PROCEEDINGS OF THE 9th INTERNATIONAL CLOUD PHYSICS CONFERENCE

VOLUME I

ТРУДЫ 9-й МЕЖДУНАРОДНОЙ КОНФЕРЕНЦИИ ПО ФИЗИКЕ ОБЛАКОВ

ТОМ I

TALLINN, ESTONIAN SSR, USSR

21—28 August, 1984

PROCEEDINGS OF THE 9th INTERNATIONAL CLOUD PHYSICS CONFERENCE

ТРУДЫ 9-й МЕЖДУНАРОДНОЙ КОНФЕРЕНЦИИ ПО ФИЗИКЕ ОБЛАКОВ

МЕЖДУНАРОДНАЯ КОМИССИЯ
ПО ФИЗИКЕ ОБЛАКОВ

МЕЖДУНАРОДНАЯ АССОЦИАЦИЯ
МЕТЕОРОЛОГИИ И ФИЗИКИ АТМОСФЕРЫ

ТРУДЫ 9-й МЕЖДУНАРОДНОЙ КОНФЕРЕНЦИИ ПО ФИЗИКЕ ОБЛАКОВ

ТАЛЛИН, СССР, 21-28 АВГУСТА 1984

ТОМ I

*ОРГАНИЗАТОРЫ АКАДЕМИЯ НАУК СССР,
МЕЖДУВЕДОМСТВЕННЫЙ ГЕОФИЗИЧЕСКИЙ КОМИТЕТ
АКАДЕМИЯ НАУК ЭСТОНСКОЙ ССР,
ИНСТИТУТ АСТРОФИЗИКИ И ФИЗИКИ АТМОСФЕРЫ
ГОСУДАРСТВЕННЫЙ КОМИТЕТ ПО ГИДРОМЕТЕОРОЛОГИИ
И КОНТРОЛЮ ПРИРОДНОЙ СРЕДЫ,
ЦЕНТРАЛЬНАЯ АЭРОЛОГИЧЕСКАЯ ОБСЕРВАТОРИЯ*

ТАЛЛИН, „ВАЛГУС“, 1984

INTERNATIONAL COMMISSION ON CLOUD PHYSICS

INTERNATIONAL ASSOCIATION OF
METEOROLOGY AND ATMOSPHERIC PHYSICS

PROCEEDINGS OF THE 9th INTERNATIONAL CLOUD PHYSICS CONFERENCE

TALLINN, ESTONIAN SSR, USSR 21—28 AUGUST, 1984

VOLUME I

SPONSORS ACADEMY OF SCIENCES OF THE USSR,
SOVIET GEOPHYSICAL COMMITTEE
ACADEMY OF SCIENCES OF THE ESTONIAN SSR,
INSTITUTE OF ASTROPHYSICS AND ATMOSPHERIC PHYSICS
USSR STATE COMMITTEE FOR HYDROMETEOROLOGY AND
CONTROL OF NATURAL ENVIRONMENT,
CENTRAL AEROLOGICAL OBSERVATORY

TALLINN „VALGUS" 1984

53
P 78

UDK 551.576

Chairman of the Conference
Yu.S. Sedunov

Председатель конференции
Ю.С. Седунов

International Scientific Programme Committee (ISPC)

I.P. Mazin - Chairman (USSR)
O.A. Avaste (USSR)
A.A. Chernikov (USSR)
G.B. Foote (USA)
W.F. Hitschfeld - President ICCP
P.V. Hobbs (USA)
P.R. Jonas (United Kingdom)
W. King (Australia)
H.R. Pruppacher (BRD)
R.R. Rogers (Canada)
Yu.S. Sedunov (USSR)
R.G. Soulage (France)

Международный научный программный комитет (МНПК)

И.П. Мазин - председатель (СССР)
О.А. Авасте (СССР)
П.Р. Джонас (Великобритания)
В. Кинг (Австралия)
Х.Р. Пруппахер (ФРГ)
Р.Р. Роджерс (Канада)
Ю.С. Седунов (СССР)
Р.Г. Сулак (Франция)
Г.Б. Фут (США)
В.Ф. Хитчфельд - президент МКФО
П.В. Хобс (США)
А.А. Черников (СССР)

National Organizing Committee

I.P. Õpik (Chairman)
O.A. Avaste (Vice-Chairman)
I.P. Mazin (Vice-Chairman)
Ü.R. Mullamaa (Vice-Chairman)
N.O. Plaude (Secretary)
I.I. Burtsev
A.A. Chernikov
A.G. Kallis
A.Kh. Khrgian
A.D. Povzner
V.A. Unt
Ch. J. Villmann
V.M. Voloschuk

Национальный организационный комитет

И.П. Эпик (председатель)
О.А. Авасте (зам. председателя)
И.П. Мазин (зам. председателя)
Ю.Р. Мулламаа (зам. председателя)
Н.О. Плауде (секретарь)
И.И. Бурцев
Ч.Й. Виллманн
В.М. Волощук
А.Г. Каллис
А.Д. Повзнер
В.А. Унт
А.Х. Хргиан
А.А. Черников

Local Organizing Committee:
Ü.R. Mullamaa (Chairman)
Institute of Astrophysics and Atmospheric Physics
202444 Tõravere, Tartu, Estonia, USSR

Местный оргкомитет:
Ю.Р. Мулламаа (председатель)
Институт астрофизики и физики атмосферы
202444 Тыравере, Тарту, ЭССР

Cover by R. Mägar
Edited by V. Russak

Обложка Р. Мягар
Редактор В. Руссак

$P \frac{1903040000 - 197}{M\ 902(16) - 84}$ Заказное

Выпущено по заказу Академии наук Эстонской ССР

CONTENTS

F O R E W O R D

It is obvious that our generation of cloud physicists is unable to solve all the problems at hand. We all have a lot to learn, but we should not forget that good ideas, foresight, persistence and courage to risk mistakes are still main ingredients for exciting research.

(R. List, 5th Int. Conf. Cl. Phys., 1968).

It becomes ever clearer that processes in cloud physics are extremely complex, as if nature protects this part of her kingdom with special care.

(H. K. Weickmann, 7th Int. Conf. Cl. Phys., 1976)

International conferences on cloud physics give a new impetus to the advancement of many areas of this science. The history of these conferences is succinctly and vividly recounted by one of the participants.[x]

"The first International Conference on Cloud Physics was held in Zürich, Switzerland, in 1954, on the initiative of Raymund Sänger, who had launched one of the first scientific experiments on hail and who was a leader of research on phase changes in water. It was this Conference which confirmed the emergence of Cloud Physics as a scientific discipline.

The second Cloud Physics Conference took place in Verona, Italy, in 1959 under the chairmanship of Ottavio Vittori. Here, for the first time, the hail problem took pride of place, and the discussions on this subject revealed to some workers the need for a return to basic research before attempting to apply a science which was still in its infancy.

The third Cloud Physics Conference was organized in 1961, in Canberra and Sydney, by the strong Australian research group led by Eugene "Taffy" Bowen. Here, the limelight was focussed on freezing nuclei and rainmaking, subjects to which the Australians had devoted considerable scientific effort. None of those present at this Conference have forgotten the epic battle over the question of the meteoric origin of freezing nuclei!

The fourth Conference was held in Tokyo in 1964, under the wing of the Japanese group headed by Kenji Isono and Choji Magono, which had devoted many years of research to the study of ice crystals and their formation.

The fifth Cloud Physics Conference was the first to be held on the American soil. It was organized by Roland List and Walter Hitschfeld, and revealed the rapid development of the subject in North America. Here again, despite good progress in observational techniques, it became clear that no useful results could be expected from the premature application of incomplete knowledge, and in the lack of the understanding which could only come from the systematic study of the basic physical problems.

Thus it was that at the sixth Conference, organized in London by B. J. Mason, weather modification was scarcely mentioned, all the emphasis being given to fundamental research.

The prospects or hopes of weather modification nevertheless remained in the background as a potential application whose immense practical importance could not be neglected. This led the Cloud Physics Commission of IAMAP and the World Meteorological Organization to arrange for the seventh Cloud Physics Conference, held in Boulder (Colorado) in 1971 under the chairmanship of Helmut Weickmann, to be followed immediately by the second WMO Scientific Conference on Weather Modification, presided over by Roland List. The Boulder Cloud Physics Conference revealed considerable progress in two fields: observational techniques, and the mathematical modelling of cloud processes."

The eighth International Conference on Cloud Physics (Clermont-Ferrand, 1980) was headed by R. G. Soulage, the author of this brief summary. As previously, it was followed by the WMO Scientific Conference on Weather Modification. At the eighth Conference for the first time greater emphasis was laid on the necessity of the deep study of interaction between microphysical processes in cloud formation and dynamics and thermodynamics of clouds. The idea proposed at the Conference about heterogeneous mixing of cloudy air with the surrounding drier air was fruitful and encouraged numerous investigations. The interest to cloud physics steadily grows because its

---

[x] R. G. Soulage. Preface to the eight International Conference on Cloud Physics. Clermont-Ferrand, 1980.

practical value becomes increasingly apparent. Just a few of the practical applications are climatology, weather forecast, self-cleaning of the atmosphere, aviation meteorology, satellite and radar research. As regards weather modification, recent years and mostly the WMO Precipitation Enhancement Project (PEP) once again demonstrated that fundamental knowledge in cloud physics is insufficient to carry out practical activities on a universal scale. Nevertheless, there is no doubt, that even at the present moment cloud seeding could and should constitute an important element of a practical experiment, the purpose of which is to study the physical processes in the clouds including precipitation formation.

Recent years were characterized by great development in experimental research and in numerical simulation of cloud processes. On the one hand, we observe the expansion of natural observations and the penetration into the fine microphysical and dynamic structure of clouds; on the other hand, we witness a more extensive experimental research of meso- and macrostructure of clouds and cloud systems, the results of which are still inadequately reflected in numerical models of clouds. At the same time, numerical models have approached much closer in many aspects to the description of real, concrete situations in the formation of clouds and precipitation.

The present proceedings of the 9th International Cloud Physics Conference have accumulated results of the last four years and provide grounds for serious deliberation. The Conference will obviously stimulate the development of initiated research thus providing a better understanding and an adequate representation in numerical models of such important processes as, for example, the generation of ice phase or the appearance of mesoscale inhomogeneities in different types of clouds and cloud systems.

As at the previous Conference, the International Scientific Programme Committee (ISPC) has received an impressive number of claims for reports (see Volume of Collected Abstracts, comprising the entire number of 252 abstracts). The three volumes of the proceedings contain all papers accepted for oral and poster presentation and reserve papers received by March 1984. The papers are arranged according to the topics of sessions and subsessions and alphabetically (by the name of the first author) within the topics.

In the name of the ISPC, I would wish to express sincere thanks to all institutions, which participated in the preparation and organization of the Conference, and to all authors of the presented papers.

In only remains to add that without an active assistance from the members of the ISPC and the Organizing Committee and primarily from Professor W. F. Hitschfeld, President of the International Commission on Cloud Physics, IAMAP, it would have been impossible to convene and hold such a conference.

I. P. Mazin

Chairman of ISPC
The 9th International Cloud Physics Conference

ПРЕДИСЛОВИЕ

"... Очевидно, что наше поколение работающих в области физики облаков не в состоянии решить все стоящие перед ними проблемы... Мы должны еще многому научиться, но не следует забывать, что наличие хороших идей, предвидение, настойчивость и отсутствие страха перед возможностью ошибки являются непременным условием получения волнующих результатов..."

Роланд Лист, 5 МКФО, Торонто, 1968.

"... Становится все очевиднее, что физические процессы в облаках чрезвычайно сложны, как будто природа особенно заботливо оберегает от нас эту часть своих владений".

Хельмут Вейкман, 7 МКФО, Боулдер, 1976.

Международные облачные конференции всегда дают новый импульс развитию физики облаков. Вот краткая история этих конференций в ярком изложении одного из ее участников[x)].

"... Первая Международная конференция по физике облаков (МКФО) состоялась в Цюрихе, Швейцария, в 1954 г., по инициативе Раймунда Сенгера, который организовал один из первых научных экспериментов по граду и был лидером в исследованиях фазовых переходов, происходящих в воде. Именно эта конференция подтвердила становление физики облаков как научной дисциплины.

Вторая МКФО проводилась в Вероне, Италия, в 1959 г. под председательством Оттавио Виттори. Здесь впервые проблема града заняла достойное место, а дискуссия по ней открыла ряду ученых, что необходимо вернуться к исследованию основ науки, а не пытаться прилагать на практике науку, находящуюся в младенческом возрасте.

Третья конференция была организована в 1961 г. в Канберре и Сиднее сильной австралийской исследовательской группой, возглавляемой Эженом Боуэном. Здесь внимание было сфокусировано на ядрах замерзания и на вызывании дождя - проблемах, решению которых австралийцы посвятили значительные научные усилия. Никто из присутствовавших на этой конференции не забудет эпических споров вокруг вопроса о метеорном происхождении ядер замерзания!

Четвертая конференция проходила в Токио в 1964 г., под покровительством Кении Исоно и Чон Магоно, которые посвятили многие годы изучению кристаллов и их формированию.

Пятая конференция впервые проводилась на Американском континенте. Она была организована Роландом Листом и Вальтером Хитчфельдом и отражала быстрое развитие физики облаков в Северной Америке. Здесь вновь, несмотря на заметный прогресс в методах наблюдений, становится ясным, что нельзя ожидать полезных результатов от преждевременного приложения несовершенных знаний, когда недостает понимания, достичь которого можно только в результате систематического изучения основных физических проблем.

Именно поэтому на шестой конференции, организованной Мейсоном в Лондое, воздействие на погоду было лишь едва упомянуто, а все внимание было уделено фундаментальным исследованиям. Однако перспективы и надежды, возлагаемые на воздействия на облака, оставались, тем не менее, за кадром, как потенциальная возможность приложений, огромное практическое значение которых нельзя сбрасывать со счета.

Поэтому Комиссия по физике облаков МАМФА и Всемирная метеорологическая организация приняли решение организовать седьмую конференцию по физике облаков в Боулдере (Колорадо) в 1971 г. под председательством Хельмута Вейкмана таким образом, чтобы следом за ней прошла вторая научная конференция ВМО по активному воздействию на облака под председательством Роланда Листа. Боулдеровская облачная конференция продемонстрировала значительный прогресс в двух областях: технике и методах наблюдений и математическом моделировании облачных процессов ..."

Следующую, восьмую облачную конференцию (Клермон-Ферран, 1980 г.) возглавил автор этой краткой истории Р.Г. Сулаж. Как и в предыдущем случае, непосредственно за ней следовала научная конференция ВМО по преобразованию погоды. На 8-й конференции впервые с большой силой была подчеркнута необходимость глубокого изучения взаимодействия микрофизических процессов облакообразования с динамикой и термодинамикой облаков. Высказанная здесь идея существования гетерогенного перемешивания облачного воздуха с окружающим его более сухим воздухом оказалась плодотворной и послужила толчком для активизации многочисленного исследования.

Интерес к физике облаков постоянно возрастает, ибо с каждым годом все яснее становится ее прикладное значение. Здесь достаточно упомянуть такие области приложений, как климатология, прогноз погоды,

---

x) Р.Г. Сулаж. Предисловие к 8-й Международной конференции по физике облаков, Клермон-Ферран, 1980 г.

самоочищение атмосферы, авиационная метеорология, спутниковые и радиолокационные методы исследования. Что касается активных воздействий на облака с целью увеличения осадков, то прошедшие годы и прежде всего Проект по увеличению осадков, разрабатывающийся под руководством ВМО вновь показали, что фундаментальных знаний в области физики облаков еще недостаточно для повсеместного развертывания практических работ. В то же время не вызывает сомнения, что засеивание облаков уже сейчас может и должно стать важной составной частью физического эксперимента, целью которого является исследование облачных процессов и в том числе процессов формирования осадков.

Последние годы ознаменовались значительным развитием экспериментальных исследований и численного моделирования облачных процессов. С одной стороны, мы являемся свидетелями расширения натурных наблюдений и проникновения в тонкую структуру микрофизического и динамического строения облаков, с другой стороны, заметно расширились экспериментальные исследования мезо- и макроструктуры облаков и облачных систем, результаты которых еще не нашли должного отражения в численных моделях облаков. В то же время во многих чертах численное моделирование приблизилось к описанию реальных, конкретных ситуаций формирования облаков и осадков.

Представляемые читателю труды 9-й облачной конференции отражают накопленные за последние 4 года знания и дают богатую пищу для размышлений. Нет сомнения, что и эта конференция послужит толчком для развития начатых исследований, что позволит, например, лучше понять и адекватно описать в численных моделях такие важные процессы, как зарождение ледяной фазы или возникновение мезомасштабных неоднородностей в облаках различных форм и облачных системах.

Так же, как и на предыдущей конференции, Международный научный программный комитет (МНПК) получил впечатляющее количество заявок на доклады (см. сборник абстрактов, в который вошли все 252 полученных абстракта). В 3 тома вошли все доклады принятые для устного прочтения или в качестве стендовых или резервных докладов и полученные до 5 марта 1984 г. Все доклады расположены группами по тематике секций и подсекций, а в каждой группе - согласно алфавита по первому автору.

От имени МНПК я рад выразить искреннюю благодарность всем учреждениям, принявшим участие в подготовке и организации конференции, и всем авторам, представившим свои доклады.

Мне остается только сказать, что без активной помощи всех членов Международного программного и организационного комитетов и прежде всего Президента Международной комиссии по физике облаков МАМФА профессора В. Хитчфельда собрать и провести такую конференцию было бы невозможно.

И.П. Мазин

Председатель МНПК
9-й Международной конференции
по физике облаков

SESSION I

MICROSTRUCTURE OF CLOUDS AND PRECIPITATION

Subsession I-1

Liquid phase in clouds

AIRBORNE STUDIES OF MICROPHYSICAL VARIABILITY IN SMALL MONTANA CUMULI

A M Blyth
Department of Atmospheric Science,
University of Wyoming, Laramie, Wyoming 82071
USA

and

J Latham
Department of Pure & Applied Physics,
UMIST, Manchester M60 1QD, England

THE STUDIES OF 27 JULY 1981

A special set of experiments was performed in CCOPE specifically to examine the evolution of the cloud droplet spectrum. They involved vertical descents by 1 or more aircraft so as to cover the whole vertical extent of the cloud in as short a time as possible. On 27 July the University of Wyoming King Air, H-2, - well-equipped with dynamical and cloud microphysical instruments - descended from the cloud top to near the base of three clouds. Each descent took about 6 minutes and involved about 6 penetrations. Table 1 presents information on the penetration for each cloud, with associated temperatures, pressures, altitudes and times. The data set therefore provides an excellent opportunity to look at the variability of cloud properties in the vertical.

The study was conducted fairly early in the day. The sky was filled with small cumulus, only a few of which penetrated much beyond the very dry layers at 650mb. All three clouds were located between 70 and 100km SSE of Miles City, and were moving at about 7ms^{-1} in a SE direction. The sounding showed light winds at all levels and little instability. Cloud base was not directly measured during the flights, but an approximate value of T=8C, p=783mb was obtained using flight notes, the sounding, a later measurement and an estimate from θq/Q plots, where θq is the wet equivalent temperature and Q is total water content.

It is difficult to form a picture of the overall dynamics of the clouds due to the problems with the vertical winds, which were severe on account of the rapid turning needed to descend in the shortest time possible. The video records revealed that each cloud was fairly simple and quite small (~1km) in horizontal extent, at least in the upper levels.

It is instructive to examine the microphysical measurements of liquid-water-content L, droplet concentration N and mean droplet diameter d, in terms of the observed wind-fields. We consider, for example, a penetration made about 10mb below the top of the cloud 2. The wind vectors show there to be a lot of turbulence across the cloud with the exception of a smaller turret where the updraught U is smoother (~ 5ms^{-1}) and there is a higher liquid water content. The spectra are very narrow in this region and adiabatic in character. There are downdraughts on either side with rolling motions at the interface. Spectra throughout the rest of the pass are broader and often bimodal. This description can be applied to any of the 3 clouds for the upper levels. Vertical winds lower down, when they can be determined, have a smaller magnitude and tend to be more variable. Scatter diagrams were produced showing, for all 3 clouds, the variations in the vertical of: L/L_A, the ratio of measured to adiabatic liquid water content; N; d; and spectral dispersion σ. It was found that at each level, in each cloud, there is a wide range of L and N. However, d increases with height. The dispersion is lower at higher levels. L/L_A varied widely at all levels but was characteristically <0.5.

It is evident that considerable entrainment of environmental air has occurred. The results indicated the presence of three types of regions in the clouds:
i) "Adiabatic", or near adiabatic where L is close to the adiabatic value, θq is near the cloud base value, the cloud is "smooth", there is an updraught, very little turbulence and the spectra are very narrow.
ii) "Smooth" regions where L is substantially sub-adiabatic, the coefficient of variability, R < 1, and spectra are quite narrow, with a large single peak.
iii) "Variable" regions where R $\gtrsim$ 2, i.e. N is highly variable, the winds are usually highly turbulent, spectra are broad and often bimodal and L is substantially sub-adiabatic. In these regions N often varies from almost a maximum to zero within a very short distance. These regions tend to be found at the cloud side.

Apparently entrainment has affected regions ii) and iii), and in different ways. A particular preliminary goal would be to find the origin of this entrained air. Paluch (Ref.4) formulated a technique for tracing the origins of a parcel of cloudy air. Figures 1 and 2 present Paluch diagrams for an individual and all penetrations through cloud 1, respectively. On these diagrams, points are marked on the sounding corresponding to the penetration level and the cloud top level, as determined by the photogrametric analysis. The cloud base point is also marked. It is shown that the two sources of air forming the cloudy mixtures found at all levels are cloud-base and cloud-top. Similar results were found for clouds 2 and 3. This clear thermodynamic picture must be consistent with the cloud dynamics, in that there must be a way for air to be brought down from the top of the cloud to the observation level. Penetrative downdraughts have been suggested as being one such mechanism. The measurements showed that there do exist parcels of air which are negatively buoyant relative to the rest of the cloud, have significant negative vertical velocity, and lower liquid water contents. There are very few such parcels at lower levels in cloud 1, but significant numbers in clouds 2 and 3. The θq/Q points calculated for these parcels, when plotted on the Paluch diagrams lie on the "mixing line". A detailed examination of the air motions within the penetrative downdraughts shows there to be a rolling flow from the downdraught into the updraught.

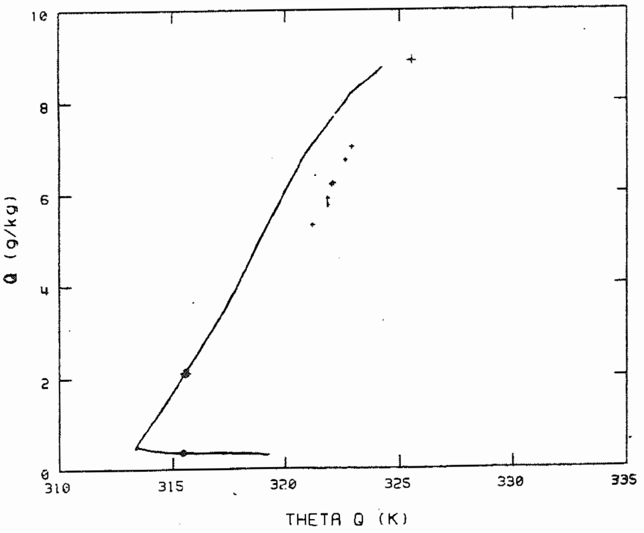

Figure 1
Paluch diagram for penetration 2 of Cloud 1. +, in-cloud points; *, penetration level; o, cloud top level, determined from video-recorder records: + cloud base level

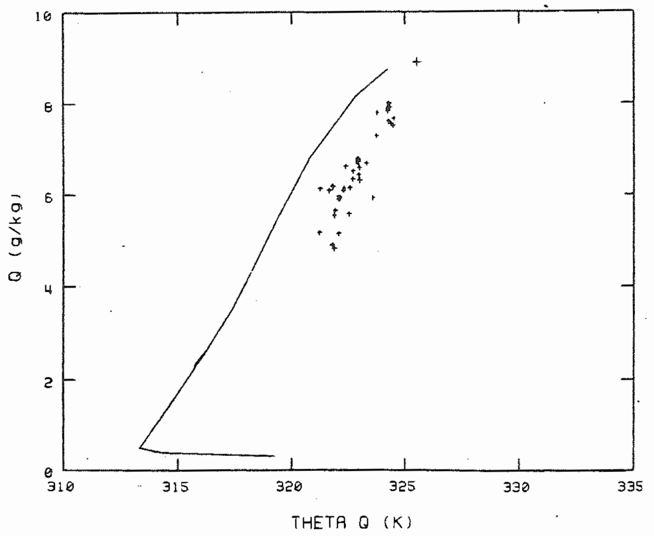

Figure 2
Paluch diagram for all 6 penetrations of Cloud 1. +, in-cloud points; + cloud-base level

TABLE 1

Cloud	Penetration	Time Interval	Altitude (m)	Pressure (mb)	Temperature (C)
1	1	183410 - 183450	4300	590	-6.0
	2	183520 - 183540	3870	630	-3.0
	3	183600 - 183650	3520	650	-1.4
	4	183715 - 183755	3200	680	+1.0
	5	183850 - 183925	2650	730	+5.0
	6	184000 - 184050	2270	770	+7.0
2	1	184630 - 184650	4260	590	-5.0
	2	184905 - 184920	4750	560	-7.5
	3	185015 - 185040	4170	600	-4.0
	4	185130 - 185205	3700	640	-2.5
	5	185245 - 185330	3350	670	0
3	1	185635 - 185650	3900	620	-2.0
	2	185840 - 185915	3950	620	-2.0
	3	190000 - 190035	3570	650	-1.0
	4	190110 - 190150	3200	680	0
	5	190235 - 190335	2700	730	+4.0
	6	190425 - 190535	2500	750	+6.0

Times, altitudes, pressures and temperatures associated with the penetrations of the 3 clouds studied on 27 July 1981. In each case the cloud base was at about 1970m, +9C. The cloud tops were at: 4460m, -7C, Cloud 1; 5230m, -10C, Cloud 2; and 4460m, -7C, Cloud 3.

Thus, there is clear evidence of negatively buoyant parcels of cloudy air in the upper regions of the three clouds, suggesting strongly - and supporting the Paluch analyses - that their sub-adibaticity is primarily a consequence of entrainment of environmental air at their upper surfaces. Although this is the general finding there were one or two situations indicative of significant entrainment from lower levels, probably the sides.

Jensen et al (Ref.3) have developed a technique for determining the effect of mixing on the droplet spectra; in all three of the clouds there is a large variation in the spectral shapes, as mentioned above. It involves plotting number concentration N in a given parcel against the fraction F of cloud-base air contained within it. F is determined from the Paluch diagram. The N-F technique presents a difficulty on this day because there are very few adiabatic parcels. However, from the few that there are, and by assuming that most points do not lie above the droplet conserving wedge, an estimate of the range of the adiabatic values of N can be made. This was found to be 370 to 530 cm^{-3}. These values agree with ones calculated from the measured CCN distribution (measured by the University of Wyoming Queen Air) using an updraught of between 1 and 4 ms^{-1}. The observational points were found generally to fall into the droplet-conserving wedge, although there are some which are ambiguous. Thus the effect of the entrainment on the majority of the droplet spectra appears to have been to conserve the total number of droplets, either by a dilution process or by classical evaporation.

Evidence was found, as mentioned earlier, of vorticity at the cloud edges and also in the centre of the cloud at the interface between updraught and downdraught. This kind of dynamical feature is described in Ref.1. It is often observed. Baker et al also predict a time evolution of the mixing process which might be simply observed in a cloud. Often, it was possible to identify distinct regions of reduced L which are different in character. Both regions are in downdraughts, near cloud top and are negatively buoyant. In one, there is considerable structure in the 50Hz droplet concentrations measured with the PMS FSSP device, while the mean diameter remains almost constant. In the other, the concentrations are more uniform into and out of the region of lower L, while the mean diameter decreases substantially. These observations are consistent with the predictions of the model, where initially there are filaments of dry and cloudy air intertwined until the Kolmogorov scale is reached, whereupon an instantaneous mixing occurs, resulting in a homogeneous mixture. In this process, depending on environmental and cloud conditions, it is likely that the mean diameter in the mixture will be lower than in the unmixed cloud. These findings are consistent with the interpretation of the N-F diagrams; which is that the mixing causes dilution (filaments of cloudy and dry air intertwined) or classical evaporation (decrease of mean diameter in the mixture). These two types of region are always found to be associated with significant vorticity.

Refs. 2, 5 predict that droplets should grow faster than adiabatically, due to the effects of entrainment. Our data can be used to examine this hypothesis, but the results of this analysis are not yet clear.

Acknowledgements
The research described herein has been supported by grants from the Natural Environment Research Council (UK) and NATO (Grant 0393/82). We are deeply grateful to Dr W A Cooper of the University of Wyoming for advice and the provision of data.

REFERENCES

1. Baker M B, Breidenthal R E, Choularton T W and Latham J 1984 The effects of turbulent mixing in clouds. J Atmos Sci (to be published)
2. Baker M B and Latham J 1979 The evolution of droplet spectra and the rate of production of embryonic raindrops in small cumulus clouds. ibid, 36,1612-15
3. Jensen J B, Austin P H, Baker M B and Blyth A M 1984 Tubulent mixing, spectral evolution and dynamics in a warm cumulus cloud. J Atmos Sci (submitted)
4. Paluch I R 1979 The entrainment mechanism in Colorado cumuli. ibid, 36, 2467-2478
5. Telford J W and Chai S K 1980 A new aspect of condensation theory. Pageoph,118, 720-742

SUPERCOOLED LIQUID WATER CONCENTRATIONS IN WINTER OROGRAPHIC CLOUDS FROM GROUND-BASED ICE ACCRETION MEASUREMENTS

Thomas J. Henderson

Atmospherics Incorporated
Fresno, California 93727 USA

ABSTRACT

An icing rate detector originally designed for aircraft is used to measure supercooled liquid water in winter orographic clouds at fixed mountain-top sites in the western United States. Supercooled liquid water concentrations have been determined using continuous records of rime ice accretion and windspeed. It is shown that supercooled liquid water is occurring within larger portions of storms than prior airborne observations over project areas have indicated, particularly below safe aircraft operational altitudes. The ground-based measurement system provides an effective tool for semi-quantitative determination of supercooled liquid water within specific cloud volumes heretofore unmeasured.

Keywords: Supercooled liquid water, weather modification, orographic clouds, instrumentation

1. INTRODUCTION

A crucial factor in any program designed to investigate the characteristics of orographic storms is the measurement of supercooled liquid water (SLW) within clouds traversing a project area. The amount and areal distribution of SLW may be the single most important indicator of precipitation potential among the enormous number of physical and chemical properties of clouds and storm systems. The scientific literature contains frequent references to the presence of SLW as a key condition to be investigated, particularly in weather modification research and applied operations programs. Past investigations have involved a variety of measurement techniques.

Modern measurement efforts involving aircraft have included the Johnson-Williams hot-wire device (Neel and Steinmetz, 1952; Neel, 1955), the Rosemount icing rate detector (Brown, 1981), the Particle Measurement Systems imaging probes (Knollenberg, 1970, 1972), and a variety of dropsondes (Hill and Woffinden, 1977). Ground-based efforts have employed microwave radiometers (Guiraud, et al, 1979), snow and ice crystal sampling and photography (Vardiman and Hartzell, 1976), and balloon borne sondes (Hill and Woffinden, 1980). Ground-based in-situ measurements of SLW include microscope slide sampling of ice crystals and the analysis of ice accretion on cylinders (Schaefer, 1945; Howe, 1960). Each technique offers unique capabilities.

An example of a large field research effort where SLW occupies an important segment of investigations is the Sierra Cooperative Pilot Project (SCPP). This is a winter precipitation enhancement research program funded by the Bureau of Reclamation and conducted in the Central Sierra Nevada Range of California. Recognition of the value of documenting the distribution of SLW has been reflected in the program's research efforts since its inception. Airborne measurement techniques employed in SCPP have included coated microscope slides, the standard Johnson-Williams instruments, a variety of probes from particle measurement systems, and certain Rosemount devices (Lamb, et al., 1976; Marwitz, et al., 1978; Marwitz, 1979; Stewart and Marwitz, 1980). Additional techniques include remote sensing by radiometer (Snider and Rottner, 1982) and ground-based snow crystal sampling and photography (Humphries and Moore, 1981; Humphries, 1982).

Since the 1977/78 winter season, the SCPP investigations have yielded a somewhat varied indication of the concentration and temporal occurrence of SLW. Although SLW has been noted during a number of the project's cloud physics measurement flights, airborne indications have rarely reached the abundant levels suggested by ground-based ice crystal sampling, moderate to heavy icing noted on commercial and private aircraft, and ground observations of heavy riming on structures and trees. This apparent discrepancy suggested that substantial quantities of SLW actually traverse the mountain barrier for extended periods and below allowable flight altitudes, generally at temperature levels warmer than -10°C. Toward resolving this particular concern, a new development in SCPP investigations has been the use of a Rosemount icing rate detector and supporting systems at a mountain-top installation to document in-cloud SLW content and distributions via ice accretion measurements. The location of the SCPP is shown in Figure 1.

This paper presents (1) a description of the icing rate detection systems, (2) the initial method used to calculate cloud SLW from ice accretion and wind data, and (3) some preliminary findings from data analyses.

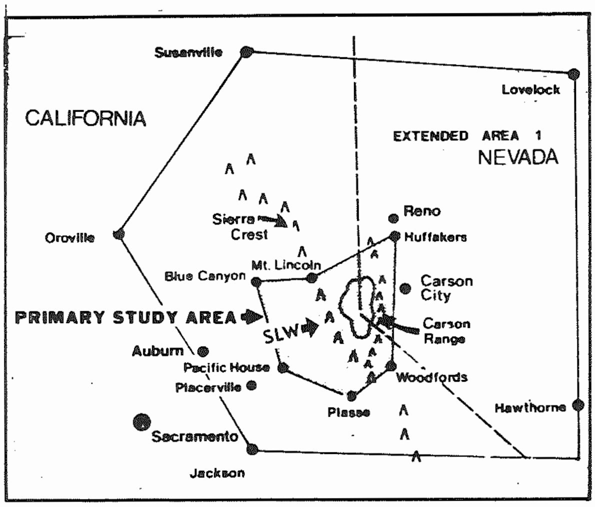

Figure 1. Research area and location of one measurement site for SLW.

2. THE ICING RATE DETECTOR

For many years, icing rate detectors have been used on aircraft and ground-based structures where measurements of icing are required for operation of deicing equipment or warning systems, as well as in engineering studies for structure design in icing-prone locations (Tattelman, 1982). Most of these instruments are labor-intensive and require on-site personnel for operations. The use of a Rosemount icing rate probe operating continuously at a fixed ground-based location for the purpose of determining specific quantities and distributions of in-cloud SLW is unique.

The Rosemount icing rate detector is an electromechanical device which transmits a signal when a specified amount of ice is present on the sensing element. This element is an axially vibrating tube (24.5 x 6.4 mm) protruding from a strut airfoil. The airfoil contains a heater for deicing the probe with the heater wires interfaced to the ice detector's electronics. The device is shown schematically in Figure 2.

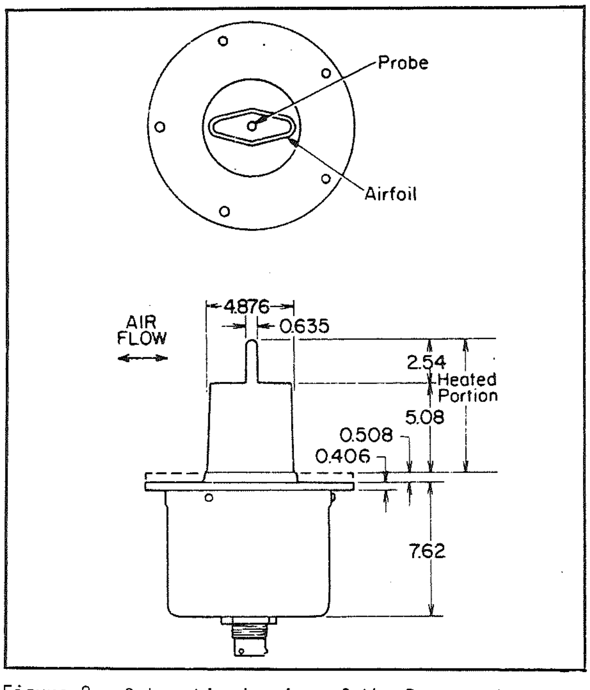

Figure 2. Schematic drawing of the Rosemount icing rate detector Model 871FA

The 40 KHz vibration frequency of the probe is of such low magnitude that it cannot be seen or felt. This is achieved through a property of certain metals known as magnetostriction and hookup to a magnetostrictive oscillator (MSO). The reference signal of the oscillator is summed with the signal from the MSO to produce a difference frequency which serves as the output of the instrument. The frequency-to-voltage converter changes the difference frequency to a voltage. When this voltage reaches a preset level corresponding to a known accumulation of ice, an output signal is provided to two timers. These timers control the duration of the 24 VDC deicing signal and the 1.8 ampere current supplied for 7 seconds to the detector deicing heaters. An analog output corresponding to ice accretion is also provided as a test point or monitoring voltage. The response time of the ice detector is inversely proportional to the liquid water content of the air times its velocity at a specified ambient temperature and water droplet diameter.

Due to the adhesion property of ice, its effect on the probe vibration is different from other substances such as oil, grease, dirt, insects or other contaminants. As a result, valid icing signals are produced only when ice is actually formed. Due to the high collection efficiency of the probe, ice forms on this sensor before it collects on other surfaces. The key to the ice detection performance is the design simplicity which virtually eliminates false signals. Additionally, if the probe is damaged the resultant frequency shift causes the unit to produce a continuous offset base line signal, thereby providing a fail-safe indication of operational status. The instrument responds to ice mass accumulated in any physical configuration on the sensing probe. This is a unique and valuable feature.

3. THE MEASUREMENT SYSTEM

Atmospherics Incorporated (AI) has organized and installed a number of individual components which comprise the total icing rate detection system. These components are:

- Rosemount Ice Detector Model 871FA
- WeatherMeasure Heated Windspeed Sensor Mod W203H
- WeatherMeasure Heated Wind Direction Sensor W204H
- AI Platinum Resistance Temperature Probe
- WeatherMeasure Signal Conditioning Modules MD
- Linseis 4-channel Recorder Model L2001
- Science Assoc. Max-Min Theremometer
- Science Assoc. Instrument Shelter
- Batteries, battery charger, inverter, control and relay boxes, cables

The electrical arrangement of each component is accomplished in such a manner that operations can be maintained throughout moderate-duration commercial power outages. The 115 VAC commercial power source is fed through a battery charger to the two series-connected 12 VDC wet cell batteries. In turn these feed a 24 VDC-to-115 VAC inverter which provides power to the relevant instrumentation. The 24 VDC requirement for certain instrumentation comes directly from the batteries. When power outages occur, the wet cell batteries are able to maintain operation of all instrumentation for a continuous period of at least 24 hours, regardless of the ice detector's deicing requirements.

The general layout of the total system as established in mountain areas of the western U.S. during the 1980-1983 season is shown in Figure 3.

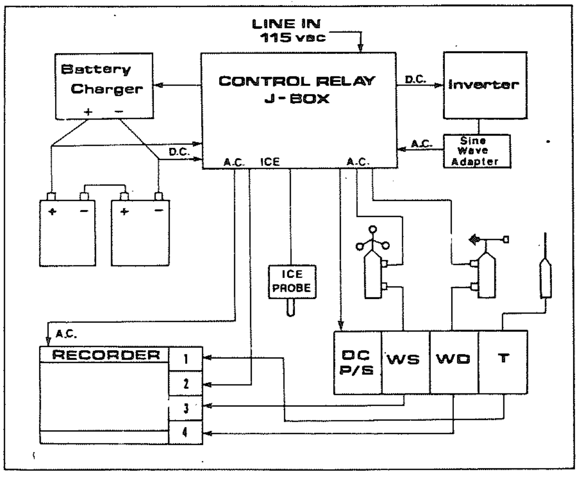

Figure 3. Supercooled Liquid Water Measurement System

4. DATA REDUCTION AND LWC CALCULATIONS

During the winter seasons of 1980 through 1983, ice accretion records were obtained in analog form on the recorder strip charts. Measurements obtained during storm periods of particular interest were coded as 15-minute average values of windspeed, wind direction, air temperature and, for the riming measurements, the number of deicing signals ("trips") of the icing rate detector.

Calculation of liquid water content from this measurement system hinges on the fact that the Rosemount device cycles when the probe senses the ice mass equivalent of a uniformly distributed 0.5 mm thick film of water. It has been assumed this mass is independent of the physical configuration of the rime ice build-up on the probe but recent laboratory tests indicate uncertainty about this characteristic.

The physical and operational characteristics of the icing rate probe pertinent to the LWC calculations are:

- Length (l) = 25.40 mm
- Diameter (d) = 6.35 mm
- Probe cross-section presented to airflow = 1.613 cm^2
- Mass of ice necessary to initiate "trip" = 0.51 mm uniform water thickness

To determine the mass of 0.51 mm water thickness on the probe we use,

$$V_3 = V_2 - V_1$$

where V_1 = volume of the dry probe and V_2 volume of the probe with a 0.51 mm thick coating of water. The volume of water required to cycle the instrument = 0.279 cm^3. Therefore, the mass of a 0.51 mm water thickness on the probe = 0.279 grams.

The volume of air sampled between "trip" points is obtained using,

$$V_4 = \bar{v}tA$$

where $\bar{v}$ = the mean wind speed (cm sec^{-1}) for the icing accumulation period since the previous "trip", t = time (sec) since the previous "trip", and A = probe area exposed to the wind (cm^2).

The uncorrected liquid water content is then,

$$LWC = V_3/V_4 .$$

LWC values through extended storm periods are calculated at 15-minute intervals using,

$$LWC = \frac{\text{number of trips} \times V_3}{V_4} .$$

As an example, a 15-minute period which includes three ice detector trips and windspeeds averaging 11.6 m sec^{-1} would yield,

$$LWC = \frac{3 \times 0.279 \text{ g}}{1160 \text{ cm sec}^{-1} \times 900 \text{ sec} \times 1.613 \text{ cm}^2}$$

$$= \frac{0.837 \text{ g}}{1.684 \times 10^6 \text{ cm}^3} = 0.497 \text{ g m}^{-3}$$

Obviously, the calculation of LWC values can be strongly influenced by the collection efficiency of the sensing probe. For cylinders, collection efficiency varies directly with ventilation rate and droplet size, and inversely with sensor diameter. The efficiency is also affected to a much smaller degree by other factors, such as the density of the sampled air. Recent work by Tattleman (1982) testing Rosemount's probes under chamber and field conditions, indicates that the instrument is a very efficient collector. Rosemount has also conducted some exhaustive laboratory tests and notes that the probe output is highly correlated with the mass and thickness of ice measured on this particular diameter cylinder.

As a confirming measurement to the ice accretion measurement system, a number of LWC calculations have been made using cloud droplet size and concentration data from both mineral oil and formvar coated slides exposed at the ice detection site during several storm periods. These data show reasonably good correspondence with the LWC values calculated from the icing rate detector system. In most cases, the comparisons between LWC calculated from measurements of supercooled cloud droplets and LWC calculated from the ice accretion system show correspondence within a factor of two or three.

Calibration checks of the Rosemount probe have also been conducted in the laboratory facilities at AI Head Office. This work involved bonding a variety of materials to the probe and documenting the mass required to cycle the device. Of particular interest has been the bonding of aluminum 10 mg balance weights with 3M adhesive products. In these preliminary tests, the analog output voltage of the icing rate detector shows excellent correspondence with each balance weight bonded to the probe, and the "trip" point occurs reasonably close to the total bonded weight of 0.279 gms.

Further calibration checks of several Rosemount probes have been conducted in the laboratory at the University of Wyoming. From tests of several probes operating simultaneously in this laboratory, there is evidence to suggest that each individual probe may have its own calibration curve and the mass required to "trip" any individual probe may be as low as 0.08 gms and as high as 0.36 gms. It should be emphasized that individual laboratory calibration work should be conducted before the assumed physical characteristics of a probe's output are accepted.

In our analysis work we have not yet attempted to adjust the results based on calculations of collection efficiency of the probe used in this particular application. More measurements are required with an observer on site during storm episodes before we can adequately address this issue. Visual observations will also be particularly helpful in determining the probe performance and identification of chart record characteristics during conditions of freezing drizzle, freezing rain, and conditions of mixed supercooled liquid water and snow.

5. ANALYSIS

As an example of analytical work, this section presents some preliminary results from analyses within the overall goals of the SCPP, including the seasonal distribution and character of SLW at the Squaw Peak site, the relationship of the occurrence of SLW with precipitation events in this project area, and the distribution and character of SLW related to specific cloud tops. The results are drawn from the 1981-1982 field season when radar and other SCPP systems were in operation.

5.1 Seasonal distribution and character of SLW

Given the availability of continuous observation:

a key question concerning the occurrence of SLW is that of seasonal distribution. Aircraft measurements conducted during past SCPP seasons suggested that significant SLW occurrence over time was disappointingly infrequent, particularly during pre-frontal stable orographic storm conditions (Marwitz, et al. 1978; Marwitz, et al., 1979; Stewart and Marwitz, 1980).

Obviously, airborne results are greatly influenced by altitude restrictions on aircraft operations over the mountainous project area, plus the limitations of on-station time during total storm periods. These airborne measurement difficulties may be somewhat offset by the limitations associated with a fixed-point sensor, but proper site locations coupled with the distinct advantage of a continuous record have produced a most useful system for assessment of SLW over this particular project area.

The 1981-1982 records have been analyzed to determine the full-season frequency of icing occurrence by tabulating positive icing indications within 15-minute intervals for the six-month period of record. These results are summarized in Table 1. The values strongly suggest a substantial occurrence of SLW during the winter season at an elevation of 2,625 m asl.

The temperature distribution at the Squaw Peak site during icing periods throughout the six-month season is shown in Figure 4. The plot is based on a tabulation of values from 15-minute intervals whenever icing was indicated. The distribution shows that nearly 60% of the total 15-minute icing periods occurred in the range of 0°C to -5°C, and that 90% occurred at -10°C or warmer. The magnitude of the full-season occurrence shown earlier, combined with the temperature distribution noted in Figure 4, supports the suspicion that significant quantities of SLW can and do occur at altitudes below safe aircraft operational limits.

Table 1. Total hours of positive icing

Month	Hours	Month	Hours
Nov'81	175.0	Feb'82	126.5
Dec'81	155.5	Mar'82	253.5
Jan'82	68.0	Apr'82	101.0
		Season total:	879.5

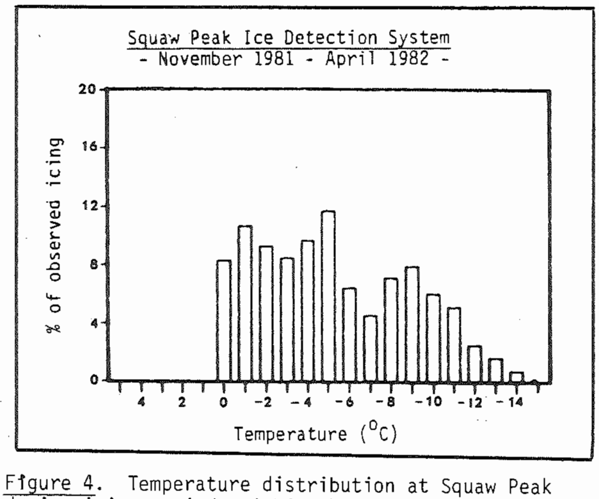

Figure 4. Temperature distribution at Squaw Peak during icing periods within the 6-month measurement season of November 1981 through April 1982. Values were determined at 15-minute intervals.

5.2 Occurrence of SLW relative to precipitation events

The monthly and seasonal values of icing indications presented in Table 1 assume additional meaning when compared with the occurrence of precipitation across the project area. Toward this type analysis, the combined duration of "significant precipitation periods" was compared with the season total icing duration. By definition, the blocks of time begin with the first measureable precipitation at any gage within the project network and end with the last precipitation at any location. Within this definition, the "significant precipitation periods" tend to over-estimate the actual duration of precipitation at any fixed point within the network's large geographical area of approximately 2,500 km^2.

The 26 precipitation periods identified during the 1981-1982 season had a total duration of 1,489.5 hours. The total season duration of icing divided by the total precipitation duration is 879.5/1489.5 = 59%. With a few notable exceptions, the icing periods at the Squaw Peak site were found to correspond well with the "significant precipitation periods". Icing indications generally preceded by one to six hours the occurrence of measureable precipitation anywhere within the SCPP gage network in approximately 35% of the observed storm sequences.

5.3 SLW character during the stable pre-frontal cloud conditions

A sample of observations in stable pre-frontal cloud conditions was analyzed to determine the character and distribution of SLW during those periods. The 137-hour sample included all storm periods classified as orographic (OR), area-wide (AW), and embedded band (EB), as described in the SCPP Operations Plan (Huggins, 1981). Tabulation of positive icing indications at 15-minute intervals within the 137-hr. sample indicated icing was in progress during approximately 45% of the periods. A collection of periods was analyzed to yield the characteristics shown in Figures 5a, 5b, and 5c. The key findings can be summarized as follows:

- $\overline{LWC}$ during riming periods = 0.40 g m^{-3}
- frequency of LWC ⩽ 0.5 g m^{-3} = 75%
- frequency of LWC ⩽ 1.0 g m^{-3} = 94%
- frequency of riming 0° to -5°C = 57%
- frequency of riming 0° to -10°C = 85%

6. CONCLUSIONS

Based on three winter seasons of operation within western mountain areas of the United States, we conclude that the Rosemount icing rate detector Model 871FA combined with reliable wind and temperature sensors provides an effective system for ground-based measurements of in-cloud supercooled liquid water. The measurements strongly support the conclusion that SLW is occurring throughout larger portions of stormy periods, particularly in pre-frontal portions, than past airborne observations over some project areas have indicated. In many cases, the SLW simply occurs over the mountainous areas below the altitudes considered safe for aircraft operations.

Like any single instrument, or assemblage of many components, this ice accretion measurement system requires fundamental knowledge of orographic cloud characteristics and considerable understanding of how the sensor responds to the various icing conditions within a field measurement program.

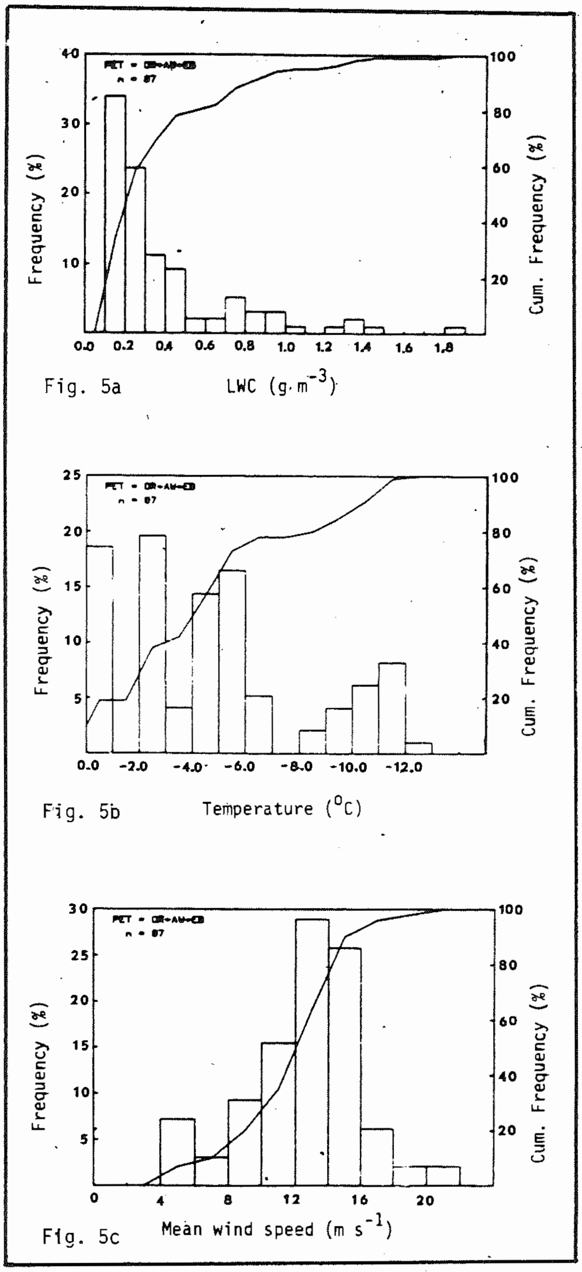

Figures 5a, 5b and 5c. Distributions of LWC, temperature and wind speed measured at 15-minute intervals during icing periods at the Squaw Peak site. The sample cinsists of periods classified as stable orographic cloud occurrences over the project area.

7. ACKNOWLEDGEMENTS

A portion of this work has been performed as part of Project Skywater, managed by the Bureau of Reclamation, under contract #9-07-85-V0020. Appreciation goes to field technicians Mike Henderson, Steve Pinion, and Ed Pinion for much of the operation and maintenance during severe weather conditions in the Sierra Nevada Range of California. Data reduction and analysis support has been provided by Mark Solak, Rand Allen and Susan Barnes. A special note of appreciation goes to Hilda Duckering for the preparation of the manuscript.

The Squaw Valley Corporation, particularly Mr. Jimmy Mott, has provided much support for winter access to a hostile mountain wilderness area.

8. REFERENCES

Brown, E.N., 1981: An evaluation of the Rosemount ice detector for aircraft hazard warning and for undercooled cloud water content measurements. NCAR Tech. Note TN-183+EDD, 13 pp.

Guiraud, F.O., J. Howard and D.C. Hogg, 1979: A dual-channel microwave radiometer for measurement of precipitable water vapor and liquid. I.E.E.E. Trans. Geosci. Electron., GE-17, 129-136.

Hill, G.E. and D.S. Woffinden, 1977: Vertical motion sensing by parachute dropsonde. J. Appl. Meteor., 16, 851-854.

Hill, G.E., and D.W. Woffinden, 1980: A balloon-borne instrument for the measurement of vertical profiles of supercooled liquid water concentration. J. Appl. Meteor., 19, 1285-1292.

Howe, J.B., 1960: Handbook for the rotating multicylinder method. Technical Note No. 568. Aeronautical Icing Research Laboratories, Air Research and Development Command, Wright Patterson Air Force Base, Ohio.

Huggins, A.W., 1981: Classification and distribution of radar echoes for the Sierra Cooperative Pilot Project. Proceedings, Eighth Conference on Inadvertent and Planned Weather Modification, Reno, Nevada, 36-37.

Humphries, J.H. and J.A. Moore, 1981: Ground microphysics characteristics from a 3-year Sierra Nevada sample. Preprints, Eighth Conference on Inadvertent and Planned Weather Modification, Reno, Nevada, 64-65.

Humphries, J., 1982: Ground based microphysical observations using a Knollenberg 2D probe. Preprints, Fifth Symposium on Meteorological Observations and Instrumentation, Toronto, CAN

Knollenberg, R.G., 1970: The optical array: an alternative to scattering or extinction for airborne particle size determination. J. Appl Meteor., 9, 86-103.

Knollenberg, R.G., 1972: Comparative liquid water content measurements of conventional instruments with an optical array spectrometer. J. Appl. Meteor. 11, 501-508.

Lamb, D., K.W. Nielsen, H.E. Klieforth and J. Hallett, 1976: Measurements of liquid water content in winter cloud systems over the Sierra Nevada. J. Appl. Meteor., 15, 763-775.

Marwitz, J.D., R.E. Stewart, T.S. Karacostas and B.E. Martner, 1978: Cloud physics studies in SCPP during 1977-1978. Univ. of Wyoming Report AS 121, to U.S. Bureau of Reclamation, 203 pp.

Marwitz, J.D., R.E. Stewart, T.S. Karacostas and B.E. Martner, 1979: Cloud physics studies in SCPP during 1978-79. Univ. of Wyoming Report AS 123, to U.S. Bureau of Reclamation, 154 pp.

Neel, C.B. and C.P. Steinmetz, 1952: The calculated and measured performance characteristics of a heated-wire liquid water content meter for measuring icing severity. NACA Tech. Note 2615, 37 pp.

Neel, C.B., 1955: A heated-wire liquid-water content instrument and results of initial flight tests in icing conditions. NACA Res. Memo. A54123, 33 pp.

Schaefer, V.J., 1945: Rotating multi-cylinder units for measuring liquid water content and particle size of clouds. General Electric Research Laboratory.

Snider, J.B. and D. Rottner, 1982: The use of microwave radiometry to determine a cloud seeding opportunity. J. Appl. Meteor., 21, 1286-1291.

Stewart, R.E, and J.D. Marwitz, 1980: Cloud physics studies in SCPP during 1979-1980. Univ. of Wyoming Report No. AS 125, to U.S. Bureau of Reclamation, 96 pp.

Tattleman, P., 1982: An objective method for measuring surface ice accretion. J. Appl. Meteor., 21, 599-612.

Vardiman, L. and C. Hartzell, 1976: Final report on an investigation of precipitating ice crystals from natural and seeded winter orographic clouds. WSSI Report No. SR-359-47, to U.S. Bureau of Reclamation, 129 pp.

THE DEVELOPMENT OF DROP SIZE SPECTRA IN CONVECTIVE CLOUDS STUDIED DURING CCOPE

T A HILL and T W CHOULARTON
Physics Department, UMIST
Manchester M60 1QD, England

1. INTRODUCTION

A long-standing, important problem in cloud physics concerns the mechanism by which continental cumulus clouds are able to produce rainfall on a timescale short compared to that predicted assuming adiabatic growth of cloud droplets on a reasonable cloud condensation nucleus spectrum, followed by stochastic coalescence. It has recently been suggested by Refs. 1 and 2 that this may occur as a result of enhanced growth of a small proportion of cloud droplets following dilution.

Firstly, entrained dry air causes evaporation to occur in a limited section of the cloud. This results in a region of much reduced water content (with small drops remaining) or, in the extreme case, a saturated, drop-free, region. This then mixes with other areas of the cloud, diluting the drops present but not causing further evaporation. If this region then rises, a supersaturation increase will occur and the drops present will grow faster than in neighbouring regions. Because reactivation of nuclei will occur, the effectiveness of the process requires frequent dilution events or the recirculation of large drops.

In this paper, we present results of penetrations into a growing ice-free cumulus cloud performed by the Wyoming King Air (H2) during the Co-operative Convective Precipitation Experiment (CCOPE) conducted in Montana, USA during July 1981. The data strongly suggests that dilution effects resulting from dry air entrainment are causing accelerated growth of a small fraction of droplets to a size at which the observed coalescence could begin.

2. GENERAL DESCRIPTION

The study was performed on 12th July 1981, 60nm to the East of Miles City, Montana. During the penetrations made by the Wyoming King Air (H-2) (varying between 5.8 and 4.5km altitude), a Queen Air (H-6) aircraft was making measurements at cloudbase. General cloud properties were: cloudbase at 2.4km, temperature 13°C, cloud top between 5.6 and 6.0km, temperature -10°C, updraughts from 3m s^{-1} at cloud base up to 15m s^{-1} at observation level. The pass discussed in detail below was typical of other passes through similar cloud regions on the same day and includes a highly buoyant region in which the largest drops were encountered.

3. DESCRIPTION OF THE MICROPHYSICS AND DYNAMICAL STRUCTURE

Figures 1a-d show the liquid water content (obtained from integrated forward scattering spectrometer probe data, FSSP) sampled at 10Hz, droplet number concentration sampled at 10Hz, the dry bulb temperature measured using the reverse flow thermometer and the vertical wind.

The aircraft flew through the cloud at 5.8km. The adiabatic liquid water content calculated from the observed cloud base of 2.4km was 8.4g m^{-3}. The observed liquid water content was typically 2g m^{-3} with a maximum of 3g m^{-3} so that it must be concluded that dry air entrainment had substantially affected all parts of the cloud. The cloud pass itself is entirely a region of positive vertical wind. The regions of highest liquid water content correspond to regions of highest temperature excess (up to 4°C).

4. EFFECTS OF MIXING ON CLOUD MICROPHYSICS

Figure 2 shows the FSSP number concentration sampled at 50Hz (about 2m horizontal resolution). With an average aircraft speed of about 100m s^{-1} the cloud can be seen to be about 2km wide. It can be seen also that the exit side has an extremely sharp boundary indicating little or no mixing is occurring at this edge. The other side, however, is less sharply defined and there are several small regions of very large fluctuations in number concentration. These are in the vicinity of the lowest liquid water content regions. These features are typical of other passes and are sometimes more clearly seen on those. See Fig.3a,b which shows 10Hz and 50Hz frequency number concentration data for a pass through another cloud on the same day. The Paluch analysis showed a single entrainment source at cloud top.

In these narrow regions, which show large fluctuations in number concentration, the droplet spectra from the FSSP plotted every 0.1 of a second, show substantial variability in number concentration and droplet size, indicating that evaporation is occurring. The large amplitude fluctuations occurring in the mixing regions is consistent with the concept discussed by Ref.3.

These observations suggest that the mixing between dry and cloudy air is intermittent and confined to relatively small regions of the cloud at any one time. However, the small scale structure in the number concentrations throughout the remainder of the cloud suggests that the dilution effect is transmitted through the remainder of the cloud. This is confirmed by the shape of the droplet spectrum.

5. DROPLET SPECTRAL SHAPE

Throughout the pass the droplet spectrum was broad with a main peak at around 10μM radius, some large drops, discussed below, and a variable number of drops down to the smallest detectable size. Many of the spectra shown in Fig.4 are bi-modal. In addition to activation of nuclei following evaporation and dilution there are three other mechanisms that could generate the bi-modal spectra observed. These have been investigated previously, as discussed in Ref.4.

1) The increase in speed of the updraught above cloud base may produce a second peak in supersaturation higher in the cloud.

This was investigated using an adiabatic

parcel growth model. The cloud condensation nucleus spectrum was based on a typical continental spectrum observed during CCOPE (we do not have data for the 12th July). It was found that no secondary activation well above cloud base occurred. This result was insensitive to the CCN spectrum chosen and to the updraught profile.
2) Fluctuations in the humidity of air entering cloud base may produce broad spectra higher in the cloud. Again, this was simulated using the temperature and humidity structure reported at cloud base by H-6 using the technique discussed in detail by Ref.4. Again, no bi-modality existed at the observation level.
3) Similarly, when the effect of turbulence in the updraught was considered, (causing variations in the number of drops activated at cloud base), or variations in the CCN spectrum between neighbouring parcels, the drop size distribution at the level of the H-2 pass was always narrow and quite different from the spectra observed.

It would therefore seem likely that the large number of small droplets and the bi-modal spectra occur as a result of fresh activation of nuclei which occurs as a result of an increase in the supersaturation following the dilution of the pre-existing droplet spectrum. Further evidence for this is now discussed.

Figure 5 shows a plot of the number of drops in the range 5-15μm sampled every 0.1sec against liquid water content. Examination of the spectral shapes in Fig.4 confirms the picture that the changes in the liquid water content are largely produced by a change in the number concentration in this size range with very little change in the position of the spectral peak. This is consistent with the molecular mixing of cloudy and environmental air, and subsequent evaporation, occurring in localised regions and not with large scale evaporation in an environment of spatially constant relative humidity.

Figure 6, in contrast, shows that the number of drops in the size range 0-5μm generally decreases with increasing liquid water content and that the largest concentration of small drops are gound in regions of low water content (L). It is this effect which accounts for the large fluctuation in L associated with roughly constant N (fig.1) throughout much of the pass.

6. 'SUPER-ADIABATIC' DROPLETS

The largest droplets obtained by growing a distribution of droplet adiabatically may be compared with largest drops measured by the FSSP. Using a reasonable continental CCN, the largest droplets were 16μm in radius with a concentrtion of about $0.1cm^{-3}$. The FSSP, in contrast, frequently detected droplets of between 18 and 20μm in concentrations typically of $0.5cm^{-3}$ and sometimes up to $1.5cm^{-3}$.

As a further check, we chose a region where strong evaporation had occurred and where mostly small, recently activated, droplets were present in a concentration comparable to the total droplet concentration at the observation level. This spectrum was grown adiabatically from the cloud base level to this level. In this case, the largest droplets were 18μm in radius with a concentration of $0.1cm^{-3}$. It must be concluded therefore that some superadiabatic growth is taking place amongst a few larger drops.

Figure 7 shows a graph of the number of droplets in the largest FSSP bin (in this case about 19.5μm) against liquid water content. This shows a result common to those regions of the cloud containing large FSSP droplets, which is that the largest drops are nearly always found to be associated with liquid water contents significantly below the maximum. This is consistent with the large drops being produced by the dilution effect and not consistent with the suggestion that giant CCN are responsible.

In this pass, the Knollenberg Optical Array Probe (1-D probe) shows that larger droplets ($r \geq 25\mu m$) are present in localised regions of this pass at concentrations of around $10\ l^{-1}$ (Fig.8). During later passes through the cloud, these drops become more widely distributed. In the pass discussed here the presence of OAP drops of radius 25μm occurred in regions in which the FSSP was detecting 18 to 20μm drops. Despite this general assoc:ated beween large FSSP drops and the 25μm OAP drops detected, (the OAP records every 1 sec only), the two are not always closely correlated. This, however, may not be very surprising in view of the gap in the detection range of the two instruments and the large difference in concentration ($\sim 10\ l^{-1}$ for the OAP and ~1 cm-3 for the FSSP).

7. CONCLUSIONS

The results described above suggest that in this particular cloud, dry air entrainment causes localised intermittent evaporation of cloud water. Other parts of the cloud are subsequently diluted and continued ascent results in a rise in the supersaturation which will re-activate nuclei producing a broad droplet spectrum and also enhance the growth of a small fraction of the largest drops apparently resulting in some droplets reaching a size of ~25μm at which coalescence can begin. This suggests that the general mixing ideas of Ref.1 and 2 are capable of producing enhanced growth in real clouds.

It must be stressed, however, that enhanced growth did not occur in some of the CCOPE clouds studied. This effect seems to be confined to actively growing clouds which are very buoyant with respect to their surroundings.

REFERENCES

1. Baker M B, Corbin R G and Latham J 1980 The influence of entrainment on the evolution of cloud droplet spectra: I. A model of inhomogeneous mixing. Quart J Roy Met Soc., 106, 581-598

2. Telford J W and Chai S K 1980 A new aspect of condensation theory. Pageoph, 118, 720-742

3. Baker M B, Breidenthal R E, Choularton T W and Latham J 1984 The effect of turbulent mixing in clouds. J Atmos Sci (in press)

4. Carruthers D J 1982 PhD Thesis (Univ. Manchester)

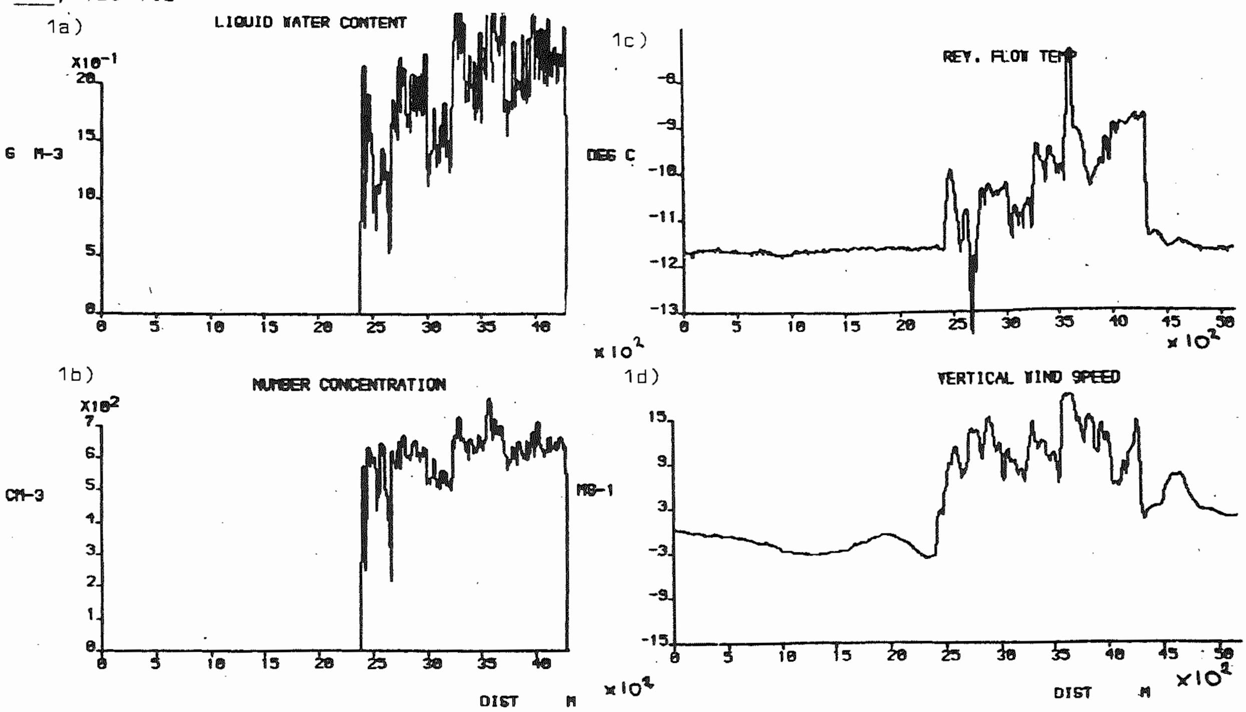

Figure 1. Graphs of a) liquid water content; b) number concentration (10Hz); c) dry bulb temperature and d) vertical wind against distance

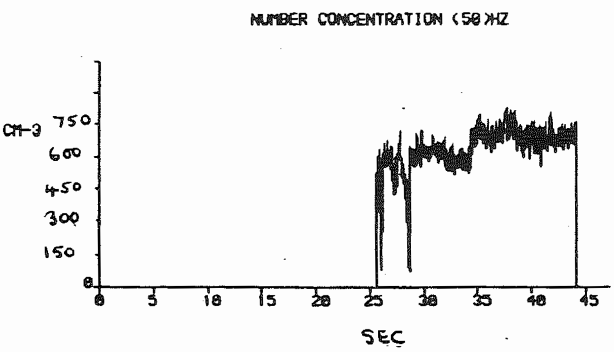

Figure 2. Droplet number concentrations sampled at 50Hz against time (Starting at 202100).

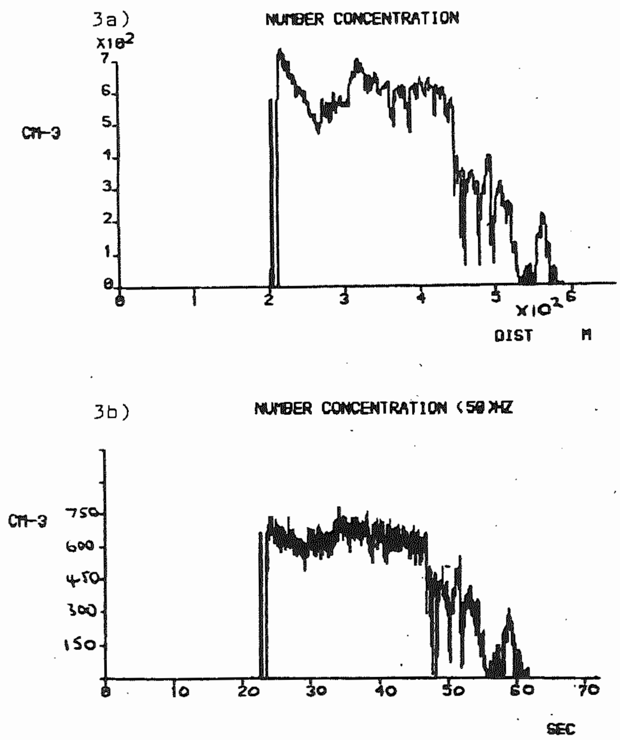

Figure 3. a) Number concentration of droplets (at 10Hz) from pass starting at 2034.00 GMT against distance.

b) Number concentration of droplets at 50Hz from pass starting at 203400GMT against time.

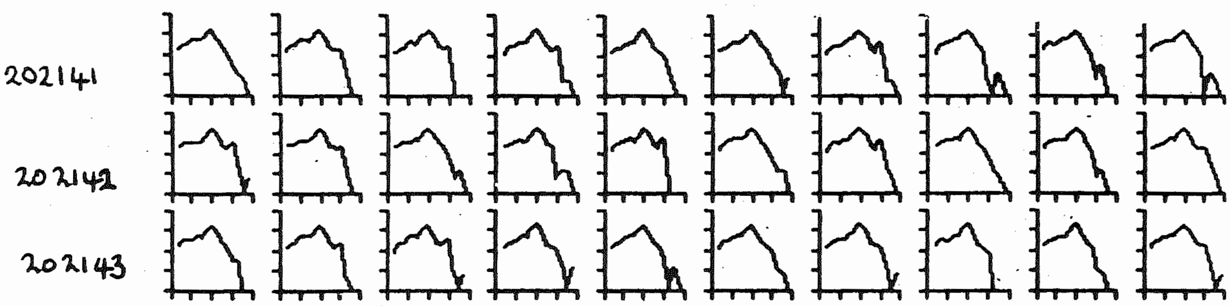

Figure 4. Neighbouring cloud droplet spectra sampled at 10Hz starting at 202141 GMT. (Corresponding to last 3 secs of pass)

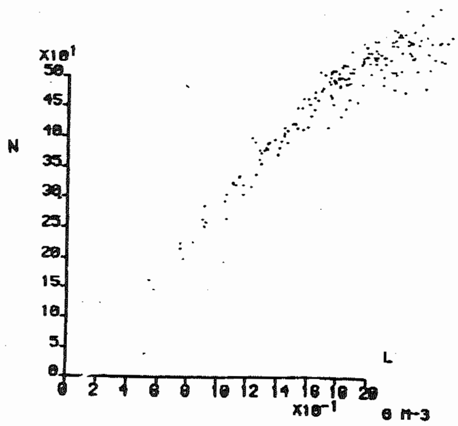

Figure 5 Number concentration of droplets in radius range 5μm to 15μm against liquid water content

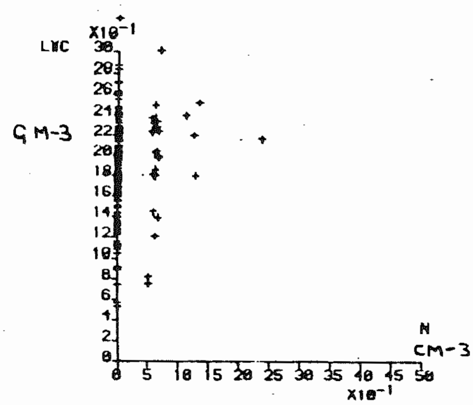

Figure 7. Liquid water content plotted against number of drops in the largest F FSSP bin

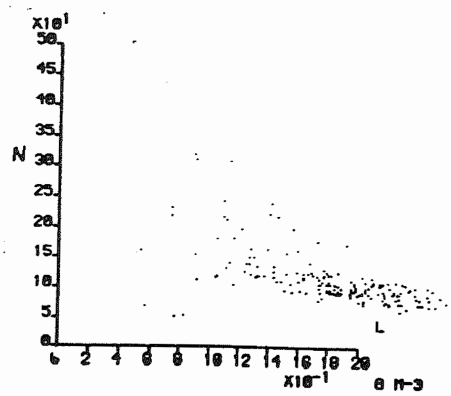

Figure 6. Number concentration of droplets in radius range 0-5μm against liquid water content

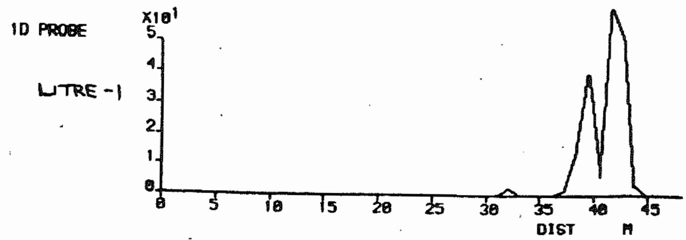

Figure 8. Drops measured by the Knollenberg 1-D probe (minimum radius 25μm) against distance through the cloud

MICROPHYSICAL OBSERVATIONS IN WARM CLOUDS

L.T.Khemani, G.A.Momin, S.K.Paul, R.Kumar
A.S.Ramachandra Murty and Bh.V.Ramana Murty

Indian Institute of Tropical Meteorology,
Pune 411 005, India

1. INTRODUCTION

The rate of coalescence within the cloud is critically dependent on the cloud droplet size distribution. The nature of the cloud droplet distribution is influenced by the physical and chemical characteristics of atmospheric aerosols. Hence measurements of atmospheric aerosols and microphysical properties of clouds are important for the physical understanding of the formation of rain in warm clouds. Aircraft observations of cloud microphysical parameters, atmospheric aerosols and chemical composition of cloud/rain water have been made in the Deccan plateau region of Maharashtra state in India as a part of the warm cloud modification experiment undertaken by the Indian Institute of Tropical Meteorology. The results of the observations are presented in this paper.

2. MEASUREMENTS

Observations of i) Aitken nuclei, ii) cloud condensation cuclei (at 0.1% supersaturation), iii) cloud droplet size distribution, iv) cloud liquid water content were made during the summer monsoon (June-September) seasons of 1979-1982. Also samples of cloud/rain water were collected during the aircraft penetrations into clouds. A DC-3 aircraft was used for the measurements.

Aitken nuclei (AN) were measured using an expansion type portable nuclei counter (Gardner Associates, USA). The instrument measures the nuclei in the size range of 0.001 to 0.1 μm. The method of sampling nuclei from aircraft and the accuracy of measurements were described elsewhere (Ref. 1). The concentrations of cloud condensation nuclei (CCN active at 0.1% supersaturation were measured using a chemical diffusion chamber (Ref. 2). The details of the sampling and the measurements of concentration of CCN were described elsewhere (Ref. 3). The cloud LWC is measured using a JW-hot wire meter (Jhonson Williams, USA). The cloud droplet sampler containing magnesium oxide coating glass slides was used for the measurement of cloud droplet size distributions. The method of sampling of cloud droplets and measurement of size distributions were described elsewhere (Ref. 4). The cloud/rain water samplers were collected using a specially designed stainless steel gadget. The details of the gadget were described elsewhere (Rs. 5). The chemical composition of cloud/rain water were determined using standard colorimetric and atomic absorption spectrophotometric methods.

3. RESULTS AND DISCUSSION

3.1 Seasonal variation of Aitken Nuclei (AN)

The mean monthly concentrations of AN at the surface are shown in Fig. 1. The average concentrations during the summer monsoon (June-September) and winter (October-March) season are respectively 1.4×10^4 cm^{-3} and $4.8 \times 10^4 cm^{-3}$. The higher concentrations of AN observed during the winter are attributed to the transport of nuclei of continental origin by airmasses travelling over land from east. The lower concentrations of AN observed during the monsoon period are due to westerly summer monsoon flow which is by and large maritime in nature.

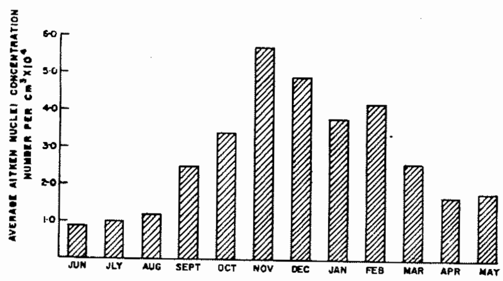

Fig. 1 : The mean monthly concentrations of Aitken nuclei during June 1980 to May 1982.

3.2 Vertical distribution of AN

The mean vertical distribution of AN in cloud-free air is shown in Fig. 2. The data shown in the figure relates to 69 days of aircraft observations made during the three summer monsoon seasons (1980-82). The concentration of AN is nearly steady from 0.9 to 2.1 km and is one order of magnitude more than that at the surface. The concentration of the nuclei up to 2.1 km showed little variation and thereafter it decreased with height. The height of the cloud-top in the region is found to be around 2 km and the concentration of AN decreased sharply above that level. Similar distributions were also reported by other investigators (Ref. 6).

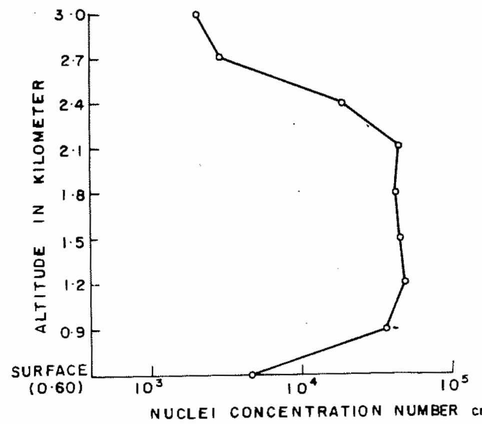

Fig.2 : Vertical distribution of AN based on observations made during the three monsoon seasons (1980-1982).

3.3 Variations of AN in cloud-air and cloud-free air

Observations of AN were made inside the stratocumulus and cumulus clouds and in the air outside the cloud at the same level during the three monsoon seasons. The results are given in Table 1. The concentration of AN is found to be significantly higher inside the cloud than that in cloud-free air. Similar feature was noticed in the measurements reported by others (Ref. 7). The higher concentrations observed in cloud-air were attributed to the higher gas-to-particle conversion rates inside the cloud by some of the investigators.

Table 1

The average concentration of Aitken nuclei ($\times 10^4 cm^{-3}$) in cloud-air and cloud-free air. Figures in brackets denote standard deviations.

Year	No.of observation	Cloud-air	Cloud-free air
1980	16	7.4 (3.38)	4.2 (2.78)
1981	28	7.1 (4.14)	3.9 (3.40)
1982	25	4.4 (2.46)	1.9 (1.31)

3.4 CCN vertical distribution

The vertical distribution of CCN and the variation of dry-bulb temperature obtained during the aircraft ascent and descent over the Arabian sea near Bombay (18° 51'N, 72° 49'E, 11 m asl) coast are shown in the Fig. 3.

The atmospheric boundary layer consisted of near isothermal layers of thickness up to 330 m with alternating layers having dry adiabatic lapse rate. The concentration of CCN at 0.1% super saturation varied between 200 and 510 cm^{-3}.

The concentration of CCN decreased in general with height. In the region of isothermal layers the concentrations are higher up to about 100 per cent than those in the respective preceding levels.

3.5 Cloud droplet size distributions

The cloud drop size distribution for different altitudes is shown in Figure 4. The total droplet concentration varied between 28 and 82 82 cm^{-3}. The concentration of bigger drops (diameter $\geqslant$ 50 μm) varied between 0.18 and 0.71 cm^{-3}. The concentration of bigger drops increased rapidly with height above the cloud-base indicating that the size distribution experiences a broadening effect with increase in distance from the cloud-base. The width of cloud drop size distribution increased progressively with height and it is maximum at 2.1 km. The percentage contribution by the drops with diameter less than 30 μm to the total LWC was computed using the data presented in the figure. It constitutes only 20% of the total LWC.

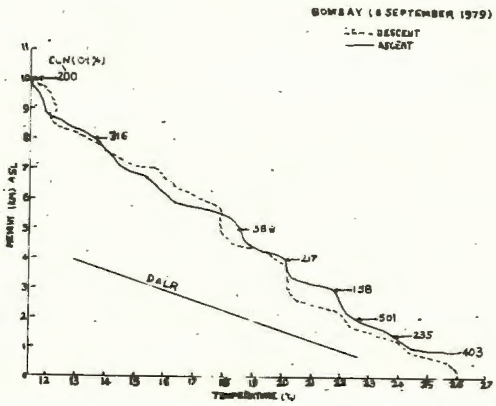

Fig. 3 : Vertical distribution of dry-bulb temperature obtained during the aircraft ascent and descent. Dry adiabatic lapse rate (DALR) distribution is also shown. Figures indicate the concentration of cloud cloud condensation nuclei (CCN) at the respective levels.

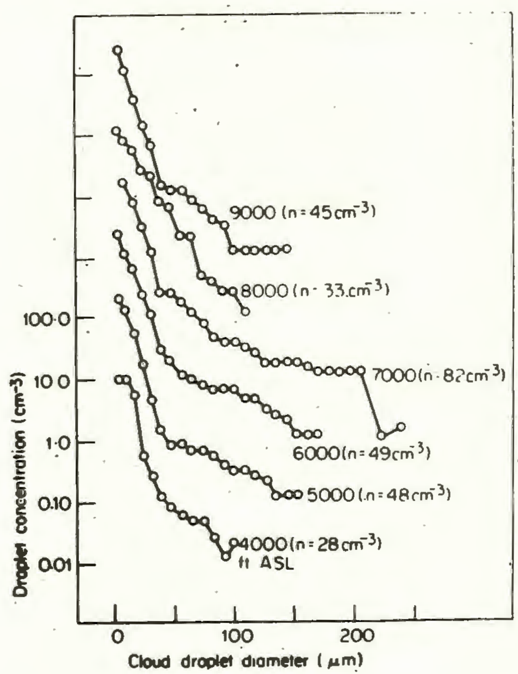

Fig. 4 : Cloud droplet size distribution at different aircraft altitudes. The total concentration (n) of the cloud droplets is also shown for each level.

The computed LWC due to the drops of diameter ⩽ 30 μm is an order of magnitude less than that measured by the JW-LWC meter. Hence it appears that the collection efficiency of the cloud droplet sampler (Ref. 8) may be low especially for the drops in the smaller size ranges. This is also seen from the very low concentrations of droplets. However, the drop size spectrum may be of some use for evaluating the collision-coalescence growth of cloud drops of diameter ⩾ 30 μm. The broadening of the drop size spectrum observed with height from the base of the cloud can lead to the conclusion that the collision coalescence growth is more effective at higher levels in the cloud. The JW-LWC also showed an increase with height from the base of the cloud.

3.6 Chemical composition of cloud/rain water

The mean chemical composition of cloud and rain water is given in Table 2. The concentrations of all the constituents measured except nitrate are higher in cloud water than in rain water. They are significantly higher for Cl, Na, Ca, NH_4 and SO_4. Petrenchuk and Drozdova (Ref. 9) have noticed higher concentrations of some constituents in cloud water than in rain water depending upon the location of observation. Bogen (Ref. 10) has observed higher concentration for Cl and Na in cloud water than in rain water. The higher concentrations of the Na, Cl, NH_4 and SO_4 observed in cloud water indicate the importance of the condensation nuclei containing ammonium sulphate and sea salt in the microphysics of clouds and coalescence process. Results of the chemical composition of cloud water collected at the hill station, Mahabaleshwar (17° 56'N, 73° 40'E, 1382 m ASL) situated on the crest of the Western Ghats (Ref.11) are in agreement with the present study.

4. CONCLUSIONS

Aircraft/surface observations of atmospheric aerosols, cloud microphysical parameters, at a tropical station in India and analysis of cloud and rain water samples collected from aircraft suggested the following :

1) The Aitken nuclei concentrations at the surface during the summer monsoon and winter seasons showed marked variations.

2) The vertical distribution of AN showed increase up to 0.9 km above the surface, little variation near the cloud-base levels and a decrease above the cloud-top height.

3) The concentration of AN is found to be significantly higher inside the cloud than that in the cloud-free air.

4) The concentration of CCN (at 0.1% supersaturation) in general decreased with height.

Table 2

The mean concentration of different ions (mg l^{-1}) in cloud and rain water, Figures in brackets indicate standard deviations.

Cl	SO_4	NO_3	NH_4	Na	K	Ca	Mg
			CLOUD WATER				
5.20	1.57	0.80	0.82	4.60	2.70	5.00	1.50
(0.10)	(0.35)	(0.10)	(0.02)	(2.75)	(1.00)	0.28)	(0.14)
			RAIN WATER				
3.95	0.95	1.36	0.61	2.96	1.75	2.72	0.65
(0.30)	(0.80)	(0.42)	(0.11)	(1.60)	(1.48)	(2.10)	(0.40)

5) The width of the cloud drop size distribution increased progressively with height above the cloud-base.

6) The concentrations of Na, Cl, NH_4, and SO_4 in cloud water are found to be higher than those in rain water.

7. REFERENCES

1. Khemani L T et al 1982, Variations in Aitken nuclei and atmospheric trace gases in the Deccan plateau, India, Proc. Conference on cloud Physics, Chicago 15-18 November 1982, 66-67.

2. Twomey S 1959, The nuclei of natural cloud formation I: The chemical diffusion method and its application to atmospheric nuclei, Geofis, Pure Appl., 43, 227-242.

3. Murty A S R et al 1978, Aircraft measurements on cloud condensation nuclei in the maritime and continential environments, Dr. **Borovikov** Memorial Volume on Cloud Physics, **Gidrometeoizdat, USSR.**

4. Paul S K et al. 1980, Calibration for studying microstructure of clouds sampled from an aircraft, J. Indian Inst. Sci., 62 (B), 83-88.

5. Khemani L T et al 1982, A simple gadget for collection of cloud/rain water from aircraft, Proc. conference on Cloud Physics, Chicago, USA, 15-18 November 1982, 303-305.

6. Bigg E K & Turvey D E 1978, Sources of atmospheric particles over Australia, Atmospheric Environment, 12, 1643-1655.

7. Hegg D A et al 1980, A preliminary study of cloud chemistry, Proc. 8th International Conference on Cloud Physics, Clermont-Ferrand-France 15-19 July 1980, 7-10.

8. Kapoor R K et al 1976, Measurement of cloud droplet size distributions in seeded warm clouds, Pure and Applied Geophysics, 114, 379-392.

9. Petrenchuk O P & Drozdova V M 1966, On the chemical composition of cloud water, Tellus 18, 280-286.

10. Bogan J 1974, Trace elements in precipitation and cloud water in the area of Heidelberg, Measurements by instrumental neutron activation analysis, Atmospheric Environment, 8, 835-844.

11. Khemani L T et al 1977, Chemical composition of cloud water at a hill station, 9th International Conference on atmospheric aerosols and nuclei, Galway, Ireland 21-27 September, 1977.

AN EXPERIMENTAL INVESTIGATION OF MICROSTRUCTURE INHOMOGENEITY IN STRATIFORM CLOUDS

A.V. Korolev, I.P. Mazin, Yu.E. Makarov and V.S. Novikov

Central Aerological Observatory, Moscow, USSR

1. INTRODUCTION

The spatial inhomogeneity of cloud microstructure has been a topic of increasing interest to cloud physicists. The information about spatial variations of concentration and cloud drop size spectra is of great importance for understanding cloud and precipitation formation mechanisms. Different authors repeatedly pointed out the necessity of a detail experimental study of microstructure including the scale of averaging influence on microstructure parameters (e.g. Refs. 1, 2).

However, until recently, cloud physicists often used the data on microstructure averaged on large spatial scale. The development of high precision probes as well as aircraft experimental techniques made it possible to study the fine structure of clouds. This is the main object of the paper. Our attention was concentrated primarily on stratiform liquid clouds (St, Sc, Ns). The choice is not accidental. On the one hand, stratiform (particularly frontal) clouds play a great role in weather formation in the middle latitudes and on the other hand, they are often thought of as rather homogeneous and stable objects.

The experimental results given below are chosen from 60 analysed cases, each of them being a part of flight made in St, Sc and Ns clouds. The flights were performed by an aircraft Il-18 (TAS = 100-150 m/s) equipped with special cloud probes including PMS FSSP-100 droplet spectrometer (Ref. 3). The data obtained by FSSP-100 form the basis of this paper. The measurements were made in one of four drop size ranges: 0.5-8 μm, 1-16 μm, 2-32 μm and 2-47 μm. Time averaging was usually selected to be equal to 0.1 sec, corresponding to the spatial length of 10 meters, so that a sample would have enough volume to contain about 1000 droplets in an individual spectrum at a concentration of 300 cm^{-3}. Some measurements were made with time averaging up to 0.01 sec, which enables us to study spatial spectrum variations with one meter averaging. Each of constant-level paths into clouds is 5-20 km long.

The experimental data were treated by an on-ground computer. The results of thorough laboratory FSSP-100 tests and calibrations of the probe by means of water drops (Refs. 4, 5) were taken into account during the treatment. It was demonstrated (Ref. 4) that utilization of the FSSP manufacture-supply calibrations would lead to the measured and real diameter discrepancy up to 3 μm. Laboratory tests also show that systematic underestimating of droplet concentration due to electronics may reach more than 100 % (it depends on air speed and concentration (Ref. 5)).

The following parameters used in the paper, are calculated from droplet size-spectra and given below:

total concentration in the used FSSP-100 range

$$N = \sum_{i=1}^{15} N_i , \tag{1}$$

where Ni is a droplet concentration in the FSSP-100 i-th channel;

concentration of large droplets

$$N1 = \sum_{i=8}^{15} N_i ; \tag{2}$$

liquid water content (LWC)

$$W = \frac{\pi}{6} \sum_{i=1}^{15} D_i^3 N_i , \tag{3}$$

where Di is a mean diameter of the i-th channel;

modal diameter of the spectrum

$$D_m = \frac{D_{i-1}N_{i-1} + D_i N_i + D_{i+1} N_{i+1}}{N_{i-1} + N_i + N_{i+1}} , \tag{4}$$

here i is the number of a channel for which $N_i = N_{max}$;

mean volume diameter (MVD)

$$D_W = \left(\frac{\sum_{i=1}^{15} N_i D_i^3}{\sum_{i=1}^{15} N_i} \right)^{1/3} ; \tag{5}$$

D_{95} - 95 % quantile, i.e. 95 % of all droplets are smaller than D_{95}. This value was calculated by means of linear interpolation.

τ_p is phase relaxation time (Ref. 6)

$$\tau_p = \frac{1}{2\pi D_V} \cdot \frac{1}{\overline{ND}} , \tag{6}$$

where D_V is diffusion coefficient of water vapour in air, D is droplet diameter. Overbar denotes averaging.

2. HORIZONTAL INHOMOGENEITY

The preliminary data analysis shows substantial spatial inhomogeneity in stratiform cloud microphysical structure. Figs. 1 and 2 show the fragments of realization of several microphysical parameters obtained in stratiform clouds in two different geographical regions. In spite of their visual similarity, there is a great difference in the average values of these parameters and in their spatial inhomogeneity. So the variation coefficients of the droplet concentration $\sigma_N/\overline{N}$ differ one from another approximately by four times and they are equal to 0.05 (Fig. 1) and 0.22 (Fig. 2). The average particle concentration LWC and τ_p are equal to N = 270 cm^{-3}, $\overline{W}$ = 0.28 gm^{-3} τ_p = 2 sec (Fig. 1), and N = 110 cm^{-3}, $\overline{W}$ = 0.05 gm^{-3}, τ_p = 9 sec (Fig. 2), respectively.

To determine which has stronger effect on LWC cloud droplet concentration or size-spectra shape, we apply correlation coefficients of particle concentration, LWC and cube of MVD (K(N, W), K(N, D^3w); K(W, D^3w)). The analysis of the accumulated data shows that the spatial variations of LWC are more closely associated with droplet size variations than with the variations of a total droplet concentration, i.e. K(W, D^3w) K(W, N). The typical values of these correlation coefficients are K(W, D^3w) = 0.7 and K(W, N) = 0.4.

It should be noted that the $K(N, D^3w)$ and $K(N, D_{95})$ are always negative (in particular, for the cases considered here $K(N, D^3w) = -0.39$ (Fig. 1), $K(N, D^3w) = 0.37$ (Fig. 2)). Fairly often, when the total droplet concentration decreases, the amount of large size droplets increases. The detailed study of spectrum variations showed two different mechanisms responsible for this effect. One of them depends on the fact that the total concentration variations are often caused by variations in small droplet (left) part of particle size distribution. Small droplets respond more rapidly than large ones to variations of relative humidity, and they may evaporate when it becomes less than 100 %. In this case the small droplets are transformed into watered nuclei (CCN), thus diminishing the measured total concentration. Large droplets due to their 'condensational inertia' cannot follow relative humidity variations. Hence, a relative increase of D^3w and D_{95} takes place when small droplets evaporate and a relative decrease - when CCN grow and are transformed into cloud droplets. Another reason for a negative correlation lies not in relative but in absolute increase of large particle concentration when the total concentration decreases. In this case it is convenient to use correlation coefficient of the total concentration N and concentration of large droplets N1. In Fig. 2 $K(N, N1) = -0.65$ when averaged over the distance of 200 meters. Due to a common trend between N and N1 for all realization $K(N, N1) = -0.2$. It is quite plausible that such an anticorrelation is caused by inhomogeneous mixing (Ref. 7), the essence of which is as follows: when a portion of relatively dry air penetrates into a cloud parcel (for example from the upper boundary of a cloud) some drops evaporate, thus diminishing the droplet concentration. When humidity increases (for example during updraft), the remained large droplets grow faster and may even reach more than 50 μm. in diameter. These droplets may later become embryos of precipitation.

Note that in Fig. 2, where negative correlations between N and D^3w or D_{95} are caused by evaporating small droplets, the correlation coefficient is rather small, $K(N, N1) = -0.05$.

Generally for correlation radii of N, W and D^3w obtained from calculated correlation functions, the following inequality is true: $R(N) \ll R(W) \lessapprox R(D^3w)$, where $R(N)$ is about some meters and $R(W)$, $R(D^3w)$ are about some hundreds of meters.

3. VERTICAL PROFILES OF SOME MICROPHYSICAL PARAMETERS

Several soundings by aircraft in stratiform clouds were made in order to explore the vertical profiles of microphysical parameters. The vertical component of the aircraft velocity was approximately constant and equal to 2-4 m/s.

Fig. 3 shows the successive transformation of drop size distributions during aircraft ascent through the lower cloud boundary. It is easy to see how CCN in the subcloud layer quickly grow up. Within the cloud the originated droplets continue to grow and approximately at 30 meters above the boundary, the concentration of 1-2 μm diameter droplets sharply diminishes (an order and more). At 50 meters, size spectrum minimum is about 1-2 μm, i.e. supersaturation here does not exceed 0.1 %. The modal diameter at this point is approximately equal to 5.5 μm and relative standard deviation of particle size distribution $\sigma = 0.2$. That is in a good agreement with the theory of regular condensation.

The modal diameter slightly increases with height up to the upper boundary. The spectrum transformation near the upper cloud boundary substantially differs from its behavior at the lower boundary. In all cases when the upper boundary was crossed, we never saw any smooth decrease of D^3w and d_{95}. Usually these variables as well as particle concentration and LWC decrease abruptly in a transitional layer with the thickness about 5-10 meters. It indicates a sharp decrease of relative humidity over the upper boundary. In this case all droplets will evaporate very quickly.

Fig. 4 shows the typical vertical profiles of some microphysical parameters. In the lower part of Fig. 4 the subcloud zone of watered CCN with the diameter 1 μm is well distinguished. In the lowest cloud layer, 100-150 meters thick, the particle concentration decreases, while the LWC and the characteristic droplet size (D^3w and D_{95}) increase. Comparatively slow further increase of D^3w and W and the invariability of average D_{95} are rather unexpected. Perhaps the process of entrainment of dry air into the cloud body and the inhomogeneous mixing which relax towards the lower boundary, play a great role here. These mechanisms suppress increase in LWC, D^3w and D_{95} with height.

Fig. 5 shows the presence of several layers (in our case three), with the vertical trends of the microphysical parameters similar to those showed in Fig. 4. The boundaries of the layers are approximately located at the levels: 1250-1450 m, 1500-1620 m, and 1720-1900 m. It may be a result of closing different cloud layers. The case represented in Fig. 5 was investigated on 11.12. 83 in the region of Penza in the rear part on the cold front, where the layering is a common phenomenon.

5. SOME OTHER FEATURES OF CLOUD MICROSTRUCTURE

The analysis of spatial variations of the droplet size spectra obtained during vertical aircraft soundings and horizontal flights in the upper half of the clouds reveals the zones, where particle concentration falls several orders. The spatial size of those cloud zones hereafter called 'caverns' is 10-100 meters and the distance from the upper boundary is tens and hundreds of meters. Fig. 6 shows a flight through a cloud cavern. Note that the abruptness of the droplet size spectrum in the cavern is similar to that at the upper boundary. This similarity implies that the origin of the cavern is due to a dry air parcel penetration from the upper boundary. As the cavern lowers down, the evaporation of droplets and turbulent diffusion provoke its erosion. The existence of caverns confirms again the hypothesis of inhomogeneous mixing in stratiform clouds.

High spatial resolution permits us to study spectrum transformation with averaging length beginning from one meter. There is an opinion (e.g. Ref. 8), that in sufficiently small cloud parcels droplet size spectra are rather narrow, but the measured spectra are essentially broader due to spatial averaging. The analysis of droplet size spectra obtained in different clouds shows that along with the above-mentioned tendency of spectrum broadening, there are cases when spectrum width is independent of averaging distance from 1 m up to 1 km. This is also true for bimodal spectra. Two types of bimodal spectra were found: i). when bimodality appears in each individual spectrum at the averaging length less than 10 meters, and ii) when bimodality appears only at averaging at large distances, while each individual spectrum is unimodal. Note that bimodal spectra usually appear in the middle part of the stratiform clouds.

5. CONCLUSION

It is impossible in a short paper to consider and even to enumerate all the features of cloud microstructure. Some of them presented here show that there are more questions than answers. Which mechanisms are responsible for the observed spatial inhomogeneity of microstructure? Which conditions are favourable for the formation of the very narrow cloud drop-size spectrum in one place of the cloud and broad enough and even bimodal in another point of a cloud? What is the role of the inhomogeneity in cloud stability and precipitation formation? How to describe it quantitatively in theoretical and numerical models?

To answer these and many other questions it is necessary to get much more information about the fine structure of spatial and time variability of cloud microphysical parameters and its relation with cloud dynamics and thermodynamics. But in our opinion, the spatial inhomogeneity of cloud microstructure plays a great role in cloud processes and even now it should be taken into account when developing numerical models of clouds, if authors wish to describe the real processes of precipitation formation, phase relaxation time τ_p and phase scale of turbulence Lp (Ref. 6) being the important parameters.

REFERENCES

1. Borovikov, A.M., Mazin, I.P., 1970. The microstructure of liquid clouds (in Russian), Trudy VIII Vsesoyuznoi conf. po fizike oblakov, Leningrad, Gidrometeoizdat, 13-21.
2. Kogan, E.L., Mazin, I.P., Sergeev, B.N., Khvorostyanov, V.I. 1984. Numerical simulation of clouds (in Russian), M. Gidrometeoizdat, 193 pp.
3. Knollenberg, R.G., 26-30 July, 1976. Three new instruments for cloud physics measurements: the 2-D spectrometer, the Forward Scattering Spectrometer Probe and the Active Scattering Aerosol Spectrometer, International Conference on Cloud Physics, Boulder, Colorado, 554-561.
4. Korolev, A.V., Makarov, Y.E., Novikov, V.S., 1984. About calibration of droplet spectrometer FSSP-100, Trudy CAO, No. 158, (in Russian).
5. Korolev, A.V., Makarov, V.E., Novikov, V.S., 1984. On the accuracy of measurements of photoelectric droplet spectrometer FSSP-100, Trudy CAO, No. 158, (in Russian)
6. Mazin, I.P., Shmeter, S.M. 1983, Clouds, their structure and physics of formation (in Russian), Leningrad, Gidrometeoizdat, 279 pp.
7. Baker, M.B., Corbin, R.G. and Latham, J., 1980. The influence of entrainment on the evolution of cloud droplet spectra: 1. A model of inhomogeneous mixing, QJRMS, 106, 581-598.
8. Udin, K.B. 1976. Some results of measurements of local characteristics in stratiform clouds, Meteor. Gidrol., No. 12, 44-48, (in Russian)

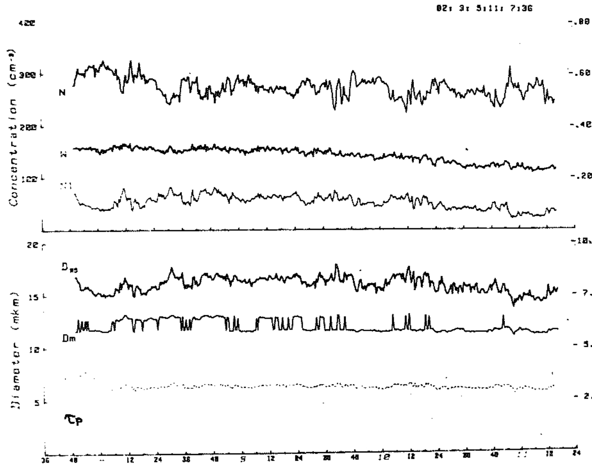

Figure 1. A part of the horizontal path in Ns, 20 km long. March 5, 1982, the Central Asia. Flight level H = 1500 m, temperature T = -3,2 °C, time of averaging Δt = 0.1 s. The FSSP-100 drop size range is 2÷32 μm. $\overline{N}$ = 273 cm^{-3}, $\overline{W}$ = 0.26 gm^{-3}, σ_N/N = 0.05. The anticorrelation of N and N1 pulsations is distinct.

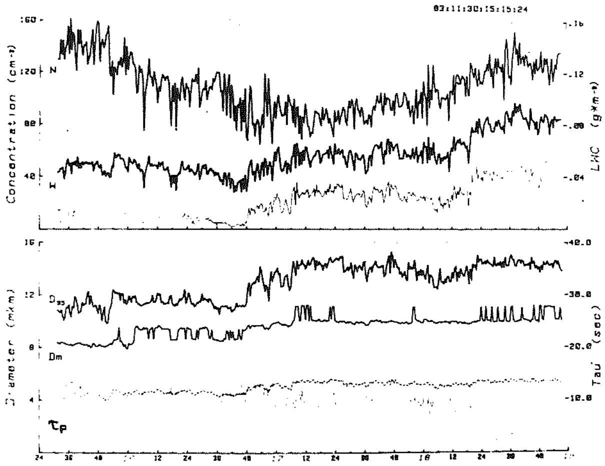

Figure 2. A part of the horizontal path in Sc, 20 km long. November 30, 1983, the region of the European part (EP) of the USSR. H = 1500 m, T = -0.3 °C, D D_{15} = 2-32 μm. $\overline{N}$ = 108 cm^{-3}, $\overline{W}$ = 0.056 gm, σ_N/N = 0.22. In this case, not only D_W, but also variations of total concentration N influence the value of LWC.

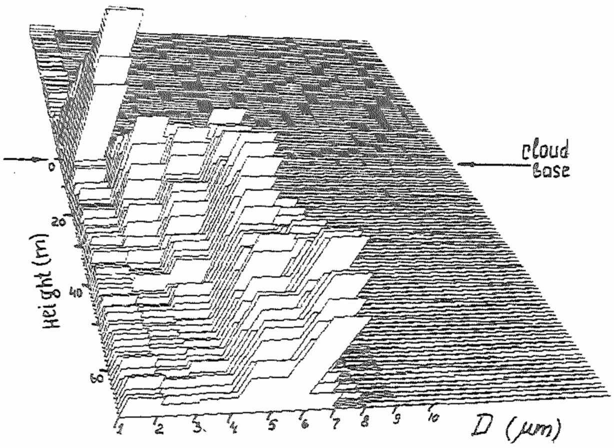

Figure 3. Consequent droplet size spectra in space, obtained during vertical sounding in SC - Ns. November 18, 1983, the region of Riga. The speed of aircraft descent is 2 m·$^{-1}$. The time of averaging, i.e. the time interval between neighbouring spectra is Δt = 1 s. In the region of lower cloud boundary (above the arrow), one can see watered CCN. The droplet modal diameter grows up to 5-6 μm (the lower part of the Figure). (The vertical profiles of cloud parameters in this case are shown in Fig. 4).

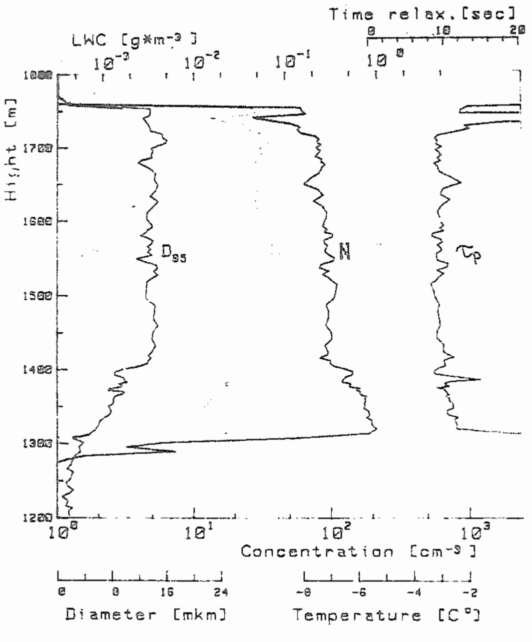

Figure 4. Vertical profiles of some parameters in Sc - Ns. November 18, 1983, the region of Riga. The droplet concentration maximum equals 280 cm^{-3} near cloud base. At 100 meters over the cloud base, the concentration decreases to 80 cm^{-3} and further changes are weak. LWC and D_W substantially increase in the lower quarter of the cloud, but the further increase becomes weak. The mean phase relaxation time τ_p is approximately constant within the cloud body and equal to 10 s.

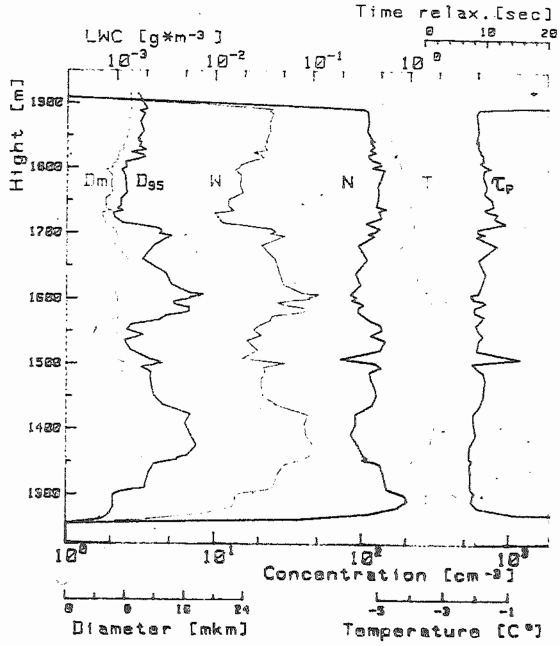

Figure 5. Vertical profiles of some parameters in Sc. November 30, 1983, central part of EP of the USSR. There is substantial vertical variability of microstructure. One can distinguish three layers, where the profiles of N, W, D_m and D_{95} are similar to those in Fig. 4.

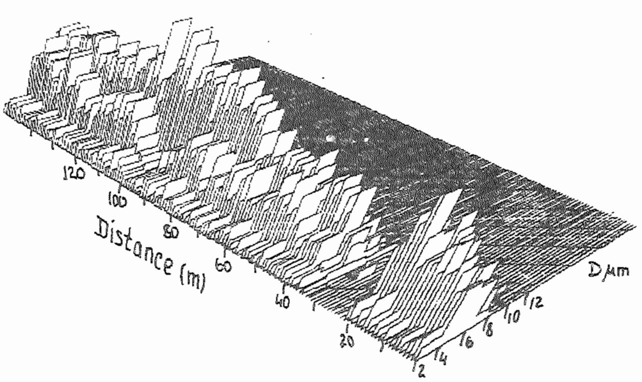

Figure 6. A part of the horizontal path in St. November 30, 1983, the central part of EP of the USSR. H = 1500 m, T = -0.3 °C. The spatial scale averaging (the distance between neighbouring spectra) is 2 meters. The arrow points to a cloud cavern - a parcel where droplet concentration falls several orders. The horizontal dimension of this cavern is about 20 meters. The cavern seems to be provoked by dry air penetration through the upper cloud boundary.

OBSERVATIONAL CASE STUDY OF MICROPHYSICS IN A GROWING CONVECTIVE CLOUD NEAR THE ALPS

P. Meischner, W. Bögel, H. Horst, R. Roth

1. INTRODUCTION

The classical descriptions of cloud droplet spectra development by condensation due to adiabatic lifting of moist air and subsequent collision / collection processes due to different fall speeds of different sized droplets do not explain satisfactorily droplet distribution development as observed in cumulus clouds. Especially natural cumulus clouds do develop faster to a mature precipitating stage mainly by a faster broadening of the initial droplet distribution. A significant increase of efficiencies of the stochastic collision-collection processes due to microscale turbulence for droplet radii of 10 - 20 µm has been discussed by ALMEIDA (1, 2, 3). A further approach to the explanation of enhanced spectral broadening is the hypothesis of inhomogeneous mixing of cloud air with environmental air laterally and from cloud top in separate blobs or continuously (4-7). Other calculations investigate the influence of turbulent velocity fluctuations near cloud base and the role of vertical coherency of turbulence on the droplet distribution (8, 9). Especially in the case of high vertical coherence of turbulence the calculations yield realistic dropsize distributions including bimodal spectra.

Most of these theoretical findings are compared with aircraft observation performed and described in very detail by Warner, 1969 (10-14). Relatively few more recent and high resolution measurements in cumulus clouds are available. Some case studies with tethered balloons in small cumulus clouds (15) and within cap clouds under various meteorological situations (16, 17) cover this field.

One aim within our field studies KOOP (Convection Oberpfaffenhofen) on convective clouds in the lower Alpine Region near Oberpfaffenhofen was to study the microphysical behaviour of small growing cumulus clouds in relation to the cloud internal dynamics by aircraft measurements. First results of a case study are to be presented here.

2. MEASUREMENTS

The observations were performed with the German Meteorological Research Aircraft FALCON operated by the Flight Facility within DFVLR - the German Aerospace Research Establishment. The equipment of interest for this study was: Sensors for pressure, total temperature, humidity (Ly-α), a Rosemount gust probe, a Knollenberg FSSP-100, a Litton INS, LTN 72.

The physical quantitites computed and presented

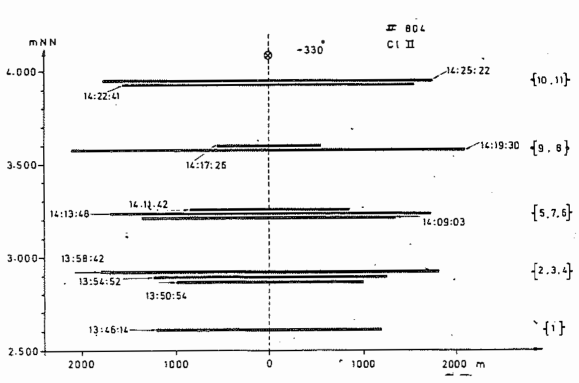

Fig. 1. Flight paths in growing Cu-cloud, II

here as time series plots with 1 Hz resolution are

1. Potential temperature TPOTC in deg C
   The relative accuracies are about 0,1 deg C in cloud free air, the in-cloud accuracy is unknown but an error of up to about -1.0 deg seems possible due to the vaporization of droplets in the total temperature probe.
2. Potential virtual temperature TPVC in deg C possible errors somewhat higher than for TPOTC.
3. Relative humidity computed from Ly-α UWLY in %. Accuracy: about 10%.
4. Water vapour mixing ratio RLY in g/kg computed from Ly-α values.
   Accuracy as in 3.
5. Horizontal wind speed WIS in m/s
   Relative accuracy ±0,5 m/s (The relative accuracy may increase for time intervals of more than 5 minutes).
6. Wind angle of horizontal wind WIA in deg. counting from north to east.
7. Vertical wind speed WWG in m/s
   Accuracy, absolute ±0,5 m/s
   relative ±0,2 m/s
8. Clouds droplet concentration CONC. in particles per cm³ from FSSP.
   Error: about -35%.
9. Mean droplet diameter M.DIAM. in µm. Accuracy ±1 µm; undersizing in more likely because of the high flight speed of the FALCON.
10. Liquid water content computed from droplet spectra LWC-KN. in g/m³
    Error: about -40%, in higher flight levels still higher because of increased flight speed.
11. Dispersion of droplet spectra DISP.

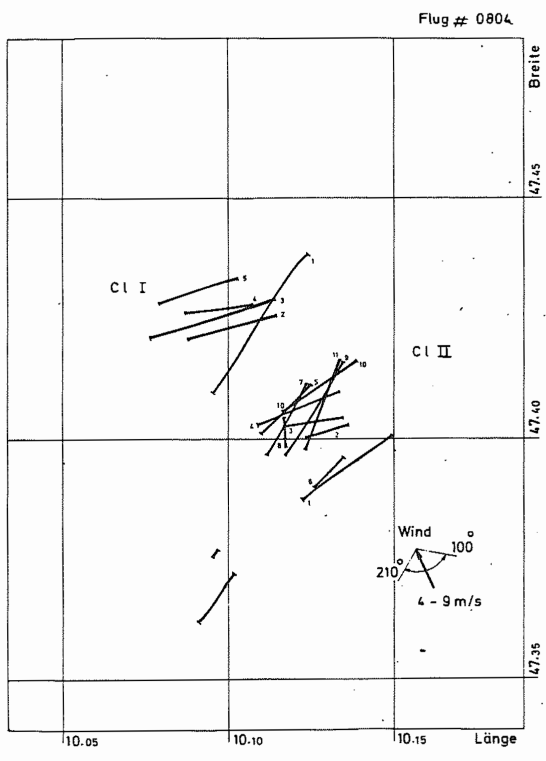

Fig. 2. Flight tracks in growing Cu-clouds

The strategy of observation was to penetrate a just developing cumulus cloud very near to its base and then successively at increasing levels during growth. At some levels successions were flown. Because of the aim to hit the cloud almost centrally, the in-cloud tracks are not stationary in space, as can be seen in fig. 1 for two clouds observed on this flight. Only cloud II will be discussed here. The corresponding flight levels, times of penetration and flight directions are given in fig. 2 which shows that the relatively stationary cloud developed to a depth of 1400 m within about 37 min. The environmental wind blew from 100 deg to 210 deg, wind speed was between 4 and 9 m/s. Because only in-cloud processes will be discussed here, no further description of environmental conditions is given but will be presented in the paper of A. Jochum in this conference using some of these observational data for model comparisons.

3. RESULTS

The observed data of only four selected traverses of cloud II are presented here, illustrating the general findings of this study. These are traverse {1} near cloud base at 2600 m NN in fig. 3, traverses {5} and {7} at 3250 m, 23 and 27,5 min later in fig. 4 and 5 and traverse {11} near cloud top at 4000 m NN about 39 min after first penetration, presented in fig. 6.

The measurements at cloud base - traverse {1}, fig. 3 - show a significant humidity excess within cloud regions up to $\gtrsim 90\%$ compared with 45% in the environment. The corresponding water vapour mixing ratio is 9 and 5 g/kg respectively. The in-cloud virtual potential temperature TPVC does not exceed the environmental values even if an error of about ∓ 1 deg is taken into account. The in-cloud humidity field shows inhomogenities. The fluctuations of horizontal wind between 2 and 7 m/s and between 40 and 120 deg in direction suggest turbulent mixing especially near the updraft core which reaches 3 m/s. The environmental wind comes from 120 deg with 6 m/s. Cloud droplets occur only in the updraft region; the concentration shows high fluctuations between about 50 and 150 per cm³ as well as the mean droplet diameter ranging between 6 and 9 µm.

Concentration and mean diameter fluctuations show the same trends and therewith the computed LWC having values between 0,01 and 0,1 g/m³. The dispersion of the droplet spectra is between 0,17 and 0,3 with the lower values for lower mean diameters and lower concentrations.

The two traverses {5} and {7}, fig. 4, 5 show in general similar dynamical and microphysical structures despite of the time shift of about 5 min. Note that these two traverses are flown in opposite directions! The relative humidity exceeds 100% and the in-cloud and environmental water vapour mixing ratios are 8 and 5,5 g/kg resp. Calculated relative humidities in excess of 100% do not necessarily indicate supersaturation, but may also be caused by droplet evaporation at the inlet of the humidity channel; see the inaccuracies mentioned above. Again there are fluctuations of humidity which extend to cloud environment especially to be seen in the later traverse {7}. Relative maxima of in-cloud temperature are observed at locations of strong updraft velocity only. Strong wind fluctuations within cloud between 1 and 8 m/s indicate turbulent mixing. The environmental wind is blowing with 7 m/s from about 180 deg. The updraft core is structured with a main peak value near 8 m/s. For traverse {7} a downward motion of 1-2 m/s outside of the visible cloud but near the edges is measured.

Cloud droplets with concentrations of about 150 /cm³ occur in regions of WWG ≥ 0 m/s only. The values of droplet concentrations and droplet diameters show equal trends in good correlation with the updraft structure. The droplet diameters vary between 7 and 12 µm for traverse {5} and 7 and 13 µm for traverse {7} with the higher updraft values. The computed LWC reaches values between 0,02 and 0,2 g/m³. The dispersion in this level clearly shows lower values for higher mean droplet diameters which means that the droplet distribution does not broaden with droplet growth in the updraft region.

Traverse {11}, fig. 6 near cloud top is characterized by frequent and strong fluctuations of all quantities measured, showing the typical cauly-flower structure of growing cumulus clouds. The relative humidity within cloud reaches values of 100% in peaks only and has a mean value of about 90%; in the environment of 50%. The corresponding in-cloud and environmental water vapour mixing ratios are at 5,5 and 3 g/kg. The in-cloud temperature again shows peaks at locations of high updrafts. A temperature increase is observed near the cloud in regions with low humidity values and small downward air motion of about 1 m/s. Obviously advected air masses are present here, which is indicated by a higher horizontal wind speed. The strong wind fluctuations between 2 and 11 m/s and between 150 and 300 deg extend far beyond the visible cloud. The updraft area is structured too with a distinct peak of $\gtrsim 4$ m/s.

Correlated with wind and updraft fluctuations there are well distinguisable parcels about 400 m in diameter containing cloud droplets with quite interesting behaviour: For the overall cloud the droplet concentration <u>decreases</u> from about 140 to 120/cm³ which corresponds to an <u>increase</u> in droplet diameter from 8 to 12 µm. In contrast to this finding <u>within the individual parcels</u> the mean droplet diamter correlates positivley with droplet concentration. The same holds for the dispersion of the droplet spectra: The dispersion increases for the whole cloud with decreasing concentration and increasing mean diamter from 0,3 to 0,4, whereas <u>within</u> the individual parcels the dispersion is negatively correlated with mean droplet diameter.

For this traverse most of the observed spectra are of bimodal type.

4. CONCLUSIONS

In-cloud measurements with the FALCON aircraft, equipped with gust probe and microphysics sensors are suited to study microphysical developments in relation to dynamics at least in small cumulus clouds.

In this case a cumulus cloud near the northern edge of the Alps has been investigated in detail. This cloud remained relatively stationary in space, despite the environmental wind blowing from southeast with a mean of appr. 7 m/s. Repeated flights through cloud at constant levels show a certain degree of stability of dynamical structure within at least some minutes. All in-cloud measurements show highly inhomogeneous structures with strong relationship between microphysics and dynamics which suggest turbulent mixing at all levels and in each state of development. The droplet concentration to some extend, but much more pronounced the mean droplet diameter is positively correlated with updraft velocity. The dispersion of droplet spectra increases with height from about 0,2 to 0,4.

At cloud base the dispersion is positively correlated with mean droplet diameter and concentration. For the later traverses {5} and {7} the correlation between dispersion and mean droplet diameter changes between positive and negative values whereas near cloud top - traverse {11} - for the individual cloud parcels the dispersion is negatively correlated with mean droplet diameter. Bimodal spectra have been observed mainly at cloud top.

5. ACKNOWLEDGMENTS

We like to thank our flight facility, especially the pilots of the FALCON for their flexible cooperation and guidance. Further thanks are due to Th. Jank and his group for their support in data evaluation software programming.

6. REFERENCES

1. De Almeida, F C 1976, The Collisional Problem of Cloud Droplets Moving in a Turbulent Environment - Part I: A Method of Solution JAS 33, 1571-1578.
2. De Almeida, F C 1979, The Collisional Problem of Cloud Droplets Moving in a Turbulent Environment - Part II: Turbulent Collision Efficiences JAS 36, 1564-1576.
3. De Almeida, F C 1979, The Effects of Small-Scale Turbulent Motions on the Growth of a Cloud Droplet Spectrum JAS 36, 1557-1563.
4. Baker, M B and Latham, J 1979, The Evolution of Droplet Spectra and the Rate of Production of Embryonic Raindrops in Small Cumulus Clouds. JAS 36, 1612-1615.
5. Baker, M B et al., The Influence of Entrainment on the Evolution of Cloud Droplet Spectra: I. A Model of Inhomogeneous Mixing. Quart. J. R. Met. Soc. 106, 581-598.
6. Jonas, P R and Mason, B J 1982, Entrainment and the Droplet Spectrum in Cumulus Clouds, Quart. J. R. Met. Soc. 108, 857-869.
7. Manton, M J and Warner, J 1982, On the Droplet Distribution near the Base of Cumulus Clouds, Quart. J. R. Met. Soc. 108, 917-928.
8. Manton, M J 1979, On the Broadening of a Droplet Distribution by Turbulence near Cloud Base, Quart. J. R. Met. Soc. 105, 899-914.
9. Baker, M B and Latham, J 1982, A Diffusive Model of the Turbulent Mixing of Dry and Cloudy Air, Quart. J. R. Met. Soc. 108, 871-898.
10. Warner, J 1969a, The Microstructure of Cumulus Cloud. Part I: General Features of Droplet Spectrum, J. Atmos. Sci 26, 1049-1059.
11. Warner, J 1969b, The Microstructure of Cumulus Cloud. Part II. The Effect on Droplet Size Distribution of Cloud Nucleus Spectrum and Updraft Velocity, Ibid. 26, 1272-1282.
12. Warner, J 1970, The Microstructure of Cumulus Cloud. Part III. The Nature of the Updraft. Ibid. 27, 682-688.
13. Warner, J 1973, The Microstructure of Cumulus Cloud. Part V. Changes in Droplet Size Distribution with Cloud Age. Ibid. 30, 1724-1726.
14. Warner, J 1977, Time Variation of Updraft and Water Content in Cumulus Clouds, Ibid. 34, 1306-1312.
15. Kitchen, M and Caughey, S J 1981, Tethered - Ballon Observations of the Structure of Small Cumulus Clouds, Quart. J. R. Met. Soc. 107, 853-874.
16. Blyth, A M et al. 1980, The Influence of Entrainment on the Evolution of Cloud Droplet Spectra: II. Field Experiments at Great Dun Fell, Quart. J. R. Met. Soc. 106, 821-840.
17. Baker, M B et al. 1982, Field Studies of the Effect of Entrainment upon the Structure of Clouds at Great Dun Fell, Qaurt. J. R. Met. Soc. 108, 899-916.

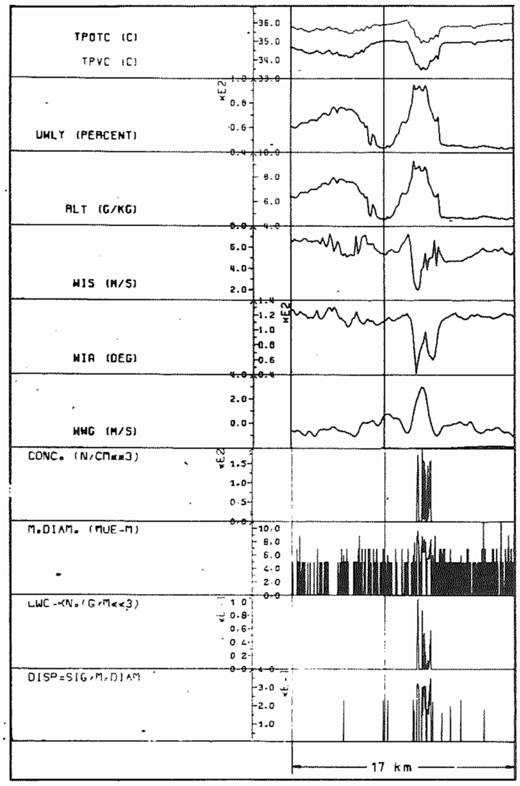

Fig. 3. Traverse {1}, see fig. 1. and 2.

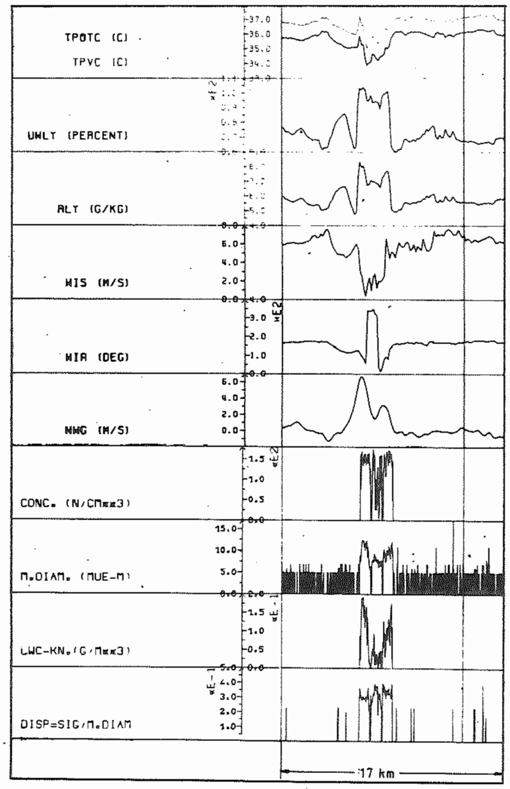

Fig. 4. Traverse {5}, see fig. 1. and 2.

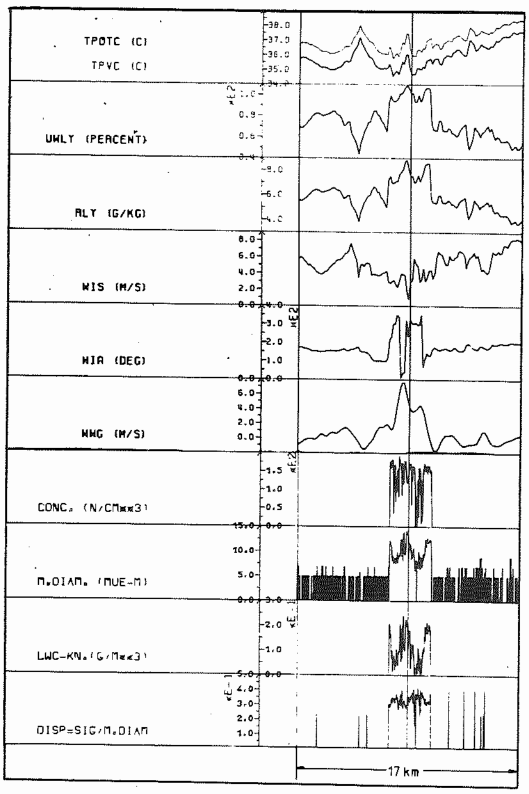

Fig. 5. Traverse {7}, see fig. 1. and 2.

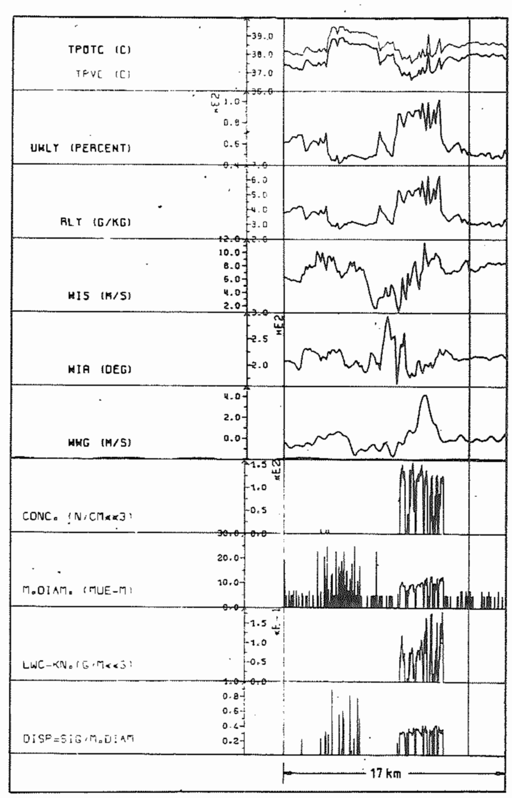

Fig. 6. Traverse {11}, see fig. 1. and 2.

MIXING AND THE EVOLUTION OF CLOUD DROPLET SIZE SPECTRA

Ilga R. Paluch

National Center for Atmospheric Research
Boulder, Colorado, 80307, U.S.A.

It has long been recognized that the rate of precipitation formation through the water phase is sensitive to the width of the cloud droplet size spectrum produced by diffusional growth, and that diffusional growth calculations in a rising, homogeneously mixed air parcel result in a narrower spectrum than is commonly observed except within a few hundred meters of cloud base. Attempts to produce a broader droplet spectrum have led to a number of microphysical models employing a variety of physical assumptions and mixing parameterizations, and presently there is disagreement over which sets of assumptions are more realistic (Refs. 1-8). In the following work aircraft data from a continental cumulus cloud are examined in an attempt to infer to what extent the observations are consistent with some model assumptions and mixing parameterizations. Because the analysis is limited to one cloud only, the present results and conclusions should not be interpreted as a general evaluation of the various modeling assumptions.

The data were collected during the Cooperative Convective Precipitation Experiment (CCOPE) in southeastern Montana on June 9, 1981, in a towering cumulus that grew in a dry, strongly sheared environment. The cloud was 4-5 km wide, 5-7 km high (from cloud base to the 0 dBZ radar top), and contained updrafts up to about 17 m s^{-1}. The cloud base was at 4°C, 790 mb, 2 km (MSL). Data from the nearest sounding and aircraft cloud base measurements from NCAR Queen Air 306D indicate that the cloud adiabatic temperature excess could be as high as 5°C. However, no adiabatic cloud regions were observed from the Wyoming King Air flying 2.3-3.6 km above cloud base.

The cloud droplet size spectra were measured with the FSSP on the Wyoming King Air (Ref. 9), averaged over 100 m (1s) intervals. Some examples of the observed spectra are shown in Fig. 1. The spectra often had more than one peak, and more frequently at the higher altitudes. During the highest cloud pass, at about -21°C, none of the observed spectra had a single peak. While the data presented here are limited to the first cloud investigated on June 9, other clouds penetrated later had rather similar droplet spectra. Droplet spectra with more than one peak are not uncommon (Refs. 10, 11), though on this flight such spectra were observed with an unusually high frequency.

In numerical models, droplet spectra with more than one peak sometimes result from activation of new droplets, when the supersaturation in an air parcel exceeds the peak supersaturation it had experienced earlier. Seeking evidence of activation of new droplets within cloud, the data were examined for correlation between the presence of large concentrations of very small droplets and an estimate of a kind of conditional supersaturation, a supersaturation that would have been attained if the small cloud droplets were not present. When the updraft velocity and the droplet size spectra are known, supersaturation can be computed using a steady state assumption that the condensation rate just balances the tendency for supersaturation to increase during ascent. For the present data, this equilibrium condition typically would be reached within a few seconds; less than 20 s even in the extreme cases of very low droplet concentration. The cloud supersaturations were calculated using the measured vertical velocities, assuming that the updraft had not changed too much since the hypothetical droplet activation occurred.

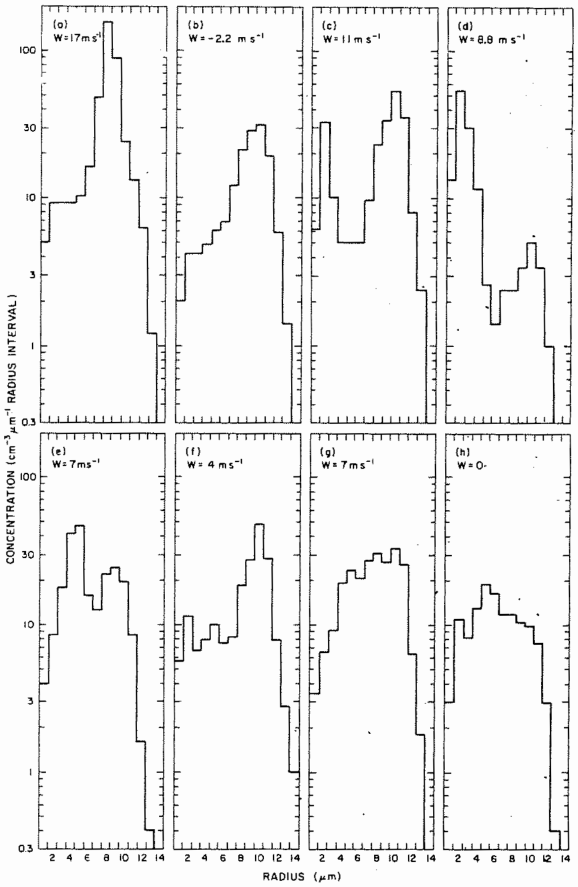

Figure 1. Concentrations of cloud droplets cm^{-3} in 1 μm radius intervals. The spectra were measured by FSSP over 100 m (1s) paths. The vertical velocity (W) is indicated above. The positions in the updraft of samples b, c, and d, are marked in the vertical velocity plots in Fig. 2.

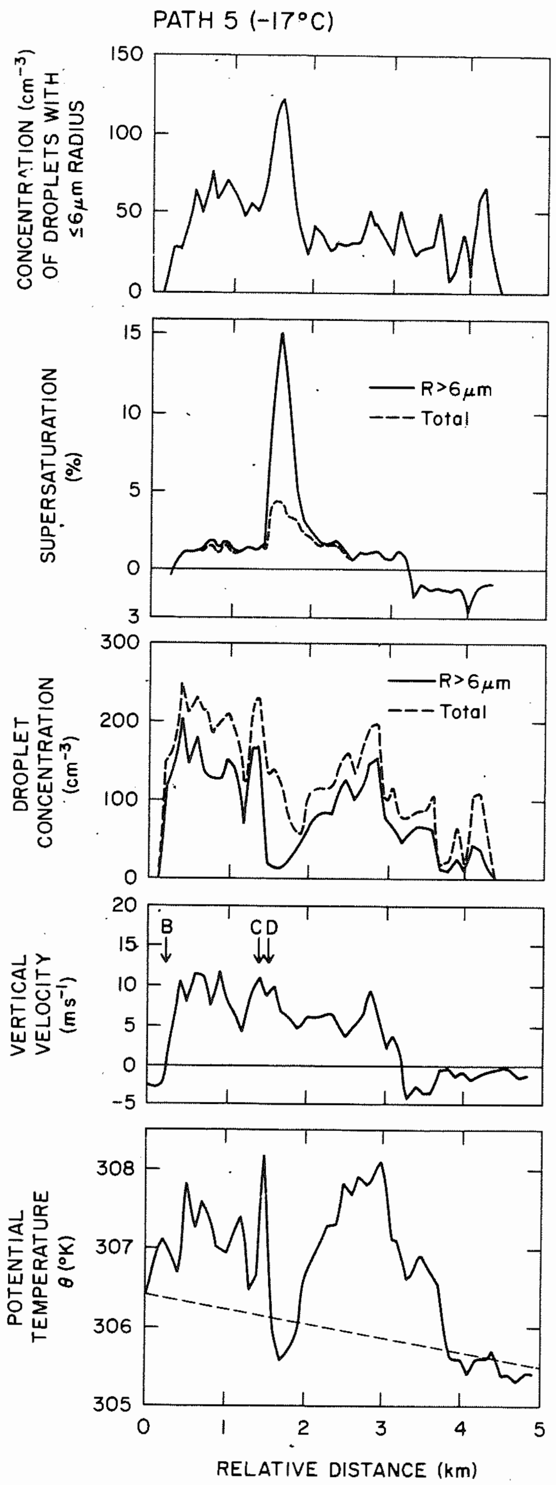

Figure 2. Data collected during the fifth cloud penetration, at about -17°C. For explanation, see text.

The first two plots in Figure 2 show concentrations of droplets ≤ 6 μm in radius and supersaturations calculated as above, but in two ways: using the droplets >6 μm in radius only (solid lines--this is the conditional supersaturation), and using all the droplets in the spectrum (dashed line). As can be seen, there is a cloud region where the supersaturation would have been very high without the small droplets, and this region is associated with a strong peak in the concentration of small droplets. Except for the most prominent peaks in conditional supersaturation, all of which correspond to the highest peaks in concentration of small droplets, the rest of the data show little correlation between the two.

It is difficult to account for the correlation between the prominent peaks except by appealing to droplet activation. Let us assume that new droplets have been activated a short time prior to the measurements, and that during this time the updraft has not changed. Then the droplets would have experienced an average supersaturation that is less than the computed conditional supersaturation but more than the supersaturation computed using all of the droplets. If supersaturation is high the growth times for small droplets are short: to reach 2 μm radius, this time is 36s and 3.6s at 1% and 10% supersaturation, and to reach 6 μm radius, 144s and 14.4s. In these estimates the length scale associated with the condensation coefficient is 5 μm. At high supersaturations the assumption that the updraft has not changed significantly since the droplets were activated does not seem unrealistic. Thus we would expect some correlation between the computed conditional supersaturation and the concentration of small droplets when this supersaturation is high, but not when it is low, as indeed the present data indicate. The correlation between only the highest peaks in the conditional supersaturation and the highest peaks in the concentration of small droplets is therefore consistent with the activation of new droplets.

The third and fourth plots in Figure 2 show droplet concentrations and vertical air velocities. The high conditional supersaturations are found in cloud regions where low concentrations of large droplets and relatively high vertical velocities coexist. The bottom plot in Figure 2 shows cloud air potential temperature calculated from data from the reverse flow thermometer. This temperature fluctuates in phase with droplet concentration indicating that mixing rather than droplet depletion by growing precipitation is the main cause of low droplet concentrations. The dashed line represents the potential temperature of the environment at the flight altitude, interpolated from King Air data collected in the clear air at ends of each penetration. As can be seen, even in highly mixed cloud regions the potential temperature is only a few tenths of a degree below that of the environment, whereas in the less mixed cloud regions the potential temperature excess is sometimes as high as 2 to 2.5°K. The potential temperature excess and the vertical velocity are not well correlated in this cloud. In clouds with less buoyancy mixing would tend to decrease or destroy the updraft, and thus the creation of high supersaturations, with concommitant activation of new droplets, would be less likely.

Aside from new droplet activation there are other processes that can produce bimodal droplet spectra. For example, numerical simulations show that bimodal spectra can be produced when droplets sediment into dry air. At an interface between cloud and dry air, the droplets only partially evaporate because as their fall speed slows down they are overtaken by larger, faster falling droplets which in turn evaporate and raise the humidity. While the sedimentation process could be disrupted by small turbulent eddies, on scales of a meter or less, it is conceivable that such eddies exist only intermittently, and that they would not disrupt the sedimentation process everywhere. It is not clear whether this process is quantitatively significant. Bimodal spectra can also result from mixing two different cloud volumes, each having a distinctly different spectral mode. Such mixing should produce an inverse correlation between the concentrations of small and large droplets. A similar trend whould also result if all the small droplets in the bimodal spectra resulted from evaporation due to mixing with dry air. However, the present data show no such trend, except in the few cloud regions associated with the highest peaks in the estimated supersaturation.

The small cloud droplets in the secondary peaks contained very little cloud water, at most .05 gm m^{-3} but usually much less, and thus they would not be expected to have had a large influence on the growth or evaporation of the larger droplets. Figure 3 shows droplet concentration at the large droplet peak as a function of the radius at the peak. As in Fig. 1, the data are 100m(1s) averages. Cases where the peak is not resolved, as in Fig. 1h, which constitute 14 percent of the data set were excluded. (This was done by excludng spectra for which, at 3 μm above the radius at peak concentration, the concentration dropped by less than one-third of the peak concentration.) The shape of the spectrum at the large droplet end is relatively constant, and when the large droplet peak is well resolved the total droplet concentration in this peak is about 3 times the value at the peak itself, using the 1 μm radius interval. Since often this peak is partially obscured by nearby peaks at smaller droplet sizes, the value of the peak itself has been used as an estimate of the total droplet concentration in the peak (left hand scale in Fig. 3).

The data in Fig. 3 show that at any given altitude the radius at the large droplet spectral peak remains nearly constant regardless of droplet concentration. This result is inconsistent with the homogeneous mixing parameterization, commonly used in the simple entraining parcel models, which predicts a shift towards smaller sizes at low concentrations. The nearly constant radius and the low droplet concentrations suggest that mixing may have taken place with already premoistened entrained air, as in the entity type entrainment mixing model by Telford and Chai (Ref. 3) or in the inhomogeneous mixing model by Baker and Latham (Ref. 2). However, the lack of variation in the droplet size at low concentrations is surprising because in this situation small adiabatic changes in altitude following mixing could be expected to produce large changes in droplet size. For example, if an airparcel contain-

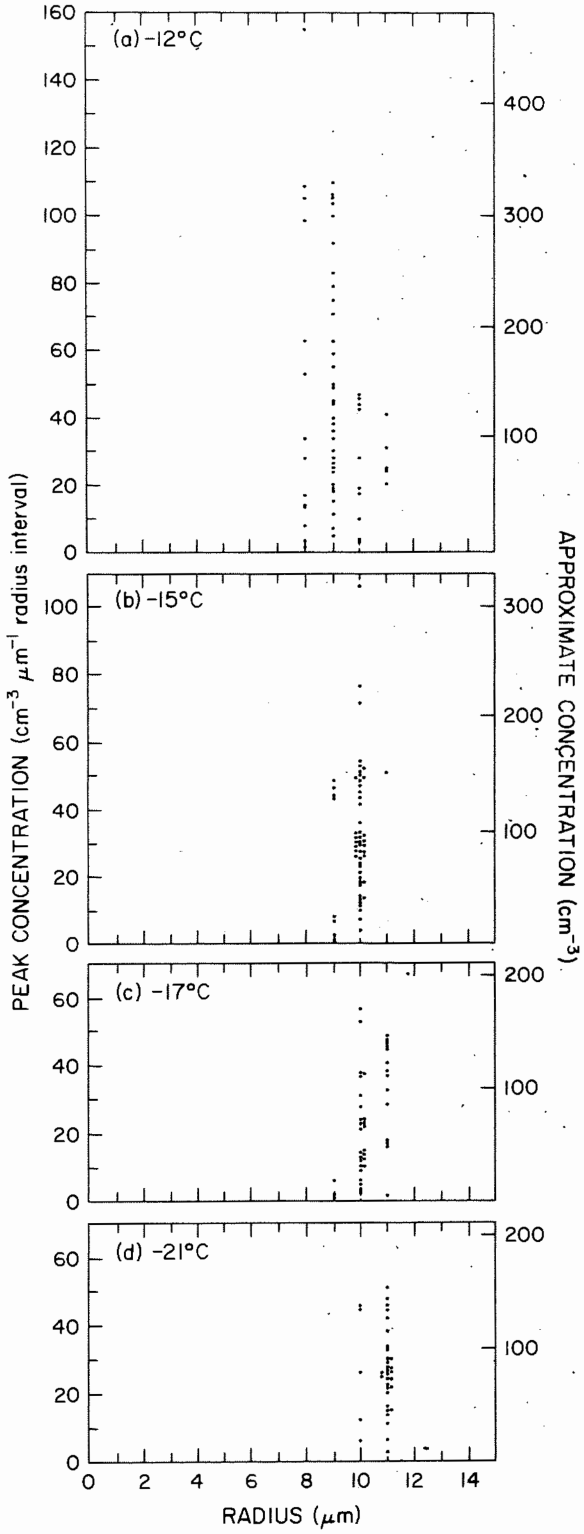

Figure 3. Observed large droplet concentration versus radius at peak concentration. Left hand scale shows the concentration at the large droplet spectral peak, right hand scale shows the estimated total concentration in this peak. The approximate penetration temperature is shown in the upper left hand corner. (a) and (b) contain two cloud penetrations each, (c) and (d) only one. The resolution of the FSSP corresponds to a 1 μm radius interval. In the plots, the data points are placed in the center of the radius interval, except when there is no room, in which case they are plotted nearby.

ing 10 μm radius droplets in concentrations of 30 cm^{-3} were raised adiabatically 200 m, then the droplets should grow to about 13 μm radius. Their size would not be significantly smaller if during ascent new cloud droplets were activated, provided that the liquid water content of the small droplets did not exceed the maximum values observed (.07 gm kg^{-1}). Similarly, if the above airparcel were lowered adiabatically 200 m, then all the 10 μm droplets should evaporate.

A possible explanation for the striking lack of change in the droplet size at low concentrations is that the measured concentrations, which are 100 m averages, may not be representative of the local concentrations that determine the supersaturation and hence the droplet growth rate. The local concentrations could be much higher and the droplet growth rates much lower if the turbulent eddies had not homogenized the mixed cloud regions down to the scale where molecular diffusion can operate effectively (which is of the order of a cm). This situation could occur if turbulence had not fully developed down to smaller scales, or if the small scale eddies were highly localized and not very efficient in homogenizing the mixed cloud regions. If such inhomogenieties do exist, then high supersaturations could develop in the cloud regions free of small droplets and there the potential for activation of new cloud droplets and ice particles could be much higher than predicted using the average supersaturation.

REFERENCES

1. Warner, J., 1969, The microstructure of cumulus cloud. Part IV. The effect on droplet spectrum of mixing between cloud and environment. J. Atmos. Sci., 30, 256-261.

2. Baker, M.B. and J. Latham, 1979, The evolution of droplet spectra and the rate of production of embryonic raindrops in small cumulus clouds. J. Atmos. Sci., 36, 1612-1615.

3. Telford, J.W. and S.K. Chai, 1980, A new aspect of condensation theory. Pure Appl. Geophys., 113, 1067-1084.

4. Kogan, Ye.L., and I.P. Mazin, 1981, Role of turbulent mixing of cloud droplets in cloud microstructure and rain formation. Atmos. and Oceanic Phys. Vol. 17, No. 9, 702-708.

5. Jonas, P.R. and B.J. Mason, 1982, Entrainment and droplet spectrum in cumulus clouds. Quart. J. R. Met. Soc., 108, 857-869.

6. Baker, M.B., and J. Latham, 1982, A diffusive model of the turbulent mixing of dry and cloudy air. Quart. J. R. Met. Soc., 108, 871-898.

7. Manton, M.J., and J. Warner, 1982, On the droplet distribution near cloud base of cumulus clouds. Quart. J. R. Met. Soc., 108, 917-928.

8. Telford, J.W., and S.K. Chai, 1983, Comment on "Entrainment and the droplet spectrum in cumulus clouds" by P.R. Jonas and B.J. Mason. Quart. J. R. Met. Soc., 109.

9. Cooper, W.A., 1978, Cloud physics investigations by the University of Wyoming in Hiplex 1977. Report No. AS119, Department of Atmospheric Science, College of Engineering, University of Wyoming, Laramie, Wyoming, 321 pp.

10. Warner, J., 1969, The microstructure of cumulus cloud. Part I. General features of the droplet spectrum. J. Atmos. Sci., 26, 1049-1059.

11. Skhirtladze, G.I., 1980, Result of a measurement of droplet size spectra in cumulus clouds. Atmos. and Oceanic Phys. Vol. 16, No. 1, 40-45.

CLOUD DROPLET SPECTRA IN WARM MONSOON CLOUDS

S.K.Paul, A.G.Pillai, A.M.Selvam, A.S.R.Murty and Bh.V.Ramana Murty
Indian Institute of Tropical Meteorology, Pune-411 005, India.

1. INTRODUCTION

Measurements of cloud drop size distributions in warm clouds are important for the physical understanding of rain-formation in tropical monsoon clouds. Cloud drop size distributions in warm monsoon clouds have been measured during aircraft penetrations into isolated warm cumulus clouds at different levels. A DC-3 aircraft was used for the above observations. The results relating to the observations made in the Pune (18° 32'N, 73° 51'E, 559 m asl), region during the summer monsoon seasons of 1981 and 1982 are presented in this paper.

2. MEASUREMENTS

A spring loaded sampler was used for collection of cloud drops on magnesium oxide coated slides. The drop sizes were measured using an optical microscope. True drop sizes from the craters were obtained using calibrations made earlier (Ref. 1). Measurements were made on 26 and 21 days during the summer monsoon (June-September) seasons of 1981 and 1982 respectively and the number of samples were 100 and 143 respectively.

3. RESULTS AND CONCLUSIONS

The average cloud drop spectra for different levels for the summer monsoon seasons of 1981 and 1982 are shown in figures 1 and 2, respectively. The standard deviations, total cloud drop concentration, N_T (cm^{-3}), computed liquid water content, LWC ($g\ m^{-3}$), mean volume diameter, MVD (μm), concentration of drops with diameter greater than 30 μm (cm^{-3}) and the shapes (modes) of the spectra are also given in the figures.

The total concentration of cloud drops in 1981 initially decreased from the cloud-base level up to 6700 feet and thereafter increased. In 1982 the drop concentration did not show systematic variation in the vertical. The average cloud-base height in the region varies between 4000 and 5000 feet ASL. The drop spectra showed, by and large, broadening with height above the cloud-base. This is marked in 1981 (Figure 1). The spectra narrowed after 7200 feet during 1981 and after 8100 feet during 1982. The total drop concentration and LWC were higher during 1982 than during 1981. The shapes (modes) of the distributions were different at various levels during both the years. The distributions were usually unimodal when the concentration of drops with diameter greater than 30 μm diameter was low and multi-modal if the concentration of the said drops was high. In general, total concentration was less when the b broadening of spectrum width was more and vice-versa. The concentration of drops greater than 30 μm diameter was higher in the lower levels during 1982.

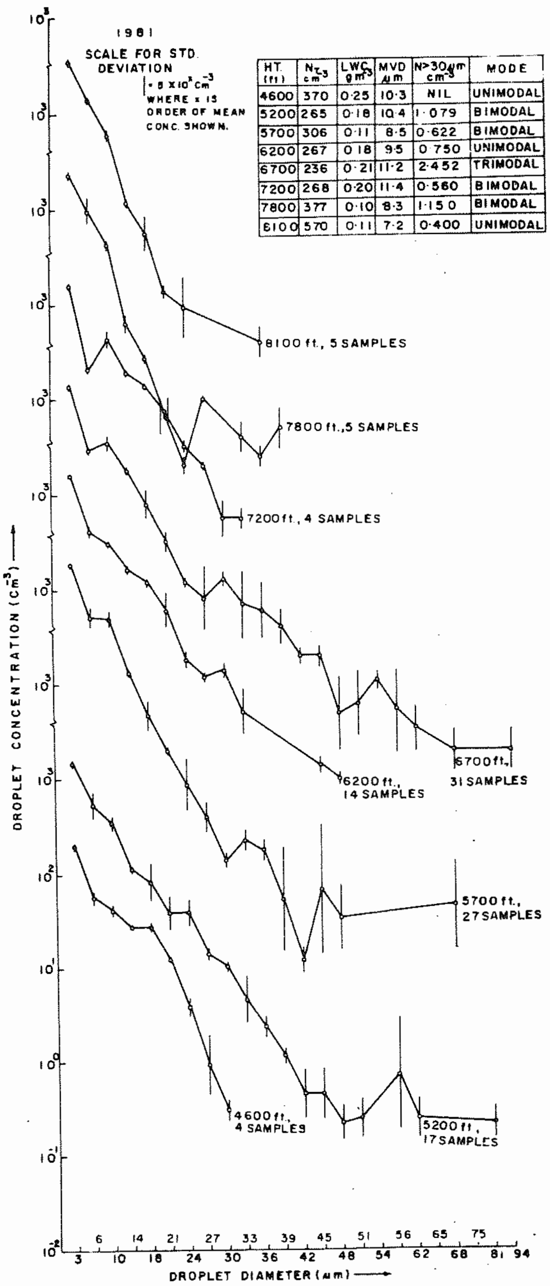

HT. (ft)	N_T cm^{-3}	LWC $g\ m^{-3}$	MVD μm	N>30 μm cm^{-3}	MODE
4600	370	0·25	10·3	NIL	UNIMODAL
5200	265	0·18	10·4	1·079	BIMODAL
5700	306	0·11	8·5	0·622	BIMODAL
6200	267	0·18	9·5	0·750	UNIMODAL
6700	236	0·21	11·2	2·452	TRIMODAL
7200	268	0·20	11·4	0·560	BIMODAL
7800	377	0·10	8·3	1·150	BIMODAL
8100	570	0·11	7·2	0·400	UNIMODAL

Figure 1 : Cloud drop size spectra - 1981. The ordinate is shifted by one scale each for the successive indicated heights.

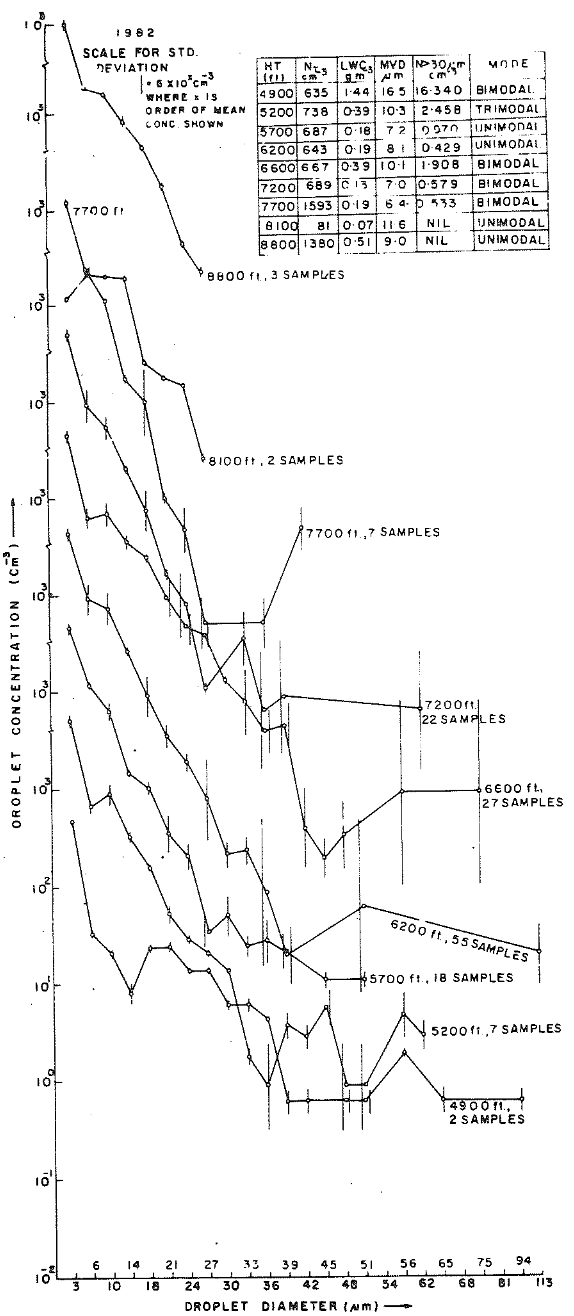

HT (ft)	N_T cm^{-3}	LWC $g\,m^{-3}$	MVD μm	$N>30\,\mu m$ cm^{-3}	MODE
4900	635	1·44	16 5	16·340	BIMODAL
5200	738	0·39	10·3	2·458	TRIMODAL
5700	687	0·18	7 2	0 970	UNIMODAL
6200	643	0·19	8 1	0·429	UNIMODAL
6600	667	0·39	10·1	1·908	BIMODAL
7200	689	0 13	7·0	0·579	BIMODAL
7700	1593	0·19	6 4	0 533	BIMODAL
8100	81	0·07	11·6	NIL	UNIMODAL
8800	1380	0·51	9·0	NIL	UNIMODAL

Figure 2 : Cloud drop size spectra - 1982. The ordinate is shifted by one scale each for for the successive indicated heights.

The multimodal drop spectra may be due to the downward transport of larger size drops from higher levels to lower levels by the cloud-top-gravity oscillations (Ref.2). The turbulent eddies originating from surface friction get amplified in the vertical by the energy released due to the condensation during the ascent of turbulent air parcels. Microscale-fractional-condensation occurs in turbulent eddis even in unsaturated environment. The turbulent eddies are inherently present all along the envelope of the large eddies as internal circulations (Fig. 3).

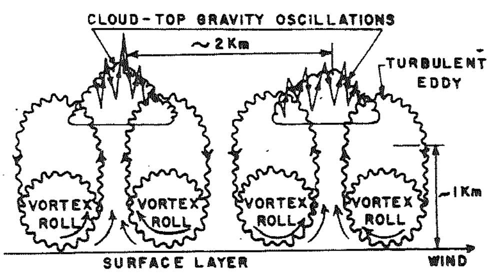

Figure 3 : Vortex rolls (large eddies) in the PBL. The turbulent eddies which are mainly caused by the roughness of the earth's surface exist all along the envelope of the large eddy. The turbulent eddes get amplified in the vertical by the latent heat released by the condensation of water vapour and generate cloud-top-gravity (buoyancy) oscillations.

The energy gained by the turbulent eddies would contribute to the sustenance and growth of the large eddy because the RMS circulation velocity of the large eddy is the integrated mean of the velocities of the individual turbulent eddies. Under favourable synoptic conditions the turbulent eddies get amplified by the energy released due to enhanced condensation and lead to the growth of the large eddy in the vertical resulting in cloud formation above LCL. Inside the cloud the turbulent eddies get amplified faster due to higher degree of condensation and generate cloud-top-gravity oscillations exclusively of buoyancy or 'gravity' type of internal waves (Ref. 2).

4. REFERENCES

1. Paul S K.et al 1980, Calibration for studying microstructure of clouds sampled from an aircraft, J. Indian Inst. Sci., 62(B), 83-88.

2. Mary Selvam et al 1982, Evidence for cloud top entrainment in the summer monsoon warm stratocumulus clouds, Preprint volume Conference on Cloud Physics, 15-18 Nov. 1982, Chicago, U.S.A. 151-154.

CONTINUOUS SPATIAL AND TEMPORAL VARIATIONS OF SUPERCOOLED WATER DURING WINTERTIME MOUNTAIN STORMS USING A PASSIVE MICROWAVE RADIOMETER

Robert M. Rauber, DaXiong Feng,* Lewis O. Grant
Department of Atmospheric Science
Colorado State University
Fort Collins, Colorado USA

and

J. B. Snider
NOAA/ERL/Wave Propagation Laboratory
Boulder, Colorado USA

1. INTRODUCTION

With the development of the dual-channel scanning microwave radiometer (Ref. 1), a new dimension of observational capability became available to determine the spatial and temporal distribution of supercooled cloud water in wintertime mountain cloud systems. Unlike aircraft or surface observations, radiometric measurements have the distinct advantage of being able to observe a large volume of the cloud system in a short amount of time. In addition, the radiometer can view regions of the cloud unapproachable by aircraft and can operate continuously in marginal weather conditions.

During the winter of 1981-82, this radiometric system was used as one part of a comprehensive field program conducted by Colorado State University in the Park Range region of Northern Colorado. The purpose of the field effort was to determine the structure and modification potential of wintertime cloud systems over the Northern Colorado River basin. One component of this program was to document the presence, spatial distribution and temporal variation of supercooled cloud water occuring in storms affecting the region.

Nine storms occured during the field program for which scanning radiometer data was available. In this paper, two of these case studies will be developed to illustrate the utility of the scanning radiometer in determining the supercooled liquid water distribution in wintertime storms. The major conclusions of this study, based on the complete nine storm data set, will also be discussed.

2. INSTRUMENTATION

This paper utilizes data collected by several instruments used during the Colorado Orographic Seeding Experiment (COSE). The field experiment was conducted during the months of December and January. Because the primary purpose of the experiment was to study the natural physical and microphysical structure of the cloud systems occuring in the region, no seeding operations were conducted. Figure 1 is a cross-section showing the major topography and the location of the instruments used in this analysis.

2.1 Microwave Radiometer

Details and references concerning the operation, theory and accuracy of measurements of cloud water and water vapor content obtained by the dual-channel radiometer are given by Ref. 1. The dual-channel radiometer is a passive instrument. Because it is passive, it can provide no information concerning the variation of liquid water content along the beam.

In the COSE program, the radiometer was mounted with a steerable antenna so that the spatial and temporal variability of the liquid water field could be studied. A standard scanning technique was adopted to observe the evolution of this field. The antenna was set at 15° elevation angle and rotated through 360° azimuth sweeps approximately every 15 minutes. Using this technique, it was possible to observe the changes in the integrated liquid water content in all directions. Because the 15° elevation angle was quite low, this technique allowed the observer to monitor the temporal and spatial evolution of the cloud water field. The data were analyzed on azimuth/time diagrams, which allowed for easy interpretation of the lifting mechanisms responsible for the production of the cloud water. The azimuth angles represent the following locations with respect to the barrier: 0° (north, parallel to barrier, 6 km west of crest); 90°(east, over barrier crest); 180° (south, parallel to barrier, 6 km west of crest); 270°(west, upwind of barrier).

2.2 Kμ band (1.79 cm) radar

During the COSE program, a vertically pointing radar was colocated with the dual channel radiometer near Steamboat Springs, Co. In this paper, the radar data are used to continuously monitor cloud top height, cloud top temperature (temperatures were obtained from special rawinsondes launched every 3 hours), and cloud maximum reflectivity.

2.3 Precipitation intensity and rime characteristics

Visual observations of snow crystal rime characteristics and special measurements of precipitation intensity were made continuously at the radiometer site (RAD). In this paper, the Magono and Lee (Ref 2) classification is simplified to examine only the rime characteristics of crystals. Unrimed crystals are classified as no rime (NR). R_{1a}, R_{1b}, R_{1c}, and R_{1d} are classified as R1. Similarly, $R_{2a,b,c}$ are classified as R2, R_{3a}, R_{3b}, R_{3c} as R3 and $R_{4a,b,c}$ as R4. Two additional categories are added for aggregates, LA for lightly rimed aggregates and MA for moderately rimed aggregates. NS indicates no snow.

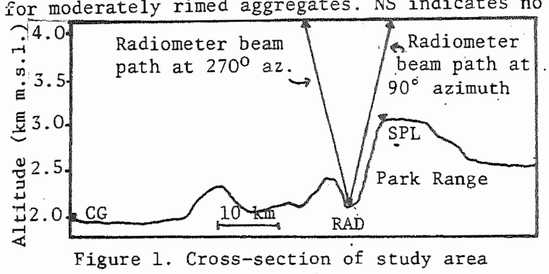

Figure 1. Cross-section of study area showing topography and instrumentation locations described in the text.

* Permanent affiliation: Academy of Meteorological Science, NMV, Beijing, China

2.4 Storm Peak Laboratory measurements

During the program, a mountaintop laboratory was established athe summit of Storm Peak (3100m msl) on the Park Range. Two of the many measurements collected at Storm Peak Laboratory (SPL) are reported in this paper. Liquid water contents in the cloud enveloping the mountain peak were measured with a rotorod device. Crystal rime characteristics were also recorded. The categories used were NS (no snow), NR (no rime), LR (light rime), MR (moderate rime) and HR (heavy rime).

2.5 Supporting data sets

Meausurements of surface temperature, pressure wind and precipitation were made continuously at RAD. Special rawinsondes were launched every 3 hours at Craig, Co (CG), 48 km upwind of RAD. Synoptic and other supporting data were obtained from standard National Weather Service products.

3. CASE STUDIES

During the COSE program, nine storm systems occured for which scanning radiometer data and other supporting data sets were available. Two of these storms will be discussed in this paper. One storm was selected to show the characteristics of a storm system prior to and during the onset of a convective band in a pre-frontal enviornment. The second was selected to show the characteristics of a post frontal decaying system with a strong orographic component.

These two cases are illustrated to show the utility of radiometric measurements. The major conclusions based on the analysis of the complete data set will also be discussed.

3.1 December 15, 1981 case study

3.11 Synoptic scale and local weather conditions

At 0600Z on December 15, 1981, a low pressure system was located in west central Nebraska and a weak high pressure system in southwest colorado. A stationary front extended from the low in Nebraska across Southern Wyoming and into Utah where it became a warm front associated with an intense weather system still off the west coast of the United States. By 1200Z, this intense storm system had moved rapidly inland. Ahead of the system, a strong, moist mid-level jet developed. The axis of this jet was located along the warm frontal boundary and strongly enhanced the development of clouds along the Wasatch mountains of Utah and in the mountains of Colorado. Winds normal to the barrier were 17 m/s. During the next hours through 1800Z, the warm frontal boundary slowly moved northward. A low pressure center developed in southwest Montana along the cold front associated with the deeply occluded system moving rapidly inland. Primarily orographically induced stratiform clouds with embedded heavy banded convective precipitation characterized the clouds present in the Park Range region during this period. The intensity of these storms slowly weakened as the warm frontal boundary moved slowly northward, the mid-level jet weakened and the strong cold front approached from the west.

3.12 Storm evolution and liquid water distribution

The cloud system of December 15, 1981 evolved through several distinct stages, each exhibiting significant variations in the cloud water distribution. These variations were associated with the passage of two wide area bands of heavy precipitation. The bands were embedded in a large scale stratiform system which extended over much of the Northern Colorado Rockies. Passage of the bands was marked by significant increases in cloud depth and precipitation intensity. This case study will concentrate on the cloud system prior to and during the passage of the first of these bands. The first band arrived at RAD at 1450Z and passed over the site in about one hour.

Rawinsondes were launched on a three hour schedule from CG during this storm. These soundings indicated that the atmosphere became progressively less stable with time. During the period of interest, a layer of potentially unstable air was present between 6400 and 8200m m.s.l. with a neutral layer extending to 4415m m.s.l., well within the stratiform layer present throughout the region. The lower region of this neutral layer became potentially unstable between 1500Z and 1800Z. The banded structure evident in the radar analysis was associated with enhanced cloud development in the middle and upper troposphere due to the release of weak potential instability and to the presence of significant amounts of middle and upper level moisture.

The time evolution of the supercooled water field is shown on figure 2. Precipitation characteristics at SPL and RAD, liquid water contents at SPL, radar characteristics and surface temperature at RAD are also shown on the figure.

During the early stage of this storm from 1310-1450Z, a stratiform cloud system with tops at 5000m m.s.l. was present over the Park Range region. Precipitation from this storm fell steadily at a rate of 1 mm/hr at RAD. During this period, radiometric measurements of the supercooled cloud water field indicated that cloud water was present throughout the cloud system, but was concentrated over the Park Range, particularly over the mountains southeast of RAD. Simultaneous measurements of rime intensity at SPL and RAD supported these measurements. At RAD, crystals were observed primarily in the R3, R2 and NR categories, indicating that significant accretion of supercooled water droplets was occuring upstream of RAD. Nearly all crystals collected at SPL were moderately rimed during this period. The lack of unrimed crystals at SPL provides strong support for the radiometric observation of increased liquid water contents over the barrier. During the early stages of this storm, mountaintop observations of supercooled cloud water gradually increased from 0.02 to 0.10 g/m^3, paralleling the observed increases in supercooled water measured by the radiometer in

With the onset of the band at 1500Z, cloud tops rapidly increased to 7000-8000m m.s.l. (-30 to -35°C). Radiometric liquid water contents rapidly decreased throughout the storm system during this stage of the storm. Prior to the onset of the band,crystals at SPL were all heavily rimed, but as the band progressed across the area, the amount of rime decreased substantially. During the passage of the band, precipitation rates increased considerably at RAD and SPL.

Within 40 minutes, all crystals observed at SPL were unrimed. Crystals observed at RAD showed a marked degree of aggregation. Many of the aggregates at RAD were lightly rimed. A few single crystals were moderately rimed. Liquid water contents at the surface at SPL reduced to 0.05 g/m^3.

These observations all suggest that the liquid water remaining in the cloud during band passage was below SPL and was horizontally distributed throughout the cloud. The rapid decrease in liquid water within the cloud system and the rapid increase in pre-
out the cloud system and the rapid increase in pre-
cipitation intensity and depth of the cloud all suggest that significant increases in the total cloud

ice crystal concentrations resulted from the enhanced convective activity. Three possible mechanisms could have produced these increases. Enhanced nucleation at cold cloud temperatures may have occured. Ice multiplication processes could have increased ice crystal concentrations during the initial stages of cloud development. Additional primary nucleation may also have occured in regions of high supersaturation in developing convective regions. Whatever the mechanism, these ice particles rapidly and efficiently removed the liquid condensate from the cloud system.

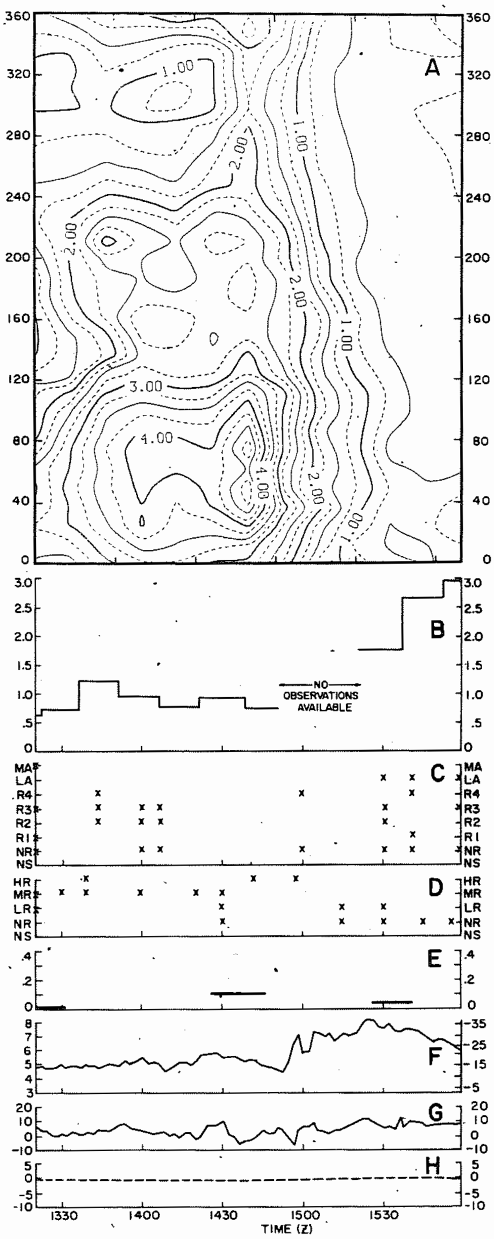

Figure 2. December 15, 1981 (1320-1600Z); (A) Radiometric precipitable liquid water as a function of azimuth from the radiometer (mm); (B) Precipitation intensity at RAD; (C) Rime characteristics of crystals collected at RAD (see sec.2.3); (D) Rime characteristics of crystals collected at SPL (see sec. 2.4); (E) Rotorod liquid water content (g/m^3) at SPL; (F) Radar cloud top (km) and cloud top temp.(C); (G) Radar max reflect.(dBZ); (H) Surf. temp. at RAD (C).

3.2 January 27, 1982 case study

3.21 Synoptic scale and local weather conditions

At 1000Z on January 27,1982 a strong cold front moved through the study area in Northwest Colorado. From the time of surface frontal passage until 1530Z precipitation fell continuously throughout the Park Range region. This precipitation was associated with an area of cloud cover which extended approximately 300 km northwest of the surface front. At 1530Z, the western edge of this cloud system passed over the region and clouds over the valleys and lower elevations rapidly dissipated. During this period, strong mid-level winds maintained localized cloud systems over higher elevations. These cap clouds persisted until well after 1900Z and frequently contained shallow convective elements. The extent of the cap cloud cover decreased during the afternoon and skies were clear by 2100Z.

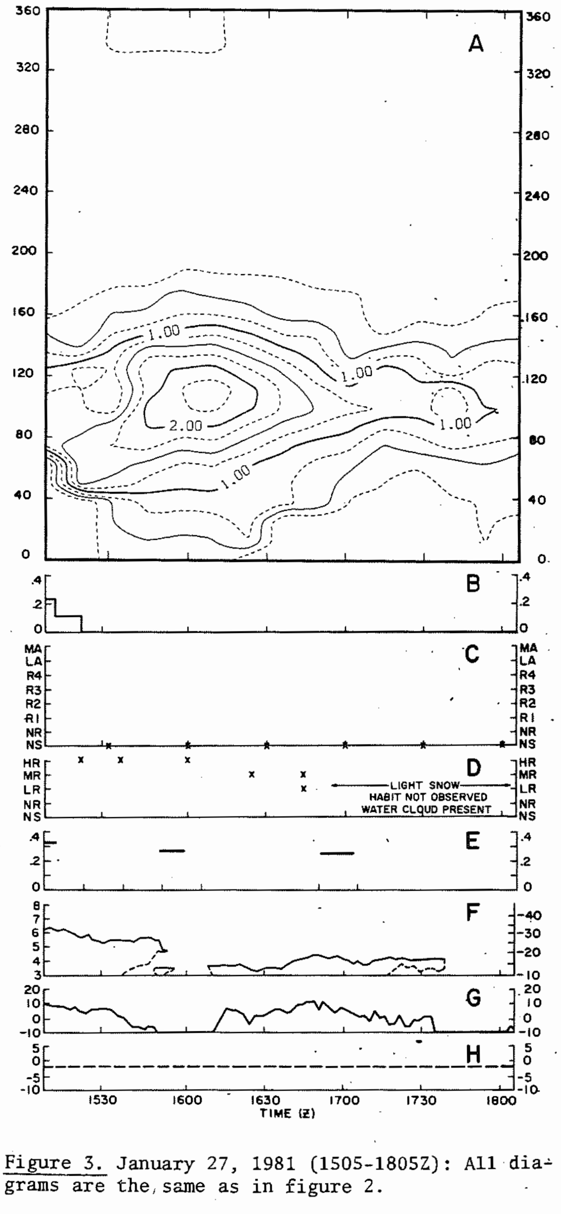

Figure 3. January 27, 1981 (1505-1805Z): All diagrams are the same as in figure 2.

3.12 Storm evolution and liquid water distribution

The January 27, 1982 storm system moved rapidly through the Park Range area, producing about seven hours of snowfall. Radiometric scans were performed during the latter disipating stages of this system. During this period, a shallow cap cloud was present over the Park Range. The edge of the cloud extended west of RAD, but the cloud produced no precipitation at RAD or other valley observation sites. The cap cloud contained shallow convective elements. These convective cells were primarily along the ridgeline embedded in the stratiform cap. More important to the production of liquid water in this cloud was the strong orographic forcing of the airflow due to exceptionally strong mid-level winds. The component of the 700 mb wind normal to the barrier was 21.7 m/s at 1600Z. Thes winds reduced substantially during the three hours following 1600Z. By 1900Z, 700 mb wind speeds normal to the barrier had reduced to 8.5 m/s. During this period, the extent of the cap cloud over the Park Range decreased. Precipitation at SPL was light in intensity between 1500 and 1800Z, gradually reducing as the mid-level wind speed declined.

The time evolution of the supercooled water field and all associated parameters are shown on figure 3. From the radiometric scans, it is evident that virtually all of the liquid water in this cloud system was concentrated over the windward slopes of the barrier. The liquid water contents decreased slowly with time, indicating that the production of liquid water was primarily due to the orographic component of the vertical motion field. It is likely that a component of this liquid water was also due to vertical motion associated with the weak embedded convection occuring along the ridgeline.

The presence of this liquid water was confirmed both by ice crystal observations at SPL and by the Rotorod liquid water content measurements. During the observation period, the cloud enveloping Storm Peak had liquid water contents ranging from 0.25 to 0.32 g/m^3. Although only light precipitation fell at the lab, all of the precipitating crystals were rimed. During the first hour of radiometric scans, crystals were heavily rimed. The amount of rime reduced with time as the cloud system slowly dissipated, but the laboratory remained in a liquid cloud throughout the period.

4. SUMMARY AND CONCLUSIONS

This paper has used two case studies to illustrate the use of the scanning dual-channel radiometer in determining the spatial and temporal distribution of supercooled water in wintertime mountain cloud systems. In the complete analysis, which included nine independant storms, several significant features of the evolution of the cloud water field were apparent. The various storms in the complete data set occured in pre-frontal,post frontal, and orographic enviornments and included systems with convective bands, cellular convection, stable wide area clouds and clouds formed primarily by orographic lifting. The cloud structure and liquid water distributions were studied with the complete network of instrumentation outlined in this paper. Details concerning additional storms will be presented at the conference. From the complete analysis, the following conclusions concerning the distribution of supercooled cloud water in wintertime storms occuring over the Northern Colorado Rockies were developed:

(1) The presence of liquid water within the cloud systems was inversely related to storm intensity. Intense storm periods with high,cold tops, heavy precipitation rates and high radar reflectivities had little liquid water present in the system. Shallow cloud systems with low precipitation rates and weak reflectivities had the highest liquid water contents.

(2) Liquid water presence in convective bands was generally limited to a short period during the developing stage of the band. In nearly all cases of band passage, cloud water present initially in the system was rapidly depleted by rapid growth of crystals by diffusion and accretion. During the majority of the time that the convective band affected the region, the entire cloud system had minimal liquid water contents.

(3) The distribution of supercooled water in the stratiform regions of the cloud system were closely related to the strength of the orographic component of the airflow. In the pre-frontal enviornment, the cross barrier component of the wind was found to vary significantly depending on the orientation of the approaching frontal system. Liquid water concentrations were highest when this component was large. In the post-frontal enviornment, this component was generally large and liquid water was commonly observed.

(4) In virtually all stratiform cloud systems, the majority of the liquid water is concentrated over the windward slopes of the mountain range. In most of these cloud systems, large enough quantities of cloud water were present upstream of the range to at least cause minimal riming of crystals falling in the valley. In some cases, values were much higher and riming was extensive.

(5) The temporal variation of the supercooled cloud water distribution in all cloud systems is large, even in systems which appear to be steady state on the mesoscale.

(6) The conversion from shallow systems with high liquid water contents and low precipitation rates to deep systems with low liquid water contents and high precipitation rates is accompanied by a systematic evolution in the microphysical characteristics of the precipitation. Prior tothe onset of the deep storm system, precipitating crystals are usually single, and are rimed. The degree of rime is a strong function of elevation, since crystals falling near the top of the mountain have to pass through the zone of high water content over the windward slopes. During the initial stages after the onset of the deep storm, the intensity of accretion increases as large numbers of crystals sweep out the cloud drops remaining in the system. Within thirty minutes, all of these particles have precipitated or were carried over the barrier. From this point onward until the system returns to a more shallow structure, the preciptation is dominantly composed of aggregates of unrimed crystals.

5. REFERENCES AND ACKNOWLEDGEMENTS

1. Hogg, D.C., F.O. Guiraud, J.B. Snider, M.T. Decker and E.R. Westwater, 1983: A steerable dual-channel microwave radiometer for measurement of water vapor and liquid in the troposphere. J. Clim. Appl Meteor. 22,5 789-806
2. Magono, C. and C.W. Lee, 1966: Meteorological classification of natural snow crystals. J. Fac. Sci. Hokkaido Univ., Series VII (Geophy.) 2, 321

The authors wish to thank the Bureau of Reclamation and the Wave Propagation Laboratory at NOAA for their support. This research was funded under NSF grant ATM-8219767.

MICROSTRUCTURE OF ANTARCTIC COASTAL CLOUDS*

V.K. Saxena and F.H. Ruggiero

Department of Marine, Earth and Atmospheric Sciences
North Carolina State University, Raleigh, NC 27650 U.S.A.

1. INTRODUCTION

During October-November, 1980 and December 1982-January 1983, the Cloud Aerosol Interaction Lab (CAIL) of North Carolina State University participated in field experiments over the Antarctic coast for investigating the cloud microstructure. In particular, measurements of the mirophysical parameters of Antarctic coastal stratus clouds were made. The objective of the field study were (1) determination of the cloud nucleation characteristics of aerosols particles that participate in the formation of Antarctic coastal clouds, (2) study of variations in the cloud droplet size spectra through direct measurements within the clouds, (3) simultaneous measurements of the Aitken nuclei concentrations, and (4) determination of the primary chemical constituents of cloud water collected directly by means of aircraft penetrations. Some of the results of the latter two objectives have previously been reported by Saxena (Refs. 1,2). This paper concerns itself with the first two objectives. We use the observations of the activity spectrum of cloud condensation nuclei in the substratus layer with simultaneous observations of cloud droplet size distribution to analyze recent models proposed for the evolution of the cloud droplet spectra. This is accomplished by examining the correlation between the CCN activity spectrum and the droplet size spectrum.

2. INSTRUMENTATION

The observational platform used for this study was an instrumented C-130 aircraft described by Hutchins and Wall (Ref. 3) and Saxena (Ref. 1). The aircraft made use of the Airborne Research Data System (ARDS) which was equipped with sensors for pressure, temperature, wind, humidity, and aircraft position. In addition the C-130 was specially equipped with a Forward Scattering Spectrometer Probe (FSSP) similar to that described by Knollenberg (Ref. 4) to measure the cloud droplet size distribution and a cloud condensation nucleus (CCN) spectrometer developed by Fukuta and Saxena (Refs. 5,6) to measure the spatial and temporal distributions of CCN.

Sampling of the cloud droplet size distribution was done at 10 sec. intervals with the FSSP. From the size distribut ons the mean diameter ($\bar{D}$), total concentration (N), liquid water content (l.w.c.), and the diameter below which 95% of the liquid water is continued (D_{95}) were calculated. The probe was operated in the size range 2-32 μm with a resolution of 2 μm.

The CCN spectrometer took samples every 60 sec and measured concentration (n) in the supersaturation range 0.15-1.2%. This lead to values of concentration and slope parameters of the conventional representation $n = CS^k$.

*Research supported by the National Science Foundation under grant no. DPP-7922058.

The sampling site is shown in Fig. 1. Sampling was carried out on days when the Antarctic Coastal Stratus Clouds were detected from the satellite imagery. Measurements of the cloud droplet size distribution were made on November 3-4, 1980, and November 5, 1980. CCN measurements are presently available for November 3-4, 1980.

3. RESULTS AND DISCUSSION

3.1 Cloud Geometry

Two dimensional cloud geometries for November 3-4 and 5 are presented in Figs. 2 and 3. The cloud boundaries were determined in part by the liquid water content calculations and notes made by one of us aboard the aircraft at the time of the observations. A l.w.c. of 0.05 g/m^3 was used as a threshold value in helping to determine cloud boundaries.

4.2 Cloud Droplet Spectra

Table 1 summarizes the measurements taken and calculations made for each cloud observed. It is noteworthy that a strong correlation between the height of the cloud base and $\bar{D}$ exists. The correlation coefficient was found to be 0.93. Although the sample size is small, the correlation seems strong enough to be significant.

The observed spectral broadening with height is also revealed by the drop size distribution for individual clouds at different heights. All the clouds sampled were found to have a bimodal size distribution (Figs. 4 and 5) with one peak of concentration of drops appearing at about 2-4 μm and another one somewhere in the range of 10 to 18 m. The diameter at which the second peak occurs seems to be a function of height. In Fig.

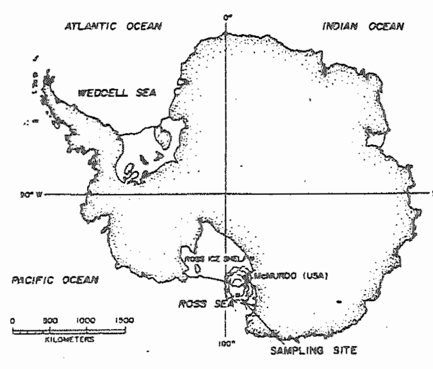

Figure 1. Sampling site in Antarctica where coastal clouds were penetrated.

Table 1. Measured and derived parameters for clouds sampled on November 3 and 5, 1980

Date	Time (GMT)	Cloud Droplet CONC (cm^{-3})	Height of Cloud Base (m)	Cloud Base Temp. °C	Conc. Parameter C (cm^{-3})	$\bar{D}$ (μm)	D95 (μm)	lwc gm^{-3}
11/3/80	23:21:10-23:27:00	79.9	700	-5.25	242	9.24	23.28	0.10
11/3/80	23:40:10-23:46:20	52.2	1450	-10.52	250	11.89	23.21	0.09
11/3/80	23:47:50-23:48:10	91.8	1400	-6.50	121	13.29	21.57	0.18
11/5/80	08:10:00-08:13:30	32.6	1900	-18.59	-	13.52	24.85	0.06
11/5/80	08:22:10-08:22:40	101.0	550	-7.89	-	9.27	19.95	0.07
11/5/80	08:29:50-08:31:30	95.1	500	-8.81	-	9.90	18.63	0.09
11/5/80	08:33:20-08:33:50	87.7	500	-7.29	-	9.77	18.57	0.07

5, the size distribution of a cloud with a base at 500m MSL is shown and it has a second peak in concentration corresponding to a diameter of 10 μm. This is contrasted to Fig. 4 which shows the size distribution of a cloud with a base at 1450m MSL and a second peak at a diameter of 18 μm. Within the cloud itself, there is a tendency for spectral broadening to occur with height. Figure 6 shows the cloud drop size distribution for two different heights within one cloud. Near the cloud base the second peak occurs at a diameter of 10 μm while near the cloud top, the second peak in concentration corresponds to a diameter of 22 μm.

Though the observation of peaks in concentration at two different diameters is interesting, it certainly is not unique. Bimodal size distributions have been observed elsewhere for cumulus (Refs. 7,8,9) and Arctic stratus (Ref. 10) clouds. Cumulus clouds were observed by Warner (Ref. 7) to have peaks at the diameters of 10 and 25 μm. In their work with Arctic stratus Tsay and Jayaweera (Refs. 1C found concentration peaks at 6 and 16 μm. They also noticed that the spectral broadening occurred at a higher level within a cloud.

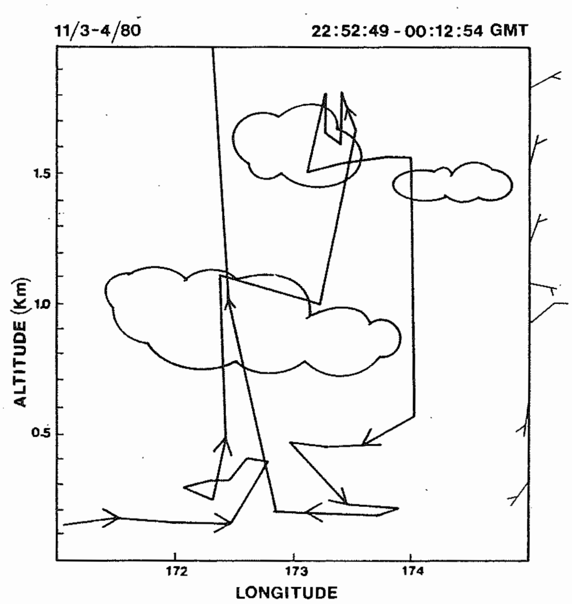

Figure 2. Two dimensional N - S reconstruction of cloud geometries observed on November 3-4, 1980.

4.3 Comparison of observations with theory

Recently three theories have been proposed to explain the coexistence of large concentrations of large and small drops in a cloud. Johnson (Ref. 11) proposed that giant and ultra-giant nuclei exist which form the large drops. A second theory proposed by Manton and Warner (Ref. 12) suggests that the spectral broadening would be the result of mixing of cloudy parcels and differential molecular absorption between the small and large drops. The third one commonly called the inhomogenous mixing model, discussed by Baker and Latham (Refs. 13,14) and Baker et. al. (Ref. 15) is based on the inhomogenous mixing of dry air with the cloudy air. The observations of the Antarctic coastal stratus clouds seem to be most easily explained by this latter model.

In the inhomogenous mixing model individual cloud drops may be involved several times in cloudy and dry air and when the time constant for the turbulent diffusion is smaller, the cloud drops may completely evaporate upon their contact with the dry air blob. This will continue to happen till the dry air is saturated. Once the saturation is achieved, the slow mixing process will separate the rest of the drops without causing any evaporation. In the model, a given number of drops in a size range is evaporated and each is reduced to the size of an activated CCN at each step of the entrainment process. Consequently, total drop concentration remains unchanged although smaller drops will be generated at the expense of larger ones thus giving the larger drops an advantage of serving as "giant nuclei" and growing bigger yet. Thus, the observed spectral broadening may be

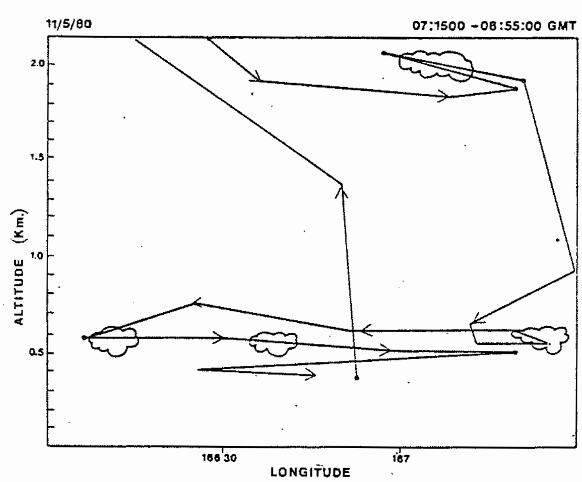

Figure 3. Two dimensional N - S reconstruction of cloud geometries observed on November 5, 1980.

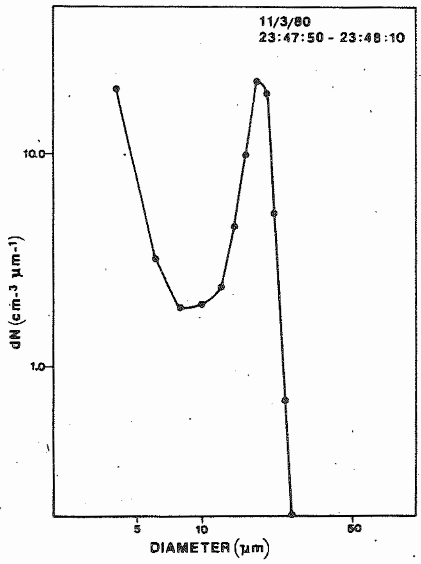

Figure 4. Droplet size distribution for a cloud with base at 1450mMSL sampled on November 3, 1980.

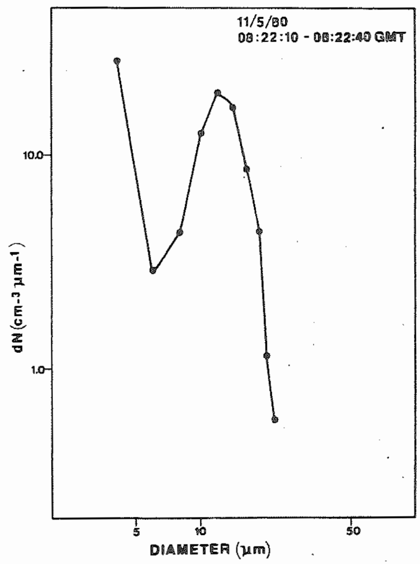

Figure 5. Droplet size distribution for a cloud with base at 500m MSL sampled on November 5, 1980.

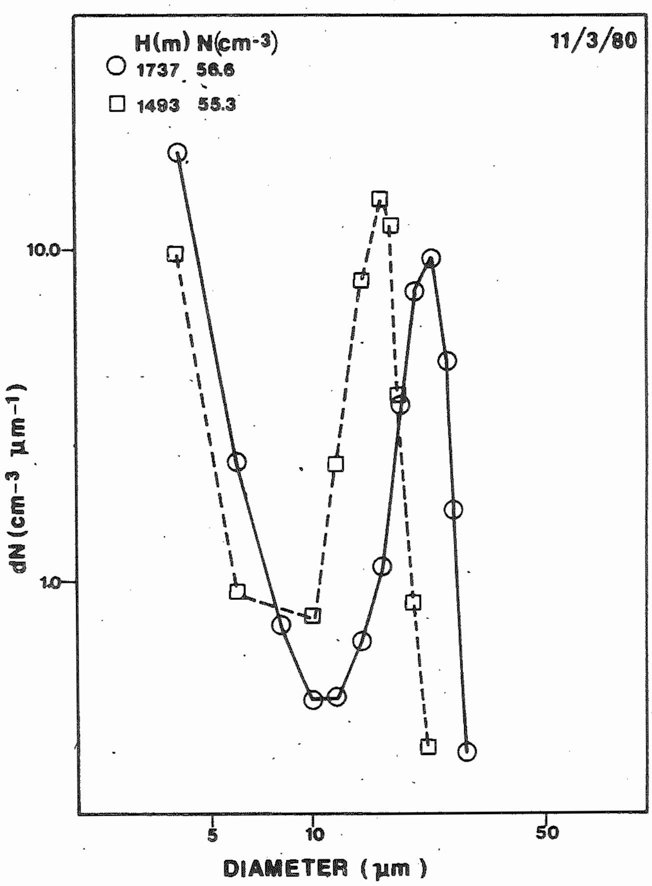

Figure 6. Droplet size distribution for near the top and near the bottom of a cloud sampled on November 3, 1980.

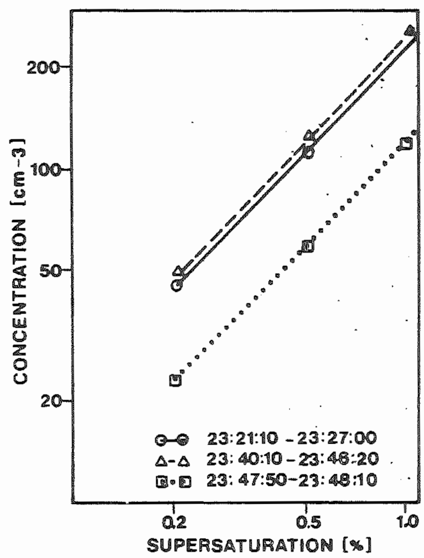

Figure 7. Observed CCN concentration as a function of supersaturation used for estimating the cloud supersaturation on the basis of the one-to-one correspondence method.

produced by the entrainment process. The small differences of size distributions between that of the Antarctic coastal clouds and other clouds (Refs. 7, 8, 9, 10) are probably due to the spatial and temporal variation in the process of inhomogenous mixing. The increase of mixing with height also could explain the spectral broadening that occurs with increasing height both within the cloud and with different clouds at different heights.

4.4 CCN Spectra

Measurements from the CCN spectrometer are available for November 3-4, 1980. The data are represented by the conventional $n=CS^k$ form. An average value of 1.03 was found for k for the entire flight. The measured values of C for the areas below each cloud are listed in Table 1. With these values for C and k and assuming that the total number of cloud drops N, represents the activated CCN (See Fig. 7), the supersaturations that are realized in the Antarctic clouds are found to be 0.34%, 0.22% and 0.76%. Supersaturations as high as 0.40% have been previously reported in fogs by Gerber (Ref. 16) and the theoretical considerations for such high supersaturations have been discussed by Saxena and Fukuta (Ref. 17). The first two values, namely 0.34% and 0.22% seem to be reasonable. However, the third value of 0.76% seems to be too high although there could be a possibility that higher than normal supersaturations may indeed exist due to the fact that with the limited concentrations of CCN available, the water vapor depletion may be very limited or nonexistent. Alternatively, it could result from some instrumental errors. It is unlikely that both FSSP and the CCN spectrometer were malfunctioning at the same time because no problems were observed from the readings of either instrument at any other times. It is in order here to mention that Telford and Chai (Ref. 18) and Telford and Wagner (Ref. 19) have argued that the CCN activity spectrum in the cloud forming air has an insignificant influence on the evolution of the cloud droplet size spectra and the one to one correspondence may not be valid.

4. CONCLUDING REMARKS

Antarctic coastal cloud-aerosol interactions are of consequential importance in understanding the hydrologic cycle of the coastal regions, the thermodynamics and the energy balance, extent of cloud cover during austral summer months, and the chemical nature of the precipitation accumulated on the surface. Despite this, the measurements reported here represent the first done of their kind.

The droplet size spectra of Antarctic coastal stratus clouds exhibit a bimodal distribution. One peak corresponds to the haze drops with diameter less than 4 µm and the other peak is associated with the diameter at which cloud droplets usually occur (10 µm <d <18 µm). The broadening of the cloud droplet spectrum as a function of height from the cloud base and also the height of the cloud base seem to be reasonably explained by the inhomogenous mixing model (Refs. 11,12,13). The CCN activation spectrum was examined and it was found that assuming a one-to-one correspondence between cloud droplet and activated CCN, rather high supersaturations (although below 1%) are needed in order to produce the total number of observed cloud droplets. Theoretical work does exist (Ref. 17) that explains how the high supersaturations could occur. Supersaturations of 0.40% have been found (Ref. 16) in mid latitude fogs so it may not be unconceivable, given the very pristine nature of the Antarctic atmosphere, that higher supersaturations would occur in Antarctic clouds due to possible absence of vapor depletion effect.

REFERENCES

1. Saxena, V.K. 1981, Microphysical measurements in Antarctic Coastal Clouds and the subcloud layer, Antarctic J. of the US. 16(5), 187-188.

2. Saxena, V.K. 1983, Evidence of the biogenic nuclei involvement in Antarctic Coastal Clouds, J. Phys. Chem. 87, 4130-4134.

3. Hutchins, R.A. and Wall, J.G. 1981, LC-130 antarctic research flights, 1980-1981, Antarctic J. of the US. 16(5), 231-232.

4. Knollenberg, R.G. 1981, Techniques for probing cloud microstructure, clouds, their formation, optical properties and effects, P.V. Hobbs and A. Deepak, Eds., Academic Press, 495 pp.

5. Fukuta N. and Saxena, V.K. 1979, A horizontal thermal gradient cloud condensation nucleus spectrometer, J. Appl. Meteor. 18, 1352-1362.

6. Fukuta, N. and Saxena, V.K. 1979, The principle of a new horizontal thermal gradient cloud condensation nucleus spectrometer, J. Rech. Atmos. 13, 169-188.

7. Warner, J. 1969, The microstructure of cumulus cloud. Part I general features of the droplet spectrum. J. Atmos. Sci. 26, 1049-1059.

8. Durbin, W.G. 1959, Droplet Sampling in cumulus clouds. Tellus 11, 202-215.

9. Eldridge, R.G. 1957, Measurements of cloud dropsize distributions J. Meteor 14, 55-59.

10. Tsay, S. and Jayaweera, K. 1983, Physical Characteristics of Arctic Stratus Clouds. Submitted to J. Clim. App. Meteor.

11. Johnson, D.B. 1982, The role of giant and ultragiant aerosol particles in warm rain initiation J. Atmos. Sci. 39 448-460.

12. Manton, M.J. and Warner, J. 1982, On the droplet distribution near the base of cumulous clouds. Quart. J. Royal Meteor. Soc. 108, 917-928.

13. Baker, M.B. and Latham, J. 1982, A diffusive model of the turbulent mixing of dry and cloudy air. Quart J. Roy. Meteor. Soc. 108, 871-898.

14. Baker, M.B. Corbin, R.G. and Latham, J. 1980. The influence of entrainment on the evolution of cloud droplet spectra: I. A model of inhomogenous mixing. Quart. J. Roy. Meteor. Soc. 106, 581-598.

15. Baker, M.B. and Latham, J. 1979, The evolution of droplet spectra and the rate of production of embayonic raindrops in small cumulus clouds. J. Atmos. Sci. 36, 1612-1615.

16. Gerber, H.E. 1981, Microstructure of a radiation fog. J. Atmos. Sci. 38, 454-458.

17. Saxena, V.K. and Fukuta, N. 1982, The supersaturation in fogs J. Rech. Atmos. 16, 327-335.

18. Telford, J.W. and Chai, S. 1980, A new aspect of condensation theory. Pageoph, 118, 720-742.

19. Telford, J.W. and Wagner, 1981, Observations of condensation growth determined by entity type mixing. Pageoph. 119, 934-965.

SOME REGULARITIES OF THE TRACER ^{210}Po DISTRIBUTION IN RAINDROPS

S.S. Shalaveyus, R.G. Krankalis, R.V. Leskauskas

Institute of Physics of the Academy of Sciences of the Lithuanian SSR

Microphysical processes in convective clouds are much more investigated than mesoscale dynamical processes. In the investigation of microphysical processes laboratory experiments are used while in the investigation of mesodynamical phenomena expensive field experiments are conducted. The investigation of the spreading and washout of the tracers injected artificially into the clouds enables to obtain new data on the dynamics of development and decay of the clouds and on the precipitation generation processes. Using radioactive tracers it is possible to reveal simultaneously a number of peculiarities of the aerosol admixtures washout by raindrops. The tracer method of the clouds investigation gives us an idea of the microphysical capture mechanisms of tracer particles by the cloud and rain droplets (Refs.1, 2, 8).

The data of 23 field experiments conducted on the proving grounds in the period 1972-1982 are used for the determination of some reguliarities of tracer ^{210}Po injected into a local space of a Cumulonimbus cloud.

The technique of conducting field experiments is described in (Refs. 5, 6). A tracer was injected into a cloud by means of a hail-suppressing rocket. The spraying of a tracer was carried out by explosions in a determined part of a Cumulonimbus cloud. The epicentre of the injection and the height of tracer injection were determined by the rocket trajectories and the given explosion time of the rocket head.

A series of subsequent samples of rain drops was collected for an approximate determination of the tracer ^{210}Po injected into a cloud spreading velocity and of the evaluation of the washout ability of different-sized raindrops during rain. Sampling was carried out on a proving ground in several points. On the proving ground with the area about 700 km there were from 7 to 13 posts for the collection of separate droplets. The raindrops left bright spots on the coloured paper. The mass of the raindrop was determined by the radius of the spot. The samples were collected every two minutes during rain. Four days after the collection of droplets the dried chromatographic paper was brought into contact with a nuclear emulsion of type A-2 and it was exposed during 40-60 days. The amount of the tracer was determined by the amount of α-tracks in the droplets of definite size.

An application of radioactive substances injected artificially into clouds for the investigation of the peculiarities of their spreading and washout by raindrops is impossible without knowing their background values in precipitations. It is known that in most cases the radionuclide background levels were determined by the summary precipitation samples, they were not concretized for the precipitations from different types of clouds and the radioactive background of droplets was not determined in dependence of their sizes (Ref. 3).

An attempt was made to determine statistically reliable distributions of natural ^{210}Po in the raindrops from Cumulonimbus clouds depending on the sizes of raindrops. Both the data obtained during the background experiments and during the experiments with artificial tracer injection into the cloud were used. The raindrops with radii 0.24-2.05 mm were investigated. More than ten thousand droplets were investigated. Measurements showed that the greatest amount of raindrops consists of droplets with radii exceeding 1.10 mm (70 %). The dependences obtained from the natural ^{210}Po distribution in droplets by their sizes were approximated using the method of least squares. The summary distribution of the natural ^{210}Po amount in raindrops depending on their sizes is of parabolic shape.

As the measurements showed the background values of ^{210}Po in droplets ranged from $3.1 \cdot 10^{-8}$Bq (for R = 0.24 mm) to $1.6 \cdot 10^{-6}$Bq (for R = 2.05 mm). It is determined that the droplets falling out at the beginning of rain were of the greatest radioactivity, i.e. a decrease of ^{210}Po concentration in raindrops during the rain was observed.

For the evaluation of time moment of the appearance of raindrops with the artificially injected ^{210}Po several criteria are selected. It is partly admitted that the time of appearance of the first maximum in the specific radioactivity time distribution in the ground measurements points coincides with the time moment of the appearance of tracer ^{210}Po (Ref. 3). It should be noted here that the maximum value of specific radioactivity is obtained both due to a change in the droplets distribution according to their sizes during rain and due to the droplets evaporation.

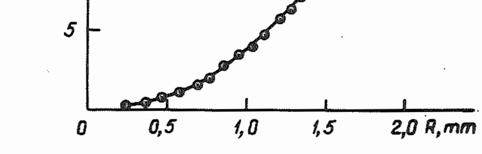

Figure 1. The summary distribution of the amount of natural ^{210}Po in raindrops of Cumulonimbus clouds in dependence of their sizes. The vertical lines denote the mean square deviations.

It is our opinion that the time of the

appearance of tracer ^{210}Po coincides with the time of appearance of the first maximum on the curves of the tracer amounts distribution in raindrops of definite size. The droplets with effective radii, i.e. the droplets which wash out the greatest amount of tracer ^{210}Po, are investigated. In some cases the droplets with predominating radii were investigated.

The vector of arrival velocity of droplets with ^{210}Po to the ground level sampling point is determined as a sum of two perpendicular vectors of vertical falling velocity and horizontal transport velocity. In this case the arrival velocities of raindrops with ^{210}Po are minimum because in reality the raindrops move at much more complex trajectories.

It is obtained that the arrival velocity of raindrops with the tracer at the ground level measuring points range from 2 to 25 ms^{-1}. The mean velocity is equal to 14 ms^{-1}. The value of the definite velocity in a given sampling point depends evidently on whether this point is located under the experimental radar cell or at some distance from it at the moment of tracer injection. In the first case the tracer arrival velocity changes from 8 to 25 ms^{-1} (mean velocity 16 ms^{-1}), in the second case - from 2 to 12 ms^{-1} (mean velocity 6 ms^{-1}). If several separate collection points of raindrops are located under the experimental cell at the moment of tracer ^{210}Po spraying, the velocity values obtained correlate with the distance from these points to the tracer injection epicentre. The closer the ground measurements point is, the faster ^{210}Po arrives in droplets to this point (Figure 2). The dependence is obtained for the sampling points located at the distance of not more than 2 km from each other. It should be noted that such tracer arrival velocity distribution in sampling points is independent of the cloud system displacement direction relative to the location of measuring points.

By the ^{210}Po injection into the frontal part of the cell the tracer spreads rapidly in the whole cell independently of the injection height. The arrival of tracers at the cloud displacement front coincides with displacement time and trajectory of the cells. The arrival velocity of tracers ranges from 12 to 25 ms^{-1}, mean value - 19 ms^{-1}. If the cell moves above the observation site at great velocity (70 -100 kmh^{-1}), ^{210}Po is rapidly transported from the injection point in the direction opposite to the movement of the cloud system. The tracer arrival velocity ranges from 20 to 24 ms^{-1} with a mean value 23 ms^{-1}.

By the tracer injection to the centre of the cell, the admixture spreads in all directions from the injection point and practically independently of the air stream direction at the cloud height. According to our data the arrival velocity of ^{210}Po with droplets at the sampling points is equal to 11-20 ms^{-1} with a mean value 15 ms^{-1}. The velocities are determined in the points located under the cell at the moment of ^{210}Po injection.

In some experiments ^{210}Po was injected into the rear part of the cell during its decay. In these cases the tracer was washed out mainly at the small area under the injection epicentre with the velocity 23-25 ms^{-1}. The velocities are determined in the zone of intensive precipitation. However, there are cases when some part of the tracer is taken away by the air streams to the other parts of the experimental cell and washed out by raindrops at a greater area. In these cases the tracer arrival velocities at the measuring points are equal to 10-11 ms^{-1}.

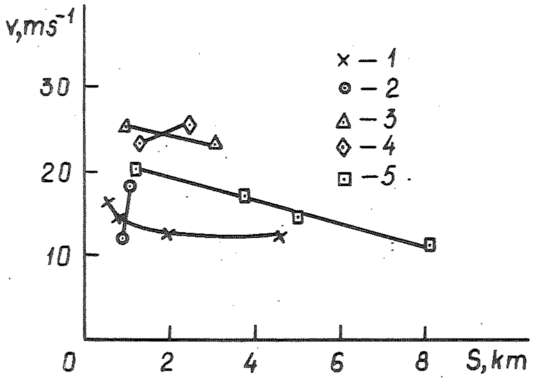

Figure 2. The dependence of the arrival velocities of tracer ^{210}Po in raindrops to the ground level sampling points located under an experimental cell at the moment of tracer injection, at the distance of the points from the epicentre of ^{210}Po injection. Curve 1 - the field experiment on 17th June, 1972, 2 - 24th June, 1972, 3 - 18th July, 1972, 4 - 2th August, 1974, 5 - 20th July, 1974.

It should be noted that the great velocities of tracer spreading were noted in the points which at the moment of ^{210}Po injection were located in opposite direction from the general air stream and from the radar cell displacement (Figure 3). It suggests that inside the cells there exist convective streams which transport the tracer at great velocities into a rear part of the cloud. Due to strong turbulence ^{210}Po is captured rapidly by the cloud and rain droplets and in consequence of descending currents it arrives rapidly at the earth surface.

Field experiments showed that in the presence of several cells in the cloud the tracer spreads mainly in the cell into which it was injected. This conclusion is true in cases when the tracer is injected into a mature cell. By the disintegration of the cell the remainders of the tracer may be transported at great distances (Refs. 6, 7).

The density of ^{210}Po fallout or its amount washed out by raindrops of definite radius on the unit of area was determined by us by multiplying the mean amount of the tracer in the droplets of the given size by their number. It was statistically determined that the greater the radius of raindrops, the greater on the average is their tracer radioactivity (Figure 4).

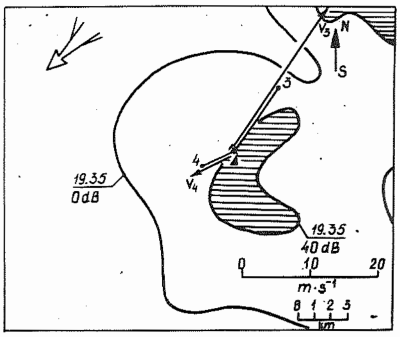

Figure 3. The distribution of the tracer ^{210}Po arrival velocities to the ground level sampling points No. 3, 4 during the field experiment on 17th July, 1972. A solid line denotes the cloud by the attenuation of radar signal by 0 dB, shaded zones - by 48 dB, a triangle - the launching place of the rocket carrying the tracer, an asterisk - the epicentre of the tracer injection.

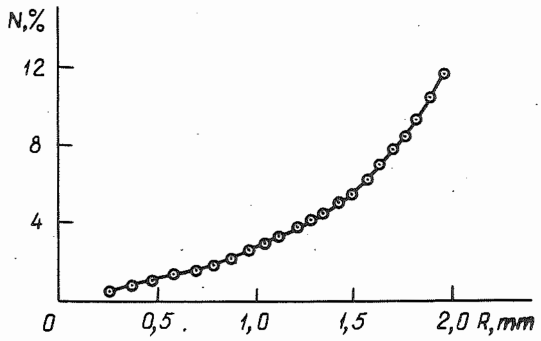

Figure 4. The distribution of the amount of tracer ^{210}Po in raindrops of Cumulonimbus clouds in dependence of their radii (after the measurements of more than $2 \cdot 10^4$ droplets). The vertical lines denote the mean square deviations.

We evaluated the amount on the unit of area of ^{210}Po washed out by raindrops by counting the number of droplets collected on the area exceeding by an order of magnitude the area of nuclear photoplates of type A-2. In most cases it was obtained that the tracer ^{210}Po fallout density distributions by the sizes of raindrops have a marked maximum in the range of radii 0,57-1.47 mm (a mean value is equal to 1.10 mm. The value of the maximum depends mainly on the raindrops amounts distribution considering the radii. In some cases a second maximum in the fallout density distributions depending on the sizes of droplets was obtained. The second maximum was usually 1.5-2 times lower than the first one and it was observed by $R > 1,19$ mm. There are also distributions in which the amount of the tracer washed out on the unit of area increased on the average with the increase of the sizes of raindrops. It should be noted that for the summary distributions of the ^{210}Po fallout densities and of the raindrops mass by the radii it was characteristic that the maxima of dependences almost coincide in majority of cases. The curve of recurrence of the raindrops sizes distribution according to their sizes intersects the range of their coincidences (Figure 5).

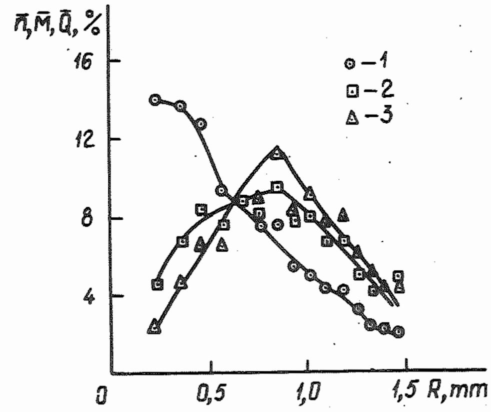

Figure 5. The summary mean distributions of the number of raindrops (curve 1), of their mass M (curve 2) and of tracer ^{210}Po fallout density Q (curve 3) by the raindrops sizes during the field experiment on 20th July, 1974. Other denotations as in Fig. 1.

The data obtained during the field experiments suggest an idea that there are raindrops of optimal sizes relative to their number, mass and amount of tracer ^{210}Po washed out by them.

REFERENCES

1. Mason, B.J., 1961. Physics of Clouds (in Russian). Gidrometeoizdat, Leningrad.
2. Shmeter, S.M., 1973. Physics of Convective Clouds (in Russian). Gidrometeoizdat, Leningrad.
3. Vebriene, B.K., 1971. Investigation of the radioactivity of separate precipitations elements and some questions of the admixture washout from the atmosphere (in Russian). Cand. dissertation, Vilnius, 174 pp.
4. Shalaveyus, S.S., Styra, B.I, Vebriene, B.K., Shpirkauskaite, N.K., Morkeliunas, L.J., Stelingis, K.M., Butkus, D.V., Lukshiene, B.I., Dinevich, L.A. and Potapov, E.I., 1977. On admixture spreading in convective clouds (in Russian). Fizika atmosfery, 3. Mokslas, Vilnius, 27.
5. Shalaveyus, S.S., Leskauskas, R.V., Krankalis, R.G. and Vebriene, B.K., 1983. Methods of studying convective storms by means of chemical tracers (in Russian). Fizika atmosfery, 8. Mokslas, Vilnius, 56.
6. Shalaveyus, S.S., Leskauskas, R.V., Krankalis, R.G., Dinevitch, L.A., Dinevitch, S.E., Potapov, E.I. and Livshits, E.M., 1983. Some peculiarities of tracer ^{210}Po spreading in convective storm (in Russian). Fizika atmosfery, 8. Mokslas, Vilnius, 60.
7. Shalaveyus, S.S., Leskauskas, R.V., Krankalis, R.G., Dinevitch, L.A., Dinevitch, S.E., Livshits, E.M. and Potapov, E.I., 1983. Time-space distribution of tracer ^{210}Po concentration and fallout density on a proving-ground (in Russian). Fizika atmosfery, 8. Moks-

las, Vilnius, 68.
8. Gatz, D.F., 1977. A review of chemical tracer experiments on precipitation systems. Atmos. Environ., II, No. 10, 945-953.

SESSION I

MICROSTRUCTURE OF CLOUDS AND PRECIPITATION

Subsession I-2

Solid phase in clouds

MICROSTRUCTURE VARIATIONS IN THE LIFE OF EXTRA TROPICAL CYCLONES

by

Arnold A. Barnes, Jr.
Ian D. Cohen, Capt., USAF

Air Force Geophysics Laboratory
Hanscom AFB, MA 01731 U.S.A.

The Air Force Geophysics Laboratory (AFGL) has used two aircraft, an MC130E turboprop transport and a Lear 36 jet to examine the microphysical structure of extra tropical cyclones. Barnes, Cohen, and McLeod (1982) describe the instrumentation on both airplanes, and list the flights conducted during the program.

The MC-130E provided data at various standard pressure levels for several storms. Varley (1980) and Cohen (1981) reported on the structure of clouds in two of these cases. Cohen (1982) summarized the findings of this part of the project. Flights in the northeast quadrant of the storm were made on consecutive days whenever possible. Data were gathered at the 400, 500, and 700, millibar levels. In some cases, the 300 mb and/or 850 mb levels were also sampled. Particle size, particle shape, and liquid (or ice) water content per unit volume were compared. Plank (1967) devised a "form factor" which describes the shape of the size distributions of the particles in a given sample.

The form factor is described by equation 1:

$$FF = \frac{\sum_{i=2}^{i=n} (2i-1)^3 \alpha_i}{\left[\sum_{i=2}^{i=n} (2i-1)^6\right]^{0.5}} \qquad (1)$$

In using it to categorize a particle distribution, the distribution is divided into size categories. In the case of our flights, the probes used provided distributions in categories. In equation 1, n represents the number of categories, and α_i is the ratio of the number of particles in category i to the total number of particles in the distribution. Each of the three probes used to gather the data has 15 channels, so in our case, a form factor for the entire distribution represents a sum of 45 channels. The value of the form factor will vary between 0 and 1; 0 indicates a completely random distribution of particles, while 1 means that all particles are in the same size category.

In general upper levels (400 millibars and above) showed the greatest consistency in size and shape. At that altitude (about 7 to 10 Km), irregular shaped crystals, called small snow, predominated. The majority of the particles were less than 100 μm in diameter. The form factors tended to be higher (generally .4 to .6) than those observed at lower levels, indicating a lognormal distribution. The warmer temperatures and complex dynamics found near the melting layer resulted in a variety of particle shapes and sizes, and form factors of .3 or less reflecting the non-uniform size distributions.

Figures 1 through 4 show the size distributions at 400 millibars (altitude about 7 Km) and 700 millibars (altitude about 3 Km) on 4 days during the storm of 23-27 March 1978. These figures, from Cohen (1982), show how the size distributions changed as the storm matured and then dissipated. With the exception of 25 March, the 400 mb level (the dotted lines) looked similar from day to day, while the 700 mb distributions vary much more as the storm moves. Shadowgraphs, taken simultaneously with these measurements, showed that the particle shapes also remained more consistent at the 400 mb level.

Dyer and Cohen (1983) made a spectral analysis of horizontal fluctuations of temperature and liquid water content in this storm system. This analysis showed that each stage of the storm had its distinctive characteristics; the earlier stages, when convective activity predominated had peaks at certain frequencies while in later stages, when stratiform activity increased, the spectra were more uniform.

The vertical structure of large scale storms was studied (Lo and Passarelli, 1981, 1982) by making spiral descents with the C-130 at approximately 200 ft/min; a rate which approximates that of a falling snow flake. As snow crystals fall, they go through three distinct stages: deposition, aggregation and breakup. Differing rates of aggregation and breakup due to local differences in temperature and vertical motion are postulated as the causes of the larger variety of particle shapes seen at the lower levels.

Schaller et al (1982) and Cohen and Sweeney (1983) have done further work with the melting layer.

The AFGL study of tenuous clouds also examined microstructure variations of clouds; in this case, thin cirrus clouds. Cohen and Barnes (1980) looked twice at a weak frontal system in New Mexico, while Varley, Cohen and Barnes (1980) looked at the cirrus canopy above a more intense storm in that same area. In the former case, the only cloudiness produced by the system was a small band of cirrus with particles as large as 700 μm ahead of the front, and very thin cirrus with unusually large (1200μm) particles behind it. The more intense storm produced denser cirrus with many particles of 1100 μm or

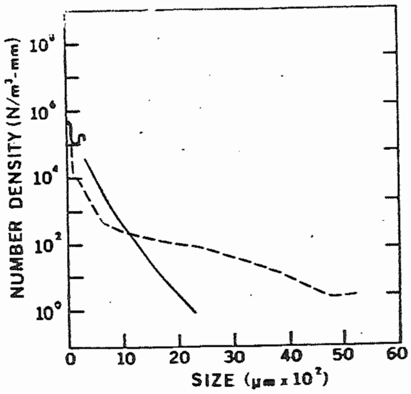

Figure 1. Size distribution of particles at 400 Mbar (solid line) and 700 Mbar (dotted line) on 23 Mar 78.

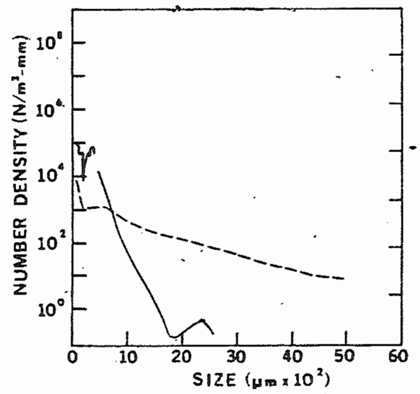

Figure 2. Size distribution of particles at 400 Mbar (solid line) and 700 Mbar (dotted line) on 24 Mar 78.

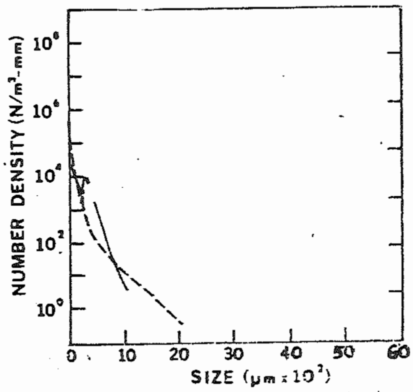

Figure 3. Size distribution of particles at 400 Mbar (solid line) and 700 Mbar (dotted line) on 25 Mar 78.

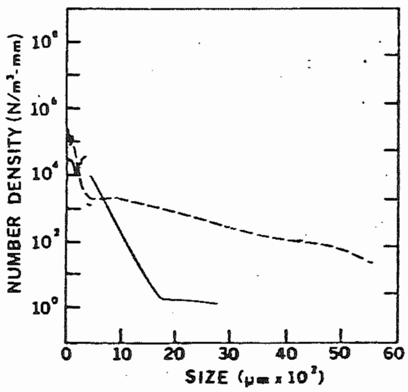

Figure 4. Size distribution of particles at 400 Mbar (solid line) and 700 Mbar (dotted line) on 26 Mar 78.

larger. This was due to stronger updrafts, which brought more moisture to the level of cirrus clouds.

The data provided by the AFGL-instrumented aircraft have been useful defining many aspects of the microstructure of extratropical cyclones. The results have increased our understanding of these storms.

REFERENCES

Barnes, A.A., Cohen, I.D., and McLeod, D.W. (1982), Investigations of large scale storms, AFGL-TR-82-0169, AD A119862.

Cohen, I.D., and Barnes, A.A., (1980), Cirrus particle distribution study, part 6, AFGL-TR-80-0261, AD A096772.

Cohen, I.D., (1982), Development of a large scale cloud system, 23-27 March 1978, AFGL-TR-81-0127, AD A077020.

Cohen, I.D., (1982), Aircraft observations of large scale cloud systems, Preprints conference on Cloud Physics, American Meteor. Soc., Chicago, IL, 15-18 Nov 1982, pp 203-206. AFGL-TR-82-0343, AD A122515.

Cohen, I.D., and Sweeney, H.J. (1983), Melting layer survey-final report, AFGL-TR-83-0200 (in press).

Dyer, R.M., and Cohen, I.D., (1983), Changes in the nature of fluctuations of temperature and liquid water content during the lifetime of a large-scale storm, J. Climate and Appl. Meteor., Vol 22, pp 385-393, AFGL-TR-83-0156.

Lo, K.K., and Passarelli, R.E. (1981), Height evolution of snow size distributions, Proceedings, 20th Conference on Radar Meteorology, American Meteor. Soc., Boston, MA, 30 Nov-3 Dec 1982, pp 397-401.

Lo, K.K., and Passarelli, R.E. (1982), The growth of snow in winter storms: an observational study, J. Atmos. Sci, Vol. 39, pp 697-706.

Plank, V.G. (1977), Hydrometeor data and analyticaltheoretical investigations pertaining to the SAMS rain erosion program of the 1972-73 season at Wallops Island, Virginia. AFGL/SAMS Report No. 5, AFGL-TR-77-0149, AD A051193.

Schaller, R.C., Cohen, I.D., Barnes, A.A., and Gibbons, L.C. (1982), A survey of melting layer research, AFGL-TR-82-0007, AD A115224.

Varley, D.J. (1980), Microphysical properties of a large scale cloud system, 1-3 March 1978, AFGL-TR-80-0002, AD A083140.

Varley, D.J., Cohen, I.D., and Barnes, A.A. (1980), Cirrus particle distribution study, part 7, AFGL-TR-80-0324, AD A100269.

DOMINANT ICE PROCESSES IN SUMMERTIME CUMULUS CLOUDS IN THE BETHLEHEM AREA

R T Bruintjes
South African Weather Bureau

1. INTRODUCTION

For the past three years, four instrumented aircraft have been operated as part of the Bethlehem Precipitation Research Project, conducted in the north-eastern parts of the Orange Free State, South Africa. The area, 200 km in diameter, is essentially a farming region with the majority of roads unpaved. Uncultivated land and exposed soil is common in the area and blowing sand and dust is a frequent occurrence. Bethlehem, as centre of the area, where the research facilities are situated, is a medium-sized town and the only significant population centre. Approximately 85% of the annual precipitation (600-700 mm) falls in the summer months between October and March. Most of this rainfall is the result of convective activity.

The origins of natural ice in summertime cumulus clouds together with the processes that contribute to the evolution of ice crystal concentrations is an important facet to be considered in any weather modification research project. In this paper, a brief account will be given of the observations which are suggestive of a primary process where ice is nucleated at fairly warm temperatures, early in the lifetime of the clouds, on what would seem to be dry soil particles. Secondly a brief account of a possible secondary process of ice generation by crystal fragmentation and via the break-up of rime will be given.

2. PRIMARY ICE

The process of ice nucleating at fairly warm temperatures on dry aerosol particles has been examined by Young (1974) who suggested that the warm temperature glaciation may be the result of contact nucleation of supercooled cloud drops at the cloud edges. Evidence for the effective forming of ice by contact nucleation has been given by Gokhale and Spengler (1972) and Pitter and Pruppacher (1973) who showed that clay and soil particles can nucleate supercooled water droplets at temperatures as warm as -3 to -4 °C. Cerni et al (1980) suggested that enhanced crystal concentrations could be explained by the creation of ice through the evaporative cooling of cloud tops as they penetrate the dry, stable layer. Mossop et al (1968) have also discussed this possibility.

Observations in natural clouds in the Bethlehem area have shown that the concentrations of ice crystal are sometimes much greater than the measured concentrations of ice nuclei at comparable temperatures. Ice crystal concentrations in young growing cumulus clouds are usually between 1 and 10 per litre with the summit temperature of the cloud top warmer than -16 °C fairly early in the lifetimes of the clouds (3-5 minutes).

Several flights with an instrumented aircraft specifically aimed at studying the appearance of first ice have been conducted during the past two years. The aircraft would, for this purpose, fly at the -10 °C level and penetrate young developing cumulus clouds which were growing through the aircraft flight level. The cloud top was always within 150 metres of the flight level. One such case occurred on 23 March 1982. This cloud was separated by more than 10 km from any other convective activity. Figure 1 represents time histories of vertical velocity, liquid water content, pressure, humidity over water and ice and the Rosemont and reverse flow temperatures of the penetration through the young growing turret. The diameter of the turret was about 1 km at the time of penetration. Environmental temperature at the penetration level was around -13 °C.

While the aircraft's true airspeed was about 100 m/s, observations during the first 400 metres showed very low liquid water content values coincident with predominating downdrafts. On the other hand a relatively high liquid water content with a peak of 1,8 g/m^3 was measured during the last 600 metres of the penetration.

Although the instruments' accuracy might be questionable it is interesting to note in Figure 1 that even the humidity over ice never reached 100% or ice saturation. A peak value of only 80% was reached. Relative humidities of 100% with respect to water were measured in other clouds studied during the same flight, which might indicate that the cloud air in this turret was subsaturated. This seems likely when it is taken into account that the aircraft was unable to do a second penetration on this turret because it evaporated and collapsed completely within a minute or two.

In figure 2 time histories of the particle concentrations measured by a PMS2DC probe (25-800 µm) and a PMS1DC probe (20-300 µm) are shown. For the 1DC probe only the concentrations of particles larger than 50 µm are shown, assuming that these particles were all ice particles, because no evidence exists from the slide photos nor replicator photos that any drops larger than 30 µm were present in the cloud. Both probes measured concentrations of between 1 and 5 per litre for the cloud penetration. The images collected by the 2DC probe are shown in figure 3 indicating the existence of plates and sector plates with branches, together with a few small graupel particles. This was supported by the stellar crystal collected on the slide and shown in figure 4. The diameter of the ice crystal is about 230 to 250 µm. Small cloud droplets are also visible on the slide photos.

Sector plates and sector plates with branches seem to be the most dominant crystal types observed in cumulus clouds in the Bethlehem area. These sector plates then apparently grow into sector plates with branches or stellar ice crystals and, after the onset of riming, into graupel particles.

An ice growth model with detailed microphysical treatment developed by Strapp (1977) was used to simulate the natural growth of ice crystals in cloud for this day. According to the model results, a PIC-s crystal nucleated at the -10 °C level would grow to a size of about 250 µm by the time it reached the -12 to -13 °C level. This corresponds well with the size of the particle found on the slide shown in figure 4. The comparison of the model results with the measurements are thus stimulating.

3. SECONDARY ICE

Fragmentation of ice crystals due to collisions has been examined as a possible ice multiplication mechanism by Vardiman (1972), by Hobbs and Faber (1972) and by Juisto and Weickman (1973). While these authors primarily considered the consequences of collisions of vapour grown ice crystals, Vali (1980) considers the breakup of rime accreted on crystals.

The observations relating to the secondary ice process were made in clouds selected according to visual criteria involving active growth, horizontal and vertical dimensions (greater than 2 000 m and 2 400 m respectively), shape, firmness of cloud base, and the absence of a radar echo. The clouds were of continental character with the concentrations and mean sizes of the cloud droplets in the ranges of 600-1100 cm^{-3} and 10 to 15 μm respectively. Cloud top temperatures were generally between -12 and -20 °C. Under these conditions, and as suggested by Vali (1980), rime usually occurs with a filamentary structure of low density.

The growth histories of ice particles are summarised in figures 5 to 7 which show the photographs of the ice crystal slides collected in the clouds. Figure 5 displays a sector plate of about 180 μm in diameter, indicating that the crystal probably nucleated at around -10 °C. The aircraft penetration level was at the -13 °C level. Interesting to note is that the crystal is also just starting to grow branches at the corners of the plate. The next stage is displayed in figure 6 where it is readily seen that the crystal has now grown branches on the corners. The diameter is about 250 μm. The cross-section of the branches is a minimum at the corners of the ice crystal indicating the weakest point in the crystal structure and they become thicker as they get longer. It can be seen that two branches are missing which must have broken off at the weak points in the structure. The missing branches were not detected on the slide, giving rise to the suspicion that they had not broken off during impact on the slide but in the cloud. This is a common finding on the ice crystal slides and the formvar particle replicator operated on another research aircraft.

The last part of the growth history is shown in figure 7 where a graupel particle of about 800 μm in diameter is displayed. From the slide it can be seen that the graupel particle is of a generally loose structure and low density. Considering the splintering on the sides, these types would seem to be very fragile.

When conditions as described above were found to exist, ice crystals in concentrations of between 10 and 100 per litre were measured within 5 minutes after the cloud top first penetrated the -12 °C level. When clouds experienced further growth and a water saturated cloud environment was maintained for more than 5 minutes even higher ice crystal concentrations were detected. In a few cases values of up to a thousand particles per litre were observed.

4. DISCUSSION

To summarize, the following scenario is suggested as the possible sequence of events:

(a) Primary ice is most likely nucleated around the -10 °C level. The mode of nucleation is still in question although the most possible mechanism may be by contact nucleation along the sides of the cloud as suggested by Young (1974).

(b) The crystal habit when crystals are nucleated is mostly sector plates. These sector plates then tend to grow branches, developing into stellar crystals as the ice is taken upward in the cloud. After the crystal dimension exceeds 300 μm further growth is enhanced by riming. These particles then develop into a very low density graupel particles as shown in the slide photographs. As soon as the graupel particles grow to millimetre sizes, collisions between ice crystals and graupel, graupel and graupel particles occur more frequently. Fragments of ice are produced during collisions, mostly due to the low density and loose structure of the graupel, which enhances the ice concentrations. The fragments grow into stellar crystals and become part of the process. Increases in crystal concentrations due to this process can be several orders of magnitude. Prerequisite conditions for this process are:

1. Sufficient moisture supply to maintain supercooled water for at least 4 minutes to start the process and for longer times to get a higher enhancement factor for ice concentrations.

2. The cloud top should reach temperatures in the order of -12 °C or colder (see Prupacher and Klett, p. 459).

3. Water saturation should be maintained long enough to stimulate the growth of stellar ice crystals.

The above mentioned process may represent the most common evolution of the ice process in the project area although there may be a scale difference. The effect of these results on reaching a seeding hypothesis with the classical seeding theories for Bethlehem clouds will have to be considered very carefully if it can show that the extent of this process is sufficient to generate rainfall naturally.

5. ACKNOWLEDGEMENTS

The author wish to thank Mr P S du Toit for his always valuable comments and suggestions regarding this research. The research was done as part of the Bethlehem Precipitation Research Project which is controlled by the South African Weather Bureau.

6. REFERENCES

1. Cerni T A & Cooper A 1980, Reprint, International Conference on Cloud Physics, Clermont Ferrand, France, p. 195.

2. Gokhale N & Spengler J I 1972, Journal of Applied Meteorology, 11,157.

3. Hobbs P V & Faber R J 1972, J. Rech. Atmos. 6,245.

4. Juisto J E & Weickman H K 1973, Bull. Amer. Meteor. Soc., 54,1148.

5. Mossop S C, Rushin R E & Hefferman K J 1968, J. Atmos. Sci., 25,889.

6. Pitter R L, Prupacher H R & Hamielec A E 1973, J. Atmos. Sci., 30,125.

7. Prupacher H R & Klett J D 1978, Micro physics of clouds and precipitation, Dordrecht, Holland, D. Reidel Publ. Co., 713 pages.

8. Strapp W 1977, M.Sc Thesis, University of Toronto.

9. Vali G 1980, Preprint, International Conference on Cloud Physics, Clermont Ferrand, France p. 195.

10. Vardiman L 1972, Atmos. Sci. Paper No. 191, Colo. St. Univ.

11. Young K C 1974, J. Atmos. Sci., 31,768.

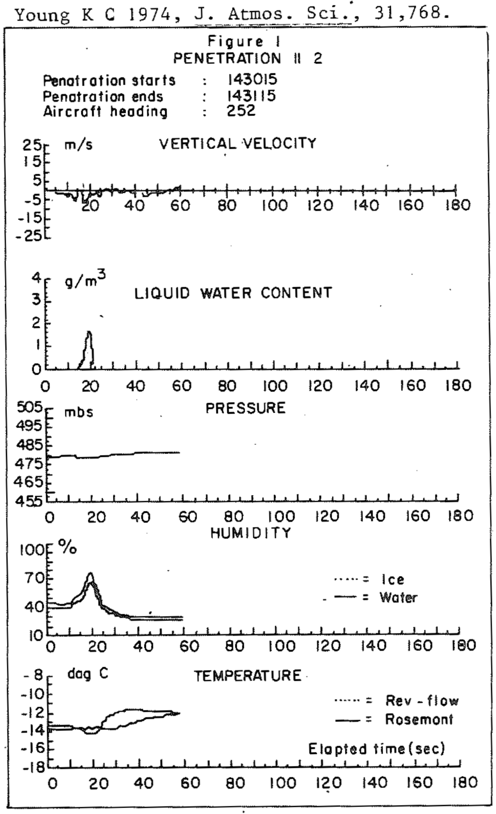

Figure 1
Time histories of microphysical parameters

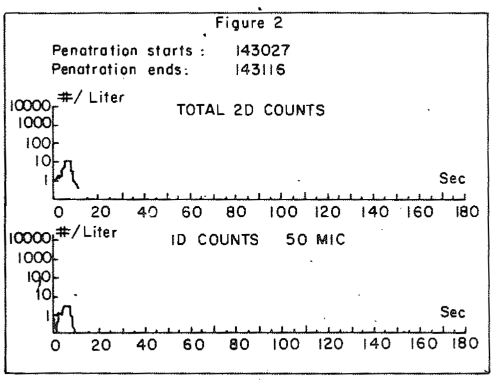

Figure 2
Time history of particle spectra

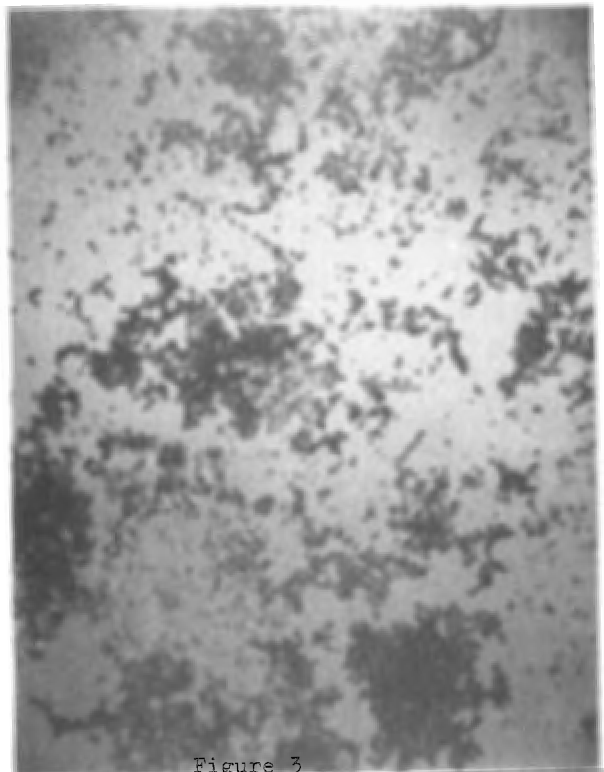

Figure 3
Stellar ice crystal (240μm diameter)

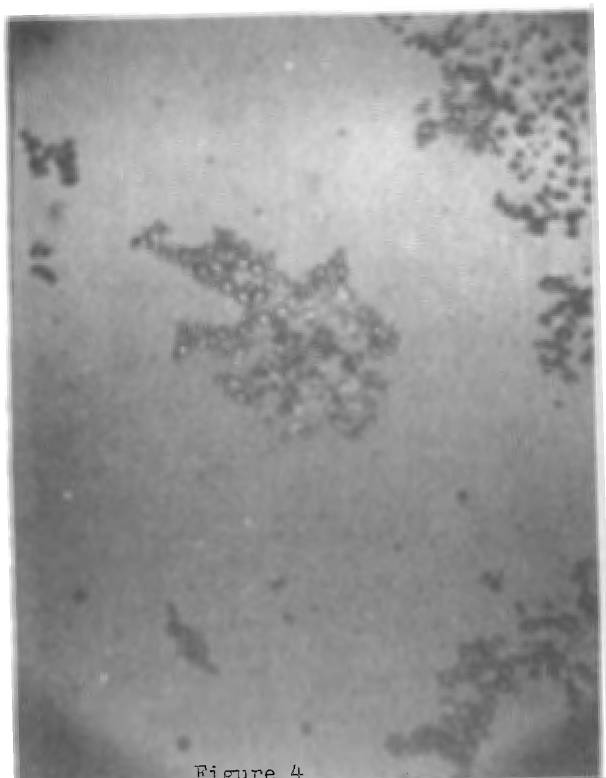

Figure 4
Sector plate (180μm diameter)

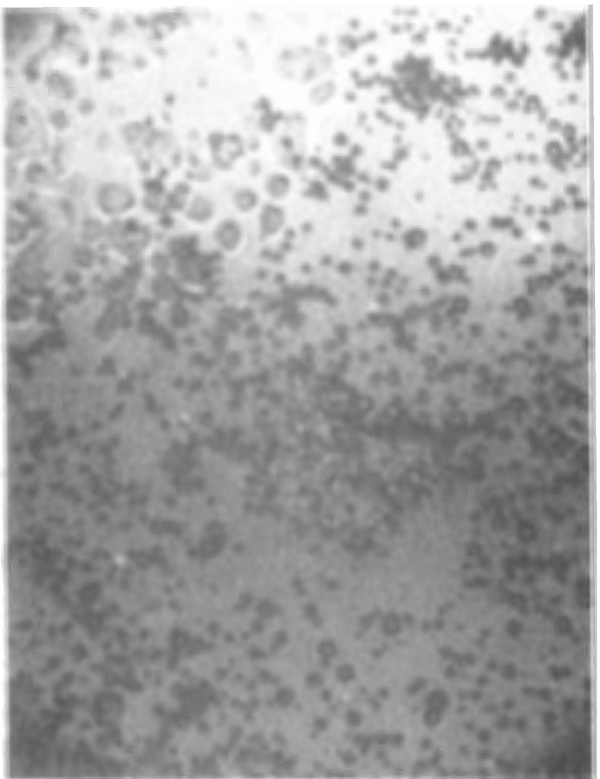

Figure 5
Sector plate with branches
(250μm diameter)

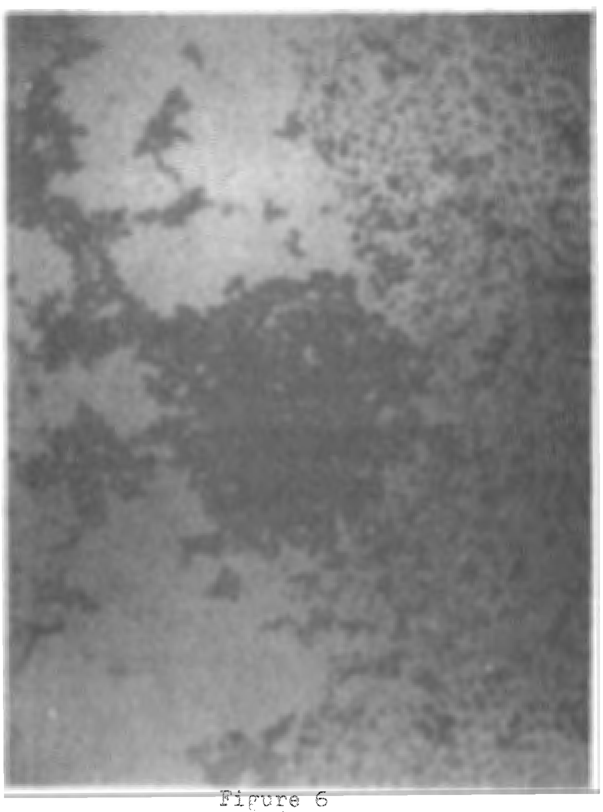

Figure 6
Graupel particle (800μm diameter)

CLOUD RIMING REGIONS FOR SNOW CRYSTALS THAT IMPACT MOUNTAINTOPS IN THE COLORADO ROCKIES

Edward E. Hindman

Department of Atmospheric Science, Colorado State University
Fort Collins, Colorado 80523 U.S.A.

ABSTRACT

Characteristics of the droplet and crystal spectra and water contents required for snow crystal riming are known. Further, surface, remote and airborne measurements of these properties have been and are being reported for wintertime Rocky Mountain clouds. The characteristics and measurements were combined to identify at least two crystal riming regions. The first region is upwind of topographic features, a short distance west of the primary barrier, and the second region is immediately upwind of the primary barrier. The contribution of each region varies with the storm and storm stage. The first region is accessible to airborne measurements; the second is not.

1. INTRODUCTION

The collection of supercooled cloud droplets by falling snow crystals is an important source of moisture to the growing snow crystals. I have estimated in Table 1 the cloud droplet contribution to be approximately 31% of the mass of snow that fell at Steamboat Springs, Colorado during December 1981 and January 1982. The remaining 69% of the mass came from diffusional growth of the crystals. The rime ice estimate was made from the snow crystal observations and measurements of Feng and Grant (Ref. 1). It was found, from their data, that rimed crystals were, on average, about twice as heavy as unrimed crystals of the same type and number flux independent of crystal type (a result consistent for rimed and unrimed dendrites as summarized by Pruppacher and Klett [Ref. 2]).

An additional source of moisture to the snowpack at Steamboat Springs is the collection of supercooled cloud droplets by the high-elevation trees and the shedding of the subsequent rime ice deposits to the snowpack. Hindman et al. (Ref. 3) estimated these deposits to contribute about 10% to the snowpack water. Combining this value with the estimated percent of rime ice on the falling snow crystals in Table 1 results in 38% of the snowpack water being due to rime ice and 62% being due to diffusion-grown ice. This result is significant because Borys et al. (Ref. 4) have shown that rime ice deposits contain the majority of the trace-chemical components of the snowfall at Steamboat Springs.

Table 1

Analysis of Feng and Grant's Snow Crystal Data

SNOW CRYSTAL TYPE	OCCURRENCE (%)	ESTIMATED % OF MASS		% OF TOTAL MASS	
		RIME	DIFFUSION GROWTH	RIME	DIFFUSION GROWTH
PLATES AND DENDRITES: RIMED -	13	50	50	6.5	6.5
UNRIMED -	8	0	100	0	8
GRAUPEL	19	90 (ASSUMED)	10 (ASSUMED)	17	2
SPATIAL PLATES AND DENDRITES: RIMED -	9	50	50	4.5	4.5
UNRIMED -	27	0	100	0	27
COMBINATION OF COLUMNS AND PLATES: RIMED -	5	50	50	2.5	2.5
UNRIMED -	14	0	100	0	14
COLUMNS: RIMED -	1	50	50	0.5	0.5
UNRIMED -	4	0	100	0	4
TOTALS	100	—		31	69

It is important to know where the falling crystals are riming in winter mountain clouds. For instance, the proper interpretation of simultaneous snow crystal and cloud water collections made by Borys et al. (Ref. 4) at their mountaintop Storm Peak Laboratory (SPL) require the cloud water collected at SPL be similar physically and chemically to the droplets collected by the falling crystals. Knowledge is increasing on the location and characteristics of the supercooled water regions in Rocky Mountain winter clouds based on recent airborne measurements reported in the literature. In this paper, these data are combined with the known physical characteristics of the droplets and crystals which collide to begin to answer the following question: Where do the crystals rime which settle onto mountaintops in the Colorado Rockies?

2. CHARACTERISTICS OF DROPLETS AND CRYSTALS

The physical characteristics of the droplets and crystals which collide have been determined through a combination of field measurements, observations and numerical simulations as summarized by Pruppacher and Klett (Ref. 2). Snow crystal riming occurs in regions of clouds where (a) drops are sufficiently large ($\geq 20\mu m$ diameter), (b) water contents are sufficiently high (≥ 0.1 gm^{-3} from calculations by Hindman and Johnson [Ref. 5]), and (c) the crystals are large enough to collect the droplets (for example, $\geq 500\mu m$ for plates and dendrites).

3. ANALYSES

The literature was reviewed to locate measurements of cloud droplet and snow crystal spectra and liquid water contents made in wintertime Rocky Mountain clouds. These measurements were anlayzed to identify regions in the clouds with the large drops, high contents and large crystals necessary for riming. Although these regions were from different storms and stages of storms, the analyses were conducted to determine if common regions existed which had the necessary properties for crystal riming. The common regions, then, are presented as first approximations of the locations of the riming regions. It must be recognized, the regions may not exist in each storm or stage of storm but they represent the most probable regions where riming occurs.

4. REGIONS WITH LARGE DROPLETS

Cooper and Saunders (Ref. 6) made extensive airborne physical measurements of winter mountain clouds upwind and over the southern Colorado Rockies. From these measurements they identified three storm-stages: stable, neutral, and unstable which occurred in that sequence. They reported droplet spectra only for the unstable stage and the regions containing drops $\geq 20\mu m$ are shown in Fig. 1. The droplet characteristics of these regions are given in Table 2. Rime ice measurements made at Wolf Creek Pass by Hindman et al. (Ref. 3) are included in Fig. 1 to augment the airborne measurements.

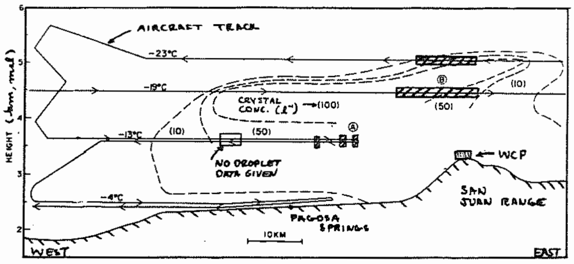

Fig. 1. Vertical cross-sections of the regions with large drops ($\geq 20\mu m$) and high water contents (≥ 0.1 gm^{-3}) for the unstable stage of the storm of 29 December 1974 in the southern Colorado Rockies from Cooper and Saunders (Ref. 6). The shaded and hatched regions indicate $\geq 0.1 gm^{-3}$. The hatched regions also contain drops $\geq 20\mu m$. The Wolf Creek Pass (WCP) data are from Hindman et al. (Ref. 3).

Table 2

Characteristics of Regions with Droplets $\geq 20\mu m$ Diameter.

$\bar{N}$ ($\geq 2\mu m$) (cm^{-3})	$\bar{N}$ ($\geq 20\mu m$) (cm^{-3})	LWC_{MAX} ($g m^{-3}$)	$\bar{d}$ (μm)	LOCATIONS OF REGIONS
511	56	~1	15	(A) in Fig. 1
210-377	85-100	≥ 1	18-20	(B) in Fig. 1
50	2.8±2	0.3-0.4	15	24 NOV 1979 in Fig. 2
185-290	1.9±0.36	0.13	6-9	26 NOV 1979 in Fig. 2
7	3.5	0.03	20	Mt Harris } Blumenstein, in Fig. 2
4-25	1.0-8.3	0.10	20	Park Range } Blumenstein, in Fig. 2
23-37	1.2-10.3	0.08	8 & 20	Park Range } Blumenstein, in Fig. 2
~40	0.9	0.03	6	SPL data in Fig. 2

Rauber (Ref. 7), Blumenstein et al. (Ref. 8), and DeMott et al. (Ref. 9,10) have reported extensive airborne physical measurements over the northern Colorado Rockies near Steamboat Springs. The regions with drops $\geq 20\mu m$ analyzed from these investigations are shown in Fig. 2. The drop characteristics are in Table 2. It must be emphasized that these measurements represent "snapshots" from a variety of storms. The storms have a spatial and temporal dependence which is illustrated by Rauber et al. (Ref. 19).

Rauber (Ref. 7) studied two storms, both were stably stratified. Blumenstein et al. studied another storm which also was stably stratified. They reported a graupel shower at the surface which was coincident with a reduction in large drops (10 to 1 cm^{-3}) overhead indicating the removal of the drops by the graupel. DeMott et al. studied a large, precipitating, stable orographic cloud. They reported few if any large drops; a result consistent with that of Politovich and Vali (Ref. 13) for similar clouds over Elk Mountain, Wyoming. This type of cloud represents a lower limit to winter clouds which contain large, collectible droplets.

Hindman (1984, unpublished) made droplet measurements at SPL near the same time Blumenstein et al. were making their airborne droplet

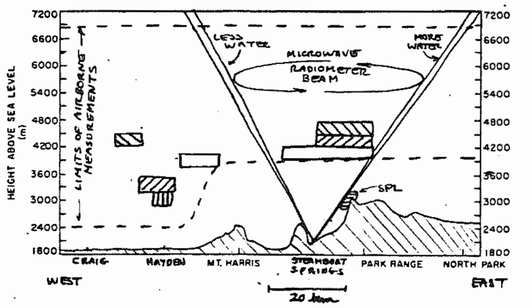

Fig. 2. A composite vertical cross-section of regions of large drops ($\geq 20\mu m$) and high water contents (≥ 0.1 gm^{-3}) for storms over the northern Colorado Rockies. The regions are as follows: drops $\geq 20\mu m$, LWC ≥ 0.1 gm^{-3} and LWC ≥ 0.1 gm^{-3} (no droplet data) on 24 and 26 November 1979 from Rauber (Ref. 7); drops $\geq 20\mu m$ on 5 January 1982 (LWC ≥ 0.1 gm^{-3}) from Blumenstein et al. (Ref. 8), LWC ≥ 0.1 gm^{-3} (no drops $\geq 20\mu m$) on 16 January 1982 from DeMott et al. (Refs. 9,10) and drops $\geq 20\mu m$, LWC ≥ 0.1 gm^{-3} on 5 January 1982 from Hindman (1984, unpublished) and Hindman et al. (Refs. 3,11) made at Storm Peak Lab (SPL). The vertically-integrated radiometer measurements are reported by Rauber et al. (Ref. 12).

measurements on 5 January 1982 as shown in Fig. 2. Droplets $\geq 20\mu m$ were measured at SPL with characteristics similar to the airborne measurements as indicated in Table 2. Also, Hindman et al. (Refs. 3,11) report the liquid clouds impact the Park Range at about 3000 m msl indicating the large $20\mu m$ drops may be even lower in the cloud than at SPL.

5. REGIONS WITH HIGH WATER CONTENT

The regions of liquid water contents ≥ 0.10 gm^{-3} which were analyzed from the literature are illustrated in Figs. 1 and 2. It can be seen from these figures that the regions which contained large drops also contained high water contents. An exception are the DeMott data. They reported small drops but high water contents probably due to high CCN concentrations and updraft speeds.

Rauber et al. (Ref. 12) operated a dual-wave length, passive microwave radiometer at Steamboat Springs as illustrated in Fig. 2. The radiometer measures the integrated liquid water (gm^2) in its narrow but long-path beam (3° by surface to top of the cloud). They report that, in general, more liquid water was detected when the beam was directed toward the Park Range than away as shown in Fig. 2. The location of the liquid water region in the beam is unknown and will be inferred from the airborne measurements and computer simulations.

Rauber (Ref. 7) developed a numerical model which predicts the condensation production rate (ice plus water) for moist air flowing over a mountain-barrier. He initialized the model using rawinsonde data collected 60 km upwind of the Park Range. The predicted condensation rates (see Fig. 3) compared favorably with his airborne water content measurements: maximum contents were predicted to be just upwind of the barrier. Tripoli and Cotton (Ref. 14) have expanded Rauber's calculations by performing multiple-barrier simulations, the results of which confirm Rauber's findings but also provide support for the water content region detected upwind of Mt. Harris in Fig. 2.

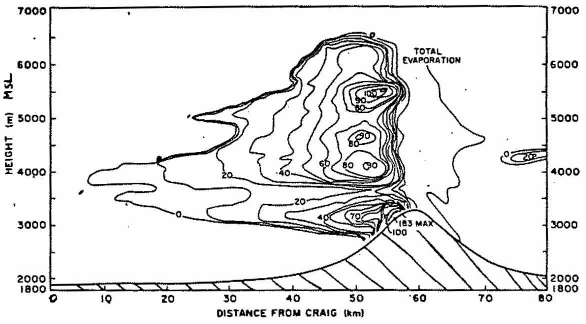

Fig. 3. Potential condensate production rates (10^5 gm^{-3} s^{-1}) for the 24 November 1979 storm from Rauber (Ref. 7).

6. REGIONS WITH LARGE SNOW CRYSTALS

The airborne snow crystal spectra measurements reported by Rauber (Ref. 7) were analyzed to identify the regions with crystals $\geq$500μm. The results of these analyses are shown in Fig. 4. It can be seen from the figure, that the majority of the largest crystals were detected below 4800 m msl.

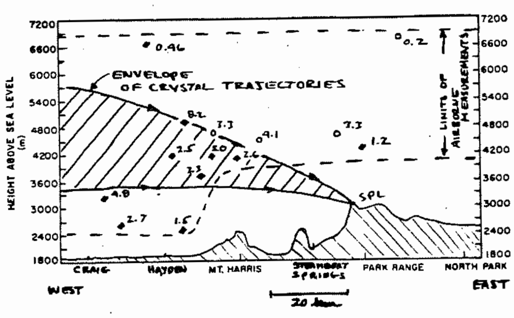

Fig. 4. A composit vertical cross-section of concentrations (ℓ^{-1}) of large snow crystals ($\geq$500μm) for storms over the northern Colorado Rockies from Rauber (Ref. 7): ◆-24 November 1979, O-26 November 1979. The envelope of crystal trajectories is also from Rauber (Ref. 7).

Rauber (Ref. 7) has computed a series of snow crystal trajectories for horizontal wind speeds of 15 to 20 m s^{-1} using his 24 and 26 November 1979 The envelope of those trajectories is given in Fig. 4. The envelope emcompasses that estimated by Cooper and Marwitz (Ref. 15) for the same wind speeds.

7. DISCUSSION

The expected regions in the winter mountain clouds with characteristics suitable for crystal riming are identified in Fig. 5 for the southern Colorado Rockies and in Fig. 6 for stable storm-stages in the northern Colorado Rockies. It can be seen from these two figures that there are at least two common crystal riming regions: the first is upwind of smaller topographic features west of the primary barriers, and the second is immediately upwind of the primary barriers. The liquid water in these regions is produced in rising air caused primarily by west winds forced over the barriers. The rising air is augmented by convection in the unstable stages as well as surface convergence zones identified by Marwitz (Ref. 16).

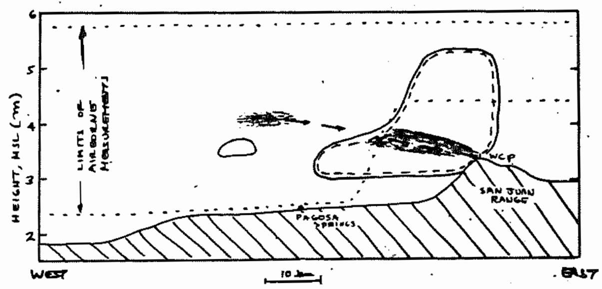

Fig. 5. Compilation of results from Fig. 1 and typical crystal trajectories (→ → →) from Cooper and Marwitz (Ref. 15) to identify riming regions (▬) in unstable storm-stages for crystals that impact Wolf Creek Pass (WCP): Regions with drops $\geq$20μm (----) and regions with LWC $\geq$0.1 g m^{-3} (——).

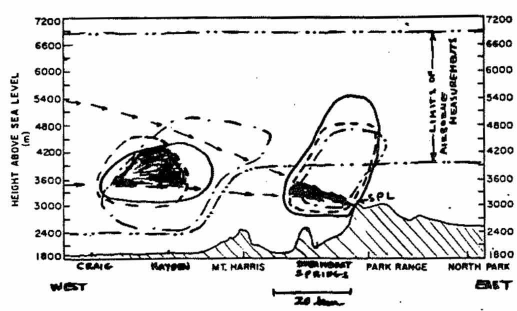

Fig. 6. Compilation of results from Figs. 2, 3 and 4 to identify riming regions (▬) in stable storm-stages for crystals that impact Storm Peak Laboratory (SPL): Regions with drops $\geq$20 μm (- - -), regions with LWC $\geq$0.1 g m^{-3}(——), regions with crystals $\geq$ 500 μm (—·—·—) and typical crystal trajectories (→ → →).

Cooper and Marwitz (Ref. 15) and Rauber (Ref. 7) have postulated, through numerical simulations based on their field measurements, that crystals are nucleated at the upwind edge of the first riming region and grow by diffusion, riming and aggregation in the region as illustrated in Figs. 5 and 6. Further, growth in the second region assures the rimed snow flakes which emerge from the first region are large enough to overcome the vertical motion just upwind of the primary barriers. In support of these thoughts, DeMott et al. (Ref. 10) measurements reveal rapid nucleation at upwind edges of liquid water zones in winter mountain clouds. Further, Tripoli and Cotton's (Ref. 14) recent numerical simulations indicate that the first riming region is required to generate aggregates which precipitate onto the primary barrier.

Another possibility exists, in that the crystals that nucleate at the upwind edge of the second riming region grow sufficiently by diffusion, riming and aggregation to precipitate onto the primary barrier. Hindman and Johnson (Ref. 5) show that crystal riming begins within two minutes of nucleation independent of temperature and water content (for contents $\geq$0.1 g m^{-3}). Further, they show graupel particles can be produced at -10 and -20C and 0.1 g m^{-3} within 11 and 15 minutes of nucleation, respectively, and heavily rimed crystals are produced at -15C. Aggregation was not simulated. Crystal transit time through the second riming regions are about 20 minutes for representative wind speeds of 15 ms^{-1}. Consequently, there is sufficient growth time and liquid water for the crystals to grow and precipitate. Aggregation will further enhance these processes.

It remains an unresolved and important question which region primary riming occurs; important because the composition of the water may be different between the two regions. Primary riming probably occurs in either region depending on the stage of the storm. Further research is required to resolve this question perhaps by employing the techniques of Warburton and DeFelice (Ref. 17) to "tag" the temperature at which riming occurred and of Borys et al. (Ref. 4) to use the chemical composition of the cloud water to infer cloud nucleus sources.

An important result from Figs. 5 and 6 is that the second riming region is below the level for safe aircraft operation; a result similar to that reported by Henderson and Solak (Ref. 18) in the Sierra Nevada Mountains. Consequently, the droplet and crystal spectra and water contents must be determined remotely as in Rauber et al. (Ref. 19), through detailed numerical simulations as in Tripoli and Cotton (Ref. 14), and from mountaintop measurements.

8. CONCLUSIONS

Rime ice deposits are important to the mass of snow crystals and determine the composition of the crystals at Steamboat Springs, Colorado: the droplets contribute 31% of the mass, the remainder comes from diffusional growth. The crystals collect the supercooled drops in at least two riming regions: the first region is upwind of smaller topographic features west of the primary barrier and the second is immediately upwind of the primary barrier. It is an unresolved question as to which region contributes a majorority of the rime deposits; it probably depends on the storm and stage of the storm. The first rime region is accessible to airborne measurements, the second is not. Thus the characteristics of the second region are being estimated using remotely sensed and mountaintop measurements and detailed microphysical/dynamical numerical simulation models.

9. ACKNOWLEDGEMENTS

This research is a portion of that funded by NSF Grant ATM8109590.

10. REFERENCES

1. Feng, D. and L.O. Grant, 1984: J. Atmos. Sci., in preparation.
2. Pruppacher, H.R. and J.D. Klett, 1978: Microphysics of Clouds and Ppt., D. Reidel Pub. Co., 714 pp.
3. Hindman, E.E., et al., 1983: Water Res. Bull. 19, 619-624.
4. Borys R.D., et al., 1982: Proc. 4th Conf. Ppt. Scavenging, Elsevier, 181-190.
5. Hindman, E.E. and D.B. Johnson, 1972: J. Atmos. Sci., 29, 1313-1321.
6. Cooper, W.A. and C.P.R. Saunders, 1980: J. Appl. Meteor., 19, 927-945.
7. Rauber, R.M., 1981: Atmos. Sci. Paper 337, CSU Fort Collins, Colorado, 151 pp.
8. Blumenstein, R.R., et al., 1982: Ppts. Conf. Cld. Phys, AMS, 491-484.
9. DeMott, P.J., et al., 1982: Ppts. Conf. Cld. Phys., AMS, 488-490.
10. DeMott, P.J. and L.O. Grant, 1984: Proc. 9th Intl. Cld. Phys. Conf., in this volume.
11. Hindman, E.E., et al., 1982: Ppts. Conf. Cld. Phys.AMS, 491-494.
12. Rauber, R.M., et al., 1982: Ppts. Conf. Cld. Phys., AMS, 477-480.
13. Politovich, M. and G. Vali, 1983: J. Atmos. Sci., 40, 1300-1312.
14. Tripoli, G.J. and W.R. Cotton, 1984: Proc. 9th Intl. Cld. Phys. Conf., in this volume.
15. Cooper, W.A. and J.D. Marwitz, 1980: J. Appl. Meteor., 19, 942-949.
16. Marwitz, J.D., 1980: J. Appl. Meteor., 19, 913-926.
17. Warburton, J.A. and T. DeFelice, 1984: Ppts. 9th Conf. Wea. Modif., AMS, in preparation.
18. Henderson, T.J. and M.E. Solak, 1983: J. Wea. Modif., 15, 64-70.
19. Rauber, R.M., et al., 1984: Proc. 9th Intl. Cld. Phys. Conf., in this volume.

ICE PARTICLES IN MARINE AND CONTINENTAL CLOUDS

Peter V Hobbs and Arthur L Rangno
Cloud and Aerosol Research Group, Atmospheric Sciences Department,
University of Washington, Seattle, Washington, 98195 USA

1. INTRODUCTION

Although there is observational evidence that ice particle concentrations in some clouds exceed measurements of ice nucleus (IN) concentrations by several orders of magnitude (Refs. 1-5), the factors that determine such ice enhancement have not been firmly established.

To provide a broader data base for elucidating this phenomenon, we have made extensive airborne measurements in a wide variety of clouds. A full description of these data and a discussion of their implications may be found in Ref. 6. Here we confine our attention to describing a sub-set of the data.

2. CLOUD TYPES AND SAMPLING PROCEDURES

Obtaining representative relationships between ice particle concentrations and other cloud parameters is a difficult task. For example, during a few hours flying on one day in Washington State (where the measurements to be described were obtained), we encountered marine cumulus mediocris with a top temperature of -6°C containing 100 L^{-1} of ice particles, single cumulus congestus clouds with a top temperature of -10°C but with no ice, a line of cumulus congestus that developed into cumulonimbus with a top temperature of -10°C and 50 L^{-1} of ice particles, orographic stratocumulus with no ice in their tops at -9°C but 15 L^{-1} of ice particles 500m below cloud top, and, no ice particles in cumulus mediocris with top temperatures of -14°C.

In view of this large variability, it is necessary to define carefully the type of cloud that is sampled, and the location and timing of the sampling relative to the lifecycle of the cloud.

Here we will confine our discussion to those clouds that had distinct origins in the boundary layer, these comprise stratocumulus clouds with bases < 2.5 km AGL and with no temperature inversion below cloud base, and cumulus and cumulonimbus clouds. Cloud base temperatures were between 10 and -10°C. Also, emphasis will be on clouds with depths > 1.5 km but with cloud top temperatures (T_T) ⩾ -20°C. These clouds are divided into three categories according to their average droplet concentrations ($\overline{N}$): marine ($\overline{N} \leqslant 300$ cm^{-3}), transitional ($300 < \overline{N} < 800$ cm^{-3}), and continental ($\overline{N} \geqslant 800$ cm^{-3}).

Clouds were sampled at several levels and at various stages in their lifecycles. For the convective clouds maximum ice particle concentrations were generally encountered in downdrafts well below cloud top and during the later stages in the cloud lifecycle.

The measurements were obtained using the University of Washington's B-23 aircraft (Ref. 5). Ice particle concentrations were measured with an optical ice particle counter (Ref. 7) and cloud droplet spectra with a PMS Axially Scattering Spectrometer Probe (ASSP) and a PMS Forward Scattering Spectrometer Probe (FSSP). Since the ASSP measurements give erroneously broad spectra, they were corrected to agree with the more reliable FSSP measurements (Ref 8).

3. RESULTS

Fig. 1 shows the measured maximum concentrations of ice particles (C_M) in "boundary-layer" clouds plotted against T_T. For $T_T \gtrsim -20°C$, C_M is essentially independent of T_T. For the marine clouds, ice enhancement occurred when $T_T \lesssim -5°C$. For continental clouds, it occurred when $T_T \lesssim -10°C$. All "boundary-layer" clouds that were ⩾ 1.5 km deep and had $T_T \lesssim -10°C$ contained ice; the lower limit to C_M in these clouds increased rapidly with decreasing T_T (dotted line in Fig. 1).

Most of the variance in C_M is accounted for by variations in $\overline{N}$ (Fig. 2). For the "boundary layer" clouds with -5°C > T_T > -11°C, the relationship between C_M (in L^{-1}) and $\overline{N}$ (in cm^{-3}) is

$$C_M = 249 \exp(-0.009\,\overline{N}) \qquad (1)$$

with a correlation coefficient (r) between these variables of 0.95. In this temperature range, the clouds are dominated by needle and columnar - type ice crystals.

Shown in Fig. 3 is the relationship between C_M and $\overline{N}$ for clouds with -13°C > T_T > -20°C. These clouds are dominated by dendritic-type ice crystals. In this case:

$$C_M = 156 \exp(-0.0037\,\overline{N}) \qquad (2)$$

with r = 0.68.

To show the effects of larger cloud droplets on C_M, we define a "threshold" cloud droplet diameter (D_T) as that for which the cumulative concentration of droplets with diameters ⩾ D_T reaches a value of 10 cm^{-3}. Hence, large values of D_T indicate droplet size distributions with "tails" extending to larger diameter droplets. The droplet spectra were measured in the upper regions of the clouds where liquid water dominated.

Plots of C_M versus D_T are shown in Fig. 4 for three classes of cloud: marine "boundary-layer", continental "boundary-layer" and altocumulus lenticularis. These three classes of cloud represent high ice producers, moderate ice producers and poor ice producers, respectively (Ref. 6).

For the high and moderate ice producers the values of D_T are relatively large, for the poor ice producers the D_T's are small. Hence, the more the "tail" of the droplet size distribution extends to larger diameter droplets the more likely is the cloud to exhibit ice enhancement.

The data in Fig 4 indicate that a D_T value of ~18 μm is required for $C_M \geqslant 1$ L^{-1}. Above this threshold, the relation between C_M and D_T is:

$$C_M = 0.003 \exp(0.33\,D_T) \qquad (3)$$

where D_T is in μm, and r = 0.86.

Acknowledgements. Work supported by N S F Grant ATM79-00948.

4. REFERENCES

1 Koenig L R 1963, The glaciating behaviour of small cumulonimbus clouds, *J Atmos Sci* 20, 29-47.

2 Hobbs P V 1969, Ice multiplication in clouds, *J Atmos Sci* 26, 315-318.

3 Mossop S C, Cottis R E and Bartlett B M 1972, Ice crystal concentrations in cumulus and stratocumulus clouds, *Quart J Roy Meteor Soc* 98, 105-126.

4 Hallett J, Sax R I, Lamb D and Murty A S R 1978, Aircraft measurements of ice in Florida Cumuli, *Quart J Roy Meteor Soc* 104, 631-651.

5 Hobbs P V, Politovich M K and Radke L F 1980, Structures of summer convective clouds in eastern Montana. I. Natural Clouds, *J Appl Meteor* 19, 645-663.

6 Hobbs P V and Rangno A L 1984, Ice particles in marine and continental clouds, *J Atmos Sci* (To be submitted).

7 Turner T M and Radke L F 1973, The design and evaluation of an airborne optical ice particle counter, *J Appl Meteor*, 12, 1309-1318.

8 Vali G, Politovich M K and Baumgardner D G 1981, Conduct of cloud spectra measurements, *Final Report to AFGL*, Contract F19628-79-C-0029, 65 pp.

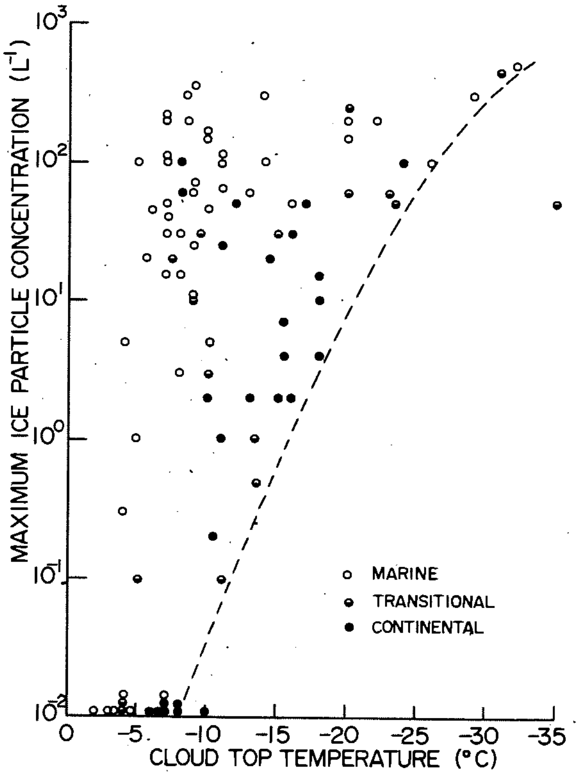

Figure 1. Maximum ice particle concentrations in "boundary-layer" clouds versus cloud top temperature.

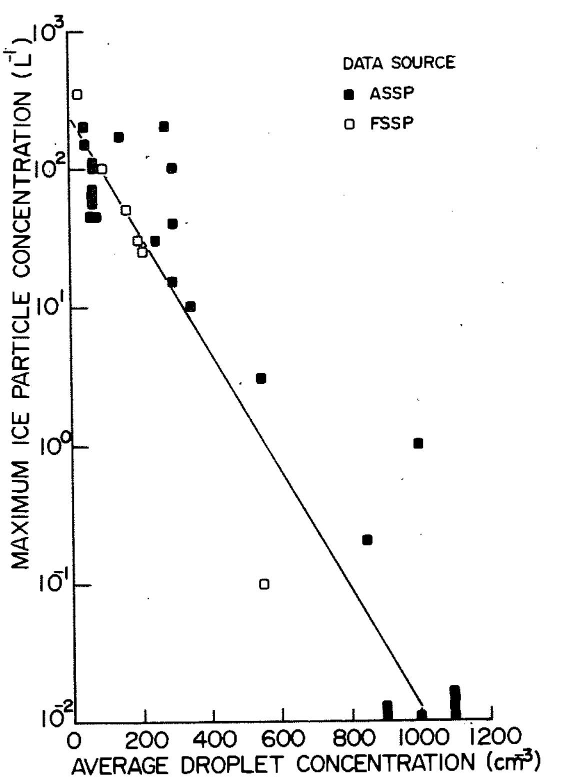

Figure 2. Maximum ice particle concentrations versus average droplet concentration for "boundary-layer" clouds with top temperatures between -5 and -11^{0}C.

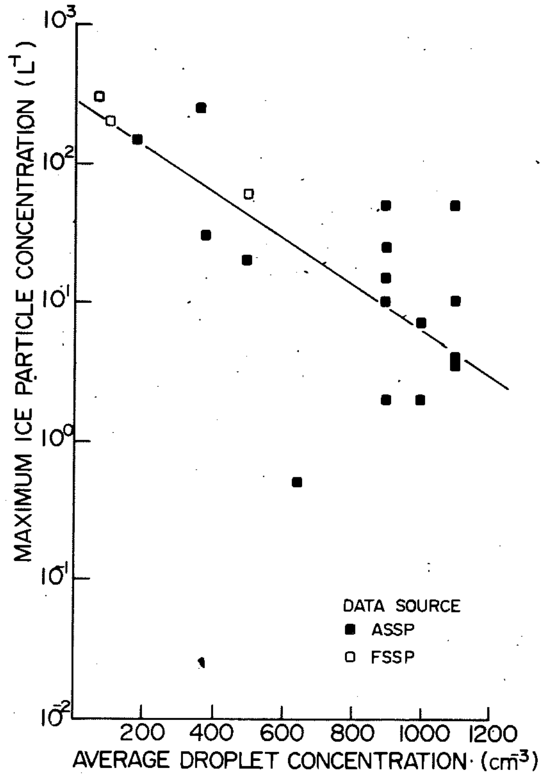

Figure 3. As for Fig 2 but for cloud top temperatures between -13 and -20^{0}C.

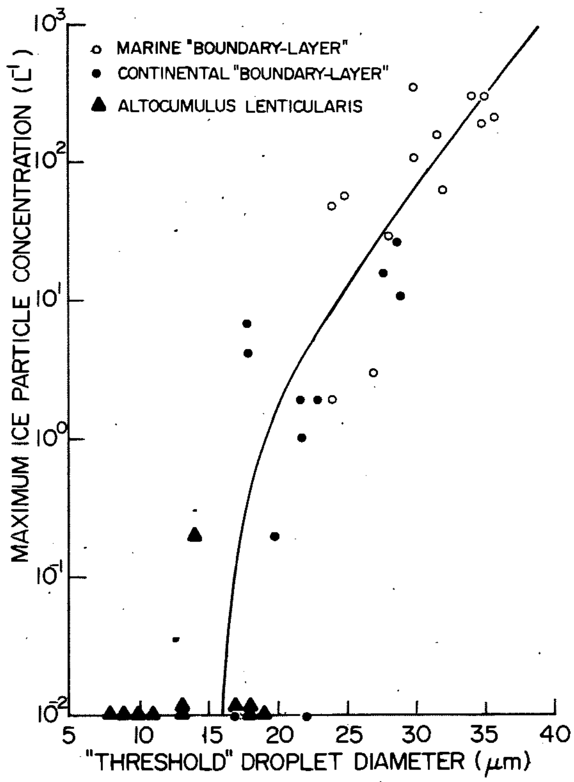

Figure 4. Maximum ice particle concentration versus "threshold" droplet diameter. Closed and open symbols indicate measurements with ASSP and FSSP, respectively.

ON THE MICROSTRUCTURE AND ICE WATER CONTENT OF HIGH CLOUDS

A. L. Kosarev, A.N. Nevzorov and F.V. Shugaev

Central Aerological Observatory, Moscow, USSR

1. INTRODUCTION

In the few available studies of high cloud microphysics (e.g. Refs.1-4, 7) the ice crystal size spectra and ice water content derived from the spectra were determined for inadequate particle size ranges, and other limitations are there for the data presented to produce sufficiently reliable, complete, and detail empirical model of cirriform cloud microphysics.

A good opportunity for collecting data on microphysical properties of ice high clouds was afforded by a series of flights of Il-18 aircraft equipped with unique cloud physics instruments developed in CAO. The flights were carried out during 1976-82 over the USSR territory. Cirriform clouds passed through were mainly of Cs type (including Cs neb, Cs fil, Cs-As, Ci sp) which this report is concentrated on. Over 25 hours of continuous recording of ice particle concentration and size spectra, ice water content (IWC), and extinction coefficient (EC) within tens of individual Cs clouds provided a large bulk of material for both case studies and statistical analyses.

Some results of sampling survey analysis of the data are summarized in this report.

2. INSTRUMENTS AND MEASUREMENT DESIGN

2.1. Measurement of crystal size spectra.

Two photoelectric particle spectrometers for different size ranges were used in our study.

Large particle spectrometer (LPS) being in routine use for over 20 years (Ref. 1) operates on the principle of partial shadowing flat-formed light beam by a single particle, the beam thickness being less than minimum size to measure. The present LPS modification involves a 12-channel pulse height analyzer scaled in drop diameters from 200 to 6000 m with increasing sequential steps. As for ice crystals, the actual measured size is the maximum of parallel chords of accidental cross-section; thus the instrument determines the spectra of crystal "effective linear" diameters. The LPS has a sampling area of 7 cm^2 and ensures measuring particle concentration up to $3\cdot 10^4\ m^{-3}$.

A more recent instrument, particle phase/size analyser (PPSA), was originally designed as a combination of light scattering drop-size probe and cross-polarization ice crystal counter both using the same optical system with operating angle of 90^o and separate photodetectors of initial and depolarized component of scattered light, respectively. A 16 mm^3 sample volume with capture area of 16 mm^2 allows the upper measurable concentration about $2\cdot 10^7\ m^{-3}$ (= 20 cm^{-3}).

A pulse hight analyser connected with the initial polarization photodetector had a threshold scale of 30-50-80-120 μm drop diameter as adjusted by the use of calibration curve. Further was presented the possibility to estimate the equivalent threshold sizes of ice crystals using the experimental results reported in Ref. (8) as well as our revelation made with the aid of PPSA that in natural Cs clouds the depolarization factor of light scattered by a single crystal at 90^o averaged 0.7-0.9. It was found that the above scale fit directly (within 20 % estimation error) for determination of distribution of effective cross-section diameters of ice crystals.

For both LPS and PPSA certain distortions of measured size spectra occur due to scatter in size-equivalent crystal responses that was estimated and taken into account in data handling. Pulse-count rate outputs of the both were continuously recorded with the time resolution of 0.5-1 sec.

2.2. Measurement of IWC.

Since 1976 a cloud water content meter, IVO CAO, based on constant temperature of impact collector-evaporator was used in our studies (Ref. 6). The instrument possesses as high as .003 gm^{-3} sensitivity and is able to measure also IWC by using a crater-shaped collector with sampling area of about 0.5 cm^2. The output time response was assigned to be 0.25 sec.

A suspicion arose from some flight tests that two main reasons, such as incomplete inertial capture of particles by the collector and taking off fractions of the captured ones before completely evaporated, are responsible for IWC measured value underestimation which reached probably 30-40 % in some clouds depending on crystal habit not less than on size spectra.

2.3. Measurement of extinction coefficient.

In cloud studies by CAO an aircraft optical transmissiometer is widely used since 1969 (Ref. 5). With its base of ~ 16 m, 25 % error limits of measureable values of EC are 2.5 and 250 km^{-1}, though mists with EC down to ~ 1 km^{-1} were reliably detected.

3. SUMMARY OF EXPERIMENTAL RESULTS

A great variability in magnitude of so-called "local" microphysical parameters in Cs (i.e. in fact belonging to cloud parcels of minimum dimensions as resolved by the instruments) is demonstrated in Fig. 1 in the form of cumulative frequency distributions of crystal concentration and maximum size, IWC, and EC, all sampled in many clouds penetrated. The spatial inhomogeneity of cirriform clouds is also characterized by the fact that the horizontal autocorrelation radius of IWC ranged widely from 0.2-0.3 to > 20 km in individual clouds. Relative stability of crystal size distribution was observed as a rule on 1-10 km length paths, so that the definition of "local" size spectrum is somewhat associated with a cloud cell of several km in diameter (Ref. 1).

3.1. Crystal size spectra.

Some examples of local spectra of crystal sizes (in terms of effective diameters d as defined above) obtained by PPSA (30-120 μm) and LPS (> 200 μm) are presented in Fig. 2. The tendency of general decrease of number concentration density per unit

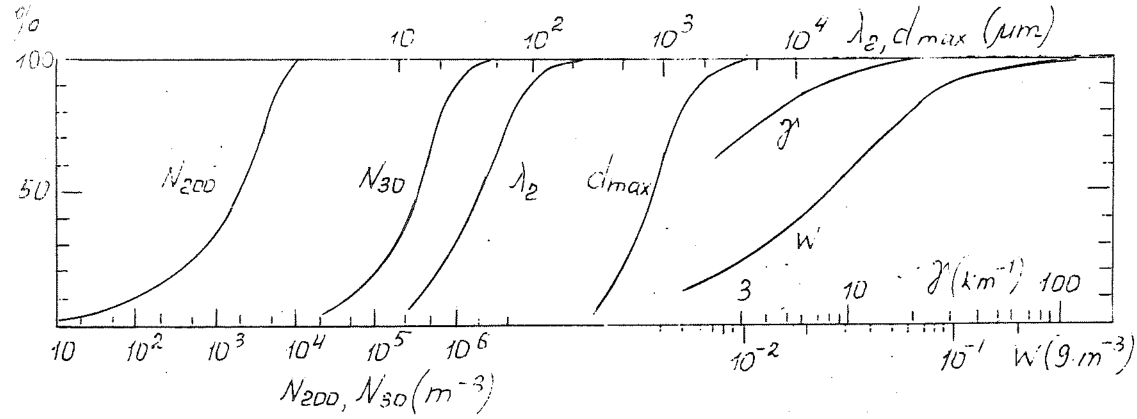

Fig. 1. Percentage of sampled Cs cloud volume wherein number concentration of crystals $> 200\ \mu m$ (N_{200}) and $> 30\ \mu m$ (N_{30}), maximum crystal effective diameter d_{max}, parameter λ_2 of Eqs (1) and (2), IWC W and extinction coefficient γ were less than abscissa values

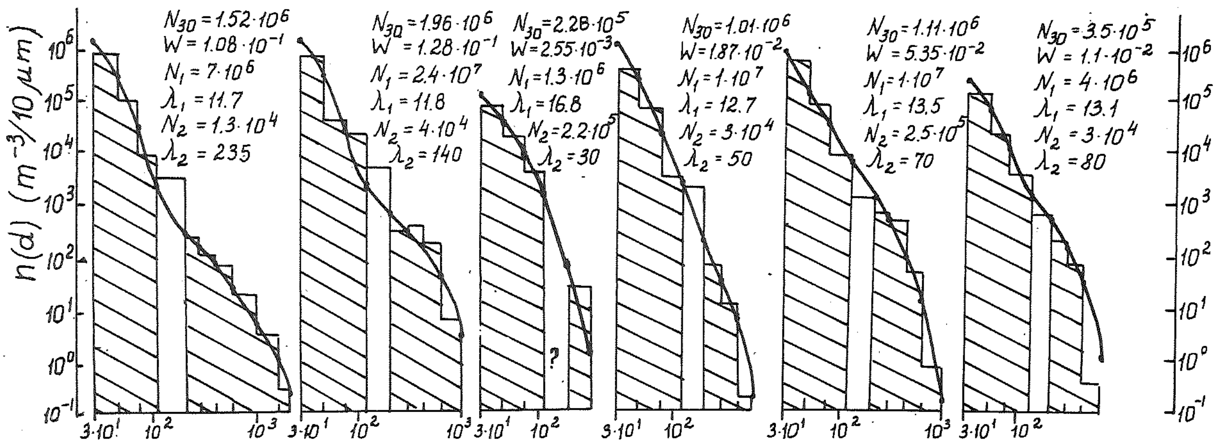

Fig. 2. Examples of local crystal size spectra obtained in Cs. Shaded are the portions determined with PPSA (left) and LPS, with rough intermediate data column unshaded. The entire curves are approximations by Eq. (2). Values of N are in m^{-3}, λ in μm, W in gm^{-3}

size, n(d), with d increasing from 30 μm is the common feature of spectra sampled within the cloud itself but not in precipitation. Of more than 1800 individual spectra, relatively weak peaks of n(d) were observed in 7 % in the region from 300 to 600 μm and in 4 % at larger d, sometimes being the second ones. In all the others 90 % n(d) descented monotonously or, perhaps, in a small part had maxima at 120-300 μm difficult to be reliably revealed, and peaks were never observed at $d < 120\ \mu m$.

The exponential character of cloud crystal $d > 150\ \mu m$ size distribution was noted earlier (Ref. 1). As for more broad size spectra in Cs, we found the most common habit of these to be well reproduced by Eq. 1 appropriate for approximation or smoothing experimental distributions in size range from 30 μm to d_{max}:

$$N(d) = N_1 \exp\left(-\frac{d}{\lambda_1}\right) + N_2 \exp\left(-\frac{d}{\lambda_2}\right), \qquad (1)$$

where N(d) is the number concentration of crystals with size exceeding d, or

(2)

for the number concentration density, as illustrated by Fig. 2. Accepting the first terms of Eqs. 1 and 2 to be responsible for smaller size portion, we have $N_1 > N_2$ and $\lambda_1 < \lambda_2$.

Now it is convenient to employ the empirical parameters N_1, λ_1, N_2, λ_2 in description of the spectra variability and, in general, for other various purposes. In all Cs sampled, the most conservative appeared to be λ_1, which varied mostly within 10-20 μm, whereas λ_2 scattered from 20-30 to over 500 μm (Fig. 1). The evidence of great scatter in magnitudes of N_1 and N_2 is given by the frequency distribution of correspondingly derived parameters N_{30} and N_{200}. Note that for N_{200} large enough the ratio of N_{30}/N_{200} was mostly within 30-300 and no more correlation between the distribution parameters was found.

3.2. Ice water content.

The mean and median values of IWC directly measured in Cs were about 0.03 and

0.025 gm^{-3}, respectively, with overall local variations from $<$ 0.003 to 0.3-0.4 gm^{-3} in infrequent record peaks. As derived from the data above, the main contribution to values of IWC is to be expected from both the smallest ($<$ 100 μm) and largest particle fraction while, in general, the IWC is one magnitude higher when large crystals contribute it.

Some appreciable relation to flight level temperature came out for IWC when averaged on tens of km flight paths. The relation displayed itself in that almost all Cs clouds at $<$ - 40 ^{o}C contained $<$ 0.01 gm^{-3} of ice against $>$ 0.01 gm^{-3} at $>$ -25 ^{o}C.

3.3. Extinction coefficient: useful evidence.

The transmissiometer used was not capable to measure such low EC as inherent in most Cs parcels (Fig. 1). Nevertheless, an important microphysical information was extracted from these measurements when compared with EC values estimated from crystal cross-section spectra determined with PPSA and extrapolated to zero by using Eq. 2. First of all, the comparison indicated that at least for most local spectra sampled in Cs actual concentrations of crystals $<$ 30 μm were markedly lower than if extrapolated, as it was demonstrated in Ref. (7). It is also of great significance that in alternative cloud regions where direct EC values, in particular when ranged 5-10 to 40 km^{-1}, were comparable with or exceeded those derived via extrapolation, the correlation between EC and crystal concentration became typically weaker than usually observed, sometimes turning even to inverse one.

The phenomenon is well pronouned in record patterns presented as examples in Fig. 3. No realistic physical interpretation of such an "anomaly" was suggested but that liquid water droplets were present within the dense Cs regions as it was hypothesized by Heymsfield (Refs. 2, 4) for cirrus generating cells. No doubt that many actually mixed cells we encountered in Cs involved liquid water phase during different stages of ice formation. Moreover, some opportunities appeared to be available to determine LWC (even roughly) and to evaluate drop mean radii r_m (by a method of LWC/EC ratio adduced in Ref. (5)), when the recorded water content corresponded to EC variations rather than to those of crystal concentration. So, the synchronous peaks of W and γ in Fig. 3 correspond to LWC of 0.01-0.04 gm^{-3} and $r_m \sim$ 2-3 μm for Ex. (a), and to those of $\sim$ 0.2 gm^{-3} and 5-8 μm for Ex. (b). In Ex. (c), LWC value remained uncertain and mean drop radius was estimated not to be more than 0.5-1 μm.

4. CONCLUSION

We consider that the determination of ice crystal size spectra in terms of effective diameters as well as direct IWC measurement provide the data to be sufficiently accurate and fairly indifferent to the crystal form. This together with the spectra parameterization is believed to be the prerequisite for effective data compressing, as needed in many up-to-date investigations.

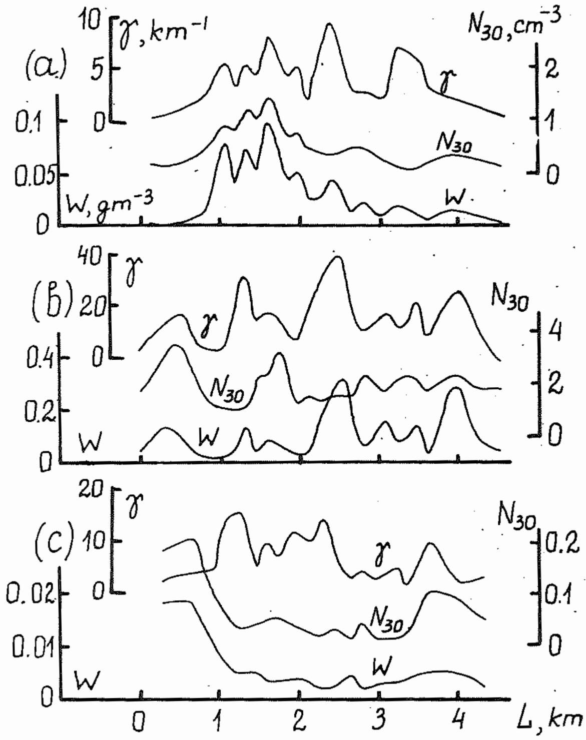

Fig. 3. Record patterns made in "anomally" dense Cs cells: EC (γ), water content (W), and total crystal $>$ 30 μm concentration (N_{30}). a) Warm front, Cs-As, 29. 10. 81, 1219 LMT, H = 7150 m, T = -30 ^{o}C, Kirov reg., b) Warm front, Cs-As, 27. 05. 82, 1021 LMT, H = 6400 m, T = -36 ^{o}C, 200 km NE from the Arkhangelsk, c) Cold front, Cs, 06. 06. 82, 1019 LMT, H = 6500 m, T = 25 ^{o}C, Vologda reg.

In this report the statistical description of "elementary" Cs parcels is presented in the form of frequency distribution of IWC and for parameters of a simple (two-esponent) function approximating or, even though, smoothing empirical spectra of crystal effective diameters in over 30 m range. The extinction coefficient measurements enabled us to witness the presence of liquid water in Cs regions considered as ice cloud generating cells.

REFERENCES

1. Borovikov, A.M., Mazin, I.P., Nevzorov, A.N., 1968. Large particles in clouds. Proc. Int. Conf. on Cloud Phys., Toronto, Canada, 356-363.
2. Heymsfield, A.J., 1975. Cirrus uncinus generating cells and the evolution of cirriform clouds. Part I. J. Atmos. Sci., 32, No. 4, 799-808.
3. Heymsfield, A.J., 1976. Particle size distribution measurement: an evaluation of the Knollenberg optical array probes. Atm. Techn., No. 8, NCAR, 17-24.
4. Heymsfield, A.J., Knollenberg, R.G., 1972. Properties of cirrus generating cells. J. Atm. Sci., 29, No. 10, 1358-1366.

5. Kosarev, A.L., Mazin, I.P., Nevzorov, A.N., Shugaev, V.F., 1976. Optical density of clouds. Proc. Centr. Aeros. Obs., No. 124, 168 p.
6. Nevzorov, A.N., 1980. Aircraft cloud water content meter. Commun. 8'eme conf. int. phys. nuag., Clermont-Ferrand, France, v. 2, 701-703.
7. Rayan, R.T. et al., 1972. Cloud microstructure as determined by an optical cloud particle spectrometer. J. Appl. Met., 11, No. 2, 149-156.
8. Volkovitsky, O.A., Pávlova, L.I., Petrushin, A.G., 1980. On the light scattering by ice crystals. Izv. Acad. Sci. USSR, Atm. and Ocean Phys., 16, No. 2, 156-163.

SESSION I

MICROSTRUCTURE OF CLOUDS AND PRECIPITATION

Subsession I-3

Hydrometeors (raindrops, snow crystals, hailstones)

OBSERVATIONS OF DROPLET AND EARLY PRECIPITATION EVOLUTION IN A CUMULUS CONGESTUS

James E. Dye[1], William A. Cooper[2], Todd A. Cerni[2], and Paul P. Lawson[2]

[1]National Center for Atmospheric Research
Boulder, Colorado 80307, U.S.A.

[2]University of Wyoming
Laramie, Wyoming 82071, U.S.A.

1. INTRODUCTION

On 19 July 1981 during the Cooperative Convective Precipitation Experiment (CCOPE) the life cycle of a cumulus congestus was investigated using four powered aircraft, an instrumented sailplane, and three meteorological radars with Doppler capability. The observations extended from before the first precipitation development through the stage of active growth and the dissipation of the cloud. The University of North Dakota Citation took time-lapse photographs of the life cycle of the cloud from which the visual history was determined; the University of Wyoming King Air made ten penetrations of the cloud, at about 5.3 to 6 km (-10 to -15°C) (all altitudes are referenced to mean sea level); the University of Wyoming Queen Air made 12 passes below cloud base at 2.7 to 3.2 km (+7° to +11°C); the National Center for Atmospheric Research (NCAR)/National Oceanic and Atmospheric Administration (NOAA) sailplane made a spiral ascent in the updraft from cloud base (3.9 km, +1.1°C) to 7.1 km (-20°C); and an Aerocommander operated for the Desert Research Institute made several passes through the cloud at 4.3 to 4.8 km (-3 to -6°C).

In previous reports on this cloud, cloud droplet measurements from the King Air were used to describe the nature of the mixing process (Ref. 1), and electric field measurements from the sailplane were briefly related to the precipitation particle measurements of the King Air (Ref. 2). In this paper we review the visual, radar, and microphysical history of the cloud and emphasize the vertical and temporal evolution of the cloud droplet spectrum. Measurements taken by the sailplane are supplemented by those from the King Air. In any study of this nature reliability and accuracy of the measurements must be a consideration. Because of limited space this topic will not be discussed, but the measurement techniques, accuracies and calibrations of the FSSP can be found in Refs. 3-6.

2. THE ENVIRONMENT AND GENERAL CLOUD HISTORY

The day was quite favorable for the development of cumulus convection but the lack of upper level support led to small individual storms rather than strong, propagating thunderstorms. A sounding composited from aircraft and rawinsonde measurements showed weak wind shear, thermal instability of 1.5 to 2° from 625 to 425 mb, and cloud tops expected to reach 11 km. The cloud base measured by the sailplane varied from 634 to 636 mb (0.8 to 1.1°C), thus yielding an equivalent potential temperature (Θ_e) of 332 to 332.6 K, at the time the sailplane entered cloud base. Measurements from the Queen Air, when corrected for a small discrepancy in temperature measurement between it and the sailplane, show that peak Θ_e's below cloud base remained within 0.5 K of the sailplane values during the active part of the cloud's life.

The time history of maximum reflectivity at a given altitude and of cloud top are shown in Fig. 1 with the cloud base passes of the Queen Air, cloud penetrations by the King Air, and the in-cloud ascent of the sailplane superimposed. The reflectivity structure was determined from the NCAR 10 cm CP-2 radar augmented by the University of Chicago-Illinois State Water Survey, CHILL, 10 cm radar for the upper levels. The figure shows the altitude of the aircraft at various times but does not necessarily imply that the aircraft penetrated the maximum reflectivity at that altitude and time.

2.1 Visual and Radar History

At 1607 local time, time lapse photographs show a cumulus mediocris with tops near 6.5 km embedded in a field of similar clouds. At about 1616 growth started on the northwest side of the cloud, followed at 1621 by rapid growth in the northeast sector of the cloud. This development dominated the growth of the cloud and reached its peak altitude of 10.5 km at about 1630, at which time an anvil began to form. By 1650 the once actively growing cloud had become a trail of precipitation from a widespread anvil.

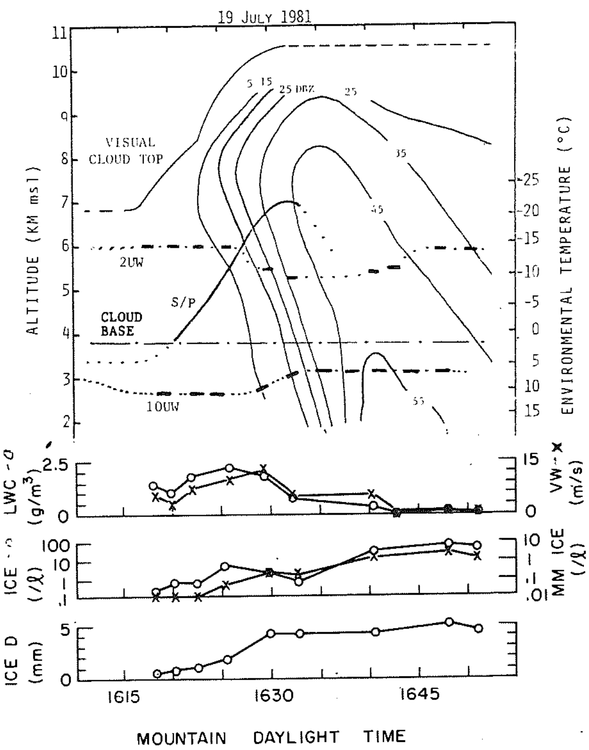

Fig. 1. The altitude time history of cloud top and the maximum radar reflectivity with the altitudes of the Wyoming King Air, (2UW) NCAR/NOAA sailplane (S/P), and Wyoming Queen Air (10UW) superimposed. The in-cloud penetrations or below cloud passes are shown by solid dark lines. The lower part of the figure shows the maximum 10 sec averages of parameters measured by the King Air during ten cloud penetrations (see Text).

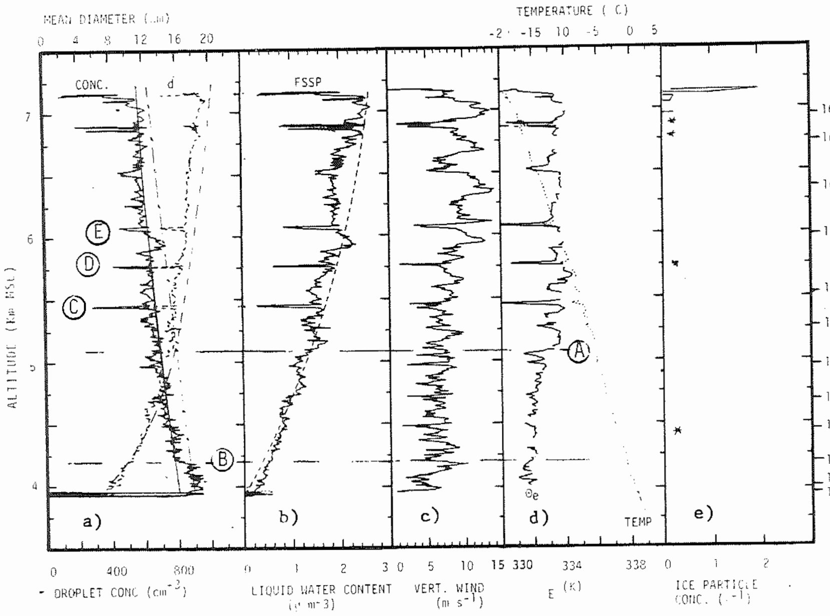

Fig. 2. One second data during the sailplane ascent from cloud base to 7.1 km. a) Total droplet concentration and mean diameter ($\bar{d}$); concentrations expected for adiabatic ascent of parcels with 900 cm^{-3} (dot-dash) and 800 cm^{-3} (solid) at cloud base; mean diameter for droplets in the 800 cm^{-3} parcel (dashed). b) Liquid water content measured by the FSSP and for adiabatic ascent (dashed). c) Vertical wind; d) equivalent potential temperature (Θ_e) and temperature (temp); e) five second averages of ice particle concentration (see text). Capital letters denote features discussed in the text.

The CP-2 radar showed sporadic, weak returns of up to 0 dBZ from 1606, the time of first coverage, to about 1614 when a more persistent 0 dBZ return appeared from 6 to 7 km. The first 5 dBZ return was detected at 1623 from 6.5 to 7.5 km, and thereafter the reflectivity rapidly increased to a maximum of 45 dBZ at 7.5 km at 1633. After 1636 the reflectivity showed the storm to be dissipating with maximum reflectivities near the surface reaching 55 dBZ. The maximum area at mid-levels was about 50 km^2 or about 8 km across. Thus, this was a small storm which briefly produced a moderate shower over a small area at the surface.

2.2 Microphysical History

Measurements from the ten penetrations of the King Air are summarized in the lower portion of Fig. 1. For each pass the maximum 10 sec average ($\sim$1 km) liquid water content (LWC) determined by the Forward Scattering Spectrometer Probe (FSSP), vertical wind speed (VW), total ice particle concentrations (ICE) from the Particle Measurements Systems 2D-C (25-800 μm) and 2D-P (200-6400 μm) probes, and concentration of ice particles >1 mm in diameter (MMICE). The lowest plot shows the maximum ice particle diameter (ICE D) for a concentration of 1 m^{-3}. The values seen for different passes are mainly indicators of temporal variations at $\sim$6 km in the cloud but also reflect variations due to the aircraft penetrating slightly different parts of the cloud on each pass. There are gradual increases in LWC and vertical wind until pass 5, (1629-1630) which is coincident with the cloud top reaching its maximum altitude. After pass 5 the vertical winds and LWC decrease and largely disappear by pass 8 (1642-1643). Ice particle concentrations and maximum diameters increased until the last pass (1650-1651) with maximum values of 10 ℓ^{-1} and 5 mm, respectively.

In summary, the King Air measurements, visual history, and radar reflectivity structure show the cloud to be in an active stage of development from about 1620 to 1630; precipitation growth and spread continue from 1630 to about 1636; thereafter the cloud is decaying with precipitation falling to the ground until somewhat after 1700. One intra-cloud lightning discharge occurred at 1637, just at the peak of precipitation development in the cloud (Ref. 2).

3. VERTICAL STRUCTURE

The observations made from the sailplane not only provide insight into the vertical structure of the cloud and the changes that occur as a parcel ascends from cloud base, but horizontal and temporal changes as well. The sailplane ascended continuously in a 1 km spiral from cloud base to 7.1 km in a region with reflectivities <5 dBZ until 6 km and <15 dBZ until the last 300 meters of the ascent. Very little ice was detected (Fig. 2e) until after 1630 (6.9 km), near the top of the ascent with maximum concentrations above this of only 2 ℓ^{-1}. The largest ice particle observed by the sailplane was a 7 mm diameter graupel.

One second measurements of droplet concentration, mean droplet diameter and LWC from the FSSP; vertical wind; temperature; and equivalent potential temperature are shown in Fig. 2 for the sailplane ascent. The ice particle concentrations are five second averages with the asterisks denoting the observation of a single ice particle. For a five second average this gives a minimum detectable concentration of approximately 0.25 ℓ^{-1}. For comparison purposes, several lines are included in the figure to show the properties of the droplet spectra and LWC for a parcel which ascends adiabatically (see figure caption).

3.1 Liquid Water Content, Equivalent Potential Temperature and Vertical Wind

The measurements of Θ_e and LWC suggest that the sailplane remained in an adiabatic or only slightly mixed region of the cloud throughout most of the ascent. Peak values of Θ_e remained near the cloud base value of 332 to 332.6 K until about 5.1 km, but then increased to 333.5

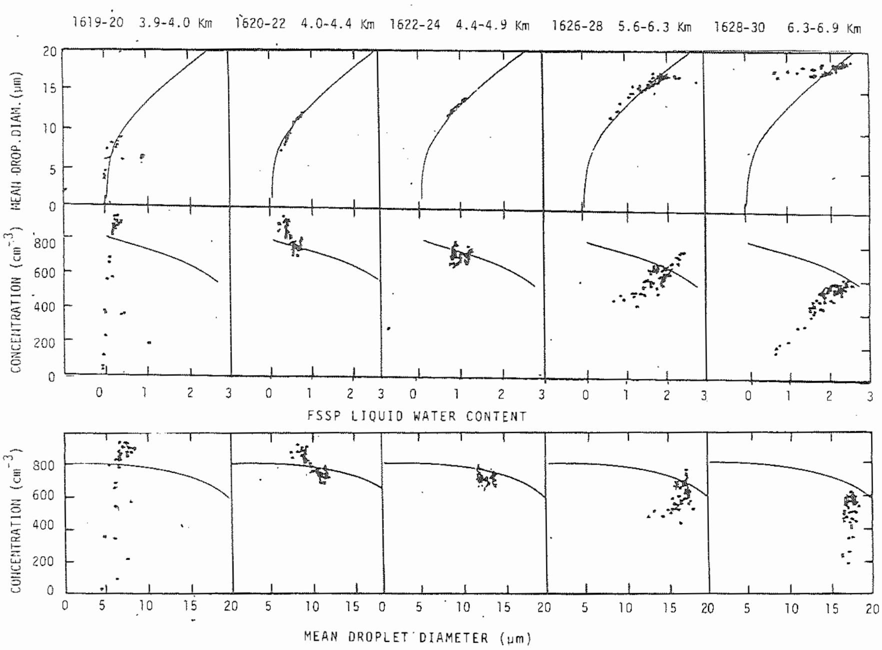

Fig. 3. Mean droplet diameter and droplet concentrations plotted as functions of the liquid water content and concentration plotted as a function of mean droplet diameter for 2-minute time periods during the sailplane ascent on 19 July 1981. The solid, curved lines show the relationship of these parameters for a parcel which initially contains 800 droplets cm^{-3} at cloud base, being lifted adiabatically.

to 334 K (point A in Fig. 2) all the way up to 7 km. Because the sailplane sinks at about 1.5 m s^{-1} in still air, this increase in Θ_e suggests that a parcel with different thermodynamic properties overtook the sailplane. A temperature increase of about 0.6°C at cloud base would be sufficient to explain the observed increase in Θ_e. This would result in an imperceptible increase in LWC of about 0.05 g m^{-3} at 6 km. A small increase in FSSP LWC of this magnitude can be seen in Fig. 2b. There is no apparent change in vertical wind at this point.

The vertical wind trace exhibits considerable variability during the entire ascent, with an average of 6 to 7 m s^{-1} up to about 5.5 km with a gradual increase in average vertical wind speed of 10 to 11 m s^{-1} by 6 to 7 km. The large excursions of vertical wind and other parameters with a periodicity of 50 to 60 s occur as a result of the sailplane flying near and then away from the core of the updraft. The LWC values measured by the FSSP (Fig. 2b) are within 20% of the adiabatic values during most of the ascent, except for the periodic times above 5.5 km when the sailplane moved away from the core of the updraft. Fully adiabatic regions were found as high as 7 km altitude in agreement with the Θ_e measurements.

3.2 Droplet Evolution

The droplet concentration and mean diameters measured by the FSSP are compared with concentrations and mean diameters calculated for adiabatic parcel ascent in Fig. 2a. The calculations were performed for cloud base concentration of both 800 and 900 droplets cm^{-3}. During the first 250 meters of the ascent and again at 5.9 km the measured concentrations are more consistent with cloud base concentration of 900 cm^{-3}. During the rest of the ascent the measured concentrations are more consistent with cloud base values of 800 cm^{-3}. Note that at 4.2 km the droplet concentration decreased rapidly with concurrent increases in mean droplet diameter and a sharp reduction in vertical wind, but no discontinuity in liquid water content.

Perhaps the reduction in droplet concentration was a result of the lower updraft speed which led to the activation of fewer cloud droplets at cloud base. However, there were large changes in vertical wind below this level but not corresponding changes in droplet concentration. Another explanation would be a change in the cloud condensation nuclei (CCN) spectra entering cloud base.

The mean diameters calculated for the ascent of the parcel with 800 droplets cm^{-3} were larger than those measured above 5 km. The mean volume diameter for the measured spectrum, was about 1 μm larger than the mean diameter, d, in these regions and would account for part of the difference. For the calculations the arithmetic mean and mean volume diameters are equivalent. However, since the calculations assumed that the water was uniformly distributed on the droplets, a comparison with the mean volume diameter seems more appropriate.

The FSSP one second measurements of concentration, mean diameter, and LWC are plotted versus each other in two minute time segments in Fig. 3 to demonstrate some characteristics of the droplet spectrum evolution at different altitudes. The solid lines in the figure show the relationship between these parameters for an adiabatic ascent of a parcel containing 800 droplets cm^{-3} at cloud base. From 1619 to 1620 the sailplane ascended through and was climbing shortly above cloud base. The rapid increase in droplet concentration, moderate change in mean diameter, and slight change in LWC illustrate the activation of droplets which occurred near cloud base. The overestimate of liquid water content at cloud base (Fig. 2b) and the minimum mean diameter of about 5 μm seen in any of the spectra suggest that the FSSP was not properly sizing the droplets in this size range even though the correction techniques described in Ref. 5 were used.

From 1620 to 1622 the abrupt droplet concentration decrease from 900 to 800 cm^{-3} can be seen. During the 1620 to 1622 and 1622 to 1624 periods the relationship between mean diameter and LWC was closely adiabatic and the droplet spectra are relatively homogeneous in nature. During the 1626 to 1628 and 1628 to 1630 periods the spectral characteristics become less uniform as more mixing occurs in the cloud. From 1626 to 1628 the mean diameter was still increasing fairly rapidly as the LWC increases, but by 1628 to 1630 little change in mean diameter was observed. The high correlation between droplet concentration and LWC which extrapolates through the origin is suggestive of an inhomogeneous mixing process through dilution. Similar relationships between concentration and LWC were present in much of the King Air data and were discussed in Ref. 1.

4. TEMPORAL AND HORIZONTAL STRUCTURE

The large scale, temporal evolution of LWC and vertical winds measured by the King Air were discussed in Section 2. The shape of the droplet spectra and modal diameters were remarkably consistent throughout the early lifetime of the cloud. Examples of spectra from representative regions of relatively high liquid water content from each of the first four passes are shown in Fig. 4. Although substantial erosion of the LWC did occur at times, the general shape, particularly the mean volume diameter, also remained nearly constant during individual passes. In most cases, King Air evidence points to a highly inhomogeneous mixing process, but with no accompanying broadening of the droplet spectrum.

5. BIMODAL DROPLET SPECTRA

Both the sailplane and King Air measurements showed bimodal droplet spectra to have been present but in quite different regions. The sailplane encountered bimodal spectra each time it came around to the mixed regions starting at 1625:30, 1626:20, and 1627:15, points C, D, and E in Fig. 2. The periodicity and location of these regions on the sailplane spiral flight track suggest vertical continuity of this region from at least 5.5 to 6.1 km. Using the observed updraft strength and droplet spectra, conditional supersaturations were calculated following the approach of Paluch (Ref. 7). The calculations suggest that the small mode of the observed spectrum could be explained by the further activation of CCN in strong updrafts. The bimodality of the spectra decreased at each successive encounter of the region, also suggesting that further growth of the droplets as they ascended was reducing the bimodality.

The King Air observed bimodal spectra in the large adiabatic region of pass 4 (Fig. 4). Since these spectra were measured in a region which was apparently unaffected by entrainment, mixing between cloud and environmental air are not possible explanations for the observation. Although instrumental effects cannot be ruled out, they seem unlikely since unimodal spectra were observed before and after these observations. One possibility is an acceleration of vertical airflow which could produce enhanced supersaturation and additional activation of CCN. If this were the case one might reasonably expect the sailplane to also have observed bimodal spectra in the adiabatic region at that

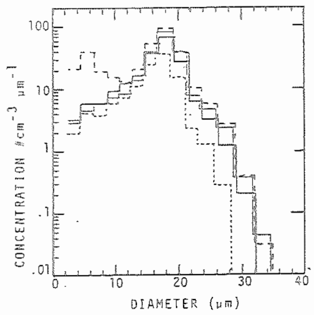

Fig. 4. Droplet spectra measured by the FSSP on the King Air in representative regions of high liquid water content on 19 July 1981. Pass 1-solid; pass 2-small dashes; pass 3-date; pass 4-long dashes.

level. A careful search did not reveal any tendency for this in the sailplane data. However, the sailplane data did show that the vertical velocity was larger above 6 km than below. It is possible that the sailplane either temporally or spatially missed the region investigated by the King Air. The King Air pass 4 data in the large adiabatic regions were remarkably uniform, whereas the sailplane data near 6 km showed considerable variability.

It is important to point out that the fraction of bimodal spectra observed by the sailplane or King Air were a very small fraction of all the measurements and, therefore, should not be overemphasized. However, the presence of the bimodal spectra help to identify processes which were occurring in the cloud.

6. CONCLUDING REMARKS

The observations made during the Early Storm Study on 19 July 1981 provide a wealth of information on the life cycle of a large cumulus congestus cloud. In this paper we have focused on the general characteristics of the storm history and precipitation development and the vertical and temporal evolution of the droplet spectrum. Additional studies on the origin of ice, details of precipitation development, evolution of the electrical structure, entrainment, and kinematic structure are being undertaken.

7. REFERENCES

1. Cooper, W. A. and A. R. Rodi: Cloud droplet spectra in summertime cumulus clouds. Preprints Conf. on Cloud Physics, Amer. Met. Soc., Chicago, IL, 1982, 147-150.
2. Jones, J. J. and W. P. Winn: Early electrification in a cumulus. Preprints Conf. on Cloud Physics, Amer. Met. Soc., Chicago, IL, 1982.
3. Cooper, W. A., 1978: Cloud Physics Investigations by the University of Wyoming in HIPLEX 1977, Rep. AS119, University of Wyoming, Laramie, Wyoming, U.S.A., 321 pp.
4. Cerni, T. A., 1983: Determination of the size and concentration of cloud drops with an FSSP. J. Cl. & App. Met., 8, 1346-1355.
5. Dye, J. E. and Baumgardner, D., 1984: Evaluation of the forward scattering spectrometer probe. Part I: Electronic optical studies. Submitted to J. Atmos. & Oceanic Tech.
6. Dye, J. E., L. J. Miller, B. E. Martner, Z. Levin: Dynamical-microphysical evolution of a convective storm. NCAR Technical Note. NCAR/TN-151+STR. NCAR, Boulder, CO, 248 pp.
7. Paluch, I. R. Mixing and the evolution of cloud droplet size spectra. Preprints 9th International Cloud Physics Conference. Tallinn, USSR, 1984.

VARIATION OF HAILSTONE SIZE DISTRIBUTIONS IN ALBERTA HAILSTORMS

Marianne English and Lawrence Cheng
Atmospheric Sciences Department
Alberta Research Council
Edmonton, Alberta, Canada

1. INTRODUCTION

Hailstone size distributions have been studied in Alberta to facilitate the remote measurement of precipitation by radar and to help evaluate hail suppression efforts.

The mathematical form for the size distributions that provides reasonable approximations to typical hailstone spectra is a truncated exponential function of the form

$$N(D) = N_o\, e^{-\Lambda D} \quad (5\text{ mm} \leq D \leq D_{max}) \qquad (1)$$

where N(D) is the number of hailstones per unit volume per unit size interval and D is the hailstone diameter (Ref. 1, 2, 3, 4, 5, 6). The size distribution must be truncated at a minimum diameter of 5 mm because of the definition of hail (Ref. 7). Since the most correlated experimental hail parameters are the maximum hailstone diameter, the maximum updraft velocity and the temperature of the updraft (Ref. 8), it appears that a storm can produce hailstones with a size up to that which can be supported by the updraft. Thus the hailstone size distributions must be truncated at some maximum diameter, D_{max}.

In addition to the exponential approximation for hailstone size distributions, it has been found that the intercept parameters, N_o, and the slope parameters, Λ, of individual size distributions can be related by a power relationship (Ref. 4) of the form

$$N_o = A\Lambda^b \qquad (2)$$

Furthermore, it appears that significant differences exist between the relationship derived for Alberta storms and that derived for a hailstorm in Switzerland, especially as far as the constant of proportionality, A, is concerned. No significant differences were found in the exponent parameter, b, between Alberta and Swiss storms.

Passarelli (Ref. 9) constructed an approximate analytical model of deposition and aggregation growth of snow assuming exponential ice crystal size distributions. He showed that an equilibrium relation should exist between the intercept and slope parameters (N_o and Λ), of the form $N_o = C\Lambda^3$, where C depends upon the cloud thermodynamics as well as microphysical parameters such as fallspeed, collection efficiency and depositional growth parameter. Elements of Passarelli's analytical model may be applicable to the growth of hailsones and so it is not unreasonable that a relationship of the form $N_o = A\Lambda^b$ should exist for hailstone size distributions and that the constant of proportionality, A, should be a function of storm thermodynamics.

A time-resolved hailstone sampling system has been operated as part of the Alberta Hail Project since 1979. (The sampling and data reduction procedures are described in Ref. 4.) In this paper, the hailstone size distributions and the thermodynamics of the storms from which the hail samples were collected are investigated. Only data from storms for which 8 or more hail samples were collected were used in this study. Furthermore, the samples had to meet the minimum criteria of at least 100 hailstones in the sample and a maximum diameter of at least 1 cm. These criteria were obtained by allowing a variable sampling duration. The criteria resulted in a data set which comprised 5 major storms.

2. RELATION BETWEEN N_o AND Λ

The N_o and Λ from our fitted hailstone distributions are plotted in Figure 1. This diagram suggests that a power relationship of the form $\log N_o = \log A + b \log \Lambda$ exists for the five Alberta storms. Least-squares regression analysis for the data points in Figure 1 gives the following expression for the line of best fit:

$$\log N_o = (1.79 \pm 0.11) + (3.86 \pm 0.25) \log \Lambda \qquad (3)$$

The standard deviations of the constant of proportionality and the exponent parameter are given inside the respective parentheses. The correlation coefficient for the data points to this line is 0.84. Equation (3) is very similar to Equation (11) in Ref. 4.

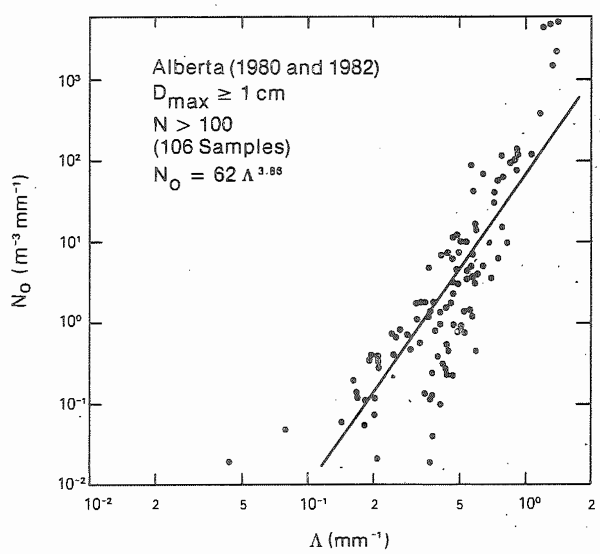

Figure 1. Variation of the intercept parameter (N_o) as a function of the slope parameter (Λ) of the exponential size distributions for the 1980 and 1982 time-resolved hailstone samples. The solid line is the line of best fit for the data.

N_o and Λ have also been examined on a storm by storm basis. Table 1 gives the coefficients of the line of best fit for each storm, the standard deviations of these coefficients and the correlation coefficient from the regression analyses. The exponent parameters, b, are all in good agreement within the standard deviations. Statistical testing of one-way analysis of covariance shows that the probability of equality of exponents is 0.98. However, the constants of proportionality, A, are quite different for the five storms. As will be shown in the next section, the differences in the constants of proportionality can be attributed to the differences in thermodynamic characteristics of the storms[1].

3. RELATION BETWEEN HAILSTONE SIZE DISTRIBUTIONS AND STORM THERMODYNAMICS

The thermodynamic properties of the 5 storms studied have been examined using the loaded moist-adiabatic (LMA) cloud model (Ref. 10). The model uses the atmospheric temperature and dew point profiles as input and calculates the available parcel energy, vertical velocity, and adiabatic water content. Upper-air data used for the 5 storms are obtained from representative rawinsondes released ahead of the storm. The

Table 1

Intercept and exponent parameters with standard deviations and the correlation coefficients of the line of best fit (of the form $\log N_o = \log A + b \log \Lambda$) obtained from regression analyses for each of the five storms studied.

Storm Date	log A	b	Correlation Coefficient r
27/7/80	1.63 ± .43	3.36 ± .79	0.85
02/8/80	2.01 ± .18	3.61 ± .34	0.97
30/6/82	0.84 ± .35	3.49 ± .88	0.67
21/7/82	1.80 ± .17	3.98 ± .45	0.84
11/8/82	2.18 ± .14	3.89 ± .29	0.92

$$\ln A = (-0.42 \pm 1.38) + (0.48 \pm 0.15)\, T_{CB} \qquad (4)$$

The correlation coefficient for this line is 0.88.

Very good relations between the maximum water mass flux M_{max} and the constant of proportionality, A, and between the product of the available parcel energy and liquid water content and the constant of proportionality, A, can also be obtained. The equations of the least-squares regression line of

Table 2

Storm thermodynamic parameters obtained with the LMA model.

Storm Date	T_{CB} (^oC)	V_{max}[1] (ms^{-1})	LWC_{max}[1] (gm^{-3})	PE_{max}[1] (Jg^{-1})	$(PE \times LWC)_{max}$ (Jm^{-3})	M_{max}[1] ($gms^{-1}m^{-3}$)
27/7/80	7.6	28.95	4.08	0.415	1.691	118.12
02/8/80	11.6	30.43	4.99	0.458	2.277	151.50
30/6/82	6.0	21.86	3.69	0.235	0.864	80.48
21/7/82	9.4	33.45	4.55	0.555	1.855	128.89
11/8/82	9.9	32.03	4.55	0.509	2.247	139.44

[1] LWC = liquid water content, PE = parcel energy, V = vertical velocity, M = water mass flux, T_{CB} = cloud base temperature

cloud base temperature is either estimated by the lifting condensation level determined from the surface temperature and moisture or by aircraft observations; aircraft observations being used when available. Table 2 summarizes the results from the LMA model for the 5 storms. Based on the classification given by Chisholm (Ref. 10), the storms of 27 July 1980 and 30 June 1982 are medium energy storms while the others are high energy storms.

The cloud base temperature for the 5 storms is plotted against the constant of proportionality, A, in Figure 2 in the semi-logarithmic form. It appears that the higher the cloud base temperature the larger N_o. The least-squares regression line of best fit is shown in the diagram and can be expressed as

[1] Two of the five storms studied (27 July 1980 and 2 August 1980) were seeded with AgI flares, the other three storms were not seeded during the period that hailstone sampling occurred. Since no conclusive evidence has yet been found that seeding with AgI flares affects hail on the ground, the seeding has been ignored in this analysis.

best fit are

$$\log A = (-8.12 \pm 1.39) + (4.71 \pm .67) \log M_{max} \qquad (5)$$

and

$$\log A = (1.01 \pm .07) + (2.97 \pm .26) \log(PE \times LWC)_{max} \qquad (6)$$

The correlation coefficients are 0.97 and 0.99, respectively. These relations simply imply that the warmer the cloud base and the more severe the storm the higher the hailstone concentration is likely to be.

4. MAXIMUM HAIL WATER CONTENT

Available evidence suggests that a maximum concentration may exist for each size category of hailstones if the relationship between N_o and Λ is valid (Ref. 4). Thus a maximum hail water content likely to have existed can be estimated for each storm once the maximum hailstone size for the storm is determined. This maximum hail water content can be compared to the maximum adiabatic water content to determine the fraction of the available water that is converted to hail by each storm. Table 3 summarizes the maximum hailstone size as estimated by volunteer observers, the

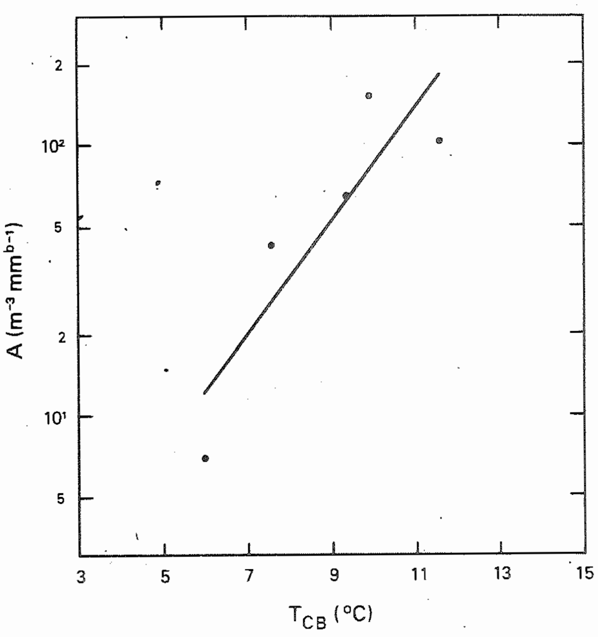

Figure 2. Variation of the constant of proportionality (A) of the $N_o - \Lambda$ relationship as a function of cloud base temperature (T_{CB}) for the five 1980 and 1982 hailstorms. The solid line is the line of best fit of the data.

maximum hail water content likely to have existed in the storm and the ratio of this maximum hail water content to the maximum adiabatic liquid water content for each of the 5 storms. Note that the percentage of available water converted to hail is rather small for all storms and is highly variable from storm to storm.

5. CONCLUSIONS

Hailstone size distributions have been determined from 106 time-resolved hail samples collected from 5 storms that occurred in Alberta in the summers of 1980 and 1982. Truncated exponential distributions have been fitted to the hailstone size and concentration data for each hail sample. Power relationships, of the form $N_o = A\Lambda^b$ have been derived for the intercept (N_o) and slope (Λ) parameters of the fitted size distributions for each of the 5 storms. No significant differences were found amongst the 5 exponent parameters (b), but significant variations from storm to storm were recognized in the constant of proportionality (A).

The variation in the constant of proportionality (A) with cloud base temperature (T_{CB}), maximum water mass flux and maximum product of parcel energy and liquid water content were investigated. (Cloud base temperature is an indication of the amount of water vapor available to the storm, while the product of parcel energy and liquid water content is an indicator of the amount of work done by the storm on the water substances.) In general, the constant of proportionality, A, increases with all of these parameters, indicating that the more water vapor available to the storm, the greater the water mass flux and the greater the availble work, the more hail is likely to fall from the storm. An exponential approximation can relate the constant of proportionality (A) to the cloud base temperature (T_{CB}), while power relationships have been derived to relate the constant of proportionality to maximum water mass flux and maximum product of parcel energy and liquid water content.

Table 3
Estimate of maximum hailstone size, maximum hail water content predicted from the $N_o - \Lambda$ relationship and ratio of maximum hail water content to maximum liquid water content.

Storm Date	D_{max} (mm)	W_{max} (gm^{-3})	W_{max}/LWC_{max} (%)
27/7/80	40–50	.50 –.60	12.2–14.8
02/8/180	30–40	.65 –.81	13.1–16.2
30/6/82	40–50	.066–.084	1.8– 2.3
21/7/82	50–60	.33 –.36	7.5– 8.1
11/8/82	20–30	.51 –.68	11.3–15.0

Using the relationship between N_o and Λ, a maximum hail water content has been determined for each storm. In comparing this maximum hail water content to the maximum adiabatic liquid water content it was found that the percentage of available water converted into hail is rather small and highly variable from storm to storm.

The relationship between N_o and Λ implies an inverse relationship between number and size of hailstones because N_o is proportional to concentration and Λ is inversely related to size.

The relationships derived in this study can greatly facilitate the measurement of hailfall by weather radar.

The relationships derived can also greatly facilitate the evaluation of hail suppression programs. Predictor values of various hail parameters can be calculated from these relationships which can then be compared to measured values to obtain an estimate of modification effects.

It should be emphasized, however, that data from many more storms are required to confirm these results. It would be desirable to examine data from other regions to see if similar relationships can be determined.

6. ACKNOWLEDGMENTS

The authors are very grateful to all the people involved in collecting the hailstone samples and in the data reduction endeavour, in particular, Mr. A. Davis, Mr. C. Ewing, Ms. M. Fong, Ms. C. Bachand, Dr. L. Wojtiw and especially Ms. B. Henderson. Special thanks are also due to Messers R. Wong, N. Chidambaram and B. Kochtubajda for their assistance. Discussions with Prof. E. Lozowski of the University of Alberta have been very helpful. The project was funded by Alberta Agriculture and the Alberta Research Council.

7. REFERENCES

1. Douglas, R.H., 1963: Size distributions of Alberta hail samples. Sci. Rep. MW-36, Stormy Weather Research Group, McGill University, Montreal, 55-70.

2. Federer, B. and A. Waldvogel, 1975: Hail and raindrop size distributions from a Swiss multicell storm. J. Appl. Meteor., 14, 91-97.

3. Federer, B. and A. Waldvogel, 1978: Time-resolved hailstone analyses and radar structure of Swiss storms. Quart. J. Roy. Meteor. Soc., 104, 69-90.

4. Cheng, L. and M. English, 1983: A relationship between hailstone concentration and size. J. Atmos. Sci., 40, 204-213.

5. Ulbrich, C.W., 1974: Analysis of doppler radar spectra of hail. J. Appl. Meteor., 13, 387-396.

6. Ulbrich, C.W., 1977: Doppler radar relationships for hail at vertical incidence. J. Appl. Meteor., 16, 1349-1359.

7. Huschke, R.E., 1959: Glossary of Meteorology, Amer. Meteor. Soc., pp. 638.

8. Dennis, A.S. and D.H. Musil, 1973: Calculations of hailstone growth and trajectories in a simple cloud model. J. Atmos. Sci., 30, 278-288.

9. Passarelli, R.E., Jr., 1978: An approximate analytical model of the vapor deposition and aggregation growth of snow. J. Atmos. Sci., 35, 118-124.

10. Chisholm, A.J., 1973: Alberta Hailstorms. Part 1: Radar case studies and airflow models. Meteor. Monogr., No. 36, Amer. Meteor. Soc., 1-36.

ON SNOW PARTICLES COMPRISING AN AGGREGATE

Yasushi Fujiyoshi and Gorow Wakahama

Institute of Low Temperature Science, Hokkaido University,
Sapporo 060, Japan

1. INTRODUCTION

Solid precipitation in winter mostly originates from band snow clouds in the coastal region of the Sea of Japan; then the amount of snowfall and precipitation intensity vary significantly with the cloud. To clarify causes giving rise to this variance counts for much in forecasting and modifying the amount of snowfall.

Snow particles often observed in this region have the form of an aggregate. Accordingly, such snow particles have been subjected to studies by many researchers on relationships of the size of the aggregate with properties such as types, size distribution and number per aggregate of snow particles (Refs 1-3). Studies on a relationship of precipitation intensity with size of the aggregate are also abundant (Refs 1, 3, 4-8). Few reports deal, however, with a relationship of precipitation intensity with types and size distribution of snow particles comprising an aggregate.

The purpose of this paper is to elucidate what kinds of microphysical processes predominantly affect the amount of snowfall and the precipitation intensity by investigating the types and size of such snow particles.

2. METHOD

Aggregates were sampled in Sapporo, Japan, from January to February in 1983. They were caught on a piece of velvet cloth and were dipped into a bath filled with cooled silicon oil at -10 °C. Each aggregate was then separated into individual snow particles as carefully as possible in a cold room at -10 °C so that they were not broken.

Precipitation intensity was measured by weighing the total mass of snow particles which had fallen into a pan 56.5cm X 40cm in size during every five minutes.

3. RESULTS

3.1. Precipitation intensity

Figure 1 shows a relationship between maximum precipitation intensities averaged for ten minutes (R_{10}, mm/hr) and one hour (R_{60}, mm/hr). As shown in the figure, R_{10} is proportional to R_{60}.

It snowed continuously from February 26 to 27 in Sapporo. The resultant accumulation amounted to 102 cm during the two days, which turned out as an extraordinarily large amount of snowfall between November 1982 and April 1983. However, both R_{10} and R_{60} for the two days were not the largest as shown in Fig. 1, from which it follows that the most necessary factor for a heavy snowfall is not precipitation intensity, but snowfall duration.

As seen from Fig. 1, the values of R_{10} of February 16 is 16 times that of January 13.

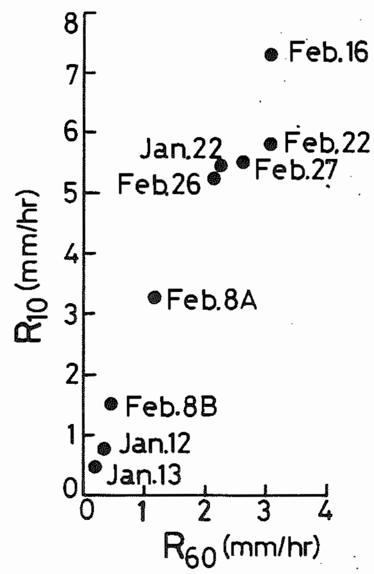

Figure 1. Relationship between maximum precipitation intensities averaged for ten minutes (R_{10}, mm/hr) and one hour (R_{60}, mm/hr).

3.2. Types of snow particles comprising an aggregate

Snow particles comprising an aggregate were classified into three types according to degree of riming; namely, (Type 1) nonrimed or lightly rimed snow crystals; (Type 2) rimed or heavily rimed snow crystals (distinguishable the type of snow crystal prior to riming); and (Type 3) heavily rimed or graupel-like snow particles. A few aggregates were sampled when R_{10} was at its maximum for examining percentage ratios of the number of snow particles of each type to the total number by counting and averaging them, the result of which is shown in Fig. 2 in the increasing order of magnitude of precipitation intensity.

When $R_{10} < 4$ mm/hr (Jan. 13, Jan. 12, Feb. 8A, Feb. 8B), the ratio of the first type decreases with increasing precipitation intensity. Meanwhile, when $R_{10} > 5$ mm/hr (Jan. 22, Feb. 22, Feb. 16), the ratio of Type 1 is slightly over 30 %. When it snowed very hard (Feb. 26 and 27), the ratio of Type 3 is fairly large in comparison with ratios of the other types. It shows that snow crystals were rimed very actively in clouds then.

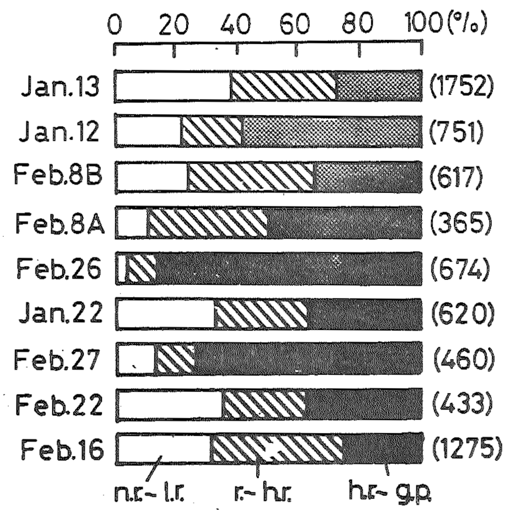

Figure 2. Percentage ratios of the number of snow particles of nonrimed or lightly rimed snow crystals (n.r. ~ l.r.), rimed or heavily rimed snow crystals (r. ~ h.r.) (distinguishable the type of snow crystal prior to riming), and heavily rimed or graupel-like snow particles (h.r. ~ g.p.) to the total number of snow particles (written in round bracket).

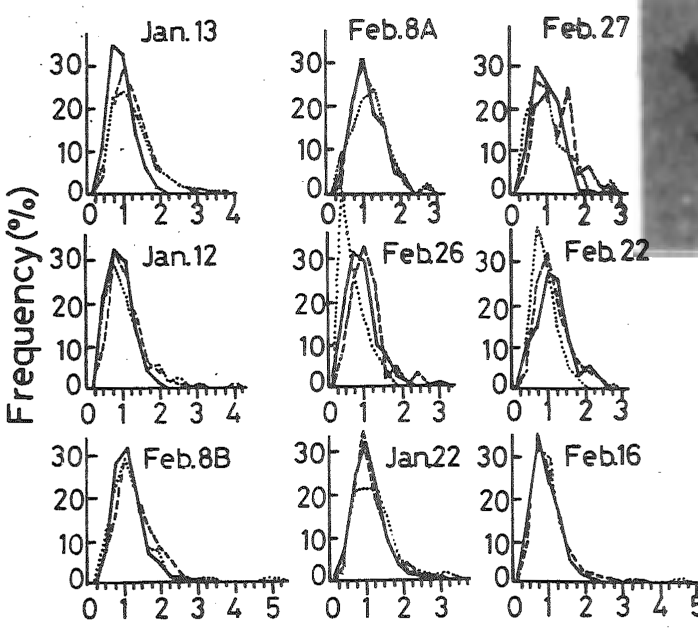

Figure 3. Size distribution of snow particles of Type 1 (dotted line), Type 2 (dashed line) and Type 3 (solid line). Size interval is taken to be 0.25 mm.

3.3. Size distribution of snow particles and types of snow crystals

Figure 3 shows the size distribution of snow particles. It is found that Type 2 and Type 3 lie mostly in a size range from 0.5 - 1.25 mm, whereas Type 1 lies mostly in a size range from 0.5 - 1.5 mm. This type shows a broader size distribution than Type 2 and Type 3.

When R_{10} < 4 mm/hr (Jan. 13, Jan.12, Feb. 8A, Feb. 8B), the size of particles of Type 3 tends to increase on an average with increasing precipitation intensity. No apparent differences exist in size distribution of snow particles between the cases in which R_{10} < 4 mm/hr and > 5 mm/hr. The size of particles of Type 3 observed on February 26 and 27 when it snowed very hard is small on an average.

All the crystals of Type 1 are stellar crystals and spatial dendrites according to International Snow Classification. When R_{10} < 4 mm/hr, snow crystals are rimed especially in the tip of branches of a crystal, as shown in Fig. 4a. On the other hand, when R_{10} > 5 mm/hr (Jan. 22, Feb. 22, Feb. 16), rimed stellar crystals with nonrimed extensions (Fig. 4b) were found very often.

When R_{10} < 4 mm/hr, the size of snow particles of Type 3 increases with increasing precipitation intensity, as seen in Fig. 3. Cone-like graupels were found especially on February 8A. When R_{10} > 5 mm/hr (Jan. 22, Feb. 22, Feb. 16), graupel-like snow particles with nonrimed extensions were found. Graupel-like snow particles with long nonrimed extensions (Fig. 4c) and rimed stellar crystals with nonrimed extensions (Fig. 4b) were found especially on February 16 and February 22.

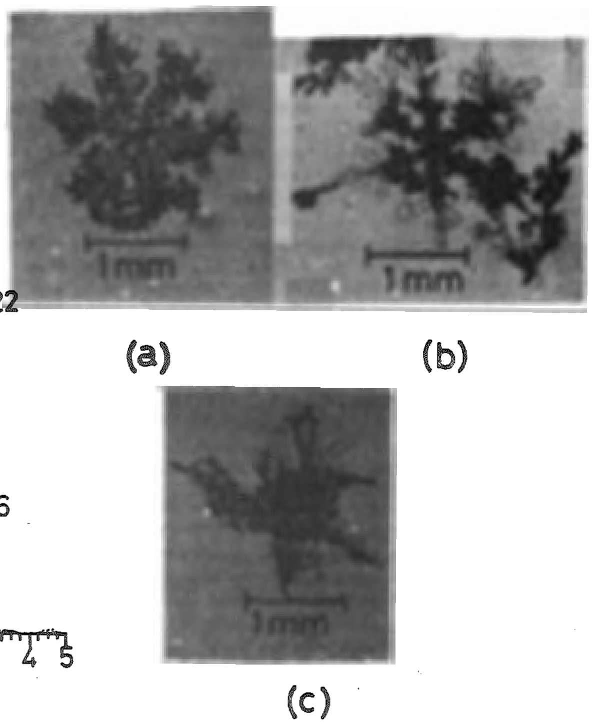

Figure 4. (a) Stellar crystal especially rimed in the tip of branches (observed on Jan 12), (b) stellar crystal with nonrimed extensions (observed on Feb. 22), (c) graupel-like snow particles with long nonrimed extensions (observed on Feb. 22).

4. DISCUSSION

When R_{10} < 4 mm/hr, the ratio of Type 1 decreases with increasing precipitation intensity, and the size of particles of Type 3 increases on an average with increasing precipitation intensity. It shows that the riming process contributes greatly to an increase in precipitation intensity then. It is obvious that the riming of a snow crystal occurs before it comes to aggregate with another snow particle.

When R_{10} > 5 mm/hr except on February 26 and 27, the ratio of Type 1 is slightly over 30 %. No apparent differences exist in size distribution of snow particles between the cases in which R_{10} < 4 mm/hr and > 5 mm/hr. Further, snow particles with nonrimed extensions are found only when R_{10} > 5 mm/hr. These facts indicate that the feeder zone where depositional growth of snow particles and snow crystals occur plays an important role in an increase in precipitation intensity.

Figure 5 shows vertical profiles of relative humidity with respect to water. It is found that the relative humidity is larger when R_{10} > 5 mm/hr than when R_{10} < 4 mm/hr. Also, the air temperature region where stellar crystals grow (around -15 °C) exists in the lower half of the layer from the ground to the level of the radar-echo top when R_{10} > 5 mm/hr. When R_{10} > 5 mm/hr, it is, therefore, suggested that snow crystals are rimed in a covective region (seeder zone), grow by deposition during their fall and aggregate with crystals of three types of snow particles in the feeder zone.

As mentioned above, snow particles with nonrimed extensions are likely to be rimed and then grow by deposition before aggregating with other particles. In contrast to them is the frequent observations of the following snow crystals in samples of aggregated snow particles originating from band snow clouds (Fig. 6, Dec. 6, 1983); namely, snow crystals, the formation process of which is likely that they grow by deposition and be rimed after aggregation. Factors controlling such properties of snow particles composing an aggregate remain to be elucidated. A difference in vertical profile of air temperature in clouds is a possible factor, as mentioned below.

As shown in Fig. 7, the -15 °C level of air temperature exists near the level of the cloud top on Dec. 6, 1983. It is considered in this case that snow crystals grew rapidly by consuming supercooled water droplets to become stellar crystals, and then aggregated with one another near the cloud top, since their size and their shape were favorable to aggregation. In contrast to this case the air temperature was lower than -15 °C near the cloud top from January to February, 1983. It is also considered that snow crystals grew slowly and hardly aggregated with other particles because of their small size, their shape and low temperature; consequently riming dominated aggregation near the cloud top.

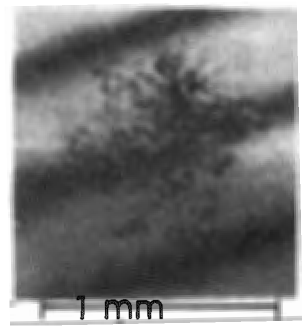

Figure 6. Stellar crystal with both nonrimed and rimed long extensions (observed on Dec. 6).

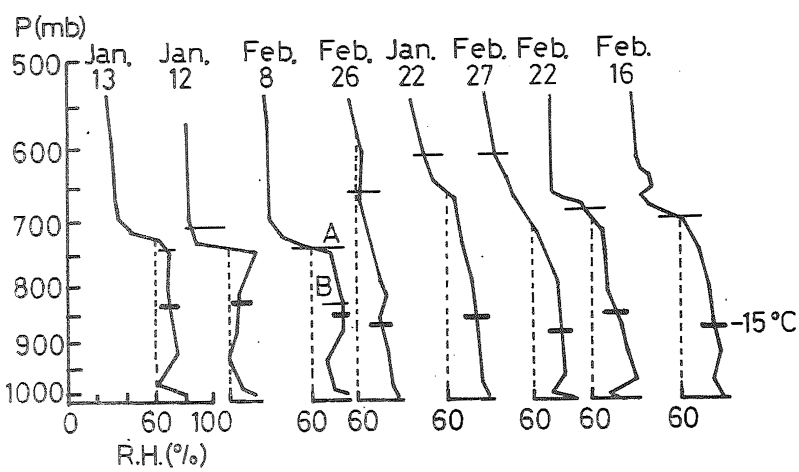

Figure 5. Vertical profiles of relative humidity with respect to water (R.H.). Vertical dashed lines mean 60 % of R.H. in each figure. Horizontal small bars mean the level of radar echo top. Horizontal small thick bars mean the level of -15 °C of air temperature.

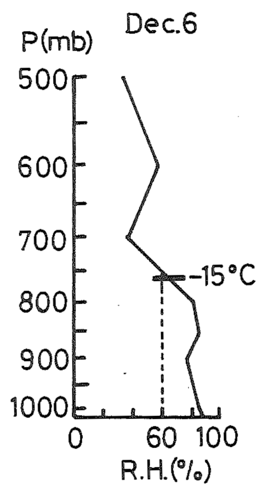

Figure 7. A vertical profile of relative humidity with respect to water.

5. REFERENCES

1. Hobbs P V, Chang S and Locatelli J D 1974, The dimensions and aggregation of ice crystals in natural clouds, J Geophy Res 79, 2199-2206.

2. Ohtake T 1970, Factors affecting the size distribution of raindrops and snowflakes, J Atmos Sci 27, 804-813.

3. Rogers D C 1974, The aggregation of natural ice crystals, Report No.AR110, University of Wyoming, Laramie.

4. Gunn K L S and Marshall J S 1958, The distribution with size of aggregate snowflakes, J Meteor 15, 452-461.

5. Magono C and Arai B 1954, On the split of snow flakes, J Meteor Soc Japan 32, 336-343.

6. Ohtake T 1969, Observations of size distributions of hydrometeors through the melting layer, J Atmos Sci 26, 545-557.

7. Sekhon R S and Srivastava R C 1970, Snow size spectra and radar reflectivity, J Atmos Sci 27, 299-307.

8. Passarelli R E Jr 1978, Theoretical and observational study of snow size spectra and snowflake aggregation efficiences, J Atmos Sci 35, 882-889.

THE MICROPHYSICAL STRUCTURES OF HAILSTONES OBSERVED ON THE XIZANG PLATEAU

Guo Enming

Institute of Weather Modification Academy of Meteorological Science State Meteorological Administration Beijing People's Republic of China

1. Introduction

The Xizang Plateau (formerly known as the Plateau of Tibet) is composed of a group of mountains, for instance, the Himalayan, the Kunlun, the Tanggula, the Nianqingtanggula and the Gandisi Mountains. These mountains have an average height of over 4,500 meters above sea level, and many of the mountain peaks are snow-capped throughout the year. Important rivers on the Xizang Plateau are the Yarlung Zanbo River, the Nujiang River, and the Lancangjiang River (known as the Brahmaputra, the Salween, and the Mekong respectively outside the territory of China). Many streams and lakes scatter over the Plateau. In summer, much more water vapour is evaporated into the atmosphere due to the melting of ice and snow, favouring the formation and development of convective clouds. The Plateau is exposed to strong solar radiation in long duration, and often strengthened by atmospheric vortices or shear lines, lead to the advantage of unstable stratification. The ascending of air along the mountain slopes spurs the convective clouds to develop into hail-bearing Cumulonimbus. Consequently, the Plateau experiences not infrequently showers, graupels or hailstones in summer days.

From June to July in 1981, we made an expedition to the Xizang Plateau with reference to colud physics. There we encountered 9 hailstorms which we studied later through photographs of hailstone structure and size distribution of hailstones. In addition, we collected historical weather data with respect to hailstorms from weather observatories in that area. Based on these information, preliminary investigations were made into the structures of hail clouds and hailstones observed on the Plateau.

2. Hail clouds

Hail-bearing clouds over the Xizang Plateau evolve mainly from single convective cells. Generally speaking, the top of these clouds are not very high, ranging from 5,000 to 8,000 meter above the surface, and usually, the cloud top temperature is below -20°C. Sometimes clouds of limited depth may also release graupels and hailstones. Fig. 1 shows a hailfall photographed at Dingri towards southwest.

The height of the cloud top was around 8,000 meters and the cloud depth about 2,000 meters. The cloud moved to the northwest after crossing the mountain peak. The hails, graupels and rain fell down from the rear part of the cloud.

Fig 1. Hail-bearing cloud (Dingri, June 25, 1981)

Fig. 2 illustrates another hailstorm observed on the Jiacuola Mountain with elevation of 5,200 meters.

Fig 2. A hailstorm cloud (Mt. jiacuola, June 24, 1981, from an elevation of 5,200 meters)

Hailstones accumulated on the hillside to a depth of 2 centimeters. The cloud in Fig. 2 was somewhat different from the hail clouds observed in lower areas (3,500-4,500 meters above sea level). The latter usually evolved from several convective cells merging into a single whole, then grew exuberantly to a higher level (some 9,000 meters above the ground). There were also hail clouds derived from single convective cells, but they produced only a small amount of hailstones for a short duration.

On the basis of the analyses of several hailstorms we encountered, we are inclined to the view that most of the hail clouds over the Plateau developed from single convective cells. Severe hailstorms derived from the merging of several convective cells were seldom seen. Such severe storms generally were caused by the passage of a depression or shearline in the lower atmosphere, accompanied with strong cold advection aloft. They were not the outcome of local convective cells.

3. The microstructure of hailstones

Most of the hailstones observed on the Xizang Plateau had an opaque outermost layer, with distinct layers of alternately clear and cloudy ice inside. Evidently this structure was formed during successive stages of wet and dry growth. The cloudy layers were sometimes compactly constructed and sometimes loosely organized. On the spot of observation, we found that the majority of hailstones had only 2-3 layers. The number of layers is less than that observed in the interior of China. We have not found bigger hailstones with more layers on the Plateau. Possibly this is due to the fact that we have not encountered severe hailstorms during our visit.

The embryos of the hailstones were mostly opaque graupels Fig. 3 although a few of the stones had a clear frozen drop in their centers.

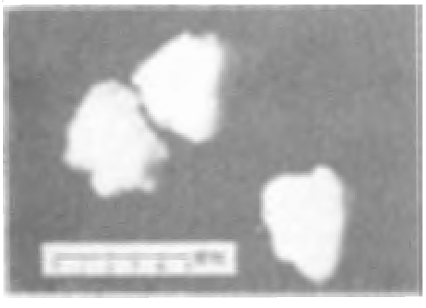

Fig 3. Opaque graupels

These are in accordance with the observations in China Interior[1].

Hailstones with multiple nuclei were observed on June 26 at 12:50 from an elevation of 5,100 meters in the northeast of the Jiacuola Mountain. Beyond our expectation, we found some of the stones had 2-4 nuclei, some others had even 5 nuclei. Most of these nuclei were opaque graupels, although some of them were clear ice pellets. In Fig. 4 we can see a hailstone with melted outer layer and four nuclei. Upon close examination, we may discern other hails with shallow protuberances on their surfaces, indicating multiple nuclei inside.

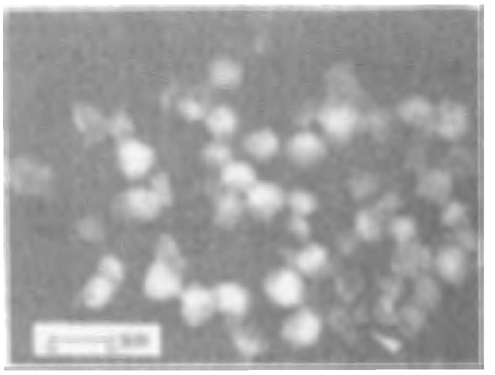

Fig 4. Hailstones with multi-nuclei (12:55, June 22, 1981.)

Hailstones of this sort were only observed during two storms from an elevation over 5,000 meters, mostly on the north-eastern side of the mountain. In our view, the hail clouds in this area were comparatively shallow, yet the vertical motion within the clouds were highly variable due to complicated topography. Consequently there was a high coalescence efficiency between the graupels and frozen drops, favouring the formation of multi-nuclei structure. Such "composite embryo" further experienced a dry growth in the cloud, wrapped in an opaque layer[2].

Hailstones with multi-nuclei structure were also observed in Beijing on July 14, 1982. Fig. 5

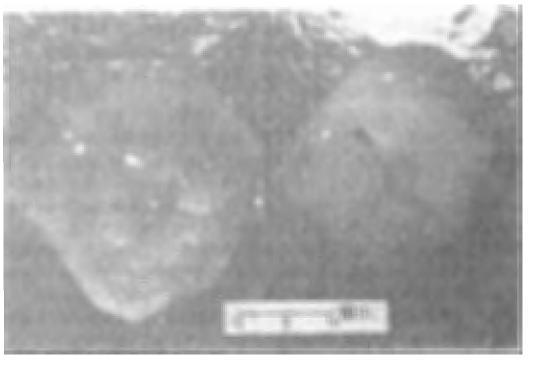

Fig 5. Multi-nuclei Hailstones (19:40, July 14, 1982. Beijing)

L.N. Rogers has shown an embryo composed of two melting particles in a hailstone slice. Yet hail embryos consisting of more than two particles so far have not been found in literature[3].

4. Shapes of hailstones

Of the four hailstorms we encountered, three storms were observed nearly from beginning to end.

The shapes of 2,628 hailstones are

classified and listed in Table 1.

Table 1
Classification of the shapes of hailstones

Place of observation	Shape spherical	ellipsoid	conical	irregular
Mt. Jiacuola (5,200 m)	315	225	124	34
Mt. Jiacuolà (5,100 m)	384	106	74	29
Mt. Mila (4,500 m)	665	279	191	202
Percentage (%)	51.9	23.2	14.8	10.1

In Table 1 we can see that the majority of the hailstones appeared in the spherical form. Since the stones were rather small, they were difficult to be classified and the "spherical" hailstones may contain some ellipsoid stones or the like. The irregular hails were of various shapes. Some were in the form of a long, narrow bar, with 1-3 transparent lobes on the surfaces, others with many ice splinters. The result of classification is similar to those observed in the interior of China and abroad. The special feature of the multi-nuclei hailstones observed from an elevation of over 5,000 meters was the irregular appearance owing to the aggregation of several nuclei. Spherical stones were observed in case the hail was wrapped in a thick layer of ice.

5. Size distribution of hails

The size distribution of hailstones is an important information for the study of hail physics. Large hailstones densely hitting the ground bring about a severe damage. Hails on the Xizang Plateau were also characterized by comparatively small size (mostly 3-5 millimeters in diameter), due to the small depth and low water content of the hail clouds. Generally, hails were accompanied by graupels and rarely covered a vast extent. Fig. 6 shows the hail spectra observed on the Jiacuola Mountain and the Mila Mountain. It can be seen that the maximum diameter of the hails amounts to 9 millimeters while the minimum is about 2 millimeters.

The size distribution of hailstones observed on the Mila Mountain and to the southwest of the Jiacuola Mountain shown in Fig. 6 both occurred in the shape of logarithmic curves with the peak values at 4 millimeters. The spectrum observed to the northeast of the Jiacuola Mountain appeared in a quite different way. It was much broader, having a maximum diameter of 9 millimeters and a minimum of 3 millimeters, with the peak value at 6 millimeters. Most of the stones concentrated within the range between 5-7 millimeters. The broad spectrum may be attributed to the fact that there were a number of multi-nuclei hailstones during the hailing process and the mechanism of the formation of hails had its particularity.

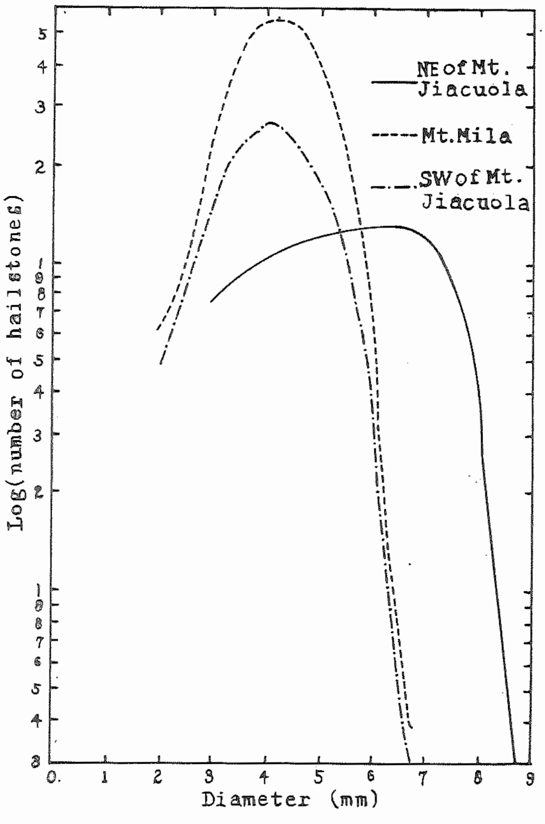

Fig 6. Size distributions of hails

In order to investigate the maximum size of hailstones on the Xizang Plateau, we plotted the curve in Fig. 7 according to the historical data of Naqu Observatory and other places. It can be seen in Fig. 7 that most of the 51 storms concerned (35.2%) produced hailstones with a maximum diameter of 3 millimeters. A few storms (11.8%) released hails with a maximum diameter of 1 millimeter.

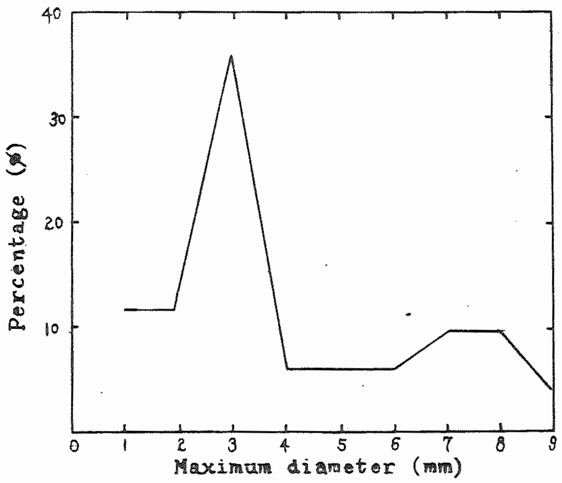

Fig 7. Occurring frequency of maximum diameter of hailstones

On the basis of the 18-year record of 672 hailstorms observed at the Naqu Observtory, only was the storm occurring on June 9, 1974 reported to rain hails with a maximum weight of 4.5 grams. On May 19, 1980 maximum stone diameter of 1.5 millimeter was observed. Although hails of the egg size have been reported by the people, there were no quantitative record was found.

6. Statistical analyses of hail observations

The Xizang Plateau is the area where hailstorms occured most frequently in China. We lay emphasis on the observational data of the Naqu Observatory, supplemented with the data of Lhasa, Rikeze and Linzhi.

The 18-year record of 672 hailstorms is summarized in Table2.

Table 2.
Monthly mean number of hailstorms at Naqu

Month	May	June	July	Aug.	Sept.	Oct.
Number of storms	18	161	163	169	159	2
Percentage (%)	2.7	24.0	24.2	25.1	23.7	0.3

Table 2 shows that most of the hailstorms occurred in summer, from June to September. The annual mean amounts to 37.3 storms per year. The earliest hails happened in May, the last in October. The maximum number of hailstorms were observed in 1976, attaining 48 storms from May to August. The minimum occurred in 1973, 21 storms hit the area from May to October.

References

(1) Guo Enming, 1983. Microphysical Structures of grauples and frozen dropes observed. *Acta Meteorological Sinica* Vol. 41, No. 3 .

(2) Browning, K.A. 1966, The lobe sturcture of giant hailstones *Quart.J.R.Meter* Soc 92. 1-14.

(3) Rogers, L.N. 1971, Two unusual hailstones. *Bull. Am. Meter* Soc 52, 994.

SOME PHYSICAL CHARACTERISTICS OF STRATIFORM CLOUD AND PRECIPITATION IN THE XIN-AN RIVER VALLEY, PROVINCE ZHEJIANG, EAST CHINA

Huang Mei-yuan He Zhen-zhen Shen Zhi-lai
Hong Yan-chao and Wu Yu-xia

Institute of Atmospheric Physics, Academia Sinica
Beijing, China

ABSTRACT

According to data observed by radar, airplane and others in the Xinan River valley, the analyses and studies are presented of (1) the precipitation features, radar echo structure and macro-physical and micro-physical characteristics of precipitating stratiform cloud, (2) the distribution of large cloud droplets and the correlation between the concentration of large cloud droplets and rainformation and (3) the vertical distribution of giant salt nuclei concentration with height in and out of cloud under different weather situation.

1. INTRODUCTION

In 1979-1980, observations were carried out through aircraft, radar and ground-based network over the basin of the Xinan River surounded by Hangzhou, Tunqi and Jiande.

An analysis based on the data of June and July shows that at this basin the appearence of various clouds is more than 20 days per month for the precipitable stratiformis (such as As, Ns, Sc), about 15 days for Cu, and about 10-14 days for rainfall. The fraction of stratiformis rainfall is above 2/3 and that of convective cloud rainfall is less than 1/3. Stratiformis rainfall is produced mainly by two kinds of clouds or cloud systems. One of them is quite thick As-Ns system. The daily rainfall amount is about 30-50 mm. The other is As, Ns or Sc, the daily rainfall amount is generally 2-15 mm. In the latter, all of Ns are precipitus, but some of As, Sc are not. In June, the rainfall probability is about 50-60% for As and about 30-40% for Sc respectively.

The analysis shows that the rainfall from the stratiform clouds in this region is much larger than the total water content in the clouds. The moisture cycles many times in clouds. The number of cycle reaches 20-50 in the deep precipitus system of As-Ns-Sc. For Ns generally it is about 20 times, but for Sc only 3-5 times. The precipitation efficiency of various clouds is analysed via estimating the moisture amount entried into the base of cloud. The precipitation efficiency in deep precipitus system of As-Ns-Sc is high, about 0.75-0.96, for Ns it is 0.38-0.48. It is lowest in the thin cloud of Sc, only 0.25.

In this region all of Sc are warm clouds. Their thickness is between 500 m and 4000m. But most of them are 2000-3000 m thick. The lowest temperature on the top of the clouds is 5° C. The liquid water content in the clouds is 0.1-1.0 g/m^3. The average value is about 0.4 g/m^3. It shows that the liquid water content of Sc over the basin of Xinan River is more than that of the same cloud in north China and USSR. In this region not all Sc are precipitus. The preliminary analysis indicates that the thickness of precipitus Sc is generally more than 2000 m; its liquid water content is not less than 0.5 g/m^3. The concentration of large droplets reaches to $10^3/m^3$ in order of magnitude.

2. INHOMOGENEOUS STRUCTURE IN STRATIFORM CLOUD

Our observations show that in Sc and sometimes in Ns and As, there are inhomogeneous constructions in the horizontal direction, which appear as some strong echo cores in the radar echoes. They may be divided into two types. One is the echo of convective cell in stratiformis (Fig.1), which develops upwards from below. The other is the inhomogeneous bright echo band which appears first near the 0° C level. Some parts of echoes in the bright band are stronger than that of others as strong echo cores. Then these strong cores develop downwards gradually and form the bright strip in the vertical direction (Fig.2) and heavy rainfall, which is called rain cores. According to the extent of aircraft bump and the data of the liquid water content and temperature which are observed continuously during the flight, it can be concluded that there are really some areas with larger liquid water content in the horizontal direction where the bump is rather strong and the temperature is high. These may be the convective cells in the stratifor-

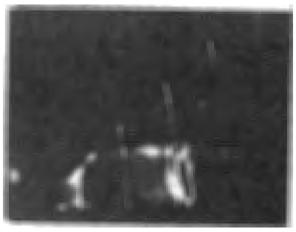

Fig.1. The radar echoes of convective cell in stratiformis.

mis. However, in other areas with much more liquid water content, there are no higher temperatures and sensible bumps than those of the surroundings. The tentative analysis shows that the inhomogeneities (the common name of both convective cell and rain cores mentioned above) are related closely to the rain formation and the increasing of rain intensity.

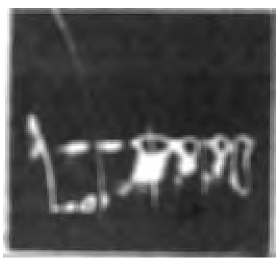

Fig.2. The radar echoes of strong cores in stratiformis.

3. LARGE CLOUD DROPLETS

We observed and analysed the large droplets (diameter more than 80μ) in the stratiformis at this region. The results show that in As, Ns and Sc precipitus, the average concentrations of large droplets are 14.0, 6.3 and 7.7/litre respectively (Table 1). For three kinds of cloud, the probabilities of more than 1/litre of large droplet concentration are 85%, 65% and 65% respectively. It shows that there are many large droplets in the precipitus stratiformis. The spectrum of large droplets is wide too. It is worthy to point out that in the thin Sc with a thickness of less than 2 km, the concentration of large droplets is also able to reach 2.6/litre and precipitation can be produced.

In general, the concentration and spectrum of large droplets in the Sc non-precipitus are less than that in Sc precipitus, but it is true that the average concentration of large droplets in Sc non-precipitus still reaches 4.8/litre. 30% probability of 1/litre of large droplet concentration was still observed. It means that although the large droplet concentration in some Sc is more than 1/litre (in other words it has already reached the concentration of natural rain drops) it still fails to produce rainfall.

The further analysis shows that there are two kinds of Sc non-precipitus. For one, large droplet concentration is too low ($10^1/m^3$) to form rain. For the other, only few precipitation elements of more than 500μ in diameter exist, though the concentration of large droplets of more than 80μ in diameter may reach to $100/m^3$, even to $1000/m^3$. It seems that although there are many large droplets of more than 100μ in diameter in these clouds, they still cannot form rainfall, because of either lower liquid water content (less than 0.2 g/m^3) or weak updraft. Most of large droplets can not grow up to 500μ.

Table 1

Cloud type	Average concentration of large droplets ($litre^{-1}$)			
	for $d\geq 80\mu$	for $d\geq 200\mu$	for $d\geq 500\mu$	for $d\geq 1000\mu$
As precipitus	14.0	0.5	0.46	0.09
Ns precipitus	6.3	1.0	0.26	0.08
Sc precipitus	7.7	1.5	0.22	0.03
Sc non-precipitus	4.8	0.63	0.001	0

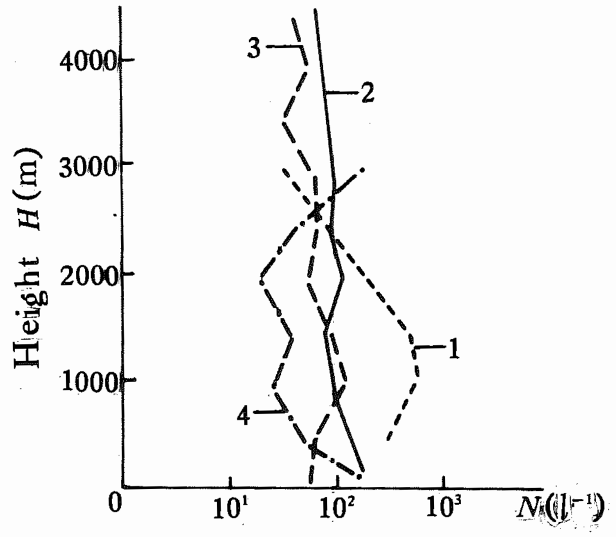

Fig.3. Vertical distribution of concentration of giant salt nuclei out of cloud under different weather.
1 - Under weather affected by typhoon.
2 - Under weather affected by front.
3 - Cloudy weather within air mass.
4 - Clear air.

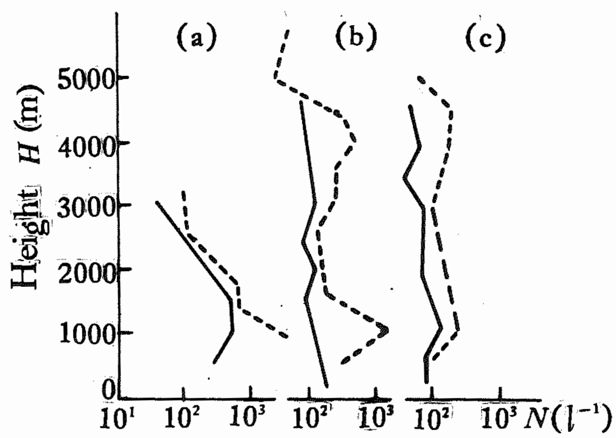

Fig.4. A comparison of giant salt nucleus concentration in cloud with that out of cloud under various weather conditions.
(a) Under weather affected by typhoon.
(b) Under weather affected of front.
(c) Cloudy weather within air mass.
Solid line - out of cloud.
Broken line - in cloud.

The above analysis shows that the existence of enough concentration (such as $10^2 - 10^5 /m^3$) of large droplets in cloud is a necessary condition of rain formation but not the only one. A cloud precipitable requires not only enough concentration of large droplets but also the appropriate thickness, updraft, as well as liquid water content. Only when the right disposition of these physical quantities exist, can rainfall occur.

4. GIANT SALT NUCLEI

We observed giant salt nuclei over the basin of the Xinan River. Fig.3 shows the vertical distribution of the concentration of giant salt nuclei out of cloud under different weather. It can be seen that under the effect of a front and in the cloudy weather of innermass, the variation of the giant salt nuclei concentration with the height is not significant. The average concentrations are 107/litre and 66/litre respectively. In weather affected by typhoon, the concentration of salt nuclei increases obviously because the air of the lower atmosphere comes from the sea. Its average amount is 317/litre. But above 1500 m, the concentration decreases rapidly with the height. However, in the clear air controlled by cold high pressure, the average concentration of giant salt nuclei in the lower atmosphere is minimal, only 57/litre. But over 2000 m, the concentration increases again. Thus it can be seen that the property of air mass can largely affect the giant salt nuclei concentration in the lower atmosphere. But near the ground, the variation of the giant salt nuclei concentration under different weather is less than that in the lower atmosphere.

A comparison of giant salt nuclei concentration in cloud with that out of cloud (Fig.4) shows that under various weather conditions, the former is consistently larger than the latter at the same height. Generally speaking, the ratio of average concentration of giant salt nuclei in cloud to that out of cloud is depentent on the weather conditions. It has a maximum of 3.9 for the weather affected by typhoon, and a minimum of 1.9 for the cloudy weather within air mass, with regard to the dependence of this ratio on the height, it is greatest at 1000 m. The difference between them is one order of magnitude for the overcast and raining days influenced by front. When it is cloudy weather of innermass, the difference is only 1.9 times. On this region the cloud base of Cu and Sc is usually near 1000 m high. On the basis of the data, the cloud base is the convergence area for giant salt nuclei. Of course, because of the condensation growth under the supersaturation condition, the giant salt nuclei observed in cloud include the part of original large salt nuclei in the air under the cloud. This effect may result in an increase of giant salt nuclei in cloud.

In fact the giant salt nuclei which we observed consist of some cloud droplets containing salt nuclei. Their spectra are similar to cloud droplets. But in cloud, the concentration of giant salt nuclei are usually $10^3 - 10^5 /m^3$ and that of the cloud droplets are usually $10^7 - 10^9 /m^3$. The concentration of giant salt nuclei in cloud is two orders of magnitude less than that of cloud droplets. This seems to show that the contribution of giant salt nuclei as condensation nuclei to the formation of cloud droplets is small.

THE SHAPE FACTOR OF HAILSTONES

Nancy C. Knight

National Center for Atmospheric Research
Boulder, Colorado, 80307, U.S.A.

1. INTRODUCTION

There are relatively few investigations of the relationship of hailstone shape to hailstone size in the literature. One of the earliest reports of a systematic study of hailstone shapes is by Weickmann (1953) who classified three principal shapes and gave the occurrence of these shapes in observer's reports of hail over a one hundred year period. List (1958) gave eight different classifications as well as details of the internal structures obtained through thin-sectioning. The most complete descriptions and illustrations of the various shapes and the frequency of their occurrence has been given by Carte and Kidder (1966, 1970) for hailstones from the South African Transvaal.

The major reasons for interest in the shape of hailstones relate to their terminal velocities, collection efficiencies, and calculations of the transfer of heat to the environment. These factors have been addressed by many researchers. More recently, the characteristics of radar return from precipitation particles, particularly from polarization diversity radars with rapid switching devices, have stimulated further interest in the hailstone shape/size relationship. These radar techniques rely on the non-sphericity of hydrometeors and on their preferential fall altitudes (e.g., Humphries, 1974).

The existence of a large body of data from several geographical regions in the form of photographs of thin-sections of hailstones, all of which were sectioned so that both the longest and shortest axes of the stones lie in the plane of the sections, made it possible to compile graphs of the shape factors as a function of the size of the stones.

2. METHOD

The shape factor for ellipsoidal hailstones is here defined as the length of the shortest axis of any given stone divided by the length of its longest axis. For hailstones with conical symmetry, the cone axis is defined as the major axis and the shortest axis is taken as the maximum dimension perpendicular to the cone axis. The data are given as a function of the longest axis.

3. RESULTS

The largest collections of hailstone thin-sections were from northeastern Colorado and central Oklahoma. The results of the measurements are given in Fig. 1 where the shape factor is plotted against the longest dimension in 5 mm intervals. The bars give the 95% confidence intervals from the t distribution where t is a function of $s/\sqrt{n}$, s is the standard deviation and n the sample number.

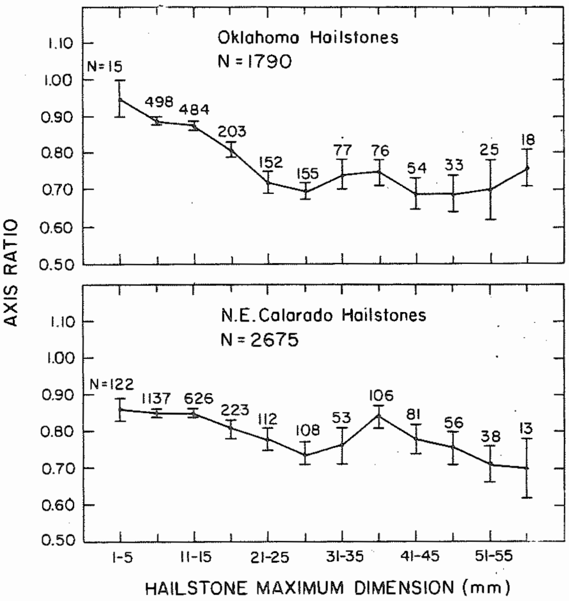

Fig. 1. Shape factors $\left(\frac{\text{shortest hailstone axis}}{\text{longest hailstone axis}}\right)$ *for Oklahoma and northeast Colorado hailstones. The curve connects the average shape factors for each size interval. The bars indicate the 95% confidence level for the average shape factor from the t distribution.*

4. DISCUSSION

The results for both regions show increasing asymmetry with size to approximately 30 mm in longest dimension. The small hail from northeastern Colorado is significantly less symmetrical than hail of comparable size from Oklahoma. This is a straightforward reflection of the difference in embryo type between these areas: Colorado embryos are predominantly conical graupel and Oklahoma embryos are predominantly frozen drops (Knight, 1981). The curves for both areas suggest a local maximum in the shape factor at about 40 mm longest dimension. This maximum is not statistically significant in the Oklahoma data, but it is significant in the Colorado sample. In fact, the 95% confidence levels of the two samples do not overlap in the size range between 36 and 45 mm.

The explanation for this peculiar bump in the data is not obvious from looking at the hailstones but one may speculate that it may be explained by the onset of tumbling. It is not unusual for Colorado hailstones to retain a conical shape until the cone axis dimension is 20 to 30 mm or even a little longer. At this point the hailstone begins to tumble and the whole growth symmetry changes (Mossop and Kidder, 1962; Knight and Knight, 1970). This sequence also occurs in Oklahoma but is much less common since the original conical shape is also less common.

Hailstones larger than 60 mm maximum dimension appear to follow a trend toward greater symmetry but the data are sparse and the trend may not be significant. It is typical for large hail to tumble very rapidly while falling so it is not easy to deduce the backscattering cross-section as a function of the direction of a radar beam. The radar return is probably dominated by 10 to 30 mm hail in any event since stones of that size are present in much higher concentrations except when local size sorting isolates the very large hail. Direct detection of large hail by its radar polarization characteristics appears to be quite uncertain.

As the shape factor curves given here indicate, the radar return from small hail may be different in different geographic areas. One might also expect it to be different from one storm to the next in the same area. The important factors are both the embryo type and whether the early growth of the hailstones is wet or dry.

5. REFERENCES

1. Carte, A. E. and R. E. Kidder, 1966: Transvaal hailstones. Quart. J. Roy Meteor. Soc., 393, 382-391.

2. Carte, A. E. and R. E. Kidder, 1970: Hailstones from the Pretoria - Witwatersrand area, 1959-1969. CSIR Research Report 197, pp. 1-44. Pretoria, South Africa.

3. Humphries, Robert G. Depolarization effects at 3 GHz due to precipitation. McGill Univ., Montreal, Canada. Stormy Weather Group, Scientific Report MW-82, March 1974, 81p. Refs.

4. Knight, C. A. and N. C. Knight, 1970: The falling behavior of hailstones. J. Atmos. Sci., 27, 672-681.

5. Knight, N. C., 1981: The climatology of hailstone embryos. J. App. Meteor., 7, 750-755.

6. List, V. R., 1958: Kennzeichen atmospharischer Eispartikeln, II. Z. Angew. Math. Phys., 3, 217-234.

7. Mossop, S. C. and R. E. Kidder, 1962: Artificial hailstones. Bull. Obs. Puy de Dome, 65-80.

8. Weickmann, H., 1953: Observational data on the formation of precipitation in cumulonimbus clouds. Thunderstorm Electricity, University of Chicago Press, 66-138.

THE EVOLUTION AND TRANSFER OF HAIL IN A SEVERE MONTANA THUNDERSTORM

Dennis J. Musil and Paul L. Smith

Institute of Atmospheric Sciences
South Dakota School of Mines and Technology
Rapid City, South Dakota 57701

and

Andy J. Heymsfield and L. Jay Miller

Convective Storms Division
National Center for Atmospheric Research[1]
Boulder, Colorado 80307

1. INTRODUCTION

The field experiment of the Cooperative Convective Precipitation Experiment (CCOPE), which was conducted in southeastern Montana in 1981, produced numerous observations of the conditions within and surrounding convective storms. The overall objective of COOPE is to develop an increased understanding of the precipitation mechanisms in convective clouds of the northern High Plains over a wide range of convective scales.

One of the more interesting storms during CCOPE occurred on 2 August 1981, and was investigated with a variety of equipment, including conventional and Doppler radar, aircraft, surface measurements, and radiosondes. One of the aircraft involved in the study of this storm was an armored T-28 (Ref. 1). In situ observations were made during three penetrations of the storm, which were analyzed and are being combined with other observations of the storm. This paper presents preliminary results of the analysis and discusses a possible hail growth mechanism that was felt to be operating in this storm.

2. STORM FEATURES

The intense storm on 2 Aug formed more than 100 km to the west northwest of Miles City, Montana, and moved east southeast at a speed of about 20 m s^{-1}, passing directly through the CCOPE research network. The storm was more or less steady for at least a 2-hour period and produced large amounts of precipitation, including baseball sized hail and a possible tornado. It later developed into a mesoscale convective complex that encompassed much of eastern Montana and the western Dakotas. The storm also exhibited a well-defined hook echo on its southern flank for an extended period and was characterized by a large weak echo region (WER) throughout much of its development. A detailed description of the storm and its development has been given by Wade (Ref. 3).

4. RADAR FEATURES

The penetration tracks and the corresponding 10-cm slant PPI radar data near the altitudes of the T-28 are shown in Figs. 1-3 for each of the penetrations. The maximum reflectivity at this level occurred well to the north of the aircraft tracks in each penetration and had a value in excess of 65 dBz. The T-28 encountered the weak echo region during Penetration 1, while on the two subsequent penetrations the track was well to the south of this region because of having previously encountered extreme turbulence. The presence of the WER, a well-developed reflectivity "notch" in the echo structure at low levels (not shown here), and the strong wind shear mark this storm as a well developed supercell. Miller (Ref. 2) examined the Doppler data for this storm from about a 2-hr time period ending about 30 min prior to the T-28 penetrations and showed the supercell characteristics of the storm at that time.

At the time of writing, Doppler data were not available for the time period encompassing the T-28 penetrations. The lack of Doppler data prevents us from making definitive statements about the precipitation mechanism present in this storm.

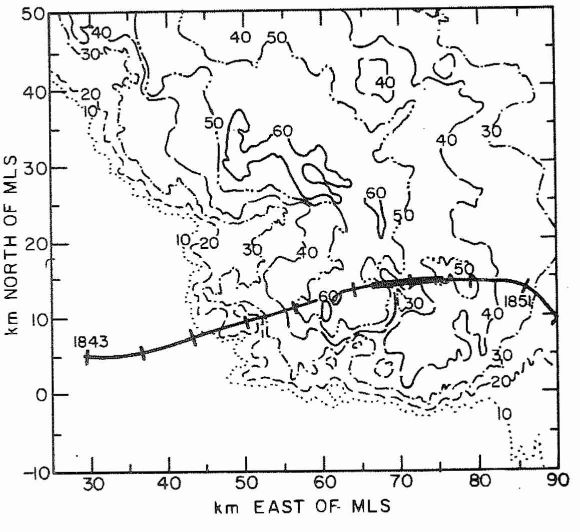

Figure 1. Plan Position Indicator plot near the altitude and time of Penetration 1 by the T-28 on 2 Aug 1981. The penetration path of the T-28 is shown with 1-min tick marks. The bold region along the flight path represents the approximate region of strongest updraft encountered by the T-28. Reflectivity contours are marked in dBz. The WER is at approximately 12N, 70E of MLS.

[1] The National Center for Atmospheric Research is sponsored by the National Science Foundation.

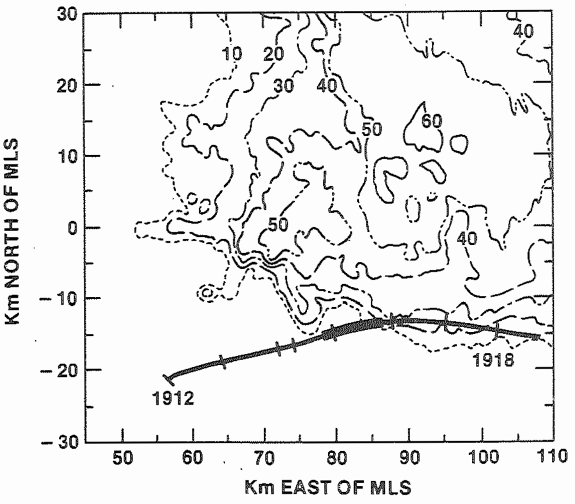

Figure 2. Same as Fig. 1, except for Penetration 2, where the WER is at approximately 2N, 97E of MLS.

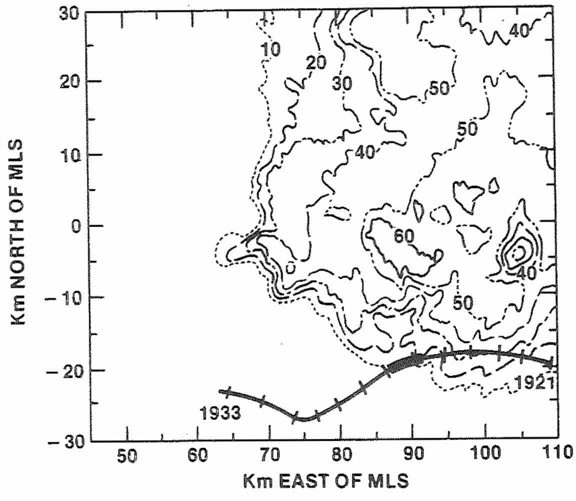

Figure 3. Same as Fig. 1, except for Penetration 3, where the WER is at approximately -5N, 105E of MLS.

Insofar as we can extrapolate from the earlier Doppler time period to the time of the T-28 penetrations, we can speculate about interactions between the hydrometeor observations from the T-28 and the motion fields represented by the Doppler data. It is planned to present more detailed information at the conference.

4. SUMMARY OF T-28 MEASUREMENTS

The T-28 measurements within and near the WER were discussed by Musil et al. (Ref. 4). Briefly summarizing, they showed the strongest updrafts were in the weak echo region beneath the overhang, while the strongest downdrafts were found in the high reflectivity regions to the west of the WER. Peak updrafts were about 40 m s^{-1}, while downdrafts existed on both sides of the WER, with peak values of -25 m s^{-1} on the west side. The WER exhibited an adiabatic core near its middle and was virtually free of ice at the level of observation (6-7 km MSL). Cloud liquid water values in updraft regions several km from the WER ranged approximately between 0.5-2.0 g m^{-3}.

Hydrometeor observations were extremely variable, but were consistent with past observations (Ref. 5). Hail was common to the west of the WER, with apparently reduced amounts to the east of the weak echo region. The highest concentrations of large hail were found along the west edge of the WER in weaker updrafts and virtually no liquid water. Hydrometeors were smaller and observed in lower frequencies during Penetrations 2 and 3, which were further removed from the WER intercepted in Penetration 1.

5. DISCUSSION AND CONCLUSIONS

Since we are forced to extrapolate motion fields some 30 min into the future to reach the time of the T-28 penetrations, we cannot at this time say for sure how the air motions will interact with the hydrometeor observations by the T-28. If the earlier Doppler measurements apply, then the suggestion is that the hailstones could be growing according to a mechanism described by Browning (Ref. 6). In any event, the details of the precipitation mechanism in this storm will remain uncertain until the Doppler data becomes available for the time period of the T-28 penetrations. At that time, a study combining air motions and Doppler data with hydrometeor observations from the T-28 can be done, which will allow an examination of detailed particle trajectories in this storm.

Acknowledgments. The research reported here was carried out with the support from the Division of Atmospheric Sciences, National Science Foundation, under Grant No. ATM-8311145.

6. REFERENCES

1. Johnson G N and Smith P L Jr 1980, Meteorological instrumentation system on the T-28 thunderstorm research aircraft, *Bull Amer Meteor Soc* 61, 9, 972-979.

2. Miller L J 1983, Kinematic structure within a severe hailstorm. Presented at the Fall Meeting, Amer. Geophys. Union, San Francisco, CA.

3. Wade C G 1982, A preliminary study of an intense thunderstorm which moved across the CCOPE research network in southeastern Montana. *Proc 9th Conf Wea Forecasting and Analysis*, Seattle, WA, Amer Meteor Soc, 388-395.

4. Musil D J, Heymsfield A J, and Smith P L 1982, Characteristics of the weak echo region in an intense High Plains thunderstorm as determined by a penetrating aircraft. *Proc Conf Cloud Physics*, Chicago, IL, Amer Meteor Soc, 535-538.

5. Heymsfield A J and Musil D J 1982, Case study of a hailstorm in Colorado. Part II: Particle growth processes at mid-levels deduced from *in-situ* measurements, *J Atmos Sci* 39, 2847-2866.

6. Browning K A 1965, Some inferences about the updraft within a severe local storm. *J Atmos Sci* 22, 669-677.

FORMATION OF FROZEN DROPS, CONGLOMERATES, AND GRAUPEL

Farn P. Parungo and Helmut K. Weickmann

Environmental Research Laboratories, NOAA. Boulder, CO 80303 U.S.A.

1. INTRODUCTION

We investigated (1) snow crystals collected at ground level, (2) hydrometeors replicated in clouds, and (3) ice crystals produced in the laboratory. Two major particle forms were observed at (-8±2)°C: noncrystalline frozen droplets and their conglomerates formed at water saturation; hexagonal thick plates or columns formed at ice super-saturation. The observations are discussed considering the mechanisms of crystal growth.

2. SNOW CRYSTALS COLLECTED AT THE SURFACE

Boulder is located close to the foothills of the Rocky Mountains. Precipitating cloud systems are often shallow upslope systems and frequently have isothermal conditions from base to top. They are ideally suited for the study of snow crystals that develop in an isothermal water cloud. We found that at -8°C±2°C and relative humidities of 100% with respect to water, snow pellets and graupel form, (Nakaya called these snow formations "lump graupel"), but crystals do not. Crystals appear, however, when the humidity drops below water saturation. Apparently, a small change in the relative humidity causes a big change of the crystal shape.

For example, on 3-31-1980, a very shallow cloud layer about 150 mb thick had formed, with a minimum temperature of -10.5 C. Figure 1 shows precipitation collected. All particles are snow grains in diameter between 0.5 mm and 1 mm. There is no regular crystal among them. A magnified view (Fig. 1, right) shows the tenuous attachment of splinters.

In the same temperature range but under conditions of subsaturation with respect to water (supersaturation with respect to ice) hexagonal crystals will form.

3. HYDROMETEORS REPLICATED IN CLOUDS

In the Florida Area Cumulus Experiment (FACE), dynamic cloud seeding with AgI was conducted (Woodley, 1970). A continuous Formvar replicator was mounted on an aircraft to collect hydrometeors on a Formvar-coated tape during the cloud penetrations (Hallett, 1976). Portions of the tape were cut and coated with carbon for examination with the scanning electron microscope. The hydrometeors can be distinguished morphologically as liquid drops, frozen drops, ice crystals in various shapes, or graupel. The concentrations of each category were measured at various stages of the cloud evolution. The results showed that seeding indeed converted many large liquid drops into frozen drops by contact nucleation. At temperatures between -6 and -10°C and at water saturation, frozen drops conglomerated to form "ice grains' which could have high falling belocity. As they fell, they scavenged liquid cloud droplets along the way to form conglomerates or graupel. However, when the humidity was subsaturated with respect to water but supersaturated with respect to ice, the frozen drops grew into column or thick plate crystals.

For example, on 24 July 1980, AgI pyrotechnic flares were released from an aircraft to seed clouds (temperature = -9±1°C, LWC=2.9 g m^{-3}). Cloud drop concentration was 10^3 cm^{-3} and no ice particle was found (Fig. 2a).

Approximately every 2 minutes, the aircraft made a cloud pass. In the second pass, the LWC reduced to 1.4 g m^{-3} after seeding. The shape and structure of the replicas indicated that 90% of the hydrometeors were liquid drops, 7% were frozen drops (Fig. 2b), 2% were conglomerated frozen drops including graupel, and 1% were columns. The columns appeared mostly at the edge of the cloud where the humidity was probably subsaturated with respect to water.

In the third and fourth passes the liquid drop concentration further decreased; on the other hand, the ice particle concentration increased and particle size also increased (Figs. 2c and 2d). More frozen drops conglomerated to form large grains, or links or large graupel. This indicates that at water saturation ice particles grow mainly by accretion of frozen drops rather than by vapor-phase growth of column crystals.

Replicas of the fifth pass showed no liquid drops, only ice particles which included 20% frozen drops, 35% columns, 15% graupel, and 30% irregulars. However, the total concentration reduced to 10cm^{-3}. The fact that the most frequent hydrometeors were columns rather than frozen drops indicates that moisture supply in the cloud at the fifth pass had been reduced to ice supersaturation and vapor-phase growth took place.

4. ICE CRYSTALS PRODUCED IN LABORATORY

We placed a beaker (500cm^3) of hot water (90°C) in the bottom of a cold box (40 cm X 40 cm X 60 cm), whose inside temperature was kept -8°C±2°C. The water vapor generated a stream of cloud which ascended with a speed of 50 cm s^{-1}. A match coated with AgI was lit to generate ice nuclei. The ice crystals produced were collected on Formvar-coated slides. In the first 2 minutes a mixture of columns, plates, frozen drops, and their accretions were observed (Fig. 3a). This suggested that the humidity throughout the box was not homogeneous because the excess AgI nuclei glaciated most cloud drops and reduced the humidity to subsaturation with respect to water in some areas. After 2 minutes when the ice nuclei were mostly consumed but clouds were still continously introduced, the humidity probably increased to water saturation. Frozen drops, conglomerated frozen drops, and graupel were now the products. The experiment demonstrated that indeed at -8°C±2°C, at water saturation, ice particles remained isometric (Fig. 3b). Only at ice saturation did vapor-phase-grown crystals develop.

5. DISCUSSION

We have demonstrated that frozen drops can be genuine precipitation particles at -8°C±2°C or, more importantly, that they can be the embryos of graupel. In order to understand that frozen drops grow isometrically and that they can easily conglomerate, one must understand the physical properties of the ice surface. The water molecules on the ice surface are understandably not so well arranged as the internal molecules. The degree of disorder increases with higher temperature and water vapor pressure of the environment. Within certain temperature and humidity boundaries, an ice surface can be covered with a quasi-liquid layer.

Faraday (1859) first noticed that an ice surface below freezing was covered with a thin film of water. Fletcher (1962 and 1968) studied the stability of a quasi-liquid layer from statistical and thermodynamical considerations. He discussed the variation of the layer thickness with temperature. Kvlividze et al. (1974) confirmed the existence of this mobile water layer at temperature warmer than -10°C by using neutron magnetic resonance spectrometry. Applications to cloud micro-physics of the quasi-liquid layer are most evident in the research of Nakaya and Matsumoto (1953) who explained the existence of a quasi-liquid layer on ice spheres. The influence of the quasi-liquid layer on crystal growth was developed by Lacmann and Stranski (1972).

The thickness of the quasi-liquid layer on ice is a function of temperature and humidity, as the temperature becomes warmer the quasi-liquid layer becomes thicker. At -8°C±2°C and at water saturation, the ice surface is probably fully covered with this layer. The growth of ice particle takes place as a two-step process: (1) condensation into the layer, and (2) crystalization into the ice surface through the two-dimensional nucleation mechanism. As a result, frozen drop is the product. However, the rate of the growth is relatively slow because the layer resembles bulk water toward the environment. Ono (1970) has observed that growth rate through diffusion at this temperature range is greatly reduced. A competitive process, collision and accretion between frozen drops, becomes an important mechanism for ice particle growth. Because of the water-like surface of frozen drops, upon collision, they cohere to form conglomerates which occur in all forms, from tenuous attachments to "lump graupel". These large ice particles will then sweep liquid drops as they move inside a cloud and convert liquid droplets to ice on their surface by contact. The riming process produces mostly snow grains or graupel but not snow crystals. However, when the humidity decreases to ice saturation, the quasi-liquid layer diminishes and ice surface is exposed to the environment; then vapor deposition growth becomes the main process and hexagonal columns or plates appear.

6. REFERENCE

1. Faraday M 1959, Note on regelation, Proc. Roy Soc. 10, 440-450.

2. Fletcher N H 1962, Surface structure of water and ice, Phil. Mag. 7, 255-262.

3. Fletcher N H 1968, Surface of water and ice II a revised model, Phil. Mag. 18, 1287-1300.

4. Hallett J 1976, Measurements of size, concentration and structure of atmospheric particles by the airborne continuous particle replicator, AFGL-TR-76-0149, 92 pp.

5. Kvlividze V I, Kiselev V, Kurzaev A 1974, The mobile water pahase on ice surfaces, Surface Science 44, 60-68.

6. Lacmann R and Stranski I 1972, The growth of snow crystals, J Crystal Growth 13-14, 235-240.

7. Nakaya U and Matsumoto A 1953, Evidence of the existence of a liquid-like film on ice surface, Research Paper 4, SIPRE, Corps of Engineers, U.S. Army, Wilmette, Illinois, 6 pp.

8. Ono A 1970: Growth mode of ice crystals in natural clouds. J Atmos. Sci. 27, 649-658.

9. Woodley W L 1970, Precipitation results from a pyrotechnic cumulus seeding experiment, J. Appl. Meteor. 9, 242-257.

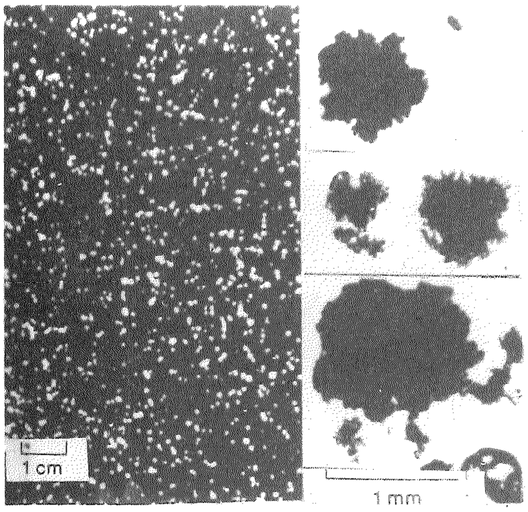

Fig. 1 Snow particles collected on 31 March, 1980

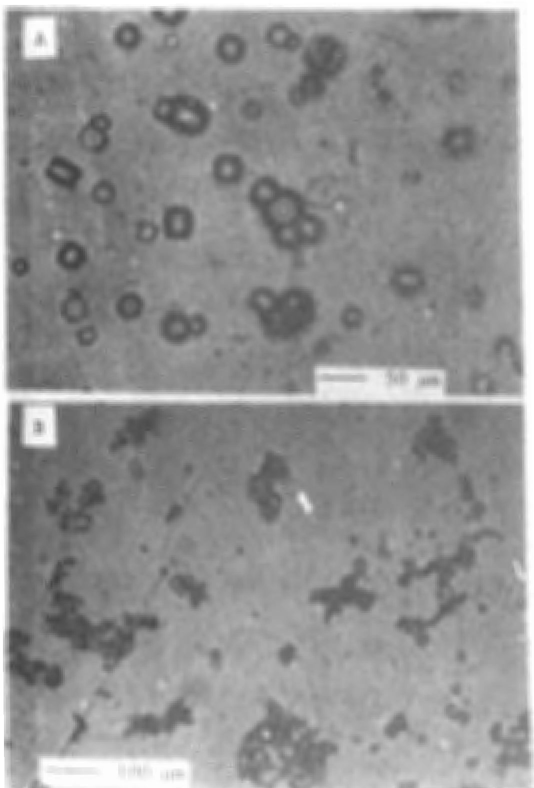

Fig. 3. Ice particles nucleated with AgI in a cold box. (A) 1 min. after seeding; and (B) 3 min. after seeding.

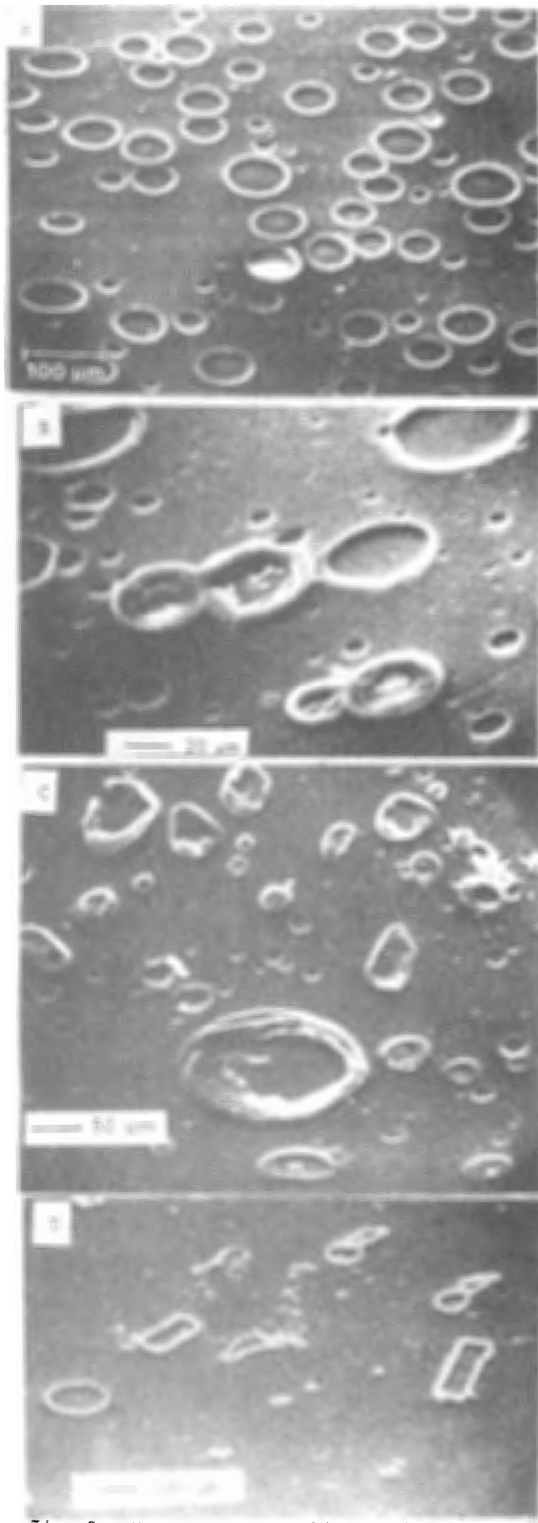

Fig. 2. Hydrometeors replicated in a Florida cumulus. (A) before AgI seeding; (B) 2 min. after seeding (C) 5 min. after seeding and (D) 8 min. after seeding.

RAIN DROPLET SPECTRA OBTAINED FROM WARM CONVECTIVE CLOUDS WITH REGULAR TRADEWINDS IN A SUBTROPICAL MARITIME AREA

C. PONTIKIS , A. RIGAUD
French Meteorological Office, 78470 Magny les Hameaux

J.P. LACAUX , B. CAMPISTRON
Aerology Laboratory, 65300 Campistrous/Lannemezan

The observations of rain drop distributions are not only important for radar applications, but also for cloud physics studies, since they allow the check of theoretical computation results.
This note summarizes the data of two different sets (S1 and S2) of rain drop size measurements obtained by classical disdrometer devices, over the flatter part of the island of Guadeloupe.
During these measurement times (March 1981 and January 1984) the tradewind was regular and only warm convective clouds were observed. Figure 1 represents a typical radiosounding (19 January 1984).

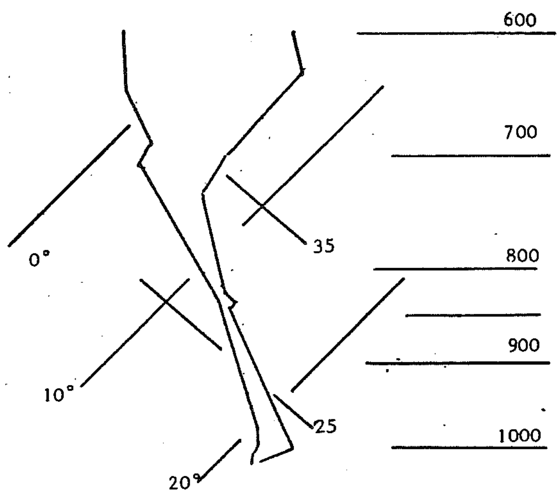

FIGURE 1

The whole data collection time was 60 minutes for S1 and 180 minutes for S2.
Drop spectra are analysed for the whole time of every individual rain event to fit the Marshall-Palmer distribution :

$$N = N_0 \cdot e^{-\Lambda D}$$

Table 1 summarizes the relation between the distribution parameters (D_o, Λ, N_o) and the rain rate R.

The agreement between observed values and classical Marshall-Palmer values is fairly good for Λ and N_o.

In a similar way, the mean values of these parameters obtained according to the formula :

$$\overline{X}_i = \sum X_i R_i \ / \sum R_i$$

are in good agreement with the classical Marshall-Palmer values for Λ and N_o (see last column of table 1). Numerous large drops are observed ($D > 3$mm). As a result, the median and mean diameter values are higher than in most other places (Austin and Geotis, Blanchard). It seems that, for a same precipitation rate, the characteristic Λ and N_o values for a subtropical event are fairly smaller than those obtained in the mid-latitudes.
Table 2 shows a comparison between two particular rain events observed during the data collection periods, and the results obtained by Waldvogel.

R (mm/h)	Λ (mm^{-1})	N_o ($m^{-3}.mm^{-1}$)	Reference
10.2	3.7	$3.5\ 10^4$	Waldvogel (Thunderstorm)
10.3	3.	$1.4\ 10^4$	S1 (warm convective cloud)
4.	3.8	$1.6\ 10^4$	Waldvogel (shower)
4.	3.	$.5\ 10^4$	S2 (warm shower)

TABLE 2

A one-dimensional warm convective cloud model (Pontikis and al.) is used to simulate the rain situations observed during the data collection periods.
This model initiates convection by introducing a small thermal instability between 0 and 200 meters, and using an entrainment coefficient proportional to the altitude :

$$\mu = A\,Z \quad \text{with} \quad A = 4.5\ 10^{-11} \text{ C.G.S.}$$

Its microphysical part is classical, similar to the one used by Ogura and Takahashi. Precipitation spectra on the ground are calculated by using the 8 a.m. radiosounding of the meteorological station in Le Rai-

Parameter	Marshall-Palmer	S1	S2	Mean Values
W_L (g/m^3)	$.072\ R^{.88}$	$.075\ R^{.85}$	$.073\ R^{.83}$	
D_o (mm)	$.09\ R^{.21}$	$.92\ R^{.24}$	$.811\ R^{.295}$	$1.112\ R^{.21}$
Λ (mm^{-1})	$4.1\ R^{-.21}$	$4.8\ R^{-.24}$	$5.3\ R^{-.272}$	$4.275\ R^{-.21}$
N_o ($m^{-3}mm^{-1}$)	$8\ 10^{3}$	$1.5\ 10^4 R^{-.31}$	$1.77\ 10^4 R^{-.252}$	$9.76\ 10^3$

TABLE 1

zet airport.
Figure 2 shows the comparison between the observed and calculated data for the 2 p.m. rain event on 16 January 1984. The whole cloud life time was 60 minutes.

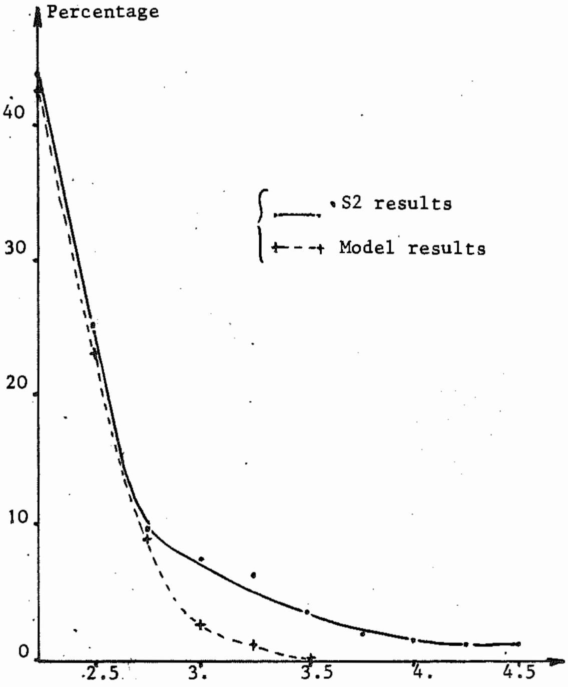

FIGURE 2

The main purpose of this paper was to present the characteristic raindrop spectra issued from warm convective clouds aver the flatter part of Guadeloupe. These spectra can be represented fairly well by using the classical Marshall-Palmer distribution. Unlike the typical mid-latitude drop spectra, high numbers of large drops ($D > 3$ mm) are observed, while a deficit exists in the class range between .5 and 1.5 mm.
An attempt to obtain the theoretical rain spectra by using a one-dimensional model leads to a fair agreement between calculated and observed drpp classes for the middle sized drops ($2 \leqslant D \leqslant 3$mm).
The model leads to a 3 mm maximum diameter after 30 minutes of cloud life, while drops up to 4.5 mm are experimentally observed. This behavior seems to be characteristic of the 1D models of this kind : usually they develop drops larger than 4 mm for cloud life times higher than 50 minutes.

BIBLIOGRAPHY

P.M. AUSTIN, S.G. GEOTIS 1979
"Raindrop sizes and related parameters for GATE"
J. Appl. Met. (18) 569

D.C. BLANCHARD 1953
"Raindrop size distribution in Hawaian rains"
J. Met. (10) 457

Y. OGURA, T. TAKAHASHI 1973
"The development of warm rain in a cumulus model"
J. Atm. Sci. (30) 262

C. PONTIKIS, G. JAUBERT, A. RIGAUD 1981
"Modèle monodimensionnel de nuage chaud"
Internal Rept, EERM N°12, October

C. PONTIKIS, A. RIGAUD 1982
"A 1D warm cloud model and measurements in Guadeloupe"
A.M.S. Conf. on Tropical Meteo., San Diego, June

A. WALDVOGEL 1974
"The N_0 jump of raindrop spectra"
J. Atm. Sci. (31) 1067

AIRCRAFT OBSERVATIONS INSIDE SWISS HAILSTORMS

Paul L. Smith and Dennis J. Musil

Institute of Atmospheric Sciences
South Dakota School of Mines and Technology
Rapid City, South Dakota 57701

and

Albert Waldvogel

Laboratorium für Atmosphärenphysik
ETH-Hönggerberg
CH-8093 Zürich, Switzerland

1. INTRODUCTION

A series of observations of the interior characteristics of Swiss hailstorms was made with the T-28 armored research aircraft (Ref. 1) during the summers of 1982 and 1983. The main objective was to determine the presence of any accumulations of supercooled raindrops in the so-called "Big Drop Zone" (BDZ); such accumulations are an important basis for the Soviet method of hail suppression seeding under test in Grossversuch IV (Ref. 2). The target zone for the aircraft penetrations was identified by radar in the same manner as used for the seeding rockets in Grossversuch IV.

This paper discusses the observations from storms on four days during the two seasons, which resulted in a total of 27 penetrations. The aircraft was directed from the ground to a point indicated by radar toward which the seeding rockets would have been fired according to normal Grossversuch IV seeding procedures. The storms penetrated were, however, not seeded.

2. IDENTIFICATION OF THE BIG DROP ZONE

The BDZ was identified by 5-cm radar measurements operating in a Range Height Indicator (RHI) mode. First, the maximum reflectivity above the 0C level (Z_m) is determined. When 45 dBz $\leq Z_m \leq$ 55 dBz, the radar-identified BDZ is that region above the -5C level where the radar reflectivities are $\geq Z_m$-10 dBz. When Z_m is > 55 dBz, the BDZ is that region where the radar reflectivities are $\geq$ 45 dBz above the -5C level. If an overhang region is identified, the radar-identified BDZ can be extended into the overhang region, even if the reflectivities there are less than the above described limits.

The above definition was used routinely during Grossversuch IV for conducting the seeding operations with rockets. The same technique was used in a real time mode to identify the target toward which the T-28 was vectored in order to investigate the characteristics of the BDZ.

3. PENETRATIONS OF THE BIG DROP ZONE

3.1 Storms considered

Storms from four days were considered in this study because they contained the best potential for penetrations of the BDZ. Table 1 shows the atmospheric conditions on the days chosen as determined from the 12Z Payerne radiosonde.

TABLE 1. Summary of atmospheric conditions for the dates shown using the 12Z Payerne radiosonde.

DATE	LLM $(g\ kg^{-1})$	CCL (mb)	CCL TEMP (°C)	LI	SHEAR $(10^{-3}\ s^{-1})$
16 Aug 82	10.7	780	10.6	-4.3	0.6
23 Jun 83	9.2	800	9.0	-2.7	0.9
13 Jul 83	7.5	705	4.0	-0.7	1.0
18 Jul 83	8.8	720	6.8	-2.7	2.6

All the days showed light to moderate instability with sufficient low level moisture to initiate and maintain deep convection in the region. The vertical shear of the horizontal wind was generally small. The storms penetrated by the T-28 during the summers of 1982-83 were mainly small, air-mass types and therefore cannot be considered to represent the whole spectrum of storms observed during Grossversuch IV (1977-1982). The implications this may have for attempting to describe the precipitation mechanism in the Swiss storms remain to be determined.

3.2 Summary of penetrations

Table 2 summarizes information pertaining to each penetration for the days studied. The altitudes and temperatures are averages for each penetration. The temperatures were generally around -8C during 1983, while the penetrations in 1982 were at slightly cooler temperatures because of a potential conflict with rocket firings into the region where the T-28 was flying at that time. Table 2 also shows on which penetrations the BDZ selection criteria were satisfied, as well as showing the effectiveness of actually hitting the intended target. There is always difficulty when attempting to coincide aircraft penetrations with the vagaries found in convective clouds. Hence, about 60% of the penetrations were made at a time when the selection criteria was satisfied. Of those, about 65% (~40% of the total) actually intercepted the BDZ, which resulted in a substantial number of cases for this study.

An example of a penetration of the BDZ on 13 July 1983 (Pen. 3) is shown in Fig. 1. The penetration was almost along the same direction as the RHI shown in the inset. It has been estimated that the BDZ at the T-28 altitude was approximately

TABLE 2. Summary of conditions pertaining to T-28 penetrations for the dates shown. OK indicates the BDZ was penetrated and NA means Not Applicable.

DATE	PEN	TEMP (°C)	ALT (km)	CRITERIA FULFILLED	ACCURACY
16 Aug 82	1	-10.9	5.6	Y	OK
	2	-11.0	5.6	Y	OK
	3	-12.8	5.6	Y	2 km S
	4	-13.3	5.6	Y	OK
	5	-12.3	5.6	Y	3 km E
	6	-12.5	5.6	Y	2 km S
23 Jun 83	1	-7.9	4.7	Y	4 km SE
	2	-7.4	4.6	N	NA
	3	-7.7	4.6	N	NA
	4	-7.6	4.6	N	NA
	5	-7.7	4.6	Y	OK
	6	-7.7	4.6	Y	OK
	7	-7.7	4.6	Y	OK
	8	-7.5	4.6	N	NA
	9	-7.6	4.6	Y	OK
	10	-7.8	4.6	Y	OK
	11	-7.6	4.5	Y	OK
13 Jul 83	1	8.9	5.1	Y	2 km SE
	2	-8.9	5.0	Y	OK
	3	-9.0	5.1	Y	OK
	4	-9.0	5.1	N	NA
18 Jul 83	1	-7.9	5.0	Y	1 km NW
	2	-7.8	5.1	N	NA
	3	-7.6	5.0	N	NA
	4	-7.6	5.0	N	NA
	5	-7.7	5.0	N	NA
	6	-7.8	5.0	N	NA

10 km^2 in this case. The time period in which the T-28 encountered the BDZ (about 153134-153203 SDT) was characterized by updrafts, which at times exceeded 15 m s^{-1}.

4. SUMMARY OF FINDINGS

A preliminary analysis of the data gathered in Switzerland by the T-28 has been made. The most important items are outlined below; these key points provide the basis for current, more detailed investigations.

4.1 Liquid water drops and accompanying ice particles

The T-28 particle camera has the capability to differentiate between ice and liquid particles, as well as to determine the relative concentrations of each. An examination of the data from the camera has shown that extremely few liquid particles were observed in the radar-identified BDZ. A typical frame of data that includes a liquid drop is given in Fig. 2. The drops are usually found in conjunction with numerous ice hydrometeors. In fact, estimates of the concentrations of liquid and ice particles for the four days considered here show the concentrations of liquid drops to be no more than about 0.1 m^{-3}, while the accompanying ice particles have concentrations ranging between approximately 10^3-10^5 m^{-3}. The survival of the drops in a liquid state in such an environment, or their chance of contributing in any meaningful way to the precipitation mechanism in these storms, is doubtful.

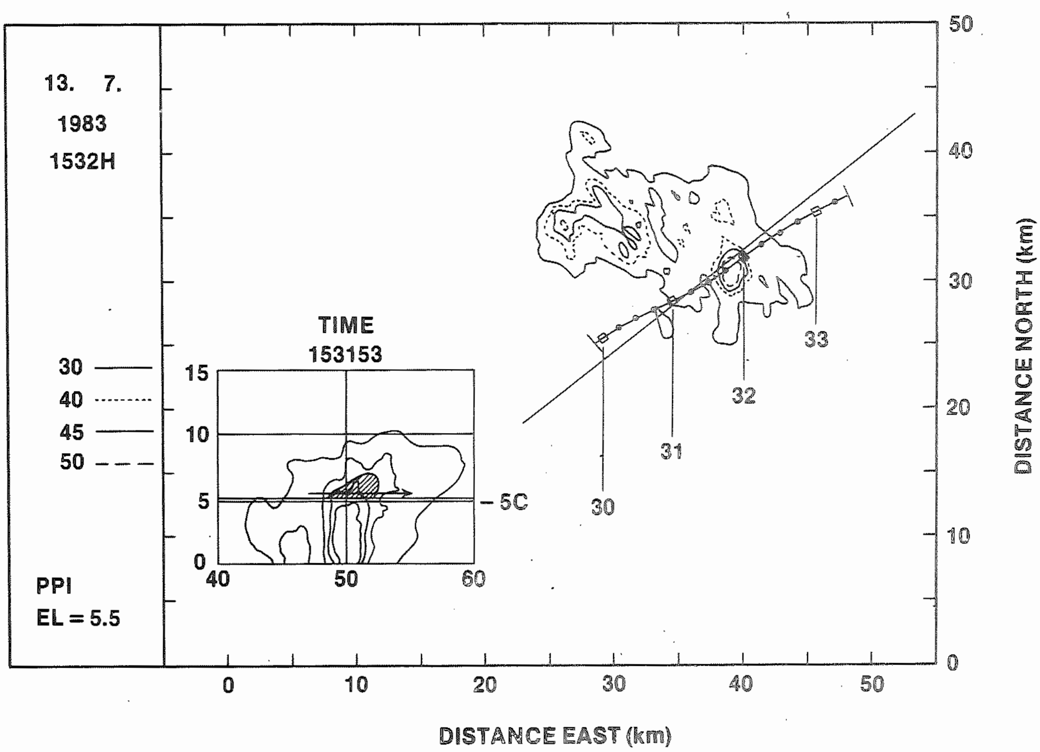

Figure 1. Radar views of a BDZ penetration on 13 July 1983. Slant PPI view (10-cm) has aircraft flight track superimposed, with squares representing minutes after 1500 SDT. RHI section (3-cm; contours 10, 20, 40, and 45 dBz) along the direction indicated shows position where T-28 crossed the RHI plane, which is almost along the flight track.

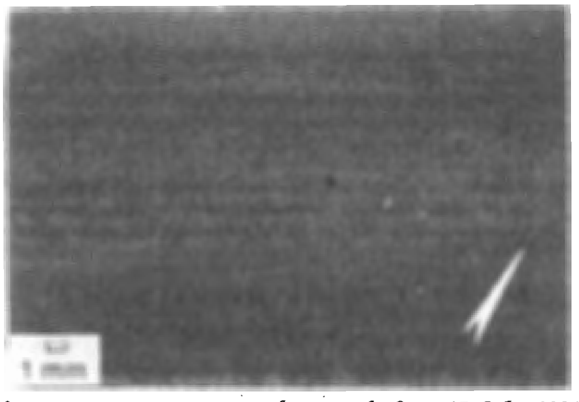

Figure 2. Cannon camera photograph from 13 July 1983 near 152537 SDT (Pen #2). Most hydrometeors are ice, with a possible drop as indicated.

4.2 Cloud droplets in the BDZ

The penetrations of the BDZ were often characterized by substantial amounts of cloud liquid water, at times ranging between 1.5-2.0 g m^{-3}. A typical frequency distribution of cloud droplets obtained from the FSSP and taken from the updraft region of the BDZ in Fig. 1 is shown in Fig. 3. The total droplet concentration is typical of maritime clouds and the spectra also shows the presence of several large cloud droplets. The cloud droplets obviously can provide the material on which hailstones grow, but the presence of the large droplets suggests the possibility that a coalescence mechanism may be active. Observations in continental clouds in the U.S.A. where an ice process has been shown to exist (Ref. 3), seldom exhibit large cloud droplets. In any event, the rather substantial amounts of cloud liquid water in the BDZ are sufficient to permit the growth of rather large hailstones.

The BDZ apparently has, at best, a seeding window of relatively short duration, but it is possible that earlier penetrations of it might have produced more evidence of supercooled raindrops and perhaps less ice. Earlier investigations of the hail falling from Swiss storms showed roughly equal occurrence of graupel versus drop embryos in the stones (Ref. 4). On the other hand, the ice particles observed in updraft regions were generally well-rimed, suggesting that they had frozen at significantly lower altitudes (higher temperatures).

4.3 Characteristics of the regions of vertical air motions

The sizes of the updraft regions in these storms were smaller than those in hailstorms of comparable intensity in the North American Great Plains, but the speeds appeared to be quite similar. The maximum observed updraft speed was about 25 m s^{-1}. Despite the smaller sizes of the storms, comparable values of maximum turbulence intensity were noted. The strongest turbulence seemed to be associated with the sharp transition from strong updraft to strong downdraft which occurred on several penetrations.

4.4 Anomalous large particles

A few large elongated particles with dimensions up to about 1x4 cm were observed during some of the penetrations. Figure 4 shows an example of one of these particles observed by the particle camera.

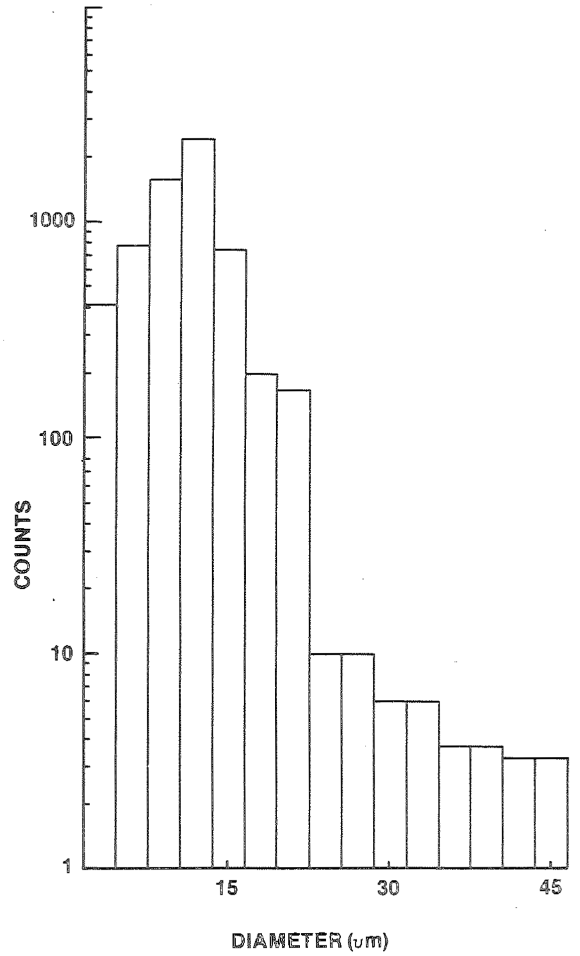

Figure 3. Average cloud droplet counts per 3-μm size category from FSSP during the time period 153134-153203 SDT, which corresponds to the updraft region of the BDZ discussed in Figure 1.

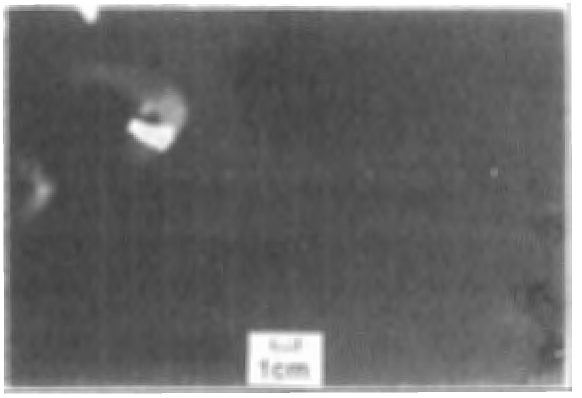

Figure 4. Cannon camera photograph of a large particle observed on 23 June 1983. Maximum dimension is about 2 cm.

The maximum dimension in this case is approximately 2 cm. The mechanism producing them is unknown, but they may be similar to the anomalous large particles previously found inside Colorado, Montana, and Oklahoma hailstorms (Ref. 5). The appearance of this particle also suggests that it might be an artifact resulting from shedding following icing on the aircraft or the instrumentation.

5. CONCLUSIONS

Recognizing the limitations that the T-28 observations are from essentially a single level and that the full spectrum of Swiss hailstorm types may not have been sampled, the following tentative conclusions can be drawn. The scarcity of large liquid drops and their occurrence in conjunction with large concentrations of ice particles suggest that the liquid drops probably do not play an effective role in the precipitation mechanisms of the storms studied. The large amounts of ice observed in these penetrations strongly suggest that an ice process is involved in the precipitation mechanism, even though there is some evidence that coalescence could also play a role. The most probable hail growth mechanism in these storms appears to involve the growth of ice particles through the accretion of cloud liquid water rather than of supercooled raindrops. The embryos for the hailstones could be either frozen drops or graupel.

Acknowledgments. We appreciate the contributions of the late Dr. Bruno Federer to making this project possible. The South Dakota School of Mines and Technology work was supported by the U.S. National Science Foundation under Grant. No. ATM-8204652, and ETH, with assistance from the Convective Storms Division of the National Center for Atmospheric Research, the U.S. Navy, and the Swiss Air Force.

6. REFERENCES

1. Johnson G N and Smith P L Jr 1980, Meteorological instrumentation system on the T-28 thunderstorm research aircraft, *Bull Amer Meteor Soc* 61, 9, 972-979.

2. Federer B, Waldvogel A, Schmid W, Hampel F, Rosini E, Vento D, Admirat P, and Mezeix F J 1979, Plan for the Swiss randomized hail suppression experiment. Design of Grossversuch IV, *Pageoph* 117, 548-571.

3. Dye J E, Langer G, Toutenhoofd V, and Cannon T W 1974, The mechanism of precipitation formation in northeast Colorado cumulus: III. Coordinated microphysical and radar observations and summary, *J Atmos Sci* 31, 2152-2159.

4. Federer B, Thalmann B, Jouzel J 1982, Stable isotopes in hailstones. Part II: Embryo and hailstone growth in different storms, *J Atmos Sci* 39, 1336-1355.

5. Smith P L, Musil D J and Jansen D C 1980, Observations of anomalous large particles inside Colorado and Oklahoma thunderstorms, *Proc VIII Intnl Conf Cloud Physics*, Clermont-Ferrand, France, 295-298.

STUDIES ON SNOW PRODUCTION PROCESSES IN A CONVECTIVE CLOUD BY THE SIMULTANEOUS USE OF RADARS AND A "CLOUD-SHUTTLE SOLID PRECIPITATION SOUNDER"

Wakahama G., Endoh, T., Fujiyoshi, Y., Irikawa, S., and Konishi, H.

Institute of Low Temperature Science, Hokkaido University

Sapporo 060, Japan

1. INTRODUCTION

Although the microphysics, structure and dynamics of clouds associated with precipitating clouds have been studied by a number of investigators by the use of radars, radiosondes, airborne devices and meteorological data collecting systems on the ground, many problems remain unsolved yet (Refs. 1, 2, 3). Airborne devices such as the Knollenberg apparatus are known to be very useful and valuable for clarifying the microphysics of the clouds. It is, however, fairly difficult for meteorologists in some countries such as Japan to conduct airborne measurements in convective clouds mainly because of the lack of suitable aircraft for meteorological observations. Instead of airborne measurements, a "cloud-shuttle solid precipitation sounder", or shortly "cloud-shuttle sonde" (CS-sonde) has been developed and used in order that microphysical data were collected in and beneath the snow-forming clouds.

Our purpose is to look into the microphysical characteristics of snowfalls in conjunction with the life cycle of convective snow clouds. This paper will present the methodology of the simultaneous use of a CS-sonde and two radars (λ = 3.2 cm, 5.0 cm) with illustrative examples.

2. METHOD

A CS-sonde is composed of (1) an ordinary "radio-sonde" for obtaining vertical profiles of air temperature and humidity, (2) a "snow crystal sonde" for collecting replicas of snow crystals or aggregates at various altitudes (Ref. 4); (3) an "aerial camera" for obtaining the concentration of aggregates and the visibility in and beneath a cloud by taking time-lapse 35 mm stereophotographs; (4) a corner reflector for tracking the sonde by the radar; (5) a main balloon filled with Helium gas; (6) a parachute; (7) a small red-coloured balloon as a "mark" when the sonde returns to the ground; and (8) a baroswitch to separate the devices from the main balloon at a specified altitude.

The exact position of the sonde was tracked by an auto-tracking apparatus and an REI radar: the altitude as well as the azimuth and distance from the site of release was obtained at all time during its flight and at the time of its landing on the ground (Fig. 1).

When a CS-sonde made a return landing, it was located easily thanks to its red balloon lying on a flat snow cover in the vicinity of the estimated landing place with an accuracy of ±0.5 km, and the

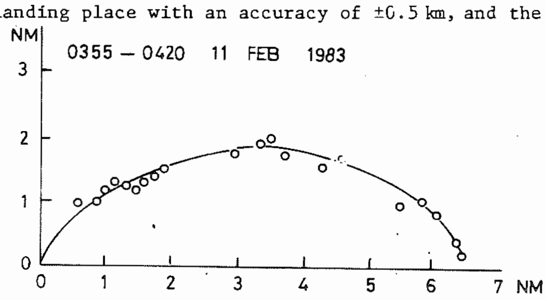

Figure 1. Trajectory of CS-sonde. Open circles indicate the positions where the corner reflector was detected by the REI radar.

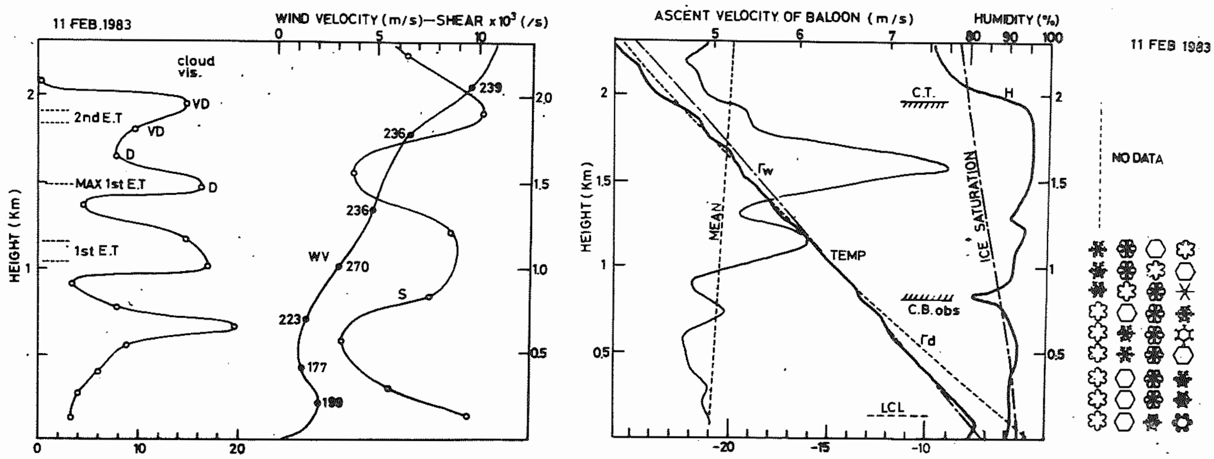

Figure 2. Vertical profiles of air temperature, relative humidity, ascent velocity of the CS-sonde, wind speed and direction, horizontal wind shear, concentration of aggregates and mode of snow crystals observed on 11 Feb., 1983.

sonde, aerial camera, and radio sonde were safely collected. Since these collected sondes and camera were reusable in the following ascent, the total system was named "Cloud-shuttle Solid Precipitation Sounder (Sonde)". The ratio of successful collection of CS-sondes was around 80 %.

In addition to the observations using the radars and sondes, ground observations were also carried out on snowfall intensity, shape and size of snow crystals, visibility, and so forth, continuously during the snowfall.

3. RESULTS

The meteorological data, replicas of aggregates and stereophotographs obtained by the CS-sonde were analyzed, and some examples are illustrated in Figs. 2, 3, 5, 6, 7, 9, and 10, together with the data obtained by the radars and ground observations.

Figure 2 shows the vertical profiles of air temperature, relative humidity, vertical air motion estimated from the ascent velocity of the balloon (Ref. 5), wind direction and speed, horizontal wind shear, concentration of aggregates, and mode of snow crystals observed on 11 February, 1983. It is obvious that there exist strong vertical fluctuations in concentration of aggregates, vertical air motion and horizontal wind shear, and that the fluctuations in concentration of aggregates and relative humidity are consistent with those in vertical air motion. The amplitude of fluctuations in concentration of aggregates increase with descending altitude of aggregates, which suggests that the degree of localization of aggregates increases during their fall.

It should be also noted that the mode of snow crystals changes from the dendritic to the broad-branched steller mode while they continue to fall beneath a cloud. It means that snow crystals grew even at such a place below the cloud base in which the air was supersaturated with respect to ice.

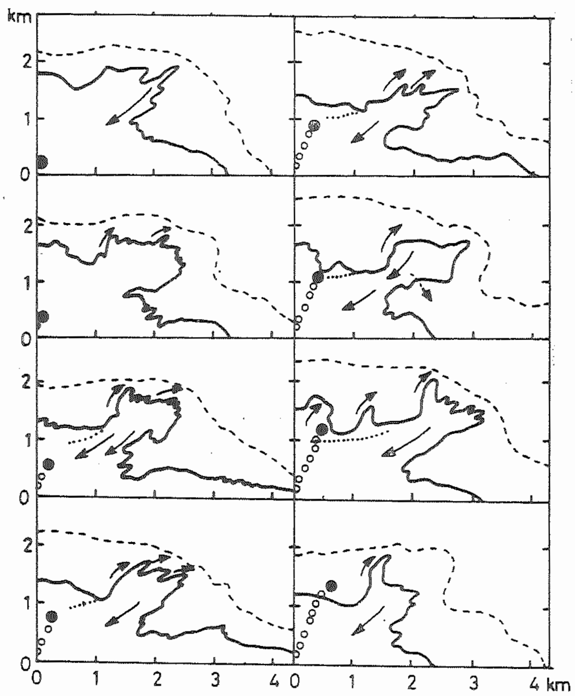

Figure 3. Change with time of the position of the sonde (solid circles) and REI radar echo patterns every 24 seconds. Arrows indicate motion of snow particles deduced from the echo shape.

Successive positions of the same CS-sonde together with the REI radar echoes taken every 24 seconds are indicated in Fig. 3. The convex and the concave shape of the convective echoes suggest the upward and the downward motion of snow particles, respectively. The motion of snow particles deduced from the shape of echoes is indicated by arrows in the figure. The upward motion of snow particles indicates the existence of updraught. It is noted that the updraught exists above 1000 m in altitude, which is consistent with the higher ascent velocity of the CS-sonde above the cloud base illustrated in Fig. 2.

On 12 March, 1983, a steady snowfall was observed from the clouds in the warm sector of a cyclone on the Ishikari Plain, Hokkaido Island. The PPI radar echoes and the snowfall intensity are illustrated in Fig. 4. A CS-sonde was then released from ILTS (Inst. of Low Temp. Sci.) at 18:00 toward the precipitating stratus snow cloud. Vertical profiles of air temperature, ascent velocity and the maximum and the averaged diameter of snow crystals obtained by the CS-sonde are shown in Fig. 5. It is noteworthy that the size of snow crystals increases with ascending altitude to 1800 m, but does not increase below it. Fractions of various crystal shapes at different altitudes were also obtained by the CS-sonde as shown in Fig. 6. It is seen in this

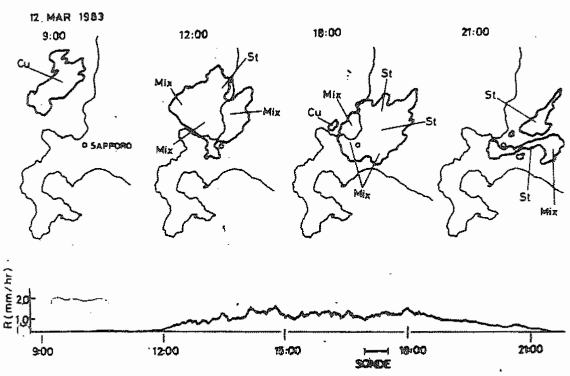

Figure 4. Time series of PPI radar echo sketches (upper) and snowfall intensity on the ground surface deduced from visibility (lower). Cu, St and Mix indicate the echoes of convective, stratified and their mixed types, respectively, on 12 Mar., 1983

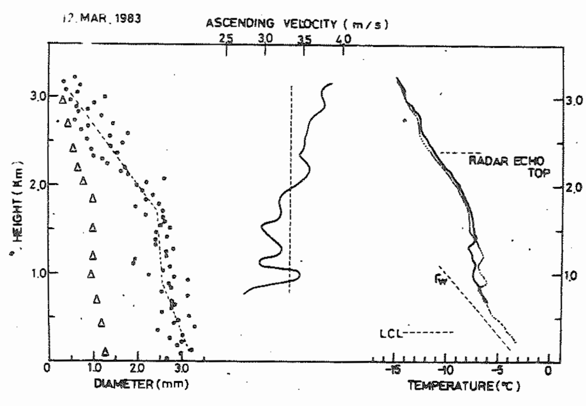

Figure 5. Vertical distribution of mean (triangles) and maximum (solid circles) diameter of snow crystals, ascent velocity of the CS-sonde and air temperature.

figure that smaller crystals with broad or sector-like branches as well as hexagonal plates are predominant at higher altitudes, while relatively larger crystals such as dendrites exist at lower altitudes.

On the basis of the results described in the previous two figures, the origin and the falling trajectories of the predominant snow crystals found at different altitudes are summarized in Fig. 7.

On 26-27 February, 1983, a series of band-shaped snow clouds brought a heavy snowfall in the Sapporo area. A sketch of a PPI radar echo on 26

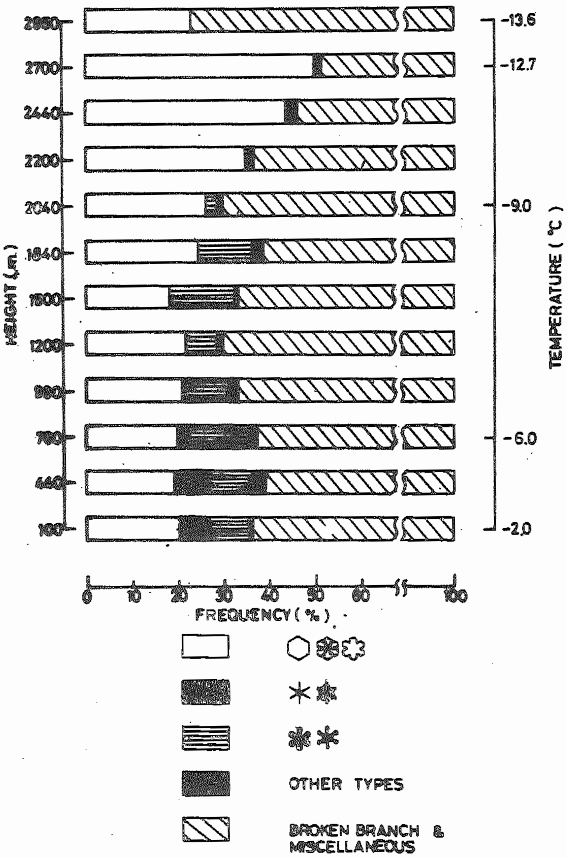

Figure 6. Change with height of fractions of each snow crystal type in percentage (%).

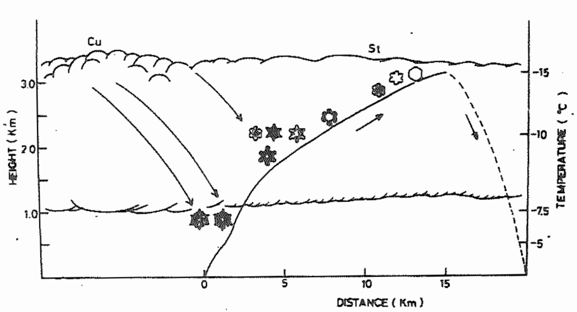

Figure 7. Trajectory of the CS-sonde and the predominant shapes of snow crystals observed at each point.

Feb. is shown in Fig. 8, in which HU indicates the site of the radar as well as the site at which the sonde was released. Figure 9 shows an REI radar echo together with the trajectory of the CS-sonde, and the continuous record of snowfall intensities deduced from visibility observations. As seen from Figs. 8 and 9, band-shaped snow clouds successively generated above the Sea of Japan are incorporated into a thick layered cloud after arriving in above the Ishikari Plain. At the same time, vertical convective clouds gradually inclined forward after the arrival.

The upper left figure in Fig. 10 shows the vertical distribution of number concentration of snow particles and that of aggregates, while the upper right figure indicates the trajectories of snow particles estimated from their averaged falling velocities observed at the ground during the snowfall. The horizontal arrows indicated near the abscissa of the upper right figure show the time when large aggregates fell. It should be noted that two trajectories intersect with each other, and the altitudes at which large aggregates are formed are consistent with the altitude at which

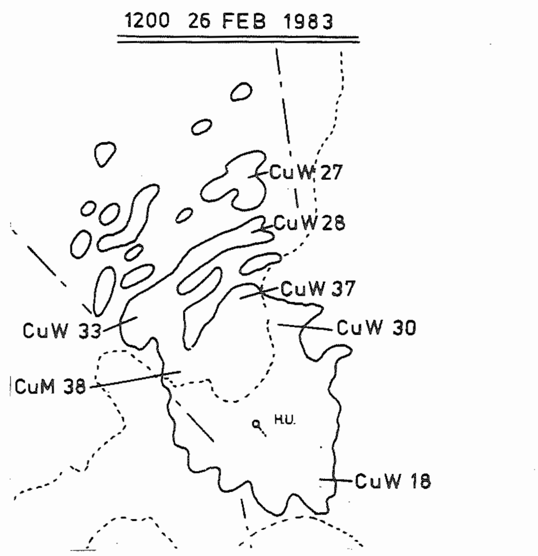

Figure 8. A PPI radar echo sketch of snow clouds on 26 Feb., 1983, when snow fell heavily. HU (Hokkaido University) indicates the position at which the CS-sonde was released and the radar was operated.

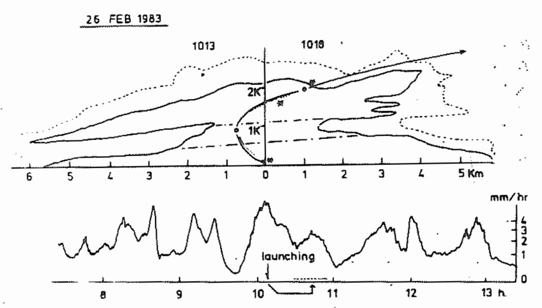

Figure 9. An REI radar echo sketch and the trajectory of the CS-sonde (upper) and the continuous record of snowfall intensity deduced from visibility (lower). Arrows indicate the time of releasing the CS-sonde and its observational duration.

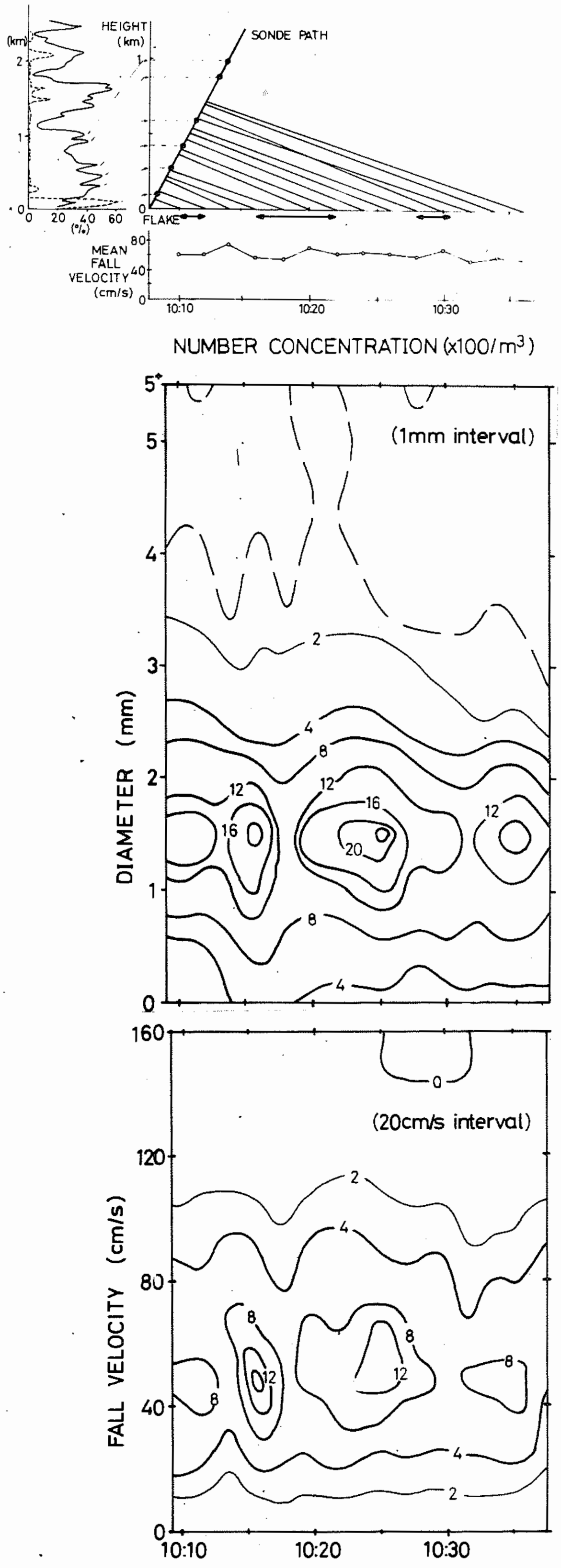

snow crystals have higher concentration, as seen in the upper left figure. It is suggested from the above that the difference in falling velocity of snow particles cause the intersection of the trajectories to form large aggregates.

4. REFERENCES

1. Winn W P et al 1975, Thunderstorm on July 16, 1975, over Langmuir laboratory: A case study, J Geophys Res 83, 3079-3092.

2. Hobbs P V et al 1980, The mesoscale and microscale structure and organization of clouds and precipitation in mid-latitude cyclones. Part I: A case study of a cold front. J Atmos Sci 37, 568-596.

3. Matejka R A et al 1980, Microphysics and dynamics of clouds associated with mesoscale rainbands in extratropical cyclones, Quart J Roy Meteor Soc 106, 29-56.

4. Magono C and Tazawa S 1966, Design of "Snow Crystal Sondes". J Atmos Sci 23, 618-625.

5. Asai T 1967, An example of cumulus updraft as revealed by rawinsonde observation, J Meteor Soc Japan 45, 493-495.

Figure 10. Relationship of the snow particles detected aloft by the snow crystal sonde and aerial camera with the particles observed on the ground surface. Upper: Vertical distribution of qualitative number concentration of snow particles (solid lines) and aggregates (broken lines) and corresponding trajectories of the sonde and snow particles in a time-height chart. Arrows indicate the observed durations of large aggregates. Mean fall velocity of snow particles is indicated below the abscissa. Middle: Change with time of size distribution spectra of snow particles observed on the ground surface. Lower: Change with time of fall velocity distribution spectra of snow particles.

THE SHAPE-SIZE DISTRIBUTIONS OF HYDROMETEORS AND THEIR EFFECTS ON CLOUD PROPERTIES

Pao K. Wang

Department of Meteorology
University of Wisconsin
Madison, Wisconsin 53706
U.S.A.

1. Introduction

The shapes and sizes of hydrometeors are among the most important physical properties of clouds and precipitation. For example, sizes of precipitation elements play a central role in the detection of storms by radar. The recently developed radar technique utilizes the linear depolarization of backscattered electromagnetic waves by hydrometeors. This depolarization property depends strongly on the shapes of the particles encountered (Refs. 1 and 2). Particles of different shapes and sizes falling in air also have different flow fields around them and therefore may be subject to different hydrodynamic drags. These drag forces have significant influences on the microphysical properties of these hydrometeors such as their fall velocities, surface heat dissipation rates, and collision efficiencies with other particles (Ref. 3).

Despite the importance of the shape-size factor, our knowledge of it is rather inadequate. So far only the *size distribution* of cloud droplets and raindrops are better understood (Refs. 4 and 5). The problems concerning ice particles remain unsolved. Furthermore, the *shape distribution* of hydrometeor, potentially most important to the new radar technique, is practically unknown (except for the case of cloud droplets where the shapes are essentially spherical). This is not to say that there are no attempts trying to understand it but merely reflecting the difficulties involved.

The main difficulty involved in the quantitative shape distribution study is in mathematically describing the many complicated shapes of hydrometeors. In order to be physically tractable, the formulas used must be simple, especially, the number of parameters involved should not be too large. The conventional shape description methods (e.g., Legendre polynomials) usually require a relatively large number of parameters, often exceeding 10, to describe a not-so-complicated shape. They are therefore not very suitable. There are some simple shapes, such as columnar ice crystals, that can be specified by two parameters (e.g., length and radius) but it fails to apply to general ice particles.

Recently Wang (Ref. 6) and Wang and Denzer (Ref. 7) developed some simple formulas for describing the shapes of conical hydrometeors (raindrops, graupel, and hailstones) and plane hexagonal snow crystals, respectively. Using only 3 parameters in the formulas, both mehtods specify not only the shapes but also the sizes of particles. It is felt that these methods should serve as a concise and consistent basis for shape-size distribution studies. In the following we briefly summarized the methods and give some actual examples.

2. Shape-size distribution of concial hydrometeors

We classify raindrops, graupel, and hailstones as concial hydrometeors here because their shapes can usually be described by the conical function given by Ref. 6:

$$x = \pm\, a[1-(z^2/c^2)]^{\frac{1}{2}} \cos^{-1}(z/\lambda c) \qquad (1)$$

where x and y are horizontal and vertical coordinates of the surface, respectively (see Fig. 1). A, c,

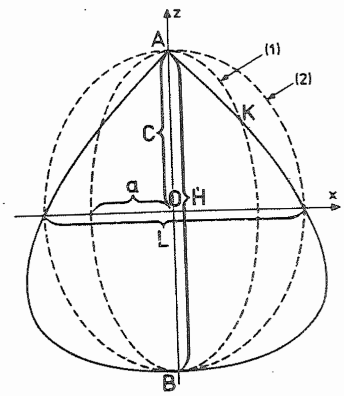

Figure 1. Definition of the coordinate system and various quantities. Solid curve is an axial cross-section of a concial body. Dashed curves (1) and (2) are the generating ellipse and limiting elipse, respectively.

and λ are parameters to be determined. a and c are semi-axes of the generating ellipse (Ellipse (1)) in the x and z-directions, respectively. Eq. (1) is thus an ellipse modified by an arc-cosine function with λ as a parameter. Note that since the principal value of the arc cosine function lies between 0 and π, the value of λ must be equal or larger than 1. When λ is small, Eq. (1) describes a conical body with sharp apex. When λ is large, the apex becomes blunt. As $\lambda \to \infty$, Eq. (1) becomes

$$x = \pm\, \frac{\pi}{2}\, a[1-(z/c)^2]^{\frac{1}{2}} \qquad (2)$$

which is a ellipse with semi-axes $\pi a/2$ and c. This is the limiting ellipse (Ellipse (2)). By changing the values of a, c, and λ, various conical shapes are obtained.

The steps of finding values of a, c, and λ for a given concial particle are (referring to Fig. 1):

(1) Determine c - This is just the half length from top to the bottom.
(2) Determine a - First draw the x-axis passing through the center point and measure the horizontal length L. a is simply L/π.
(3) Determine λ - There are two cases:
   (A) The concical curve intersects with the generating ellipse - λ is determined by

$$\lambda = z_K/(0.5403\ C) \qquad (3)$$

where z_K is the z-coordinates of point κ (see Fig. 1).

(B) The concial curve does not intersect with the generating ellipse - λ is determined by

$$\lambda = [(cx_g{}^3/x_m z_m a^2)^2 + (z_m/c)^2]^{\frac{1}{2}} \qquad (4)$$

where x_m and z_m are the maximum x coordinate of the conical curve and the corresponding z coordinate, respectively. x_g is the corresponding x coordinate of the generating ellipse.

Using the method, various shapes of graupel, hailstones, and large raindrops can be simulated quite closely, as shown in Figs. (2) and (3). Note that Eq. (1) can also describe spheres and prolate and oblate spheroids if we let $\lambda \to \infty$. Then the semi-axes of them are given by $\pi a/2$ and c, respectively.

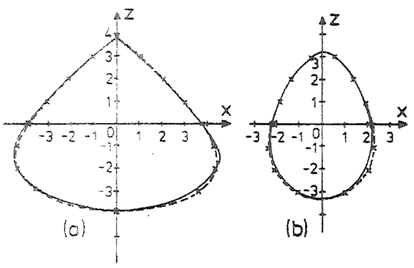

Figure 2. Examples of fitting conical graupel and hailstones by Eq. (1). (a) $a = 1.48$ mm, $c = 2.32$ mm, $\lambda = 1.0$; (b) $a = 0.85$ mm, $c = 1.95$ mm, $\lambda = 1.72$.

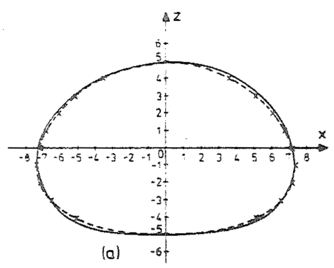

Figure 3. Example of fitting a large freely falling raindrop by Eq. (1). $a = 2.29$ mm, $c = 2.5$ mm, $\lambda = 14.79$.

We now come to the analysis of the shape-size distribution of samples of a particular precipitation event. As a preliminary example, a sample of 63 hailstones from June 22, 1976 storm in Colorado (shown in Fig. 4) was analyzed. The photo-

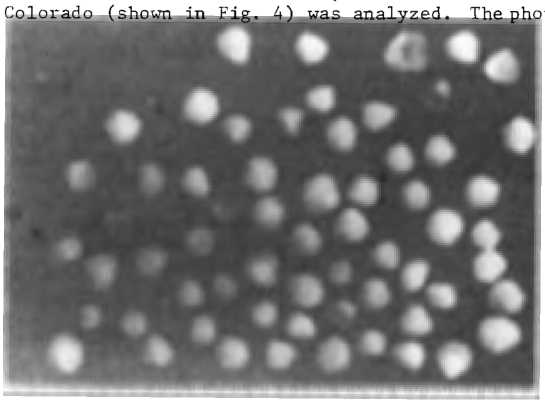

Figure 4. A sample of 63 hailstones fall in Boulder, Colorado in 22 June, 1976.

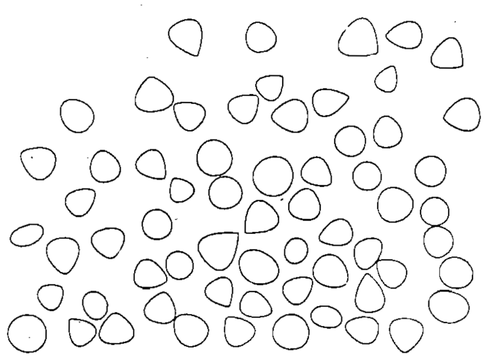

Figure 5. Simulated hailstone shapes of the sample in Fig. 4 using Eq. (1).

graph was kindly provided by Drs. Charles and Nancy Knight of NCAR. A perfect simulation is impossible, of course, considering the surface irregularities. During the fall, the tip of some concial particles melted considerably (Knight, 1983, private communication). In the present study we artifically "made up" these melted tips. This does not result in a large deviations from the shapes in the photo, as can be seen if we compare the simulated shapes (Fig. 5) and the original photo. In fact, it may be that the simulated (unmelted) shapes are closer to the shapes of these hailstones when they were still suspended higher above in clouds and which are of the greater concern for radar observations. The distributions of various geometrical properties of this particular sample are given in Figs. 6-11. Note that the volume, axial cross-sectional area, and area of the surface of revolution are calculated according to (Ref. 6):

$$V \approx \pi^2 ac(3.2889 + \frac{0.2667}{\lambda^2} + \frac{0.0382}{\lambda^4} + \frac{0.0046}{\lambda^8} \qquad (5)$$

$$\frac{0.0024}{\lambda^{10}}),$$

$$A_x = \pi^2 ac/2, \text{ and} \qquad (6)$$

$$A_R \approx 2\pi^2 ac, \qquad (7)$$

respectively. A_x is independent of λ, V and A_R are only weakly dependent on λ. Due to this fact, the ratios between these quantities are nearly constant. i.e.,

$$V/A_x \approx 7,\ V/A_R \approx 1.7,\ A_R/A_x \approx 4 \qquad (8)$$

These expressions may be used as handy rules for estimating the geometrical quantities.

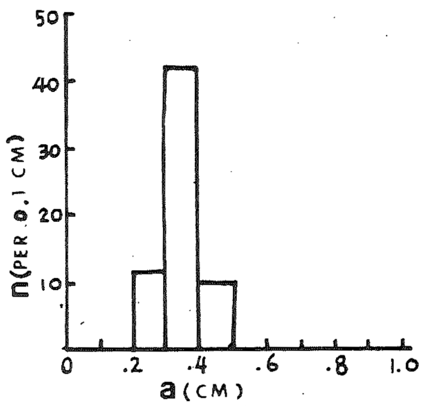

Figure 6. A-distribution of hailstones in Fig. 5.

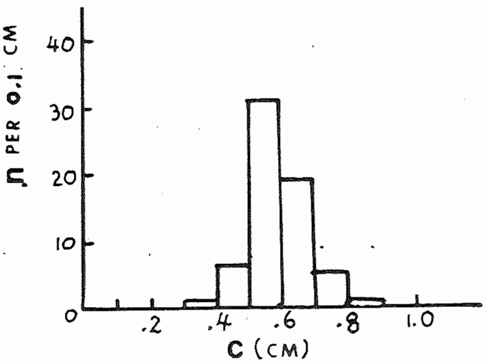

Figure 7. C-distribution of hailstones in Fig. 5.

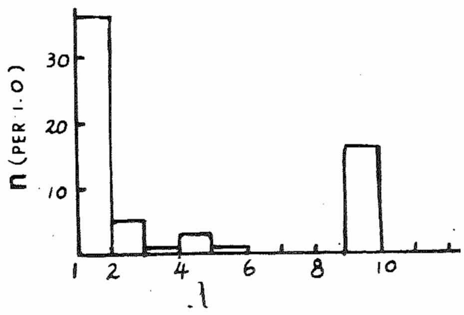

Figure 8. λ-distribution of hailstones in Fig. 5.

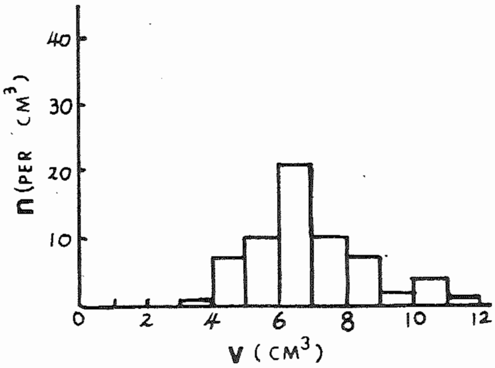

Figure 9. Volume distribution of hailstones in Fig. 5.

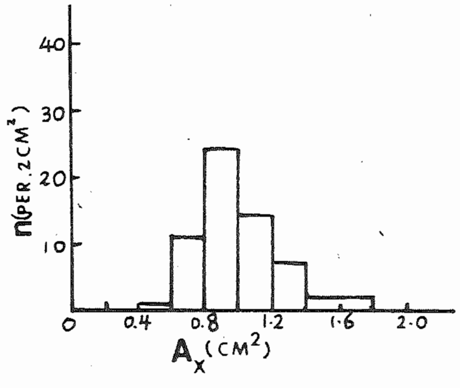

Figure 10. Axial cross-sectional area distribution of hailstones in Fig. 5.

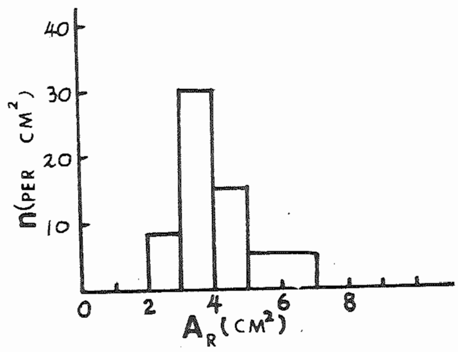

Figure 11. Area of the surface revolution distribution of hailstones in Fig. 5.

It is seen from these figures that the distributions are not irregular but show rather distinct characteristics. For example, both a- and c- distributions show a distinct peak close to its respective median value, especially the a-distribution. Perhaps the single quantity that can be thought as representative of the concept "size" is the axial cross-section A_x which is independent of the shape factor λ while V and A_r are somewhat dependent on λ, although only weakly. It is seen from Fig. 10 that A_x-distribution is close to a χ^2-distribution. Actually, V and A_r also have the similar type of distribution. A_r-distribution is almost the same as A_x which is to be expected from Eqs. (6) and (7). V-distribution is also close to χ^2-type but of higher frequency. The quasi-χ^2 property of these quantities may be of importance. The properties of χ^2-distribution is well-known and we recall here that the Maxwell distribution of the kinetic energy of molecules is a χ^2-type whose physical interpretation is wellknown. Thus the χ^2 property of hailstone distribution, if confirmed by further analysis, may one day afford a physical-dynamical interpretation of hail formation. Of course, the above conclusions are based on this 63 hailstone samples which is definitely inadequate to say anything certain.

Fig. 8. shows another interesting property. Since λ is the main factor that determines the shape, the λ-distribution may be considered as the shape distribution. It is seen here that λ-distribution has two distinct peaks, i.e., it is a bimodal distribution. Remember that when λ is close to 1 the curve is concially shaped with a sharp tip, i.e., a vertically highly asymmetric shape. On the other hand, large λ represents symmetrical shapes such as spheres and spheroids. The bimodal distribution seen here thus can be interpreted as that there are two main types of hailstone shapes in this sample, one type with sharp cones and the other are spheroids. Since the differential scattering between horizontally and vertically polarized waves depend strongly on the particle shapes and fall orientations, it is possible that this bimodal property of λ-distribution may be observed directly by radar. If this λ-property can be proved to be well-correlated with radar differential scattering, then it may become a useful tool for severe storm observations. It is to be noted here that the values of λ of the second peak are put near 10. Changing these λ-values to much larger numbers will not change significantly the shapes. Hence the absolute position of this second peak is not definite. But the importance is that the two-peak structure will remain regardless of the absolute position of the second peak.

Again it is stressed that the above are merely preliminary results based on the analysis of a rather limited sample. A more extensive analysis based on much larger samples is currently underway. The results will be reported at the time of the conference. Similar method can be applied to analyze the shape-size distributions of raindrops. This work is also underway and the results will be reported later.

3. Shape-size distributions of snow crystals

The shapes and sizes of snow crystals can also be described by 3-parameter functions, as have been shown in Ref. 7. For example the following formulas produce the shapes shown in Figs. 12 and 13:

(1) Type-1.

$$\gamma = a\,(\sin^2\,(3\theta))^{\lambda} + c \qquad (9)$$

(2) Type-2

$$\gamma = a[1-(\sin^2\,(3\theta))^{\lambda}] + c \qquad (10)$$

respectively. Here the parameters are a, c, and λ where a is the branch length, c is the radius of the center disk, and λ is the shape factor regulating the width of the branch. It is conceivable that these 3 parameters can be used as the bases of shape-size distribution analysis. Results will be reported later.

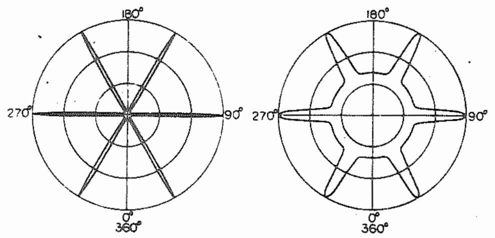

Figure 12. Hexagonal crystal shapes generated by Eq. (9). Left: a=7.37, c=0.25, λ=50; Right: a=4.22, c=3.4, λ=12.

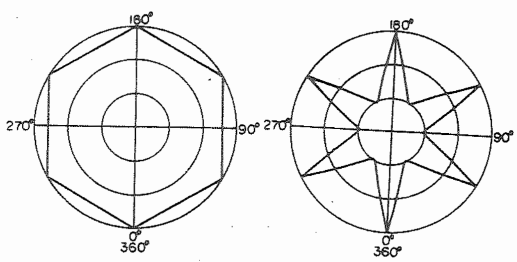

Figure 13. Hexagonal crystal shapes generated by Eq. (10). Left: a=1.02, c=6.6, λ=0.35; Right: a=5.12, C=2.50, λ=0.35.

4. Conclusions

It is seen from above discussions that analyzing shape-size distributions of hydrometeors using simple formulas is possible. In the examples shown here, only 3 parameters are involved, thus serving as a concise base of the shape-size categorization. The preliminary results for conical hydrometeors show interesting properties which may be important for understanding the physical processes involved. The present sample is a ground sample. The actual in-situ air sample is becoming available through the use of 2D probe. These insitu sample will be our future subject of analysis.

5. Acknowledgements

I am indebted to Drs. Charles and Nancy Knight of NCAR for providing the photographs of hailstones. This work is partially supported by U.S. Environmental Protection Agency under Gront No. R-809371-01-0. Although the research described in this article has been funded in part by EPA, it has not been subject to the Agency's required peer and administrative review, and, therefore, does not reflect the view of the Agency and no official endorsement should be inferred.

6. References

1. Seliga, T.A. et al. 1981, A preliminary study of of comparative measurements of rainfall rate using the differential reflectivity radar technique and a raingauge network. *J. Appl. Meteor.*, *20*, 1362-1368.

2. Seliga, T.A., and V.N. Bringi, 1978, Differential reflectivity and differential phase shift: Applications in radar meteorology, *Radio Sci.*, *13*, 271-275.

3. Pruppacher, H.R., and J.D. Klett, 1978, *Microphysics of Clouds and Precipitation*, D. Reidel, 714 pp.

4. Khrgian, A. Kh., and I.P. Mazin, 1953, in Borovikov et al., *Cloud Physics*, p. 65. English Translation, U.S. Dept. of Commerce.

5. Marshall, J.S., and Palmer, W.M., 1948, *J. Meteor.*, *5*, 165.

6. Wang, P.K., 1982, Mathematical description of the shape of concical hydrometeors, *J. Atmos. Sci.*, *39*, 2615-2622.

7. Wang, P.K., and S.M. Denzer, 1983, Mathematical description of the shape of plane hexagonal snow crystals. *J. Atmos. Sci.*, *40*, 1024-1028.

SESSION II

MICROPHYSICAL PROCESSES IN CLOUDS AND PRECIPITATION

Subsession II-1

Cloud droplet growth

RAINDROP OSCILLATION MODES

K. V. Beard

Department of Atmospheric Sciences, University of Illinois
Urbana, Illinois 61801, U.S.A.

1. INTRODUCTION

Although our quantitative knowledge of drop oscillations dates from 19th century hydrodynamic theory and the important contribution of Ref. 1 on the normal modes, the oscillation of drops falling in air had not been studied in detail until the subject was pioneered by Ref. 2 at the beginning of the modern era of cloud physics. Our knowledge of drop oscillations has been advanced by more recent theoretical (Ref. 3) and observational studies (Refs. 4-6). An important indication that raindrops undergo frequent non-equilibrium distortions is found in the photographic study of Ref. 7. His work has been often cited, but usually only as evidence for an average oblate distortion. Support for a strong source of raindrop oscillations is presented in Ref. 8 based on a balance between collisional energy and viscous dissipation. With the advent of dual-polarization radar it has become increasingly important to quantify drop shape since it is the key microphysical parameter needed for determining the rainfall rate (Ref. 9).

2. OBSERVATIONS OF DROP OSCILLATIONS

The most important observational knowledge of oscillating water drops falling in air originated from wind tunnel investigations (Ref. 2) followed by field investigations (Ref. 7) and subsequent wind tunnel work (Refs. 4-6). Large amplitude distortions were observed which increased with drop size. Two types of deformation were noted for very large drops (Ref. 2 for D = 6-9 mm, where D is the diameter of an equivalent volume sphere): rotations about the vertical minor axis as a rigid ellipsoid with the major axis horizontal; and oscillations between ellipsoidal shapes with alternating major axes 90° apart in the horizontal plane. As pointed out by Ref. 3 this latter type of oscillation is a degenerate mode of the fundamental harmonic ($m = 2$, Ref. 10). In contrast the type of oscillation observed by Ref. 4 for drops (D = 3.7-5.6 mm) were "approximately of the prolate-oblate type" (according to Ref. 11), corresponding to the axisymmetric oscillation of the fundamental harmonic ($m = 0$) described by Ref. 1. This was the only type of oscillation for small drops (D = 1-3 mm), and large drops (D = 4-7 mm) exhibited various other shapes near the fundamental frequency with no evidence for higher harmonics (Ref. 5). There is photographic documentation (see Refs. 4, 6) that the approximate prolate-oblate oscillation noted by Ref. 11 contains features of both the axisymmetric oscillation and the remaining degenerate mode at the fundamental frequency ($m = 1$), one in which the drop elongates in alternate orthogonal directions tilted at 45° from the vertical in a vertical plane.

These wind tunnel observations of water drops falling in air have shown that the majority of oscillations occur near the fundamental frequency with some evidence of a few higher harmonics but at greatly reduced amplitudes (Refs. 4, 6). Small drops oscillate in the most symmetrical manner, whereas larger drops whose equilibrium shape is notably different than a sphere exhibit characteristics of all three degenerate modes for the lowest harmonic.

In his raindrop study, Ref. 7 considered average axis ratios obtained using two orthogonal cameras. Although the prolate and oblate distortions were found, no details were given on their relative orientation which could be used in determining the type of oscillation. These results are shown in Fig. 1 for comparison with observations of drop oscillations in a wind tunnel. The mean axis ratio line was obtained by Ref. 7 for 1783 raindrops. A slight correction was made to account for a systematic error in the vertical dimension due to the (10 μs) flash duration (Ref. 12) which leads to a .02-.03 decrease in axis ratios. The upper and lower dashed lines provide an envelope to the raindrop measurements. The wind tunnel data show means and extremes observed for oscillating water drops. Although the mechanism that causes raindrop oscillations is most likely different than in the wind tunnel experiments (collisions not turbulence) the responses seem to be remarkably similar. This comparison provides indirect evidence that the shift observed by Ref. 7 is due to oscillations. A more direct form of evidence for oscillations is the scintillation seen in raindrop streaks under dark field illumination (Refs. 13, 8).

3. THEORY FOR RAINDROP OSCILLATIONS

A brief description of the theory for oscillations about the equilibrium raindrop distortion is found in Ref. 14 with an account of the potential flow aspects given in Ref. 15. In these studies an ellipsoidal shape constraint was used for the lowest harmonic because of the relative ease in evaluating the surface area compared to the Rayleigh shape.

The kinetic energy of constant volume ellipsoid assuming potential flow (Ref. 16) is expressed in terms of the mass (m) of the drop and the rates of changes for the semi-axis as

$$E_k = \frac{m}{10}\left(\dot{a}^2 + \dot{b}^2 + \dot{c}^2\right) \qquad (1)$$

For axisymmetric (vertical) drop oscillations Eq. 1 is reformulated as a differential equation for the change in axis ratio with time using the following definitions for the axis ratios, $\alpha = c/a = c/b$, and the volume constraint $D^3 = 8\,abc$, so that

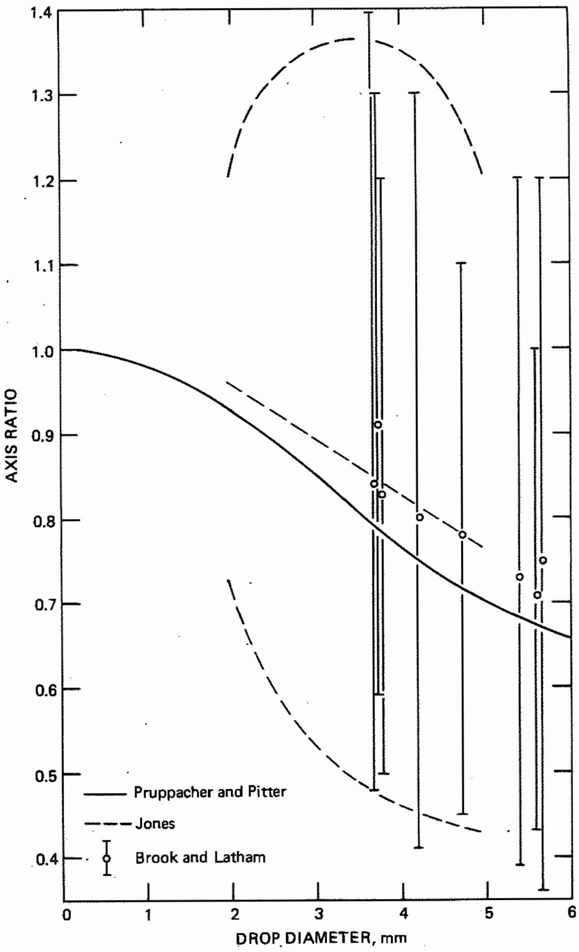

Figure 1. Observed axis ratios as a function of drop diameter. Solid curve is the equilibrium value. Dashed lines are the mean and extremes for raindrops. Open circles and vertical bars show mean and extremes for water drops in a wind tunnel.

$$\dot{\alpha} = 6\,\alpha^{4/3}\,(5E_k/m)^{\frac{1}{2}}\,(1+2\,\alpha^2)^{-\frac{1}{2}}\,D^{-1} \qquad (2)$$

The change in axis ratio with time of the asymmetric mode can be obtained from Eq. 1 by assuming that oscillations occur as ellipsoidal variations in drop size. The horizontal mode has two axis ratios $\alpha_x = c/a$ and $\alpha_y = c/b = \alpha_o^2/\alpha_x$ where the vertical semi-axis, $c = D^3(8ab) = D\alpha_o^{2/3}/2$, is assumed to be invariant for consistency with theory for the analogous asymmetric oscillation about a sphere (Ref. 10). With these definitions the time rate of change for α_x is

$$\dot{\alpha}_x = 2\,\alpha_x^2\alpha_o^{-2/3}\,(10E_k/m)^{\frac{1}{2}}\,(1+\alpha_x^4/\alpha_o^4)D^{-1} \qquad (3)$$

The task of integrating Eq. 2 or 3 for the temporal behavior of the axis ratio requires an expression for the instantaneous kinetic energy which can be obtained using conservation of energy with dissipation. Thus two additional equations are needed, one that accounts for the relative amount of kinetic and potential energies, $E = E_p + E_k$, where the total energy (E) determined at an oscillation end point from the potential energy function (E_p); and one for viscous dissipation, $\dot{E}_k = -B\,E_k$, where B can be approximated assuming linear dissipation.

The potential energy function is $E_p = E_s + mgc$, or in terms of the axis ratio,

$$E_p = \pi\sigma D^2\,F + \pi\rho g D^4\,\alpha^{2/3}/12 \qquad (4)$$

where F is the dimensionless area (area/πD^2) for an oblate or prolate spheroid. This equation is equivalent to the potential energy of a spheroidal drop on an idealized non-wettable surface. A minimum in Eq. 4 occurs because the gravitational energy decreases whereas the surface energy increases as the drop becomes more oblate. The predicted axis ratios using Eq. 4 are generally within 1% of the force balance (Ref. 17) which included an aerodynamic pressure. The agreement shows that the equilibrium axis ratio is determined almost entirely by a balance between the curvature of the hydrostatic pressures in the manner of a sessile drop.

Time average axis ratios for the vertical mode ($\hat{\alpha}_v$) were computed by integration of Eq. 2 and found to be predicted by $\bar{\alpha}_v = 1/2\ \alpha' + 1/2\ \alpha_o^2/\alpha'$, where α' is the initial axis ratio. The computed deviations, $(\hat{\alpha}_v-\bar{\alpha}_v)/(\hat{\alpha}_v-\alpha_o)$, were found to be independent of amplitude for $\alpha_o - \alpha' \leq 0.35$ and to vary with raindrop size yielding values of 14, 7, 0, -7, -18 and -30% for D = 1, 2, 3, 4, 5 and 6 mm. As a consequence $\bar{\alpha}$ provides a useful approximation to $\hat{\alpha}_v$ for raindrops up to moderate sizes (D $\leq$ 5 mm).

The computed time averages for the horizontal mode ($\hat{\alpha}_h$) were predicted by $\bar{\alpha}_h = 1/2\ \alpha_o + 1/2\ \alpha' + 1/2\ \alpha_o^2/\alpha'$ with deviations, $(\hat{\alpha}_h-\bar{\alpha}_h)/\hat{\alpha}_h - \alpha_o)$, in the range ±5% for D = 1-6 mm and amplitudes $\alpha_o - \alpha' \leq 0.35$.

4. COMPARISON OF MODEL RESULTS WITH OBSERVATIONS

4.1 Oscillation Frequency

Quantitative observations have been made of the oscillation frequency for water drops in wind tunnel experiments (Refs. 18, 4-6, 19). A comparison of frequency data is shown in Fig. 2 along with findings from the potential flow model. For drop sizes above 2 mm the model results for the vertical oscillation diverge from the fit labeled "Nelson & Gokhale". Most of the frequency data obtained by photographic measurements are above the Rayleigh result about halfway between the theory for the vertical and horizontal oscillations for drops in the range 3 to 7 mm.

The comparison of the computed frequencies with the modulation frequency from microwave laboratory studies is also shown in Fig. 2. The data labeled "Brook & Latham" were obtained with the transmitted wave polarized vertically, whereas the measurements labeled "Goodall" were made with the transmitted wave polarized vertically and also horizontally. The microwave data show two distinct frequency variations with drop size. The lower set can be attributed to the horizontal mode because it was detected only with horizontal polarization and because it was directly observed in the "Blanchard" frequency measurements for very large drops (D = 6-10 mm). The computed frequencies for the horizontal mode correspond well with the lower data set although agreement is best for the largest drops at small amplitudes. Breakup would probably occur for large amplitude ($\Delta\alpha$ = 0.3) as expected for maximum horizontal dimension exceeding 1.0 cm.

Photographic sequences of large oscillating drops (D = 5 mm, Ref. 5; and D $\approx$ 4.5 mm, Ref. 6) show features of both the vertical and transverse (m = 1) modes. Therefore it is possible that the upper fre-

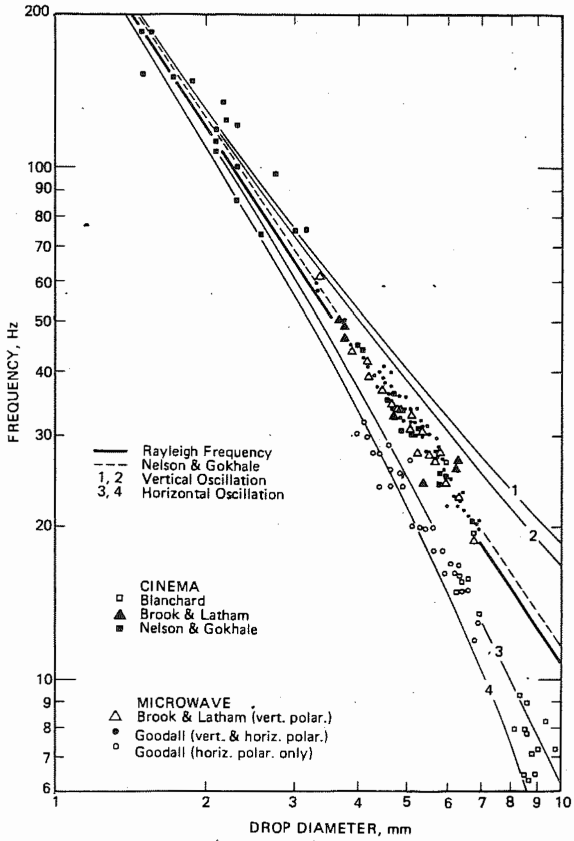

Figure 2. Oscillation frequency for water drops as a function of equivalent volume diameter. Data points and dashed line are from observations; solid lines are theory. Curves 1 and 3 are model results for small amplitude and 2 and 4 for $\Delta\alpha = 0.3$.

quency set corresponds to drops oscillating in some combination of the vertical and transverse modes.

Although the potential flow model with gravity is capable of simulating many features of drop oscillation it fails to predict the oscillation frequency for many drops in the range of 2-7 mm diameter (an important size range for microwave scattering). Oscillations of the transverse mode may be partly responsible for the difference between model results and observations. However, it is possible that the model frequencies are too high because the sessile drop analog of the vertical mode is inadequate. Clearly the frequency shifts seen in Fig. 2 for small amplitude are the result of gravity since the Rayleigh frequency can be recovered for g = 0 or as $D \rightarrow 0$. The decrease in frequency for the horizontal oscillation must be due to the gravity induced distortion because the potential energy of the horizontal mode is the result of changes in surface area only. In fact the ratio of the computed frequency to the Rayleigh frequency (f/f_R) for small amplitude was found to be a function of only $\alpha_o (f/f_R = \alpha_o^n$, with n = 0.6).

For the vertical mode, changes in gravitational energy occur during the oscillation and n was found to vary from -0.9 to -0.6 monotonically with increasing size from D = 1 to 10 mm. The drop oscillates on an imaginary surface causing a varying hydrostatic pressure. A raindrop oscillates with a varying drag force as the cross section changes producing a varying acceleration and hydrostatic pressure. This mechanism couples to the vertical mode by driving axisymmetric shape changes (Ref. 20). Since the acceleration mechanism provides a positive feedback to the vertical mode it may be responsible for the higher frequencies seen in the upper data set in Fig. 2 (i.e., the upwards shift from the pure distortion case of the horizontal mode).

Although the sessile drop analog may not predict the exact oscillation frequency for the vertical mode, it is adequate for estimating the time average axis ratio. The formula for predicting the average for the vertical mode with gravity $(\overline{\alpha}_v)$ actually has less error when compared to model calculations $(\hat{\alpha}_v)$ without gravity as the deviation, $(\hat{\alpha}_v - \overline{\alpha}_v)/(\hat{\alpha}_v - \alpha_o)$, is less than 3% for amplitudes $\Delta\alpha \leqslant 0.35$. Thus the role of gravity is a minor one in the time average problem and the different dependencies for the vertical $(\hat{\alpha}_v)$ and horizontal $(\hat{\alpha}_h)$ oscillations must be primarily the result of shape changes unique to each mode.

4.2 Average Axis Ratios

The axis ratio curves shown in Fig. 3 are from the above formulas for $\overline{\alpha}_v$ and $\overline{\alpha}_h$. Most of the observed averages are consistent with model amplitudes of 0.20-0.25 for the horizontal mode and 0.30-0.35 for the horizontal mode. Since the data are measured for drops with maximum amplitudes of 0.25-0.30 the formula for $\overline{\alpha}_v$ appears to be a better predictor of the observed averages. The oscillations from wind tunnel measurements (labeled "Brook & Latham", Ref. 4) were "approximately of the prolate-oblate type" corresponding to the vertical mode (Ref. 11). In addition the photographic sequence by Ref. 6 shows a vertical motion that would be absent in the horizontal mode. Thus these wind tunnel averages most likely do not involve the horizontal mode.

The raindrop data in Fig. 3 (labeled "Jones", Ref. 7) correspond to the linear fit on Fig. 1. There are probably too few data for larger raindrops to determine a reliable average since there were only 88 axis ratios for D > 4 mm and 15 for D > 5 mm. However, for smaller raindrops ($D \leqslant 4$ mm), where the number of measurements appears to be adequate (1595), the predicted average $(\overline{\alpha}_v)$ is consistent with the wind tunnel observations and indicates the presence of the vertical mode.

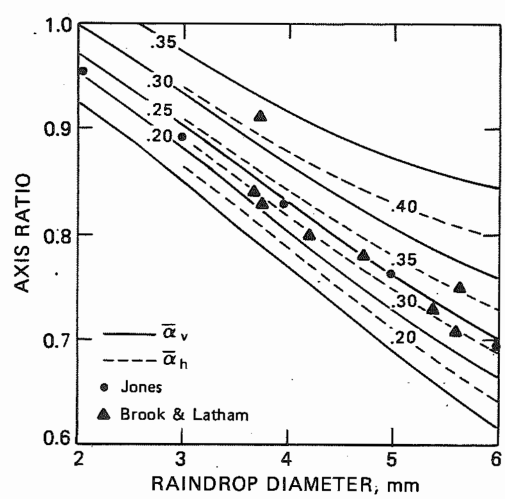

Figure 3. Average axis ratios as a function of drop diameter. Lines are labeled with oscillation amplitudes ($\Delta\alpha = \alpha_o = \alpha'$).

5. CONCLUSIONS

Axisymmetric oscillations were simulated by the vertical motion of a drop on a surface in which the gravitational potential energy was proportional to the displacement of the center of mass. The resultant oscillation frequencies were higher than the Rayleigh result (and the data for large drops) but agreed with measurements for D < 2 mm. Asymmetric oscillations were modeled for a horizontal mode whereby the potential energy increases with the surface area for ellipsoidal variations about a spheroid. The computed frequencies were lower than the Rayleigh result and compared favorably to observations. Simple formulas with good accuracy were developed for the time dependent and average axis ratios as a function of oscillation amplitude. The comparison between the prediction for the average axis ratio with measurements suggests the dominance of the vertical mode.

Acknowledgements. The author thanks Brant Foote, Dave Johnson and Art Jameson for some invaluable discussions about raindrop oscillations. This work was supported, in part, by the National Science Foundation (ATM82-16847).

6. REFERENCES

1. Rayleigh Lord 1879, On the capillary phenomena of jets, *Proc Roy Soc London* 29, 71-97.
2. Blanchard D C 1950, The behavior of water drops at terminal velocity in air, *Trans Amer Geophys Union* 31, 836-842.
3. Foote G B 1973, A numerical method for studying liquid drop behavior: Simple oscillation, *J Comput Phys* 11, 507-530.
4. Brook M and Latham D J 1968, Fluctuating radar echo: modulation by vibrating drops, *J Geophys Res* 73, 7137-7144.
5. Nelson A R and Gokhale N R 1972, Oscillation frequencies of freely suspended water drops, *J Geophys Res* 77, 2724-2727.
6. Musgrove C and Brook M 1975, Microwave echo fluctuations produced by vibrating water drops, *J Atmos Sci* 32, 2001-2007.
7. Jones D M A 1959, The shape of raindrops, *J Meteor* 16, 504-510.
8. Beard K V, Johnson D B and Jameson A R 1983, Collisional forcing of raindrop oscillations, *J Atmos Sci* 40, 455-462.
9. Seliga T A and Bringi V N 1976, Potential use of radar differential reflectivity measurements at orthogonal polarizations for measuring precipitation, *J Appl Meteor* 15, 69-76.
10. Landau L D and Lifshitz E M 1959, *Fluid Mechanics*, Addison-Wesley, 536 pp.
11. Latham D J 1968, The modulation of backscattered microwave radiation by oscillating water drops. *Ph.D. Thesis*, New Mexico Institute of Mining and Technology, Socorro, NM, U.S.A.
12. Jones D M A and Dean L A 1953, A raindrop camera, Research Report No 3, 19 pp. [NTIS DA 36039].
13. Blanchard D C 1962, Comments on the breakup of raindrops, *J Atmos Sci* 19, 119-120.
14. Beard K V 1981, Raindrop oscillations, *Proc Second Int Colloq Drops and Bubbles*, Monterey, CA, 244-246.
15. Beard K V 1982, Raindrop oscillations, *Preprints Conf Cloud Physics*, Chicago, 416-419.
16. Lamb H 1932, *Hydrodynamics*, Dover Publications, 738 pp.
17. Pruppacher H R and Pitter R L 1971, A semi-empirical determination of the shape of cloud and rain drops, *J Atmos Sci* 28, 86-94.
18. Blanchard D C 1948, Observations on the behavior of water drops at terminal velocity in air, *Occas Rep 7* Gen Elec Res Lab, Schenectady, NY.
19. Goodall F 1976, Propagation through distorted water drops at 11 GHz, *Ph.D. Dissertation*, Post Graduate School of Electronic and Electrical Engineering, University of Bradford, UK.
20. Beard K V 1977, On the acceleration of large water drops to terminal velocity, *J Appl Meteor* 16, 1068-1071.

ON COAGULATION OF CHARGED AND NEUTRAL CLOUD DROPS

S.P.Belyaev, V.M.Kim, V.N.Matveev

The Institute of Experimental Meteorology,
Obninsk, USSR

I. INTRODUCTION

The attempts to estimate the effect of electric forces on the gravitational coagulation process important for the precipitation generation process in clouds were undertaken long ago. From this point of view mean Reynolds numbers ranging between I0-I00 are less investigated both experimentally and numerically. The effect of electric forces(Refs.I,2) on collection efficiency of water drops colliding with small spherical particles at the charge Q on drops with the maximum values occurring in thunderstorm clouds(Ref.3) was studied in the experimental paper(Ref.2) for $N_{Re} \leqslant$ I0 and numerically(Ref.I) for N_{Re} = I–400. It is found that such magnitudes of charges are of great importance for drop growth with radii $R \leqslant$ I00μm and their role decreases with increasing drop size. In the experimental paper(Ref.5) a strong effect is shown of drop large charges identical with the limiting Rayleigh charges which are assumed(Ref.4) to be present in the vicinity of the lightning channels at N_{Re} = 5–I5.

In this paper the experimental(Ref.I4) and numerical results are given on collection efficiency with which charged water drops of radii from 90 to 250μm with a charge exceeding the maximum one in thunderstorm collect(capture) neutral fog droplets at N_{Re} = 7–70. The charge on drops changed from I.I0^{-13} to 3.I0^{-11} C and reached I7-55% of the limiting Rayleigh charge.

2. EXPERIMENTAL PROCEDURE AND THE INSTRUMENTS

The experiments were carried out in a vertical wind tunnel of the Institute of Experimental Meteorology(diameter - 2 m, height of the work part of the tunnel - 20 m)(Ref.I5). Thus the coagulation process was not affected by the walls and instruments. Charged collector drops of equal sizes were injected into the central part of the wind tunnel top to the cloud of small neutral droplets ascending in the work part of the tunnel with the mean velocity smaller than the terminal velocity of collector drops. The integral collection efficiency was estimated from more than a hundred of measurements of size increase of collector drops after their passage a distance of I9-37 m in the cloud. Its value was attributed to the liquid water content weighted mean value of cloud droplets radius(Ref.6), r_W.

If cloud droplets have relatively narrow drop size distribution as it is shown in (Ref.7) the expression for drop growth rate in supposition of continuous collector drops growth model is in the form

$$\frac{dR}{dt} = K(R, r_W, Q) \cdot W , \qquad (I)$$

where W is the liquid water content. In Eq.I the kernel of coagulation is expressed by

$$K(R, r_W, Q) = \frac{1}{4\rho R^2} \cdot E \cdot (R + r_W)^2 (U_R - U_{r_W}), \quad (2)$$

where E is the collection efficiency, ρ - water density, U_R and U_{r_W} the terminal velocity of a collector drop and a cloud droplet having the liquid water content weighted mean value radius

$$r_W = \frac{1}{W} \sum_{i=1}^{n} r_i \cdot \Delta W_i \quad . \qquad (3)$$

In Eq.3 r_i is the mean droplet radius in the i-th interval of droplet size distribution, ΔW_i – contribution to drop water content of this interval.

Such representation of the collector drop growth rate is possible under the condition of linear dependence of K on r for a given size R of a collector drop. This condition is approximately realized for the neutral collector drops and for the cloud droplets spectrum with $r \leq 10 \mu m$, and this is true for the charged collector drops up to $r \leq 7 \mu m$ (Refs.I,8).

From Eq.I for the integral coagulation kernel at a small increase of charged collector drop size and the time of their passage we obtain

$$K(\bar{R}, r_w, Q) = \frac{1}{W} \; \frac{\Delta R}{\Delta t} \quad , \qquad (4)$$

where ΔR is the increase of a collector drop, Δt is the time of their passage within the cloud, $\bar{R} = 0.5\,(R_{in} + R_t)$ is the mean drop radius, R_{in}, R_t are the initial and terminal drop radii. Experimental measurements of ΔR, Δt, W and r_w allow to obtain the coagulation kernel K and the collection efficiency E

$$E(\bar{R}, r_w, Q) = \frac{4 \rho \bar{R}^2 K}{(\bar{R} + r_w)^2 \, (U_{\bar{R}} - U_{r_w})} \, . \qquad (5)$$

In experiments the collector drops were generated by a piezoceramic generator of monodisperse drops at frequency from 4 to 20 kHz. The initial and the terminal collector drop sizes were estimated by identical laser meter(Ref.9) fixed on two levels of vertical wind tunnel at the distance of I5, 45 m from each other.

The cloud of small droplets was generated by water spraying with pneumatic nozzles. The cloud droplet size distribution $f(r)$ was measured with a television counter(Ref.IO) and was closely approximated by the gamma-distribution with the parameters of $-0.2 \leq b \leq +0.2$ and $2.5 \leq \tilde{r} \leq 3.8 \mu m$

$$f(r) = \frac{(b+3)^{b+1}}{\Gamma(b+1) \cdot \tilde{r}^{\,b+1}} \cdot r^{b} \cdot \exp\left(-\frac{b+3}{\tilde{r}}\, r\right), \quad (6)$$

where $\Gamma(b + 1)$ – the gamma-function, $\tilde{r} = r_3^3 / r_2^2$ – the size making a maximum contribution to the liquid water content of the cloud, r_2, r_3 is the root-mean-square and root-mean-cube radii of cloud droplets. When b changes in the given interval the relationship between r_w and $\tilde{r}$ has the form $r_w = k\,\tilde{r}$, where k changes from I.3I to I.37. The droplets size r_w remains constant during the experiment, but it changes from $(3.4 \pm 0.2) \mu m$ to $(5.0 \pm 0.3) \mu m$ from one experiment to another experiment. The contribution of the droplets with radius less than $7 \mu m$ to the liquid water contents accounts for $\simeq 80\%$ and of droplets with radius less than $10 \mu m$ accounts for $\simeq 95\%$, that allow to represent the collector drop growth rate in the form of Eq.I.

The liquid water content was measured with the device described in(Ref.II). It was generated under the conditions of a small increase of collector drops. Maximum increasing of the collector drops radii did not exceed I0%, the liquid water content changed from I.35 to 4 g/m³. In general cloud droplets were neutral ones; the maximum charge on the individual largest droplets did not exceed several hundreds of elementary charges; the distribution was symmetrical in respect to the charge sign. The collector drops were charged by the induction method. The drop charge was measured from the charging current which the charged drops carried on and from the frequency of their generation.

The total relative measurement error of the collection efficiency E $(\bar{R}, r_w, Q)$ ranged from 4.5 to 7% according to the given experimental procedure.

3. NUMERICAL MODEL

For comparison of the obtained experimental results with the theoretical ones a numerical gravitational coagulation process model was developed. This model took into account the electrical forces and was identical to the one given in (Ref.I). The model supposed that the cloud droplets had no effect on the flow field around the collector drops. The resistance force for the small droplets was calculated from the Stokes-Cunningham formula. The charge on the cloud droplets was small enough and this permitted to neglect the effect of the coulomb forces and to consider the induction forces as the electric ones. The induction forces consideration was taken from (Ref.I3).

As distinguished from the numerical model(Ref.I)in our computations we used stream functions of the flow around a fluid sphere obtained by Rivkind V.J. and Ryskin G.M.(Ref.I2) for mean Reynolds numbers N_{Re}= I0,I5,40,50,70 and for the distance $\leq$I0 R from the collector drop center. Our model computations showed that the collision efficiencies of the neutral droplets and collector drops(computed by the given model) coincided with the values obtained in (Ref.I) with the error up to 3%.

4. DISCUSSION OF RESULTS

The experimental results obtained are given in Figure I. This figure shows that the electric charges on drops of radii from 90 to 200 μm have a considerable effect on the collection efficiency E. For the collector drops of radii ⩾ I24 μm, i.e. at $N_{Re} \geqslant$ I6 a nonmonotonous dependence of the collection efficiency on collector drops charge was found. The curve bend zone tends to larger charges and becomes more pronounced as the collector drop size grows.

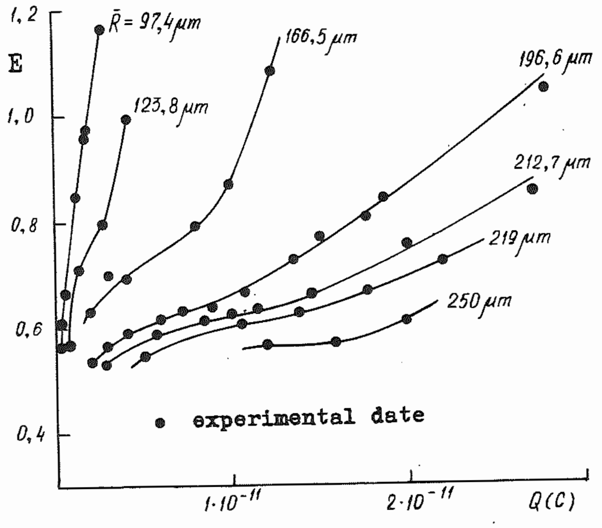

Figure I. The dependence of the drop collection efficiency on its size and charge (τ_W = 3.4 - 5.2 μm). Adapted from Ref.I4.

The comparison of the experimental and theoretical data is given in Fig.2. This figure(solid line) gives as an example experimentally measured efficiency E with which a collector drop of $\bar{R} \simeq 97$ μm ($N_{Re} \simeq 40$) collects cloud droplets with their τ_W from 5.0 to 5.2 μm depending on the charge of a collector drop. The cloud droplet size distribution f(r) is characterized by the parameters: b = -0.2 , $\tilde{\tau}$ = 3.8 μm. Dashed lines represent calculated collision efficiences E for the same value N_{Re} and monodisperse cloud droplets with radii of 5.0 μm and 5.5 μm. As seen from Fig.2 the calculated and experimental values E are in a good agreement, but the behaviour of the experimental curve differs from the calculated one. The cause of difference of the experimental and theoretical dependence of collection efficiency E on Q is now under study.

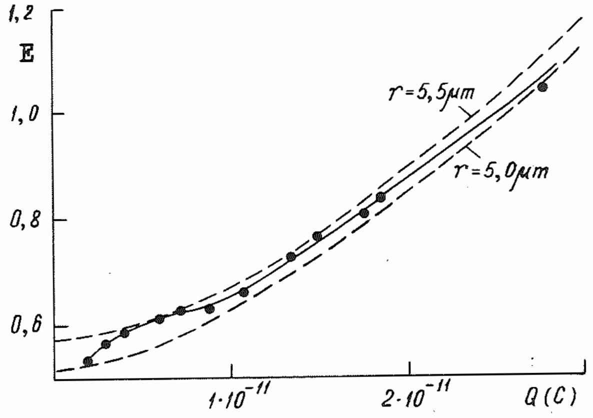

Figure 2. The experimental and theoretical dependence of the collection efficiency E on a collector drop charge for $N_{Re} \simeq 40$.

5. REFERENCES

I. Grover, S.N., Beard, K.V., I975, A numerical determination of the efficiency with which electrically charged cloud drops and small raindrops collide with electrically charged spherical particles of various densities, J.Atm.Sci., 32, No.II, 2I56-2I65.

2. Dayan, N., Gallily, J., I975, On the collection efficiency of water droplets under the influence of electric forces I : experimental, charge-multiple effects, J.Atm.Sci., 32, No.7, I4I9-I429.

3. Gunn, R., I949, The free electrical charge on thunderstorm rain and its relation to droplets size, J.Geoph.Res., 54, 57-63.

4. Vonnegut, B., Moore, C.B., I960, A possible effect of lightning discharge on precipitation formation processes, Geophys.Monogr., No.5, Amer.Geophys. Union, p.287-290.

5. Smith, M.N., I976, The collection efficiences of highly charged water drops for uncharged cloud droplets, J.Atm. Sci., I5, No.3, 275-28I.

6. Belyaev, S.P., Zakharjuzhenkov, P.I., Kim, V.M., Matveev, V.N., I976, Some experimental results of the kernel of cloud droplet collisions. Trudy IEM, I4(59), p.4I-49.

7. Beard, K.V.. Pruppacher, H.R., I968, An experimental test of theoretically calculated collision efficiencies of cloud drops, J.Geoph.Res., 73, No.20, 6407-64I4.

8. Grover S.H.,Beard K.V.,I974, Numerical collision efficiencies for small raindrops colliding with micron size particles, J.Atm.Sci., 3I,No.2,543-550.

9. Alexandrov, M.M.,Kim, V.M.,Matveev, V.N., I980, Laser meter of aerosol sizes. Trudy IEM, 25(93), p.43-5I.

IO. Smirnov, V.V., Shmakov, V.N., Yaskevich, G.F.,I98I, The television system of image analysis of spatial microobjects ensembles. Automated image processing systems. Abstracts of papers presented at the First All-Union Conference, Moscow,Nauka, p.I77.

II. Kim, V.M., Matveev, V.N.,I980, Liquid water content meter of warm fogs. Trudy IEM, 25(93),p.64-78.

I2. Rivkind, V.J.,Ryskin, G.M.,I976, Structure of the flow about a spherical drop moving in a liquid medium at intermediate Reynolds numbers,Fluid and Gas Mechanics, No.I, p.8-I5.

I3. Davis, M.N.,I964, Two charged spherical conductors in a uniform electric field: forces and field strength, Quart.Journ. Mech. and Appl.Math.,XVII,Pt.4,499-5II.

I4. Kim, V.M.,Matveev, V.N.,I983, The collection efficiency of strong charged water drops colliding with weak charged cloud droplets, Trudy IEM, 30(I04),p.50-57.

I5. Belyaev, S.P.,Zakharyuzhenkov, P.I.,Kim, V.M.,Matveev, V.N.,Tret'yakov, N.D.,I976, Investigations of the vertical wind tunnel characteristics.Trudy IEM,I4(59), p.60-66.

OSCILLATION ENERGIES OF COLLIDING RAINDROPS

David B. Johnson and Kenneth V. Beard

Illinois State Water Survey
Champaign, Illinois U.S.A.

1. INTRODUCTION

When two raindrops collide, they can either bounce off one another, coalesce, or break into fragments. In every case however, some of the kinectic energy involved in the collision will manifest itself in mechanical oscillations of the drop or group of drops that survive the collision. While there are a variety of other energy sources that at times may be capable of driving drop oscillations (such as turbulent air motions, wake shedding, or fall into strongly sheared environments), the collisional energy source is particularly intriguing since it provides an inherent oscillation mechanism that does not require special conditions or circumstances.

The degree to which a colliding raindrop stays in an agitated state, of course, will depend on the collision rate and amount of energy provided by each collision as well as the rate at which the oscillations are damped by viscosity. In a recent paper (Ref. 1) we examined the collisional mechanism for raindrop oscillation by means of a model which produced an estimate of the average energy levels associated with a balance between dissipation of oscillational energy and its rate of supply by collisions with other raindrops. That study concluded that collisions could provide sufficient energy to produce large-amplitude oscillations in moderate-to-heavy rainfall. Under such circumstances drop collisions are likely to be the dominant energy source for oscillations. In the present work, we reexamine the question of collision-induced drop oscillations using a probabilistic interpretation of the coalescence equations similar to that employed in stochastic collection models to generate an estimate of the full distribution of oscillation energies as a function of drop diameter and rainfall rate.

2. MODEL FORMULATION

The goal of this model is to calculate the oscillation energies of large raindrops resulting from collisions with smaller drops. The model starts with the same basic assumptions as were invoked in Ref. 1, but extends the calculations to produce estimates of the full distribution of oscillation energies. Computations are performed for each of a number of different raindrop distributions. Each distribution is assumed to be at least quasi steady-state, so any changes in the distribution resulting from coalescence or breakup can be ignored. To adequately describe the raindrop distribution, 112 logarithmically-spaced drop categories were used to cover the diameter range from 30 µm to 5 mm with the number of drops in each class assigned as a function of rainfall rate using the equations of Sekhon and Srivastava (Ref. 2). The overall approach is based on the average collision rates between a large drop of diameter D and each smaller raindrop category, the collisional energy associated with each collision, and the expected rate at which the collision-induced oscillations are dissipated by viscosity in the liquid drop. The final product of each calculation is a distribution showing the fraction of large drops of diameter D having oscillation energies in any specified range.

The average number of collisions that a drop of diameter D experiences in a time step Δt with smaller drops of diameter d_i is given by

$$C_i\ (D,d_i) = \frac{\pi}{4}\,(D+d_i)^2 \left[v(D) - v(d_i)\right]\, n(d_i)\ \Delta t, \quad (1)$$

where $v(D)$ and $v(d_i)$ are the terminal velocities of the drops and $n(d_i)$ is the concentration of the smaller drops. If $\Sigma C_i \ll 1$, then an individual collision rate $C_i\ (D,d_i)$ can be directly interpreted as the probability that the large drop will undergo a collision with a drop of diameter d_i in the time interval Δt.

The excess kinetic energy associated with a collision between a large drop of diameter D and a smaller drop of diameter d_i can be expressed as

$$E_{ki}\ (D,d_i) = \frac{1}{2}\,Mv(D)^2 + \frac{1}{2}\,mv(d_i)^2 - \frac{1}{2}\left[Mv(D) + mv(d_i)\right]^2/(M+m), \quad (2)$$

where M and m are the masses of the drops of diameters D and d_i, respectively and, as before $v(D)$ and $v(d_i)$ are their terminal velocities.

The dissipation of energy by a vibrating drop of diameter D can be estimated by the relation

$$\frac{dE}{dt} = \frac{-2E}{\tau}, \quad (3)$$

where τ, the time constant of amplitude decay for the fundamental mode, is given by $\tau = D^2/(20\nu)$, and ν is the kinematic viscosity of liquid water. Since the energy decays exponentially, it is convenient to introduce discrete energy categories that are spaced logarithmically. In this case, the time step, Δt, can be selected so that the energy dissipation during one time step always reduces the energy by a single category. In the present model, 55 logarithmically spaced energy categories are used to describe the oscillation energies non-dimensionalized by the surface energy of the drop ranging from .001 to .5. The upper limit on the energy classifications is assumed to correspond to the maximum oscillation that can be supported by a raindrop without breakup while the lower energy limit represents an estimate of the smallest oscillation energies that are likely to produce significant deviations from equilibrium shapes (Refs. 1 and 3). An additional energy category ($E = 0$) is used to keep track of all drops that are not yet oscillating or whose oscillations have decayed below the .001 energy level.

A separate calculation is performed for each raindrop distribution specified by its rainfall rate (see Ref. 2) and for each large drop diameter, D. The fundamental parameter to be followed is N_j, the number of raindrops of diameter D having oscillation energies in category j. If the probability of a drop D striking a smaller drop d_i during a time step Δt is C_i and the collisional kinetic energy associated with that collision is E_{ki}, then $N_j C_i$ drops are transferred from category E_j to a new energy category E_m that corresponds to an energy level of $E = E_j + E_{ki}$ while $(1-C_i) N_j$ drops remain in the category j. If $E_j + E_{ki} > 0.5$, then breakup is invoked with the assumption that each of these collisions produces one large fragment, corresponding to the initial large drop, that survives the breakup and carries away the maximum energy permitted ($E = 0.5$). Excess energy beyond this level is ignored, as are the other fragments produced during breakup. After redistributing the drops in each of the 56 energy categories for every possible collision

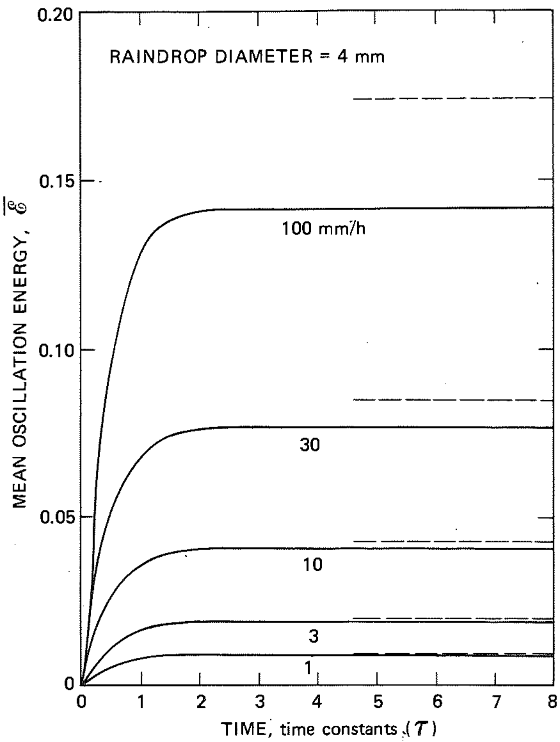

Figure 1. Time evolution of the non-dimensionalized mean oscillation energy for five different ensembles of 4 mm diameter raindrops. Each curve corresponds to a different raindrop distribution and is labeled in terms of the overall rain rate of the distribution. The thin dashed lines represent the corresponding estimates of the mean energies from the steady-state energy balance model (Ref. 1).

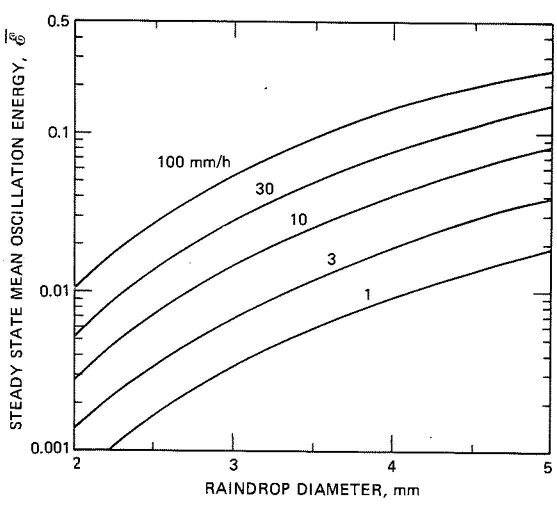

Figure 2. Steady-state mean oscillation energies (in non-dimensionalized units) from the energy model as a function of drop size and rain rate.

such that $d_i < D$, time is incremented and all drops decay to the next lower energy level.

Initially, all drops are assigned to the non-oscillating category. Once the computations begin, however, all possible energy states become occupied as the average energy increases and the distribution converges toward steady-state. Figure 1 shows one aspect of the evolution of the model. This example illustrates the build up of the mean oscillation energy of 4 mm drops for five different droplet distributions. After a rapid initial rise, the mean energy quickly levels off at, or slightly below, the level predicted by our earlier steady-state energy balance model. Figure 2 shows the steady-state mean energies predicted by the energy distribution model as a function of drop diameter and rainfall rate. These mean energies, as well as the energy distributions discussed in the next section, were obtained after a time interval of 8τ from the start of the computations in order to ensure that model predictions reflect steady-state conditions.

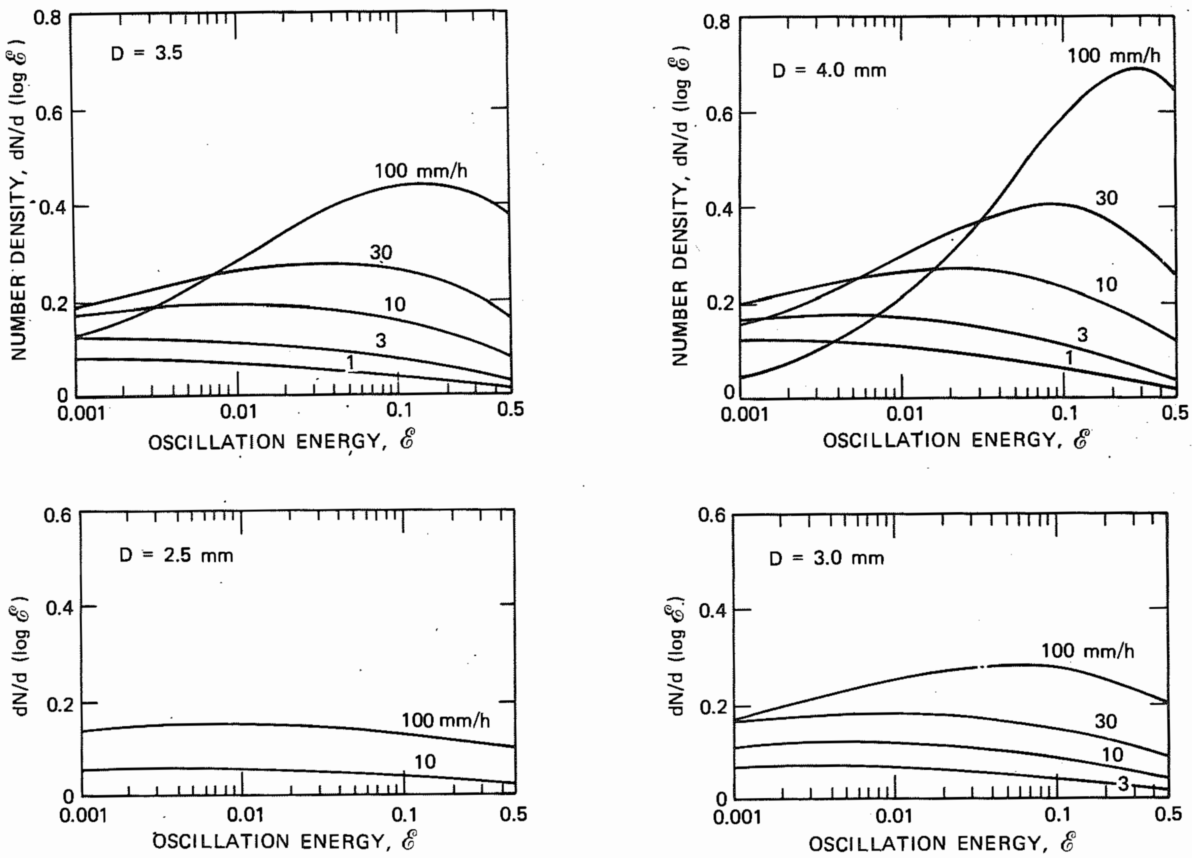

Figure 3. Steady-state number density distributions for large raindrops as a function of the non-dimensionalized oscillation energy. Separate curves are shown for rainfall rates up to 100 mm/h.

3. MODEL RESULTS

Figure 3 illustrates the steady-state number density distributions of raindrops with diameters ranging from 2.5 to 5.0 mm as a function of the non-dimensionalized oscillation energies. Within each plot, separate distributions are shown for rainfall rates up to 100 mm/h. In this type of presentation the area under each curve is proportional to the total fraction of drops oscillating within the range of energies plotted. The increase in area beneath the curves for higher rainfall rates and larger drop diameters merely reflects a larger fraction of drops having oscillation energies between .001 and .5.

Taken collectively these results indicate that at any instant, a suitable ensemble of colliding raindrops will contain drops having oscillation energies that range from intense to imperceptible. At the level of the individual drops, this distribution of energies is understandable since the collisional mechanism for generating oscillations is inherently unsteady with irregularly repeated cycles of sudden energy input followed by gradual decay. If drops with non-dimensionalized oscillation energies smaller than 0.001 are classified as not oscillating, there is almost always a significant number of non-oscillating drops. This remains the case even when the mean oscillation energies are quite high. In every case, however, both the fraction of drops oscillating and the severity of the oscillations increase as the drop diameter and rainfall rate increase. For example, the model suggests that 86% of the 3 mm diameter raindrops in a 3 mm/h rainshaft would be expected to have oscillation energies less than .001 (not oscillating), while only 2% are oscillating intensely with energies > .1. With an increase in the rainfall rate to 30 mm/h, 58% of the drops are not oscillating, while 9% are oscillating intensely. On the other hand, if we consider drops as large as 5 mm, then the model predicts that 32% of these drops will not be oscillating in a 3 mm/h rainfall and 13% will have oscillations with energies > .1. With a 30 mm/h rain rate, only 1% of the 5 mm raindrops would not exhibit appreciable oscillations while 53% would exhibit strong oscillations.

4. DISCUSSION

This study reinforces our earlier conclusion that drop collisions can be an important energy source for drop oscillations, while emphasizing that there will always be a wide range of intensities of oscillation in any ensemble of drops undergoing collisional excitation. Although other energy sources may also contribute to oscillations in special situations, the collisional energy source would seem to have widespread applicability since it will always be present when drops exist in sufficient numbers to collide with one another. Although it may be possible to find an example of

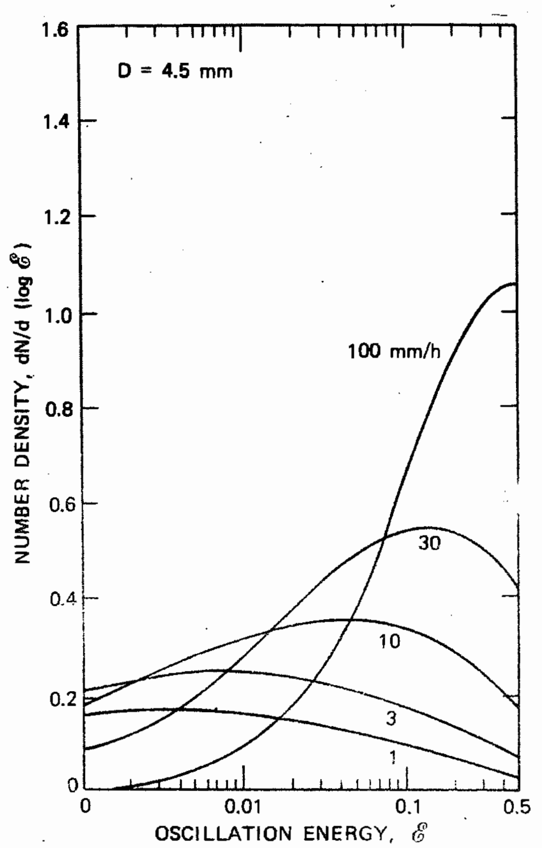

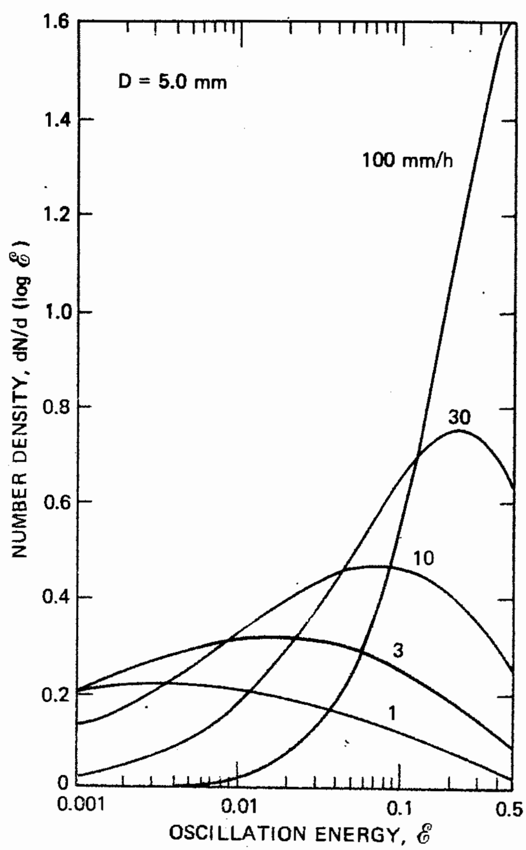

Figure 3(cont.). Steady-state number density distributions for large raindrops as a function of the non-dimensionalized oscillation energy.

almost any level of oscillation within a single rainshaft, ranging from drops oscillating at the verge of breakup to those with motions that are so thoroughly damped that they seem to be at rest, the number of drops oscillating and the intensity of the oscillations will always increase with increasing drop size and rainfall rate.

While these results should be useful in understanding some of the general features of the collisional forcing of raindrop oscillations, the specific numbers produced by the model should be taken with some caution. The model includes only one energy source and is by no means a complete description of that one. For example, the smaller fragments resulting from breakup and their oscillations are not considered by the model. Furthermore, it should be noted that there will be situations in which the model predictions may significantly overestimate or underestimate the intensity of the oscillations. Our previous study, for example, revealed the sensitivity of the model results to the small end of the raindrop distribution, and any process that modifies the relative concentration of these drops will have a direct impact in the intensity of the collisional forcing. Size-sorting of particles within a precipitation shaft is one example of a process that will clearly impact on the collisional forcing. In addition, any residual fragments of unmelted ice (or even air bubbles left in the process of melting) may be expected to enhance the speed with which oscillations are damped (Refs. 4 and 5) and may produce significant shifts in the expected energy distributions. Similarly, the introduction of oscillation energy in modes higher than the fundamental is likely to speed damping and shift the energy distributions toward lower energies.

Acknowledgments This work was supported by the National Science Foundation under grants ATM81-08455 and ATM82-16847.

5. REFERENCES

1. Beard, K. V., D. B. Johnson and A. R. Jameson, 1983: Collisional forcing of raindrop oscillations. *J. Atmos Sci.*, 40, 455-462.

2. Sekhon, R. S., and R. C. Srivastava, 1971: Doppler radar observations of drop-size distributions in a thunderstorm. *J. Atmos. Sci.*, 28, 983-994

3. List, R., T. B. Low, N. Donaldson and E. Freire, 1980: Experiments and models on coalescence and breakup of raindrops. *Proc. Int. Conf. Cloud Physics*, France, 165-168.

4. Blanchard, D. C., 1950: The behavior of water drops at terminal velocity in air. *Trans. Amer. Geophys. Union*, 31, 836-842.

5. Blanchard, D. C., 1957: The supercooling, freezing, and melting of giant waterdrops at terminal velocity in air. *Artificial stimulation of rain*, Pergamon Press, 233-249.

AN EXPERIMENTAL INVESTIGATION OF THE EFFECT OF WEAK TURBULENCE ON THE COAGULATIONAL GROWTH RATE OF CLOUD DROPS.

Neizvestny A.I., and Kobzunenko A.G.

Central Aerological Observatory, Moscow, USSR.

1. INTRODUCTION

The data on the effect of turbulence on cloud drops coagulation growth rate (CDCGR) given in the literature are rather inconsistent, since CDCGR theoretical estimates (Refs.1-3) using the model convective diffusion of drops have shown that the effect of turbulence on CDCGR can be neglected, while the numerical simulation (of the process) of drops random movement in the field of turbulent pulsations of air flow velocities (Ref.4) gives a drop collection efficiency increase of one order of magnitude, if the drop sizes are comparable, the greater drop radius is $r_1 < 25$ µm, and the rate of turbulent kinetic energy dissipation $\varepsilon = 1$ cm^{2}s^{-3}.

Regarding the turbulent flow as an aggregate of velocity shears of different scales, Jonas and Goldsmith (Ref.5) have estimated collection efficiency of drops in a laminar flow with a constant shear. They have found that for shears of 10 to 20 1/s, $r_2/r_1 \geqslant 0.4$, collection efficiency of drops also increases by an order of magnitude. Thus, the lack of experimental data on the effect of turbulent pulsations on CDCGR and marked diversity of data from different calculated models of drops interaction in a turbulent flow strongly necessitates experiments for in situ CDCGR determination in a turbulent flow.

This paper presents data on the relative change of collection efficiency for drops of radius $r_1 \doteq 14$ to 27.5 µm and droplets of radius $r_2 = 9$ to 11 µm interacting in turbulent and laminar flows.

2. THE EXPERIMENT

A certain number of drops and droplets are injected into a horizontal tunnel. Entrained by an air flow the drops interact and then precipitate onto a collecting plate introduced into the flow. A certain part of drops capture droplets with the probability $F = n_c/n_t$, where n_c is the number of drops which have captured droplets and n_t is the total number of drops which have precipitated on the collecting plate. If the distribution of drops in the tunnel is Poissonian and their number density is so low that the probability of double, triple, ets. captures is negligible, then the collection efficiency K is estimated from the expression (Ref.6)

$$K = -\ln(1-F)\left[\pi(r_1 + r_2)^2 N \cdot v_s \cdot t_i\right]^{-1}; \qquad (1)$$

where N is the mean numbers density of droplets in the tunnel, v_s is sedimentation rate of drops, t_i is the drops-droplets interaction time (see Table 1). It should be noted that relationship (1) coincides with Picknett's one (Ref.6) only in case of gravitational coagulation, when the condition $h = v_s t_i$ is fulfilled. Yet, in a turbulent flow drops move randomly due to turbulent pulsations, which makes the "height h" notion of the column, washed out by drops in a droplets' layer, physically meaningless. The product $v_s t_i$ in this case actually shows, what portion of the height h the drops passed interacting and what portion h they moved due to turbulent transport of a mole of air across the tunnel.

The experimental apparatus, shown in Fig.1, is a tunnel, 290cm long with 9x10 cm^2 cross-section. Filtered air is injected into straightening chamber 11, further

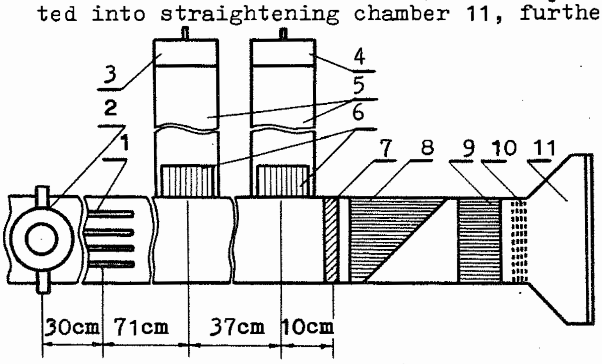

Fig.1 Diagram of the experimental apparatus. 2 is photodetector for measuring the droplet number density. 8 is honeycomb with a 45° shearing angle. The rest of the signatures are given in the text.

straightening of air flow is done with rectangular honeycomb section 9 of 1.5 mm mean cell diameter and 10 cm length and with four rows of nets 10 with a 0.5 mm cell diameter. For producing a turbulent air flow, grating 7 with a 25 mm rods diameter is placed in the tunnel.

Drops and droplets are produced by generators 3 and 4 with a dissipating jet described in paper (Ref.8), with the exception, that in the present case a pneumatic dissipation of a droplet chain is performed. To neutralize a spontaneous charge of drops (droplets) a constant voltage is applied between the jet and the discharge electrode. The drops' generator has an orifice with a 28 µm diameter and uses a water solution of 30% of glicerine, 6% of NaCl and 10% of black ink. The droplets' generator has an orifice with a 17 µm diameter and uses a water solution of 10% of glicerin and 1% fluoresceine - Na. This composition of solutions and the dimensions of the orifices provide that after partial drying of the drops we obtain scarlet glicerine droplets with the spectrum, shown in Fig.2, and

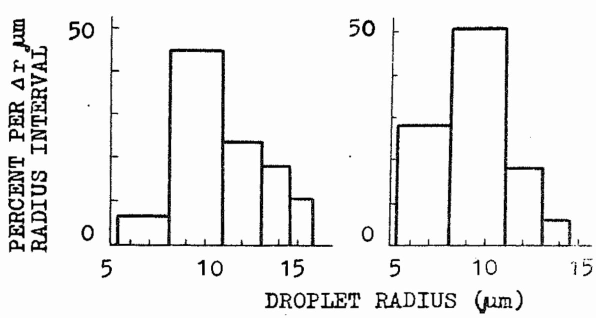

Fig.2 Droplet size spectra: left-regime 1, series 1 and 2, regime 4, series 2 and 3, right - the rest of the regimes and series (see Table 2).

dark-blue glicerine drops with a discrete spectrum of 14 to 27.5 µm.

Before getting into the horizontal tunnel drops and droplets pass at a 5-6 cm/s speed through vertical chambers 5 of an 11 cm diameter and a 70 cm length and honeycombs 6 with cells of a 4 mm mean diameter and a 3 cm length. Sampling within the flow is done using glass plates of 6 x 9 cm^2 size. The plates are placed into holder 1 which can be inserted at different heights into the slits in the side walls of the tunnel.

Experiments are conducted in the following succession. After starting droplets' generator, neutralizing the integrated charge of the droplets, and measuring their balanced size in the lower portion of vertical chamber 6 (Fig.1), the number density N is determined. Then the drops' generator is started and after the charge neutralization and drops size measurement the flow is sampled. For this purpose the holder with a plate is exposed in the flow for 3-10 s. Repeated exposure provides 60 plates for each regime, which after processing are divided into three series.

For estimating the collecting plate is placed upon a transparent backing with a reference grid on it. Drops and droplets are seen through a binocular microscope as round spots with the diameter 2.4 times the diameter of the original spherical drops, differing significantly in colour. Coalescence of dark-blue drops and scarlet droplets results in specifically coloured drops which can be easily discriminated from dark-blue ones. When successively surveying through the microscope the whole of the collecting plate, the total number $n_t(r_1)$ of drops for each size fraction is counted and the number of drops which have collected droplets, $n_c(r_1)$, is determined.

3. CHARACTERISTICS OF THE FLOWS

The characteristics of turbulent and laminar flows in the tunnel without drops (droplets) are determined with a constant temperature thermoanemometer DISA, model 55A01, with the detector thread diameter of 5 µm and length of 2 mm. Frequency and wave number spectra are obtained using a quartz filter spectrum analyser with a 5 Hz passband. The spectrum of longitudinal pulsation (Fig.3) spans two orders of wave numbers and five orders of parameter $2S(\Omega)\bar{v}^{-2}$ has a specific form and is governed by "the law of -5/3" up to the

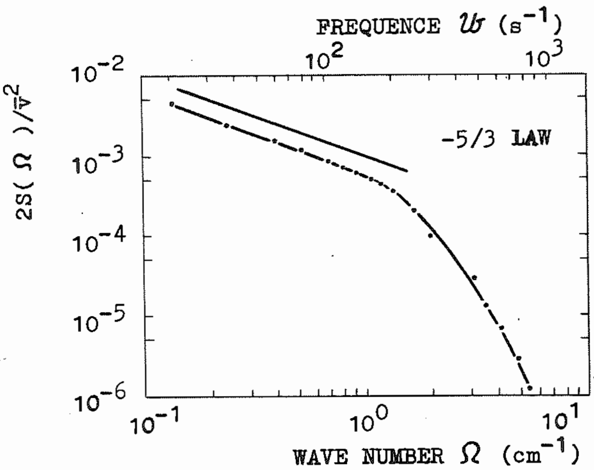

Fig.3 Spectrum of the longitudinal component of turbulent pulsation versus frequency (wave number).

frequency $\omega \approx 160$ Hz ($\Omega = 0.5$ cm^{-1}). So, all further measurements of $S(\Omega)$ were performed at a single frequency $\omega = 80$ Hz (where $\Omega = \omega/\bar{v}$ (1/cm) is the wave number; $S(\Omega) = 1/2\ \tilde{v}^2$ is the spectrum density of turbulent kinetic energy in a 1 Hz frequency band; $\tilde{v}$ (cm/s) is the turbulent pulsation rate at the wave number Ω; $\bar{v}$ (cm/s) is the mean air flow velocity in the detection zone). The value of ε is estimated from the relationship:

$$\varepsilon = [1/c^3\ S(\Omega)^3 \Omega^5]^{1/2}\ (cm^2 s^{-3}); \quad (2)$$

which has been obtained using "the law of -5/3". The constant c = 0.14, if Ω is measured in cm^{-1}.

Fig.4 shows the profiles of mean flow velocities at the level of the horizontal tunnel. Table 1 gives the mean flow velocity shears and other measured parameters. It can be seen that for regime 1 the mean shear does not exceed 2 s^{-1}. A honeycomb with a 45° shearing angle, introduced into the flow, increases the mean shear up to 8.8 s^{-1} (regime 3). Further $\bar{v}$ growing (regime 4) causes the shear to grow up to 10 s^{-1} (this shear is conditioned by a Poiseuille profile of the flow velocities in the tunnel).

The value of ε remains constant over the height of the tunnel under regime 4 (Fig.5) and $\varepsilon = 0$ under regime 1. Under regimes 2 and 3, in the central portion of the chamber $\varepsilon = 0$, while near the walls

Table 1 The apparatus operational regime. H is the vertical distance from the upper portion of the tunnel to the collecting plate; $t_i = L/\bar{v}$ is the time of drops-droplets interaction; L = 71 cm is the distance from the point of drops' injection into the tunnel to the center of the collecting plate; N_1 and N_2 are the mean number densities of drops and droplets, precipitated on 1 cm^2 of the collecting plate, respectively; h=5 cm for all regimes.

Regime No	Elements introduced into the flow	Flow state	$\bar{v}$ (cm/s)	Mean shear (1/s)	ε (cm^2/s^3)	t_i (s)	N (cm^{-3})	H (cm)	N_1 (cm^{-2})	N_2 (cm^{-2})
1	-	laminar	48	2	0	1.48	166.5	9 (5)	26	6.4
2	-	by-the-wall turbulence	97.6	3.8	0.15	0.73	60.2	5	10.5	5.8
3	honeycomb	laminar	79.2	8.8	0	0.90	56.2	5	15.4	5.8
4	grid	turbulent	133	10	1	0.53	29.4 (23.8)	5 (5)	11.6 (16.8)	1.9 (1.83)

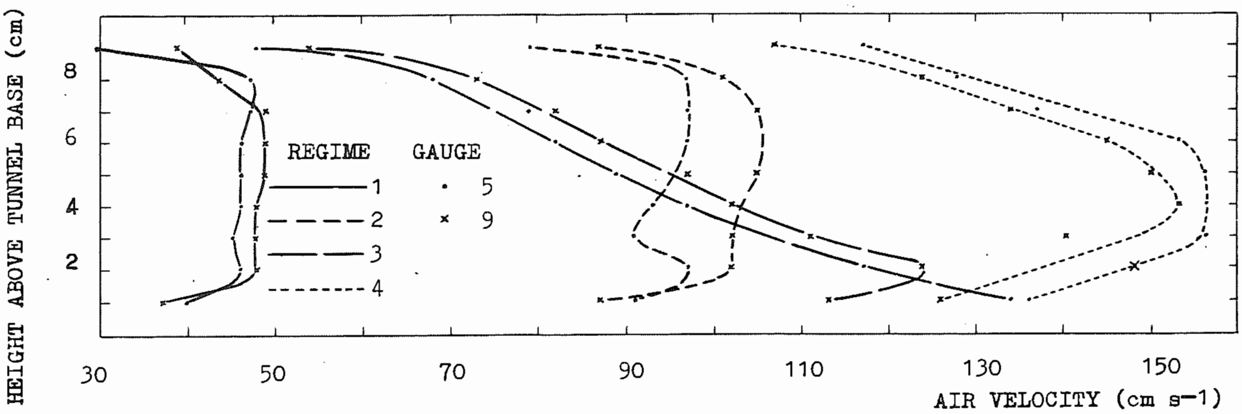

Fig.4 Profiles of the mean flow rate over the height of the horizontal tunnel.

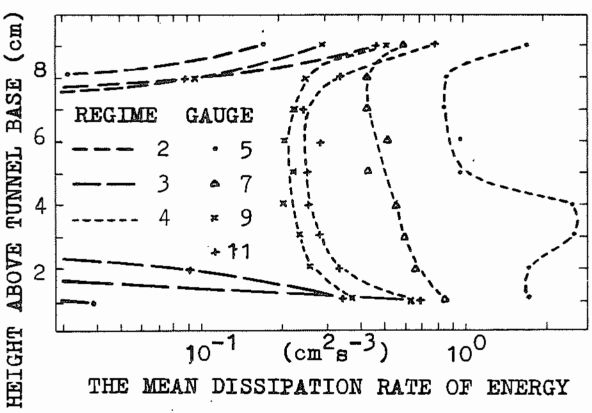

Fig.5 Profiles over the height of the horizontal tunnel. Regime 1, where ε = 0, is not shown.

turbulence develops (at the bottom under regime 3 and at top under regime 2).

The analysis of Table 1 and Figs. 4 and 5 shows that the chosen regimes of the apparatus operation allows of studying gravitational and turbulent-shear coagulations (regimes 1 and 4 respectively). A comparison of collection efficiencies obtained under regimes 3 and 4 will make it possible to isolate a pure turbulent pulsation effect. Likewise, a comparison of K values obtained for regimes 1 and 2 with those for regime 3 allows of the determination of a pure stationary shear effect.

4. RESULTS

The interacting drops radia r_1 and r_2, collection probabilities F, and other measured parameters are given in Table 2, which shows that K value for drops with r_1= 25-27.5 µm under each of the regimes and in all the series remains constant. This proves the reliability of the technique of determining K and the insensitivity of the collection efficiency of such drops to neither turbulent pulsations nor stationary shears. Moreover, K values for any r_1 under regime 1 and those for $r_1 \geqslant 21.5$µm under regime 3 agree well with collection

Table 2 Experimental collection efficiencies of glicerine drops (ρ =1.37 g/cm^3 for drops and ρ =1.26 g/cm^3 for droplets, where ρ is the density of the drops). Σn_c and Σn_t are the number of drops which have collected droplets and the total number of drops in the given experimental series, respectively. K^* is the collection efficiency evaluated for ρ =1 g/cm^3. K_s/K_g is the ratio of the shear coagulation collection efficiency to that of the gravitational one (Ref.5). The results for N,H and h in both series under regime 4 in Table 1 are given in brackets.

Regime No.	Series No.	r_1 µm	r_2 µm	Σn_c	Σn_t	$(F\pm\Delta F)\cdot 10^3$	$K \pm \Delta K$	K^*	K_s/K_g	K_t^*	K_t^*/K_g^*
1	1	18.0	9.2	62	33188	1.87±0.21	0.061±0.007	0.035	1		
	2	14.0	9.2	12	17670	0.68±0.2	0.050±0.015	0.029	1		
		16.5	10.6	24	14599	1.60±0.52	0.35 ±0.11	0.20	1	0.20	6
2	1	21.5	10.6	31	14282	2.2 ±0.52	0.20 ±0.05	0.12	1	0.12	1.8
		27.5	10.6	33	3607	9.8 ±3.1	0.40 ±0.13	0.23	1	0.23	1
		16.5	10.6	11	11134	0.94±0.5	0.18 ±0.1	0.10	3		
3	1	21.5	10.6	49	33697	1.43±0.2	0.11 ±0.015	0.064	1		
		27.5	10.6	40	3946	10.2 ±1.6	0.36 ±0.06	0.21	1		
		16.5	10.6	11	6884	1.58±0.14	0.98 ±0.09	0.57	3	0.19	5.8
	1	21.5	10.6	15	4671	3.2 ±0.2	0.84 ±0.05	0.49	1	0.49	7.6
		27.5	10.6	12	3135	3.5 ±0.2	0.41 ±0.02	0.24	1	0.24	1
4		16.5	9.2	17	21784	0.83±0.24	0.70 ±0.2	0.41	3	0.14	4.2
	2	21.5	9.2	31	2626	3.2 ±0.09	1.14 ±0.03	0.66	1	0.66	10.3
		27.5	9.2	12	3394	3.4 ±1.2	0.53 ±0.19	0.31	1	0.31	1.4
		14.0	9.2	38	19859	1.87±0.2	2.71 ±0.02	1.6	5.7	0.29	7.9
	3	19.5	9.2	20	8554	2.4 ±1.02	1.18 ±0.5	0.68	1.2	0.57	10
		25.0	9.2	3	1531	1.97±0.2	0.42 ±0.04	0.24	1	0.24	1

efficiency results for gravitational coagulation. The occurrence of even relatively weak by-the-wall turbulence (regime 2) entails K increase for drops with radia of 16.5 and 21.5 µm, while an 8.8 s^{-1} shear results in K increase for r_1 = 16.5 µm under regime 3. A combined turbulent-shear coagulation increases the collection efficiency of drops with $r_1 \leqslant 16.5$ µm several tens fold. The isolation of the pure turbulent pulsation effect*) under regime 4 shows that at the investigated ε value turbulent pulsations increase K, on average, 6 or 8 fold, if $r_1 \leqslant 21.5$ µm.

It should be noted that all our K values are slightly overestimated, since in the experiment $\rho > 1$ (see Table 2). To reduce K values to K* values use is made of the calculated K as function of Stokes's number (Ref.9). If in Stokes's number droplets density is increased 1.26 fold, then Stokes's number itself will increase 1.74 fold, hence, $K^* = 0.58 \cdot K$.

5. ERROR ESTIMATION

Finally, we shall consider the experimental errors and analyse the factors affecting the accuracy of determining K.

The main source of error in the determination of K is random errors in the estimation of the collection probability F. The empirical confidence intervals of the determination of F at a 0.68 confidence probability for each of the experimental series are given in Table 2. The root-mean-square error obtained from 10 measurements of N in each series does not exceed 6-8%. The determining error in estimating the drop size lies in the width of the interval r in the drops' discrete spectrum. At Δr=2 µm the maximum error grows from 6 to 12%.

A certain not easily estimated bias in the determination of F is present in series 1 and 2, regime 4, and under regimes 2 and 3, when a drop with r_1=16.5 µm collects a droplet from the large-size fraction of the droplets' spectrum (Fig.2), which results in a drop large enough to be registered when counted on the collecting plate as a drop of the second drop's size fraction (r_1=21.5 µm). This effect results in a certain underestimation of K for drops of the first size fraction and overestimation of K for those of the second fraction.

A possible source of error in the determination of F may be the background value of n_c which can, in principle, occure in a turbulent flow when the drops bounce away from the walls of the horizontal tunnel, polluted by fluorosceine sodium, and thus take on the colour of the collecting drops. An additional experiment under regime 4 with the droplets' generator switched off showed the absence of the background value of n_c.

A possibility of the coalescence of drops and droplets right on the collecting plate is prevented by selecting properly the time of the plate's exposure in the flow. The time and consequently the number densities N_1 and N_2 (1/cm^2) (see Table 1) are selected so as to make the collection probability on the plate negligible. Also, N_2 for regime 4 has always been several times smaller than for the rest of the regimes. Hence, K increase under regime 4 is not connected with this effect.

6. CONCLUSION

Thus, the experimental results show that small-scale turbulence which is always present in clouds, even when ε =1 cm^{2}s^{-3}, increases the collection efficiency of cloud drops with $r_1 \leqslant 21.5$ µm and $r_2/r_1 \geqslant 0.5$, almost by an order of magnitude in comparison with the case of a purely gravitational coagulation. In this connection it is necessary to revise fundamentally the modern notions of the atmospheric turbulence effect on the coagulational growth rate of cloud droplets.

A c k n o w l e d g m e n t. The authors wish to express their sincere gratitude to Prof. I.P.Mazin and Dr. V.I.Smirnov for valuable discussion of the results.

7. REFERENCES

1. Levin, L.M., and Sedunov, Iu.S., 1965, On turbulent-gravitational coagulation of cloud droplets. DAN USSR, 164, No.3, p.552-555.
2. Mazin, I.P., 1971, Theoretical evaluation of coagulation efficiency in clouds. Trudy Central. Aerolog. Obs., No.95, p.12-25.
3. Smirnov, V.I. 1969, Coagulation and condensational growth rate of aerosol particles. Trudy Central. Aerolog. Obs., No.92, p.3-106.
4. Almeida, F.C. de, 1975, On the effects of turbulent fluid motion in the collisional growth of aerosol particles. Rep. N 75-2. Grant G1-31287, University of Wisconsin, 186 pp.
5. Jonas, P.R. and Goldsmith, P., 1972, The collection efficiencies of small droplets falling through a sheared air flow. J. Fluid Mech., 52, Part 3, pp. 593-608.
6. Picknett, R.G., 1960, Collection efficiencies of water drops in air. Intern. J. Air Pollut., No. 1-3, pp. 160-167.
7. Neizvestny, A.I. and Kobzunenko, A.G. 1980, Experimental determination of the collection efficiency of water droplets of comparable sizes. Izv. Acad. Sci.USSR, Atmospheric and Oceanic Physics. 16, No.4, 1980, pp.389-396.
8. Neizvestny, A.I. and Kobzunenko, A.G. Experimental determination of coefficient of gravitational coagulation for water droplets in a wide range of sizes. ($10^{-3} \leqslant$ Re $\leqslant 10$). Proc. of the VIII-th Intern. Conference on Cloud Phys., Clermont-Ferrand, pp. 81 - 84.
9. Voloshcuk, V.M. and Sedunov, Iu.S., 1975, Coagulation process in dispersion systems. Leningrad, Gidrometeoizdat, p.172

*) For this purpose the experimental K values were divided by K_s/K_g, which has been obtained from the comparision of regimes 1 and 3 (r_1=16.5 and 21.5 µm) as well as from (Ref.5) for r_1=14, 18 and 25 µm.

ACCRETION OF CLOUD DROPS BY PRECIPITATION

Harry T. Ochs III and K. V. Beard

Illinois State Water Survey, P. O. Box 5050, Station A
Champaign, Illinois 61820 U.S.A.

1. INTRODUCTION

The evolution of warm-rain precipitation has been divided into two processes (Ref. 1). The first of these is autoconversion in which cloud water is transferred to precipitation water by the collection mechanism within the cloud water distribution. The second is accretion in which precipitation hydrometeors collect cloud water. A third warm rain process is self collection which is responsible for increasing the dispersion of the precipitation water distribution (Ref. 2). Of these three processes the second, accretion, is the most efficient for increasing the precipitation water content. Thus a knowledge of collection efficiencies for small precipitation drops collecting cloud drops is essential for understanding warm-rain precipitation development.

There are almost no experimental data for accretion in the critical size ranges covered in this paper. Early experiments (Refs. 3-4) for very small cloud droplets (about 5 μm mean radius) collected by 70 to 300 μm radius drops have been improved by Ref. 5. Good agreement was found by Ref. 5 with theoretical collision efficiencies in Refs. 6-8. The accretion of 20 to 24 μm radius cloud droplets by 95 to 114 μm radius collector drops have been studied (Ref. 9) and collection efficiencies between 0.11 and 0.23 were measured. Refs. 10-11 concluded that the efficiencies in Ref. 9 were anomalously low and resulted from spurious experimental errors. Thus adequate measurements of collection efficiency are unavailable for cloud drops greater than 10 μm radius. The modeling results (e.g., Ref. 2) suggest that the mean size of the cloud droplet distribution must be at least 10 μm before significant collection can occur. In the study presented in this paper, collection efficiencies were measured in the important size regime for accretion of cloud droplets between 10 and 20 μm radius by small precipitation drops of 100 to 400 μm radius.

2. EXPERIMENTAL DESIGN AND PROCEDURE

The collection efficiency was determined experimentally by measuring the amount of tracer captured by a stream of widely spaced drops falling at terminal velocity through a monodisperse cloud of chemically tagged droplets (see Fig. 1). The method was an extension of the experiment reported in Refs. 12-13. The cloud was produced by a vibrating orifice device (TSI Model 3050), whereby a liquid jet was disrupted into a stream of uniform size droplets. Both the dilution and dispersion air streams were saturated slightly above room temperature to prevent evaporation and provided saturation in the cloud chamber. The tracer solution of lithium sulfate (0.1% Li^+) was fed to the cloud droplet generator from a reservoir under pressure. An electrically neutral cloud was achieved with an ion discharge device (TSI Model 3054). The cloud was continuously generated during the experiment and flowed at 11 liters min^{-1} through the cloud chamber (1.3 m long by 10.6 cm in diameter).

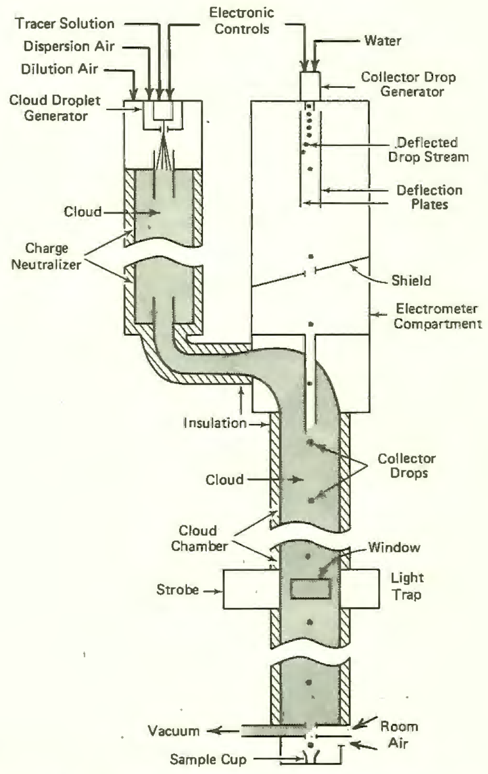

Figure 1. Diagram of experimental apparatus.

Sampling ports were located in the chamber to permit the insertion of slides coated with dye and gelatin mixture for an evaluation of the droplet sizes. The stain produced by the droplets was calibrated with an accuracy of ±0.5 μm by using the direct output of the droplet generator. For typical experiments droplets in the chamber were found to be of one size (dispersion of 0.1 μm) except for an occasional doublet (< 2%). The droplet concentration was measured from strobe photographs with illumination arranged in a vertical plane of well-defined thickness by two cylindrical lenses and two slits. A typical concentration for 11 μm cloud droplets was about 100 cm^{-3}, and about 6 cm^{-3} for 17 μm droplets.

An orifice device was also used to produce the collector drops (Ref. 14). Drops with a wide vertical spacing (several centimeters) were separated from the main stream using a charging electrode and high voltage deflection plates. The drops reached terminal velocity within the electrometer compartment before entering the top of the cloud chamber.

During an experiment the drops were collected beneath the cloud chamber in a polypropylene jar.

After chemical analysis the collection efficiency was determined from experimental parameters using the equation

$$\bar{E} = M[\pi(R + r)^2 \Delta V n m X t N]^{-1}. \qquad (1)$$

The number of collector drops (N) was calculated from the drop generation rate and the experimental time. The mass of lithium from each experiment (M) was determined by atomic absorption analysis. The collector drop radius (R) and cloud droplet radius (r) was used to obtain the relative terminal velocity (ΔV) from the equations in Ref. 17. The cloud droplet concentration (n) was determined photographically by the method discussed above. The initial droplet mass (m) was determined from the rate and generation frequency whereas the mass fraction of lithium (X) was the initial concentration of the tracer in the cloud water solution. The interaction time (t) was determined from the fall speed of the collector drop, the downward air velocity in the cloud chamber and the cloud chamber height. A more complete description of this equation can be found in Beard and Ochs (1983).

3. ERROR ANALYSIS

Chemists trained in microanalysis performed the atomic absorption measurements necessary to determine the amount of Li^+ in each sample. The total error from chemical contamination and analysis was found to be less than 3%.

Spurious electrical forces could have altered either the collision or coalescence efficiencies. Therefore the charge on the small cloud droplets was minimized by a charge neutralizer (Fig. 1) designed to achieve a Boltzmann charge distribution. We have computed that the mean magnitude of charge on a cloud droplet was $< 2 \times 10^{-18}$ C. The charge on the collector drop was also minimized. The measured magnitude was $< 3 \times 10^{-16}$ C for the smaller collector drops and $< 5 \times 10^{-15}$ C for the largest. Previously reported effects on coalescence suggests that magnitudes of $> 10^{-14}$ C on oppositely charged drops are necessary to affect coalescence (e.g., Refs. 16-17). The force from opposite charges of this size is orders of magnitude larger than the electrical forces in our experiment. A brass experimental chamber was used to minimize electric fields. Since the charges and fields were too small to affect the collision efficiencies for our drop sizes (Ref. 18), we conclude that our measured collection efficiencies (collision and coalescence) were unaffected by electric forces.

4. RESULTS

Table 1 shows values of R, r, p, and $\bar{E}$ for six drop size pairs derived from 38 experiments. The stated measurement uncertainty was based on the sum of the 90% confidence intervals estimated for the mean cloud droplet concentration from counting 2000 to 13,000 drops for each group of experiments and the mean tracer mass collected per collector drop in a sequence of 4 to 8 experiments. There is an additional uncertainty (not included in the table) of about 5% from the rms combination of measurement and calibration errors. The reported collector drop size is known to ±0.1% and the cloud droplet size to ±0.5 μm. The measured collection efficiency was used with the collision efficiency from Ref. 19 to obtain the coalescence efficiency ($\varepsilon = \bar{E}/E$).

Fig. 2 shows the measured collection efficiencies and curves based on the collision efficiencies from Ref. 19. The data show a trend of decreasing efficiency with increasing cloud droplet size which is consistent with the finding of Ref. 13. The measured efficiencies also decrease with increasing collector drop size. It is clear that the measured collection efficiencies are significantly below the computed values. Table 1 shows that for the 326 μm collector drop and the 17 μm cloud droplet, the measured collection efficiency is only 54% of the computed collision efficiency (i.e., ε = 54%). The estimated uncertainty of about ±10% in both the measured and computed efficiencies is not large enough to account for this difference.

Fig. 2 also shows the mean collection efficiencies from the measurements of Ref. 5 for collector drops in the size range of the present

Table 1. Experimental Results

Drop Radius (μm) R	r	Radius Ratio p	Efficiency (%) Measured Collection $\bar{E}$	Computed Collision E	Inferred Coalescence ε
113	11	0.097	70 ± 4	85	82 ± 4
139	17	0.123	65 ± 3	94	70 ± 3
213	11	0.053	68 ± 2	89	77 ± 2
217	17	0.078	61 ± 6	94	65 ± 6
326	17	0.052	51 ± 3	94	54 ± 3
371	11	0.030	63 ± 2	90	70 ± 2

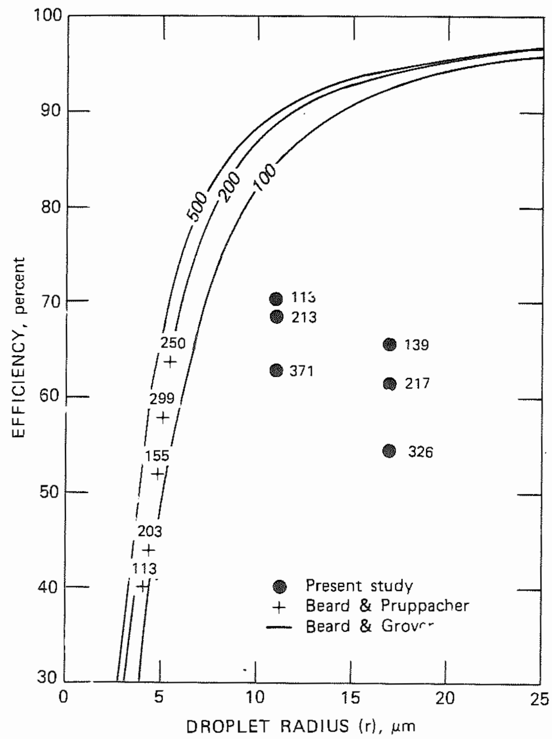

Figure 2. Measured collection efficiencies and computed collision efficiencies as a function of droplet radius. Numerical values are the collector drop radii in microns.

study. They concluded that their data agreed with theoretical collision efficiencies since the error bars overlap the computed collision efficiencies. However, the mean collection efficiencies for R > 113 m are from 4 to 19% below theoretical values.

In Fig. 3 the empirical coalescence efficiencies are presented. The present data show a decreasing coalescence efficiency with increasing cloud droplet size. Thus the higher coalescence efficiencies for 4 to 5 μm cloud droplets calculated from the data in Ref. 5 are consistent with this trend. In addition the coalescence efficiencies also decrease with increasing collector drop size. The dashed curves in Fig. 3 are contours of constant coalescence efficiency interpolated from the present data. Fig. 3 also shows the semi-empirical coalescence efficiencies from Refs. 20-21. Both formulations were developed from data taken outside the size ranges used in the present study and apparently cannot be extrapolated to the sizes shown in Fig. 3.

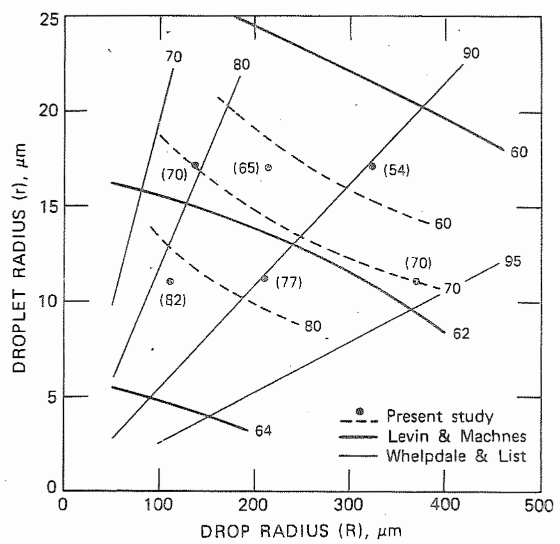

Figure 3. Coalescence efficiencies from present data using theoretical collision efficiencies. Also shown are empirical curves from coalesence studies. Data and curves are labeled with coalescence efficiencies in percent.

5. DISCUSSION

There are two distinct yet related physical mechanisms that can prevent coalescence for colliding drops (Ref. 13). Both depend on drop deformation and the resulting entrapped air to reduce the closure velocity. Bouncing occurs by the <u>rebound mechanism</u> if the restoring force of surface tension causes the drops to spring apart before the air film can drain. In contrast, bouncing occurs by the <u>grazing bounce mechanism</u> if the tangential velocity of the droplet carries it past the collector drop before the air film drains. Of course, in actual drop interactions bouncing could occur as a result of some combination of these mechanisms.

Photographs of bouncing drops can help to distinguish between the rebound and grazing bounce mechanisms. Fig. 3b in Ref. 21 shows a drop interaction where the small drop leaves the surface of the stationary large drop with a nearly tangential trajectory, an indication that bounce was due to the grazing bounce mechanism. A clear indication of the more elastic rebound mechanism is found in Ref. 20. There is also evidence to suggest that grazing bounce is primarily responsible for our coalescence efficiencies. In experiments with supported drops (Refs. 20-21) and with two drop streams (Ref. 17) bouncing was found to be a function of closure velocity and impact angle. Extrapolation to our sizes suggests that coalescence should always be expected for direct collisions. These studies also suggest that the likelihood of bouncing increases with impact angle. A geometric interpretation of our measured collection efficiencies results in critical impact angles of > 45° (i.e., for ε > 50%). In actuality the critical impact angle is increased and the droplet trajectory becomes more tangential because of hydrodynamic deflection. Thus we believe that the grazing bounce mechanism is primarily responsible for our results. The collector drop with its lower curvature pressure apparently indents, entraps additional air and allows the closure velocity to vanish so that the tangential velocity can carry the droplet past the collector drop.

Both the rebound and grazing bounce mechanisms depend on drop deformation to entrap air and retard contact. The Weber number is the relevant parameter governing the deformation of equal size drops colliding along their line of centers (Ref. 22). It is proportional to the ratio of an inertial force to a surface tension force and can be defined as

$$We = \rho \hbar U^2/\sigma \qquad (2)$$

where ρ is the density of water, $\hbar$ is a characteristic curvature radius for the deformation, U is the an impact speed and σ is the surface tension. For unequal size drops there is a Weber number that characterizes each drop deformation. However, in our study we assumed that the cloud droplet was rigid and the curvature of the deformation in the collector drop was characterized by the radius of the cloud droplet. Since the impact speed for small size ratios scales with the collector drop velocity (V), the Weber number for our drop interactions is

$$We = \rho r V^2/\sigma. \qquad (3)$$

When the Weber number is small, then the collector drop does not deform and the collection efficiency is equivalent to the hydrodynamic collision efficiency. Thus as the cloud droplet or collector drop becomes smaller (r or V smaller) the coalescence efficiency should approach 100%. Conversely the coalescence efficiency is reduced by grazing bounce as the Weber number increases in both the increasing drop and droplet size directions. The tendencies in our data (see Fig. 3.) are consistent with Weber number projections.

It is interesting to compare our inference of grazing bounce to the phenomena investigated by Whelpdale and List (1971). They noted a "low velocity bounce" at the lowest impact speeds (We of 0.1 to 1.7) and high angles of incidence (i.e., the most grazing interactions). At somewhat higher impact speeds they found that the droplet bounced "after deformation of the drop" (We of 1.7 to 3.5). They also found partial coalescence at still higher impact speeds (We of 3.5 to 7.7). The Weber numbers for our sizes ranged between 0.1 and 1.6. Thus the interactions that we have studied are well below the impact regime for partial coalescence and within the range for low velocity bounce.

6. CONCLUSIONS

Collection efficiencies for accretion were measured for six drop pairs. Cloud droplets from 11 to 17 μm radius and collector drops between 100 and 400 μm radius were used. The resulting efficiencies were in the 56-72% range and all values were significantly below computed collision efficiencies. Coalescence efficiencies between 54 and 82% were found to decrease with increasing drop and droplet size. Poor agreement was found between our results and extrapolated values using the semi-empirical formulations in Refs. 20-21.

The mechanism of grazing bounce (Ref. 13) has been reasserted as the physical explanation for our coalescence efficiencies. The capture of cloud droplets by larger collector drops is important to the initiation of warm-rain precipitation and is the most important mechanism for transferring liquid water content from the cloud droplet to the precipitation distribution (Refs. 1, 23-24). Thus our findings of significantly reduced collection efficiencies should encourage the inclusion of coalescence effects in modeling studies of warm rain processes.

Acknowledgments. The authors appreciate several helpful suggestions by Roland List and the careful chemical analysis performed by Loretta Skowron. This material is based upon work supported by the Atmospheric Research Section of the National Science Foundation under Grant ATM 8121390 and ATM 8314072.

7. REFERENCES

1. Kessler, E., 1969, On the Distribution and Continuity of Water Substance in Atmospheric Circulation, Meteor. Monogr., No. 32, Amer. Meteor. Soc., 84 pp.

2. Berry, E. X, and R. L. Reinhardt, 1974, An analysis of cloud drop growth by collection: Part I-IV, J. Atmos. Sci., 31, 1814-1831, 2118-2135.

3. Kinzer, G. D., and W. E. Cobb, 1956, Laboratory measurements of the growth and collection efficiency of rain drops, J. Meteor., 13, 295-301.

4. Kinzer, G. D., and W. E. Cobb, 1958, Laboratory measurements and analysis of the growth and collection efficiency of cloud droplets, J. Meteor., 15, 138-148.

5. Beard, K. V., and H. R. Pruppacher, 1971, A wind tunnel investigation of collection kernels for small water drops in the air, Quart. J. Roy. Meteor. Soc., 97, 242-248.

6. Davis, M. H., 1965, The effect of charges and fields on the collision of very small cloud drops, Proc. Int. Conf. Cloud Physics, Tokyo, 118-120.

7. Klett, J. D., 1968, The interaction and motion of rigid spheres falling in a viscous fluid at low Reynolds numbers, Ph. D. thesis, University of California, 113 pp.

8. Shafrir, U., and M. Neiburger, 1963, Collision efficiencies of two spheres in a viscous medium, J. Geophys. Res., 68, 4141-4147.

9. Neiburger, M., Z. Levin, and L. Rodriguez, Jr., 1972, Experimental determination of the collection efficiency of cloud drops, J. Rech. Atmos., 6, 391-397.

10. Abbott, C. E., 1977, A survey of waterdrop interaction experiments, Rev. Geophys. Space Phys., 15, 363-374.

11. Pruppacher, H. R., and J. D. Klett, 1978, Microphysics of Clouds and Precipitation, Reidel, 714 pp.

12. Beard, K. V., H. T. Ochs, and T. S. Tung, 1979, A measurement of the efficiency for collection between cloud drops, J. Atmos. Sci., 36, 2479-2483.

13. Beard, K. V., and H. T. Ochs, 1983, Measured collection efficiencies for cloud drops, J. Atmos. Sci., 40, 146-153.

14. Adam, J. R., R. Cataneo and R. G. Semonin, 1971, The production of equal and unequal size droplet pairs, Rev. Sci. Instrum., 42, 1847-1849.

15. Beard, K. V., 1976, Terminal velocity and shape of cloud and precipitation drops aloft, J. Atmos. Sci., 33, 851-864.

16. Sartor, J. D., and C. E. Abbott, 1972, Some details of coalescence and charge transfer between freely falling drops in different electrical environments, J. Rech. Atmos., 6, 479-493.

17. Park, R. W., 1970, Behavior of water drops colliding in humid nitrogen, Ph. D. thesis, University of Wisconsin, 577 pp.

18. Schlamp, R. J., S. N. Grover and H. R. Pruppacher, 1976, A numerical investigation of the effects of electric charge and vertical external electric fields on the collision efficiency of cloud drops, J. Atmos. Sci., 33, 1747-1755.

19. Beard, K. V., and S. N. Grover, 1974, Numerical collision efficiencies for small raindrops colliding with micron size particles, J. Atmos. Sci., 31, 543-550.

20. Levin, Z., and B. Machnes, 1977, Experimental evaluation of the coalesence efficiency of colliding water drops. Pure Appl. Geophys., 115, 845-867.

21. Whelpdale, D. M., and R. List, 1971, The coalescence process in raindrop growth, J. Geophys. Res., 76, 2836-2856.

22. Foote, G. B., 1975, The water drop rebound problem: Dynamics of collision, J. Atmos. Sci., 32, 390-402.

23. Ochs, H. T., and R. G. Semonin, 1979, Sensitivity of a cloud microphysical model to an urban environment, J. Appl. Meteor., 18, 1118-1129.

24. Johnson, D. B., 1982, The role of giant and ultragiant aerosol particles in warm rain initiation, J. Atmos. Sci., 39, 448-460.

COLLECTION EFFICIENCIES FOR SMALL PRECIPITATION DROPS

Harry T. Ochs III, K. V. Beard and Robert Czys

Illinois State Water Survey
Champaign, Illinois 61820 U.S.A.

1. INTRODUCTION

Numerical computations of the collection efficiencies for small precipitation drops (100 through 400 μm radius) have been presented in Refs. 1-2. In these computations the drops are assumed to be rigid spheres and the method of superposition obtained from solutions of the Navier Stokes equation for single spheres was employed. There is very little experimental evidence available in the literature to evaluate the accuracy of these results. A comparison of results for a 75 μm collector drop with data from Refs. 3-5 show reasonable agreement for the radius ratio, p, between about 0.55 and 0.8 (Ref. 2). No comparisons are given for larger collector drops.

Collections between drops in the size range of 100 to 400 μm may be important in the evolution of precipitation by warm rain microphysical processes. The rate of growth of the drop having the size corresponding to the mean of the mass density distribution (the "predominant" size), after this size exceeds 50 μm radius, is formulated in Ref. 6. The growth of the drop with the predominant mass results from continuous collection of the cloud water distribution by the precipitation drops and stochastic collection within the precipitation distribution. In addition, the self-collection process (precipitation drops collecting other precipitation drops) is essentially responsible for the spreading of the precipitation distribution. The rate at which this spreading proceeds is proportional to the precipitation liquid water content which is in turn governed by accretion of cloud water. The rate coefficient for stochastic collection was related to the kernel for the capture of the predominant sized drops by drops 1.5 times larger (i.e. p = 0.67) (Ref. 6). Thus collections between small precipitation drops at intermediate values of p may be important in the evolution of precipitation.

An important factor that cannot be treated by the superposition method of computing collision efficiencies is the coalescence efficiency which is typically assumed to be equal to unity for drops of 100 to 400 μm radius. Experimental studies of drop coalescence have been carried out at various impact speeds (Refs. 7-8). Partial coalescence or drop bounce (without coalescence) was not indicated in Ref. 7 as long as both drops are smaller than 300 μm. A large probability of partial coalescence and also bounce for a 225 μm radius drop collecting a 75 μm drop at a relative impact speed similar to the difference in terminal velocities was found in Ref. 8. The inconsistency between these findings may result from differences in the angle between the drop trajectories and drop speeds (i.e., differences in the vector drop velocities). In addition, there is evidence in Ref. 7 of pronounced oscillations before collision. These experiments may not adequately simulate the situation in clouds where drops are initially at terminal velocity and collide under the influence of aerodynamic forces appropriate to their environment. The theoretical superposition method is also subject to uncertainty in the aerodynamic forces. It is therefore important to carry out experiments that incorporate a more complete modeling of collision and coalescence in clouds.

The purpose of this paper is to present results from an experiment that has been designed to measure the collection efficiency of small precipitation drops. The drops studied (100 to 400 μm radius and $p > 0.65$) interacted under free fall conditions at terminal velocity.

2. EXPERIMENTAL APPARATUS

The fundamental principal by which uniform droplets are produced by perturbing a liquid jet was developed by Ref. 9. A method for producing pairs of unequal sized drops from a single jet was demonstrated in Ref. 10. A sinusoidal voltage was applied to a piezoeolectric transducer which induced capillary waves on the jet resulting in uniform droplet production. The excitation frequency was periodically switched between two values to produce a group of drops of one size followed by a group of a second size. The drops could be charged and deflected between high voltage electrodes. Pulses of controlled width and voltage were used to isolate a drop with negligible charge from each group. Fig. 1 shows a photograph of an uncharged drop pair

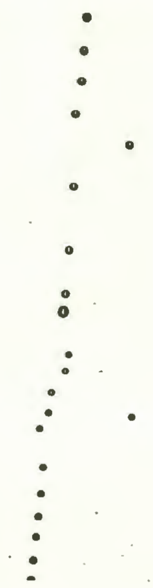

Figure 1. Photograph of drop stream between deflection electrodes showing uncharged drop pair.

and the main drop stream being deflected between the high voltage electrodes. In practice the uncharged drops in each pair were generated at a much larger separation to allow them to achieve terminal velocity.

Several design changes and improvements have been made to the system in Ref. 10. First TTL digital logic has been adopted for the majority of the electronic controls. By using a 10 MHz crystal controlled oscillator good long term frequency stability was achieved. Digital counters divided the oscillator frequency thus producing square waves of controllable frequency that were amplified and applied to the piezoelectric transducer. Satellite drops were almost never formed in the stable range of drop generation frequencies. This may have resulted from sharper edges on the perturbations imposed on the liquid jet. The size ratio of the drop pair produced by this generator was extendable using a lower harmonic to form a larger drop outside of the normal operating range of this type of generator. A disadvantage of this generator was that both drops were produced at the same speed (i.e. the jet speed). Thus a practical lower limit of $p = 0.65$ resulted from the criteria that both drops be at terminal velocity when they interacted.

The deionized water for the drop generator was supplied by a large pressurized reservoir (Fig. 2) consisting of two 55 gallon drums. The vibration absorbing platform minimized the transmission of building vibrations to the drop generator and liquid jet.

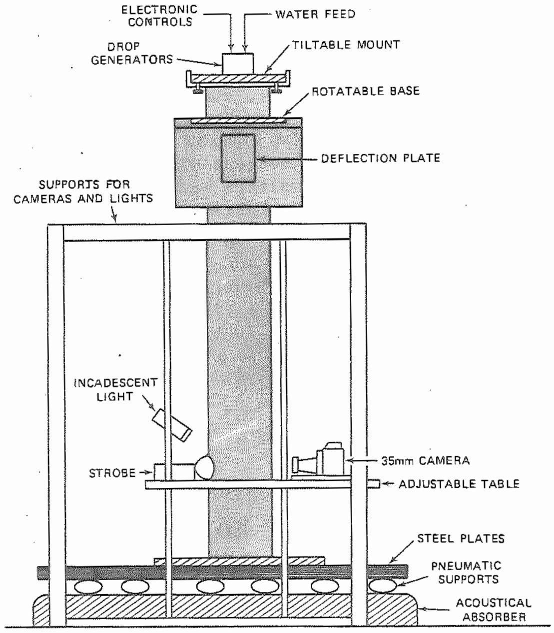

Figure 2. Experimental apparatus

At the beginning of each experiment the uncharged jet was directed vertically. After the deflection field was applied the uncharged drop pairs were adjusted to fall vertically. The drop charges were minimized by this method and were $< 3 \times 10^{-16}$ C for the smaller drops to $< 5 \times 10^{-15}$ C for the largest. Previously reported effects on coalescence suggests that magnitudes of $> 10^{-14}$ C on oppositely charged drops are necessary to affect coalescence (e.g., Refs. 8,11).

The uncharged drop pairs fell vertically between the high voltage electrodes and through a 1 m plexiglas column with a 10 cm by 10 cm cross section (Fig. 2). The experimental chamber was located on a vibration absorbing platform to reduce the affects of building vibrations on drop generation. The electronic controls, camera, and lighting systems were attached to a large metal frame that was set on the floor so that vibrations that these devices caused would not be transmitted to the drop generator.

3. RESULTS

Streak and strobe photographs of the type shown in Fig. 3 were used to obtain the data necessary to deduce the collection efficiency. The streaks were created by an incandescent lamp located about 45° above the camera axis and on the opposite side of the chamber (see Fig. 2) and were taken at the point where the large drop overtook the smaller one. The streak photographs were used to determine the type of interaction (miss, bounce, or collection) and the initial horizontal separation. The first photograph in Fig. 3 shows the signature of a coalescence whereas the second shows a drop bounce. The bounce in Fig. 3 is caused by an entrapped air film resulting from a deformation in the colliding drops, and the wavering in the diverging streaks after bounce is evidence of drop oscillation resulting from the distortion of the drop surfaces during collision. A free running strobe positioned about 45° to one side of the optical axis created successive exposures on the film. The fall speed of each drop was computed from the displacement and frequency.

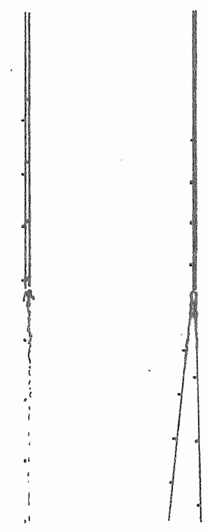

Figure 3. Streak and strobe of coalescing and bouncing drop interactions.

The results of this study are presented in Table 1. Both the measured collection efficiency (accuracy of ±10%) and the theoretical collision efficiencies (Ref. 1) are shown for each drop pair studied. The measured collection efficiencies are consistently and significantly below the theoretical values. Additional data is being obtained for larger collector drops.

Table 1. Measured collection efficiencies

Drop Radius (μm) R	r	Radius Ratio p	Efficiencies (%) Measured Collection E	Computed Collision E
128	111	0.87	0.90	1.04
249	204	0.82	1.00	1.06
270	249	0.92	0.86	1.02
271	202	0.75	0.60	1.00
277	187	0.68	0.31	1.00

Acknowledgments. This research was supported by the Atmospheric Sciences Program of the National Science Foundation under grant NSFATM 8314072.

4. REFERENCES

1. Shafrir, U., and T. Gal-Chen, 1971, A numerical study of collision efficiencies and coalescence parameters for droplet pairs with radii up to 300 microns, J. Atmos. Sci., 28,741-751.

2. Lin, C. L., and S. L. Lee, 1975, Collision efficiencies of water drops in the atmosphere, J. Atmos. Sci., 32, 1412-1418.

3. Telford, J. W., N. W. Thorndike, and E. G. Bowen, 1955, The coalescence between small water drops, Quart. J. Roy. Meteor. Soc., 81, 241-250.

4. Woods, J. D., 1965, The collision and coalescence of water droplets, Ph.D. thesis, University of London.

5. Beard, K. V., and H. R. Pruppacher, 1968, An experimental test of theoretically calculated collision efficiencies of cloud drops, J. Geophys. Res., 73, 6407-6414.

6. Berry, E. X., and R. L. Reinhardt, 1974, An analysis of cloud drop growth by collection: Part III-IV, J. Atmos. Sci., 31, 2118-2135.

7. Brazier-Smith, P. R., S. G. Jennings, and J. Latham, 1972, The interaction of falling water drops: coalescence, Proc. R. Soc. Lond., A, 326, 393-408.

8. Park, R. W., 1970, Behavoir of water drops colliding in humid nitrogen, Ph.D. thesis, Dept. of Chemical Engineering, University of Wisconsin.

9. Rayleigh, Lord, 1878, On the instability of jets, Proc. Lond. Math. Soc., 10, 4-13.

10. Adam, J. R., R. Cataneo, and R. G. Semonin, 1971, The production of equal and unequal size droplet pairs, Rev. Sci. Instr., 42, 1847-1849.

11. Sartor, J. D., and C. E. Abbott, 1972, Some details of coalescence and charge transfer between freely falling drops in different electrical environments, J. Rech. Atmos., 6, 479-493.

A STUDY OF SOME CHARACTERISTICS OF A WARM CONVECTIVE CLOUD BY REGULAR TRADEWINDS IN A SUBTROPICAL MARITIME AREA WITH A ONE-DIMENSIONAL MODEL AND IN SITU MEASUREMENTS.

C. PONTIKIS[+], A. RIGAUD[+], C. ASSELIN de BEAUVILLE[++], M.C. MARCEL[+++]

+ French Meteorological Office, EERM, Magny les Hameaux
++ University of Antilles, Guedeloupe
+++ French Meteorological Office, MN, Guadeloupe

Studies of the physical processes in warm convective subtropical clouds are helpful in the understanding of more complicated cloud systems (Ref. 6-10).
In view of a detailed study of this convection type, daily meteorological observations made in Guadeloupe are used to associate the precipitation measurements on the ground with the dynamic and microphysic properties of the theoretical cloud obtained by using a 1 D model.
Unlike classical models of this type initiating convection by introducing either a small temperature perturbation from the ground up to the cloud basis, or a non-zero advection velocity, this model starts convection by using a small temperature excess between 0 and 200 meters (Refs 4-9-11).
The equations are classical (Refs 3-4) :

(1) Vertical velocity U(Z,t)

$$\frac{\partial U}{\partial t} = -U\frac{\partial U}{\partial z} + g\left(\frac{T_V - T_{VE}}{T_{VE}} - w_L\right) - \mu U^2$$

(2) Temperature T(Z,t)

$$\frac{\partial T}{\partial t} = -U\left(\frac{g}{C_p} + \frac{\partial T}{\partial z}\right) - \frac{L}{C_p}\cdot\frac{\partial w_V}{\partial t} - (w_V - w_{VE})\frac{\mu U L}{C_p} - \mu U(T - T_E)$$

(3) Entrainment coefficient

$$\mu = \frac{1}{m_a}\cdot\frac{dm_a}{dz} = A.z$$

where A is a constant
(4) The complete microphysics treatment used the droplet radii distribution F(Z,t) defined according to the classical cinetic growth equation :

$$\frac{\partial F}{\partial t} = Q_P - Q_D$$

Q_P and Q_D terms contain the collision-coalescence and break-up processes.

The flat part of the island of Guadeloupe is convenient for that kind of experiment (Grande Terre). Routine measurements are made between 8 am and 3 pm (local time): daily radiosoundings, precipitation measurements (11 points in the North), estimated cloud top heights.
During 2 weeks in February 1981, combined flying telepiloted saucer S.A.M. (P;T;U) and photogrammetric measurements were associated to the routine ones. These observations allow the check of some general properties of the sub-tropical boundary layer, limited by the trade inversion.
These properties can be summarized as follows :

-- There is a well-mixed subcloud layer, even over land. Its upper limit, between 500 and 1,000 meters, often coincides with the beginning of the conditional convective instability. So thermals have to reach this altitude to give a cumulus cloud (Refs 5,8). In fact, convection only starts if air masses near the ground are heated enough to go beyond this level.

For example, the temperature and mixing ratio behavior in this layer for February 17 are given in figures 1 and 2, as obtained by S.A.M. measurements.

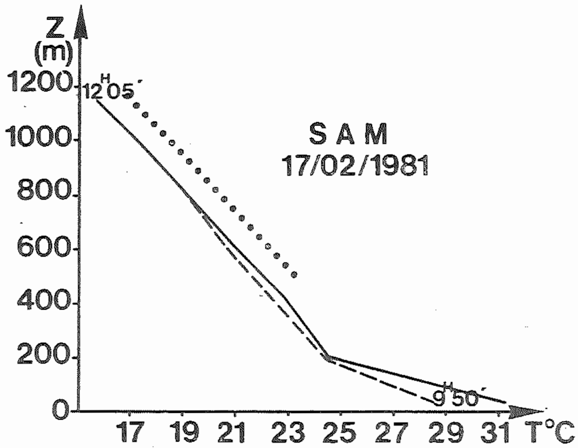

FIG.1 : S. A. M. SOUNDING

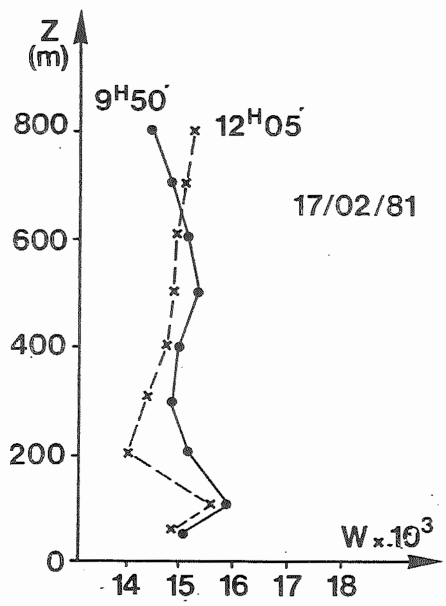

FIG.2 : WATER CONTENT (g/kg)

The temperature decreases adiabatically with height and the mixing ratios are approximately constant. From these results, it seems reasonable to conclude that the layer heated to give thermals is situated between 0 and 200 meters.

-- The mean features of the convective cloud formation layer are :
  + the conditional instability described in Refs 1 and 5,
  + the sporadic existence of a shear in the trade-wind velocity and direction (limiting the cloud top height at about 1,400 m).

The above conclusions obtained after analysis of the routine daily measurements in relation with the model (Ref 7) lead to two discrete values of the entrainment constant A :

$$1.5\ 10^{-10} \text{ and } .45\ 10^{-10} \quad cm^{-2}.$$

Five days are chosen from the period of February 1981. The calculated cloud basis and top heights and top advection velocity agree fairly well with the observed ones. Table 1 summarizes the analysis results obtained by using three different versions of the 1 D model (non-precipitating a, parametrized microphysics b /Ref 2/, and complete microphysics c versions. The last one is described in this paper). The precipitation values on the ground are first classified following the goemetrical cloud characteristics (cloud top and basis heights, cloud diameters) for the period between January 1981 and January 1983.
For approximately equal maximum diameters and cloud depths, 2 different classes of observed cloud top and basis heights are obtained (Table 2).

TABLE 2

	Mean Basis Height	Mean Top Height	Diameter (m)	Depth (m)
Class 1	800 m	1,600 m	700-900	800-1100
Class 2	1000 m	2,100 m		

A second classification is drawn according to the maximum liquid water content and the maximum updraught velocity (for approximately equal mean cloud droplet numbers and diameters) for the theoretical cloud produced by the 1 D model in connection with daily radiosounding data.
For a nearly constant maximum liquid water content ($w_L \sim 2$ g/kg air), 3 cloud classes are obtained, leading respectively to .5, 1.1 and 4.1 mm of mean precipitation on the ground. Their mean characteristics are represented on the figure 3.

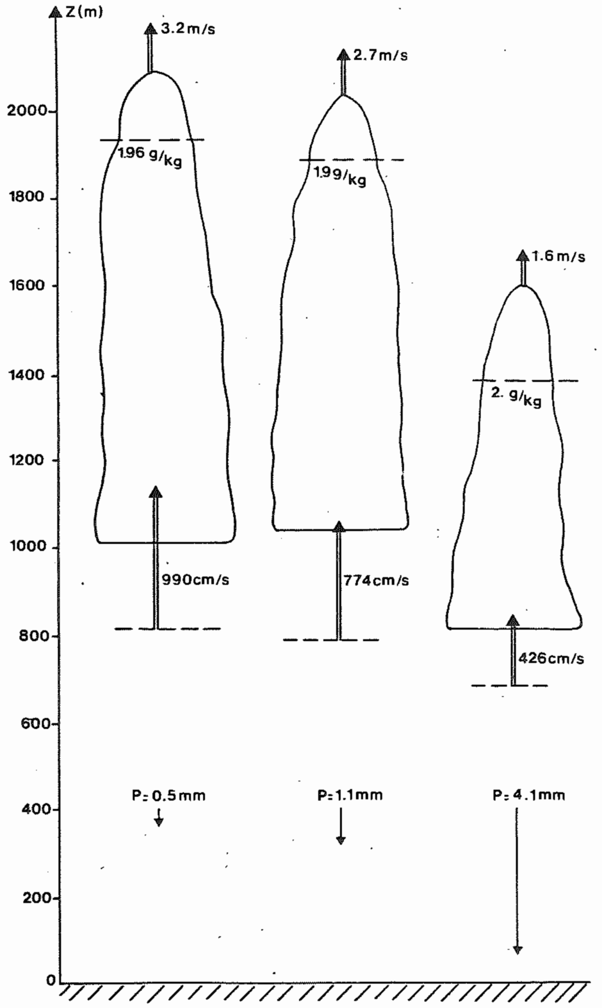

FIG. 3 : CLOUD CLASSES WITH $W_L \sim 2$ g/kg

The top advection and maximum updraught velocities are strongly linked to the précipitation on the ground. Generally, the maximum updraught velocity is located near the cloud basis, below the level of the maximum liquid water content. So droplets have to grow large enough to overcome the barrier of the maximum updraught velocity.
There is also a coupling between the subcloud layer properties and precipitation on the ground : In fact, a well-mixed subcloud layer is observed for almost all cases of high precipitation ($>$ 3mm) while stra-

TABLE 1

Date	Cloud Basis/Top Height (m)				Top Advection Velocity (m/s)			
	Obs.	1 Da	1 Db	1 Dc	Obs.	1 Da	1 Db	1 Dc
17/2/81	750/1600	800/1800	800/1800	800/1800	1.5 - 3.	2.	2.	2.1
19/2/81	700/2000	800/2200	800/2200	800/2200		3.3	3.2	3.3
20/2/81	800/1700	800/1600	800/1600	800/1800		2.	2.	2.1
21/2/81	700/1600	800/1600	800/1600	800/1600	1.6	2.	1.9	2.
26/2/81	800/1200	900/1200	900/1200	900/1200	0.8 - 1.3	1.2	1.2	1.3

tified subcloud layers occur for precipitation less than 3 mm.
The precipitations obtained using the 1 D model for the three cloud classes are in agreement with the observed ones.
The main purposes of this paper were to present the connection between observed characteristics of a warm convective cloud by regular tradewinds and mean theoretical features obtained by using a 1 D model.
It was possible to calibrate the model to predict fairly well the top heights, mean top velocities and precipitations, by using two different values of the entrainment coefficient constant A, and the thermodynamic properties of the subcloud layer.
It appears that, by observed equal cloud thickness and theoretical equal maximum liquid water contents, there is an inverse relation between cloud top height and observed precipitation on the ground.
Updraught velocities and subcloud layer seem to play an important role in this case.

List of symbols

C_p specific heat
g gravity acceleration
L latent heat of evaporation
m_a ascending air
T_E temperature of environmental air
T_v virtual temperature
T_{vE} virtual temperature of environmental air
W_L liquid water content /g air
W_v water vapor mixing ratio
W_{vE} water vapor mixing ratio for environmental air

Bibliography

1- Falkovitch A.I. (1977)
Meteorologya I Gidrologiya (9) 85-99
2- Kessler E. (1969)
A.M.S. Monograph 10 (32)
3- Ogura Y. and Takahashi T. (1973)
J.Atm. Sci. (30) 262
4- Orville H.D., al. (1975)
Pageoph. (113) 983
5- Pontikis C., Rigaud A., Oger H.,Asselin C.(1980)
La Météorologie (22) 61
6- Pontikis C., Rigaud A. (1982)
Conf. on Tropical Meteorol.,San Diego, Calif.(June)
7- Pontikis C., Rigaud A. (1983)
Preprints AMS, Conf. Hydromet.,Tulsa, October
8- Riehl H. (1954)
Météorologie Tropicale, McGraw Hill
9- Sarthou J.P. (1977)
Thèse Dr es Sciences, Toulouse, N°769
10- Takahashi T. (1982)
J.Met. Soc. Japan, II (60) 508
11- Weinstein A.L. (1970)
J. Atm. Sci. (27) 46

A WIND TUNNEL INVESTIGATION OF THE RIMING OF MODEL ICE CRYSTAL AGGREGATES

Roy M. Rasmussen

Convective Storms Division
National Center for Atmospheric Research
Boulder, CO 80307 (USA)

Jeffrey K. Lew

Department of Atmospheric Sciences
University of California
Los Angeles, CA 90024 (USA)

Hans R. Pruppacher

Institut für Meteorologie
Johannes Gutenberg-Universität
D-6500 Mainz, Postfach 3980 (FRG)

1. INTRODUCTION

Recent observations on the growth of hydrometeors in the July 22, 1976 hailstorm in northeastern Colorado (ref. 1) suggest that snowflakes (or ice crystal aggregates) may serve as the initial hail embryo. These authors suggest that aggregates formed in the forward regions of the storm (in a region with weak updrafts), are introduced into the storm near the boundary of the Weak Echo Region (WER). Rapid growth is thought to occur in this region because the depletion of liquid water by particles other than the growth particle is lowest along the WER boundary. An attempt to verify this hypothesis was made by Heymsfield (ref. 2), where he modelled the growth and trajectories of various particle types and sizes in a three-dimensional Doppler radar-derived wind field for this same storm. He found that the particles most likely to become hail were aggregates (snowflakes) of 5.0×10^{-3} to 1.5×10^{-2} m [5 to 15 mm] diameter. The results of this model, however, depend critically on the collection kernels assumed for these aggregates. The collection kernels for aggregates used by Heymsfield (ref. 2) was based on the collection efficienty for a *solid* sphere of the same diameter as the aggregate. However, since snowflakes are *porous* by nature, one might expect a different collection kernel because significant amounts of air can pass through them, as suggested by Magono and Nakamura (ref. 3). They analyzed snowflake fallspeeds and found that on the average, the drag coefficient equals 1.3 for snowflakes. For solid spheres with Reynolds numbers between 100 and 1000, the drag coefficient ranges between 1.0 and 0.45, considerably less than 1.3. Magono and Nakamura (ref. 3) attributed this discrepancy to the flow of air through the snowflakes. Since the collision efficiency between hydrometeors and cloud droplets depends critically on the flow field around the hydrometeor, one may expect the riming rate of a snowflake to depend critically on the amount of air that passes through the snowflakes. To date, there have been no experimental or theoretical studies on this problem.

2. EXPERIMENT

This study attempts to experimentally determine how the fallspeeds and porosities of aggregates affect their accretional growth rates in order to find an "optimum" snowflake for graupel and hailstone production. Aggregates were modelled by ice disks molded with circular holes evenly spaced on its surface. These models had two ranges of diameters, 5.0×10^{-3} - 6.0×10^{-3} m [5-6 mm] and 1.0×10^{-2} - 1.1×10^{-2} m [10-11 mm], and had thicknesses in the range 7.9×10^{-4} - 1.6×10^{-3} m [0.79-1.6 mm]. The number of holes and the hole sizes were varied, resulting in 12 models (see Table 1 for a description of each model). Table 2 shows the Reynolds numbers for our models for the fallspeeds used in our experiment. These models were suspended on a 1×10^{-4} m [0.1 mm] diameter fiber or rigidly on the end of a thin wooden stick. They were taken into a refrigerated walk-in cold chamber and weighed to get an initial mass and then placed into the UCLA Cloud Tunnel. An airflow in the tunnel carried cloud droplets condensed from steam past the models at either one of four constant speeds (1.5, 2.0, 2.5, and 3.0 m s^{-1}) or at the terminal velocity of the crystal (which varied with time). The temperature was monitored with a copper-constantan thermocouple and the liquid water content of the cloud was computed from a measurement taken by an E G & G Dewpoint Hygrometer. The cloud liquid water content averaged around 2×10^{-3} kg m^{-3} with some runs under 1×10^{-3} kg m^{-3} and some over 3×10^{-3} kg m^{-3}. The drop size distribution was estimated using the rod impaction method (ref. 4) and was found to be very narrow with a median size of about 5×10^{-6} m [5 μm] radius. After a period of time, the models were transferred back into the refrigerated walk-in chamber where they were photographed and weighed to determine the mass of rime accumulated. The density of the rime on the models was then measured by the mercury displacement method (ref. 5).

3. OBSERVATIONS

The model aggregates rimed only on the side facing the air stream, never on the "back" side. Most rime grew around the outer rim of the disk while a substantial amount accumulated around the edges of the holes and often inside the holes themselves, clogging them. The smaller holes tended to clog fairly early in the growth period, creating what was essentially a solid disk and preventing further growth in the center of the disk. The models with larger holes clogged at a much later time and usually had much greater amounts of rime around the holes than on the smaller-hole models. The clogging effect appeared to be largely due to diffusional growth inside the holes on which cloud particles rimed. The rime around the outer rim appeared to grow inward toward the center of the disk as well as

Table 1. Model specifications and experimental results

Model No.	Overall diam. (10^{-3}m)	Hole diam. (10^{-3}m)	No. of holes	X-sect. area (10^{-5}m^2)	Porosity (%)	$\overline{E_c}$ at constant velocity* m s^{-1} 1.5	2.0	2.5	3.0	$\overline{K}$(10^{-6}m^{3}s^{-1}) at constant velocity* m s^{-1} 1.5	2.0	2.5	3.0
1	6	1.65	4	1.97	30.3	.20	.31	.50	.42	5.76	11.21	24.63	23.81
2	11	1.65	14	6.51	31.5	.12	.22	.32	.33	10.44	28.80	52.53	63.95
3	6	1.22	4	2.36	16.5	.15	.19	.27	.22	5.23	9.31	15.95	15.35
4	6	2.06	4	1.49	47.2	.32	.43	.66	.61	7.23	12.94	24.44	27.15
5	11	1.22	14	7.87	17.2	.06	.10	.13	.15	6.96	15.15	25.89	35.31
6	11	2.06	14	4.84	49.1	.28	.35	.43	(.52)	19.96	34.67	51.70	(74.80)
7	10	.86	21	6.62	15.7	.02	(.07)	(.10)	---	1.88	(9.35)	(17.00)	---
8	10	1.09	21	5.89	25.1	.03	.09	(.25)	---	2.89	10.53	(36.97)	---
9	5	.51	17	1.59	19.0	.11	---	---	---	2.72	---	---	---
10	5	1.02	7	1.40	28.9	.18	---	---	---	3.71	---	---	---
11	10	.51	74	6.17	21.4	.07	---	---	---	6.46	---	---	---
12	10	1.02	32	5.26	33.0	.11	---	---	---	8.84	---	---	---
disk	6	.00	0	2.83	.0	.02	.08	.14	---	.78	4.28	9.89	---
disk	10	.00	0	7.85	.0	.004	.02	.07	---	.49	2.90	13.74	---

*Parentheses denote tentative values.

Table 2. Reynolds numbers for aggregate models

Model No.	N_{Re} at constant velocity m s^{-1} 1.5	2.0	2.5	3.0
1,3,4	600	800	1000	1200
2,5,6	1100	1467	1833	2200
7,8,11,12	1000	1333	1667	2000
9,10	500	667	833	1000
6 mm diam. disk	600	800	1000	1200
10 mm diam. disk	1000	1333	1667	2000

downward as the growth time lengthened. We speculate that the rime was growing along the flow streamlines around the model. Many of the string-suspended disks swung from side to side or helically and some would shake. However, the string did not allow the disk to flip over and rime on the other side, as was observed in our preliminary experiments with freely-floating natural aggregates. A film showing the accretional growth of our models in the Cloud Tunnel will be presented at the Conference.

Although the string suspension of the aggregate models allowed them to move freely in the air stream and thus more closely simulate their natural motions, the early rime growth habits of these crystals did not differ much from rigidly mounted crystals in appearance nor in collection efficiency. Assuming the cloud droplets are very small compared to the aggregate models, the collection efficiency E_c was calculated from

$$E_c = \frac{\Delta m/t}{w_L U A_c} \qquad (1)$$

where Δm is the mass of the rime (or change in mass of the model), t is the time of growth, w_L is the liquid water content of the cloud, U is the airflow speed in the Cloud Tunnel, and A_c is the effective cross-sectional area of the model perpendicular to the airflow. The collection kernel K is the effective volume swept out by the model in unit time and represents a nondimensional growth rate. It is given by

$$K = E_c A_c U \qquad (2)$$

or

$$K = \frac{\Delta m}{t\, w_L} \qquad (3)$$

where we have assumed that the cloud droplets are very small compared to the model and have negligible fall velocities in calm air. Table 1 compares collection efficiencies and collection kernels for the various aggregate model configurations. By comparing the results of model 3 with models 1 and 4, and model 5 with models 2 and 6, one observes that larger holes in the disk models resulted in higher mass growth rates (larger collection kernels) despite the smaller cross-sectional area. This suggests that the collision efficiency increases at a faster rate than the cross-sectional area decreases, resulting in a higher growth rate for the more porous aggregate models.

Consider the results for the different fallspeeds. One observes that in general, as the fallspeed increases to a point, so does the collection efficiency and collection kernel, regardless of hole size. This implies that aggregates with the highest initial terminal velocities are the fastest rimers. The effect of increased collection efficiency at higher speeds can also be seen in the Stokes impaction parameter, N_{Stk}. The Stokes number N_{Stk} gives a relative ranking of the likelihood of collisions between bodies due to their inertia (ref. 6):

$$N_{Stk} = \frac{2V_\infty r^2 \rho_d}{9\mu a} \qquad (4)$$

where r is the cloud droplet radius, ρ_d is the density of a cloud droplet, μ is the dynamic viscosity of air, V_∞ is the terminal fall velocity of the disk, and a is the radius of the porous disk model (we chose to represent the overall dimensions of the porous model rather than the equivalent radius of the solid disk of the same cross-sectional area in order to compare the effects of different holes in the same size disk). The Stokes number is therefore proportional to fallspeed and cloud droplet size. A plot of N_{Stk} versus the collection efficiency E_c (fig. 1)

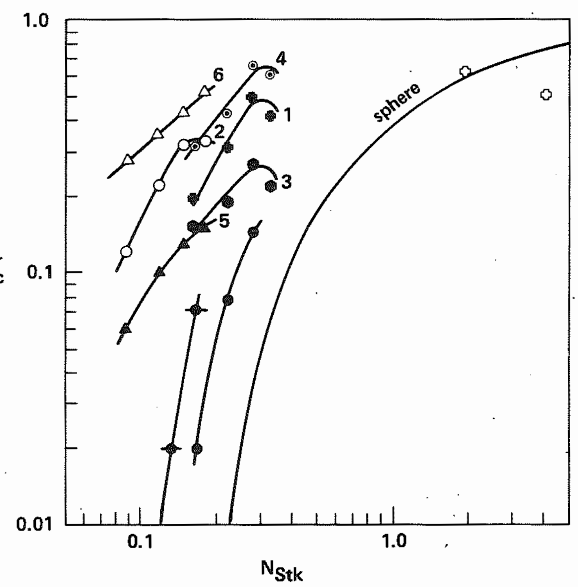

Figure 1. Collection efficiency $\bar{E}_c$ vs. Stokes number N_{Stk}. Present results: model 1: ✚ ; model 2: ○ ; model 3: ● ; model 4: ⊙ ; model 5: ▲ ; model 6: △ ; 6.0×10^{-3} m [6 mm] diam. disk: ● ; 1.0×10^{-2} m [10 mm] diam. disk: -●- . Solid line "sphere" for N_{Re} = 400 sphere (ref. 7); solid disk N_{Re} = 25, 51: ✿ (ref. 6). See table 1 for model specifications.

shows again that for the same disk size, the higher the porosity and the greater the Stokes number (higher relative speed or larger cloud droplets), the greater the collection efficiency. Also plotted on fig. 1 are values for a solid disk and a sphere (ref. 6, 7) and our own experimental results for two solid disks with diameters similar to our aggregate models. Note that our collection efficiencies are higher than both the disk and sphere collection efficiencies. Also note that the solid disk collection efficiencies lie closer to our model aggregate results than a

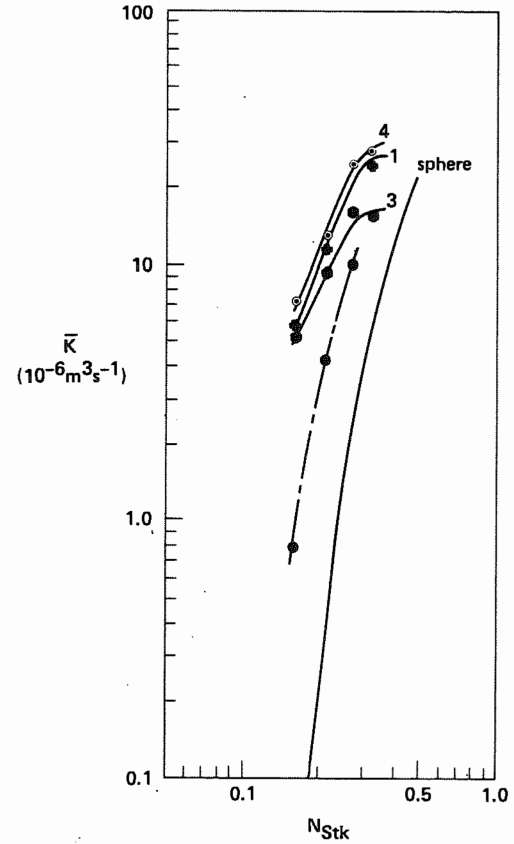

Figure 2. Collection kernel $\bar{K}$ vs. Stokes number N_{Stk} for 6.0×10^{-3} m [6 mm] diam. models. Present results: model 1: ✚ ; model 3: ⬢ ; model 4: ⊙ ; 6.0×10^{-3} m [6 mm] diam. disk: ● . Solid line "sphere" is kernel for 6.0×10^{-3} m [6 mm] diam. sphere adapted from N_{Re} = 400 collection efficiency data (ref. 7). See table 1 for model specifications.

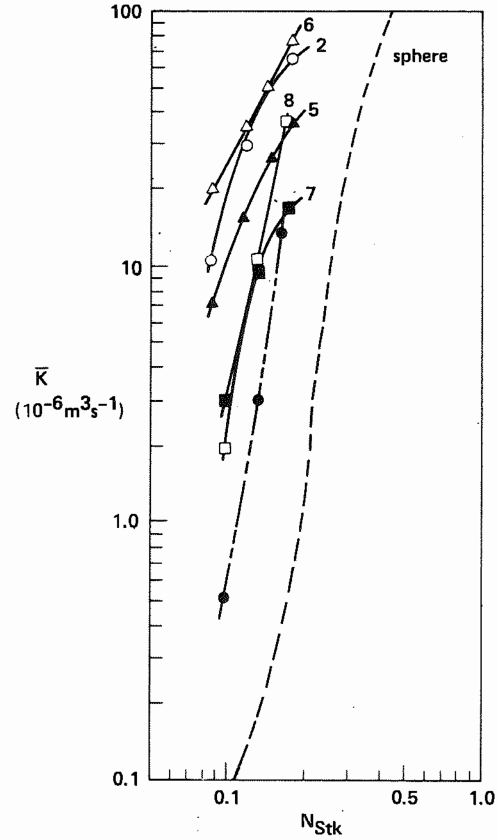

Figure 3. Collection kernel $\bar{K}$ vs. Stokes number N_{Stk} for 1.0 to 1.1×10^{-2} m [10-11 mm] diam. models. Present results: model 2: ○ ; model 5: ▲ ; model 6: △ ; model 7: ■ ; model 8: □ ; 1.0×10^{-2} m [10 mm] diam. disk: ● . Dashed lined "sphere" is kernel for 1.1×10^{-2} m [11 mm] diam. sphere adapted from N_{Re} = 400 collection efficiency data (ref. 7). See table 1 for model specifications.

sphere with the same Stokes number. This would imply that one cannot use the data for solid spheres to describe the early growth habits of porous disks.

While the more porous models have higher collection efficiencies, the relative rate of growth of the different models (as expressed by the collection kernel) may reflect a different trend, since the kernel depends on the models' cross-sectional areas perpendicular to the air flow. In figs. 2 and 3, we plot the collection kernel K versus the Stokes number N_{Stk} for our models and our own experiments with solid disks. Also plotted are collection kernels for similarly-sized solid spheres computed from the collision efficiency data in ref. 7. These plots show that the more porous models (with correspondingly smaller cross-sectional area) have higher relative growth rates, as previously mentioned. The collection kernels of the solid disks were nearly an order of magnitude smaller at small Stokes numbers, reducing to a factor of two to three less at higher Stokes numbers. More interesting is the comparison between our models and solid spheres. The collection kernels for our aggregate models are one to two orders of magnitude higher than the kernels for spheres of the same Stokes number.

These results suggest that a porous aggregate may have a growth rate which is significantly higher than a sphere or non-porous disk of the same overall diameter and falling at the same terminal velocity, at least during its early stages of riming growth.

The density of the rime is important to our studies since it may affect the fallspeed of rimed aggregates. The rime density depends on the air temperature, cloud droplet size (which remained fairly constant throughout the series of experiments), liquid water content of the cloud and impact velocity of the droplets. The measured densities varied from about 5.0×10^1 to 2.5×10^2 kg m^{-3} [0.05-0.25 g cm^{-3}] with the higher densities observed at higher temperatures. This is expected since the growth is "wetter" and therefore becomes more dense at higher temperatures (ref. 8). With respect to the constant fallspeeds used in our experiments up to now, there was little apparent variation in the rime density. There was a slight tendency toward higher rime densities at higher cloud liquid water contents.

This study is mainly concerned with the initial growth of aggregates by collisions with cloud droplets. As growth continues, porosity is reduced because of the aforementioned mechanism of diffusional growth in the holes followed by riming. This will result in a reduced growth rate due to the lower porosity as long as the aggregate does not change its terminal velocity. In free-fall, the aggregate may or may not change its fallspeed as it grows, depending on parameters such as its growth mode, rate of hole clogging, density, etc. As shown in table 1, the growth rate for a given aggregate size and porosity increases with its fallspeed. In order to properly model the growth of aggregates in nature, we must know how the fallspeed varies with the amount, density, and growth pattern of mass accreted. In order to study these aspects and to verify the results obtained in our experiments thus far, we are currently riming natural snowflakes. Early results from riming freely-floating natural aggregates in our Cloud Tunnel are as expected--that the larger, more porous aggregates rime more quickly, and increase their terminal velocities significantly in a shorter period of time than the smaller, less porous aggregates.

4. REFERENCES

1. Heymsfield, A. J. and D. J. Musil, 1982: Case study of a hailstorm in Colorado, Part II: particle growth processes at mid-levels deduced from *in-situ* measurements. *J. Atmos. Sci.*, 39, 2847-2866.

2. Heymsfield, A. J., 1983: A technique for investigating graupel and hail development. *J. Clim. Appl. Met.*, 22, 1143-1160.

3. Magono, C. and T. Nakamura, 1965: Aerodynamic studies of falling snowflakes. *J. Met. Soc. Japan*, 43, 139-147.

4. Liddel, H. F. and N. W. Wootten, 1957: The detection and measurement of water droplets. *Quart. J. Roy. Met. Soc.*, 83, 263-266.

5. Knight, N. C. and A. J. Heymsfield, 1983: Measurement and interpretation of hailstone density and terminal velocity. *J. Atmos. Sci.*, 40, 1510-1516.

6. Prodi, F., M. Caporaloni, G. Santachiara and F. Tampieri, 1981: Inertial capture of particles by obstacles in the form of disks and stellar crystals. *Quart. J. Roy. Met. Soc.*, 107, 699-710.

7. Grover, S. N., 1980: A numerical investigation of the efficiency with which aerosol particles collide with cloud and small rain drops. *Ph.D. Thesis*, University of California, Los Angeles, 275 pp.

8. Pruppacher, H. R. and J. D. Klett, 1978. *Microphysics of Clouds and Precipitation*. D. Reidel Publishing Co., 714 pp.

SESSION II

MICROPHYSICAL PROCESSES IN CLOUDS AND PRECIPITATION

Subsession II-2

Ice particle growth

THE MECHANISM OF HABIT DEVELOPMENT IN DIFFUSIONAL ICE CRYSTAL GROWTH

N. Fukuta and A.-S. Wang*

Department of Meteorology, University of Utah
Salt Lake City, Utah 84112, U.S.A.

1. INTRODUCTION

Ice crystals, when growing from small seeds in the atmosphere, gather water vapor on their surfaces and release the generated latent heat to the environment. It is this process that leads to a variety of and often beautiful forms of snow crystals. It has become increasingly evident that ice crystals of different shapes play different roles in summer convective and winter layer coluds (Ref. 1).

The basic shape of snow crystals, hexagonal column, changes depending on the condition of the environment. Variation of the diameter (2a) to height (c) ratio, or the growth habit, appears to depend mainly on the temperature (Refs 2-7) and dendrite development or morphological instability to depend on the supersaturation. It is now widely believed that as the temperature drops from the freezing point, the ice crystal shape grown by the diffusional mechanism varies from thick plates to columns (-6°C) to thin plates and dendrites (-15°C) and back to cloumns (below -20°C) (Refs 7,8). The mechanism of this growth habit variation puzzled many researchers and a number of experimental and theoretical studies have been carried out. Ice crystals epitaxially growing on cleaved covellite surfaces provided behaviors of giant growth steps (Refs 9,10)(see Fig. 1), reflecting the habit

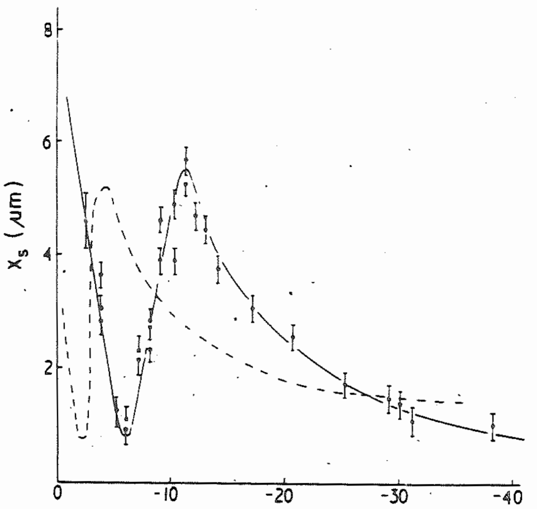

Figure 1. The variation with temperature of the mean migration distance x_s of a water molecule on: ——— the basal face (measured); ------- the prism face (hypothetical)(Ref. 9 with changes).

variation. Similar variations were confirmed on both prism and basal faces of single ice crystals (Ref. 11).

Recently, surface kinetic processes of crystal growth including quasiliquid layer (Ref. 12) and adhesive growth mechanism (Refs 13,14) were applied to explain the habit variation. However the problem still remains unsettled.

In this paper, we shall first report an upgraded Nakaya diagram determined in an ice thermal diffusion chamber and introduce two new surface kinetic processes to explain the habit variation mechanism.

2. THE REVISED NAKAYA DIAGRAM

To analyze the process responsible for habit variation, accurate knowledge of it is essential. Utilizing the stable, steady state fields of vapor and temperature of a wedge-shaped ice thermal diffusion chamber (Refs 15,16), growing the crystals on a fine fiber and rotating them for accurate measurement, the habit parameter, 2a/c, has been determined as a function of ice supersaturation (S_i - 1) and temperature T and is shown in Fig. 2, in comparison with the frequently

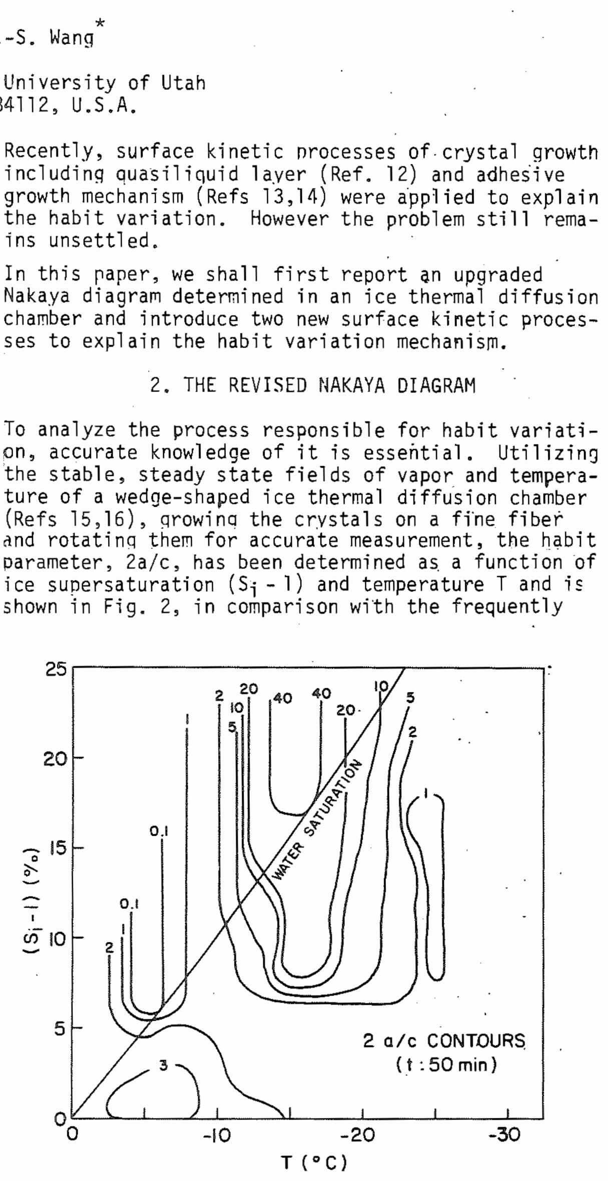

Figure 2. Contours of ice crystal diameter to height ratio 2a/c plotted as a function of temperature T and ice supersaturation (S_i-1) afer 30 min of growth.

quoted diagram reported by Kobayashi (Fig. 3). Our diagram is closer to Hanajima's (Ref. 5) than Kobayashi's and give a 2a/c minimum and a maximum at -5 and -15°C, respectively, instead of at -8 and -13°C of Kobayashi. The extremum positions at -5 and -15°C are also confirmed with ice crystals grown under free fall in our vertical supercooled cloud tunnel (Ref. 17). In Fig 2, it can be seen that the extrema occur when the environmental conditions are close to water saturation, suggesting a possible effect of transitional liquid layer that appears on the crystal surface during the growth.

*On leave from Institute of Atmospheric Physics, Academia Sinica, Beijin, The People's Republic of China

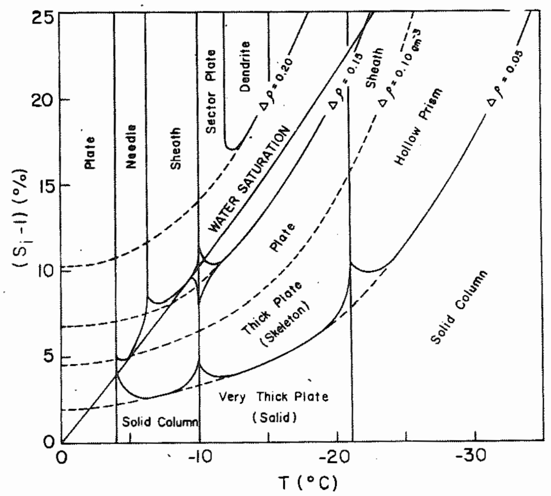

Figure 3. The form of ice crystal plotted as a function of temperature and ice supersaturation reported by Kobayashi (Ref. 8).

Under very low (S_i-1) at $T < -15°C$, $2a/c$ approached a limiting value of 1.4 instead of Kobayashi's 1,25. Applying Wulff's theorem to $2a/c=1.4$, we obtained

$$\sigma_{SG,P}/\sigma_{SG,B} = \sqrt{3}a/c = 1.21,$$

where $\sigma_{SG,P}$ and $\sigma_{SG,B}$ are surface free energy at ice-air interface on prism face and that on basal face, respectively.

3. MECHANISM OF GROWTH HABIT DEVELOPMENT

3.1. Habit Variation

Before proceeding to theoretical analysis of the habit process, let us try to understand relationships among observed surface kinetic processes and the new Nakaya diagram, since some of the processes are obviously responsible for the habit development under the restriction of vapor and heat trnsport process and the shape and size of crystal or boundary conditions. Upon inspecting Figs. 1 and 2, one may notice that the step migration velocity data of Fig. 1 are merely isolated behaviors of crystal planes. However, the data and others (Refs 10,11) clearly show existence of a maximum as well as a minimum of the velocity, an important but rather unique feature of ice crystal habit development. Figs. 4 and 5 show 2a and c values

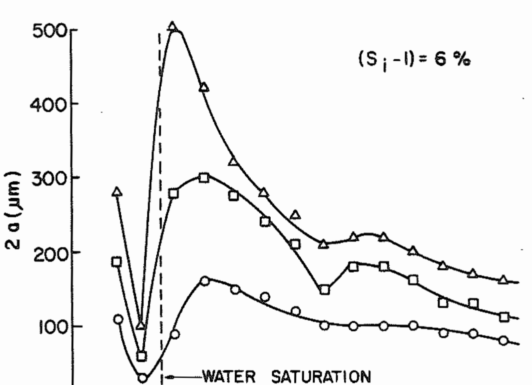

Figure 4. 2a measured as a function of T at different growth periods under $(S_i-1)=6\%$.

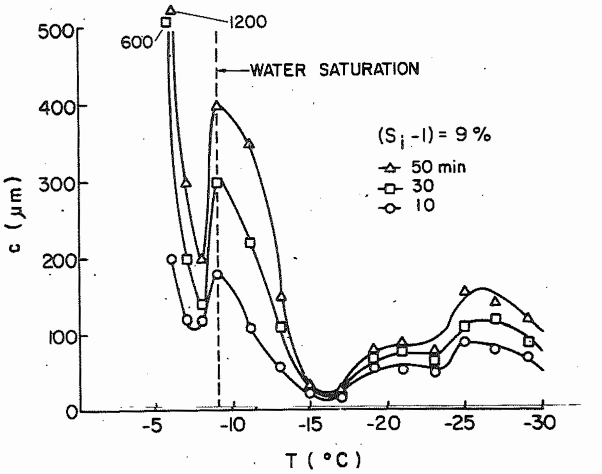

Figure 5. Ice crystal height c measured as a function of T at different growth times under $(S_i-1)=9\%$.

determined in our diffusion chamber, also showing the extrema. The problem of habit variation, therefore, boils down to identifying the surface kinetic process responsible for formation of the extrema.

3.2. The two-dimansional nucleation

In the process of crystal growth, molecules migrate to steps, causing step advance. There seems no plausible factor of surface migration that can cause a steep maximum and a sharp minimum in step velocity. The observed step velocity variation must therefore be caused by the behavior of microsteps which, after bunching, become visible. Two types of step are known. One is associated with spiral dislocation which rotates upon step advance and remains during the growth. However, it has a high energy and its formation is difficult (Ref. 18). Ice crystal growth in the atmosphere takes place at temperatures near the melting point of ice where annealing tendency is so strong that the dislocation, even if formed, will move to the edge and disappear. In fact, McKnight and Hallett (Ref. 19) reported absence of dislocation in their X-ray topographic studies on vapor grown crystals. The other is so-called "two-dimensional (2D) nucleation" which generates islands without dislocations. Once formed, an island spreads collecting molecules on the step, often bunching up with others to become visible and disappears at the crystal edge. For this reason, it requires repeated nucleation of the islands. At the air-ice interface, however, this 2D deposition nucleation is practically impossible due to relatively large surface free energy there (Ref. 20). Application of this mechanism under the coverage $\theta < 0.02$ without evaluation of the rate (Refs 13,14) cannot be justified. Thus, there is no existing mechanism at present that provides steps for the crystal plane growth.

Under $1 > \theta > 0.02$, Kuroda (Ref. 13) and Kuroda and Lacmann (Ref. 14) proposed the "adhesive mechanism" to capture water molecules on roughened surface by adsorbed molecules without 2D nucleation. On the crystal surface, clusters of molecules maintain a dynamic equilibrium resulting in the Boltzmann distribution

$$n_i/n_1 = \exp(-\Delta F/kT), \qquad (1)$$

where n_i and n_1 are the number of cluster containing i molecules per unit area and that of single molecules, respectively, ΔF_i the free energy of cluster formation and k Boltzmann's constant. Addition of a molecule to a cluster will create a "current" to the direction of single molecules of the distribution to lower cluster free energy and merely changes the population of the latter and eventually a molecule will be emitted back. Therefore, the adhesive mechanism hardly leads to capture of molecules on the surface. Thus, even under large θ, 2D nucleation cannot be avoided. Nevertheless, our experiments clearly showed growth of ice crystals even under low (S_i-1) where the previous 2D nucleation-growth theory fails to provide a sufficient rate.

The conventional theory of 2D nucleation assumes no mutual interactions among adsorbed molecules. Since σ_{SG} is involved in ΔF_i, as we shall see later, this effect of θ on σ_{SG} has to be evaluated based on fundamental concept of surface free energy σ. Fig. 6 shows

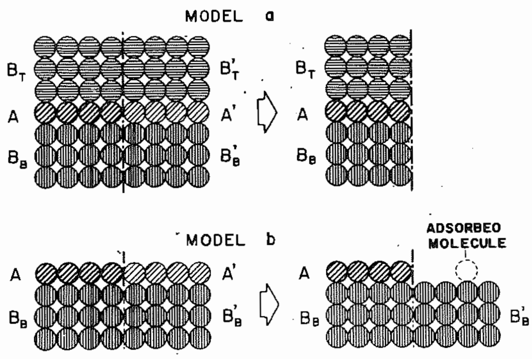

Figure 6. Interactions involved for formation of a flat surface and side of monomolecular step.

interactions in the surface layer. When a surface increases the area, there appears a resisting force. This resistance is due to the work against the intermolecular potential existing in the surface layer when molecules in the bulk are brought to the surface to fill the gap. σ is therefore the normal component of imbalanced total surface potential (Fig. 6 MODEL a). For the side of a semi-infinite molecular layer, the interaction lost due to step formation on a flat surface is AA' in Fig. 6 MODEL b. If all the A' molecules are brought back in the original phase, the σ on the side surface will disappear. If they are brought back in liquid phase, a 2D σ_{SL} should result. Assuming additive molecular potential and adsorbed layer is liquid-like,

$$\sigma_{SG,A} = \sigma_{SG,2} - (\sigma_{SG,2} - \sigma_{LS,2})\theta, \qquad (2)$$

where subscripts A and 2 stand for adsorbed and 2D, respectively.

The free energy required for formation of a disk-like embryo is

$$\Delta F = \pi r^2 h\Delta\mu + 2\pi r h\sigma_{SG,A}, \qquad (3)$$

where r is the radius of the embryo, $\Delta\mu$ the chemical potential difference per unit volume of ice between ice and water vapor and h the height. ΔF shows a maximum which is to be overcome during nucleation. By differentiating Eq. 3 with r and setting to 0, we have the radius of critical embryo

$$r^* = -\sigma_{SG,A}/\Delta\mu. \qquad (4)$$

Using Eq. 2 for σ of flat surface which is an overestimate, and Eq. 4 in Eq. 3, the free energy of critical embryo formation

$$F^* = -\frac{\pi h}{\Delta\mu}\sigma^2_{SG,A} = -\frac{\pi h}{\Delta\mu}[\sigma_{SG}-(\sigma_{SG}-\sigma_{LS})\theta]^2. \qquad (5)$$

Since our estimate involves a number of crude assumptions, we use an approximate formula for nucleation rate

$$J \simeq 10^{25}\exp(-\Delta F^*/kT)\ (\mathrm{cm^{-2}s^{-1}}). \qquad (6)$$

Fig. 7 shows J computed as a function of θ at -10°C

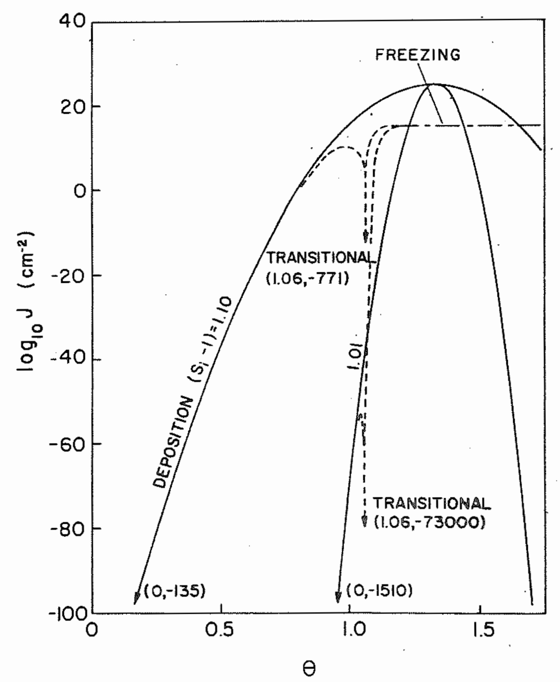

Figure 7. Log J plotted as a function of θ at -10°C on the basal plane of ice. The numbers in the brackets are coordinate positions.

on the basal plane. σ_{SG} and σ_{LS} are taken to be 10.9 and $2.7\times10^{-2}\,\mathrm{Jm^{-2}}$ and $h = 3.68\times10^{-10}$m. The previous treatment corresponds to $\theta = 0$ and shows clearly the nucleation difficulty with $J \simeq 10^{-135}\,\mathrm{cm^{-2}s^{-1}}$ for $(S_i-1) = 0.10$ and $10^{-1510}\mathrm{cm^{-2}s^{-1}}$ for $(S_i-1) = 0.01$. However, as θ increases, J gradually becomes recognizable or $J > 1\ \mathrm{cm^{-2}s^{-1}}$. At $(S_i-1) = 0.01$ at -10°C, the BET (Brunauer-Emmett-Teller) adsorption equation gives $\theta = 1.34$ which is the portion above the ice saturation (transient adsorbed layer in which the 2D nucleation is possible). Furthermore, as pointed out above, the σ used for this computation are the overestimate and if proper values were used, J is likely to increase considerably. Thus the difficulty of 2D nucleation previously thought is eased by the interaction between the embryo and adsorbed molecules.

3.3. <u>The transitional nucleation mechanism</u>
As we have seen above, the 2D nucleation is possible on ice crystal faces and when θ and therefore T increase under (S_i-1)=const., it becomes faster. Whereas, the adhesive mechanism does not. However, the 2D deposition nucleation alone is still insufficient to explain the maximum and the minimum of the face growth rate. When the (S_i-1) increases, θ in the transitional layer accordingly becomes larger and eventually exceeds the critical embryo height. Then, formation of the critical embryo demands exposure of the top of embryo to the gaseous phase (see Fig. 8). Then,

$$\Delta F = \pi r^2 h\Delta\mu + 2\pi r h\sigma_{LS,2} + \pi r^2\Delta\sigma, \qquad (7)$$

where $\Delta\sigma = \sigma_{SG,2} - \sigma_{LS,2} - \sigma_{LG,2}$. Applying the same procedure discussed above, we have

$$r^* = -h\sigma_{LS,2}/(h\Delta\mu + \Delta\sigma). \qquad (8)$$

Then, because $r^* > 0$,

$$h > h_c = -\frac{\Delta\sigma}{\Delta\mu}, \qquad (9)$$

where h_c is the critical height below which $r^* < 0$. Since adsorption occurs on the solid surface to reduce σ there, $\Delta\sigma > 0$. Replacing Eq. 8 in Eq. 7,

$$\Delta F^* = -\pi h \sigma^2_{LS,2}/(\Delta\mu + \Delta\sigma/h). \qquad (10)$$

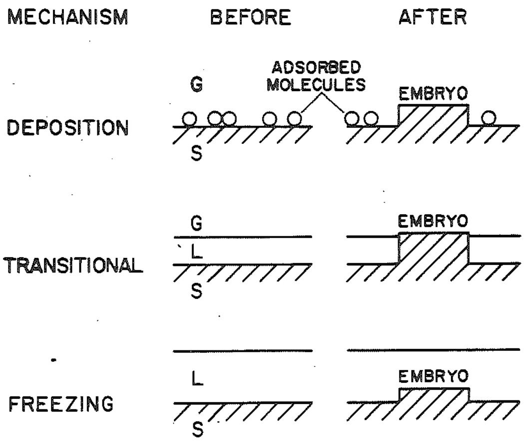

Figure 8. Three possible mechanisms of 2D nucleation on ice crystal planes. G, L and S denote gaseous, transitional liquid and solid phase, respectively.

At $h=h_c$, $\Delta F^* \to \infty$ suggesting an extreme decrease of J. For $(S_i-1)=0.10$ and T=270°K assuming $\Delta\sigma=10^{-3}Jm^{-2}$, h_c $=8.75\times10^{-11}$m or 24% of the monolayer height h_m. This restriction becomes effective only when $\theta > 1$. Thus, when $\theta \geq 1$ and $h_m\theta > h_c$, J becomes very low. Under the condition, molecules arriving at the surface accumulate in the form of transitional liquid layer and the mechanism shift to faster 2D freezing nucleation. However, during this shift, vapor pressure of the layer increases and reduces the vapor flux arriving at the surface, causing slow down of crystal face growth. When $\theta \gg 1$, the layer becomes bulk supercooled water and the 2D freezing nucleation proceeds easily. This change of nucleation mechanism explains occurrence of the two extrema for the crystal face growth rate. To explain the habit variation, however, the shift of growth rate between the basal and prism face must be analyzed.

From our experiments, $\sigma_{SG,P} > \sigma_{SG,B}$, and considering interactions responsible for σ, it is reasonable to expect $\sigma_{LS,P} > \sigma_{LS,B}$. For growth of the basal face in c-axis direction, as can be seen in Eq. 10, $\sigma_{LS,P}$ is involved. So, ΔF^* becomes small to nucleate when $-\Delta\mu$ or (S_i-1) is large. Under such a condition, h_c is small and the restriction from the mechanism switch-over becomes effective. As T increases under water saturation, the basal plane or c-axis growth slows down leading to plate formation. Whereas, the growth slow down happens in a-axis direction on the prism plane, where $\sigma_{LS,B}$ is involved, under low (S_i-1), which occurs at higher T. Thus, the growth slow down at low T and high (S_i-1) on basal face or in c-direction, and that at high T and low (S_i-1) on prism face or in a-direction explain the observed habit variation. It should be pointed out, however, for computation of surface kinetics which involves feedbacks of many processes, basic constants such as surface free energies of the embryo and adsorbed molecules must be evaluated first based on correct and fundamental molecular interactions.

Acknowledgments. This work was supported by Div. of Atmos. Sci., N.S.F. under Grant ATM-8106792 and Senior Academician Program (N.F.) of N.O.A.A.

4. REFERENCES

1. Fukuta N 1980, Development of fast falling ice crystals in clouds at -10°C and its consequence in ice phase processes, *Preprints, 8th Internat Conf Cloud Phys,* Clermont-Ferrand 15 Jul '80, 97.
2. Nakaya U et al 1938a, Preliminary experiments on the artificial production of snow crystals, *J Fac Sci Hokkaido Univ Ser II*, 2, 1 - 11.
3. Nakaya U et al 1938b, Further experiments on the artificial production of snow crystals, *J Fac Sci Hokkaido Univ Ser II*, 2, 13 - 57.
4. Hanajima M 1944, On the conditions of growth of snow crystals, *Low Temp Sci A1*, 53 - 65.
5. Hanajima M 1949, On the growth conditions of man-made snow, *Low temp Sci A1*, 23 - 29.
6. Hobbs P V & Scott W D 1965, A theoretical study of the variation of ice crystal habits with temperature, *J Geophys Res*, 70, 5025 - 5034.
7. Fukuta N 1969, Experimental studies on the growth of small ice crystals, *J Atmos Sci*, 26, 522 - 531.
8. Kobayashi T 1961, The growth of snow crystals at low supersaturations, *Phil Mag*, 6, 1363 - 1370.
9. Mason B J et al 1963, The growth habits and surface structure of ice crystals, *Phil Mag*, 8, 505 - 526.
10. Kobayashi T 1965, The growth of ice crystals on covellite and lead iodide surfaces, *Rept Low Temp Sci Inst Hokkaido Univ Ser A*, 20, 1 - 22.
11. Lamb D & Hobbs P V 1971, Growth rates and habits of ice crystals grown from the vapor phase, *J Atmos Sci*, 28, 1506 - 1509.
12. Lacmann R & Stranski I N 1972, The growth of snow crystals, *J Crystal Growth*, 13 - 14, 236 - 240.
13. Kuroda T 1982, Growth kinetics of ice single crystal from vapour phase and variation of its growth forms, *J Meteor Soc Japan*, 60, 520 - 534.
14. Kuroda T & Lacmann R 1982, Growth kinetics of ice from the vapour phase and its growth forms, *J Crystal Growth*, 56, 189 - 205.
15. Schaller R C & Fukuta N 1979, Ice nucleation by aerosol particles; Experimental studies using a wedge-shaped ice thermal diffusion chamber, *J Atmos Sci*, 36, 1788 - 1802.
16. Fukuta N et al 1982, Experimental and theoretical studies of ice crystal habit development, *Preprints Conf on Cloud Phys*, Chicago 15 - 17 Nov 1982, 329 - 332.
17. Fukuta N et al 1982, Determination of ice crystal growth parameters in a new supercooled cloud tunnel, *Preprints Conf on Cloud Phys*, 15 - 17 Nov 1982, 325 - 328.
18. Fletcher N H 1960, Nucleation and growth of ice crystals on crystalline substrate, *Aust J Phys*, 13, 408 - 418.
19. McKnight C V & Hallett J 1978, X-ray topographic studies of dislocations in vapor-grown ice crystals, *J Glaciology*, 21, 397 - 407.
20. Ohara M & Reid R C 1973, *Modeling Crystal Growth Rates from Solution*, Prentice-Hall, Inc., 267pp.

LABORATORY SIMULATIONS OF GRAUPEL GROWTH

D J GRIGGS , J P ROUYET, B E STEWART , R LIST
Physics Department, University of Toronto
Toronto, Ontario, M5S 1A7, Canada.

1. INTRODUCTION

The growth of ice particles by accretion in natural clouds is one of the fundamental precipitation forming processes. One step in the formation of hail is the graupel stage, and graupel melting to form raindrops is the final stage of precipitation formation in many clouds. Relatively little work has been directed towards understanding graupel growth. This is partly due to the difficulty of appropriate field observations providing quantitative information on the growth.

The object of this paper is to present preliminary results of a laboratory study on graupel growth. To achieve this, graupel has been grown in an icing tunnel using various initial embryos. The shape evolution of the particles was studied and, in some cases, density measurements of the resulting particles were made.

2. EXPERIMENTAL

2.1. Apparatus

The experiments were performed in the cloud physics wind tunnel at the University of Toronto, (Fig. 1). A full description is presented in reference 1. The facility was originally used for studying the growth and melting of hailstones, and a number of modifications had to be made before the graupel study could be performed. With the changes, temperatures between +10°C and -30°C, wind speeds between 1 m s^{-1} and 28 m s^{-1}, and pressures down to 25 kPa can be obtained.

Cloud droplets are produced by an atomizing nozzle and calculations show that they reach thermal equilibrium with the surroundings before entering the measuring section.

2.2. Measurement techniques and experimental conditions.

Seven different embryo models were used for the graupel growth experiments. These were 1,2 and 3 mm diameter circular discs, 1,2 and 3 maximum dimension hexagonal plates and conical ice particles of 3.5 mm base dimension with a cone angle of 75° . All the circular discs and hexagonal plates were made from mylar ∿ 80 μm thick and were suspended in the tunnel with the plane of the disc perpendicular to the flow, using a 250 μm thick glass fibre, which has the advantage of very good thermal insulation. This method was not used for the conical embryos because it was not rigid enough at the higher terminal velocities of these particles. The conical embryos were mounted in the wind tunnel with either the base or the apex pointing downwards into the stream of droplets, using stainless steel wire 300 μm diameter. These orientations were chosen as they are both known to be possible free fall modes, (reference 2). The relative air speeds were chosen to be equivalent to the terminal velocities of the particles.

During each experiment the temperature, dew point, pressure, relative humidity and air velocity were continuously monitored. Liquid water content was measured to a first approximation by icing a cylinder at high velocity (25 m s^{-1}) and low temperature (-20°C) and by assuming a collection efficiency of unity.

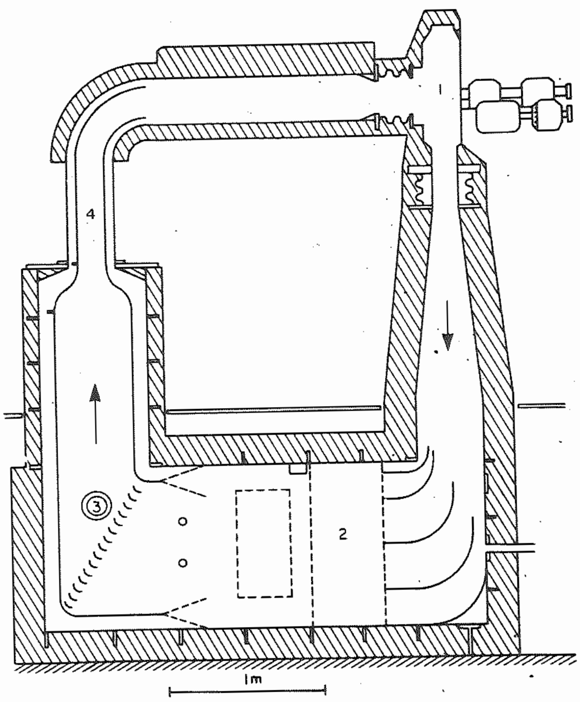

Figure 1. Schematic diagram of the University of Toronto icing tunnel: 1) Fan 2) Cooling elements 3) Atomizing nozzle port 4) Measuring section

The liquid water content reading was calibrated before the experiments began and was checked after completion. The nozzle produced a spray with a mean diameter of ∿ 15 μm in the measuring section, as measured by the magnesium oxide coated slide technique. Photographs were also taken at regular intervals during the growth.

On completion of growth, the graupel was immediately placed into a cooled container and transferred to a cold room. Analysis in the cold room consisted of photographing the final graupel and measuring mass and then the volume to determine the density. In these latter cases, accretion was only allowed to take place for ∿ 5 minutes so that the actual terminal velocity of a freely falling particle would have remained relatively constant. Mass was measured to an accuracy of ± 0.1 mg and volume was calculated using the buoyancy technique described in references 3 and 4 to an accuracy of ± 0.15 mm^3.

In these preliminary studies, all the experiments were conducted at -15°C, at laboratory pressure, and in liquid water content of ∿ 1 g m^{-3}. The value of updraft velocity for the discs and hexagonal plates of 1.0 m s^{-1}±16% was chosen using drag coefficient data from references 2 and 5 and these experiments ran for ∿ 20 min.

Six updraft velocities were used for the conical embryos. Three values were used for each initial embryo orientation and these corresponded to the terminal velocities associated with three densities. The values of air velocity used in all the experiments and corresponding initial densities are shown in Table 1. Because of the higher velocities used with the conical embryos, the duration of these experiments was reduced to 10 min.

Embryo	Diameter [mm]	Velocity [m s^{-1}]±16%	Corresponding density [g cm^{-3}]
Discs and hexagonal plates	1.0	1.0	0.91
	2.0	1.0	0.91
	3.0	1.0	0.91
Cone base pointing down	3.5	1.4	0.2
	3.5	1.7	0.3
	3.5	2.2	0.5
Cone apex pointing down	3.5	2.1	0.2
	3.5	2.5	0.3
	3.5	3.4	0.5

Table 1. Size of the various embryo models and the air velocity used for riming. Drag coefficients of 1.2 were used for the discs, hexagonal plates and cones with the base down. A value of 0.5 was used for cones with apex down.

3. RESULTS

In all cases, the graupel grew in the dry growth regime. Their appearance was white and they were very fragile. In nearly all cases the graupel also grew into a conical shape although the cone angle changed as the conditions varied. The results for circular discs, hexagonal plates and conical embryos will be dealt with consecutively.

A quantitative description of the variation of the cone angle with disc size has not yet been obtained since only a small number of preliminary experiments have been performed. However, in all cases, the cone angle was between 60° and 100°. This is not unrealistic when compared to natural graupel. Examples of the conical structure are shown in Figs. 2a and 2b.

For all sizes of disc, accretion occurred preferentially around the edges rather than in the centre. Thus, on completion of riming, a distinct indentation could be seen in the base of the graupel. This point is illustrated by Figs. 2c and 2d which show the indentation for two sizes of initial disc. In general the circular shape of the embryo was preserved into the graupel phase although the shape became more irregular as time progressed (see Fig 2e). It was also noticed, on occasion, that irregularities in the growth occurred early in the riming process, and that these irregular growths generally grew larger with time. This point is illustrated in Figs. 2f and 2g. Fig 2f, taken 5 min after the start, shows a small protuberance whereas Fig 2g, taken after riming is complete, shows that this additional growth has become larger.

The results obtained with hexagonal plates of all size categories were consistent with the results found with discs. The cone angles were again in the range of 60° to 100°, and again the indentation in the base of the final graupel was always present. In most cases using a hexagonal plate embryo, the initial shape tended to be preserved throughout the growth so that the hexagonal shape could still be distinguished on completion of riming (as shown in Fig 2h), even though the diameter of the particle had increased by a factor of ∿ 2.

When a cone with its base downwards was used, the cone angle varied with velocity (See Figs. 2i and 2j). At high velocities (2.2 m s^{-1}) the growth eventually produced a cylindrically shaped particle, whereas at low velocities (1.4 m s^{-1}) the angle of growth much more resembled those found using the discs and the plates, i.e. 60° to 100°. At all velocities the indentation in the base was present and its general appearance did not vary significantly as the velocity was changed.

When a cone with its apex pointing downwards was used, a growth pattern was observed whereby the area around the apex of the cone tended to fill-in as growth progressed. This continued until the shape of the particle had reverted to a cone with its base downwards. This is illustrated in Figs. 2k and 2l.

The density of graupel was found for two different conditions. The density of growth produced by riming a 2 mm circular disc was found to be 0.30 ± 0.05 g cm^{-3}. Using a cone with the base down in an updraft of 1.7 m s^{-1}, the value for the density was again found to be 0.30 ± 0.05 g cm^{-3}. Thus for these two conditions, the density was invariant.

4. DISCUSSION

Many of the accretional growth results were not unexpected. First, the photographs and visual impressions indicated that the growth became less fragile at the higher velocities. This is consistent with an increased spreading of the droplets on impact with the substrate. Second, the experiments tended to produce conical shapes with realistic cone angles. This is important when relating the results to nature. Third, the common occurrence of an indentation in the base of the graupel may be due to increased collection of droplets around the edge due to inertial and aerodynamic coupling. This has been studied theoretically, reference 6, in the laboratory, reference 7, and in the field, reference 8. However, the field observations indicate that the indentations do not exist or perhaps do not persist to the size of particles examined here. The reason for this is not clear from this study, although the fact that the embryos in this experiment were fixed whereas in nature they are free to oscillate in some manner might provide a possible explanation. Drop sizes and their distribution could be crucial aspects of the problem because larger drops would be less deflected before accretion and thus an indentation would be less likely. Fourth, the preservation of the embryo shape (i.e. hexagonal plate) into the graupel phase could simply be due to the airflow around the crystal causing more drops to be deposited at the corners of a hexagonal crystal than at the edges. This is in agreement with previous work, (reference 7). However, a detailed study of the flow pattern around a growing hexagonal plate would have to be performed

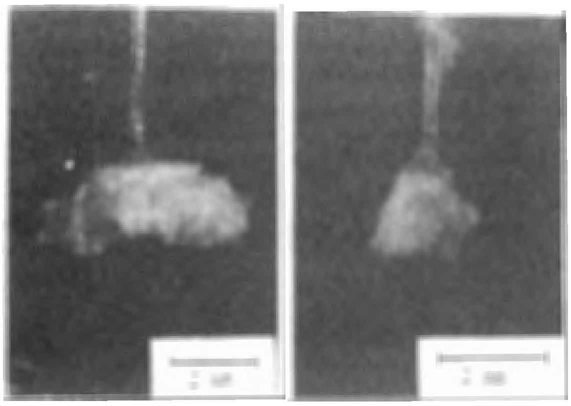

Fig. 2a
3mm hexagon

Fig. 2b
1mm disc

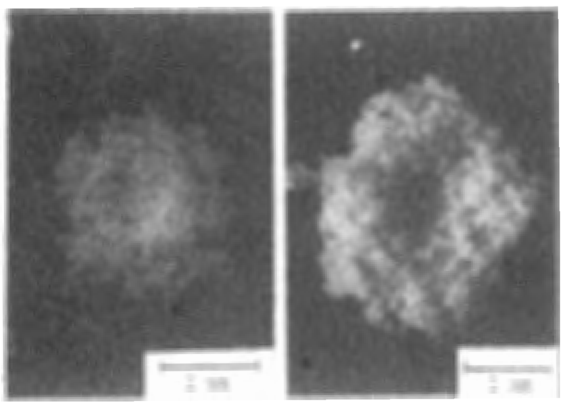

Fig. 2c
2mm hexagon

Fig. 2d
3mm disc

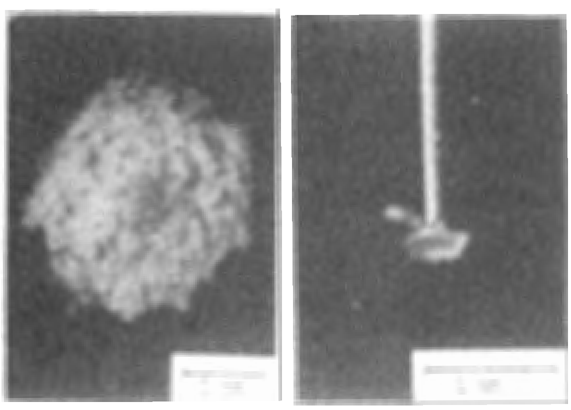

Fig. 2e
3mm disc

Fig. 2f
2mm hexagon

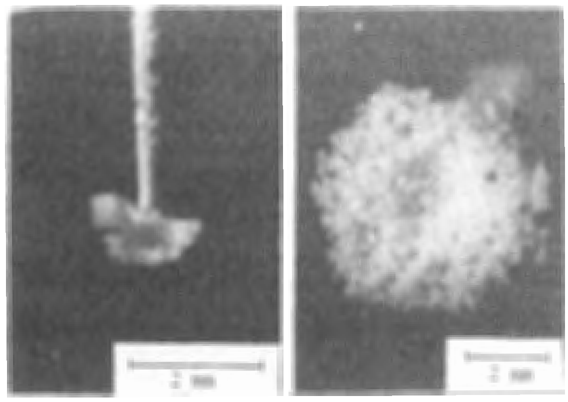

Fig. 2g
2mm hexagon

Fig. 2h
3mm hexagon

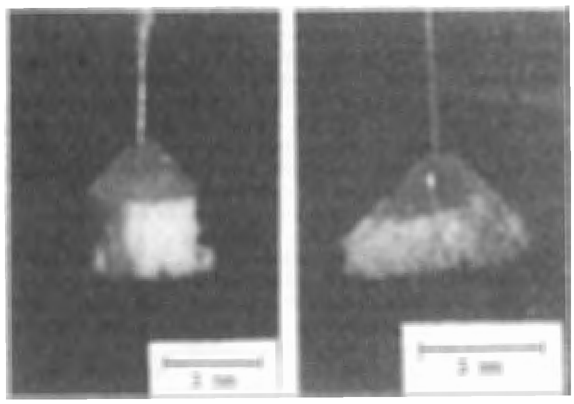

Fig. 2i
cone, base down

Fig. 2j
cone, base down

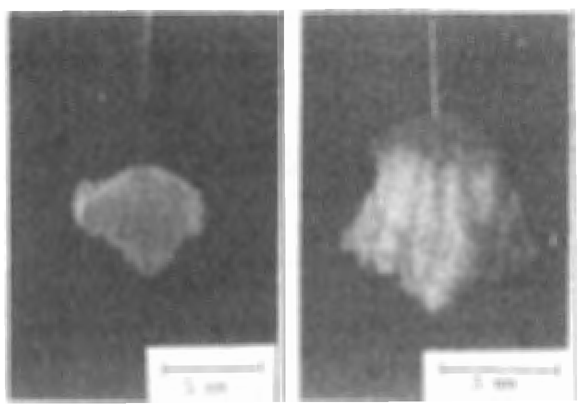

Fig. 2k
cone, apex down

Fig. 2l
cone, apex down

Fig. 2 Photographs illustrating various aspects of the growth of the graupel. Embryo size is given below each photograph.

before this could be confirmed. The irregularities often observed on the completion of riming are probably due to the increased collection efficiency of a small irregularity which protrudes into the flow. Thus it will tend to grow with respect to the rest of the surface. The original irregularity could be present on the crystal itself or could just be caused by statistical variations in the accretion process. Fifth, the densities measured in the two cases were not unrealistic (~ 0.3 g cm^{-3}). Such densities have been measured in the laboratory by others (reference 9). However, they are much too low compared with some field observations (reference 10) which recorded densities mostly around 0.7 g cm^{-3}.

The new features which were found with a conical embryo were the variation in cone angle with velocity and the reversal in the growth of a cone originally placed with the apex directed towards the flow. Both these effects may be explainable when the airflow around the embryo is considered.

5. CONCLUSIONS

Experiments have been conducted on the accretional growth of particles in a vertical icing tunnel in which the conditions simulated a natural graupel growth environment. Results were focused towards shape evolution of initial discs, hexagonal plates and cones. Some attention was directed to measuring the density of the deposit. The graupel evolved towards a conical shape in nearly all cases, and in the base of the cones there were often indentations. These observations were independent of the size and shape of embryo used. When a conical embryo was used with the base directed towards the flow the cone angle was found to change systematically with velocity. When a conical embryo with the apex directed towards the flow was used, the cone reverted to a cone with a base down. The density of the graupel tested was 0.3 g cm^{-3} although only two sets of data were obtained.

Future experiments will elucidate these and other aspects of graupel growth. Such results will enhance our understanding of precipitation formation via icing processes.

6. ACKNOWLEDGEMENTS

Research was carried out under the sponsorship of NSERC Canada, AES Canada and NSF Switzerland.

7. REFERENCES

1. Lesins G B 1983, Hailstone studies in an icing tunnel, PhD thesis, Department of Physics, University of Toronto.

2. List R and Schemenhauer R S 1971, Free fall behaviour of planar snow crystals, conical graupel and small hail, J Atmos Sci 28, 110-115.

3. List R 1961, Physical methods and instruments for characterizing hailstones, Bull Amer Meteor Soc 42, 452-466.

4. Knight N C and Heymsfield A J 1983, Measurement and interpretation of hailstone density and terminal velocity, J Atmos Sci 40, 1510-1516.

5. Hoerner S F 1965, Fluid dynamic drag, Hoerner publishing corporation.

6. Pitter R L and Pruppacher H R 1974, A numerical investigation of collision efficiencies of simple ice plates colliding with supercooled water drops, J Atmos Sci 31, 551-559.

7. Oleskiw M 1976, Cloud chamber simulation of graupel growth, MSc Thesis, U of Alberta.

8. D'Errico R E and Auer A H 1978, An observational study of the accretional properties of ice crystals of simple geometric shapes, Conf on Cloud Phys and Atmos Elec, Washington, 114-121.

9. Pflaum J C and Pruppacher H R 1979, A wind tunnel investigation of the growth of graupel initiated from frozen drops, J Atmos Sci 36, 680-689.

10. List R 1958, Kennzeichen Atmosphaerischer Eispartikeln, Z. angew. Math. Phys. 9A, 180-192.

REGIONAL CHARACTERISTICS OF GRAUPEL FORMATION

Toshio Harimaya

Department of Geophysics, Hokkaido University, Sapporo 060, Japan

1. INTRODUCTION

In previous papers (Refs. 1,2), it was shown that both snow crystals and frozen drops could become graupel embryos. The following question is what meteorological conditions determine that snow crystals or frozen drops become graupel embryos. On the other hand, it was shown in another paper (Ref. 3) that the internal structures of graupel particles were classified into three types, that is porous ice with small crystals, porous ice with large crystals and compact ice with large crystals.

The thresholds of meteorological conditions which classify the types of embryo and internal structure can be obtained from observational results. It is described in the present paper that predominant embryo and internal structure of graupel are estimated at 6 places in the Japanese Islands using the thresholds and regional characteristics are studied concerning the embryo and internal structure of graupel.

2. REGIONAL CHARACTERISTIC OF EMBRYO

The temperature at the cloud base and thickness of mixed clouds were calculated from aerological data in order to examine the relationship between embryo type and meteorological conditions. Fig.1 shows the meteorological conditions at the time when each embryo was observed. Frozen drop embryos belong to the upper region above boundary A and snow crystal embryos belong to the lower region below boundary B.

Next, we must examine whether there are large cloud droplets in the snow clouds under the meteorological condition on the upper right corner in Fig.1. The temperature at the cloud base and thickness of mixed clouds at the time when cloud droplets were observed by snow crystal sondes (Refs. 4, 5, 6) were calculated from aerological data. These values are added in Fig.1. It is seen that small cloud droplets and large cloud droplets are situated at the lower left corner and at the upper right corner respectively. Since warmer temperatures at the cloud base provide a higher liquid water content, the meteorological condition corresponding to the upper right corner is suitable for liquid coalescence owing to a higher liquid water content and greater thickness of mixed clouds (Ref. 7). Therefore, it is reasonable that large cloud droplet and frozen drop embryo are situated at the upper right corner in Fig.1.

Next, the predominant types of embryo were estimated at the places on the western shore of the Japanese Islands using the threshold regarding the embryo. Wakkanai, Sapporo, Akita, Wajima, Yonago and Fukuoka were selected as representative places, because aerological observations were carried out at these places.

Statistical analysis was made using only the aerological data at the time when graupel particles precipitate for one hour before and after the aerological observation time. The temperature at the cloud base and thickness of mixed clouds at the time were calculated from the adopted aerological data (1967/68~1976/77). These values are shown in Fig.2 in the same manner as shown in Fig.1. As the region occupied by frozen drop embryos could not be distinguished from the region occupied by snow crystal embryos using a boundary line in Fig.1, the middle line between boundary line A and B may be adopted as the boundary line between both regions. The boundary line is indicated by a solid line in Fig.2 and the line is the threshold regarding the embryo. Fig.2 shows the ratios of snow crystal

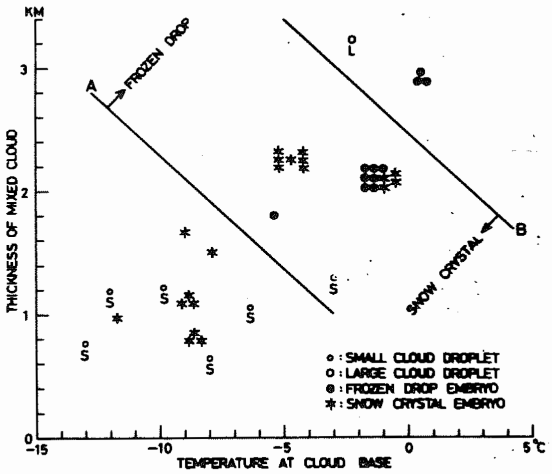

Figure 1. Relationship between embryo type and meteorological conditions.

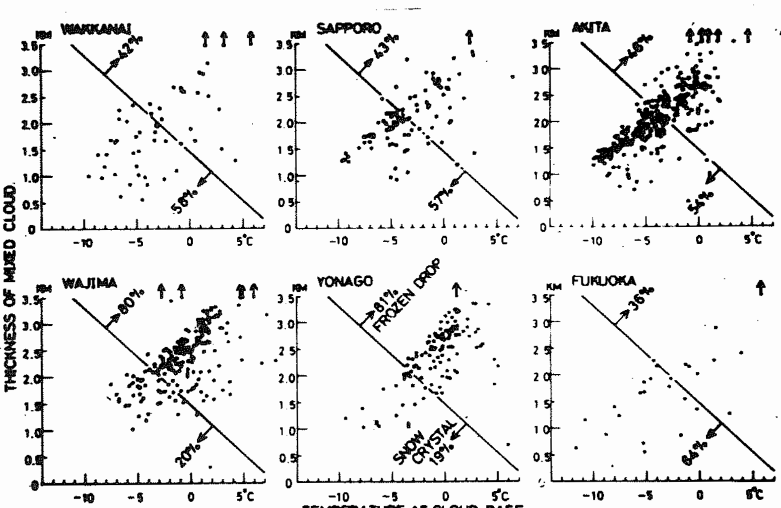

Figure 2. Regional characteristics in embryo type.

embryo number and frozen drop embryo number to total number at each place. It is seen that snow crystals are superior to frozen drops as embryos in the group of northern region such as Wakkanai, Sapporo and Akita while frozen drops are superior to snow crystals as embryos in the group of southern region such as Wajima and Yonago. But, it is an unusual case that snow crystals are superior to frozen drops as embryos at Fukuoka in the group of southern region. It is an important result that the distribution of predominant embryo type is not arranged randomly but is arranged systematically corresponding to the latitude.

3. REGIONAL CHARACTERISTIC OF INTERNAL STRUCTURE

Combining the appearance with crystal size, the internal structures of graupel particles were classified into three types, that is porous ice with small crystals, porous ice with large crystals and compact ice with large crystals (Ref. 3). Based on the experimental results of appearance and crystal size regarding the accreted ice, contributing factors to internal structure of graupel are considered to be environmental temperature and surface temperature of graupel. As wet-bulk potential temperature was uniform in clouds, it was adopted as the environmental temperature. And the temperature at cloud base was adopted as the other parameter instead of liquid water content which is effective to control the surface temperature of graupel. Fig.3 shows the relationship between the internal structure and meteorological conditions above-mentioned. It is seen that each type of internal structure occupy different positions on the diagram respectively and each type is classified clearly by two thick solid lines.

Next, the predominant types of internal structure were estimated at the places on the western shore of the Japanese Islands using the threshold regarding the internal structure in the same manner as carried out regarding the embryo. It was characteristic result that porous ice with small crystals (P-S) type was observed in the group of northern region such as Wakkanai, Sapporo and Akita whereas the same was not observed in the group of southern region such as Wajima and Yonago. But, it was an unusual case that (P-S) type was observed at Fukuoka in the group of southern region. The distribution of predominant internal structure type is not arranged randomly but is arranged systematically corresponding to the latitude. And the boundary line was observed at the same position as obtained in the case of predominant embryo type.

4. REGIONAL CHARACTERISTICS OF GRAUPEL FORMATION AND CLIMATE

It is important in the regional characteristics of predominant embryo and internal structure types that each was divided into two groups of northern and southern regions. As the Japanese Islands elongate along the latitude, this is expected to cause considerable difference in air temperature between northern and southern ends of the Japanese Islands. Therefore, it is considered that this regional characteristic of graupel formation reflects the climate. On the other hand, the thresholds regarding predominant embryo and internal structure were closely related to the air temperature and humidity at the ground. After due consideration of the facts above-mentioned, monthly mean values were examined regarding the air temperature and humidity at 6 places during 10 winters (1967/68~1976/77). Each place had the same value

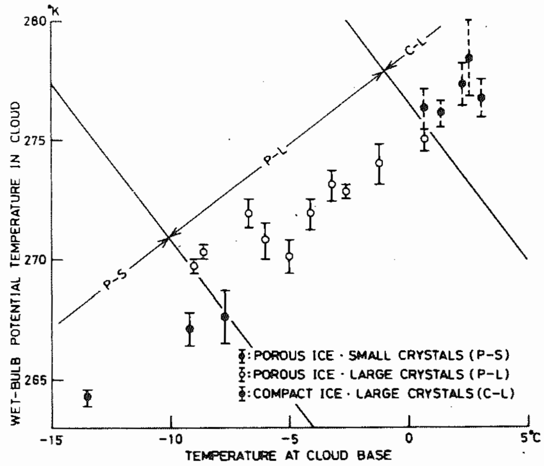

Figure 3. Relationship between internal structure type and meteorological conditions.

as one another regarding humidity except Fukuoka, but the temperature of Wakkanai was about 12°C colder than that of Fukuoka. The boundary line concerning graupel formation corresponded to the +2°C isotherm of monthly mean temperature in the coldest month. When graupel particles precipitate, the temperature at cloud base in northern region is colder than that in southern region and the thickness of mixed clouds in northern region is thinner than that in southern region.

5. CONCLUDING REMARKS

The regional characteristics based on the difference of climate were detected in the formation process of graupel. This kind of study offers informations regarding artificial cloud modification theories and techniques in the case of their application in different geographical areas.

6. REFERENCES

1. Harimaya T 1976, The embryo and formation of graupel. J Meteor Soc Japan 54. 42-51.

2. Harimaya T 1977, The internal structure and embryo of graupel, J Fac Sci Hokkaido Univ Ser VII 5, 29-38.

3. Harimaya T 1983, A further study on the internal structure of graupel, J Fac Sci Hokkaido Univ Ser VII 7, 227-238.

4. Magono C and Tazawa S 1966, Design of "snow crystal sondes", J Atmos Sci 23, 618-625.

5. Magono C and Lee C W 1973, The vertical structure of snow clouds, as revealed by "snow crystal sondes", Part II, J Meteor Soc Japan 51, 176-190.

6. Taniguchi T and Magono C 1978, Observations of the electric charge and snow crystals in winter thunderclouds using sondes, Paper presented at the meeting of the Meteor Soc Japan held in Sendai.

7. Singleton F and Smith D J 1960, Some observations of drop-size distributions in low layer clouds, Quart J Roy Meteor Soc 86, 454-467.

ON THE SNOW CRYSTALS OF COLD TEMPERATURE TYPES

Katsuhiro Kikuchi and Noboru Sato

Department of Geophysics, Hokkaido University, Sapporo 060, JAPAN

1. INTRODUCTION

Various kinds of unknown and peculiar shapes of snow crystals discovered in the antarctic region were first reported by Kikuchi (Refs. 1-4). Further, most of them were observed within the arctic region (Refs. 5, 6). It was recognized that the temperature conditions of the growth of these crystals were colder than -20°C. Therefore, they were called "Snow crystals of cold temperature types". The main external shapes of these snow crystals of cold temperature types were "Tetragon", "Seagull", "Gohei" types, and so on (peculiar shapes) except columns, combinations of bullets, and crossed-plates. A "Gohei" is a Japanese word for the pendant paper strips hanging from a sacred rope at a Shinto shrine. Almost all of these crystals were of polycrystalline types. Since the first report on the peculiar shapes, the crystal structures and formation mechanisms of polycrystalline snow crystals including the peculiar shapes have received wide attention. The origin of polycrystalline snow crystals is becoming clear by the observations of snow crystals, the freezing experiments of water droplets, and the consideration of models on the formation mechanisms of polycrystalline snow crystals. In order to clarify the formation mechanisms of polycrystalline snow crystals, freezing experiments of supercooled water droplets were carried out by many workers (Refs. 7-12). Kobayashi et al. explained the structure of polycrystalline snow crystals by the "Generalized Coincidence Lattice Site" theory (Ref. 13). Further, Kobayashi et al. proposed a "Cubic Structure Model" at a junction between each component of polycrystalline snow crystals (Ref. 14). Regarding the peculiar shaped crystals, the c-axis of several types of peculiar crystals and their crystalline structure were decided using a polarizing microscope (Ref. 4). The frequency of occurrence of the peculiar shapes in the natural snowfalls was examined in the Arctic Canada (Ref. 15). In order to study the crystal structure, formation mechanisms, and growth mechanisms of the peculiar shaped crystals below -20°C in detail, a new diffusion type of cold chamber was constructed. The purpose of the work reported here is to investigate the production frequency, formation mechanisms, structures, and growth mechanisms of the peculiar shaped crystals growing from the vapor by the use of the new cold chamber.

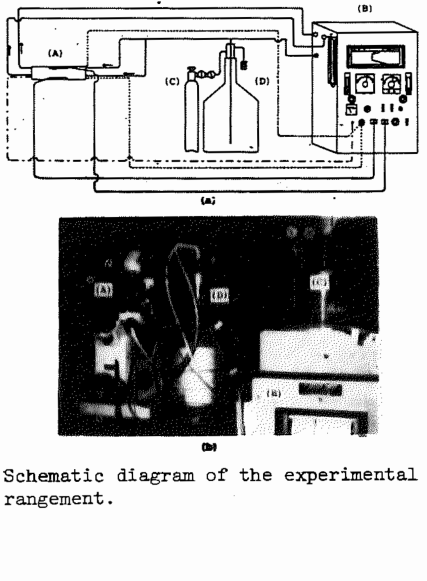

Fig.1. Schematic diagram of the experimental arrangement.

2. EXPERIMENTAL METHOD

A thermal diffusion type cold chamber has been de-igned in order to investigate the peculiar shapes of snow crystals. An outline of the apparatus used in the experiment is shown in Fig.1. It consists of four parts, that is, a cold chamber (A), temperature controller (B), nitrogen gas vessel (C), and a jar of liquid nitrogen (D). The cold chamber was mounted on a stage of an inverted microscope. It is possible to cool or warm the temperatures of upper and lower stages in the chamber independently. Liquid nitrogen in the jar was poured onto the stages of the chamber by the pressure of the nitrogen gas vessel. The flow rate of liquid nitrogen was controlled by the temperature controller in such a way that the temperatures of the upper and lower stages were set up at any desired temperatures. Temperatures of the upper and lower stages were measured with fine thermocouples attached immediately to the surfaces of the stages. A heater is imbedded in the lower stage to control the temperature automatically. The temperature and the rate of temperature change in the chamber can be controlled by the temperature controller programatically. On the other hand, the upper stage can be maintained at the constant temperature desired. Therefore, the temperatures of both stages can be maintained at any desired temperature down to -70°C. The surfaces of both stages were lined with ice sheets formed by freezing of the distilled and deionized water. The ice sheets were the source of water vapor to induce snow crystal growth. At the center of the stages, there are small windows through which the growing snow crystals were observed under a transmitted light. The observation windows were exposed to heated nitrogen gas in order to prevent window frost. Prior to the starting of the experiment, two or three fine filaments using silk threads on which snow crystals were grown, were stretched on a plastic frame with intervals of 1.5 mm apart horizontally through the center of the chamber. The diameter of the filaments was 5 to 20 μm. The temperature of ambient air near the filaments, Ta, was measured by means of a fine thermocouple, likewise. Therefore, three kinds of temperatures at the upper and lower stages, and ambient air, Tt, Tb, and Ta, were recorded by a recorder.

The temperature difference between the upper and lower ice surfaces formed on the upper and lower stages was controlled in such a way that the germs of snow crystals could be nucleated. When a temperature difference, $\Delta T = Tt - Tb$, was given, the snow crystals grew from certain points on the silk filaments. After the appearance of germs on the filaments, Tt and Tb were fixed and steady state conditions were readily achieved. Hence, snow crystals were grown on the filaments under constant temperature. Various types of snow crystal were grown by changing the temperatures of Tt and Tb. The growth of crystals was recorded by taking photographs at appropriate intervals through a microscope, and the growth rate of crystals was measured. Moreover, the c-axis of crystals was determined by use of crossed nicols and sensitive color plates. Experiments were repeated many times, and a number of snow crystals were found to grow in this chamber at

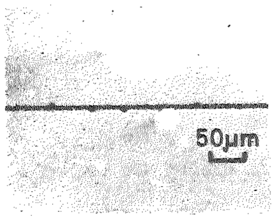

Fig.2. Small water droplets on a thread.

temperatures between -20° and -40°C.

3. RESULTS AND DISCUSSION

3.1 Formation condition of artificial snow crystals

The distance between the two stages in the cold chamber was 6 mm. The temperature profile was measured at intervals of one millimeter by a very fine thermocouple. As a result, the measured temperature showed an almost linear profile. The state of thread at the nucleation stage was indicated in Fig.2. It was found from this photograph that the artificial snow crystals passed through a liquid phase. The condition of supersaturation was at or near water saturation. From the simple experiments, the supersaturation was about 10% after about 10 minutes elapsed from the nucleation of crystals. If the influence of the interface kinetics is taken into account, supersaturation will be about two fold (Ref. 16). Moreover, the supersaturation depended on the number of crystals nucleated in this manner.

3.2 Peculiar shapes of snow crystals made artificially

A number of experiments were carried out and repeated under various air conditions in the cold chamber. Many kinds of peculiar shapes were made artificially. The various types of peculiar shapes were as follows. Typical peculiar shapes of snow crystals made artificially were shown in Fig.3 (a) to (f). Crystal (a) shows one of the typical peculiar shapes of snow crystals with Ta = -23°C. This crystal as seen in figure grew predominantly toward one direction from the center of the crystal which was mainly composed of columns. The hexagonal plates were seen growing on the linear assemblage of columnar crystals. An average growth rate of this crystal was about 0.4 $\mu m \cdot s^{-1}$. This growth rate was greater than theoretical growth rate along the [10$\bar{1}$0] and [0001] directions at water saturation. Crystal (b) grown at -22.5°C is an example of the crystal in which incomplete columns appear on the linear growing part. A c-axis of the linear growing part was different from that of incomplete columns. In these two crystals the structure of coupling is unknown. The crystal which grew alternately on both sides of the growth direction is shown in (c). The c-axes were different between both sides of the growing part of the crystal. The growth temperature of this crystal was -20°C. The average growth rate of this crystal was 0.12 $\mu m \cdot s^{-1}$. The scrolls at the initial stage of growth changed to incomplete columns as the crystal grew. The crystal shown in (d) seems to correspond to "Gohei"

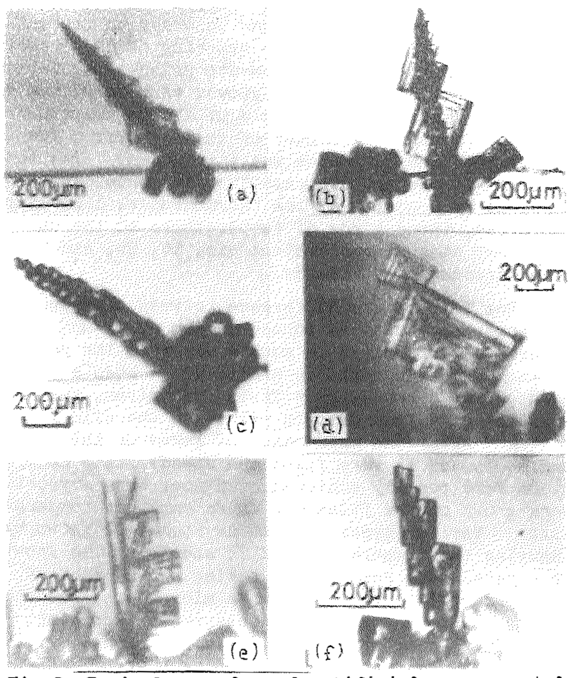

Fig.3. Typical examples of artificial snow crystals of peculiar shapes.

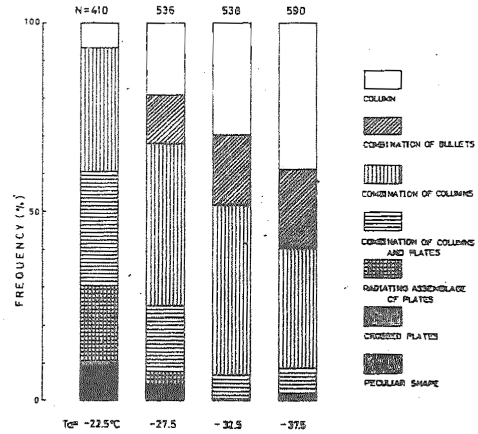

Fig.4. Frequency histograms of the production of each shape of snow crystals.

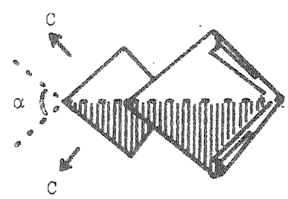

Fig.5. Schematic figure of "Gohei" type crystals.

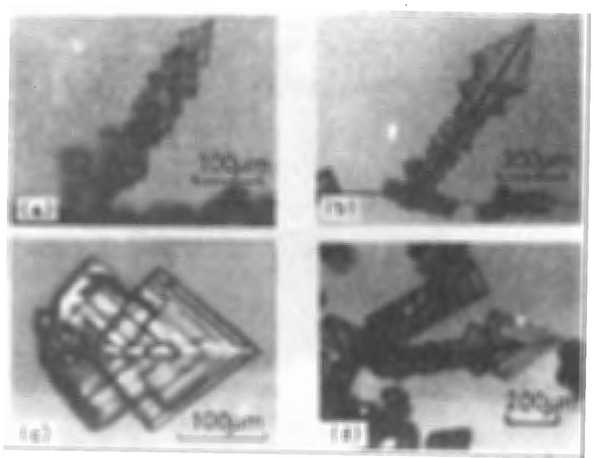

Fig.6. Photographs of "Gohei" type crystals. (a) and (b): artificial, (c) and (d): natural.

type which has a twin structure. Using the cross nicols on this crystal, it was clear that the c-axes were different between both sides of the center line of the crystal. This crystal continues to grow at -24°C. Crystal (e) is a polycrystalline snow crystal which had many columns. The direction of the c-axis of the long scroll was made at a right angle to that of the short scrolls. A scroll continuously originated and grew to a column as time passed. The temperature which this crystal grew was -30°C. Crystal (f) was made at -25°C and was a linear assemblage of incomplete columns. The crystals made artificially as described above had been already observed in the natural environment (Refs.1-6).

3.3 Frequency of occurrence of peculiar shapes of snow crystals

The frequency of occurrence of peculiar shapes of snow crystals was examined in Arctic Canada (Ref. 15). It was reported that the falling frequency of the peculiar shapes against other basic and regular shapes was 3 to 4% on the average although sometimes this rate reached a maximum value of 9%. To compare the frequency of occurrence of peculiar shapes of artificial snow crystals against that of natural snow crystals, experiments were made using a newly constructed diffusion type cold chamber. Artificial making of snow crystals was carried out under the conditions of Ta = -22.5°, -27.5°, -32.5°, and -37.5°C and ΔT = Tt-Tb = 20°C. The crystals grown on filaments in the chamber were classified into seven types depending their shapes, namely, columns, combination of bullets, combination of columns, combination of columns and plates, radiating assemblage of plates, crossed-plates, and peculiar shapes. The percentages of these crystals to the total numbers examined were calculated at each temperature. Results are shown in Fig.4. The numbers in the upper part in the figure show the total numbers of snow crystals made at each air temperature, Ta, in the chamber. The ordinate shows the frequency of occurrence of each shape of snow crystals. The percentages of occurrence of peculiar shapes were 9% at -22.5°C, 4% at -27.5°C, 1% at -32.5°C, and 2% at -37.5°C, respectively.

The frequency of occurrence of the peculiar shapes to the basic and regular shapes of snow crystals was 3.4% on the average of all data. The result seems to be equal to the frequency of peculiar shapes in natural observations (Ref. 15).

3.4 Formation mechanisms of "Gohei" type crystals

"Gohei" type snow crystals which are the most typically polycrystalline peculiar crystals in natural conditions were also made artificially. These crystals were defined as follows; (1) polycrystalline, (2) symmetry, (3) closed tip, (4) multiplicity. A Gohei type crystal is shown in Fig.5, schematically. Examples of Gohei type crystals are shown in Fig.6. The tip angle α (Fig.5) of artificial Gohei type snow crystals were 78° (Fig.6 (a)) and 55° (Fig.6 (b)).

In order to study the presence of a rule in the tip angle of Gohei type, microphotographs and replicas of Gohei type crystals which were taken and replicated in the polar region were available for examination (Refs. 1-6). The total number of crystals examined in this analysis was 116 of which 53 were taken by microphotographs. The result is shown in Fig.7. It was found that the number frequencey of tip angle had a maximum peak around 77° and a minor peak around 54°. The distribution around 66° was indistinct. The Gohei type crystals which were observed in the polar region are indicated in Fig.6 (c) and (d).

The formation condition of Gohei type is be-

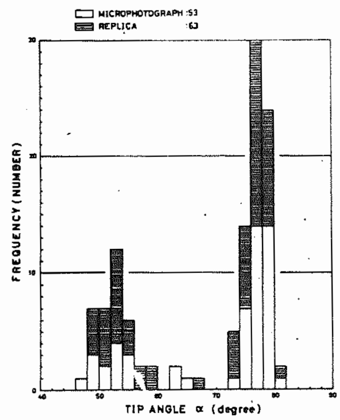

Fig.7. Frequency histograms of the tip angle (α).

coming clear by the observation of snow crystals in natural environment and the experiments of artificial making of snow crystals. (1) There was a rule in the tip angle of Gohei type, (2) Gohei type crystals grew as a part of combination of bullets, and (3) the condition of saturation at the nucleation was at or near the water saturation. Therefore, it was concluded that Gohei type crystals grew from frozen cloud droplets. From these results, it was considered that a polycrystalline snow crystal was defined by their c-axes when a cloud droplet was frozen, and if at that time two prism planes grew and crossed each other having a small angle, their crossing planes grew as a Gohei type crystals.

The formation processes of axial angle between the c-axes were considered by the same manner as Uyeda and Kikuchi (Ref. 17). It was assumed that the polycrystalization in a frozen water droplet was formed according to the cubic structure model on a basal plane of ice (Ref. 14). When polycrystalization commenced on a basal plane of a hexagonal ice, the direction of the c-axes of C_1, C_2, ...and C_6 indicated in Fig.8 would be constructed in the water droplet. Further, if a cubic structure was formed again on a basal plane of the crystal, of which c-axis was one of the c-axes of C_1, C_2, ...and C_6, six new directions of the c-axes would be made as shown on the right hand side in Fig.8.

Here new directions C_1, that is, six new directions C'_{11}, C'_{12}, ...and C'_{16}, were taken toward C_1. Similary, six new c-axes were formed on each of C_2, C_3, ...and C_6. The six new c-axes on C_2, C_3, ... and C_6 were symbolized as C'_2 (C'_{21}, C'_{22}, ...and C'_{26}), C'_3 (C'_{31}, C'_{32}, ...and C'_{36}), ...and C'_6 (C'_{61}, C'_{62}, ...and C'_{66}). Thus, new c-axes of 36 directions were formed. By the combination of two of the new c-axes, the axial angle between the c-axes was calculated.

Selecting one of the directions of these c-axes and one of the directions of three a-axes, one prism

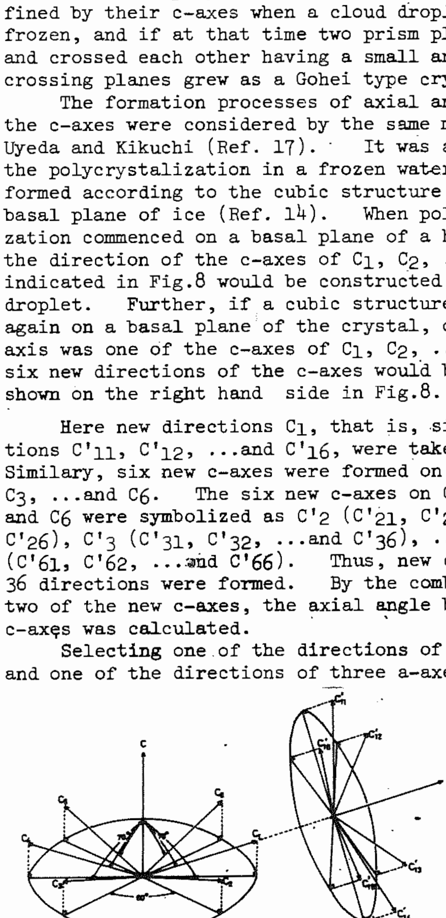

Fig.8. An arrangement of the c-axes.

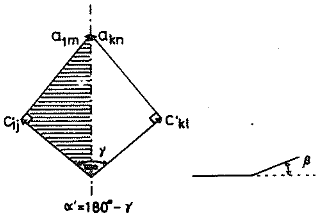

Fig.9. ^ngles of α' and β of "Gohei" type crystals.

	α'	β
C'_1-C'_1	* 56°	19°
	39°	19°
C'_1-C'_2	* 66°	11°
C'_1-C'_6	* 78°	13°
	32°	16°
	* 56°	19°
	39°	19°
C'_1-C'_3	* 66°	11°
C'_1-C'_5	32°	16°
	* 56°	19°
	39°	19°
C'_1-C'_4	* 66°	11°
	* 68°	18°
	* 56°	19°
	39°	19°

Table 1. Calculation results of the angles of α' and β.

plane was decided. The crossing angle of two prism planes, β, was calculated. A combination of two prism planes satisfying the following two conditions is listed in Table 1. The conditions were (1) $\beta < 20°$ and (2) two c-axes were in symmetry with respect to the crossing line of two prism planes (Fig.9). An α' indicates a supplementary angle of angle between c-axes of two prism planes γ. $\alpha' = 78°$ and $\beta = 13°$, $\alpha' = 56°$ and $\beta = 19°$, and $\alpha' = 68°$ and $\beta = 18°$ ($\alpha' = 66°$ and $\beta = 11°$) which were marked by (*) in Table 1 seem to correspond to the peaks $\alpha = 77°$, 54°, and 66°, respectively. The reason why the peak 77° is predominant seems to be that the density of coincidence sites on a composition boundary is large.

4. CONCLUSION

Using a new diffusion type cold chamber, various kinds of peculiar shaped crystals were made artificially, which had already been observed in natural condition. And the production frequency of the peculiar shapes was the same value as natural snowfalls found in Arctic Canada. Moreover, the Gohei type crystals which were the most attractive peculiar shapes were produced artificially. Assuming that a crystal took a cubic structure twice on the basal planes of (0001) of frozen cloud droplet at the nucleation stage and prism planes $(10\bar{1}0)$ of crystals grew at the initial growth stage, this rule in the tip angle of Gohei type crystals may be acceptable as one of the formation mechanisms of Gohei type crystals.

5. REFERENCES

1. Kikuchi K 1969, Unknown and peculiar shapes of snow crystals observed at Syowa Station, Antarctica, J Fac Sci, Hokkaido Univ, Ser VII , 3, 99-116.
2. Kikuchi K 1970, Peculiar shapes of solid precipitation observed Syowa Station, Antarctica, J Meteor Soc Japan, 48, 343-349.
3. Kikuchi K and K Yanai 1971, Observation on the shapes of snow crystals in the South Pole region in the summer, Antarctic Record, Polar Res Center, Tokyo, 41, 34-41.
4. Kikuchi K and A W Hogan 1976, Snow crystal observations in summer season at Ammundsen-Scott South Pole Station, Antarctica, J Fac Sci, Hokkaido Univ, Ser VII , 5, 1-20.
5. Kikuchi K and C Magono 1978, General description of the meteorological conditions and shapes of snow crystals during the observation period at Inuvik, N.W.T., Canada, Snow Crystals in the Arctic Canada, Hokkaido Univ, Japan, 172pp. (Edited by C. Magono).
6. Kikuchi K et al 1982, Observation of wintertime clouds and precipitation in the Arctic Canada (POLEX-North) Part 2 : Characteristic properties of precipitation particles, J Meteor Soc Japan, 60, 1215-1226.
7. Hallett J 1964, Experimental studies of the crystallization of supercooled water, J Atmos Sci, 21, 671-682,
8. Higuchi K and T Tosida 1966, Crystallographic orientation of frozen droplets, Physics of Snow and Ice, Vol. 1 (Inst Low Temp Sci, Hokkaido Univ Sapporo) 79-93.
9. Aburakawa H and C Magono 1972, Temperature dependency of crystallographic orientation of spatial branches of snow crystals, J Meteor Soc Japan, 50, 166-170.
10. Murray W and R List 1972, Freezing of water drops, J Glaciology, 11, 415-429.
11. Uyesa H and K Kikuchi 1976, On the orientation of the principal axis of frozen water droplets, J Meteor Soc Japan, 54, 267-275.
12. Uyeda H and K Kikuchi 1979, Measurements of the principal axis of frozen hemispheric water droplets, J Meteor Soc Japan, 58, 52-58.
13. Kobayashi T et al 1976, On twinned structures in snow crystals, J Crystal Growth, 32, 233-249.
14. Kobayashi T et al 1976, Cubic structure models at the junctions in polycrystalline snow crystals, J Crystal Growth, 35, 262-267.
15. Kajikawa M et al 1980, Frequency of occurrence of peculiar shapes of snow crystals, J Meteor Soc Japan, 58, 416-421.
16. Beckmann W 1982, Interface kinetics of the growth and evaporation of ice single crystals from the vapour phase III, Measurements under partial pressures of nitrogen, J Crystal Growth, 58, 443-451.
17. Uyeda H and K Kikuchi 1982, Some considerations on combination of bullets which have the axial angle between the c-axes of 90°, J Fac Sci, Hokkaido Univ, Ser VII , 7, 145-157.

AERODYNAMIC CONDITIONS OF ICE CRYSTAL GROWTH BY AGGREGATION AND DROPLET DEPOSITION

Josef Podzimek

Department of Mechanical and Aerospace Engineering
and Graduate Center for Cloud Physics Research
University of Missouri-Rolla, MO 65401, USA

1. ICE CRYSTAL MOTION INVESTIGATIONS

Much attention has been paid in the past to the motion and aggregation of planar and columnar crystals. As long as the crystal remains steady on its trajectory, one can describe its behavior by simple terms, such as the aerodynamic drag or the steady settling velocity. Both parameters are functions of the corresponding Reynolds number (Re) and Best number (Be). The last parameter can be expressed as a function of the corresponding drag coefficient (C_D) and Re. From the extended discussion of this subject by Pruppacher and Klett (Ref. 9) and other investigators, one can make the following conclusions:

In most of the theoretical studies a good agreement between the numerical solution and experimentally found flow field around a thin disk was found for Re $\leq$ 100. From the experiments by Willmarth et al. (Ref. 15) we learned that the shedding of vortices behind a thin disk starts at Re ~ 100. At this Re it is assumed that a thin disk starts to oscillate and its amplitude increases with increasing Re, until a glide-tumbling motion originates.

The fall of columnar-type models, approximated often by cylinders of different ratio of the cylinder diameter, d, and length, L, was investigated theroretically and experimentally as well. Analytical solutions are usually related to the classical approach by Lamb who calculated the drag per unit length of an infinite cylinder as a function of Re. For Re > 0.2 one has, however, to resort to a numerical solution which was presented by several authors. The standing eddy on the reverse side develops at Re ~ 6.0 and grows linearly with increasing Re until Re ~ 40.0. At Re > 40.0 the shedding of vortices was observed in accordance with the numerical models.

The non-steady motion of falling planar models was studied by Podzimek (Refs. 4, 5, 6, 7), Schemenauer (Ref. 11) Stringham et al. (Ref. 14), List and Schemenauer (Ref. 3), and Sasyo (Ref. 10). These investigations are based on several simplifying assumptions and present often only the simple description of the model trajectory, without any casual relationships between the observed parameters. First attempts to analyze in detail the motion of a free falling disk at 2200 < Re < 4450 were made by Stewart (Ref. 12) and Stewart and List (Ref. 13).

The purpose of this contribution is to review the old measurements with planar and columnar models falling in liquids, Podzimek (Refs. 4, 5, and 6) and to complete them with the studies of falling planar models in the air, Podzimek (Ref. 8). Further, an attempt will be made to summarize some of the measurements with several aerodynamically interacting models.

2. EXPERIMENTAL FACILITIES

The experiments with aluminum models falling in a mixture of glycerol and water were performed in a glass tank of main dimensions 1.5 x 0.6 x 0.6 m^3. The motion of a falling model was recorded by two movie cameras, one placed approximately 100 cm in front of the side wall and the other 50 cm above the top of the tank. Records with 24 frames per second were made after the model resumed its steady mode of motion (between 30 cm and 50 cm from the liquid surface). The correction on the hydrodynamic effect of the wall proximity was usually less than 1%. The liquid viscosity was controlled before each experiment during which the liquid temperature was kept constant within $\pm$ 0.05°C. Probable errors in determining the model fall velocity from the projected pictures were smaller than $\pm$ 3% (resp. $\pm$ 7%) for planar models falling at Re < 200 (resp. Re < 6000). For columnar models these errors were slightly lower. The models were made of aluminum with the diameter of the circle circumscribed to plates and stars 50 mm (thickness h = 1.5 mm), 20 mm (h = 0.5 mm) and 10 mm (h = 0.2 mm). The diameters of columnar models were 20 mm, 10 mm, 5 mm with the d/L ratios 1; 1/2; 1/4; 1/6.

Experiments with falling paper models were made in a large plexiglass cylinder or in a large environmental chamber adapted for the photographing of the models illuminated by strobo-flash. Estimates about the third dimension of the model trajectory were made from the comparison with the scale picture distorted by the perspective. That explains larger errors ($\pm$ 15%) in determining the model position in the direction of the photographic camera optical axis in comparison with the two coordinates perpendicular to it (mean error smaller than $\pm$ 6%). The evaluation of the mean errors in determining the model position refers to the projection of the 35 mm film record on the screen at a magnification 10:1. The influence of a side wind (0.7 m/s to 1.0 m/s) on the mode of settling of planar models has been studied in the same environmental chamber (4.10 x 1.70 x 2.00 m) which was converted into a low speed wind tunnel with the cross-section of the experimental space of 1.80 m x 1.67 m. A detailed description and sketch of the tunnel was published elsewhere, Podzimek (Ref. 8). The models falling in the air were cut out of high quality paper of the density, ρ_p = 0.97 g cm^{-3}, and thickness h = 0.017 cm. A few models were made of styrofoam 0.15 cm and 0.50 cm thick.

3. CHARACTERISTICS OF THE STEADY FALLING MODELS

3.1 Plate-Type Crystals

Figure 1 summarizes the results of experiments with disks made in liquids, Podzimek (Refs. 4, 5, 6) and in the air, Podzimek (Refs. 7, 8). At Re < 2 the measured data agree very well with the theory and experiments of other investigators. For 2 < Re < 30 the measured values of C_D are closer to the curves obtained by Oseen or Pitter than to that calculated by Oberbeck [Pruppacher and Klett (Ref. 9, p. 333)]. Between Re = 30 and Re = 100 a transition from a quiescent fall to markable oscillatory motion develops. At Re > 100 a substantial difference between the observed motion in the liquid and in the air is apparent and the values of C_D vary considerably over the domain of Re between 100 and 1500. The increase in C_D beyond Re = 1000 is explained by the fact that C_D is related to the vertical component of the settling velocity v_z (and therefore to Re_z) which, however, becomes smaller than the horizontal component v_x at an intense swinging. There is a large scatter and poor response of the C_D points calculated from the measurement in liquids (mixture of glycerol and water - marked in Fig. 1 by circles o) and in the air (marked by □). The disk motion in the air is characterized often by temporary gliding or tumbling, especially at side wind conditions (marked by Δ). This will be discussed in the section of unsteady model motion.

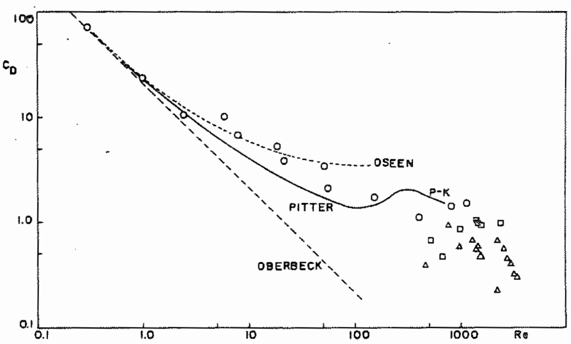

Fig. 1

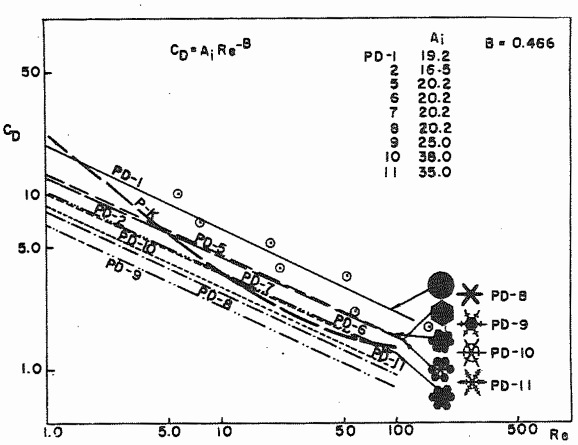

Fig. 2

Plates with outgrows and star-like crystals show much greater stability of movement than simple plates and plates with large sectors. In Fig. 2 are plotted curves of $C_D = f(Re_z)$ for a disk (PD-1) and several planar models (PD-2 and PD-5 to PD-11) the shapes of which are drawn next to the lines representing a simplified relationhip $C_D = A_i Re^{-B}$. The lines are the best fit to the points calculated from the velocity of falling models, their geometry, weight and parameters characterizing the state of the fluid. Only the individual points for a disk (PD-1) are plotted. Practically, all lines in Fig. 2 are parallel for 1.0 < Re < 100.0. The lines are normalized and refer to an "equivalent disk" corresponding to the main cross-section of a hexagonal plate (PD-2). After comparison of the position of individual lines, one concludes that the lines for plate, plate with outgrows and star with large sectors (PD-2, PD-5, PD-6) are almost identical, while star-type and dendritic models deviate considerably from the "equivalent disk" substitution suggested by Jayaweera (Ref. 1).

3.2 Columnar-Type Crystals

The steady falling columnar crystals are characterized by the curves $C_D = f(Re)$ where Re is referred to the diameter of the circle circumscribed to the hexagonal base of the column, d, C_D depends also on the ratio d/L, where L is the column length. For the range 1 < Re $\lesssim$ 100 is suggested a simple relationship $C_D = A_c Re^{-Bc}$, which is simpler than the empirical formula suggested by Jayaweera and Cottis (Ref. 2).

In Fig. 3 are plotted lines representing the best fit of measured data to the relationship $C_D = A_c Re^{Bc}$ for cylinders with the ratio of the hexagonal base diameter, d, to the length of the column, L, 1:1(C-1), 1:2(C-3), 1:4(C-5) and 1:6(C-6). The model C-3 (with an axis ratio of 1:2) was slightly different than the other three. It had a hollow conical space on both ends the depth of which was equal to the radius of the base. From Fig. 3 and other experiments one can deduce the following characteristics of falling columns:

The formula $C_D = A_c Re^{Bc}$ is a reasonably good approximation to the measured values for a long cylinder [P-K line in Fig. 3 was replotted from Pruppacher and Klett (Ref. 9)] especially if compared to long columns (C-5, C-6).

Model C-1 (with an axis ratio 1:1) fell at 7 < Re < 150 with the main axis in the direction of its vertical path. Around Re = 150 the model started to fall with its main axis in horizontal position. At Re corresponding to several hundreds the model started to oscillate along its main axis (in horizontal position) and performed a slight trochoidal movement along its path. The trajectory was slightly inclined from the vertical (3° to 8°).

Columns C-3 and C-5 remained steady with the main axis in horizontal position until Re = 200 and then began to swing slightly and deviate (6° to 11°) from the vertical.

The influence of hollow spaces at the ends of columnar crystals on the value of the drag coefficient, C_D, is insignificant. The ratios of C_D (solid model)/C_D (with hollow space) have the following values for Re = 50 and Re = 200 (in parenthesis): For axis ratio 1/2 1.1207 (1.1580), for 1/4 1.0430 (1.0672) and for 1/6 1.0325 (1.0517).

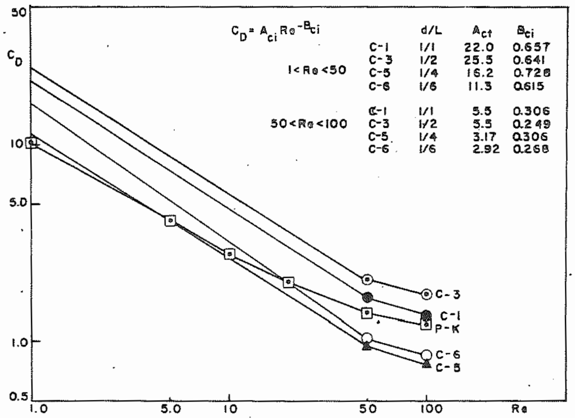

Fig. 3

The behavior of pyramidal models with the angles at the top 60° (model PY-1) and 30° (PY-2) can be characterized in the following way: PY-1, at Re between 13.4 and several thousands, usually fell with the tip down. However, the position was not stable. At Re = 39.2 the model fell a long distance with the tip up. Model PY-2 settled quietly with the tip up at Re below 25. Around Re = 50, it increased the amplitude of the processional movement. At Re = 100 the model started to fall with sideways its main axis approximately in horizontal position. The C_D values for steady fall (tip down or up) were:

$$\text{PY-1 } C_D = 4.7\ Re^{-0.364};\ \text{PY-2 } C_D = 3.95\ Re^{-0.213}.$$

Several columnar models with a pyramid at the end were investigated: Two columns with the height of one diameter of the base. One had a pyramid with the angle 60° (PJ-3), the other with 30° (PJ-4). Two columns with the height of two diameters of the base and the pyramid top angle 60° (PJ-5) and 30° (PJ-6). In general, it can be said that bullet-type models of crystals fall quietly with their major axes in horizontal position up to Re = 100. For this region of Re_z (related to the vertical component of the velocity of a falling model) the C_D values are:

$$\text{PJ-5 } C_D = 3.05\ Re_z^{-0.165};\ \text{PJ-6 } C_D = 2.55\ Re_z^{-0.132}.$$

Due to the hydrodynamic forces acting on a column with a pyramid at the end, the model moved in the direction opposite the tip of the pyramid during its fall. This horizontal component of the velocity of falling bullet-type models is apparent in Fig. 4.

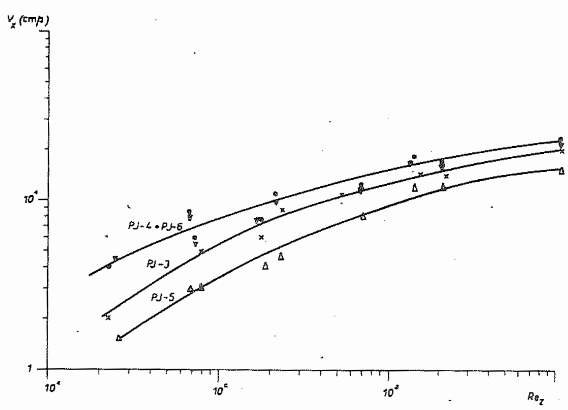

Fig. 4

4. UNSTEADY MOTION OF SWINGING MODELS

4.1 Planar Models

Time lapse camera and stroboscopic pictures allowed identification of the following parameters featuring each fall experiment: Model velocity, $V(V_x, V_y V_z)$, angular velocities of motion, $\omega\ (\omega_x, \omega_y, \omega_z)$, angle of attack of a planar model, , frequency, n, amplitude δ and "wave" length of the oscillatory motion, λ. From these parameters and from the knowledge of the model weight, geometry and from the known fluid properties (viscosity, density) the parameters of similarily were deduced such as Re, Best number, Willmarth's stability number and Strouhal number. An attempt was also made to relate some of these parameters to planar models performing an oscillatory motion during their fall in fluids, Podzimek, (Ref. 7). The main conclusions from these studies are the following:

The comparability of the experiments with swinging models made in liquids and in the air is poor, and the author believes, impossible. In Fig. 5 we plotted the amplitudes, δ, of regularly oscillating planar models in a mixture of water and glycerol and the amplitudes of a paper disk falling in the air. The difference in slope of both curves for $700 < Re_z < 3000$ (unrealistic in nature) is obvious. It can be explained by energy transfer during a model motion in liquid and in the air which causes a spectacular difference in model acceleration in a liquid (up to 200 cm s^{-2} and in the air (up to 1000 cm s^{-2}).

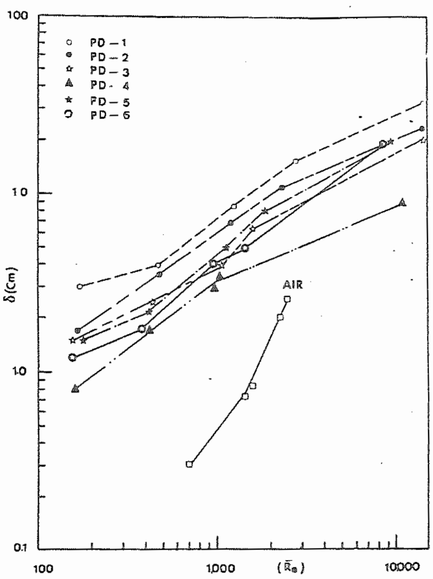

Fig. 5

Slight side wind (0.7 m s^{-1}) has a markable effect on the mode of falling models for Re > 900, however, it does not affect much the mean velocity of settling models.

4.2 Columnar Models

The studies of the falling columnar models were performed mainly in liquids, where it was possible to follow the model slight oscillatory motion at Re > 200 with high accuracy. At Re exceeding several hundreds the columnar models start to twist around their main axis and their wave-like path reminded a trochoid-type curve.

The swinging of bullet-type (column with a pyramid on the end) models is featured by a sideways component of fall motion (Fig. 4) and usually by a complicated precession of the main axis. The periodically appearing instability of movement is fully developed after the models surpassed Re = 2000 and started at smaller Re in the case of shorter pyramids and shorter columns (PJ-3).

5. AERODYNAMIC INTERACTION OF SEVERAL FALLING MODELS

Planar crystals interact if they are closer than one diameter sideways and less than five diameters in the wake of their precursors at $50 < Re < 80$. In Fig. 6 are plotted positions z of hexagonal plate models (measured in diameters, D, of the leading plate) in the wake of the plate of the same size. The position, z, of the leading plate settling at a mean velocity of 13.1 cm s^{-1} is expressed also in plate diameters, D. Two different observations are plotted in the same figure: a) leading plate falling at mean Re = 55.7 is followed by the same plate which will acquire in the wake of its precursor the mean velocity corresponding to Re = 78.2. At the time t = 0 their distance was 3.15 D. b) Two plates follow the "leader" of the same size and aggregate successively with it. The leading plate is falling at a mean velocity corresponding to Re = 49.4, the third one aggregated first with the second one and then both reached in the "leader's" wake a velocity corresponding to Re = 60.2.

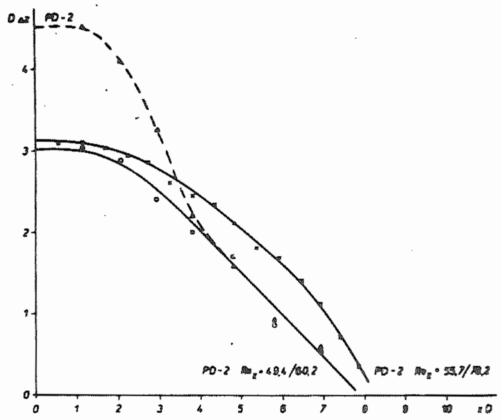

Fig. 6

A series of systematic experiments with falling columns concentrated on the aerodynamic interaction of long columnar models (C-6) with crossed and parallel main axes.

6. CONCLUSION

Useful relationships were found between the mode of movement of falling planar and columnar models simulating the fall of ice crystals in the atmosphere and the important parameters such as C_D, Re and Best number.

The fall of compact planar models can be approximated by an "equivalent disk" diameter for Re < 70.

The effect of a side wind of 0.7 m s^{-1} on the mode of motion of a planar crystal is considerable. However, it affects only slightly the settling velocity of planar models.

The comparison of model settling characteristics in liquids and in the air is satisfactory for Re < 200. However, for Re > 500 the deviation of calculated C_D is large due to the different mode of oscillatory motion in both media.

7. REFERENCES

1. Jayaweera, K.O.L.F., 1972, An equivalent disc for calculating the terminal velocities of plate-like ice crystals, J. Atmos. Sci., 29, 596-598.
2. Jayaweera, K.O.L.F., and Cottis, R.E., 1969, Fall velocities of plate-like and columnar ice crystals, Quart. J.Roy. Meteor. Soc., 95, 703-709.
3. List, R., and Schemenauer, R.S., 1971, Free fall behavior of planar snow crystals, conical graupel and small hail, Bull. AMS, 47, 110.
4. Podzimek, J., 1965, Movement of ice particles in the atmosphere, Proc. Int. Conf. Cloud Phys. Tokyo-Sapporo, May, 224.
5. Podzimek, J., 1968, Aerodynamic conditions of ice crystal aggregation, Proc. Int. Conf. Cloud Phys., Univ. Toronto, 295-299.
6. Podzimek, J., 1969, The Growth of an Ice Crystal in a Mixed Cloud (in Czech), Part I and II, D.Sc. Thesis, Charles University, Prague.
7. Podzimek, J., 1981, Clearing of Military Smoke Cloud with Scavenging Technique, Final Rep. DAAG 29 79 C 0073, Univ. of Missouri-Rolla, GCCPR, Rolla, June.
8. Podzimek, J., 1982, Study of the motion of bodies simulating the fall of ice crystals, Prepr. Vol. Conf. on Cloud Physics, Chicago; AMS, Boston, 103-105.
9. Pruppacher, H.R., and Klett, J.D., 1978, Microphysics of Clouds and Precipitation, D. Reidel, Publ. Dordrecht.
10. Sasyo, Y., 1971, Study of the formation of precipitation by the aggregation of snow particles and the accretion of droplets on snowflakes, Pap. Meteor. Geophys, 22, 69-142.
11. Schemenauer, R.S., 1969, Measurements of the Drag Coefficients and Characteristic Motions of Snow Crystals, Gaupel and Small Hail Models, M.S. Thesis, Univ. of Toronto.
12. Stewart, R.E., 1977, Experimental Investigation of the Aerodynamics of Freely Falling Disks, Ph.D. Thesis, Univ.of Toronto.
13. Stewart, R.E., and List, R., 1980, The aerodynamics of freely falling disks and implications for understanding the free fall motions of atmospheric particles, Proc. Int. Conf. Cloud Physics, Clermont-Ferrand, 299-302.
14. Stringham, G.E., Simons, D.B., and Guy, H.P., 1969, The Behavior of Large Particles Falling in Quiescent Liquids, Geol. Survey Prof. Paper 562-6, Washington, D.C.
15. Willmarth, W.W., Hawk, N.E., and Harvey, 1964, Steady and unsteady motions and wakes of freely falling disks, Phys. Fluids, 7, 197-208.

THE COLLECTION EFFICIENCIES OF SOFT-HAIL PELLETS FOR ICE CRYSTALS

C P R SAUNDERS and N JALLO
Physics Department, UMIST, MANCHESTER M60 1QD, ENGLAND

1. INTRODUCTION

There is little data available of the collection efficiencies of soft-hail pellets for ice crystals. In laboratory experiments, the numbers of ice crystals collected by 360μm and 3mm diameter ice targets were determined and corresponding values of collection efficiency of around 0.1-0.2 and 0.3 respectively were found (Ref.1,2) These workers used small vapour grown ice crystals up to a mean size of 8μm for which they assumed a collision efficiency of unity with the ice target. In clouds, the ice crystals have time to grow to larger sizes for which collection efficiency data is not available.

Recently, a new method of measuring collection efficiencies has become available following studies of the electric charge that is separated when ice crystals bounce off a riming ice target. This work had an objective of simulating thunderstorm charge transfer processes in the laboratory. The techniques developed proved to give reproduceable results as long as the cloud conditions, which were closely monitored, were reproduced. (Ref. 3). In these studies, ice crystals were grown in a cold room, up tc 100μm in size, from a cloud of supercooled water droplets. The cloud was nucleated by the brief presence of a fine wire cooled in liquid nitrogen. A target rod, representing a soft-hail pellet, was either moved through the cloud on a rotating frame or was held stationary while the cloud was drawn past it. During the interactions of the ice crystals with the riming target, the current to the target was measured. The moving target was used up to speeds of about 3.6m s^{-1}, but above this speed, unwanted rotational forces were avoided by using a stationary target.

During ice crystal collisions with the riming target, electric charge was transferred across the crystal/rimer interface, so that crystals which separated from the rimer removed charge. The nett effect of many such interactions was to produce a current to the rimer which passed through an amplifier to earth and could be measured. Thus, with a knowledge of the ice crystal concentration, the charge transfer per collision could be estmated by assuming a collision efficiency of unity. Also of interest is the size of the charge removed by each separating crystal. The separation probability is a function of whether most of the colliding crystals leave the rimer with a small charge or whether only a few of the colliding crystals separate but with a larger charge. The product of the separation probability (the fraction of colliding crystals that separate) and the collision efficiency (the fraction of crystals in the geometric path of the rimer that impact) is here called the Event Probability, (EP).

By simultaneously measuring the current to two riming targets of different diameter, the ratio of the currents may be obtained which is related to the ratio of their EP values. One of the targets consisted of a fine stainless steel wire of 0.25mm diameter, for which the Event Probability may be taken as being close to unity. An upper value of EP for the other, thicker, riming target can then be determined. If d and D are the diameters of the thin and thick riming targets, of equal length, then:

$$EP_D = \left(\frac{I_D}{I_d}\right)\left(\frac{d}{D}\right)EP_d$$

where I is the current to each target.

2. THE EXPERIMENT

Two riming targets were mounted across the end of an open tube of diameter 38mm, the other end of which was connected to a suction pump. The tube was mounted within the cold room so that a cloud of supercooled water droplets and ice crystals could be drawn past the targets at a known speed. Both targets thus experienced identical cloud conditions. The targets were insulated from the supporting tube and the currents to them were monitored during crystal interactions.

The figure shows the results at three temperatures and three velocities for a target of diameter 5mm. Because the small currents were hard to measure at low velocities, the results at 3.6m s^{-1} were obtained with 30cm long targets on a rotating frame which provided a higher rate of interactions than did the shorter stationary targets. Rotational effects were not found to cause problems at low v .ocities. Each point on the figure is the average of about 30 individual experiments. Throughout each experiment, the ice crystals grew to a maximum size of about 100μm before they fell out of the cloud; however, at large sizes, there were so few crystals left that the current was immeasurable. The effect of crystal size on the EP values was not found to be as great as that of temperature, hence all values plotted on the figure shown are average results obtained for ice crystals in the size range 30 to 60μm. The error bars for each point indicate the standard deviation of the mean of the 30 values of EP while the lines are best fits having coefficients of determination close to 0.9. The values of EP for the thicker target were calculated assuming that for the thinner target EP_d =1. EP_d may be slightly less than unity but in view of the size of the errors involved, small changes in EP_d do not significantly alter EP_D values. In any case, the values shown are maximum values of EP_D.

3. CONCLUSIONS

The results show that the event probability increases at colder temperatures in line with the generally observed decrease of "stickiness" of ice at lower temperatures. The collision efficiency is unaffected by temperature, hence the graphs represent the effect of temperature on the separation probability of ice crystals impacting on a riming target. There is no evidence here of the observation (Ref.1) that the collection efficiency is higher at -11°C than at warmer or colder temperatures.

The increase of EP values with higher velocities indicates that the impacts are not modelled well by the concept of deformable ice crystals hitting a soft ice surface - the crystals behave more like rigid spheres bouncing off a firm surface. However, there may be break-up of the crystals during the collision and evidence for or against this is being sought at present.

The values of EP are surprisingly low. If a collision efficiency of unity is assumed, then the event probability ranges between 0.1 and 0.5 corresponding to adhesion efficiencies of between 0.9 and 0.5. The results indicate that soft-hail and hailstones will collect ice crystals in clouds although this is not a well-documented observation. In order to verify that ice crystals are retained on the rimer surface, a fresh rime sample was scraped off a rimer target and was viewed through a microscope. Indeed, ice crystals could clearly be seen trapped in the lattice of frozen supercooled droplets.

REFERENCES

1. Hosler C L and Hallgren R E 1960 The aggregation of small ice crystals. Disc. Faraday Soc., 200-207

2. Latham J and Saunders C P R 1970 Experimental measurements of the collection efficiencies of ice crystals in electric field. Quart J Roy Met Soc, 96, 257-265

3. Jayaratne E R, Saunders C P R and Hallett J 1983 Laboratory studies of the charging of soft-hail during ice crystal interactions. ibid, 109, 609-630

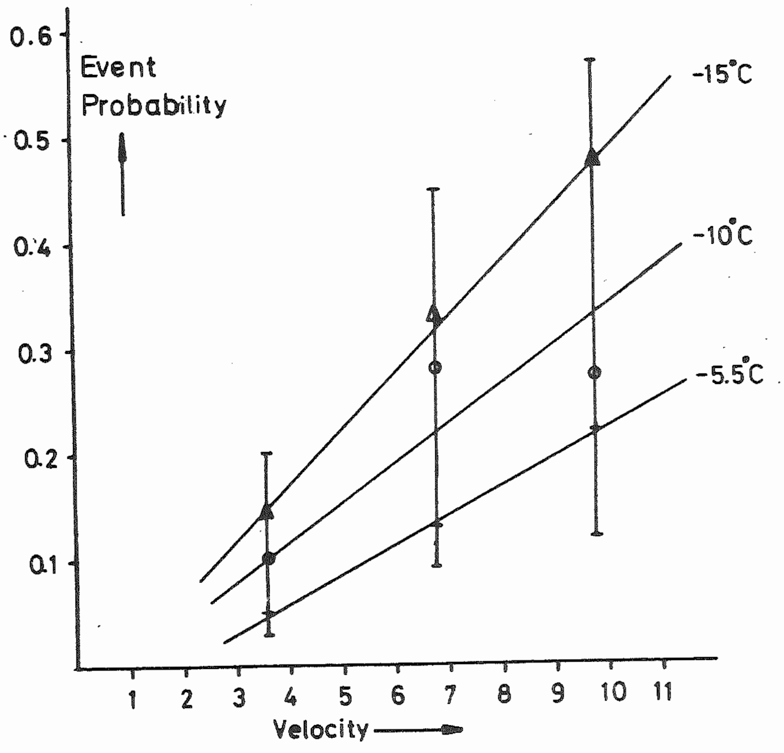

The event probability of ice crystals impacting on a riming target as a function of velocity.

NEW MODELS OF ICE CRYSTAL GROWTH LAW IN TEMPERATURE - ICE SUPERSATURATION OR VAPOR DENSITY EXCESS FIELD

Ang Sheng Wang

Institute of Atmospheric Physics, Academia Sinica
Beijing, The People's Republic of China

ABSTRACT

On the basis of a great number of our experimental data in new wedge-shaped chamber whicw has stable enviromental conditions and we can measure three dimension sizes of ice crystal easy in here. A new model of ice crystal habit variation with temperature and ice supersaturation, and another new model of ice crystal habit variation with temperature and vapor density excess have been presented in the paper. In lower ice supersaturation, they are different from former models which were used about 20 years. New models are much better than former models, and more closed natural observational results.

Keywords: Cloud Physics, Ice crystal, Chamber, Model, Experiment.

1. FORMER MODELS

It is well know, the law of ice crystal in temperature - ice supersaturation field is a very important and basis problem. During recent 30 years, many scientists engaged a lot of experimental works, and got a volume of data of ice crystal growth. Many models of ice crystal growth law had been summarized by use of above data.

On the basis of M. Hanajima's (1949, Ref.1), U. Nakaya's (1951, 1954 and 1955; Ref.2, 3, 4), and J. Hallett and B. J. Mason's (1958, Ref. 5) etc. experiments, J. Hallett and B. J. Mason (1958) presented first model in which there hadn't data of lower ice supersaturation region. In 1961, T. Kobayashi (Ref. 6) firstly got a few data of ice crystal growth in lower ice supersaturation region, and gave his famous model on the basis of former models and his new data. During recent 20 years, many scientific papers and books on Cloud Physics or Atmospheric Physics applied his result. For example, N. H. Fletcher's book (1962, Ref.7), P. V. Hobbs's book (1974, Ref.8), D. Rottner and G. Vali's paper (1974, Ref.9), Takehiko Gonda's paper (1974, Ref. 10), R. R. Rogers's book (1976, Ref.11), R. Lacmann's paper (1977, Ref.12), H. R. Pruppacher and J. D. Klett's book (1978, Ref.13), T. Kuroda and R. Lomann's paper (1980, Ref.14), and H. R. Pruppacher's paper (1981, Ref. 15) etc. That means T. Kobayashi's model was very important and basic. In 1978 only, H. R. Pruppacher and J. D. Klett (Ref.13) modified his model a little according to B. J. Mason's (1971, Ref. 16), J. Hallett and B. J. Mason's (1958, Ref.5), and D. Rottner and G. Vali's (1974, Ref.9) etc.works.

Now, a former variation model of ice crystal habit with temperature and ice supersaturation and another model of ice crystal habit with temperature and vapor density excess (H. R. Pruppacher and J. D. Klett, 1978, Ref.13) are shown in Fig.1 left and right. They are former basic models which were got by T. Kobayashi (1961, Ref.6) and were used about 20 years. Fig.1 is a new modified models by H. R. Pruppacher and J. D. Klett (1978,Ref.13), but there are three problems in the model.

(1). They were qualitative data, so it was very difficult for distinguishing many kinds of ice crystals, specially near the boundary.

(2). There were a few data in lower ice supersaturation (i. e. below water saturation line), and it was not good to use them for deciding model.

(3). T. Kobayashi's (and et. al) data weren't accurate, for example, he gave the temperature range was $-10^{\circ}C > T_a \geq -20^{\circ}C$, or $-23^{\circ}C > T_a > -32^{\circ}C$ etc.

We believe that it is very necessary to do more experiments and get a lot of accurate data, then to improve former models.

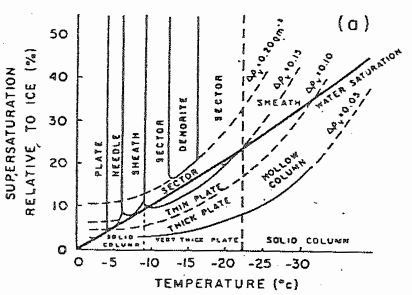

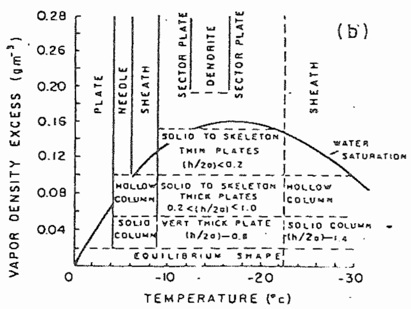

Fig. 1. Variational models of ice crystal habit with temperature and supersaturation (a, left), and temperature and vapor density excess (b, right) (from H. R. Pruppacher and J. D. Klett,).

2. A NEW MODEL OF ICE CRYSTAL HABIT VARIATION WITH TEMPERATURE AND ICE SUPERSATURATION

During recent three years, we got accurate and a great number of data of ice crystal growth by use of a new wedge-shaped ice thermal diffusion chamber which has stable enviromental conditions and can measure three dimension sizes of ice crystal easy (N. Fukuta, G. D. Swoboda and Ang Sheng Wang, 1982 Ref.17; Ang Sheng Wang and N. Fukuta, 1983, Ref. 18). According to above a volume of data and other conditions, we studied the law of ice crystal growth and gave new models.

Firstly, a quantitative classification of ice crystal has been given in Table 1 (Ang Sheng Wang and N. Fukuta, 1983, Ref.19) and will be used in this paper. Their objective definition is different from qualitative and subjective definition of ice crystal form. So it will be careful to compare our data with former author's data.

Secondly, quantitative experimental results of ice crystal habit variation with temperature and supersaturation have been presented in Fig.2. The number of every points in Fig.2 is 2a/c value in thatpoint when growing time of ice crystal is equal 50 minutes. It represents the form of ice crystal in that point according Table 1. At same time, isolines of 2a/c (for example 0.1, 1, 2, 5, 10, 20, and 40 etc. isolines) is drawn in Fig.2 for distinguishing different kinds of ice crystal as Table 1. There are about 120 points in lower ice supersaturation region (i.e. below water saturation). The number of data is much more than former auther' data, and every 2a/c is got from measuring 2a and c, so this result is better than former data.

According to quantitative experimental results as Fig.2 (time: 50 min.) and similar data (but different time) (Ang Sheng Wang and N. Fukuta, 1983a, Ref. 18),a new variational model of ice crystal habit with temperature and ice supersaturation has been presented in Fig.3. It is very clear that the new model is similar to Fig.2, but it is more ideal and different from former model (see Fig.1 left) in lower ice supersaturation (i.e. below water saturation) region. Two centers of this model are needle ice crystal region ($2a/c \leq 0.1$, near $T=-5°C$ and ($S_i - 1$) is higher than 6 %) and dendrite or spatial plate — very thin plate region ($2a/c > 20$, temperature is from near $-12°C$ to $-18°C$, and (S_i-1) is higher than 8 %). Around above two centers, all kinds of ice crystal change gradually . For example, there are thin plate, thick plate, prism and needle ice crystal, and 2a/c changes from about 20 to 10, 5, 2, ···to 0.1 gradually, and so on (temperature is from $-15°C$ to $-5°C$). We can find that the distribution of ice crystalkinds as close as symmetric to two centers of dendrite and needle ice crystal regions. Another characteristics of our model is a " Wulff's theory region " which is in ($S_i - 1$)=0 - 6 % region and temperature is from about -10 or $-15°C$ to $-30°C$. In this region, 2a/c is close about 1.5 or $c/2a \simeq 0.7$. This value is close Wulff's theory (H. R. Pruppacher and J. D.

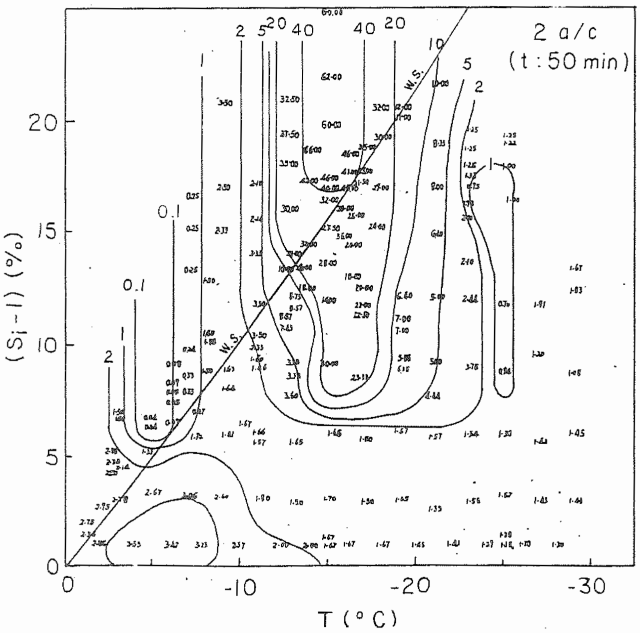

Fig. 2 Quantitative experimental results of ice crystal habit variation with temperature (from 0°C to -30°C) and ice supersaturation (from 0 to 25 %) at time=50 minutes in new wedge - shaped chamber.
*W.S.= Water Saturation.

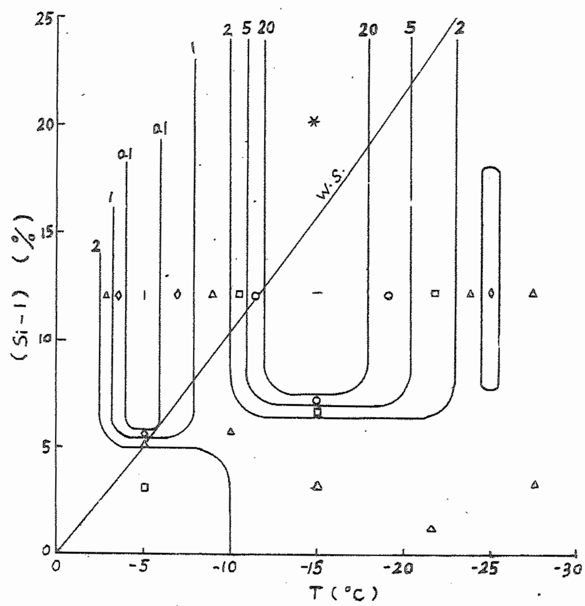

Fig. 3 A new variational model of ice crystal habit with temperature and ice supersaturation.

Table 1. A quantitative classification of ice crystal by (2a/c)

Sign	*	—	○	□	△	◊	∣
Name of ice crystal	Dendrite or Spatial plate	Very thin plate	Thin plate	Thick plate	Prism	Long prism	Needle
2a/c	2a/c > 20	2a/c > 20	20 ⩾ 2a/c > 5	5 ⩾ 2a/c > 2	2 ⩾ 2a/c > 1	1 ⩾ 2a/c > 0.1	0.1 ⩾ 2a/c

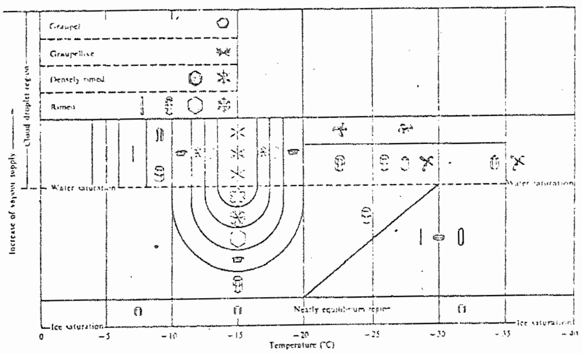

Fig. 4 Temperature and humidity conditions for the growth of natural snow crystals. (from C. Magono and C. Lee, 1966. Ref. 20).

Klett, 1978), and $c/2a \simeq 0.81$. In this condition, ice crystal grow in equilibrium situation closely.

It is very interesting to find that our model is similar to C. Magono and C. Lee's (1966, Ref. 20) observational result of natural snow crystal growth as in Fig. 4. Although their result hadn't quantitative data and ice supersaturation, then their qualitative observational result of natural snow crystal growth gave similar tendency which is like our model.

when compare our model (Fig. 3) and observational natural result (Fig. 4), they are similar very much in needle, dendrite, very thin plate etc. ice crystal regions and their near regions; specially in symmetric characteristic of different kinds of ice crystals between -10°C and -20°C. In lower ice supersaturation region (near ice saturation), it is clear, we only find prism or thick plate in Fig. 3 or Fig. 4. In above region, there are close equilibrium condition, and ice crystals grow according to Wulff's theory, so the form of ice crystals is prism closely. In addition, ice crystal form changes gradually from prism to thick plate, thin plate, very thin plate and dendrite and so on in near -15°C, when ($S_i - 1$) increases, we can see this similar phenomenon is in above both figures. So we can think that Magono's work supports our model by his natural observation of snow crystal growth.

3. A NEW MODEL OF ICE CRYSTAL HABIT VARIATION WITH TEMPERATURE AND VAPOR DENSITY EXCESS

Same as second section, firstly we give our qualitative result of ice crystal form in temperature and vapor dinsity excess field in Fig. 5. This is first result of a volume of measuring data. As like as second section, many isoline of 2a/c (for example, 40, 20, 10, 5, 2, 1 and 0.1 etc.) was drawn in Fig. 5, according to quantitative data (Ang Sheng Wang and N. Fukuta, 1983 b, Ref. 19). In comparision of our data (in Fig. 5) with former data (in Fig. 1 right), it is very clear that their model was ideal too. In the situation of lacking data, former authers (for example, J. Hallett and B. J. Mason, 1958; T. Kobayashi, 1961; H. R. Pruppacher and J. D. Klett, 1978 et. al) used isothermohyps and vapor density excess isolines to decide ice crystal form. But, our acture data show that later isn't good, because of most boundaries of different kinds of ice crystals are slope from higher to lower temperature, and aren't parallel to vapor density excess isolines.

According to our a lot of data, a new variation-model of ice crystal habit with temperature and vapor density excess has been presented in Fig. 6. It is different from former model, specially in low ice supersaturation region (i.e. below water saturation). Its characteristics are similar to Fig.3. Of course, same as former work, isothermohyps are main factor to decide ice crystal form still; but, vapor density excess is another factor, and it changes with different temperature, so most boundaries of different kinds of ice crysrals are slope and aren't parallel to vapor density excess isolines. This is very important result.

4. REFERENCES

1. Hanajima, M.,1949: On the growth conditions of man - made snow. Low. Tem. Sci., A2, 23 - 29.

2. Nakaya, U., 1951: The formation of ice crystal. Compendium of Meteorology. Amer. Met. Soc., Boston. 207.

3. ______, 1954: Snow Crystals. Horvard University Press. 510.

4. ______, 1955: Snow crystals and aerosols. J. Fac. Sci. Hokkaido University. Ser. 2, 4, 341.

5. Hallett, J.,and B. J. Mason, 1958: The influence of temperature and supersaturation on the habit of ice crystals grown from vapor. Proc. R. Soc., A247, 440 - 453.

6. Kobayashi, T., 1961: The growth of snow crystals at low supersaturations. Phil. Mag., 6, 1363 - 1370.

7. Fletcher, N. H., 1962: The physics of rainclouds. The Cambridge University Press. 386.

8. Hobbs, P. V., 1974: Ice Physics. Oxford University Press. 827.

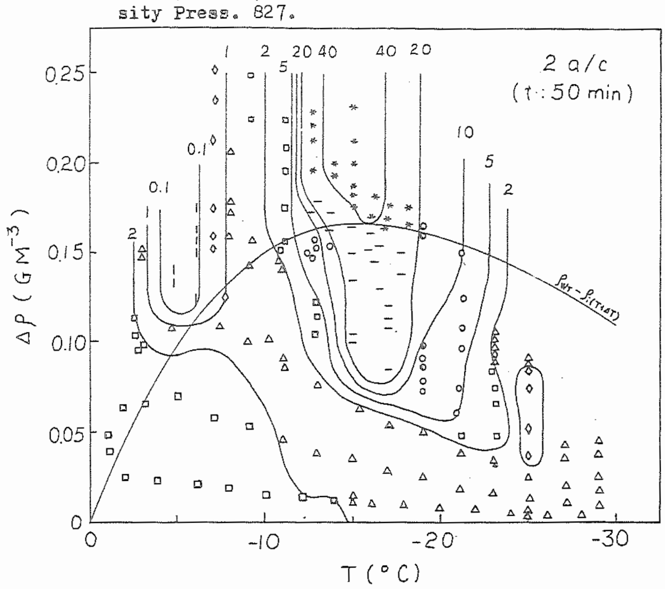

Fig. 5 Quanlitative result of ice crystal form in temperature and vapor density excess field (time: 50min).

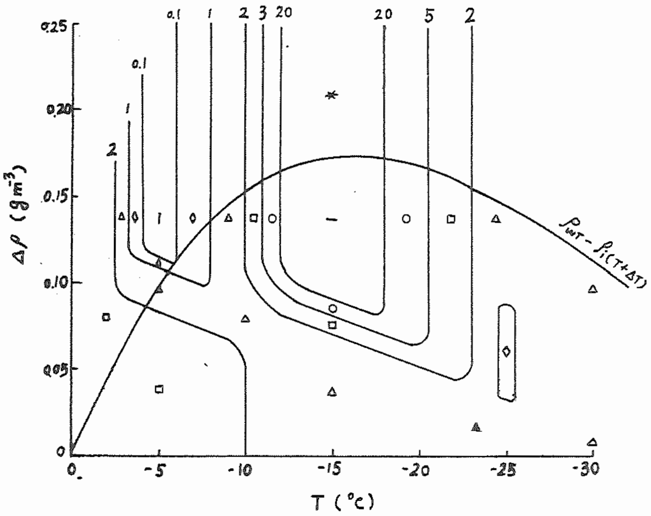

Fig. 6 A new Variational model of ice crystal habit with temperature and vapor density excess.

9. Rottner, D. and G. Vali, 1974: Snow crystal habit at small excess of vapor density over ice saturation. J. Atmos. Sci., 31, 560-569.

10. Takehiko Gonda, 1974: Experimental studies on the growth of snow crystals. Kisho kenkyn Note 123, 95-118.

11. Rogers, R. R., 1976: A short course in cloud physics. Pergamon Press. 227.

12. Lacmann, R., 1977: Zür Deutung der wachstums-formen des Eises Zonschrift fur Physikelische chemie Neue Fulge. (Z. Physik. Chem.,(N. F.)) Bd. 104, 1. s. 1-9.

13. Pruppacher, H. R. and J. D. Klett, 1978: Microphysics of cloud and precipitation. D. Reidel. 714.

14. Kuroda, T. and R. Lacmann, 1980: Growth kinetics of ice from vapour phase and its growth forms. International Conference on Cloud Physics. France, July 15-19, 1980, 109-112.

15. Pruppacher, H. R., 1981: The microstructure of Atmospheric cloud and precipitation. Clouds, their formation, optical properties, and effects. Academic Press. 93 - 186.

16. Mason, B. J., 1971: The Physics of Clouds. 2nd ed. Oxford University Press. 671.

17. Fukuta, N., G. D. Swoboda and Ang Sheng Wang, 1982: Experimental and theoretical studies of ice crystal habit development. Conf. on Cloud Physics. AMS. Nov. 15-18,1982. Chicago. 329-332.

18. Wang Ang Sheng and N. Fukuta, 1983a : Quantitative studies on the growth law of ice crystal. (Submitted for publication to Scientia Atmospherica Sinica.).

19. ______, and ______, 1983b : Studies of ice crystal habit development in new wedge-shaped ice thermal diffusion chamber. (Submitted for publication to Chinetia Sinica).

20. Magono, C. and C. Lee, 1966: Meteorological classification of natural snow crystals. J. Fac. Sci., Hokkaido University, Ser. 7, 2, 321-335.

THE STUDIES OF GROWTH RATES OF ICE CRYSTAL AT DIFFERENT TEMPERATURE AND ICE SUPERSATURATION

Ang Sheng Wang

Institute of Atmospheric Physics, Academia Sinica
Beijing, The People's Republic of China

N. Fukuta

Department of Meteorology, The University of Utah
Salt Lake City, Utah U.S.A. 84112

ABSTRACT

An overall and quantitative studies of growth rates of ice crystal at different temperature and ice supersaturation have been introduced in this paper. Authors point out that d(2a)/dt and dc/dt plotted as a function of temperature at ($S_i - 1$) = 1, 3, 6, 9, 12, 15 and 18 %; their changes with time; and their characteristics at water satura - tion etc. We can quantitatively calculate 2a and c of ice crystal, and decide the form of ice crystal by use of those results.

Keywords: Ice crystal, Cloud Physics, Microphysics, Cloud Chamber, Ice supersaturation, Temperature.

1. INTRODUCTION

During the fifties of this century, qualitative characteristics of ice crystal form had been found (M. Hanajima, 1949, Ref.1; U. Nakaya, 1954, Ref. 2; J. Hallett and B. J. Mason, 1958, Ref. 3; et. al), so many scientists tried to explain this phenomenon by use of the growth rate of ice crystal. The linear growth rate of the basal face of ice crystal is different from one of prism face had been found, and it can be using for explaining ice crystal form. But it was very difficult to measure linear growth rates. So B. J. Mason et. al (1963, Ref.4) firstly measured the mean surface migration distance of basal surface only, and they suggested the mean surface migration distance of prism surface, and used them to explain the forms of ice crystals. In 1971, D. Lamb and P. V. Hobbs (Ref.5) used experimental method to measure the linear growth rates of the basal and prism faces of ice crystals as a function of temperature under water vapor, and the excess vapor pressure was constant at 10 μm of mercury. Although their data were dispersion, but that was first quantitative data, and explained some ice crystal form. Because of an overall quantitative data of ice crystal growth hadn't been got, so quantitative explaintion of ice crystal form was difficult still.

In 1982 and 1983, the wedge-shaped ice thermal diffusion chamber had been used to get a lot of quantitative data of ice crystal growth, and we got more than 4000 data of the largest linear size of the basal surface (2a) and the height of prism surface (C) at different ice supersaturation (from 0 to 25 %) and temperature (from 0 to - 30°C) during about one hour (Wang Ang Sheng and N. Fukuta, 1983, Ref. 6). According to those data, first overall and complete quantitative growth characteristics of ice crystal had been presented. On the basis of above results, we studied the growth rates of ice crystal at different temperature (T) and ice supersaturation ($S_i - 1$). The main result has been given as follows.

2. d (2a)/dt AND dc/dt PLOTTED AS A FUNCTION OF TEMPERATURE AT DIFFERENT ICE SUPER - SATURATION

As you well know, the temperature is a very important factor which decided the growth characteristics of ice crystal, so it is necessary to study that d (2a)/ dt and dc/dt plotted as a function of temperature.

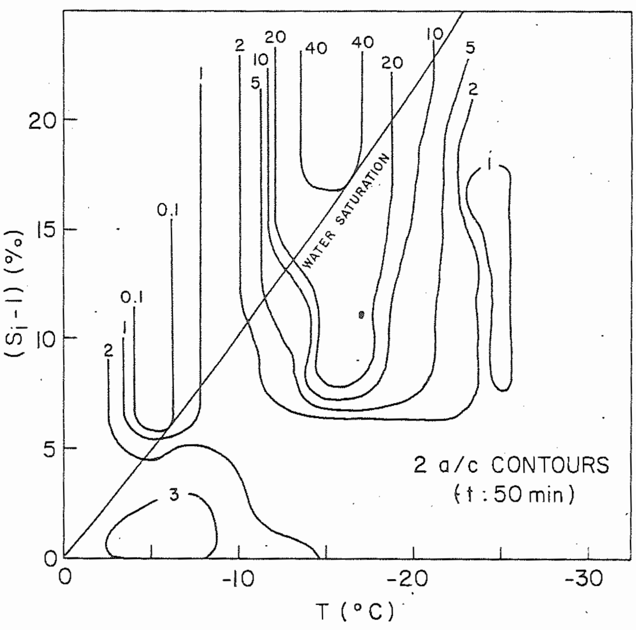

Fig. 1 The variation of 2a/c ratio plotted as a function of temperature and ice supersaturation at 50 minutes of ice crystal growth.

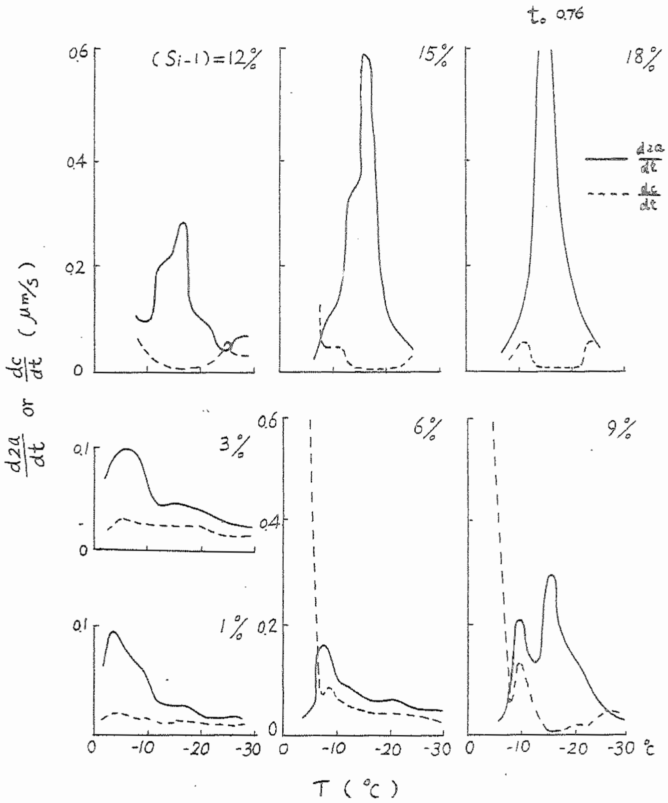

Fig. 2 Average d(2a)/dt and dc/dt plotted as a function of temperature at (S_i-1) = 1, 3, 6, 9, 12, 15, and 18 %, and time = 50 minutes.

First, let us introduce a main result of quantitative characteristics of ice crystal in Fig. 1. Fig. 1 consists of about 400 data of 2a and c. There is an interval of every 5 minutes for 2a/c field (like Fig. 1) which was been got from our data (Wang Ang Sheng and N. Fukuta, 1983a, Ref. 6). As you see from Fig. 1, we can find any quantitative datum in this T and (S_i-1) field; and can use the figures which had been got in different time to compute the growth rates of ice crystal at different temperature and ice supersaturation (Wang Ang Sheng and N. Fukuta, 1983b, Ref. 7).

Now, average d(2a)/dt and dc/dt plotted as a function of temperature at ice supersaturation (S_i - 1) = 1, 3, 6, 9, 12, 15 and 18 % have been shown in Fig. 2 (time = 50 minutes). According to those data, we can find main results as following:

(1). Because of ice crystal forms in (S_i-1) — T field are complex, so d(2a)/dt and dc/dt are complex too. d(2a)/dt and dc/dt change with either temperature or ice supersaturation.

(2). In lower supersaturation (for example, 1 % or 3 %), dc/dt were near 0.01 (1 %) or 0.025 μm/s (3 %); then d(2a)/dt were simple, only had a peak of curve which are near -4°C (1 %) and -6°C (3 %).

(3). In lower ice supersaturations (from 1 % to 6 %) and colder temperatures (from -10 or -15°C to -30°C), the curves of d(2a)/dt and dc/dt were parallel each other, so 2a/c values in this region were closely about 1.4. That means the form of ice crystal is the prism ice crystal, and this growth likes Wulff's growth (H. R. Pruppacher and J. D. Klett, 1978, Ref. 8).

(4). dc/dt has a rapid increace had been found in (S_i - 1) = 6 - 9 % and T = -5°C; at same time, d(2a)/dt rapidly decreaced. In here, dc/dt increaced from about 0.1 to 0.67 μm/s. Because of c increased rapidly and 2a increased slowly, so needle formed near -5°C region. Due to the measurement of ice crystal size wasn't easy, so there weren't data in (S_i - 1) = 12, 15 and 18 %, but same tendency had been found.

(5). An obvious d(2a)/dt peak region and dc/dt concave region had been found between -10 and -20°C and over (S_i - 1) = 9 %. When (S_i - 1) is heigher, d(2a)/dt is much heigher. For example, when (S_i - 1) increases from 12 to 18 %, and d(2a)/dt increases from 0.28 to 0.76 μm/s. We can find that the maximum of d(2a)/dt is near -15°C. In this region, dendrite, spatial plate and very thin plate etc. ice crystal have been found.

Above results tell us that the growth rates of ice crystal in (S_i - 1) — T field are complexer than D. Lamb and P. V. Hobbs's work (1971).

3. THE GROWTH RATES OF ICE CRYSTAL CHANGE WITH TIME

In static experiment of ice crystal growth, we found that the growth rates of ice crystal is faster during starting period, and one is slower during latter period. In Fig. 3, we can find this phenomenon. As an example, d(2a)/dt and dc/dt which are mean values either from 0 to 10 minutes or from 0 to 50 minutes have been shown in Fig. 3, their temperature is - 15°C.

From Fig. 3, we can find that either d(2a)/dt or dc/dt, the mean values which are from 0 to 10 minutes always bigger than the values which are from 0 to 50 minutes. Of course, their changing values are different at different ice supersaturations. That means small ice crystal during starting period grows faster, but bigger ice crystal grows slower in static experiment.

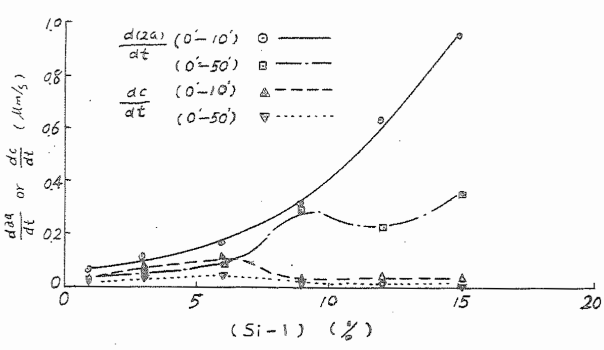

Fig. 3 Mean d(2a)/dt and dc/dt (from 0 to 10 minutes or from 0 to 50 min) plotted as a function of ice supersaturation at - 15°C.

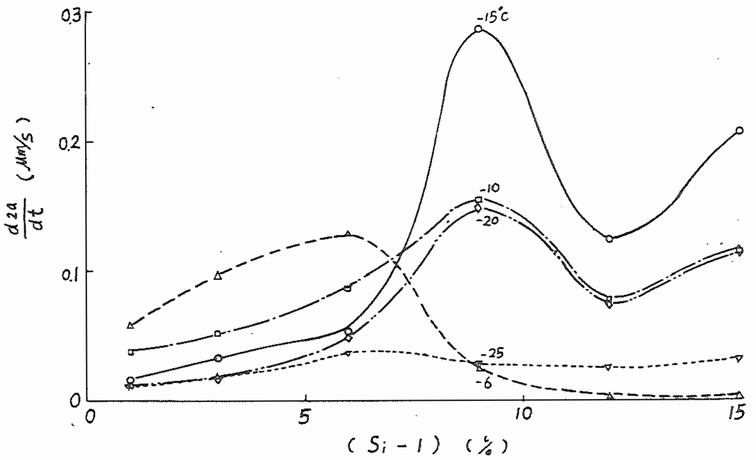

Fig. 4 d(2a)/dt plotted as a function of ice supersaturation at -6, -10, -15, -20 and -25°C, from 10 to 50 minutes.

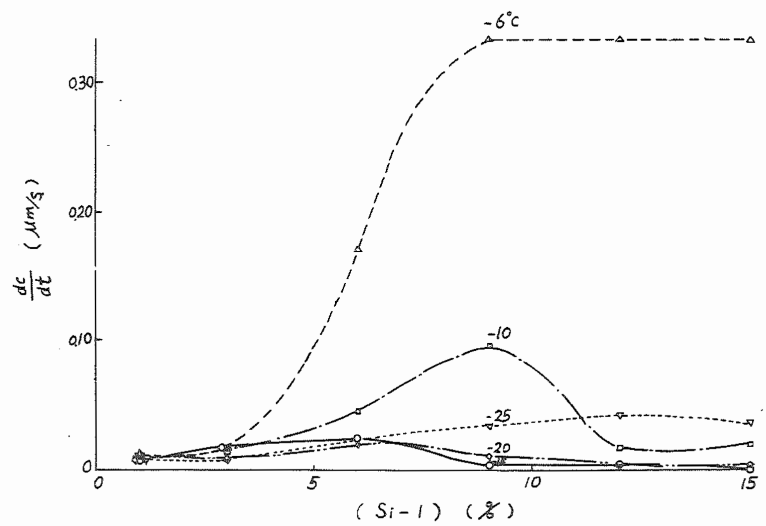

Fig. 5 dc/dt plotted as a function of ice supersaturation at -6, -10, -15, -20 and -25°C, from 10 to 50 minutes.

4. d(2a)/dt AND dc/dt PLOTTED AS A FUNCTION OF ICE SUPERSATURATION

Although the temperature is very important factor for ice crystal growth, the ice supersaturation is another very important factor. From Fig.1 and Fig. 2, we can find that the ice supersaturation influences the growth rates of ice crystal.

Now, d(2a)/dt and dc/dt plotted as a function of ice supersaturation at -6,-10, -15, -20 and -25°C have been given in Fig. 4 and Fig. 5 respectively. In Fig. 4, we can see that d(2a)/dt which are as a function of ice supersaturation are different at different temperature. For example, when the temperature is equal -6°C, d(2a)/dt increases from (S_i-1) = 1 % to 6%, and the value of d(2a)/dt decreases from (S_i-1) = 6 % to 15 %. Than d(2a)/dt changes a little and is equal about 0.02 — 0.04 at -25°C. When ice supersaturation is lower than 7 %, d(2a)/dt increases with the ice supersaturation; and when temperature is warm, the d(2a)/dt is bigger. Than when the ice supersaturation is higher than 7 %, we can find that d(2a)/dt increases with cold temperature; and the value of d(2a)/dt decreases with cold temperature only from -15 to -25°C, but the former temperature region is from -6 to-15°C.

The data of dc/dt which had been shown in Fig.5 are different from d(2a)/dt. At -6°C, dc/dt grows faster, specilly when (S_i - 1) ⩾ 9 %, the dc/dt is equal about 0.35 μm/s. Than when temperature is cold, dc/dt decreases. But they change complexly as same as Fig. 5.

We can use above data at same time, and compare them. According to our data, we can point out the ice crystal form in different (S_i - 1) and temperature region and the explanation of ice crystal forming. For example, when temperature is equal -6°C and ice supersaturation is higher than 6 %, dc/dt > 0.17 μm/s (as we see) and d(2a)/dt changes from 0.1 to 0.01 μm/s, so c increases rapidly than 2a; and the needle ice crystal will form in this region. The dendritic and very thin plate ice crystal have been found in near -15°C and (S_i - 1) > 9 % region, because of d(2a)/dt is bigger than about 0.15 μm/s, and dc/dt is smaller than 0.004 μm/s.

5. d(2a)/dt AND dc/dt AT WATER SATURATION

Usually the form of ice crystal at water saturation has been applied in the research work on Atmospheric Physics, because of it is like natural situation. According to our data, we can calculate the

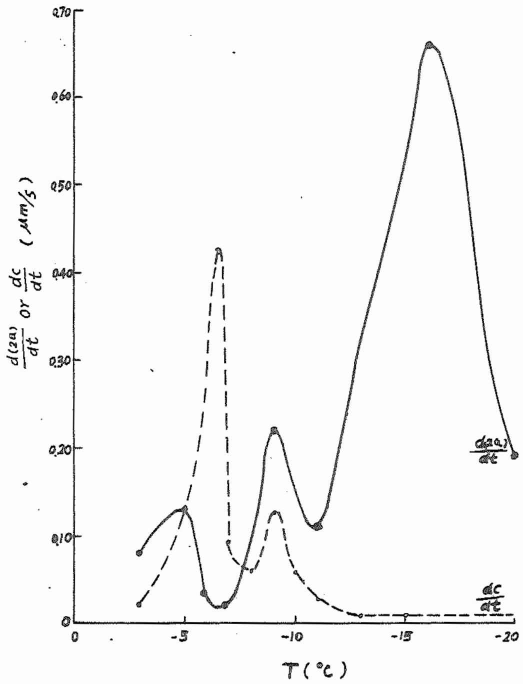

Fig. 6 d(2a)/dt and dc/dt plotted as a function of temperature at water saturation (time: 50min.).

d(2a)/dt and dc/dt at water saturation and give them in Fig. 6. Above data are mean value of d(2a)/dt and dc/dt from 0 to 50 minutes. A main peak of d(2a)/dt has been found in -16°C and is equal 0.66 µm/s. We can see another main peak of dc/dt in -6.5°C, and it is about 0.43 µm/s. The main peak of d(2a)/dt and dc/dt respond to minimum of dc/dt and d(2a)/dt respectively, they are 0.01 and 0.02 µm/s. So at water saturation and -6.5°C, a typical needle ice crystal had been found. Than at water saturation and -16°C conditions, a typical dendritic ice crystal had been found too.

When we compare Fig. 1 and Fig. 6, it is very clear to find that the needle and dendritic ice crystal regions are over water saturation. So the maximum of d(2a)/dt and dc/dt in (S_i - 1) —— T field aren't in water saturation line. According to our research in water saturation line from zero point (0, 0) to another side, the form of ice crystal will be orderly: thick plate ($2a/c > 2$), prism ($2 \geqslant 2a/c > 1$), long prism ($1 \geqslant 2a/c > 0.1$) to needle ($2a/c \leqslant 0.1$); than long prism, prism, thick plate ($5 \geqslant 2a/c > 2$), thin plate ($20 \geqslant 2a/c > 5$), very thin plate ($2a/c > 20$) and dendritic or spacial plate ($2a/c > 20$) etc. (Wang Ang Sheng, 1984, Ref. 9). Our data of d(2a)/dt and dc/dt at water saturation in Fig.6 show above phenomena are true. We can use those data to calculate quantitatively ice crystal growth and decide their forms.

6. REFERENCES

1. Hanajima, M., 1949: On the growth conditions of man - made snow. Low. Tem. Sci., A2, 23-29.

2. Nakaya, U., 1954: Snow Crystals. Harvard University Press. 510.

3. Hallett, J., and B. J. Mason; 1958: The influence of temperature and supersaturation on the habit of ice crystals growth from vapour. Proc. R. Soc., A247, 440-453.

4. Mason, B.J., G. W. Bryant and A. P. Van den Heuvel, 1963: The growth habits and surface structure of ice crystals. Phil. Mag., 8, 505-526.

5. Lamb, D. and P. V. Hobbs, 1971: Growth rates and habits of ice crystals grown from the vapor phase. J. Atmos. Sci., 28, 1506-1509.

6. Wang Ang Sheng and N. Fukuta, 1983a: Quantitative studies on the growth mechanism of ice crystal. (Submitted for publication to J. Atmos. Sci.).

7. ______, and ______, 1983b: The growth characteristics of ice crystal at lower ice supersaturation. (Submitted for publication to Acta Meteorologica Sinica).

8. Pruppacher, H. R., and J. D. Klett, 1978: Microphysics of clouds and precipitation. D. Reidel. 714.

9. Wang Ang Sheng, 1984: New models of ice crystal growth law in temperature and ice supersaturation or vapor density excess field. 9th International Conference on Cloud Physics. Tallinn, USSR. August 21-28, 1984.

SESSION II

MICROPHYSICAL PROCESSES IN CLOUDS AND PRECIPITATION

Subsession II-3

Ice crystal generation and multiplication

THE KINETICS OF ICE CRYSTAL FORMATION IN "DYNAMIC" CLOUD CONDITIONS

P. J. DeMott, W. G. Finnegan, R. D. Horn and L. O. Grant

Department of Atmospheric Science, Colorado State University
Fort Collins, Colorado, 80523, U.S.A.

ABSTRACT

A knowledge of the rates and mechanisms of ice crystal formation by artificial ice nuclei may be critical in their application for cloud modification. Previous laboratory studies in an isothermal cloud at water saturation, have shown that different silver iodide nucleating aerosols demonstrate different characteristic nucleation rates and mechanisms that could differently affect the magnitudes (spatially and temporally) of ice crystal concentrations in the same seeded cloud volume. It is necessary, therefore, to define the rates of ice crystal formation by nucleating aerosols, under variety of cloud conditions. Toward this end, a controlled slow-expansion(dynamic) cloud chamber is being used. The chamber is described in its operating mode for cold cloud studies and preliminary results of below-cloud base seeding simulations are discussed.

Keywords: Ice Nucleation, Ice Nuclei, Cloud Seeding

1. INTRODUCTION

The temporal and spatial development of ice crystal concentrations in clouds can be affected by the mechanisms and rates of ice crystal formation by natural ice nuclei (Ref. 1). Based on laboratory studies, this will also be true for artificial nuclei used for weather modification. Experiments in a large isothermal cloud chamber have shown that various silver iodide nucleating aerosols function be different rates and mechanisms under identical cloud conditions (Refs. 2-4). Therefore, it would be desireable to quantify the character of nucleation by different aerosols, under a variety of environmental conditions and in simulations of various seeding methodologies. To achieve this, a large slow-expansion cloud chamber has been instrumented for use. The Dynamic Cloud Chamber (DCC) can simulate a wide variety of parcel/cloud conditions including warm or cold cloud formation, various controlled droplet spectra, high versus low vertical velocity, and cloudless ice nucleation at low temperatures.

At this writing, preliminary studies have been performed to evaluate the function of various nuclei in simulations of seeding below cloud base. This is important information for weather modification programs in which seeding is done from the surface, or by aircraft below cloud base. It also serves to demonstrate the importance of rates and mechanisms to the development of the initial ice crystal structure of a cloud after seeding. Continuing experiments and development of quantitative methods are discussed briefly.

2. THE DYNAMIC CLOUD CHAMBER

The DCC is a slow expansion cloud chamber capable of simulating adiabatic ascents. This device was first operated in 1976 (Ref. 5) with a crude control system and no aerosol/cloud physics instrumentation. In the past two years the system has been upgraded through physical refinements, automation and the installation of particle sensing instrumentation. The chamber consists of a 2 m^3 stainless steel outer pressure vessel which houses an inner liquid-cooled copper liner. The total observational working volume is 1.19 m^3. In operation, air is evacuated from the pressure vessel at a controlled rate, producing true adiabatic cooling of the air inside. Simultaneously, the inner liner is force cooled to match the mean air temperature due to expansion. This produces a large homogeneous (free of large temperature gradients) working volume. Expansion is controlled by ocmputer generated code containing ascent profile data, as determined by initial temperature, dewpoint temperature and pressure data. Nuclei can be inserted at any point during an expansion. Useful working ranges presently are, temperature: +40°C to -38°C ± 0.2°C, pressure: 900mb to 150mb ± 0.5mb, relative humidity: 0.1% to >110% ± 0.2% steady state, and simulated vertical velocity: $0.2\,m\,s^{-1}$ to $20\ m\,s^{-1}$.

Particle sensing instruments currently within the observational volume of the DCC include a Particle Measuring System (PMS) ASASP-X aerosol probe for pre-cloud/haze detection, a PMS FSSP-100, modified and adapted to facillitate non-intrusive droplet spectra measurement, and a PMS 2D-c probe adapted to detect ice crystal formation rate in a mode directly verifiable by cold-stage microscopy. Additionally, a developmental laser based, axial extinction/depolarization sensor has been installed to provide measurement redundancy for small ice crystal detection.

3. PRELIMINARY EXPERIMENTS

Two nucleating aerosols that are known to be mechanistically different in function at water saturation were tested for their ice nucleation ability after injection below cloud base at 0°C. The first nucleus, silver iodochloride (AgI·AgCl), has been shown to function primarily as a contact nucleus at water saturation and temperatures -16°C and warmer (Ref. 2). The nucleation rate at these temperatures is controlled by the transport rate of nuclei to cloud droplets. At colder temperatures, it can also function as a deposition nucleus. Contrasted to the AgI·AgCl nuclei are silver iodochloride - sodium chloride (AgI·AgCl-NaCl) ice nuclei. These aerosols have been shown to function rather rapidly by a condensation-freezing mode of nucleation (Ref. 4). These two nucleating aerosols provide and excellent comparison due to their nearly equivalent activity spectra at water saturation.

The results of a particular set of experiments are shown in Figure 1 and 2. These were repeatable with high confidence. Cloud droplet concentrations are rather high at warm temperatures (3000 cm^{-3}), but subsequently decay by fallout and pumping losses. Droplet sizes at peak concentrations is about 10 μm mean diameter. These results may be summarized as follows:

1) Detectable ice crystal concentrations (30 $^{-1}$) were produced at -6.9°C by AgI·AgCl versus -9.5°C by AgI·AgCl-NaCl nuclei for initial seeding concentrations of approximately $10^{6}\ ^{-1}$.
2) Rates of ice crystal formation (indicated by the slope of the cumulative ice crystal number plot) by AgI·AgCl nuclei are slow at warmer temperatures and characteristic at any temperature of both contact nucleation and immersion-freezing nucleation (of drops collided with, but not nucleated at warmer temperatures).

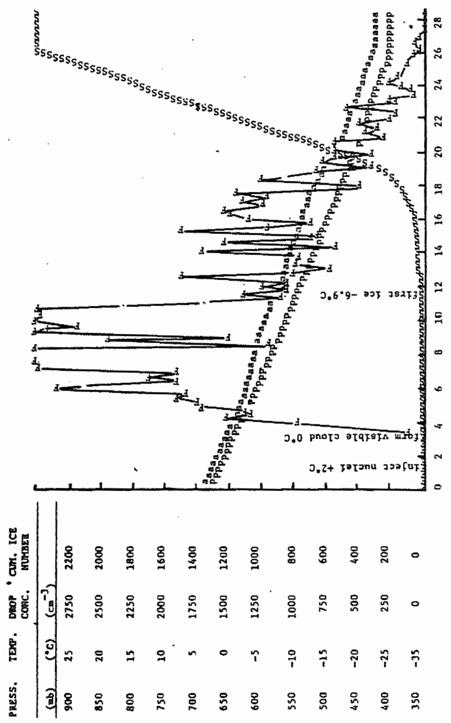

Figure 1. Plot of ascent data for AgI·AgCl seeding test. Air temperature (a), Pressure (p), FSSP drop concentration (F) and cumulative ice crystal number

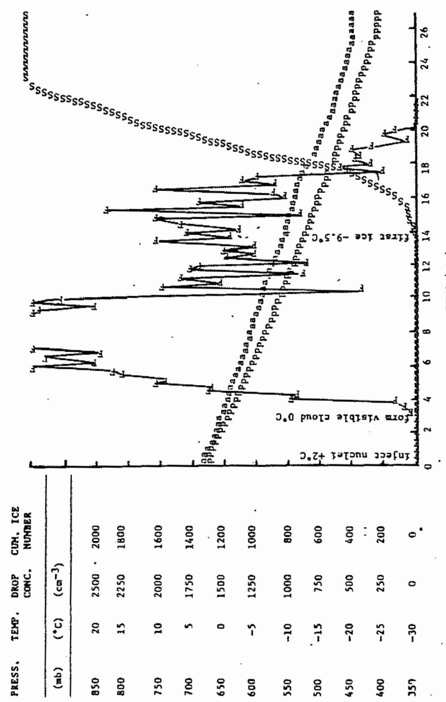

Figure 2. Same as in Figure 1, but for test of AgI·AgCl-NaCl nuclei.

3) AgI·AgCl-NaCl nuclei are apparently immersed in droplets during cloud formation. This is consistent with its behavior as a condensation-freezing nucleus and observations of ~1000 cm^{-3} higher peak concentrations. As a result, the ice crystal formation rate is rapid after nucleation begins, such that cloud glaciation occurs at -15°C. Interestingly, nucleation persists after glaciation, indicating depositional nucleation behavior at colder temperatures.
4) It is apparent that very high seeding rates may be necessary, using either of these highly efficient nucleating aerosols, to achieve significant ice crystal concentrations at temperatures warmer than -10°C by seeding through cloud base.

4. SUMMARY

A cloud chamber to simulate "dynamic" cloud conditions has been described. Using this device, it has been demonstrated that the rates and mechanisms of ice crystal formation by ice nucleating aerosols influence the development (in time) of ice crystal concentrations. Quantitative analysis methods and formulation fo nuclei depletion effects will follow methodologies based in chemical kinetics (Ref. 2). These methods and further results of experiments will be reported on at conference time.

Acknowledgements. This research was performed under contract No. 9514 with the Alberta Research Council.

5. REFERENCES

1. DeMott P J and Grant L O 1984, Development of ice crystal concentrations in stably stratified orographic cloud systems, *Preprints of Conf. on Cloud Physics*, Tallin, U.S.S.R.

2. DeMott P J, Finnegan W G, and Grant L O 1983, An application of chemical kinetic theory and methodology to characterize the ice nucleating properties of aerosols used for weather modification, *J Clim Appl Meteor* 22, 1190-1203.

3. Blumenstein R R, Finnegan W G, and Grant L O 1983, Ice nucleation by silver iodide-sodium iodide: A reevaluation, *J Wea Mod* 15, 11-15.

4. Finnegan W G, Daxiong F, an Grant L O 1984, Composite AgI·AgCl-NaCl ice nuclei: Efficient, fast functioning aerosols for weather modification experimentation, *Preprints of Conf on Cloud Physics*, Tallin, U.S.S.R.

5. Garvey D M, Lillie L L, Grove T C, and Grant L O 1976, Determination of the rates of ice crystal formation in two large cloud chambers, *Preprints Conf on Wea Mod*, Boulder, Colorado, U.S.A, 121-125.

DEVELOPMENT OF ICE CRYSTAL CONCENTRATIONS IN STABLY STRATIFIED OROGRAPHIC CLOUD SYSTEMS

Paul J. DeMott and Lewis O. Grant

Department of Atmospheric Science, Colorado State University
Fort Collins, Colorado, 80523, U.S.A.

ABSTRACT

Primary processes responsible for the development of ice crystal concentrations in stably stratified winter orographic clouds in Northwest Colorado have been studied using airborne instrumentation. Initial ice forms rapidly at the upwind liquid cloud edge. Crystal concentrations are maintained in the absence of fallout or additional primary ice crystal nucleation. Nucleation zones are primarily observed in association with orographic lifting and additional condensate formation. A chemical kinetic analysis of the rates of ice crystal formation on a particular case study day shows that a single nucleation mechanism is functioning. A strong relation between ice crystal appearance rates and concentration changes with estimates of water supersaturations generated in the cloud supports condensation-freezing nucleation as the primary ice nucleation mechanism.

Keywords: Ice Nucleation, Ice evolution, Ice Crystal Concentrations, Cloud Microphysics, Orographic Clouds

1. INTRODUCTION

Basic knowledge about the formation of ice in the atmosphere is incomplete. Large discrepancies have been shown to exist between ice nucleus concentrations and ice crystal concentrations in some clouds (Ref. 1). Although measured ice nucleus concentrations increase exponentially with decreasing temperature, a large scatter of ice crystal concentrations as a function of cloud top (coldest) temperature is frequently found (Ref. 2). In some cases, the concentration of ice crystals measured at relatively warm temperatures are several orders of magnitude higher than measured ice nucleus concentrations. Secondary ice nucleation mechanisms have been described to explain such observations (Refs. 3-4). However, it is also recognized that ice nucleus measurement methods may not be representative because they do not properly simulate the natural nucleation mechanism. Only a few observational studies have made inferences to primary processes functioning to form ice crystals in natural clouds (Refs. 5-6). The identification of specific processes of ice generation and the conditions on which they depnd would help determine how much of the variation in measured ice crystal concentrations (at a given temperature) might be explained by primary nucleation mechanisms. In addition, it would add to the basic knowledge of such processes. This goal is being pursued by examining detailed aircraft microphysical observations of orographic cloud systems in the Northern Colorado Rockies.

In laboratory studies (Ref. 7), rates of ice crystal formation, measured as a function of cloud parameters, were used to define the nucleation mechanisms of an artificial nucleant. Similar methods can be applied in natural clouds if the development of ice can be traced into and through the cloud. Stratified orographic clouds thus provide an excellent natural laboratory to perform such studies. In the case examined in detail here, the aircraft flight track was designed to be along the path of the wind in a relatively thin orographic cloud that was precipitating only lightly. By choosing an altitude within a few hundred meters of cloud top, the influence of ice crystal fallout was minimized. Thus, ice crystal concentration changes should reflect nucleation. Changes in cloud droplet concentrations and sizes, in association with changes in ice crystal concentrations, are then used to infer that nucleation proceeds by a condensation-freezing nucleation process versus a contact nucleation process. Due to the nature of this mechanism, definition of nucleation activity at a given temperature is not possible without a simultaneous definition of supersaturation.

2. DATA COLLECTION

The Colorado International Corporation Cheyenne II instrumented aircraft was used for data collection. Ice crystals were continuously sampled using a PMS (Particle Measuring Systems) 2D-c spectrometer probe. Spot samples for microscopic examination were collected using a decellerator. Cloud droplets were observed using a PMS Forward Scattering Spectrometer Probe (FSSP). These measurements of cloud droplet concentrations and sizes were used to determine droplet size distributions and to calculate cloud liquid water content. Ice crystal size analysis was also performed on the data. Both ice crystal and cloud droplet data were averaged for 5 second intervals at true air speed to obtain statistical samples. Only "streakers" were rejected from the 2D data. Emphasis was on small ice crystals and it was felt that unrealistic spectra were obtained by the rejection of zero images.

3. A CASE STUDY

An orographic cloud was studied on 16 January, 1982, as part of Colorado State University's COSE (Colorado Orographic Seeding Experiment) III program in the Northwest Colorado Rocky Mountains. Snow fell during the morning hours, but ended at all but the highest elevations by 1130 local time. At flight time (1230 local), the cloud extended approximately 50 km upwind of the primary mountain barrier (Park Range) perpendicular to the wind. Aircraft measured cloud top varied from 4100 to 4300 m MSL while cloud base was at 2800 to 2900 m MSL based on surface observations. The aircraft entered the upwind cloud edge at 3900 m and maintained constant altitude. Cloud temperature was approximately -16.5°C at this level. Horizontal wind speed was 15 m s^{-1} as interpolated from an upwind sounding at 1200 local time. The equivalent potential temperature profile from this sounding indicated a stable atmosphere and radar reflectivities (from a vertically pointing Ku-band radar at the base of the Park Range) were nearly invariant during the flight.

A cross-section of relevant measurements as a function of the topography along the flight track is shown in Fig. 1. Of immediate note is the relation between ice crystal concentration and liquid water content. Both rise in coincidence at cloud leading edge and subsequently level off. This is consistent with observations of cap clouds at nearby Elk Mountain, Wyoming (Ref. 6). Unlike the case observed in that particular study however, both ice crystal concentrations and liquid water content increase in coincidence at locations within

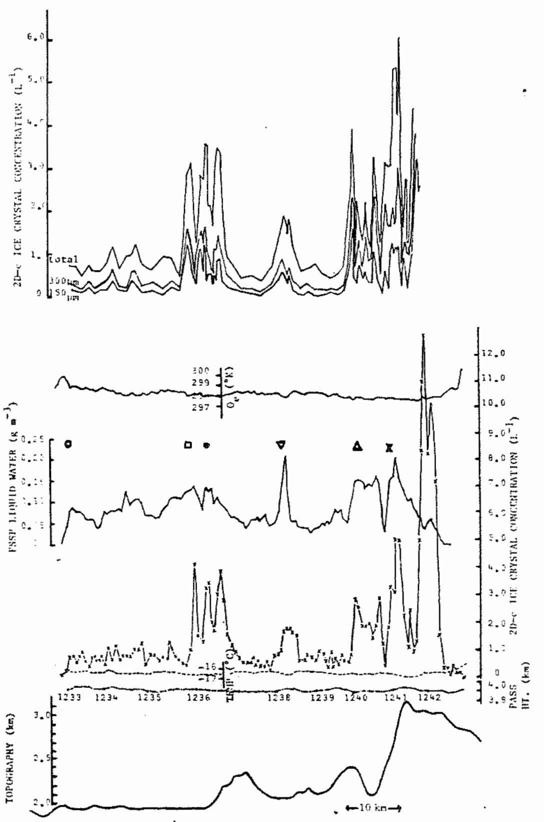

Figure 1. FSSP liquid water content (·), 2D ice crystal concentration (x), temperature and equivalent potential temperature (θ_e) in the pass through the 16 JAN 1982 cloud. Average topography along the flight track is shown at the bottom. At the top of the figure, the crystal concentrations are differentiated for sizes ≤150 μm and ≤300 μm. Location of various ice crystal formation zones are denoted by large symbols.

the cloud (with one exception, discussed later). These locations appear primarily associated with elevation increases in the underlying topography. Thus, the formation of new ice crystals appears connected to the orographic lifting which is causing the new condensate formation as well. The mechanism behind the formation of ice crystals could be either contact nucleation or condensation-freezing nucleation based only on this information. The temperature at flight level precludes the possibility of the Hallett-Mossop ice multiplication mechanism functioning. Secondary production by dendritic collisional fracturing (Refs. 8-9) was possible since this crystal habit predominated in the 2D images and some aggregates were observed at the surface. However, very few aggregates were evident at flight level. Secondary mechanisms are thus ruled out. The coincidence of ice crystal and liquid water peaks also argues against the possibility that new crystals are being mixed from cloud top. That ice crystal concentration increases result from newly formed ice crystals, receives strong support from the size differentiated data in Figure 1. Most concentration changes in inferred nucleation zones occurs for crystals ≤150 μm.

A kinetic analysis of the rates of ice crystal formation in the nucleation zones reveals that a single mechanism is likely responsible for ice crystal formation. The rates of ice crystal formation are displayed in Figure 2 for the various locations. Time in the figure is not aircraft time, but parcel transit time based on the horizontal wind speed at flight level. The assumption is made that over the short times considered, the same air parcel is sampled. This is supported by the fairly constant θ_e on the flight track (Figure 1). Each point in Figure 2 is an average of 5 seconds of aircraft data. This smooths out any horizontal inhomogeneities. The ice crystal formation rates are very rapid and are exponential in nature. This has been noted in previous studies (Ref. 6). These plots can be converted into more meaningful plots of the Ln (100 - %IC) versus parcel time, where %IC is the percent of new ice crystals formed at any time after the onset of nucleation in each case. At time zero, the ice crystal concentration is the initial stable concentration. The maximum concentration after the onset of nucleation is the value used to normalize to obtain the %IC. These plots represent the rate of depletion of nuclei (which can function under the given conditions) to form ice crystals and the slopes display the apparent rate constants in each case (see Ref. 7). In a contact nucleation process, an increase in the rate constant would be caused by a substantial increase in droplet concentrations. In a condensation-freezing process, an increase in slope (at the same temperature) would be a manifestation of an increase in vapor concentration (or alternately supersaturation). The singularity of the slopes (in all but one case) is indicative of a single, psuedo-first order process in action(see Figure 3).

The possible mechanisms are now considered. The rates are extremely rapid and cannot be explained by a conventional (Brownian) contact nucleation mechanism for reasonably sized natural nuclei and for the slight changes in droplet concentrations that occur in the nucleation zones(see Figure 4). Concentration changes at in-cloud locations are only on the order of 30 cm^{-3} across the nucleation zones. Even at cloud edge the concentration of approximately 130 cm^{-3} would not result in a rapid contact nucleation rate by Brownian motion alone. Calculations

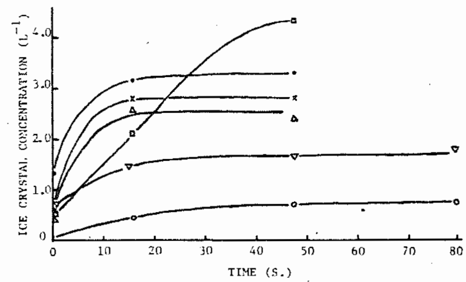

Figure 2. Rates of ice crystal formation through the various locations denoted by symbols in Figure 1. Time in this figure is parcel transit time.

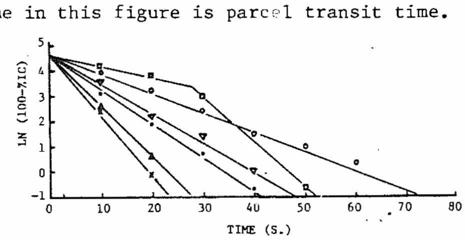

Figure 3. Kinetics plots of ice crystal formation. The percent of ice crystals (new) formed at any time (%IC), is computed based on zero crystals at the onset of nucleation and the total at the maximum value at any location.

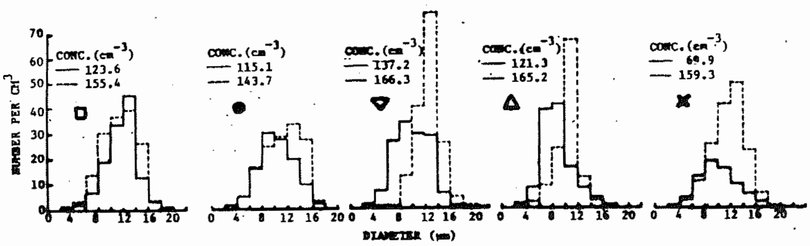

Figure 4. Cloud droplet spectra (five second averages of aircraft data) immediately preceeding (——) and immediately following (---) nucleation zones. Location is denoted by characteristic symbol.

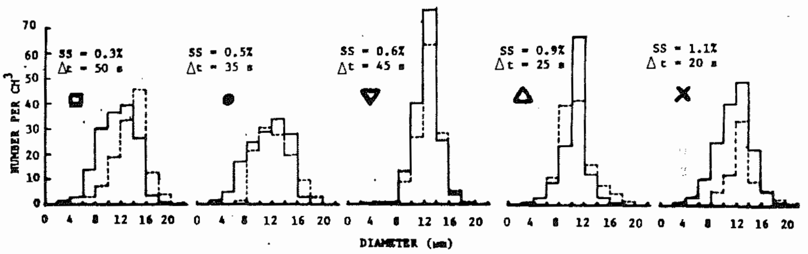

Figure 5. Supersaturation (SS) estimation based on droplet growth calculations. Spectra (---) computed from initial spectra in Figure 4 under given supersaturations are matched with the observed final spectra(——). Integration time (Δt) is the time separating observed initial and final spectra and is determined by the completion time for new ice crystal formation.

have also shown that contact nucleation can be enhanced by phoretic forces, but this occurs only in zones of evaporation (Ref. 10). It has also been postulated that an upper limit to the contact nucleation rate is set by the collision rate of nuclei treated as a molecular species in the presence of condensing droplets (Ref. 6). This mechanism can be ruled out because the fastest nucleation rate is predicted at cloud edge and this does not occur. Also, a concentration gradient between aerosols and droplets is well established within the cloud and the molecular processes would no longer govern the transport process. Thus, a process of elimination alone, would predict condensation-freezing nucleation as the mechanism responsible for ice crystal concentration increases.

Additional support for condensation-freezing nucleation on the natural aerosols (which may or may not be preactivated) lies in the indications of slight water supersaturations present and the correlation of estimated values of supersaturation with both the rates of nucleation and the numbers of ice crystals nucleated. From the cloud droplet distribution changes across nucleation zones (assuming horizontal flow for the short elapsed times), it is seen that the primary contribution to the increases in liquid water content is due to growth of the droplets already present. This is a strong indication of water supersaturation. It is curious that the new droplets do not appear in the smallest bins. However, the response of droplet distributions to supersaturations in mixed-phase clouds is not well documented and the growth of newly nucleated droplets to 3-4μm radius sizes is not inconsistent with the growth times in Figure 4. It is therefore attempted to estimate supersaturation based on the changes in the droplet spectra using a simple droplet growth model and ignoring new nucleation. This supersaturation is that in excess of what can be immediately used by growing ice crystals (can be viewed as a competing rate process). New droplets would not be nucleated if this excess did not exist. Integration times over which the supersaturation is assumed constant are based on the times for the formation of 99% of the new ice crystals in each case. The simplified droplet growth expression is (Ref. 11),

$$r\frac{dr}{dt} = \frac{(S-1)}{\rho_L} \cdot G \quad , \qquad (1)$$

where r is the droplet radius, S is the ratio of ambient to saturation vapor pressure, ρ_L is liquid water density and G is the thermodynamic function. Assumptions of quiescent droplets, steady state thermal and vapor fields and linearly distributed temperature and vapor density are inherent in Eq. 1. Integration gives,

$$r = \left(r_0^{\,2} + \frac{2(S-1)G}{\rho_L}\Delta t\right)^{\frac{1}{2}} . \qquad (2)$$

Also,

$$G = \left(\frac{R_v T}{D\, e_s} + \frac{L^2}{R_v T^2 \kappa}\right)^{-1} , \qquad (3)$$

where R_v is the gas constant for water vapor, L is the latent heat of vaporization, e_s is the saturation vapor pressure at an infinite distance, κ is thermal conductivity (from standard meteorological tables) and D is the diffusivity of water vapor in air. The relation given by Ref. 12 is used for D.

The results of computations are shown in Figure 5. The best fits between the droplet distribution predicted from the initial spectra (dashed line) and the observed final spectra (solid line) are displayed. These define the supersaturation necessary to produce the observed change. All SS values are reasonable atmospheric values, but may be quite surprising for orographic clouds. A comparison between the diagnosed SS values and the rates of formation and concentrations of ice crystals can now be made. This comparison is shown in Table 1. Entries are ordered by the diagnosed SS values. Supersaturation is not known for cloud edge and the apparent rate constant at location □ is not given due to the dual kinetic slope. For the values

Table 1
Comparison of computed supersaturation values (SS) with the apparent rate constant of ice crystal formation and the change in ice crystal concentration in various nucleation zones.

Location	SS(%)	Rate Const.(s^{-1})	ΔIC Conc. (L^{-1})
○	---	0.077	0.73
□	0.3	(dual slope)	3.82
●	0.5	0.137	2.01
▼	0.6	0.125	1.02
△	0.9	0.200	2.15
X	1.1	0.244	2.27

given, the correlation between rate constant and the change in ice crystal concentration is very good. In the comparison between these and SS, only the values at ● and ▼ are reversed in order, but these are very close. If only SS and rate trended together, it could be argued that the rate observed is ice crystal growth , but the correlation also with ice crystal numbers nucleated is most consistent with a condensation-freezing nucelation process for which condensation is rate determining.

One region of prolific apparent ice crsytal nucleation that is anomolous to the behavior discussed previously occurs to the lee of the primary topographic barrier in Figure 1. Crystal concentrations rise sharply in coincidence with strong liquid water depletion. This is a frequent feature in data collected during the COSE program. The source of these ice crystals is not known, but there are a few possibilities. Mixing of crystals from the mountain surface is not likely due to the stability and the height of the aircraft. However, droplet distributions and visual observations from aircraft indicate that this is a region of strong evaporation and descending air. Therefore, more conceivable mechanisms are the local accumulation of ice crystals in this region (that may have nucleated near cloud top) or enhanced contact nucleation by phoretic forces (Ref. 10).

4. COMMENTS AND SUMMARY

For the case study of an orographic cloud presented, natural nuclei at this continental location are shown to function primarily in a condensation-freezing nucleation mode. This result has been inferred previosly at a separate location in the Rocky Mountains (Ref. 6). As a result, variations of supersaturation (inferred from cloud droplet measurements), at the same temperature in the cloud examined, were responsible for variations in ice crystal concentrations by a factor of 2 to 5. The data set is small and therefore the generality of this result and its relevance to more complex cloud systems cannot be concluded. Larger scale storm systems have been studied at this same location and detailed analyses of sources of ice crystal concentrations in the clouds are continuing. Already, spatial distributions of ice crystal concentrations that are contrary to those expected on the basis of ice nucleus activation spectra , have been noted (Ref. 2). Namely, higher concentrations of ice crystals are frequently found at the warmer temperatures (lower altitudes) in stable orographic cloud systems, that cannot be explained by sedimentation or secondary nucleation. These are cloud regions most affected by lifting effects of topography and thus more susceptible to supersaturations.

If condensation-freezing nucleation is an important mechanism for natural ice nucleation, as it was found to be in the case described here, the definition of nucleation activity at a given temperature is a function of supersaturation. This will also be an important consideration in the seeding of clouds with artificial nuclei for the purposes of snowpack enhancement. The processes responsible for primary nucleation can strongly affect the spatial and temporal development of ice crystal concentrations in clouds.

Acknowledgements: This research was supported by the National Science Foundation Grant 8109590. The authors would like to thank Colorado International Corporation for providing the cloud physics aircraft, Dr. William Finnegan for suggesting the case study, and Mr. Robert Rauber and Ms. Taneil Uttal for assistance in data reduction.

5. REFERENCES

1. Hobbs P V and Atkinson D G 1976, The concentrations of ice particles in orographic clouds and cyclonic storms over the Cascade Mountains, *J Atmos Sci* 33, 1362-1374.

2. Grant L O, DeMott P J and Rauber R M 1982, An inventory of ice crystal concentrations in a series of stable orographic cloud systems, *Preprints Conference on Cloud Physics*, AMS, 584-587.

3. Hallett J and Mossop S C 1974, Production of secondary ice particles during the riming process, *Nature* 249, 26-28.

4. Mossop S C and Hallett J 1974, Ice crystal concentrations om cumulus clouds: Influence of drop spectrum, *Science* 186, 632-634.

5. Auer A H 1971, Observations of ice crystal nucleation by droplet freezing in natural clouds, *J Atmos Sci* 28, 285-290.

6. Cooper W A and Vali G 1981, The origin of ice in mountain cap clouds, *J Atmos Sci* 38, 1244-1259.

7. DeMott P J, Finnegan W G and Grant L O 1983, An application of chemical kinetic theory and methodology to characterize the ice nucleating properties of aerosols used for weather modification, *J Clim Appl Meteor* 22, 1190-1203.

8. Hobbs P V and Farber R 1972, Fragmentation of ice crystals in clouds, *J Rech Atmos* 6, 245-258.

9. Vardiman L 1978, The generation of secondary ice particles in cloud crystal-crystal collisions, *J Atmos Sci* 35, 2168-2180.

10. Young K 1974, The role of contact nucleation in ice phase initiation in clouds, *J Atmos Sci* 31, 768-776.

11. Fletcher N H 1962, *Physics of Rain Clouds*, Cambridge University Press, London.

12. Hall W D and Pruppacher H R 1976, The survival of ice particles falling from cirrus clouds in subsaturated air, *J Atmos Sci* 33, 1995-2006.

SECONDARY ICE MULTIPLICATION BY "SPLINTERING" IN LOW STRATOCUMULUS CLOUDS

by

C. Duroure, J.F. Gayet and R.G. Soulage
(Laboratoire Associé de Météorologie Physique, Université de Clermont II, B.P. 45
63170 Aubière, France)

1. INTRODUCTION

Stratocumulus clouds are generally characterized by the presence of embedded convection into the stratiform layer. As a function of the convective intensity, the stratocumulus clouds may present very different microphysical and dynamical structures (from quasi-stratiform layer to small cumulus field).

The precipitations given by these clouds are very reliable in type and intensity and the production of precipitating particles can have several causes. Some observations in low non-glaciated clouds (Ref.1) show that occasionally precipitation drops can appear from the coalescence process alone.

Other measurements in low summer stratocumulus (cloud top warmer than - 12°C) (Ref. 2) show that the clouds were weakly glaciated (10 l^{-1}) and the secondary ice multiplication processes were not active.

On the contrary, this paper describes measurements carried out in heavily glaciated low stratocumulus with evidence of ice multiplication processes. These measurements have been obtained during the W.M.O. Precipitation Enhancement Project in Spain (Valladolid site) from March to May 1981.

2. AIRCRAFT INSTRUMENTATION

The measurements were obtained from the instrumented Piper Aztec aircraft of the "Météorologie Nationale".

The available instrumentation was the following :

- usual thermodynamical and dynamical probes ;
- a hot-wire Johnson-Williams liquid water content probe (reliable for drop size smaller than about 30 µm) ;
- a PMS* FSSP for the measurement of the droplet spectra ($3 \leqslant D \leqslant 45$ µm) ;
- a PMS 2D-C imaging probe ($25 \leqslant D \leqslant 800$ µm with 25 µm resolution).

The data of this probe have been processed using a pattern recognition method (Ref. 3) able to discriminate six usual particle shapes (size larger than 150 µm).

The 2D-C data for particles smaller than 100 µm are used in a qualitative way because of the lack of reliable sampling volume of the probe (the maximum overestimation factor for the total ice concentration is around 3).

3. MAXIMUM ICE PARTICLE CONCENTRATION VERSUS THE TEMPERATURE

In this chapter are presented and discussed the results concerning the ice particle populations sampled with the 2D-C probe during all the stratocumulus cloud penetrations in which the maximum ice particle** concentration was locally greater than 100 l^{-1} (with 180 m averaging). With this criterion, the study concerns 17 penetrations of 8 distinct embedded convective cells.

Figure 1 displays the maximum ice particle concentration versus the temperature at the penetration level. Cross and circle symbols refer to columns and graupels respectively (size larger than 150 µm). Triangle symbols concern the total ice concentration of particles larger than 25 µm.

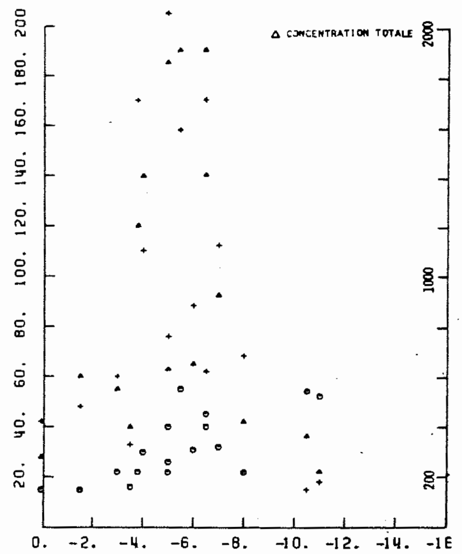

Fig. 1. Maximum pass concentration of ice crystals ($D \geqslant 150$ µm) and total ice concentration ($D \geqslant 25$ µm) versus temperature of the sampling level (15 cloud passes during PEP 81).

This figure shows :

- the total ice concentration (triangle) and the column concentration (cross) are maximum for temperatures ranging from - 3°C to - 7°C. In this range of temperatures the total ice concentration is higher than 400 l^{-1} and reaches 2000 l^{-1} during some cloud penetrations at a temperature of - 5°C ;
- in this same range of temperatures, the column population is dominating with regards to the other ice particle shape (graupels).

These observations displayed in Figure 1 are not in agreement with the hypothesis of a glaciation governed by a primary ice generation process alone (via ice nuclei). Indeed, on the one hand, the maximum concentrations of ice particles found at - 5°C level are about three orders of magnitude higher than the concentration of ice nuclei active at this temperature ($\sim$ 1 to 10 m^{-3}) (Ref. 4) ; on the other hand, the active ice nuclei concentration always presents an increase as temperature decreases.

This well-marked stratification of ice concentration versus the temperature has also been found from the larger sample of measurements (59 penetrations in glaciated stratocumulus) obtained during the 1979 PEP experiment (same site) supposing as in Ref. 5 that hydrometeors larger than 100 µm were ice crystals. Nevertheless, because of the lack of imaging probes the ice shape was unknown.

* PMS : Particle Measuring Systems, Boulder, Co.
**Particle size larger than 150 µm.

Figure 2 represents the maximum ice concentration of particles larger than 100 µm versus the temperature at the penetration level.

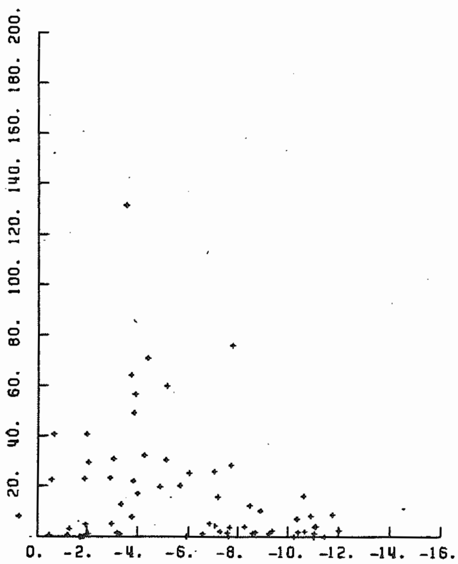

Fig. 2. Maximum pass concentration of hydrometeors (D ⩾ 100 µm) versus temperature of the sampling level (59 cloud passes during PEP 79).

This figure (PEP 1979) shows the same result as Figure 1 (PEP 1981). 63 % of penetrations carried out at temperatures ranging from − 3°C to − 7°C have a maximum ice particle concentration higher than 20 l^{-1}, against only 11 % of penetrations realized at temperatures colder than − 7°C.

The high concentrations of ice crystals observed between − 3°C and − 7°C temperature levels cannot be explained without secondary ice generation processes. These processes and the localization of the cloud zones where they are efficient are discussed in the next chapter through a case study.

4. EVIDENCE OF ICE CRYSTAL MULTIPLICATION BY SPLINTERING IN MIXED ZONES LOCATED BETWEEN THE CONVECTIVE AND THE STRATIFORM CLOUD REGIONS.

The discussed case corresponds to a study at three levels (− 11°C, − 6.5°C and − 3°C) of a convective cell embedded in a stratiform layer. These three penetrations have been performed during a period no longer than 15 mn and the general characteristics of this situation have been frequently encountered during the study of this cloud type.

The radiosounding carried out near the flight zone is characterized by a wet unstable low layer leading to the development of a convective activity embedded in the stratiform layer (1.6 km depth). The convection was nevertheless limited by a well-marked temperature inversion at 700 mb, − 12°C and corresponded to the cloud top.

From 10 cm radar observations (Ref. 6), the formation of precipitation particles was efficient in spite of a small thickness of the cloud layer. No upper cloud was observed during the experiment flight thus leading to suggest, that the heavy glaciation of cloud system which was observed, was not due to a natural seeding of the lower layer by crystal sedimentation.

Figures 3-a, 3-b and 3-c represent for the three penetrations : (a) T = − 11°C : ∿ convective cell top, (b) T = − 6.5°C : ∿ stratocumulus layer top, (c) T = − 3°C : ∿ cloud base, the evolution along the flight track of the following parameters :

- the concentration of ice particles greater than 800 µm ;
- the concentration of graupels (⩾ 150 µm) ;
- the concentration of columns (⩾ 150 µm) ;
- the total ice particle concentration (⩾ 25 µm) ;
- the concentration of large drops ranging from 25 to 45 µm in diameter ;
- the cloud droplet concentration ;
- the liquid water content.

The spatial resolution was about 90 m.

An example of images sampled with the 2D-C probe is given on Figure 4 for five zones labelled A, B, C D and E. These letters are indicated on Figures 3 and give the localization of these zones.

The analysis of Figures 3 and 4 leads to the following comments :

a/ Near the cloud base (Fig. 3-c : T = − 3°C), the glaciated zone is more extended (∿ 20 km) than on the active zone (∿ 4 km), which is defined by a significant liquid water content.

The regions of high concentrations of crystals (with columns as dominant shapes, Fig. 4, zones D and E) are located on both sides of the condensation zone (Fig. 3, zone C) in which the column concentration is much smaller. The presence of large aggregates of columns (precipitating) is correlated to the zones where the concentration of single columns is the largest and reaches 30 l^{-1} (D ⩾ 150 µm) (Fig. 4-C).

b/ Near the top of the stratiform layer (Fig. 3-b), T = − 6.5°C), the ice concentrations were much higher than the one measured near the cloud base. This cloud penetration reveals two convective heavily glaciated zones.

The total ice concentration reaches (on about 160 m) 1800 l^{-1} near the zones of maximum liquid water content. This ice population is mainly composed of small columns (< 100 µm) as shown on Figure 4-B. The small size of the columns sampled in the regions of high ice concentration indicates that these regions are ice generating zones of ice crystals (indeed, the column growth rate − at 6.5°C and at water saturation − being about 1 µm s^{-1}, a column growing under these conditions takes nearly 1 min. to reach 60 µm).

Furthermore, Figure 3-b reveals the presence of precipitating graupels (D ⩾ 800 µm) with concentration locally higher than 1 l^{-1}.

Figure 3-b also reveals that the ice generating zones are not located in the zones of maximum liquid water content, but on their edges.

c/ Near the top of the convective cell (Fig. 3-a, T = − 11°C), the sampled ice crystals are mainly composed of graupels, the initial ice crystal of which is frequently a column (Fig. 4-A). The ice concentration is weaker than the one measured at the − 6.5°C level (∿ 40 l^{-1}).

Discussion

The microphysical characteristics of the generating zones (small columns, large graupels, concentration of large droplets (D ⩾ 24 µm) higher than 10 cm^{-3}) found at a temperature of − 6.5°C suggest that the secondary ice production by splintering (Ref. 7) is efficient in these regions.

In addition, the possibility to measure its characteristics with a spatial resolution of about 100 m, allows the following comments :

- the observation of zones in which the conditions required for the splintering process are got, correspond indeed to the observation of a lot of young crystals. (Fig. 4-B gives a particularly good example of this type of splintering zone) ;

- these glaciation zones are located in mixed regions of the active cells rather than in their center. The causes of this localization may be linked to the dynamics of these convective zones which favours the precipitation of large particles (graupels) on the edges of the updrafts (Ref. 8). For strato-cumulus clouds, the existence of an extended mixed zone (embedded convection) allows these precipitating particles to go through regions having large conden-sation droplets, the collection of which causes the splintering.

This hypothesis, which neglects the time evolution of the convection, is put forward due to the long time life of the convective cells observed in this cloud type (up to 1 hour). Nevertheless, the aircraft data being quasi-instantaneous, it is difficult to conclude on the origin of large graupels found near the maximum liquid water content zones. These large particles can be either generated by the cell itself, as discussed above, or come from an older cell in dissipating stage.

Whatever the cause, this localization of ice gene-rating zones outside the convective regions is confirmed by the observation of the maximum ice concentration stratification versus the temperature at the penetration level (Fig. 1). Indeed, this stratification shows heavy ice concentrations for temperatures warmer than − 8°C, and suggests a bad efficiency of stratocumulus in glaciation phase to carry (via the updrafts) the generated ice crystals from the lower to the upper regions of clouds.

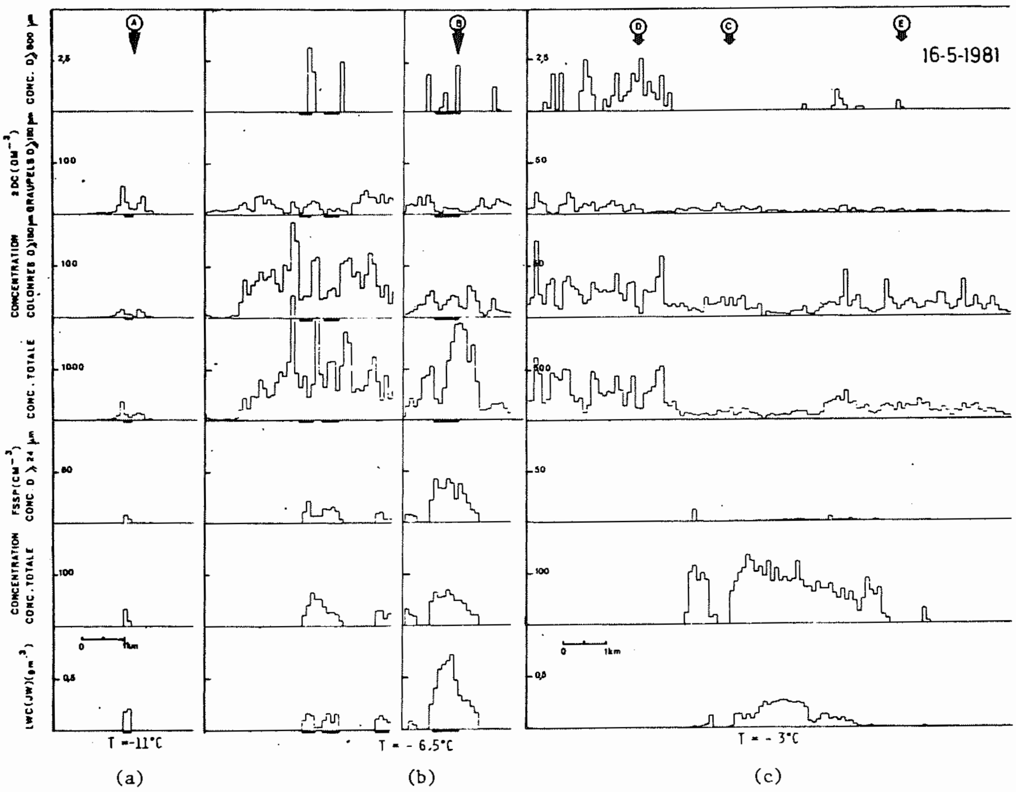

Fig. 3. Microphysical data of the four penetrations at three temperature levels :
(a) T = − 11°C (near the top of the convective tower),
(b) T = − 6.5°C (near the top of the stratiform layer),
(c) T = − 3°C (near the cloud base).
Time axis are underlined when the liquid water content is greater than the half of the maximum liquid water content of the pass. The circled letters on the top refer to the representative 2D-C images displayed on Fig. 4.

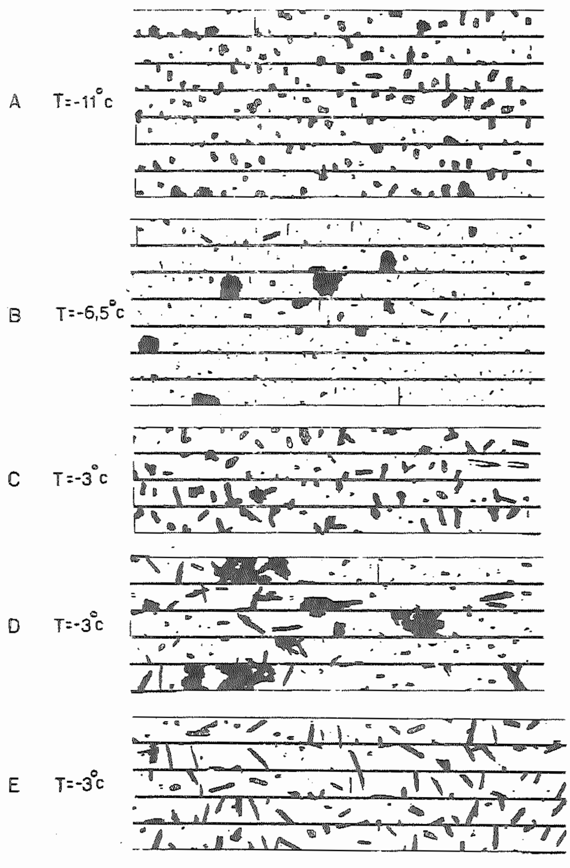

Fig. 4. Representative 2D-C images (0.8 mm width) which were sampled at the time indicated by accompanying letter designations on Fig. 3.

5. CONCLUSIONS

This study shows an original stratification of the maximum ice concentration versus the temperature. The largest concentrations are found at temperatures ranging between - 3°C and - 7°C and can reach 200 l^{-1} for the particles larger than 150 μm, and much more than 1000 l^{-1} for the particles larger than 25 μm.

Due to the cloud top temperatures generally warmer than - 15°C, these heavy ice concentrations are not compatible with a glaciation governed by a primary nucleation on ice nuclei. Through a case study, one of the secondary ice multiplication processes responsible for the heavy ice concentration has been identified to the splintering described in Ref. 7. Furthermore, the preferential glaciated zones are located on the edges of the high liquid water content regions rather than in their center. This last point is important for the microphysical and dynamical cloud evolution after the formation of the ice phase.

6. AKNOWLEDGMENTS

The authors would like to express their appreciation to C. Baraduc for the typing of the manuscript.

The research was supported by the Direction des Recherches Etudes et Techniques under contract DRET/Université n° 80.34.294.

7. REFERENCES

1. Soulage R G et al 1981, Particules précipitantes dans des stratocumulus peu épais au-dessus de Valladolid : conséquences pour la modifiabilité des nuages dans PAP, *J. Rech. Atmos.* 15, 131-142.

2. Mossop S C et al 1972, Ice crystal concentrations in cumulus and stratocumulus, *Quart. J. Roy. Meteor. Soc.* 98, 105-123.

3. Duroure C 1982, Une nouvelle méthode de traitement des images d'hydrométéores données par les sondes bidimensionnelles, *J. Rech. Atmos.* 16, 71-84.

4. Soulage R G 1961, Origins, concentrations and meteorological importance of atmospheric freezing nuclei, *Nubila* anno IV, 1, 43-67.

5. Vali G 1980, Cloud microphysics studies at the Spanish site for the Precipitation Enhancement Project. *Proc. Third WMO Sci. Conf. Weather Modification*, Clermont-Ferrand, France, 21-25 July, 259-263.

6. Duroure C. 1982, Mécanismes de glaciation secondaire dans les stratocumulus : importance du "splintering" dans les zones de mélange des régions convectives, *J. Rech. Atmos.* 16, 353-367.

7. Hallett J & Mossop S C 1974, Production of secondary ice particles during the riming process, *Nature* 249, 26-28.

8. Soulage R G et al 1980, Etude de cas de zones d'accumulation d'eau dans un cumulonimbus tropical au cours de Moussafrica 1977, *J. Rech. Atmos.* 14, 477-486.

SECONDARY ICE PARTICLE PRODUCTION BY RIME FRAGMENTATION AND CRYSTAL BREAKUP

D J GRIGGS and T W CHOULARTON

Physics Department, UMIST, PO Box 88,
Manchester M60 1QD, England

1. INTRODUCTION

The hypothesis that rime and vapour grown crystals may fragment due to collision with other cloud particles has been proposed in various forms for a number of years. Experiments have been performed with the intention of testing this hypothesis. The experiments were carried out by impacting small glass beads with the ice and thus measuring the impact parameter required to break both rime and vapour grown crystals. Rime grown in the temperature range -1°C to -24°C was tested. During some experiments the rime was left in an undersaturated environment before testing. Vapour grown crystals of various habits found in the range -3°C to -25°C were tested, in both ice saturated and undersaturated environments. In some cases accretion was allowed to take place on the vapour grown crystals before testing. The results of these experiments are compared to the findings of other workers and their relevance to natural conditions is discussed.

2. EXPERIMENTAL APPARATUS AND MEASUREMENT TECHNIQUE

The experiments used to test rime breakup were carried out inside a chamber of dimensions 30 x 30 x 75cms located within a walk-in cold room. The target rod was attached horizontally to a constant speed motor. The rod rotated within the chamber with its axis normal to the direction of rotation, so rime collected on the leading edge. The speed of rotation of the rod was fixed at 2m s^{-1}.

A cloud was introduced into the chamber by injection of steam from a boiler. The liquid water content in the chamber could be varied throughout an experiment by altering the power input to the boiler. Liquid water content was measured using a two-stage impactor of the type described by May(1). These results were compared with those obtained by collecting the rime of the rod, weighing it and using the expression

$$RAR = L \times E \times A \times v$$

where RAR = Rime accretion rate = mass of rime collected per second, L = liquid water content, E = collection efficiency of target rod for cloud droplets, A = area of target rod normal to axis of rotation, v = velocity of target rod.
The results obtained by the two methods were consistent. Temperature was measured using a thermocouple and was monitored throughout an experiment.

In order to test the rime, air from a cylinder was passed into a vertical glass tube with a nozzle of known diameter. The target rod was fixed so that air from the nozzle could be directed onto any part of the rime. Impacts with the rime were obtained by individually inserting thermalised glass beads of various sizes into the flow of air.

The flow rate of air was continuously monitored using a flowmeter, hence the velocity at the nozzle was also known. The air used to test the rime could either come directly from a compressed air cylinder or it could be saturated with respect to ice by first passing the air through an ice filled vessel.

When ice particles broke off during testing they were either detected by eye, or they were collected on a slide coated with silicone oil which was then examined under a microscope.

The apparatus used to test vapour grown crystals was very similar. Because of the heat introduced into the chamber as a cloud was formed, the temperature of the chamber was slightly warmer than the air outside the chamber. Thus the target rod was disconnected from the motor and attached to a large metal heat sink located outside the chamber. The temperature of the target rod was thus slightly colder than the air in the chamber and ice could be grown from the vapour. The test apparatus was the same for vapour grown crystals as for rime.

A combination of the two experiments was also carried out by first growing crystals from the vapour and then rotating the rod so that the crystals became rimed. The time for which riming took place was adjusted, depending on how heavily the crystals were to be rimed. (Ref.2) suggested that vapour grown crystals which had subsequently rimed might be the most suitable form of ice for fragmentation.

3. RESULTS

3.1 Rime breakup

After several preliminary experiments, it was decided that a suitable amount of rime (~3mm) was obtained when riming took place for about 20 mins. Photographs taken of the rime showed that it became increasingly less dense as the temperature at which it was grown was lowered.

Two different sizes of glass bead were used to test the strength of the rime. Grade 4 beads with diameter 1075μm ± 200μm and grade 8 beads with diameter 485μm ± 45μm. The values given for the velocity required to break the rime are the values at which the first fragment broke off at a particular temperature. Figures 1 and 2 show the velocity required to break the rime for grade 8 and grade 4 beads respectively. From comparison of both curves it can be seen that the velocity required to break rime decreases as the temperature is lowered. Also, that the larger the impacting mass the lower the velocity required to break the rime at a particular temperature. In all cases, however, at temperatures higher than -2°C, when the rime was grown in the wet growth regime, the velocity required to break the rime was greater than 115m s^{-1}, the maximum velocity the system was able to record. On each of the graphs the error bars on the ordinate axis refer to the accuracy with which velocity was measured. The error bars on the abscissa refer to the range in temperature over which an experiment was conducted. The temperature was found to vary somewhat during an experiment and therefore was adjusted, with a time lag of several minutes, by changing the power input to the boiler.

The results presented have been for air supplied directly from a cylinder. Various experiments were performed to see if evaporation of the rime occurred due to the air being undersaturated. From these experiments it can be stated that any evaporation which took place had no significant effect on the strength of the rime.

The effect of allowing the rime to evaporate during accretion was also studied. In the experiments described to date calculation shows the rime surface to be growing by vapour diffusion as well as accretion. By increasing the liquid water content and reducing the temperature it was possible to rime in conditions where the rime surface was evaporating. This could weaken the ice structure due to partial evaporation of ice bridges linking frozen droplets. For liquid water contents of about 2g m^{-3} at temperatures between -15°C and -21°C the velocity required to break the rime on impact with grade 8 beads increased by approximately 10m s^{-1} when compared to results obtained at lower liquid water contents at the same temperature. It would appear therefore that any weakening due to evaporation is more than compensated for by the increase in the surface temepraturе, due to the high liquid water content, causing the impacting drops to pack more closely. A similar result was found at higher temperatures. An experiment was also performed in which riming was carried out at low temperatures ($\sim$ -20°C) and low liquid water content ($\sim$0.3 g m^{-3}) to grow fragile rime, and then the temeprature and liquid water content were increased to $\sim$ -7°C and $\sim$ 1g m^{-3} respectively to examine the possibility that this might weaken by evaporation the rime grown in the first stage of the experiment. The strength of the rime was found not to differ from that grown in the first stage of the experiment alone. However, in a single case, this method did produce the lowest velocity of all experiments of 17m s^{-1} on impact with grade 8 beads.

3.1.1 <u>Effects of variations in liquid water content</u> The results presented so far have not taken into account possible errors due to the variation of liquid water content between experiments. This was found to be 0.2g m^{-3} to 0.4g m^{-3} below -8°C and between 0.5g m^{-3} and 1.2g m^{-3} at higher temperatures. Further experiments and calculations were performed in order to assess any effect due to this variation. A series of experiments were carried out in which the strength was tested for rime grown in the range of liquid water contents found during the experiments but with the temperature the same in each case. No difference in the strength of the rime could be detected within the errors already shown. In addition, a calculation was performed to solve the equation (Ref.3)

$$(Ewv[L_f + C_w(Ta-Tm) + C_i(Tm-Ts)])/4 = \chi Re^{0.5} \times \frac{(Pr^{\frac{1}{3}}k(Ts-Ta) + Sc^{\frac{1}{3}}LvD(\rho s-\rho e))}{2R}$$

where E is the collection efficiency of the rimer for cloud drops (Ref.4); W = liquid water content; v is the collection speed; L_f and Lv are latent heats of fusion and vapourisation respectively. C_i, C_w are the specific heats of ice and water respectively. Ta, Tm, Ts are the ambient, melting and surface temperatures; Re is the Reynolds number, Pr and Prandtl number, k is the thermal conductivity of air. Sc is the Schmidt number, D is the diffusion coefficient of water vapour in air, ρs, ρe are the densities of water vapour at the riming surface and in the environment, R is the radius of the rod and χ is a roughness parameter and was taken to be 0.76 the value for a relatively smooth sphere. The results of this calculation show the maximum rise in the surface temperature of the rime to be 1°C. If figure 2 is inspected it can be seen, for example, that for grade 8 beads, the difference in velocity required to break the rime at -4°C and -5°C is 5m s^{-1}. However, the density and hence the strength of the rime is not dependent only on the surface temperature of the riming surface. As all other relevant parameters have remained constant this will tend to reduce further any effect due to an increase in liquid water content. Hence the sensitivity to changes in liquid water content will again be concealed within the $\pm$6m s^{-1} error bars.

3.2 <u>Vapour grown crystal breakup</u>
It was found that a suitable amount of ice grew from the vapour in 2 hours. This time was required due to the small difference between the temperatures inside and outside the chamber. The crystal length varied considerably between experiments, but as near as possible crystals were grown of length 3mm. The temperature was constantly monitored throughout the growth and was kept as constant as possible by adjusting the power to the boiler.

In addition to grade 8 and grade 4 beads, grade 10 beads with diameter 270μm + 60μm were used to test the strength of the vapour grown crystals. The testing of the strength was performed in the same way as already described.

It was not possible to obtain values for the velocity required to break the various crystal types with grade 4 or grade 8 beads as at all temperatures the crystal were found to break on impact with the beads with the air supply turned off.

The values obtained for the velocity

required to break different types of crystal with air alone and grade 10 beads are shown in Table 1. As can be seen from the table the velocity required to break dendritic crystals with grade 10 beads is below the limit of detection of the experiment, namely 1.2m s^{-1}. As this is the weakest crystal type it would appear to be the most likely to undergo fragmentation. If the results for other crystal types are extrapolated to determine a value for dendritic crystals on impact with grade 10 beads the velocity required is estimated to be about 1m s^{-1}.

The same experiments as those already described, with respect to evaporation during testng were again performed for vapour grown crystals. Again no differences in the velocity required to break the crystals were found.

4. DISCUSSION

The strength of rime grown under different conditions was measured by finding the velocity at which a glass bead must impact with the rime before it breaks. The results are shown in Figures 1,2 and 3. The strength of the rime was found to decrease as the temperature decreased. This is reasonable as the drops will freeeze quicker and spread less at lower temperatures, with only narrow points of contact between individual frozen drops.

By considering their relative fall velocities, the size of hailstone, of density 0.9g cm^{-3}, with the same kinetic energy with respect to the rime can be found. For rime which breaks at 17m s^{-1} on impact with a grade 8 glass bead, (the weakest value found during experiments), the size of hailstone with the same kinetic energy was found to be about 6mm diameter. Similarly for rime grown at ~ -15°C the size of equivalent hailstone, with the same kinetic energy, which could fragment the rime was found to be about 7.5mm diameter. Particles of this size are found only rarely even in quite vigorous clouds and hence from these results it would appear that rime fragmentation is unlikely to have any significant effect in most natural clouds.

The results obtained with vapour grown crystals are shown in Table 1. It is clear that the vapour grown crystals grown in this manner are much weaker than rime grown at the same temperature. These results have been compared with Ref.5, see Table 2. These values were obtained by estimating the maximum impact speeds which natural ice crystals could withstand without fragmentation when they impact upon a mylar film coated with a wet 4% solution of Formvar in chloroform 150μm thick. Qualitatively the results show good agreement with dendrites the weakest crystal habit and prisms and plates the strongest. Thus it seems more likely from these results that vapour grown crystals, particularly dendrites, could fragment under natural conditions.

However, there are many possible objections as to the quantitative applicability of results of this type to natural conditions. An objection to the test method whereby an ice crystal is grown and then collided with an object of known mass and velocity was raised (Ref.2). That is, the most delicate fragments could be broken in catching and mounting the crystal. This was overcome by growing the crystal on the rod on which it was to be tested.

In attempting to apply these results it must be recognised that the nature of the impacting particle differs between the experiment and natural clouds. Thus the differences caused by using glass as opposed to ice as the impacting medium must be accounted for. The density of the glass bead is greater than that of an ice particle and hence, to impart a corresponding force the ice particle must be larger than the glass bead.

In addition, any possible differences in contact times must be considered as this will also affect the force on impact. When the Hertzian theory of elastic collision is applied to the various interactions it is found that the differences in contact times are minimal, although this does not take into account the changing surface nature of ice as the temperature changes. Since plastic flow of ice can give rise to apparent higher strength the difference in contact times could be important.

Calculations were also performed to compare the experimental results with the calculations where a cantilever expression was used. (Ref.5)

Firstly, considering dend ritic crystals, the size and velocity of glass beads required to break a dendritic crystal can be found from the experiment. Then by calculating the size of hailstone or graupel particle (density 0.9g cm^{-3}), which has the same kinetic energy available with respect to the crystal when falling at their terminal velocities, a comparison can be made with the cantilever expression. Thus the experiment predicts that any graupel particle greater than about 550μm diameter will be able to break a crystal 3mm long. The cantilever expression predicts that a 400μm diameter graupel particle will be needed to break a crystal of the same length, width 150μm and thickness 150μm. Thus there is very close agreement between the two methods. Using the same method for a columnar crystal, the experiment predicts that a 1500μm graupel particle will break the 3mm long crystal whereas the cantilever expression, when a crystal of the same length and with an end radius of 250μm is used, predicts that a graupel particle of 850μm is required. Thus in this case the agreement is not as good. Both these methods have further doubts as to their quantitative applicability to natural clouds.

1. The crystal in the experiment is fixed to a target rod. This forbids a degree of rotational freedom which a natural crystal would have. This lack of rotation gives an enhanced stress at the

point of impact and an enhanced moment at the suspension point. A natural crystal would be able to dissipate some of the energy of impact in the form of rotation.
2. The lack of rotation interferes with the flow of air around the target crystal on impact.
Thus it can be deduced from these experiments that vapour grown crystals appear to be much more likely to fragment than rime grown at the same temperature with the possible implication that vapour grown crystal fragmentation, particularly that of dendrites, could provide a significant number of secondary ice crystals to some natural clouds.

Any quantitative estimation of the effect is limited however by the inherent differences between the experiment and natural conditions. Further studies, particularly in the field need to be carried out before any reliable estimates can be made.

REFERENCES

1. May K R 1945 The cascade impactor. An instrument for sampling coarse a·rosols. J Sci Instr., 22, 187-193
2. Vardiman L 1978 The generation of ice particles in clouds by crystal-crystal collision. J Atmos Sci, 35, 2168-80
3. Macklin W C and Payne G S 1967 A theoretical study of the ice accretion process.Quart J Roy Met Soc.,94, 195
4. Ranz W E and Wong J B 1952 Impaction of smoke and dust particles on surface and body collectors. Ind Eng Chem, 44, 1371
5. Hobbs P V and Farber R J Fragmentation of ice particles in clouds. J Rech Atmos, 6, 245-257

TABLE 1

Crystal Habit	Temperature (°C)	B.V. with air alone ($m\ s^{-1}$)	B.V. with 270μm diameter beads ($m\ s^{-1}$)
Needles	-3 to -5	9	5
Prisms	-5 to -8	11	6
Plates	-8 to -12	11	6
Dendrites	-12 to -16	2	Terminal velocity
Plates	-16 to -25	8	4

(B.V. Breaking Velocity)

TABLE 2

Crystal Type	Maximum dimension of crystal (mm)	Maximum impact speed at which crystal remains intact (ms^{-1})
Dendritic	3	9
Thin hexagonal plate	1	14
Hollow column	3	18
Needles	3	9

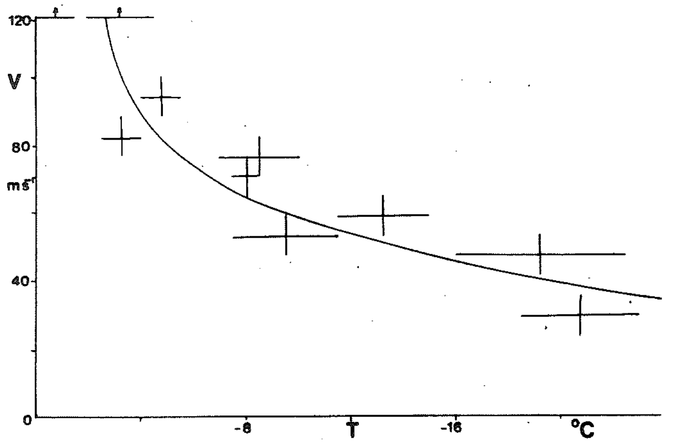

Figure 1. Velocity, V, at which rime was observed to break on impact with 485μm diameter glass beads, plotted against temperature T.

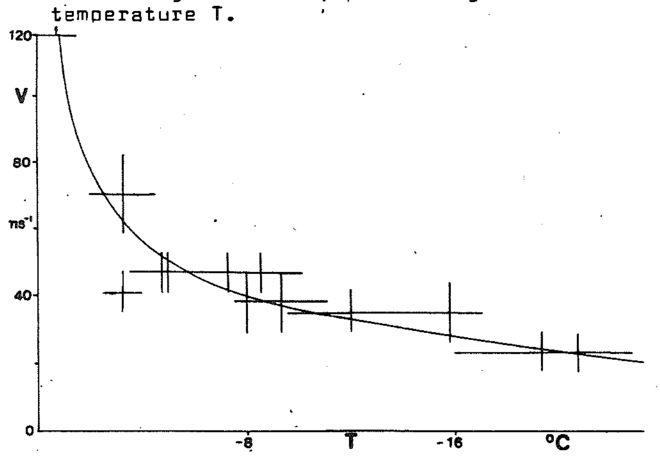

Figure 2. Velocity, V, at which rime was observed to break when impacted with 1075μm glass beads, plotted against temperature T.

SIMULTANEOUS OBSERVATION OF STRUCTURE OF LAYER CLOUDS AT UPPER- AND MIDDLE-LEVELS BY LASER RADAR AND 8.6MM RADAR

Takao Takeda, Mitsuaki Horiguchi and Kenji Akaeda

Water Research Institute, Nagoya University
Nagoya, Japan

1. INTRODUCTION

Layer clouds at upper- and middle-levels, which are often formed around a cyclone, have an important role in the water budget and heat budget in the atmosphere. One of interesting problems of these layer clouds is the formation of ice particles and their growth in them. The observational study of layer clouds around a cyclone has been made at Nagoya since 1980, mainly using a vertically-pointing radar of 8.6mm wave length and a laser radar by which the depolarization ratio of clouds is also measured. In this paper the fine structure of layer clouds and the spatial distribution of ice particles in them are described on the basis of observational results by both radars.

2. RESULTS OF OBSERVATION

2.1. Observation of layer clouds at upper-levels by 8.6mm radar

All of observations were made when it was not rainy and visible layer clouds at upper-levels were recognized. The observation by the vertically-pointing 8.6mm-radar often showed that layer clouds had the fine structure of radar echo shown in Fig. 1. In most of cases in which the radar echoes of large reflectivity (larger than $4x10^{-10}\ cm^{-1}$) were observed, they had a tendency to appear with period of about 10 min in the time-height cross section of reflectivity. Interestingly the cluster of radar echoes (for example, the echo region of reflectivity larger than $3x10^{-10}\ cm^{-1}$) also appeared with period of 40 to 60 min sometimes, as shown in Fig. 1.

2.2. Simultaneous observation by a laser radar and a 8.6mm radar

A laser radar of 0.6943μm wave length was sometimes used for the observation of layer clouds together with the 8.6mm radar. The laser radar can detect super-cooled cloud droplets as well as small ice particles, while our 8.6mm radar can detect only rather large particles. One example of simultaneous observation is shown in Fig. 2, which corresponds to the echo region between 16.30 and 17.00 in Fig. 1. Echoes of two radars show a much different structure, though intensive echoes appeared with period of about 10 min in both cases similarly. Detailed analysis of observational data suggests that this cloud system consisted of upper-level clouds and middle-level clouds and the latter clouds were mainly composed of super-cooled cloud droplets.

2.3. Measurements of depolarization ratio

The depolarization ratio of clouds ($\delta = P_{\perp}/P_{\parallel}$) measured by the laser radar is very useful for identifying whether cloud-composing particles are ice or liquid. Our measurements made for many kinds of clouds, which are summarized in Fig. 3, indicate that ice clouds showed the depolarization ratio of 40% or more, liquid cloud did the ratio of 10% or less and mixed clouds the ratio between 10 and 40%.

2.4. Case study of layer clouds observed on July 20 in 1983

On July 20 in 1983 the fine structure of layer clouds was observed using both the 8.6mm radar and the laser radar simultaneously, including the measurement of depolarization ratio. The data of channels 3 (3.55~3.93μm) and 4 (10.5~11.5μm) of satellite NOAA were also used in the analysis. It is seen from Fig. 4 (actually from more detailed figure) that generating cells appeared with period of 12 to 17min in the time-height cross section of reflectivity and streaks falling from these cells were identified. The measurement of depolarization ratio indicates that middle-level clouds, the radar echo of which is shown in Fig. 4, included many super-cooled cloud droplets and some streaks fell through cloud regions composed of cloud droplets. Figure 5 indicates the vertical profiles of reflectivity along streaks 2A, 2H and 3A and depolarization ratio in each part of clouds.

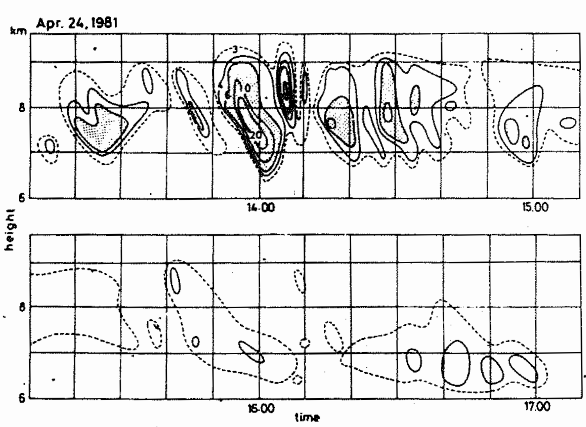

Fig. 1 Time-height cross section of radar reflectivity observed by a vertically-pointing radar of 8.6mm wave length on April 24 in 1981. Contours of 3, 4, 6 10 and 20 x $10^{-10}\ cm^{-1}$ are drawn.

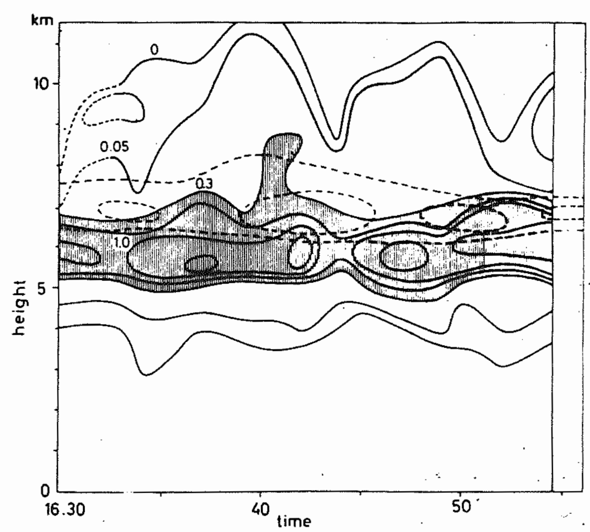

Fig. 2 Time-height cross section of backscattering coefficient observed by a laser radar on Apr. 24 in 1981. Contours of 0, 0.05, 0.3, 1.0 and 2.0 km^{-1} are drawn. Contours of radar reflectivity are also shown by dotted lines.

Figure 6 is the horizontal distribution of brightness temperature of channel 4 of NOAA 8. Radar echoes of Fig. 4 correspond to clouds shown in the right half part of Fig. 6. It is possible to infer the structure of upper part of clouds from the quantitative analysis of the data of channels 3 and 4. On the basis of the analysis of observational data of the laser radar and the 8.6mm radar and satellite data, the fine structure of layer clouds and the formation of ice particles in them will be discussed.

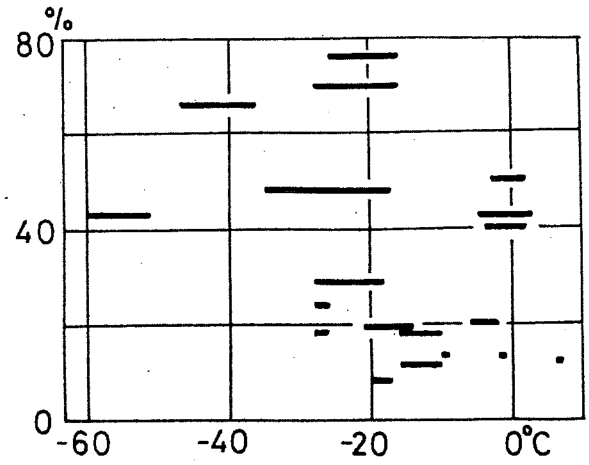

Fig. 3 Relationship between depolarization ratio (ordinate) and air temperature range of cloud layers observed by the laser radar (abscissa).

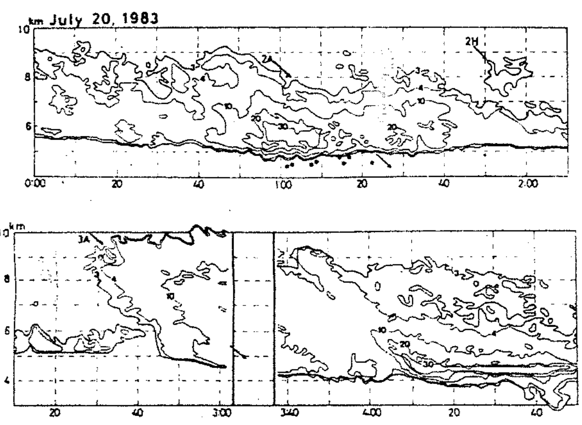

Fig. 4 Time-height cross section of radar reflectivity observed by the 8.6mm radar on July 20 in 1983. 2A, 2H and 3A indicates examples of streaks and dots are cloud bases determined by the laser radar. Contours of 3, 4, 10, 20 and 30 x 10^{-10} cm^{-1} are drawn.

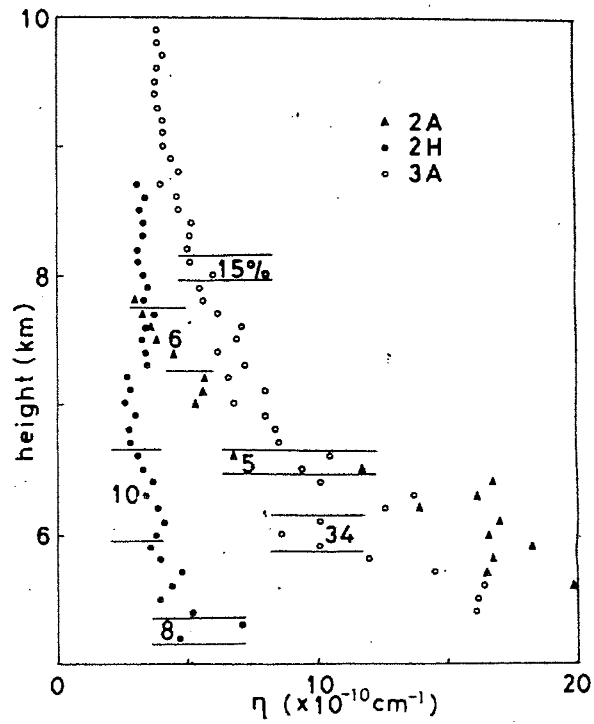

Fig. 5 Vertical profiles of radar reflectivity along streaks 2A, 2H and 3A, and depolarization ratios in each part of clouds.

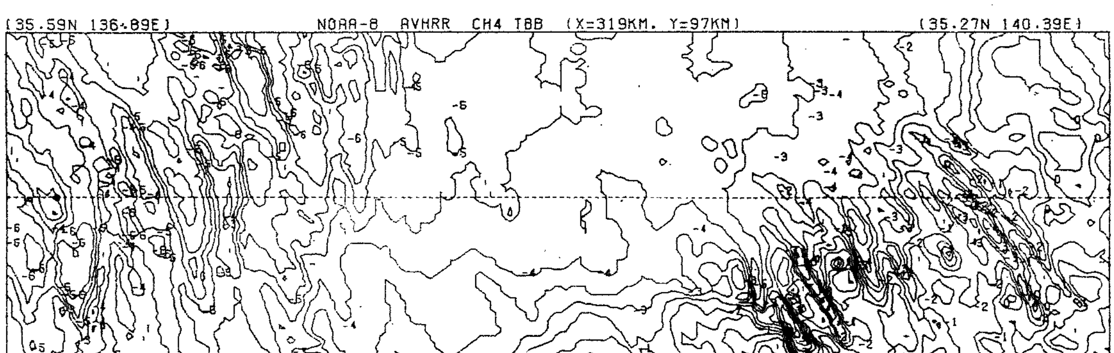

Fig. 6 Horizontal distribution of brightness temperature observed by NOAA 8 channel 4 at 7.47 JST on July 20 in 1983. A dot shown in the left part of the figure is the position of Nagoya. Radar echoes shown in Fig. 4 correspond to roughly the right half part of the figure. Contours are drawn every 10°C.

SESSION II

MICROPHYSICAL PROCESSES IN CLOUDS AND PRECIPITATION

Subsession II-4

Cloud droplet size-spectrum formation

MODELLING THE VARIATION OF AEROSOL CONCENTRATION IN DROPS AS A RESULT OF SCAVENGING AND REDISTRIBUTION BY COAGULATION

K.D. Beheng and F. Herbert

Institut für Meteorologie und Geophysik der Universität Frankfurt/Main
D-6000 Frankfurt 1, Fed. Rep. Germany

1. INTRODUCTION

The importance for cleansing the atmosphere from pollutants has been motivation for many investigations to the removal of aerosol particles (AP) by in cloud- and below cloud-scavenging of drops and ice particles. Usually, the efficiency of these processes is described in terms of a characteristic scavenging parameter formerly referred to as wash out- and rain out coefficients. These parameters are defined as fractional removal rates of airborne AP depending on the size distributions of both the AP and the particles removing the AP as well as on the scavenging collection kernel which is a decisive quantity in numerical scavenging models. In our companion article (Ref.1) we discussed in detail how this kernel function has been modelled analytically under the aspect of considering the effects of the microphysical atmospheric scavenging mechanisms in combination.

For estimating the scavenging effect by observational data it is common to combine mean bulk quantities such as liquid water content, total AP concentration in air and number or mass of AP in cloud or precipitation water in an empirical formula. This illustrates the present situation that, on the one hand, theoretically required microphysical quantities are not sufficiently known while, on the other hand, many measurements are made without taking notice of the microphysical character of the processes to be investigated. To overcome this discrepancy partially, theoretical models can be developed to account for the spectral character of scavenging and pollution and to investigate how microphysical quantities are related to the empirical bulk formula mentioned above. Such a model is subject of this study. Here we formulate the equations describing the degree of pollution of an evolving droplet spectrum by considering two mechanisms: the directly acting scavenging process and the indirectly operating redistribution of AP by coagulation of polluted drops.

2. MODEL DESCRIPTION, INITIALIZATION

The process of pollution of drops as well as the decrease of airborne AP are appropriately described in terms of kinetic equations for the size distribution functions. In order to simulate the degree of pollution we introduce, besides the drop mass x, a further internal coordinate n_p, counting the number of particles captured. As a consequence of this, the kinetic equation of the drop distribution function has been extended and reformulated in two aspects. First, by adding a flux divergence expression which considers the effects of direct scavenging of AP analogous to the formulation of drop condensation or evaporation. In doing so the 'pollution velocity' is determined by a specific mass balance condition so that the divergence term results in shifting the droplet spectrum towards increasing AP numbers. It is thereby assumed that all AP colliding with drops are incorporated as insoluble, non-reactive matter. As second aspect besides this direct pollution process just described it is considered that the AP number in a drop is changed by mutual coagulation between drops. The coagulation integrals then are defined in taking into account balance conditions for both the drop mass and the particle number within each drop. The kinetic equation for the AP distribution function representing the depletion of airborne AP is merely changed in so far as a droplet spectrum referenced to the new coordinate n_p has to be considered.
This description represents two coupled integro-differential equations then must be solved numerically.
Basis of the numerical scheme is a suitably defined discretization grid for particle mass, drop mass and AP number in drops. As initial size distribution of smaller AP we used a gamma function and for larger AP a Junge power law. For the two case studies presented in section 3 the same AP distribution is chosen with a mean radius of 0.03 µm and a total number concentration of $8 \times 10^3\,cm^{-3}$ according to values typically observed over industrial regions. The initial distribution function of polluted drops is given as $f(x,n_p) = g(x)\, h(n_p)$, where both $g(x)$ and $h(n_p)$ are given by modified gamma functions each specified by appropriate parameters. Note that the drop spectrum is yet polluted to some degree at the beginning of the model time. All distribution functions are transformed according to the known suggestions of Berry (Ref.2). The scavenging collection kernel is defined and computed as reported in Ref.1. The coagulation kernel is calculated according to Scott and Chen (Ref.3)

3. TWO CASE STUDIES

Numerical integrations of the kinetic equations have been carried out for different atmospheric situations and assuming that pollution is described (i) without drop coagulation effects, as e.g. scavenging by fog and (ii) by inclusion of the redistribution term by drop coagulation, simulating a cloud with relatively high liquid water content.
In case I we have considered the direct pollution term only. It is evident that for each drop category the corresponding liquid water content and droplet number density are constant with time. In contrast, we expect a considerable increase of the mass-dependent mean AP number per drop

$$\overline{N}_p(x) = \int_0^\infty n_p\, f(x,n_p)\, dn_p \,/\, N_d(x)$$

as well as the total mean AP number per drop

$$\overline{N}_p = \int_0^\infty \overline{N}_p(x)\, dx \,/\, N_d$$

where $N_d(x)$: number density of drops with mass x and N_d: total number density of drops.

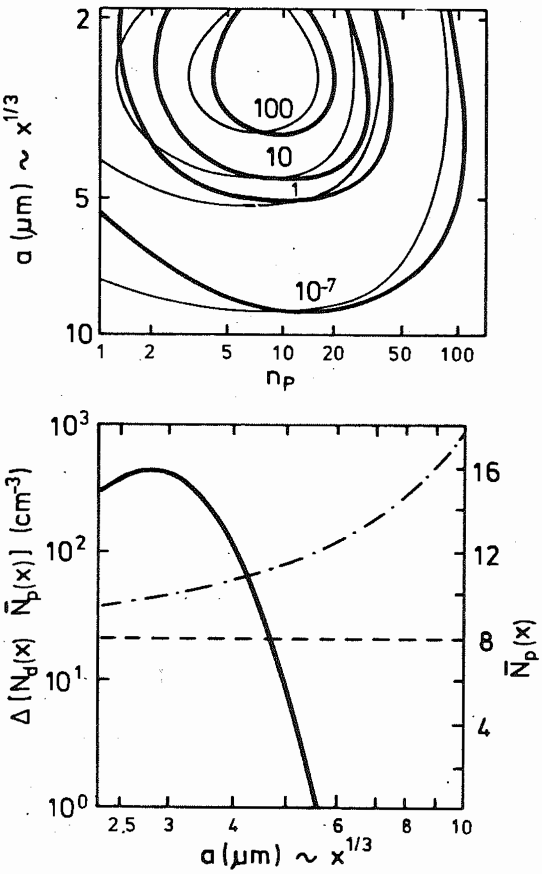

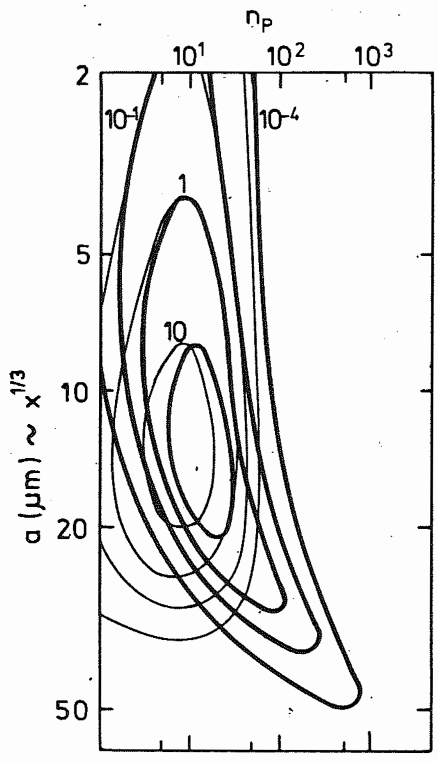

Fig.2: Isolines $f(x,n_p) = 10, 1, 10^{-1}, 10^{-4}$ cm^{-3} for t = 0 s (———) and t = 900 s (▬▬) for the same ambient parameters as in Fig.1.

Fig.1: (a) Isolines $f(x,n_p) = 100, 10, 1, 10^{-7}$ cm^{-3} as function of drop radius a and AP number n_p for t = 0 s (———) and t = 3000 s (▬▬);
(b) mass-dependent AP number per drop $\bar{N}_p(x)$ at t=0 s(– – –) and t=3000 s(–·–·–) and AP number increase in drops, $\Delta[\bar{N}_p(x)N_d(x)]$ in cm^{-3}, during the total model time as function of drop radius a
Ambient conditions: RH = 100.5%, T = 5 °C, p = 900 mb

In omitting the coagulation impact we chosed a fog droplet distribution with a mean radius of 2.5 μm, a liquid water content of 0.1 g m^{-3} and a total number concentration $N_d = 10^3$ cm^{-3}. The ambient conditions are listed in the figure captions. Computed isolines $f(x,n_p)$ = const. are presented in Fig. 1a for initial time and for t = 3000 s where $\bar{N}_p(x,t=0) = \bar{N}_p(t=0) = 8$. During the integration time the distribution function moves towards larger AP contents whereby larger drops are quicker advected than smaller. This property of relatively large drops, i.e. incorporating many AP, is also documented by the large $\bar{N}_p(x)$-values in Fig.1b. However, large drops are in so low concentration that their contribution to the depletion of particles is negligibly small. On the other hand, as shown by the solid line in Fig.1b, small drops present in high concentration are very effective in removing AP from air despite the only slight increase of $\bar{N}_p(x)$. At t = 3000 s the total mean AP number per drop $\bar{N}_p$ is raised to 10. Expressing $\bar{N}_p(x)$ in a mean AP number per unit water mass these results correspond to about 10^9 particles per gram in good agreement with estimates of Rosinski (Ref.4).

In case II we studied the effect of the redistribution term disregarded in case I. To realize this effect a drop size distribution is given with a liquid water content of 1.0 g m^{-3} and an initial mean drop radius of 14 μm. In contrast to case I, we recognize in Fig.2 that after 900 s model time larger drops highly polluted have been developed by coagulation in relatively small number concentrations. However, it is expected that for longer model times larger drops in appreciable concentration will be formed. The total mean AP number per drop $\bar{N}_p$ amounts to 15.5 compared to the initial value of 8. A definite influence of the drop size on the depletion of AP by means of using $\bar{N}_p(x)$ cannot be found out because the number of drops per mass category has been changed by coagulation processes in contrast to case I.

4. REFERENCES

1. Herbert F and K D Beheng 1984, A mathematical model of aerosol scavenging microphysics, this proceedings.
2. Berry E X 1967, Cloud droplet growth by collection, J Atmos Sci 24, 688-699.
3. Scott W T and Chen C Y 1970, Approximate formulas fitted to the Davis-Sartor-Shafrir-Neiburger droplet collision efficiency calculation, J Atmos Sci 27, 698-702.
4. Rosinski J 1967, Insoluble particles in hail and rain, J Appl Met 6, 1066-1074

CLOUD MICROPHYSICAL CHARACTERISTICS RELATED TO OROGRAPHIC AIR FLOW IN THE DUERO RIVER BASIN (SPAIN)

J.L. Brenguier

Centre National de Recherches Météorologiques
31057 Toulouse Cedex - FRANCE

1. INTRODUCTION

The quantitative prediction of precipitations is a complex objectif because of unstable processes, which can completely change the rain rates depending if they occur or not during the lifetime of clouds. These are principally the rapid growth of large droplets for coalescence and the ice multiplication mecanisms for cold clouds. The frequency of occurence of these processes has been compared in various parts of the world (Ref.1), but little is known to explain the high variability of microphysical properties of the clouds in the same place and during the same season, as it has been observed during the PEP* experiment in North West Spain (Ref. 2).

In this paper, a large and homogeneous cloud data set is analysed in order to relate the production of large droplets and the occurence of ice multiplication with primary cloud microphysical properties, like the droplet concentration and with thermodynamical characteristics, like the cloud top temperature. In the same time, an attempt is made to see if the origin of the air masses is able to explain the variability of these microphysical characteristics.

2. THE PEP SITE

The site, located in North-West Spain, is an area 100 km in radius, centered on Valladolid (5°W,42°N). Its most important features for our study are that the target area is :
- situated at 300 km from the ocean. Sufficiently close for the maritime properties of the air to be sensible, sufficiently far for the continental pollution to occur.
- very homogeneous over 10000 km², without appreciable change of relief (average altitude MSL = 900m; annual rainfall between 300 and 600 mm).
- very inhomogeneous in the environment since it is surrounded by 2700 m high mountains over 270° and open towards the ocean, in the South-West, by a slowly sloping plateau.

That appears on Fig.1 where different air mass circulations have been symbolized. Maritime air masses, flowing from West and South-West, penetrate in the Duero basin without strong orographic effect. They are called hereafter Maritime (M). Maritime Air masses, flowing from the South, the North-West or the North, give generally heavy precipitations upwind of the mountains before penetrating in the basin. They are called Modified Maritime (MM). Finally, continental airmasses, flowing from the East and the North, and maritime air masses, flowing from the East and South-East after having turned around Spain, have been put together into the Continental categorie (C). The number of cloud systems studied in each categorie are indicated in the arrows. The percentage of the precipitation for the 1981 period is indicated for each category.

More climatological characteristics of the site are available through a series of special reports published by WMO.

*PEP : Precipitation Enhancement Project of the World Meteorological Organization.

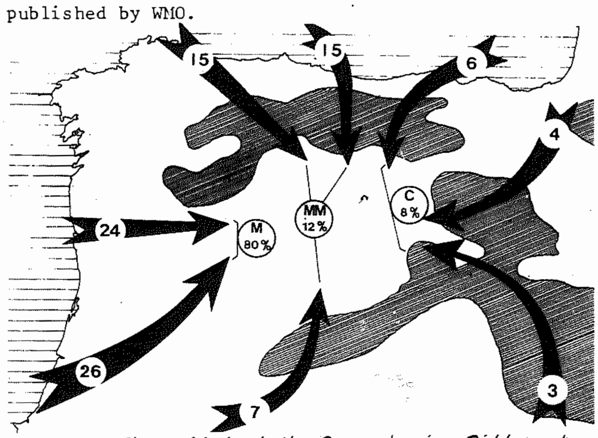

Figure 1. The relief of the Duero basin. Different air flows are indicated by arrows and classified into 3 categories. The number in the arrows represent the number of cloud systems studied by air flow regime. The percentage of the precipitation for the 1981 period is indicated for each category.

3. DATA BASE

The clouds were sampled by a cloud physics aircraft, the University of Wyoming's Queen Air. The periods of observation extended from February to May 1980 and 1981. The data used in this study have been obtained with a scattering probe (PMS ASSP) for the condensation droplet spectra, with a PMS 2D-C probe, which records the shadow images of particles with 25 µm resolution, for the crystal distribution and current aircraft measurement systems for thermodynamical parameters.

The maximum droplet concentration (C_M) has been estimated on vertical profile of the droplet concentration, in regions where the ice concentration was smaller than 0.1 ℓ^{-1}. Because the mean value and the maximum of C_M for 1981 were 20% smaller than the mean value and the maximum for 1980, all the 1980 values have been reduced by 20%. This discrepancy can result from change of the probe sample area or of the processing technique used to correct the coincidence effects.

To characterized the droplet growth at cloud base, the volume weighted size distribution has been calculated. The maximum mode of this distribution ($\emptyset_M$) has been estimated 500 m above cloud base, when the ice concentration was smaller than 0.1ℓ^{-1}.

The maximum ice concentration (IC_M) has been estimated in the University of Wyoming by processing the 2D images and noted in the detailed flights reports. In these reports have been noted too : the cloud base altitude (Z_B) and the cloud top temperature (T_T).

The air trajectories have been classified, as indicated in the preceding paragraph, using synoptical maps at different levels and the radiosounding winds measured in the Valladolid airport during the experiment.

4. CONDENSATION PHASE

Figure 2 shows the variability of the maximum droplet concentration (C_M) and its dependence on cloud base altitude above ground (Z_B). For $Z_B \leq 1600$ m, C_M is varying from 80 cm^{-3} up to 620 cm^{-3}, characterizing modified maritime clouds. (The uncorrected 1980 C_M values reached up to 800 cm^{-3}). Above 1600m, the C_M values remain smaller than 350 cm^{-3}. Except for this observation, the droplet concentration for the whole data set does not show strong correlation with cloud base altitude, whereas the data collected on the same day in multi-layers clouds do. 13 situations of multi-layer clouds have been studied during 1980 and 1981. Up to 4 super-imposed cloud layers have been sampled and the corresponding data points are joined on Figure 2. They show similar decreases of C_M versus Z_B of about 100 cm^{-3} per km. Somes cases (noted by ★) indicate the presence of distinct homogeneous layers separated by an inversion, with constant values of C_M in the same layer and a rapid change of C_M for clouds located on both sides of the inversion. On the other hand, Figure 2 suggests that the C_M values of maritime clouds are smaller that those of the maritime modified and the continental ones. In order to appreciate this difference more quantitatively, the mean values and the variances of C_M have been calculated for the three categories. To take into account for the decrease of C_M versus Z_B, virtual concentrations C'_M reported to the ground altitude have been calculated by the relation :

$C'_M = C_M + 0.1 * Z_B$, where Z_B is the cloud base altitude above ground in meters.

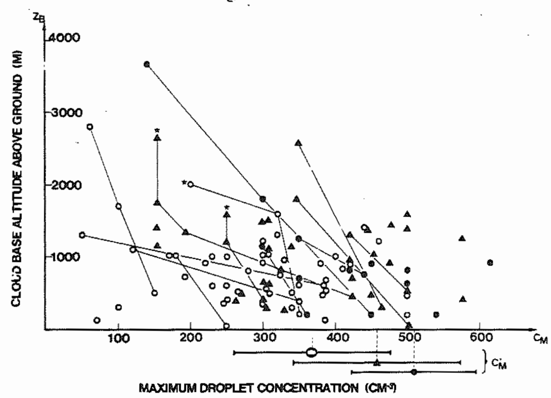

Figure 2. Maximum condensation droplet concentration C_M (cm^{-3}) versus cloud base altitude above ground Z_B (meters)

o : maritime air masses

▲ : modified maritime air masses

● : continental air masses

Superimposed cloud layers, sampled on the same day, are connected by thin line. Virtual maximum droplet concentration, C'_M, reported to the ground altitude (see text) are reported below the concentration scale.

We note that the results obtained without correction, for cloud base altitudes lower than 1600 m, are similar to those presented here, but the correction allows to take into account all the data points. The concentrations of the clouds classified as maritime are well distinct from those classified as continental, with mean values of C'_M respectively equal to 370 cm^{-3} and 510 cm^{-3} and with variances respectively equal to 108 cm^{-3} and 85 cm^{-3}. Clouds classified as maritime modified have intermediate droplet concentrations, with 460 cm^{-3} for the mean value and 115 cm^{-3} for the variance. These values are added on Figure 2 below the concentration scale.

These differences can appear insignificant compared to differences between true maritime (C_M<100 cm^{-3}) and true continental (C_M >1000 cm^{-3}) clouds. In fact, they affect the droplet growth at cloud base which is represented on Figure 3 by the maximum mode of the volume weighted droplet spectrum, 500 m above cloud base ($\emptyset_M$) versus C_M. Less data points have been plotted on Figure 3 because the maximum values of the mode have been estimated only when measurements of the droplet spectrum were available 500 m above cloud base and in regions where the ice concentration was lower than 0.1 l^{-1}.

Figure 3 shows that droplet concentrations smaller than 400 cm^{-3} are able to produce large droplets ($\emptyset_M$>20 µm) in the first 500 meters of cloud depth. Hence, due to their lower droplet concentrations, the maritime clouds have more chance to produce large droplets rapidly.

This analysis of the condensation phase reveals that air masses penetrating the Duero basin through the South-West Valley, can preserve their maritime characteristics even in the lowest levels (C_M<250 cm^{-3} for Z_B<700 m). On the contrary, maritime air flows from the North and North-West, crossing the Cantabric barrier, can change their condensation characteristics even for high cloud base altitudes (C_M>450 cm^{-3} for Z_B>1200 m) These modifications are important for warm rain initiation because of the sensitivity of coalescence processes to the large droplet concentrations.

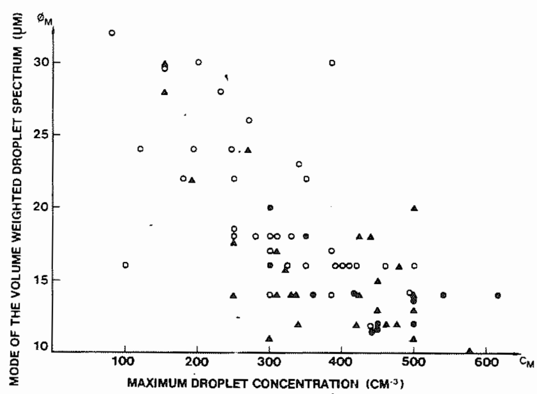

Figure 3. Maximummode of the volume weighted droplet spectrum $\emptyset$M, (µm) measured 500 m above cloud base, versus maximum droplet concentration C_M(cm^{-3})

o : maritime air masses

▲ : modified maritime air masses

● : continental air masses

5. ICE PHASE

Most of the clouds sampled in the Duero basin during PEP, have cold top temperature and produce rain by ice processes. Based on a 43 cases analysis, Vali(Ref.2) has shown that in about 45% of the non convective clouds and in 81% of the convective ones, secondary ice processes were evident. Different mecanisms, called the Hallet-Mossop Splintering,(Ref. 3), the crystal fragmentation (Ref.4) and the rime break-up (Ref.5), have been proposed to explain the high ice concentrations observed in clouds with moderately cold top temperatures (T_T>-10°C). For the Hallet-Mossop process, large drops of about 25 µm in diameter and larger are essential. It follows that the cloud base temperature, governing the maximum condensate available at -8°C, and the droplet concentration are critical for ice multiplication (Ref. 1) . On the other hand, though the ice nuclei concentrations have shown a very strong dependence on temperature , the ice crystal concentrations do not (Ref.6). Discrepancies can be due to ice multiplication processes, but even after selection of clouds to study primary ice production the ice concentration is not well correlated with cloud top temperature for the complete set of clouds (Ref.7). On the contrary, the correlation is remarkable for individual days, on which many clouds were penetrated over a wide range of temperatures (Ref.7). On the same location, changes in air mass, ice nucleus concentration and condensation characteristics can explain this observation. This hypothesis has been tested by plotting on Figure 4. the maximum ice concentration (IC_M) measured in a given cloud as a function of the maximum droplet concentration (C_M) and the cloud top temperature (T_T).

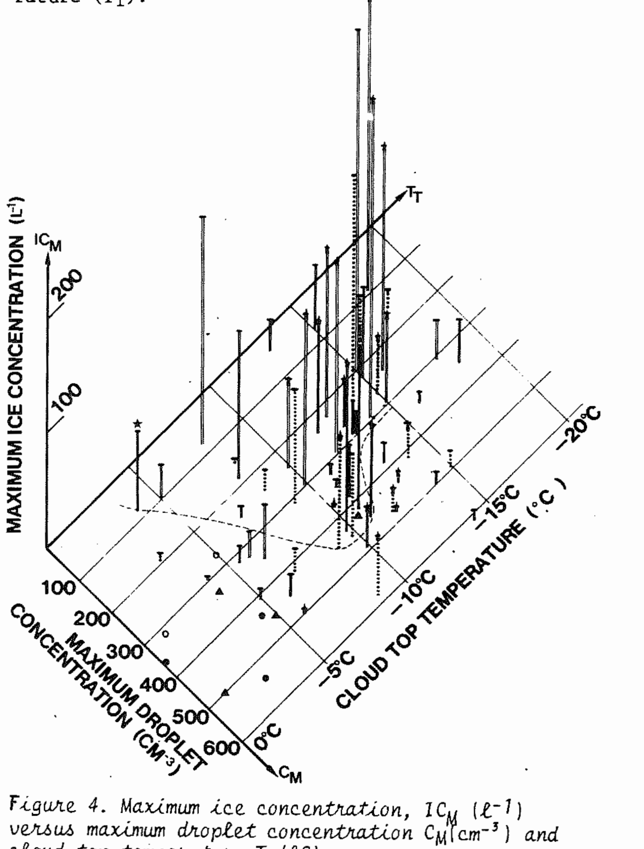

Figure 4. Maximum ice concentration, IC_M (ℓ^{-1}) versus maximum droplet concentration C_M (cm^{-3}) and cloud top temperature T_T (°C)

- : *maritime air masses*
  - o : *if $IC_M<1$*
- : *modified maritime air masses*
  - ▲ : *if $IC_M<1$*
- : *continental air masses*
  - ● : *if $IC_M<1$*
- ★ : *C or D type clouds*

Viewed as a whole, Figure 4 shows that for cloud top temperatures warmer than -5°C, ice multiplication occurs only for very low droplet concentrations. Particularly in the situation noted by (★) where the merger between a Sc (base temperature = + 10°C) and an As layer (top temperature = -4°C) was sampled by the Queen Air. Due to the warm temperature of the cloud base, the cloud depth of about 2 km and the very low droplet concentration measured ($C_M<80$ cm^{-3}), the coalescence was very active and at the highest level (T = -3°C) a mixing of needles and semi round water or ice particles were observed by the 2D probe in concentration up to 100 ℓ^{-1} (Queen-Air flight reports).

For cloud top temperature between -8°C and -10°C, most of the clouds produce high ice concentrations, for droplet concentrations up to 450 cm^{-3}. For C_M larger than 450 cm^{-3} and the same temperature interval, two cases have been sampled showing ice concentrations of about 50 ℓ^{-1}. One of these cases, C_M = 580 m^{-3} and T_T = -9°C, correspond to a situation where a high pollution spreading all over the Duero basin was noted by G. Vali, with possible very high ice nucleus concentration.(Queen-Air flight reports).

For cloud top temperatures colder than -10°C, the droplet concentration threshold for ice multiplication seems to decrease rapidly until 300 cm^{-3}. Clouds with tops colder than -20°C, are not reported on Figure 4 for two main reasons. First of all, at these temperatures, ice concentration is less dependent on condensation droplet characteristics and the origin of the air masses. Secondly, the cloud top temperature is not so well known because the Queen Air has flown at lower levels and cloud tops were estimated by visual observations or echotop radar measurements.

Due to differences in droplet concentration between the maritime clouds and the maritime modified or the continental ones, the maritime clouds appear to have more chance to produce high ice concentrations. Moreover, maritime modified clouds with low droplet concentrations are able to produce similar high ice concentrations. On the other hand, continental clouds even with low droplet concentrations give smaller concentrations of ice.

This observation suggest that the condensation droplet concentration is an important factor governing ice multiplication for clouds growing in air masses of recent maritime origin, whereas ice multiplication is less efficient in clouds of continental origin and less dependent on the droplet concentration.

6. SUMMARY

The observations described in the two preceding paragraphs, show that the rain formation in clouds growing in maritime air masses are different according to the air mass trajectories. For air masses crossing the mountains (South, North-West and North flow), the inefficiency of the microphysical processes to produce large droplets and high ice concentrations, appears to be related with an increase of the condensation droplet concentration. An alternative explanation could be that this inefficiency is due only to different dynamical properties of the clouds growing downwind of the mountains.

In order to test this hypothesis, the distribution of cloud types in each air mass category has been studied. In 1980, G. Vali has proposed a classification ot the cloud systems based on morphological properties of the clouds : class A - Deep, non convective (NS, merging layers) ; class B - Shallow clouds (St, As, Cuhum, Sc, Ac) ; class C - deep widespread convection (Cu cong, Cu med) ; Class D - isolated deep (Cb calv.). The relative frequency of A, B and C + D types of situations is roughly even, while the A type systems are responsible for two thirds of the total rain, the C + D clouds systems for the other one third, and the B cloud systems yield only 1% of the total precipitation (Ref.2)

air mass cat. / cloud type	M maritime	MM modified maritime	C continental	virtual drop conc / max ice conc.
A Ns, merging layers	346 103 34% (17) 26% (9) 87 98	387 119 27% (10) 18% (4) 31 31	465 39 46% (6) 60% (6) 20 14	380 108 33% 28% (19) 54 74
B St, As, Sc, Ac	355 106 24% (12) 31% (11) 30 40	466 88 51% (19) 50% (11) 33 62	548 108 46% (6) 30% (3) 7 6	443 117 37% 37 25 29 49
C+D Cu med, Cu cong, Cb calv	400 110 42% (21) 43% (15) 124 85	550 115 22% (8) 32% (7) 38 33	540 8% (1) 10% (1) 80	445 128 30% 34% (23) 96 81
$\bar{x}$ σ p% (n) / p% (n) $\bar{x}$ σ	370 108 50% 52% (35) 85 86	460 115 37% 33% (22) 34 48	510 85 13% 15% (10) 22 24	(100) / (67)

$\bar{x}$: mean value, σ : variance } of C'_M (upper left), IC_M (lower right)

p% : percentage of clouds in the given class

(n) : number " " " " " "

Table I. Distribution of the analyzed clouds into the three air masses categories (columns) and the three cloud type classes (rows)

The distribution of the clouds used in this analysis into the three cloud types (A, B and C + D) and into the three air mass categories (maritime, modified maritime and continental) has been reported in Table I. In each box , the upper left corner corresponds to the data set used for droplet concentration analysis and the lower right corner to the ice production analysis. These two sets are not equivalent because the warm top clouds and those with top colder than -20°C have not been used for the ice production analysis. Inversely the same cloud base values can correspond to more than one maximum ice concentration for clouds of different depths and top temperatures. The numbers in the boxes give the percentage of the total number of clouds of the air mass category indicated on top of the Table which belong to the cloud type class indicated on the left. The number in brackets indicates the true number of clouds. In the column on the right, the data are summarized by cloud type class with the mean value and the variance for the virtual concentration C'_M and the maximum ice concentration IC_M. The true number of clouds for the droplet concentration is the same than the percentage because the total number is just equal to 100. In the lower row, the data are summarized by air mass categories.

The numbers of the column on the right indicate that the data sets used for C_M and IC_M are well representative of the general cloud type distribution (1/3 in each cloud type class). On the contrary, 50% of the clouds (35% for IC_M) belong to the maritime category for only 13% (10% for IC_M) to the continental one and moreover, the cloud types are not homogeneously distributed into the air mass categories.

Concerning the droplet concentration, the A type clouds have a lower value of C'_M (380 cm^{-3}) than the B and C + D type clouds (445 cm^{-3}), but their distribution into the three air mass categories cannot explain the result of paragraph 4. Table I shows indeed that the mean values of C'_M, respectively in each of the 3 cloud type classes, are smaller in the maritime category than in the two other ones.

Concerning the ice production, the number of C + D type clouds is very different in the maritime category (15) than in the continental one (1) and the mean value of IC_M for the C + D type clouds (96 ℓ^{-1}) is very high compared to its mean value for the A type clouds (54 ℓ^{-1}) and the B type clouds (29 ℓ^{-1}). To verify that this observation does not change the conclusion of paragraph 5, the C + D type clouds have been symbolized on Figure 4 by black arrows. They correspond to cloud top temperatures between -10°C and -15°C. In this temperature interval, the modified or continental C + D type clouds have effectively low values of IC_M, which confirms the interpretation of these observations.

7. CONCLUSIONS

In spite of the variability of the cloud microphysical characteristics, the analysis of a large and homogeneous data set allowed to document in detail the dependence of the droplet growth and ice production on droplet concentration, cloud base altitude and cloud top temperature. In particular, the occurrence of ice multiplication, favoured by warm cloud bases (Ref.1), is generally reduced in our case, because of the high droplet concentrations of the clouds with low cloud base altitudes above ground. On the other hand, the maritime air masses seems to have a reduced precipitation efficiency due to the increase of their droplet concentration when they penetrate the Duero basin through the surrounding mountains.

Acknowledgments. This research is supported by the French Institut National d'Astronomie et Géophysique (N°4666).

8. REFERENCES

1. Mossop S C 1978, Some Factors Governing Ice particle Multiplication in Cumulus Clouds, *J.Atmos Sci.* 35, 2033-2037.

2. Vali G et al 1982, Ice evolution versus precipitation in the Duero basin, *Proc. Conf. on Cloud Physics*, Chicago 15-18 November 1982, 218-221.

3. Mossop S C, and Hallet J 1974, Ice cristal concentration in cumulus clouds : influence of the drop spectrum. *Science* 186, 632-634.

4. Vardiman L 1978, The generation of secondary ice particles in clouds by crystal-crystal collision, *J. Atmos. Sci.* 35 (11), 2168-2180.

5. Vali G 1980, Ice multiplication by rime breakup, *Proc. VIII International Conf. on Cloud Physics*, Clermont-Ferrand 15-19 July 1980, 227-228.

6. Hobbs P V et al 1980, The structures of summer convective clouds in Eastern Montana. I : natural clouds, *J. Appl. Meteor.* 19, 645-663.

7. Cerni T A 1982, Primary ice crystal production in cmlus congestus clouds of Eastern Montana, *Proc. Conf. on Cloud Physics*, Chicago 15-18 November 1982, 346-349.

A MATHEMATICAL SIMULATION MODEL OF AEROSOL SCAVENGING MICROPHYSICS

F. Herbert and K.D. Beheng

Institut für Meteorologie und Geophysik der Universität Frankfurt/Main
D-6000 Frankfurt 1, Fed. Rep. Germany

1. INTRODUCTION

Essentially influenced by the previous works of Greenfield (Ref.1) and Young (Ref.2), in recent time, numerical simulation models of the complex particle removal process by cloud and rain drop scavenging have been developed on the basis of improved theoretical concepts. Central points in such mathematical models are the following two questions. First, how one can describe the significant atmospheric scavenging processes in combination and second, which removal rates, i.e. the portion of aerosol mass absorbed by drops (or ice particles), can be computed on the basis of stochastic-kinetic continuity equations?

While earlier models operate with partially incomplete and partially erroneous mathematical concepts for the particle transport with the result that the so-derived scavenging collection kernels are not uniformly applicable in the whole particle size range, extended theoretical simulations of the basic scavenging microphysics developed more recently (Refs.3,4,5) provide successively improvements over those earlier calculations. From a physical point of view these flux models are not yet complete in so far as they ignore effects by mechanic inertial impaction and therefore only apply (in the case of uncharged drops and particles) to relatively small particles with radii smaller than about 0.1-0.5 µm. However, to apply generally in the whole particle size range the flux method should permit the quantitative computation of the scavenging collection kernel between aerosol particles and water drops (or ice particles) due to the combined impact of all responsible internal and external driving forces, i.e. the simultaneous action of Brownian and phoretic diffusion as well as Coulomb and mechanic inertia forces. Such a closed flux model (Ref.9) has been developed with relatively simple assumptions about the effective collision cross sectional area.

A generalization of this simulation method is subject of the present study. It is shown that this model allows, for the first time, to describe the effect of particle scavenging in the whole radius size range $10^{-3} < r < 10^{2}$ µm as function of all known dynamic influences and geometric parameters. The model operates, compared to earlier models, with an inertia-corrected scavenging collection kernel as well as with kinetic equations for the time evolution of the drop and particle size spectra.

2. THE SCAVENGING KERNEL FUNCTION

In this context the first question concerning the microphysical mechanisms is answered with the help of a thermodynamically derived particle flow equation with which the combined action of purely stochastic forces by Brownian, pressure and phoretic diffusion as well as inertial impaction of the paricles can be considered. Associated with specific 'dynamic closure' conditions for the inertia terms, this equation finally leads to a purely diagnostic flux equation for the particles in which gravitational and Coulomb forces now become additionally effective.

This flux velocity equation and specific kinematic constraints and boundary conditions for the particle flow are combined together in a mathematical concept general enough to model the fine structure of the collection mechanism between large drops and relatively small particles. The result of this analysis is a significant kernel function K representing an effective volume of collection per unit time. According to this we assume that Brownian diffusion as well as phoretic and Coulomb forces provide via a simultaneous action a spherically symmetric particle transport to the drop surface $4\pi a^2$ equivalent to that K-expression used in Ref.3, whereas gravity and other dynamic forces are assumed to provide an additional contribution which strongly depends on an effective collision cross sectional area πy_c^2 (see schematic illustration in Fig.1).

While the terms due to Brownian, phoretic and Coulomb forces in the K-expression can be evaluated according to Ref.3 or 5, a numerical evaluation of the gravitational term requires an explicit formulation of the effective cross sectional radius y_c. The y_c-specification might generally be a very complicated kinetic-dynamic problem, whereas for practical estimations a quite useful approximation appears to be already given by $y_c=a$, hence the cross sectional area is πa^2. This simple approach holds for pure gravity impaction having a collision efficiency of about 1. From the basic flux concept, however, it is clear that

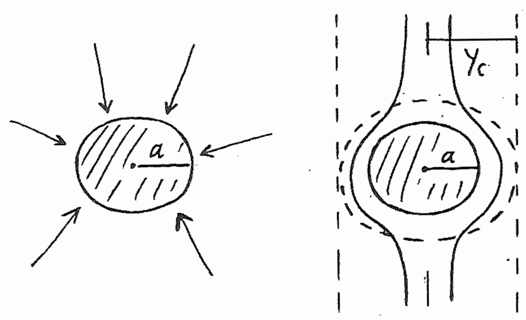

Fig.1: Effective collision surface for Brownian, phoretic and Coulomb induced scavenging (left sketch) and effective cross sectional area for gravitational induced scavenging (right sketch)

inertial impaction represented by the gravitational term is not a function of gravity only but also of other hydrodynamic influences which may gradually enhance the impaction process as larger the particles are. Although such effects are not in all cases dominant, of course, they should be associated with the fine structure of K using a more general definition for the effective collision radius. For doing this a polynomial approach should be successful, its constants being computed to give a precise fit to observed collection kernels for particles with radii of about >0.5-1 μm. At time, however, there are not enough observational data of this size range available to compute a representative polynom with reliability. As a way out of this dilemma we therefore choosed a simpler, semi-empirical concept setting $y_c = a(r/r_0)^{\alpha}$. In this case one needs far less kernel-data to compute realistic values of the two parameters α and r_0. For some few special cases such fitting values could be found with the scavenging efficiency data of a trajectory model by Grover et al. (Ref.6) as well as the few observations of Leong et al. (Ref.7) where α and r_0 then have been determined by numerical interpolation to fit each two of these data sets.

Numerical evaluations have been made for particle radii between $10^{-3} < r < 10$ μm and drop radii between $10 < a < 500$ μm and for alternate ambient temperatures, pressures and relative humidities. The collector drops and the particles were assumed either to be uncharged or to carry an electric charge of the magnitude of mean thunderstorm charges on drops measured by various authors (see Ref.8). The ventilation coefficients and terminal velocities were calculated according to the schemes recommended in Refs.10, 3.
For the air-particle conductivity ratio which plays a role in the phoresis correction we assumed either the value 0.05 as it was used in other numerical studies (e.g. Ref.3) or the value 0.005 estimated (Ref.7) from observations.

One example of the computed variations of the collection kernel with the particle radius is presented in Fig.2. The calculations have been carried out for the conditions RH = 30%, T = 24 °C, p = 1000 mb for uncharged particles and for the collector drop radii a = 72 μm and 66 μm. These case studies exhibit the effects of diffusio- and thermophoresis and particularly of the inertial impaction term represented alternatively with the simplest and with the inertia corrected y_c-form.

In summary for all numerical case studies we can state that, independent of whether y_c could be determined inertia corrected or not, the results provide the typical structure of the kernel mentioned before. This means, in contrast to the predicted K-curves of former flux models, a minimum of K in a certain size range ($0.1 < r < 1$-2 μm; so-called Greenfield gap range) and a rapid increase for larger particles. With characteristic values α and r_0 it is found that K increases $\sim r^n$ ($n>4$) up to particle radii of about 5-7 μm, whereas with a non-corrected gravitational term it is found that the right branch of the curves increases uniformly $\sim r^2$.

	Leong et al. (Ref.7)		Grover et al. (Ref.6)	
	interpolation interval (μm)			
	1.7/2.09	2.09/3.16	1.6/2.0	2.0/3.0
r_0 (μm)	1.84	1.47	1.72	0.95
α	7.95	2.85	8.49	1.74

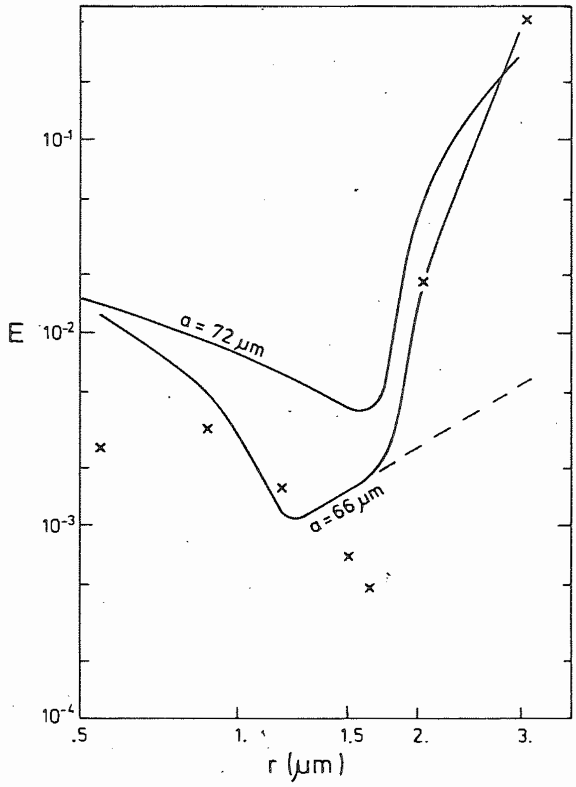

Fig.2: Collision efficiency E as function of particle radius r. For the drop radius a = 72 μm E has been fitted to the trajectory model values of Grover et al. (Ref.6) and for a = 66 μm to the experimental data of Leong et al. (Ref.7) indicated by crosses, respectively. The interpolation parameters α and r_0 are listed in the Table. For further parameters see text.

Although from a microphysical point of view this ascent $K \sim r^2$ is really too flat for larger particle radii $r > 1$-2 μm, nonetheless one may expect that, when using y_c=a, numerically predicted wash out effects in natural particle size spectra are not considerably underestimated.

3. CALCULATED PARTICLE SCAVENGING EFFECT

The second question quoted in the Introduction is associated with the more general task that the particle scavenging micromechanism is to be treated as a part of a numerical cloud simulation model with which in particular the wash out effect of airborne particles under given external conditions can be predicted. Obviously in this case we have to solve kinetic continuity equations for the particle and drop size spectra. Here the key problem is the numerical integration of these equations using given kernel functions by which the evolution of the size spectra as well as especially the decrease of number and mass of the particles by the scavenging impact are determined.

In this study we operate with a reduced calculation scheme for the drop and particle microphysics. This makes use of the assumptions that the drop size spectrum $f_w(\varepsilon)$, ε: drop mass, is varied due to drop coagulation and break-up terms, only, while the time variation of the particle spectrum $f_p(m)$, m: particle mass, is exclusively described by the loss of particles due to their absorption by drops. The numerical scheme allows to calculate the scavenging impact on the spectral distribution function $f_p(m)$ as well as for any derived mathematical moment

$$\int_0^\infty m^\nu f_p(m)\, dm$$

as e.g. the number density (ν=0) and the mass density (ν=1) of particles.

Because the removal rates of particles essentially depend on the structure and time variation of the drop size spectrum the loss integral in the particle equation can numerically be solved in detail or by approximation. Here both methods are applied and compared with one another. The approximation method is based on a specialized theoretical concept so that the particle collection effect can be described more simply as the result of a relaxation process in the sense of chemical reaction relaxations. Central point of this treatment is a characteristic relaxation time

$$\tau = \left(\int_0^\infty K(m,\varepsilon)\, f_{w,o}(\varepsilon)\, d\varepsilon\right)^{-1} \quad \text{in which,}$$

for practical applications, the drop size distribution is set to be stationary, i.e. $f_w(\varepsilon) = f_{w,o}(\varepsilon)$, and the phoresis-Coulomb corrected term in the scavenging kernel $K(m,\varepsilon)$ is developed into a polynomial form. Practical advantage of such a relaxation approach is a considerably reduced numerical work compared with that needed to compute non-specialized kinetic equations. Some explicit calculations of our numerical studies are presented in Fig.3 and 4. For these as well as for all other numerical evaluations with variable ambient temperature, pressure, relative humidity, particle and liquid water content etc. we can summarize the following main aspects:

1) The model predicted removed aerosol mass is strongest in the beginning of the scavenging process and decreases gradually with increasing time (Fig.3, curve 1). This result could be expected due to observations of in-cloud and below-cloud scavenging.

2) Characteristic for the time development of the particle spectrum is a strong decrease of small particles which diminishes gradually (under the main impact of Brownian and phoretic diffusion forces) towards the Greenfield minimum. Beyond this range the capture of larger particles again increases rapidly. This size range of the

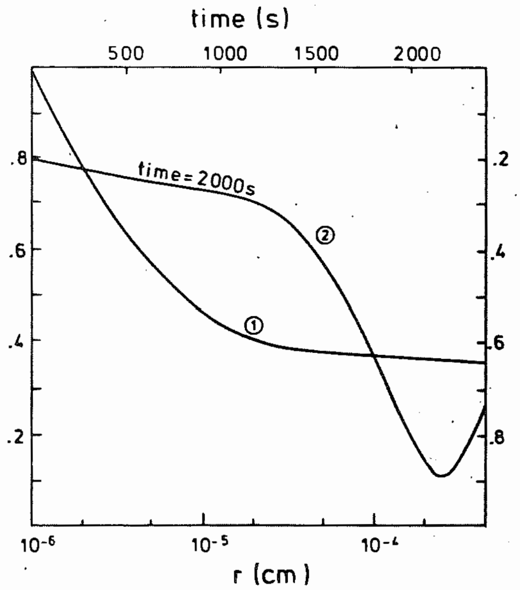

Fig.3: Fraction of particle mass removed (curve 1) as function of time (upper abscissa, right ordinate) and fraction of particle number removed (curve 2) as function of particle radius r for t = 2000 s (lower abscissa, left ordinate). Ambient conditions: RH = 50%, T = 10 °C, p = 900 mb.

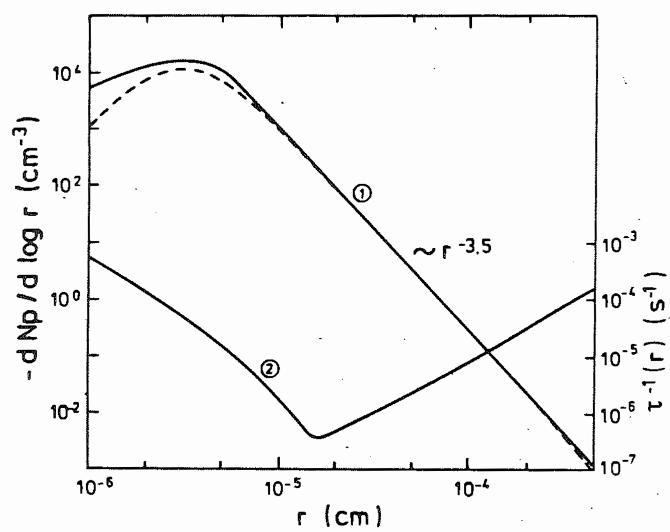

Fig.4: Development of the particle size distribution, $-dN_p/d \log r$ (curve 1), from the initial time (solid line) to t = 3000 s (dashed line) as well as the relaxation coefficient $\tau^{-1}(r)$ (curve 2) as function of particle radius r. Ambient conditions: RH = 100.5%, T = 10 °C, p = 900 mb.

particle spectrum contributes the main portion to the removed aerosol mass although the concentration of larger particles is relatively small.
Curve 2 in Figs.3 and 4 represents computations of the scavenging effect in spectral resolution; its integral influence is included implicitly in curve 1 of Fig.3.

3) For a natural drop size spectrum $f_{w,o}$ the spectral structure of the relaxation coefficient $1/\tau(r)$ has been computed in the form shown in Fig.4. It is characteristic that the $1/\tau$-curve consists of two branches separated by a (small) minimum range similar to the Greenfield minimum in the kernel spectrum (cf. Fig.2). It might be clear that this similarity is not self-evident.

ACKNOWLEDGMENT

The studies presented here and in our companion article of this proceedings are part of a cloud physical research program in the Sonderforschungsbereich 'Atmosphärische Spurenstoffe' supported by the Deutsche Forschungsgemeinschaft. Also, we wish to thank our colleague R.W. Unfug for his expert help in preparing the manuscript.

4. REFERENCES

1. Greenfield S 1957, Rain scavenging of radioactive particulate matter from the atmosphere, J Meteor 14, 115-125.
2. Young K C 1974, The role of contact nucleation in ice phase initiation in clouds, J Atmos Sci 31, 768-776.
3. Wang P K, Grover S N and H R Pruppacher 1978, On the effect of electric charges on the scavenging of aerosol particles by clouds and small raindrops, J Atmos Sci 35, 1735-1743.
4. Martin J J, Wang P K, Pruppacher H R and Pitter R L 1981, A numerical study of the effect of electric charges on the efficiency with which planar ice crystals collect supercooled cloud drops, J Atmos Sci 38, 2462.2469.
5. Herbert F 1981, On the flux and collision mechanism of the scavenging process of atmospheric aerosol particles, in Atmospheric trace constituents, Vieweg, Braunschweig, 117-128.
6. Grover S N, Pruppacher H R and Hamielec A E 1977, A numerical determination of the efficiency with which spherical aerosol particle collide with spherical water drops due to inertial impaction and phoretic and electric forces, J Atmos Sci 34, 1655-1663.
7. Leong K H, Beard K V and Ochs III H T 1982, Laboratory measurements of particle capture by evaporating cloud drops, J Atmos Sci 39, 1130-1140.
8. Takahashi T 1973, Measurements of electric charge on cloud drops, drizzle drops and rain drops, Rev Geophys Space Phys 11, 903-924
9. Herbert F, Roos M and Beheng K D 1983, Ein Modellexperiment zum Auswaschen von Teilchen durch Wolken- und Regentropfen, Meteorol Rdsch 36, 130-134.
10. Beard K V 1976, Terminal velocity and deformation of raindrops aloft, J Atmos Sci 33, 851-864.

DROPLET ACTIVATION, GROWTH AND EVAPORATION IN A SLOW-EXPANSION CLOUD CHAMBER

Edward E. Hindman
Research Institute of Colorado[1]
Fort Collins, CO 80526 USA

ABSTRACT

A controlled, slow-expansion cloud chamber was used to investigate droplet activation, growth and evaporation. The resulting measurements reproduced the droplet activation and growth behavior first predicted by Howell. The measurements revealed possible evaporation of certain cloud droplets in supersaturated conditions.

1. INTRODUCTION

The formation of cloud droplets in an adiabatically rising air parcel, in its simplest form, is a function of the sizes, numbers and compositions of the nuclei and the temperature, moisture and parcel rise-rate. Howell (Ref. 1) first predicted the following features of a droplet population in a rising air parcel.

1. The initial population of solution droplets in subsaturated conditions, grow by condensation as the relative humidity (RH) in the parcel increases.
2. As the RH exceeds 100%, the larger droplets "activate" (exceed their critical sizes) and form cloud droplets.
3. A maximum supersaturation is reached which represents an equilibrium between moisture available for condensation and the growth of the cloud droplets.
4. Finally, certain droplets with critical supersaturations greater than or equal to the maximum supersaturation remain "unactivated", or haze droplets.

Fitzgerald (Ref. 2), among others, tested these predictions with careful subcloud nucleus, temperature, moisture and updraft measurements and cloud base droplet measurements. He used the subcloud measurements to predict cloud-base droplet spectra. The general features of Howell's theory were confirmed by Fitzgerald's work. Further, he found the predicted spectra dispersion to be narrower than the measured dispersion: More large drops were measured than were predicted. This discrepancy is presently unresolved. The discrepancy may be resolved through a combination of laboratory tests and droplet activation and growth calculations.

As a first step in this direction, Fitzgerald's field experiment has been simulated in the CSU slow-expansion cloud chamber. Nuclei of known sizes, numbers and composition were exposed to the chamber environment which simulates an adiabatically rising parcel. The purpose of the experiment was to determine how accurately the chamber and measurement systems reproduce the activation and growth of cloud drops and to provide droplet evaporation data. According to the summary in Pruppacher and Klett (Ref. 3), there is a derth of droplet evaporation data.

[1]Permanent affiliation: Department of Atmospheric Science, Colorado State University, Fort Collins, CO 80523 USA.

2. CLOUD CHAMBER SYSTEM

The chamber and data collection system are shown in Fig. 1. Briefly, referring to the figure, the ~1m³ chamber was expanded at 3.5 mb min^{-1} [the values which can be achieved range between 850 and 275 mb ($\pm$ 0.5 mb) and between 30 and -35C ($\pm$ 0.5C)]. The walls were cooled (Tw) to track the chamber air temperature (Ta). The nuclei for droplet formation were primarily NaCl or $(NH_4)_2SO_4$ particles generated by bubbling solutions using the system described by Hindman and Blumenstein (Ref. 4).

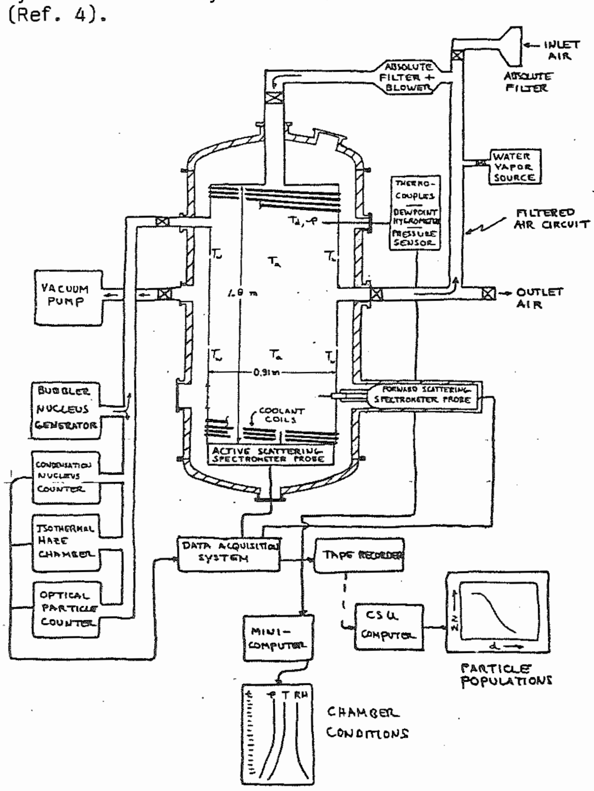

Figure 1. The CSU slow-expansion cloud chamber and measurement systems. Details are given in the text.

The sizes (0.01 to 30 μm dia.) and concentrations (10^{-4} to 10^{4}cm^{-3}) of the particles in the chamber were determined by combining measurements from a condensation nucleus counter (CNC) (Environment/One), and a series of optical particle counters (Particle Measurement Systems - Active Scattering Spectrometer Probe (ASASPX) and Forward Scattering Specrometer Probe (FSSP-100), Ref. 5, and a Royco Model 200). The FSSP was modified to sample through a capillary which restricted the flow to 1 cm^{3}s^{-1} and avoided the "dead-time" problems discussed in Refs. 6, 7 and 8. The sizes and concentrations of haze droplets in equilibrium at 100.0% were determined prior to chamber expansion using an isothermal haze chamber (IHC) described by Hindman (Ref. 9).

As seen in Fig. 1, the data from the CNC, ASASPX, FSSP, Royco and IHC were collected on magnetic tape for post-experiment reduction and size distribution and number concentration analyses. The pressure, temperature and dewpoint (Td) measurements were continuously processed, relative humidity was calculated and the resulting values were continuously displayed to aid conduct of the experiment.

3. PROCEDURES

Between 27 September and 1 October 1982, ten cloud formation and evaporation experiments were conducted in the CSU chamber. Results from the 30 September experiment using a 1% NaCl solution are available for presentation. The procedures and the times they occurred during the experiment as well as the resulting chamber conditions are listed in the table. As seen in the table, the experiment was divided into three periods: -34 min to 0 min, initialize the chamber; 0 min to 42.3 min, expansion period and 42.3 min to 49.5 min, constant low-pressure period.

TABLE

CHAMBER CONDITIONS, 30 SEPT 1982, 1% NaCl SOLUTION

TIME FROM START OF EXPANSION (min)	AIR TEMPERATURE (°C)	AIR PRESSURE (mb)	RELATIVE HUMIDITY MEASURED (%)	RELATIVE HUMIDITY ESTIMATED (%)	PROCEDURE
-34.0	20.0	843	71.0	—	• PURGE CHAMBER AND ADJUST HUMIDITY
-28.0	20.0	843	70.0	—	• SEAL CHAMBER
-25.0	20.0	843	72.0	—	• START BUBBLER
-20.0	20.0	843	72.0	—	• STOP BUBBLER
-15.0	19.0	843	72.0	—	• START ROYCO/CN SAMPLES
-10.0	20.0	843	72.0	—	• STOP ROYCO/CN SAMPLES
0.0	20.0	843	72.0	—	• START EXPANSION AT ~0.6 mb s⁻¹, BEGIN ASASP/FSSP SAMPLES
8.3	17.5	816	80.0	—	
18.5	14.3	783	91.0	—	
22.5	12.9	767	96.0	—	• FIRST LARGE DROPS OBSERVED
24.0	12.3	766	98.0	—	
24.5	12.2	764	98.3	98.0	
25.0	12.1	761	98.5	98.5	
25.5	12.0	760	99.2	99.0	
26.0	11.8	759	100.0	99.5	
26.5	11.7	758	100.0	99.8	
26.7	11.6	757	100.0	100.0	• CLOUD FORMED
27.0	11.5	756	100.0	100.06	
27.5	11.4	755	100.0	100.15	
28.0	11.3	753	100.5	100.37	
28.5	11.2	752	100.8	100.45	
29.0	11.1	751	100.8	100.28	
29.5	11.1	748	101.2	100.50	
30.0	11.0	746	100.5	100.35	
30.5	11.0	745	101.2	100.23	
36.5	9.9	726	101.2	100.27	
42.3	9.0	710	101.0	100.34	• STOP EXPANSION
43.5	9.0	710	100.5	100.18	• MEASURED 100% RH AT 44.0 MIN
45.0	9.1	710	99.2	100.15	
45.3	9.1	710	99.2	100.14	
45.8	9.1	710	99.2	100.12	
46.0	9.1	710	99.2	100.0	
46.2	9.1	710	99.2	99.8	
47.0	9.1	710	99.0	99.0	
48.0	9.1	710	98.5	98.5	
49.0	9.2	710	98.0	98.0	
49.5	9.3	710	98.0	98.0	• UNSEAL CHAMBER

Cloud droplet spectra were measured every 4s and averaged over 12s intervals for analyses. The spectra measured during the 20 min period between bubbler termination and chamber expansion were analyzed to estimate rate of particle loss by coagulation and diffusion to the walls (0.9% min^{-1}). The rate of particle loss due to evacuation of the chamber was estimated from the pumping rate (0.34% min^{-1}). The FSSP flow rate changed with reducing pressure causing an apparent particle loss of 0.46% min^{-1}. The rate of particle loss due to sedimentation were estimated from the fall speeds to range from 0.16% min^{-1} for 1 μm diameter particles to 46% min^{-1} for 20 μm particles. Each analyzed droplet spectra was corrected for these losses.

As can be seen in the table, two procedures were used to evaluate the chamber relative humidity. The first procedure was to calculate RH values from the Ta and Td measurements. The calculated RH values greater than 100.0% were caused by Td > Ta due to droplets partially evaporating in the Td sensor. The second procedure was to estimate the subsaturated and saturated RH values by matching the analyzed droplet spectra to expected spectra as a function of RH from the Köhler curves of Low (Ref. 10). In Fig. 2, the dry particle spectra and spectra at 99.8, 100.0 and 100.06% were estimated from the spectra measured at 72% RH.

The supersaturated RH values in the table were estimated using the following iterative procedure which is illustrated in Fig. 2: First, a supersaturation value was assigned and the corresponding Köhler curve was plotted; Second, the cumulative concentration for the intersection between the Köhler curve and analyzed droplet spectra was evaluated; Third, the smallest dry particle size that accounted for the cumulative concentration was read off the plots; Fourth, from Fitzgerald (Ref. 11) the critical supersaturation was calculated from the dry particle size. If the calculated supersaturation was less than (greater than) the first estimate, then the second estimate was less (greater) than the first. The steps then were repeated until the calculated and estimated supersaturations were equal.

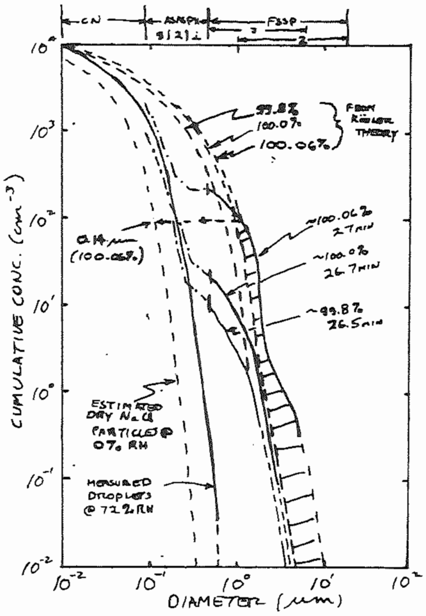

Figure 2. Estimation of chamber relative humidity by matching measured droplet spectra with expected spectra from Köhler theory. The ▨ area is the region of activated droplets. The size ranges of the CN, ASASPX and FSSP particle counters are indicated.

4. RESULTS

The chamber temperature, pressure and dew point measurements taken during the experiment are plotted on an adiabatic diagram in Fig. 3. It can be seen from the figure that the chamber environment reproduced first a dry-adiabatically rising air parcel. After cloud formation, the chamber reproduced a moist-adiabatically rising parcel.

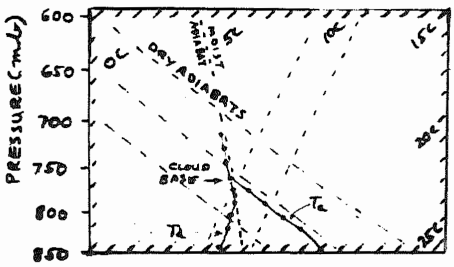

Figure 3. The temperature, pressure and dewpoint measurements from the 30 September experiment that employed at 1% NaCl solution.

The cloud droplet spectra measurement during the 30 September 1982 experiment are illustrated in Fig. 4. Three distinct stages are apparent in the figure (the chamber conditions are detailed in the table): 0 min to 26.7 min, haze droplet formation and growth, 26.7 min to 42.3 min, cloud droplet activation and growth, 42.3 min to 49.5 min, cloud droplet evaporation to haze drops.

5. DISCUSSION

Köhler theory is strictly valid for monodisperse droplets and equilibrium RH conditions. Gerber et al. (Ref. 12) followed these constraints and experimentally verified the theory for both NaCl and $(NH_4)_2SO_4$ particles 0.02 to 0.12 μm diameter. Nevertheless, the use of Köhler theory in the slow-expansion chamber experiments is justified. First, the polydispersion of droplets was sufficiently low in concentration ($N(\geq 0.01\ \mu m) = 10^4 cm^{-3}$) that the droplets were separated by 46,000 times their diameters. They acted as individual droplets. Second, the rates of changes of relative humidity ($0.024\% s^{-1}$ subsaturated conditions, $0.003\% s^{-1}$ supersaturated conditions) were slow enough so the droplets were always at equilibrium size. For example, Hindman (Ref. 9) reported that dry NaCl particles 0.2 and 0.6 μm diameter reach their critical sizes 20 and 1200s after being exposed to their critical supersaturations of 0.04 and 0.0075%, respectively. This translates to equilibrium growth at rates less than or equal to $3.3\% s^{-1}$ and $0.08\% s^{-1}$, respectively. The chamber rates were well below these upper-limit rates.

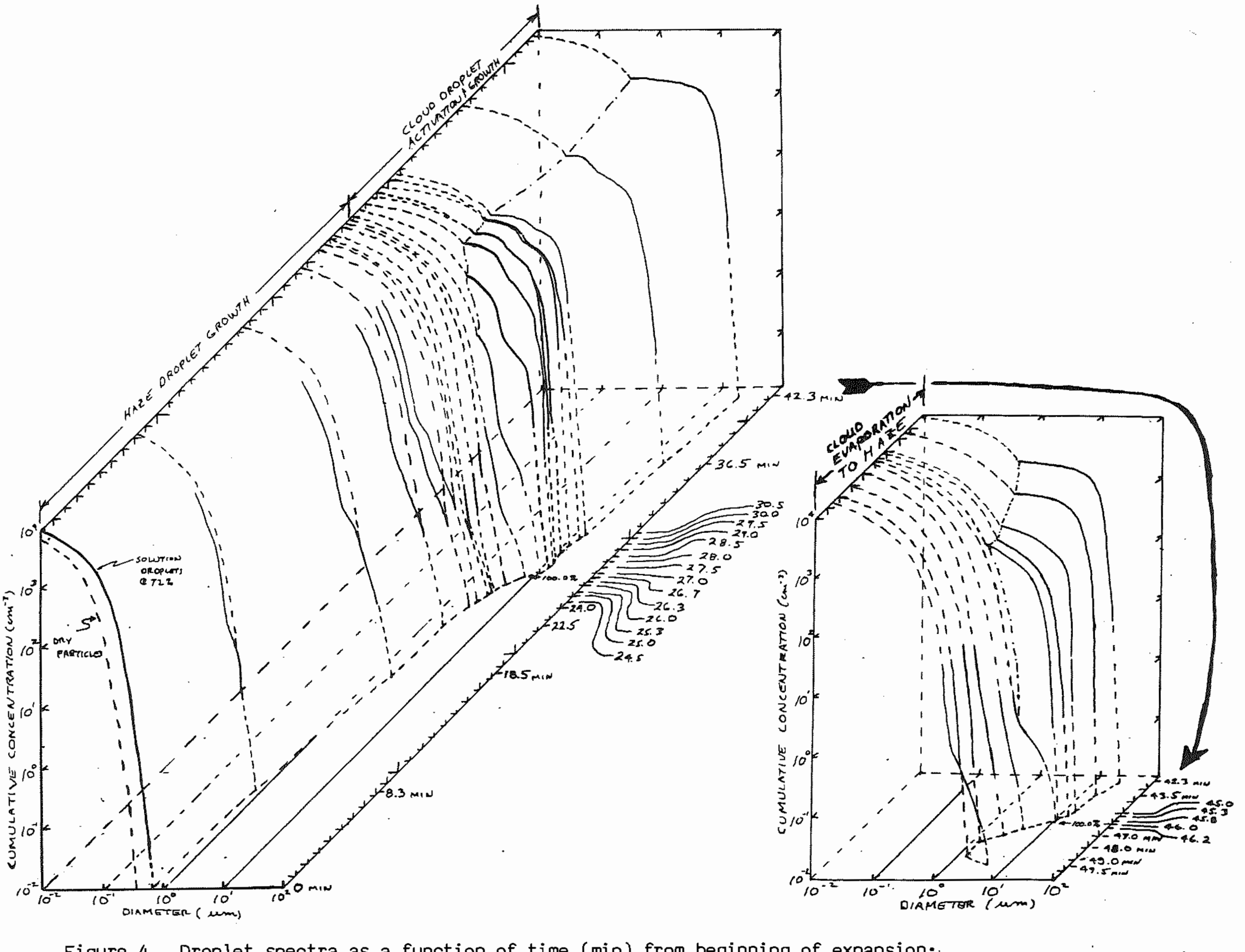

Figure 4. Droplet spectra as a function of time (min) from beginning of expansion; 30 September 1982 experiment, 1% NaCl solution. The upper dashed-segments of the spectra are expected spectra using Köhler theory. The solid lines are measured spectra and the lower dashed-segments are reasonable extrapolations of the measurements. The —·— curve separates the unactivated and activated droplet populations. The chamber conditons corresponding to the indicated times are given in the table.

Consequently, because of the low droplet concentrations and slow-expansion rate, it is expected that the measured droplet behavior, up to the critical superaturation values, will conform to Köhler theory. It can be seen in Figs. 2 and 4 that only the larger droplets ($\gtrsim 1$ μm) conformed to theory. The concentrations of submicron droplets are lower than predicted with theory. The particle concentrations were not large enough to cause coincident errors in the ASASPX and FSSP instruments (significant errors occur when N(≥0.09 μm) ≥ $10^5 cm^{-3}$ and N(≥0.5 μm) ≥ 1500 cm^{-3}). So the low concentrations of submicron droplets in the ASASPX data are probably due to partial evaporation of droplets in the 14 cm sampling tube between the chamber and sensor. The FSSP sensor was in situ so evaporation should have been a minimum. A complete analysis of the remaining nine experiments will be required before final conclusions can be made about the measured low concentrations of submicron droplets.

As can be seen in the table, the measured and estimated relative humidity values up to 99.0% are in good agreement. The measured values reached 100% sooner than the estimated values because of partial evaporation of large droplets in the Td sensor. During the constant pressure period the measured RH values plateaued at 99.2 while estimated RH values reduced from 100.15 to 99.8%. From this analysis, it appears measured RH values ≤99.0% are reliable. Values above 99.0% should be inferred using Köhler theory. To avoid this inference in future experiments, the hygrometer of Gerber (Ref. 13, 14) should be employed which accurately measures RH between 95 and 105%.

Combining the droplet spectra in Fig. 4 with the supersaturation variations listed in the table produces laboratory confirmation of the droplet growth behavior first predicted by Howell (Ref. 1): Haze droplets grow as relative humidity increases, activation of drops and gradual increase of supersaturation to s_{max} (0.50%) and then continued growth of drops but diminishing of the supersaturation. The maximum supersaturation of 0.50% is consistent with that reported by Hudson (Ref.15) for stratus clouds and lies between values for fog (0.1%) and cumulus (1.0%). Droplet activation and growth calculations, initialized with chamber data, are underway by Fitzgerald using an adaptation of his warm-fog model (Ref. 16). The model has realistically reproduced the formation of warm fog at sea. The purpose of these calculations is to compare the measured spectra of active droplets with expected spectra.

As seen in Fig. 4, droplet evaporation began after 42.3 min, the point at which the pressure was held constant at 710 mb. However, the bimodal droplet spectra indicated supersaturated conditions persisted. It may be possible to have newly activated cloud droplets evaporating in supersaturated conditions as soon as the supersaturation reduces below the critical supersaturations of the droplets. The most rapid droplet evaporation occurred between 45.8 and 46.0 min (0.2 min) for droplets 0.5 to 5 μm diameter. For droplets of similar sizes, an equivalent amount of growth occurred between 26.7 and 27.5 min (0.8 min). Thus, in this experiment, droplet evaporation rates exceeded droplet growth rates.

6. CONCLUSIONS

From the one experiment presented, droplet activation and growth measurements in the slow expansion cloud chamber, in general, followed what was expected from theory for drops ≥1 μm. Measurement difficulties prevented resolution of growth below this size. Evidence is presented that newly activated droplets may evaporate in supersaturated conditions as soon as the supersaturation reduces below the critical supersaturations of the droplets. Droplet evaporation was measured to be somewhat faster than droplet growth for droplets 0.5 to 5 μm diameter.

7. ACKNOWLEDGEMENTS

This study is a portion of the research funded by ONR Grant N00014-79-C-0793 administered through the Research Institute of Colorado. The experiment was conducted by Randy Horn, Rochelle Blumenstein, DaXiong Feng and William Finnegan while the author was unavoidably on travel. Brian Morrison and Philip Durkee assisted with computer programming and data analyses.

8. REFERENCES

1. Howell, W. E., 1949: J. Meteor., 6, 134.
2. Fitzgerald, J. W., 1972: Ph. D. Thesis, U. of Chicago, 144 pp.
3. Pruppacher, H. R. and J. D. Klett, 1978: Microphysics of Clouds and Ppt., D. Reidel Pub Co., 714 pp.
4. Hindman, E. E. and R. R. Blumenstein, 1982: [IN] Hygroscopic Aerosols in the Planetary Boundary Layer, Spectrum Press, Hampton, VA. In press.
5. Knollenberg, R. G., 1976: Ppts. Int'l Conf. Cloud Physics, AMS, Boston, 554-561.
6. Mossop, S. C., 1983: J. Clim. Appl. Meteor., 22, 419-428.
7. Baumgardner, D., 1983: J. Clim. Appl. Meteor., 22, 891-910.
8. Cerni, T. A., 1983: J. Clim. Appl. Meteor., 22, 1346-1355.
9. Hindman, E. E., 1981: J. Rech. Atmos., 15, 235-244.
10. Low, R., 1969: Part I, ECOM-5249, ASL, White Sands, NM, 553 pp.
11. Fitzgerald, J. W., 1973: J. Atmos. Sci., 30, 628-634.
12. Gerber, H. E. et al., 1977: J. Atmos. Sci., 34, 1836-1841.
13. Gerber, H. E., 1980: J. Appl. Meteor., 19, 1196-1208.
14. Gerber, H. E., 1981: J. Appl. Meteor., 38, 454-458.
15. Hudson, J. G., 1983: J. Atmos. Sci., 40, 480-486.
16. Fitzgerald, J. W., 1978: J. Atmos. Sci., 35, 1522.

J.G. Hudson and C.F. Rogers
Desert Research Institute
Reno, Nevada, U.S.A.

1. INTRODUCTION

An earlier work (Ref. 1) presented the first cloud interstitial measurements of CCN spectra. This was accomplished by separating cloud droplets from the samples. Comparisons with total within-cloud CCN spectra, which included nuclei within droplets, were then interpreted in terms of various models of cloud mixing. The results suggested that classical or homogeneous mixing processes were occurring.

Further experiments are now described which employed improved droplet size cuts which were also varied during the experiments. The results not only confirm the previous study but also establish a correlation between cloud droplet size and nucleus critical supersaturation.

These mixing models which attempt to explain how large droplets are formed can be classified into two categories depending on the assumed mode of mixing. The homogeneous mixing models (Ref. 2 and 3) explicitly state that the largest surviving cloud droplets should be those which were nucleated upon the largest (most active and lowest S_c) CCN. An inhomogeneous mixing model (Ref. 4) explicitly states that no such linkage exists and we infer the same for an entity mixing model (Ref. 5) which states that the development of large drops is independent of CCN concentrations.

As pointed out in Ref. 1, interstitial CCN spectra can be used to differentiate between these two mixing modes. Homogeneous mixing should result in steeper interstitial spectra because more of the lower S_c nuclei should be within droplets. The interstitial spectra in an inhomogeneously mixed cloud should not display this characteristic steepness because droplet growth is more of a function of the dynamics rather than the nucleus S_c. Interstitial measurements with cuts at larger sizes emphasize the differences between the two types of mixing processes and more directly address the important question of large droplet formation. For homogeneous mixing, many of the smaller droplets grown on high S_c nuclei would now show up in the interstitial spectrum. Multiple cycles of evaporation and recondensation as well as mixtures of parcels with different supersaturation histories would still display a characteristic steepness in the interstitial CCN spectrum. For inhomogeneous or entity mixing, the interstitial CCN concentration for all S_c's should be raised below S_{eff} (effec-tive cloud supersaturation) because the nuclei within small droplets which would appear in the "interstitial" sample have approximately equal potential of having any S_c below S_{eff}. If either mixing scenario actually influences the development of large droplets, then the predicted characteristics of the "intersti-tial" spectra should persist to size cuts as large as the drop sizes which are influenced by mixing.

2. DESCRIPTION OF EXPERIMENTS

The measurements were carried out at Henninger Flats (765 m elevation) near Pasadena, California. CCN were measured with a continuous flow diffusion chamber (Ref. 6) and an isothermal haze chamber (Ref. 7). Droplet size cuts were achieved with a cyclone separator (Ref. 8) attached to the sample inlet tube. The flowrate through the cyclone was periodically changed to achieve various desired droplet size cuts. The cyclone was also periodically removed from the tube in order to make direct "total" within-cloud CCN measurements. Since this does not exclude the cloud droplets from the sample, these "total" CCN measurements include all nuclei within the measured volume of the cloud. Droplets are evaporated within the sampling tube inside the instrument trailer before the sample enters the cloud chambers where the nuclei form droplets. These droplets are counted in standard practice by the optical counters on each cloud chamber.

Table 1 presents all of the data for one cloud event including both interstitial and total CCN measurements. The remarkable consistency of the concentrations of high S_c nuclei even with various droplet size cuts attests to the fact that these smaller nuclei had little droplet involvement.

TABLE 1 - HENNINGER
June 8-9, 1983

			Number cm^{-3} (Within S_c Intervals) (S_c %)						
Time	Cy-clone	Size Cut µm Diam.	0.3–0.14	0.14–0.10	0.10–0.08	0.08–0.036	0.036–0.022	0.022–0	LWC $gm\ m^{-3}$
2038-2045	On	5.1	413	104	96	178	114	43	
2050-2100	On	2.5	329	88	77	132	115	17	
2104-2112	On	9	399	91	90	176	124	44	0.381
2115-2127	On	2.5	384	81	69	118	65	18	0.433
2125-2140	Off	Total	393	97	85	165	152	70	0.432
2141-2148	Off	Total	384	88	85	167	164	54	0.822
2149-2156	Off	Total	410	88	94	166	161	92	0.592
2157-2205	Off	Total	412	87	78	153	160	105	1.060
2208-2215	On	9	412	93	79	159	150	62	0.658
2217-2227	On	2.5	388	81	70	126	93	35	0.310
2228-2236	On	2.5	326	70	57	95	68	22	
2238-2244	On	4.8	384	68	59	107	73	23	0.751
2245-2252	On	4.8	388	70	54	88	53	14	0.868
2255-2305	On	5.1	475	83	75	137	108	37	1.380
2308-2322	On	9	471	81	80	161	161	67	0.662
2323-2332	Off	Total	435	79	74	147	184	143	0.027
2334-2339	On	9	399	78	72	145	170	120	0.285
2340-2347	On	9	423	79	73	139	155	99	0.349
2348-2357	On	5.1	407	77	70	136	142	70	0.619
2358-0007	On	5.1	420	76	69	127	135	86	0.016
0008-0017	On	5.1	359	74	62	112	89	58	1.480
0018-0027	On	5.1	364	70	58	91	50	12	2.360
0029-0037	Off	Total	424	82	70	129	142	89	2.221
0038-0046	Off	Total	438	86	72	127	122	103	3.166
0049-0056	On	9	413	82	71	125	101	41	2.310
0057-0106	On	9	424	82	64	109	88	34	1.980
0107-0115	On	9	502	85	64	104	89	34	2.058
0119-0125	On	5.1	475	90	63	95	50	11	2.000
0128-0135	On	5.1	465	88	65	101	48	7	1.860
0138-0145	On	2.5	425	79	62	96	43	5	0.835
0148-0154	On	5.1	478	83	70	122	112	41	0.537
0155-0205	On	5.1	465	81	67	120	117	70	0.428
0206-0215	On	5.1	440	79	67	121	123	81	0.077
0218-0225	On	5.1	441	80	67	119	123	91	0.0016
0228-0237	On	2.5	414	79	66	119	120	88	0.00031
0238-0252	On	9	468	78	67	120	127	102	0.022
0253-0258	Off	Total	482	80	67	122	136	110	0.00087
0300-0306	Off	Total	477	83	69	134	135	109	0.0315
0307-0315	On	5	473	83	67	121	130	106	0.377
0316-0324	On	5	517	88	71	125	111	38	0.634

The measured total within-cloud CCN concentrations indeed showed a remarkable degree of consistency with time during cloud events (Fig. 1). These results show that non-nucleation aerosol scavenging by cloud droplets was not an active process. Moreover, chemical conversion within droplets was also apparently not significantly changing the CCN concentrations. These observations indicate conservation of CCN within clouds; therefore, even though the measurements were not simultaneous, the interstitial CCN concentrations could be subtracted from the total concentrations to deduce the spectrum of CCN which were within cloud droplets greater than the cut sizes.

3. RESULTS

The significant aspect of this work is the changes in the concentrations of the lower S_c nuclei as the cyclone size cut was varied (Table 1). These concentrations are also understandably a function of cloud density as shown in Fig. 2.

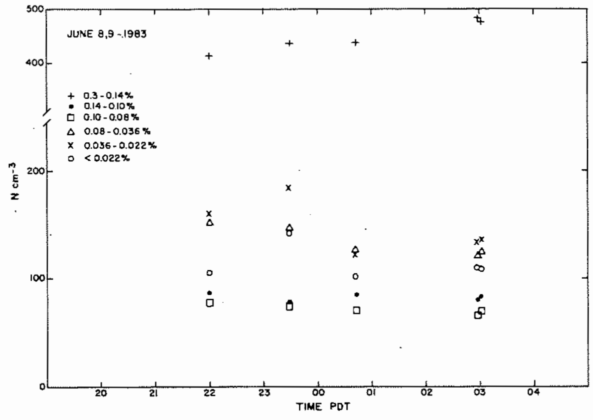

Figure 1. Total CCN concentrations for various S_c intervals during a cloud event.

Higher LWC generally resulted in lower concentrations of the lowest S_c interstitial CCN for all size cuts whereas total concentrations of these nuclei were usually unaffected by LWC variations.

A measurement cycle representing the total CCN spectrum and the interstitial spectra for three inlet size cuts is displayed in Figs. 3-6. Also displayed on Figs. 4, 5 and 6 are the percentage decreases in concentration with respect to Fig. 3

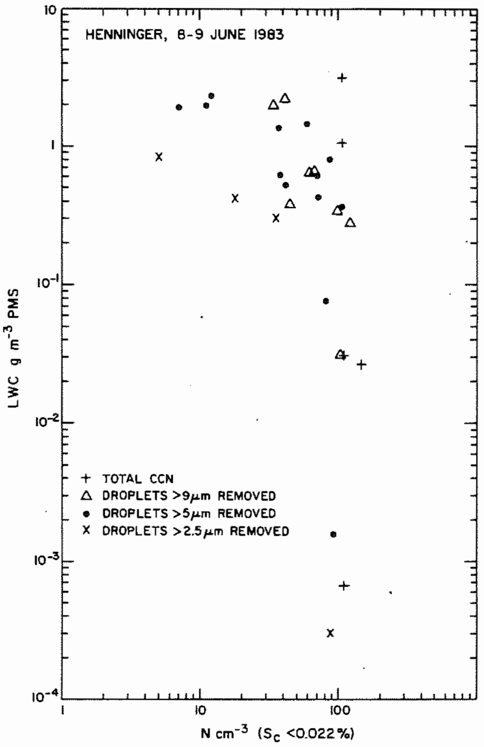

Figure 2. Cloud liquid water content calculated from a PMS droplet spectrometer vs. concentration of largest nuclei in the interstitial aerosol.

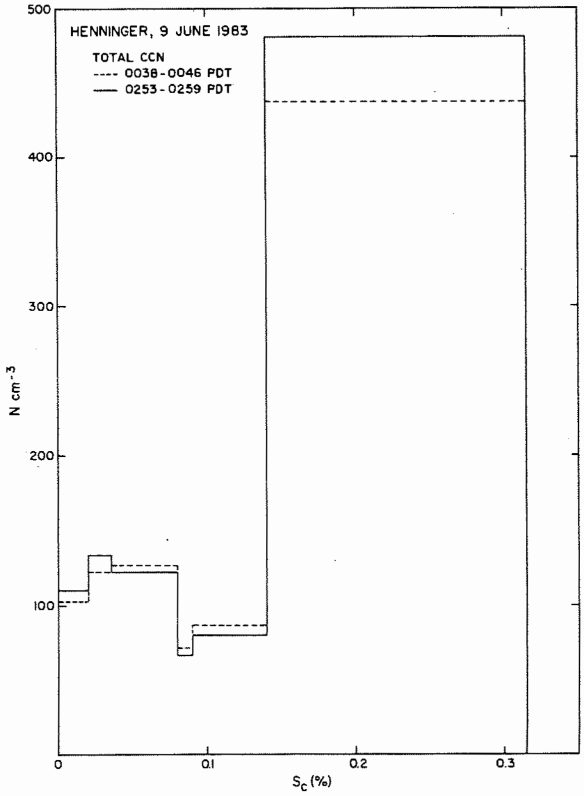

Figure 3. CCN concentrations within the specified S_c intervals for all CCN within the clouds for periods before and after the interstitial measurements (displayed in Figs. 4, 5 and 6).

(total CCN) for each S_c interval. This represents the percentage of nuclei within droplets.

Since the very small percentages for the higher S_c's are within experimental uncertainty, this indicates that virtually none of these nuclei are involved in droplets. An interpretation of the mixing mode can be obtained from the percentages displayed in Figs. 4, 5 and 6. Since these percentages monotonically increase for lower S_c's for each figure, homogeneous mixing is indicated. Note also that these percentages are lower for the larger drop size cuts (lowest for Fig. 6) because larger size cuts allow more nuclei into the interstitial samples. Nevertheless, the similarities of Figs. 4, 5 and 6 indicate that homogeneous mixing affects droplet size up to 9 μm. The similarities of the percentages between Figs. 4 and 5 show that there are very few droplets between 2.5 and 5 μm diameter.

The relationship, or correlation between droplet size and nucleus S_c is further revealed by comparisons of Figs. 5 and 6. Seventy-six percent of the lowest S_c nuclei which are within droplets larger than 5 μm are also within droplets larger than 9 μm (comparing 90% and 68%). Proceeding similarly, only about 50% of the nuclei in the next two S_c intervals which are within 5 μm droplets (Fig. 5) are also within droplets greater than 9 μm (Fig. 6) (61% vs. 31% and 24% vs. 12%). The reader may calculate that it makes little difference whether we choose the 5 μm cutoff of Fig. 5 or the 2.5 μm cutoff of Fig. 4 to compare with Fig. 6 arriving at this conclusion for these three S_c intervals. Figs. 4, 5 and 6 illustrate the

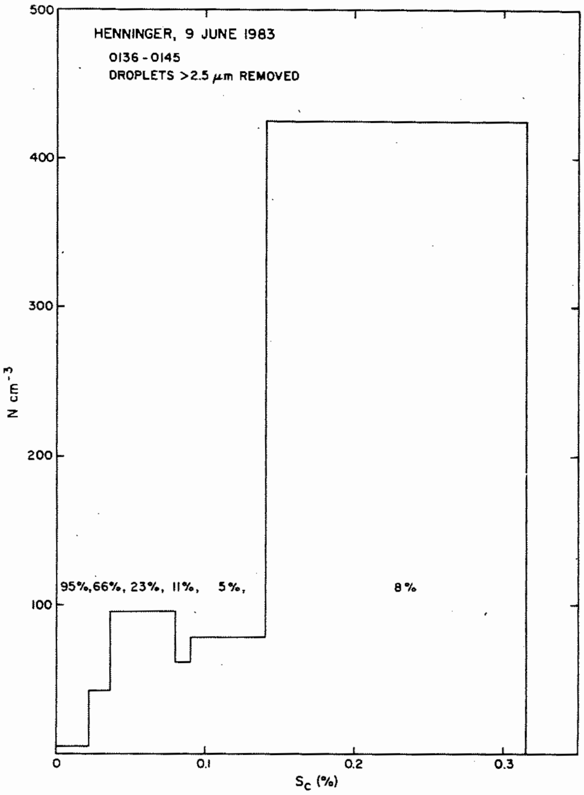

Figure 4. Similar to Fig. 3 except that nuclei within droplets greater than 2.5 μm have been excluded. Also displayed here are the percentage differences for each S_c interval relative to the data in Fig. 3. This represents the percentage of nuclei within droplets.

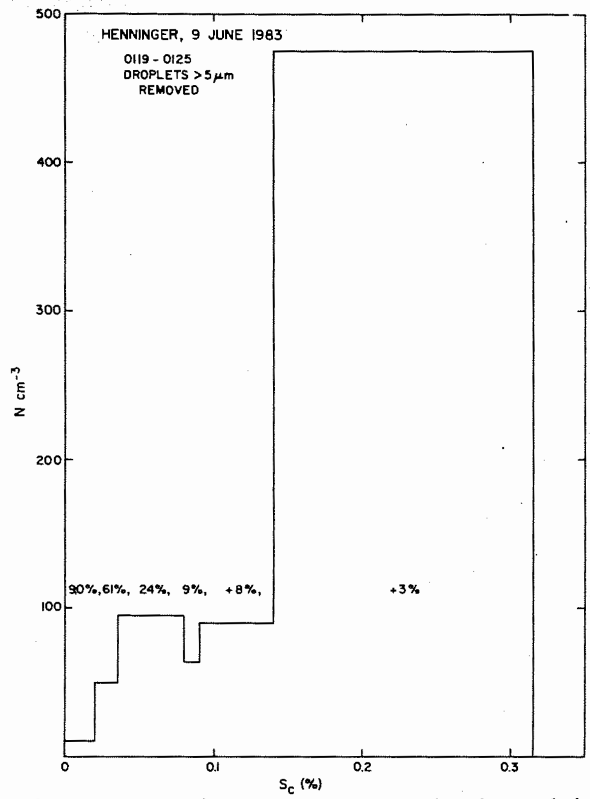

Figure 5. As Fig. 4 except that only the nuclei within droplets greater than 5 μm have been excluded.

typical monotonically-decreasing percentage of nuclei found within cloud droplets, as the cyclone size cut is held constant and the nucleus S_c is increased in the analysis. Furthermore, as the cyclone size cut is reduced, these data generally show increased involvement of intermediate- and low-S_c nuclei within droplets.

The above analysis is now applied to the entire 1983 Henninger data, shown in a compressed, tabular form (Table 2). Although a wide range of cloud conditions are included the consistency of the results is noteworthy. The percentage of nucleus involvement in droplets is shown in parentheses and like Figs. 4-6 these generally increase for lower S_c's (to the right), showing that lower S_c nuclei are more likely to be incorporated into droplets. As with the figures comparisons of the average percentages for the different size cuts reveals a correlation between droplet size and nucleus S_c. Eighty percent of the lowest S_c nuclei found within droplets > 5 μm are also within droplets larger than 9 μm, (32% out of 40%), whereas only 64% of the next S_c group are in the largest drops while this is the case for only about half of the third nucleus interval (0.08 to 0.036% S_c). Furthermore, while only 7% (3 of 43) of the lowest S_c nuclei which are detected to be within droplets, are within droplets between 2.5 and 5 μm, 36% (8 of 22) of the next nucleus interval (0.022% to 0.036% S_c) and 80% (8 of 10) of the nuclei in the next S_c interval which are within droplets are within these same relatively small droplets.

The comparisons made in this table must be taken with the warning that there may have been some uncharted changes in the total CCN concentrations over the entire course of the cloud events even though Fig. 2, Table 1 and similar data for the other events show this to be unlikely. It must also be remembered that variations in cloud density throughout each event affected the interstitial percentages even for constant size cuts (Fig. 2). Nevertheless, for each event (date) there is a monotonic increase downward reflecting the fact that lower size cuts remove more nuclei. The systematic differences between cloud events (dates) are mostly due to systematic differences in cloud density.

The consistently low percentages for the high S_c's confirm the low S_{eff}'s of stratus clouds (Ref. 9 and 1). However, many of the experiments in Tables 1 and 2 took place when the cloud was not as dense as for Figs. 4-6, few CCN were contained within droplets and thus the average decreases from the total CCN concentrations were minimal. Nevertheless the results always followed the same pattern with larger drops associated with low S_c nuclei.

4. CONCLUSIONS

A new technique for cloud microphysical investigation has been developed which has demonstrated the existence of a correlation between cloud droplet size and nucleus S_c. This in itself could have important implications for cloud physics as it may be determined that only a subset of activated CCN or the shape of the CCN spectrum are really important for the development of large droplets and precipitation.

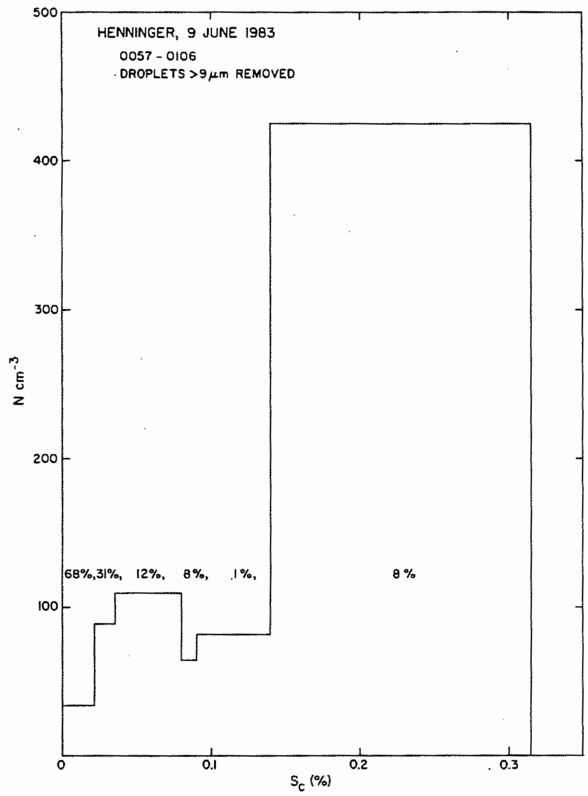

Figure 6. As Fig. 4 except that the droplet cutoff is 9 μm.

TABLE 2 - HENNINGER, 1983

Number cm^{-3} (Percentage of Nuclei Involved in Droplets for Same Date Within S_c Intervals) (+ Indicates Increase Over Total) (S_c %)

Date	Cut Size and No. of Cases	0.3 – 0.14	0.14 – 0.10	0.10 – 0.08	0.08 – 0.036	0.036 – 0.022	0.022 – 0
	Total						
June 9	5	448	83	72	134	147	114
11	1	1347	261	130	209	152	65
21	9	966	126	73	165	149	66
22	8	1287	172	103	200	158	67
25	3	1455	246	142	247	181	103
26	12	1066	156	92	184	150	60
	9 μm Diameter						
June 9	9	434 (3)	78 (6)	73 (+1)	138 (+3)	129 (12)	67 (41)
11	5	1306 (3)	253 (3)	127 (2)	203 (3)	127 (16)	29 (55)
21	3	933 (3)	128 (+2)	76 (+4)	170 (+3)	143 (4)	49 (26)
22	0	----	---	---	---	---	---
25	3	1386 (5)	240 (2)	135 (5)	231 (6)	171 (6)	80 (22)
26	8	926 (13)	139 (11)	85 (8)	184 (0)	141 (6)	50 (17)
	Average for all dates	(5)	(4)	(2)	(1)	(9)	(32)
	5 μm Diameter						
June 9	14	442 (1)	83 (0)	60 (4)	122 (9)	104 (29)	54 (53)
11	15	1306 (3)	270 (+3)	134 (+3)	208 (0.5)	117 (23)	13 (80)
21	6	923 (4)	132 (+5)	76 (+4)	172 (+4)	143 (9)	56 (15)
22	4	1336 (+4)	183 (+6)	104 (+1)	195 (3)	143 (9)	50 (25)
25	3	1352 (7)	235 (4)	136 (4)	236 (4)	159 (12)	55 (47)
26	1	1162 (9)	171 (+10)	98 (+7)	188 (+2)	152 (6)	47 (22)
	Average for all dates	(3)	(+3)	(+1)	(2)	(14)	(40)
	2.5 μm Diameter						
June 9	6	374 (16)	80 (4)	67 (7)	114 (15)	84 (43)	31 (73)
11	1	1208 (10)	225 (14)	103 (21)	139 (33)	62 (59)	2.5 (96)
21	2	930 (4)	132 (5)	74 (+1)	164 (1)	146 (2)	61 (8)
22	12	1325 (+3)	186 (+8)	105 (+2)	184 (8)	131 (17)	44 (34)
25	14	1410 (3)	251 (+2)	143 (1)	231 (6)	147 (19)	56 (46)
26	4	1041 (2)	154 (1)	97 (+5)	190 (+3)	158 (+5)	58 (3)
	Average for all dates	(5)	(2)	(4)	(10)	(22)	(43)

These measurements have been used to distinguish between the effects of certain cloud droplet growth models which address a central problem in cloud physics--bridging the size gap between condensation growth and the size necessary for initiation of the coalescence process. The vast majority of the data tend to support the homogeneous mixing interpretation, confirming the earlier work (Ref. 1).

5. ACKNOWLEDGEMENTS

This research was supported by the meteorology program of the Atmospheric Sciences Division of the National Science Foundation, Grant ATM-82-10344.

The droplet measurements shown in Table 1 and Fig. 2 were provided, courtesy of the California Institute of Technology, Dept. of Environmental Engineering Science, by Michael Hoffmann, Jed Waldman, Daniel Jacob and William Munger.

The site was provided by the Forestry Division of the Los Angeles County Fire Dept. whose cooperation is gratefully acknowledged.

6. REFERENCES

1. Hudson, J.G., 1984: CCN measurements within clouds. J. Climat. Appl. Meteor. In press.
2. Mason, B.J., and P.R. Jonas, 1974: The evolution of droplet spectra and large droplets by condensation in cumulus clouds. Q.J.R. Meteorol. Soc., 100, 23-38.
3. Lee, I.Y., G. Hanel, and H.R. Pruppacher, 1980: A numerical determination of the evolution of cloud drop spectra due to condensation on natural aerosol particles. J. Atmos. Sci., 37, 1839-1853.
4. Baker, M.G., R.G. Corbin, and J. Latham, 1980: The influence of entrainment on the evolution of cloud droplet spectra: I. A model of inhomogeneous mixing. Q. J. R. Meteorol. Soc., 106, 581-598.
5. Telford, J.W., and S.K. Chai, 1980: A new aspect of condensation theory. Pure Appl. Geophys., 118, 720-742.
6. Hudson, J.G., and P. Squires, 1976: An improved continuous flow diffusion cloud chamber. J. Appl. Meteorol., 15, 776-782.
7. Hudson, J.G., 1980: Relationship between fog condensation nuclei and fog microstructure. J. Atmos. Sci., 37, 1854-1867.
8. Chan, T., and M. Lippmann, 1977: Particle collection efficiencies of air sampling cyclones: an empirical theory. Environ. Sci. Technol., 11, 377-382.
9. Hudson, J.G., 1983: Effects of CCN on Stratus Clouds. J. Atmos. Sci., 40, 480-486.

DROPLET GROWTH KINETICS IN CLOUDS AND PRECIPITATION FORMATION

A.A. Lushnikov

Karpov Institute of Physical Chemistry,
Moscow, USSR.

ABSTRACT

The coagulation growth of cloud particles is considered. Assuming the particle overgrown a critical mass G to be removed instantly from the cloud the equation governing the time evolution of the particle mass spectrum is solved analytically for three model coagulation kernels. In addition to the time dependence of the coagulating particles mass distributions the precipitation mass spectra are found. A special attention is given to the problem of the precipitation formation in the case when a giant superparticle might arise in the corresponding coagulating system without sinks. It is shown that there exist then two clearly distinguished stages: i. the coagulation growth of the particles without the total cloud mass loss, ii. the stage of the active rain droplets formation being accompanied with the total cloud mass exhaustion owing to the release of precipitation from the cloud. The characteristic time of the first stage is occurred to be asymptotically independent of G, and the precipitation mass spectrum be of the form:

$$G^{-2}f(g/G)$$

where g is a droplet mass.

Keywords: Coagulation, Cloud Particles, Precipitation, Mass Spectra

1. INTRODUCTION

Among numerous processes responsible for the cloud particles size spectrum formation and affecting considerably the dynamics of the release of precipitation, the coagulation plays a very important role, especially in warm clouds that are entirely beneath the level of the 0°C isotherm.

The coagulation leads to the growth of small cloud particles with radii of the order 10 up to relatively large rain droplets the size of which lies within the range 0.5 - 5mm and larger. These droplets are released then as a rain, the dynamics of which is thus governed by the kinetics of the coagulation process.

It is frequently assumed that the rate of a single coalescence act (the coagulation kernel) has the form (1) (the gravitational kinematic coagulation):

$$K = K_0(l_1^{1/3}+l_2^{1/3})^2\left|l_1^{2/3}-l_2^{2/3}\right| \qquad (1)$$

where

$$K_0 = 2g\pi r_0^4\,\rho/\nu\rho_w\,,$$

$g = 9.81\mathrm{m/s}^2$, ρ_w, ρ are the water and air densities respectively and l_1, l_2 are the masses of colliding particles measured in units of a minimal mass of a monomeric particle of the radius r_0 (below $r_0 = 10\mu$).

The coagulation kernel (1) is a homogeneous function of its arguments whose homogeneity exponent is $\lambda = 4/3 > 1$. As has been shown in refs. [1,2] in the case $\lambda > 1$ a giant superparticle must appear during a finite interval of time. This superparticle has the mass comparable with the total mass of a coagulating cloud. The fact of appearance of the superparticle in a finite coagulating system had been confirmed by a numerical experiment in ref. [3], where the characteristic time for the superparticle formation had been evaluated

$$t_c = 10\ /L(s) \qquad (2)$$

where $L(\mathrm{kg/m}^3)$ is the cloud water content. According to eq.(2) the superparticle should be formed very quickly (during the time of the order of several minutes).

Of coarse, it is very difficult to imagine that a large object can be retained in a cloud. Moreover, sufficiently large particles of the coagulation origin responsible for the superparticle formation should also be released from the cloud as precipitation. This means that the coagulation process is affected considerably by the presence of sinks of large particles.

The rate of the particle removal depends on the particle size. This dependence is assumed below to have a threshold nature, i.e. particles with masses larger than a critical mass G (in units of the monomeric mass) are removed instantly from the cloud. The value of G is extremely large: $G \sim 10^6$ ($r_0 \approx 10\mu$, $r_G \approx 1$mm). It is also assumed that the smaller particles are retained in the cloud for a sufficiently long time to grow up to the critical mass. The model described above is seemed to be quite reasonable and suitable for a qualitative solution of the following problems:

i. How the sink affects the form of the particle mass spectrum in a coagulating system?
ii. How the possibility of forming a superparticle affects the form of the mass spectrum and times of the precipitation formation?
iii. What form has the precipitation mass spectrum and what can be said about the dynamics of the precipitation formation?
iv. How the sink affects the source enhanced coagulation?
The latter question is not related straightforwardly to the cloud processes. Nevertheless, the answer to it is very important for solving other problems of physics of atmospheric aerosols.

The reminder of the paper is organized as follows. In the next section some mathematics is given related to the model used. Section 3 is devoted to the results concerning free coagulation in systems with sharp sinks. In section 4 the form of the steady state mass spectra is discussed for the case of source enhanced coagulation in systems with sharp sinks. Some concluding remarks concerning the possibility of application of the results obtained are contained in section 5.

3. BASIC EQUATIONS

Assuming the particles with masses exceeding the critical value G are removed instantly from the system, the equation governing the time evolution of the mass spectrum has the form:

$$\partial_t c(g,t)=I(g,t) + \int k(g|x,y)c(x,t)c(y,t)\,dxdy \qquad g<G \qquad (3)$$

Here $c(g,t)$ is the concentration of the particles of mass g, $I(g,t)$ is the intensity of the source of fresh particles,

$$k(g|x,y)=\tfrac{1}{2}K(x,y)\left[\delta(g-x-y)-\delta(g-x)-\delta(g-y)\right]\theta_G(x)\theta_G(y) \qquad (4)$$

$K(x,y)$ is the coagulation kernel, $\delta(x)$ is the Dirac delta function and $\theta_G(x)=1$ at $x<G$, $\theta_G(x)=0$ otherwise.

The sink of large particles is modelled by introducing the cut off factor forbidding the presence of particles with masses exceeding G. These particles form the precipitation whose mass spectrum is contained within the interval [G, 2G]:

$$c^{+}(g,t)=\frac{1}{2}\int K(x,y)\theta_G(x)\theta_G(y)c(x,t)c(y,t)\delta(g-x-y)\,dxdy \qquad (5)$$

Equation (3) should be supplemented with the initial condition. Below initially monodispersed particles are considered, i.e.

$$c(g,0)=\delta(g-1) \qquad (6)$$

After eq.(3) having been solved the precipitation mass spectrum is readily restored with the aid of eq.(5).

The function $I(g,t)$ is either put equal to 0 (free coagulation) or $I(g,t)=I(g)=\delta(g-1)$ (source enhanced coagulation). In the latter case only the steady state mass spectra are considered defined by eq.(7)

$$0=I(g)+\int k(g|x,y)c(x)c(y)\,dxdy \qquad (7)$$

Model coagulation kernels are chosen in the form:

$$K_1=2, \quad K_2=2(x+y-1), \quad K_3=xy \qquad (8)$$

the second of which had been used for modelling the dynamics of development of cloud particle mass spectra (see e.g. ref.[4]). The coagulation process with the kernel K_3 leads to the superparticle formation in coagulating systems without sinks.

Some results are also found for the coagulation kernels of more general form:

$$K=\frac{1}{2}(x^{\alpha}y^{\beta}+x^{\beta}y^{\alpha}) \qquad (9)$$

where $\lambda=\alpha+\beta>1$.

4. FREE COAGULATION

In absence of sources and for initially monodispersed particles exact solutions to eq.(3) had been found in a recent papers [5,6] for three model coagulation kernels (8). Below the main results of these papers are presented along with some supplementary comments bearing on physics of the precipitation formation.

Free coagulation in systems with sharp sinks proceeds in three stages. At the initial stage when the coagulating particles are still small the mass spectrum does not feel the sink, and the solution to the coagulation kinetic equation is close to that obtained without accounting for the sink. As far as the spectrum is developed enough and the average mass of particles has become comparable with the critical value G the active precipitation release is begun. At this moment the total concentration of the precipitating particles becomes comparable with that of actively coagulating particles. After this the final stage follows during which the final precipitation mass spectrum is formed. The characteristic times for the initial stage have the order G, lnG, 1 for the kernels K_1, K_2 and K_3 respectively. The transient period proceeds during the time G, lnG and 1/ G respectively for the same sequence of kernels. The final stage takes up all remaining time.

A remarkable fact is that the time interval of the initial stage for the third model is independent of G whereas the time interval of the transient period tends to 0 at $G\to\infty$. This is a general feature of all coagulating systems in which the superparticle can grow. It is also interesting to notice that the superparticle is not formed in systems with sharp sinks. It is explained by the fact that the superparticle formation requires a different limiting transition. Namely, it is necessary to consider a finite coagulating system with the total mass m and then shift G to infinity fixing the ratio $G/m \neq 0$. The situation discussed above corresponds to the case $\lim G/m = 0$ at $G \to \infty$, so the superparticle embryo has precipitated before it grows sufficiently to form the superparticle.

Below some results are listed concerning the precipitation mass spectra. In the limit of large G one has for the kernel K_1:

$$c^+(g,\infty) = G^{-2}(1-r)e^{-2C}\int_{-\infty}^{\infty}\exp\left[(1+r)s - 2\int_0^s \frac{e^u-1}{u}du\right]ds, \quad r=\frac{g-G}{G}, \quad C = 0.577.. \quad (10)$$

For the remaining two models the precipitation spectra are similar:

$$c^+(g,\infty) = \pi^{-1}G^{-2}e^{q(1+r)}(1-r)/(1+r)^2 r^{1/2}$$

where $q = 0.854032657...$. The total particle concentration in the precipitation is:

$$N^+(\infty) = \int_0^G c^+(g,\infty)dg = 0.7923G^{-1} \quad (11)$$

for the first model, and for the latter two it is:

$$N^+(\infty) = qG^{-1} \quad (12)$$

For the third model after the critical moment $t = 1$ (corresponding to the time of the superparticle formation in the sink free case) the time dependence of the precipitation mass spectrum has the form:

$$c^+(g,t) = c^+(g,\infty)(1-t^{-1}) \quad (13)$$

At $t > 1$ the total mass concentration M begins to decrease with time:

$$M = \int gc(g,t)dg = 1/t \quad (14)$$

It should be emphasized that the dependence (14) is a consequence of the initial condition (6).

For initially polydispersed particles the dependence $M(t)$ can be easily found at $G=\infty$. Let $F(p)$ be the Laplace transform of $gc(g,t)$. Then for $M(t)$ eq. (15) is obtained:

$$\dot{M} = F(M - t\dot{M}) \quad (15)$$

This equation is solved exactly. Derivating eq.(15) with respect to t and introducing the function Q inverse to $-F'$ yield:

$$M = F(Q(t^{-1})) \quad (16)$$

The critical moment t_c (after which the precipitation release begins) is readily found from eq.(16):

$$t_c^{-1} = -F'(0) = \int g^2 c(g,t)dg \quad (17)$$

The form of the mass spectrum is conserved in the postcritical period:

$$c(g,t) \propto M(t)g^{-5/2}\exp(qg/G) \quad (18)$$

The remarkable fact brought up by the influence of the sink is the appearance the exponentially growing factor on the right hand side of eq.(18). As will be shown a little below this is rather general feature of coagulating systems with sharp sinks.

Some analytic results may be obtained for the kernel K given by eq.(9). If $1 < \lambda < 2$ and $\mu < 1$, where

$$\mu = |\alpha - \beta| \quad (19)$$

then at $G \to \infty$ there exists a critical moment t_c after which the active release of precipitation begins. In the postcritical period the mass spectrum of actively coagulating particles is of the form:

$$c(g,t) \propto M(t)g^{-(3+\lambda)/2}\exp(q_\mu g/G) \quad (20)$$

where the parameter q is the solution of eq.(21):

$$\int_0^1 (e^{q_\mu g} - 1)g^{-(3-\mu)/2}dg = 2/(1-\mu) \quad (21)$$

A closed equation similar to eq.(15) does not exist for the kernel K , though the low $M = t_c/t$ holds for the initially monodispersed mass spectra.

The precipitation mass spectrum looks as follows:

$$c^+(g,t) \propto (1-t_c/t)G^{-2}\exp q_\mu(1+r) \int_0^1 (1-x)^{-(3+\lambda)/2}(r+x)^{-(3-\lambda)/2}dx \quad (22)$$

Of coarse, the integral on the right hand side of eq.(22) can be expressed in terms of special functions.

In sinkless coagulating systems with the kernel K the superparticle is formed. However, unlike to the case of the kernel K_3 this superparticle is passive at $\alpha, \beta < 1$, i.e. its appearance does not affect the mass spectrum of smaller particles. It serves just as a sink of the total mass concentration, whereas the mass spectrum is defined by eq.(3) at $G=\infty$. The superparticle formed is unique.

This is a consequence of the following simple consideration. The rate of coalescence of two superparticles with masses comparable to m has the order $K(m,m)/m \propto m^{\lambda-1}$ ($K/V \propto K/m$ is the rate of the superparticle collision the concentration of which $\propto 1/V \propto 1/m$, where V is the volume containing the finite coagulating system with the total mass m). At $\lambda > 1$ and $m \to \infty$ this rate becomes infinitely large, therefore only one superparticle can exist in the system. On the other hand, the rate of coalescence of the superparticle with smaller particles the concentration of which is finite in the thermodynamic limit is estimated as $K(1,m)/m \propto m^{\alpha-1} \to 0$ ($\alpha > \beta$) at $\alpha < 1$ and $m \to \infty$. Thus the presence of the superparticle does not affect the particle mass spectrum in this case.

4. SOURCE ENHANCED COAGULATION

In this section the steady state regimes of coagulation in the presence of a source of small particles.

For the kernel (9) eq.(7) has the steady state solution approaching asymptotically (at large $g<G$) to

$$c(g)\propto g^{-(3+\lambda)/2}\exp(q_{\mu}g/G) \qquad (23)$$

where q_{μ} is again defined by eq.(21). The mass concentration M grows with G as:

$$M=\int_0^G gc(g)dg \propto G^{(1-\lambda)/2} \qquad (24)$$

These results hold for $\mu<1$, when the steady state regime exists at $G=\infty$.

5. CONCLUDING REMARKS

The above consideration allows one to make several qualitative conclusions about the behaviour of the coagulating system with sharp sinks and the kernel (1). In this case the superparticle can be formed, thus the dynamics of the coagulation process is expected to be similar to that for the model system with the kernel K_3. Three stages should be observed:

i. Active coagulation without the precipitation formation (till the moment t_c given by eq.(2)). The mass spectrum of coagulating particles can be found by solving numerically eq.(3).

ii. A very short transient period the duration of which decreases with G.

iii. The stage of the precipitation formation ($t<t_c$). One may anticipate that at $t<t_c$

$$c(g,t)= c(g)t_c/t \qquad (25)$$

Substituting eq.(25) into eq.(3) yields:

$$\int k(g|x,y)c(x)c(y)dxdy + c(g)/t_c=0 \qquad (26)$$

The precipitation mass spectrum is then found from eq.(27):

$$c^+(g,t)= (1-t_c/t)\int K(x,y)\theta_G(x)\theta_G(y)\cdot \delta(g-x-y)c(x)c(y)dxdy \qquad (27)$$

Even in the framework of such oversimplified approach the problem of calculating the particle mass spectrum remains very complicate, but not hopeless one.

REFERENCES

1. Lushnikov,A.A.,1977, Coagulation in systems with probabilistic initial conditions. Dokl. Acad. Sci. USSR. 236, No3, p.673-677.

2. Lushnikov,A.A.,1978, Some new aspects of the coagulation theory. Izv. Acad. Sci. USSR, Atmospheric and Oceanic Physics. 14, No.10, p.1046-1055.

3. Domilowskii,E.R., Lushnikov,A.A. and Piskunov V.N., 1978, Monte-Carlo simulation of coagulation processes. Dokl. Acad. Sci. USSR. 240, No. 1,p.108-110.

4. Voloschuk,V.M., Sedunov,Yu.S.,1975, Processes of coagulation in dispersed systems. Leningrad, Gidrometeoizdat, 320 pp.

5. Lushnikov,A.A. and Piskunov,V.N.,1982, Three new exactly soluble models in the coagulation theory. Dokl. Acad. Sci. USSR. 267, No.1, p.127-132.

6. Lushnikov,A.A. and Piskunov,V.N.,1983, Analytic solutions in the theory of coagulating systems with sinks. Applied Mathematics and Mechanics. 47, No.6,p. 931-939.

MIXING AND PRECIPITATION INITIATION

Harry T. Ochs III and David B. Johnson

Illinois State Water Survey
Champaign, Illinois 61820 U.S.A.

1. INTRODUCTION

Traditionally, entrainment has been assumed to retard precipitation development. However, a number of studies have suggested that mixing between the cloud and the environment or between the cloud and residues of previous thermals would tend to broaden the cloud droplet distribution and, under some circumstances, would actually accelerate precipitation development (Refs. 1-4). This paper presents results of an explicit test of the effect of mixing on precipitation initiation. This study uses a modified version of the microphysical parcel model discussed in Ref. 5.

2. INITIAL CONDITIONS

The CCN (cloud condensation nuclei) distribution used for the calculations is similar to those used in Refs. 6-7, but with the distribution truncated at 3 micrometers diameter. The parcel's starting temperature, pressure and relative humidity were set at 16.7°C, 886 mb, and 83%, respectively. The parcel was lifted at a constant ascent rate of 4 m s^{-1} until a liquid water content of 0.1 g m^{-3} was achieved. At this point entrainment was initiated.

3. MODEL EXPLORATIONS

After modifications, the model was structured to permit two general types of mixing: homogeneous and inhomogeneous. In both cases the general approach employed was based (loosely) on the study in Ref. 8. The environmental air entrained into the cloud was assumed to have the same temperature as the cloud and a relative humidity of 80%. For simplicity, in these exploratory calculations environmental air was mixed into the rising parcel at every time step. The net rate was picked to result in parcel liquid water contents that were maintained at approximately half the adiabatic value.

Homogeneous mixing was relatively easy to simulate. Near the end of the calculation within a condensation time step, the desired quantity of environmental air was mixed into the cloudy parcel. A mass-weighted mean temperature and mixing ratio were computed with the liquid water content being adjusted appropriately. A new supersaturation could then be computed. Nuclei entrained into the main parcel were assumed to have relative size distributions equivalent to the size distribution of cloud droplets (or potential cloud droplets) obtained at the point where the liquid water content was 0.1 g m^{3} (see Fig. 1).

Inhomogeneous mixing assumes that the entraining parcel mixes relatively slowly with the cloudy air so that some droplets are almost completely evaporated while others remain essentially unaffected. The number of cloud droplets evaporated was determined by the amount of vapor required to saturate the incoming parcel. In this calculation drops larger than 30 micrometers radius were assumed to be unaffected by possible evaporation. All drops smaller than 30 micrometers were possible candidates for evaporation to saturate the incoming parcel. The evaporated droplets were then reintroduced into

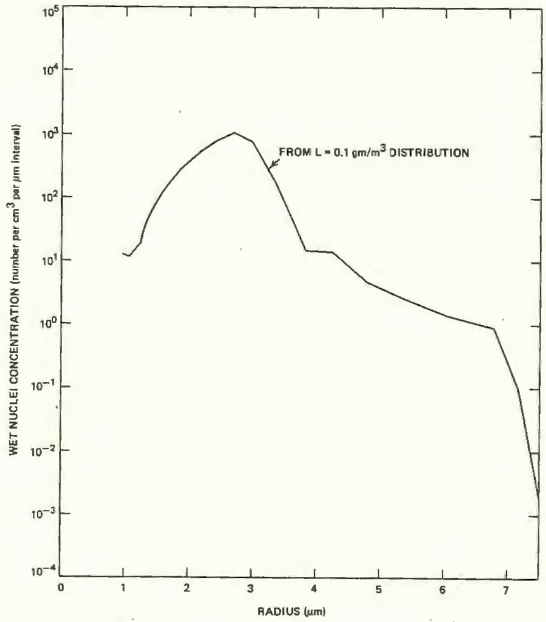

Fig. 1. Wet CCN distribution.

the parcel in the relative CCN distribution of Fig. 1 while the appropriate adjustments were made in the temperature. The parcel now completed mixing with the remaining cloudy air in a manner identical to the treatment of homogeneous mixing. As in the homogeneous cases the entrained air could contain nuclei or be nuclei free.

As a benchmark the model was run without mixing; i.e., an "adiabatic" simulation. Fig. 2 shows five variables as functions of height derived from this calculation. Four are self explanatory. The fifth variable, R_m, is the droplet radius at which the droplet distribution falls below 10^{-3} drops per cm^{3}, per micrometer interval. This variable is intended to serve as a measure of the rate at which the cloud droplet distribution spreads to larger sizes. The predicted cloud droplet distributions are highly monodisperse, as would be expected for an adiabatic calculation.

The results of two simulations with homogeneous mixing are presented in Figs. 3 and 4. The only difference between the homogeneous-mixing simulations is in the nuclei in the entrained air. One case (Fig. 3) had no nuclei in the entrained air while the other had nuclei in the same concentration as were present at cloud base. As in the adiabatic case the cloud droplet distributions resulting from the case depicted in Fig. 3 were highly monodisperse. Fig. 4 depicts the results obtained when the entrained nuclei were assumed to immediately form into the same relative size distribution exhibited at the 0.1 g m^{-3} level. The simulation that included nuclei in the entraining air produced cloud droplet distributions that showed significant broadening (mostly toward the small end of the spectrum), but were still dominated by a pronounced peak in the distribution.

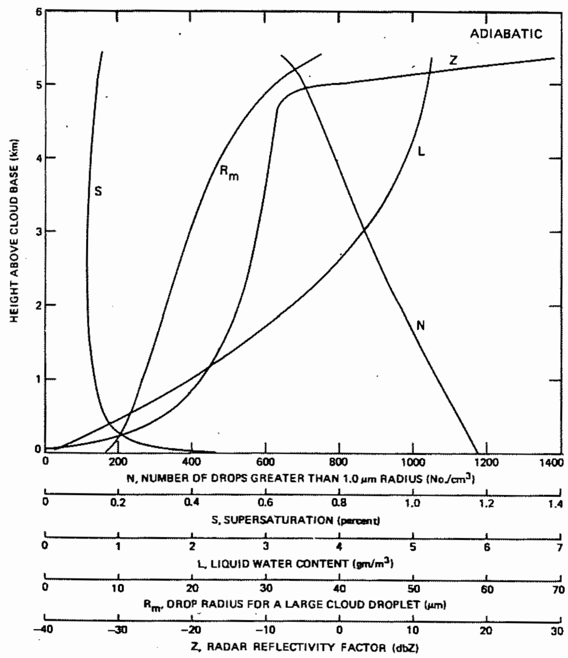

Fig. 2. Parameters computed in an adibatic simulation.

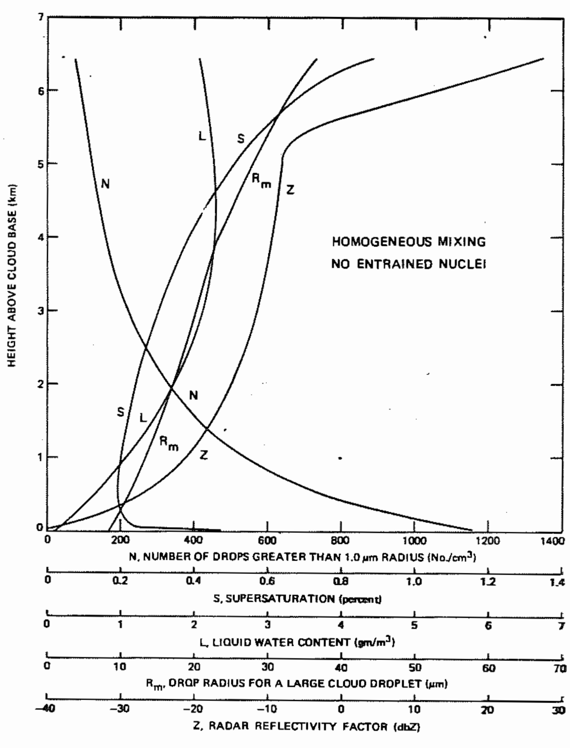

Fig. 3. Parameters computed in a parcel simulation with homogeneous mixing.

Figs. 5 and 6 depict the results of two cases in which inhomogeneous was simulated. In both cases the nuclei distribution in Fig. 1 was used. In the case depicted in Fig. 5 no nuclei were contained in the entraining air and drops that evaporated to saturate the entraining parcel were reintroduced with a relative size distribution based on the

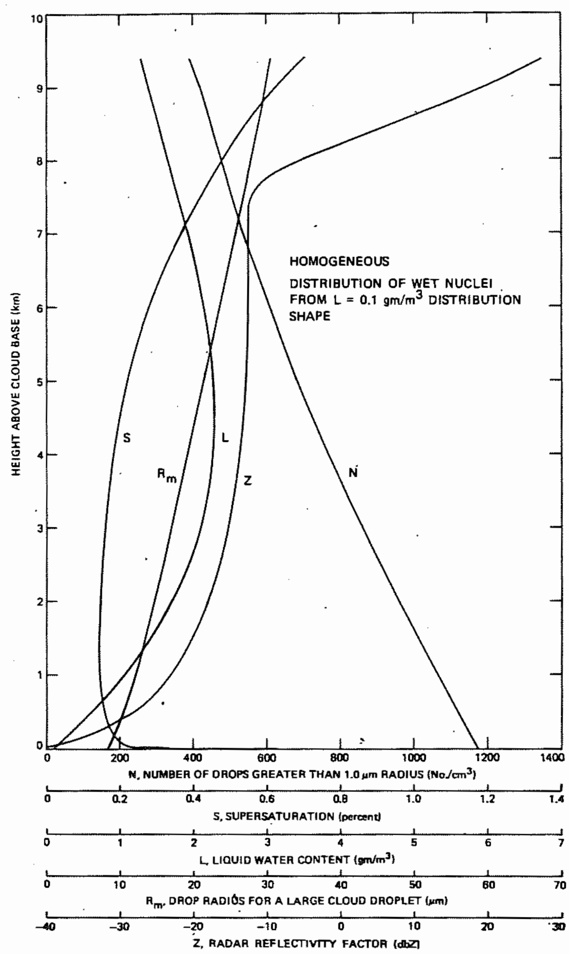

Fig. 4. Parameters computed in a parcel simulation with homogeneous mixing.

distribution shown in Fig. 1. Fig. 6 illustrates the results of the case where nuclei were included in the entraining air. The corresponding cloud droplet distributions for this simulation are shown in Fig. 7.

4. OTHER CALCULATIONS

Several other model simulations were used to investigate other aspects of precipitation initiation. The adiabatic simulation and two of the mixing cases were repeated with the CCN distribution extended to larger sizes in the same manner as in Refs. 6-7. These results suggest that if large particles are present in the air entering cloud base, they can be very effective in initiating precipitation. In addition, other calculations are being performed to investigate the effect of entraining air discontinuously in larger units (blobs) than simulated in the cases discussed here.

5. DISCUSSION

These calculations suggest that inhomogeneous mixing can enhance the rate of precipitation development compared to corresponding homogeneous mixing simulations. However, the cases presented in both Figs. 3 and 5 develop precipitation faster than the corresponding cases with nuclei in the entrained air, which suggests that dilution of the droplet

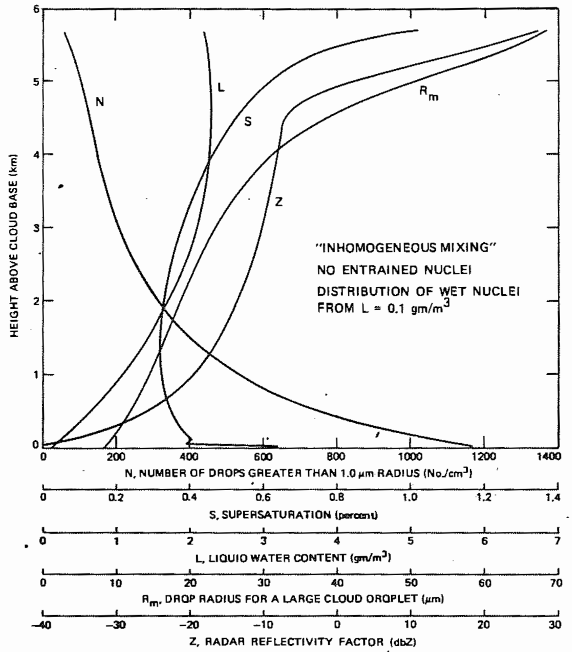

Fig. 5. Parameters computed in a parcel simulation with "inhomogeneous mixing".

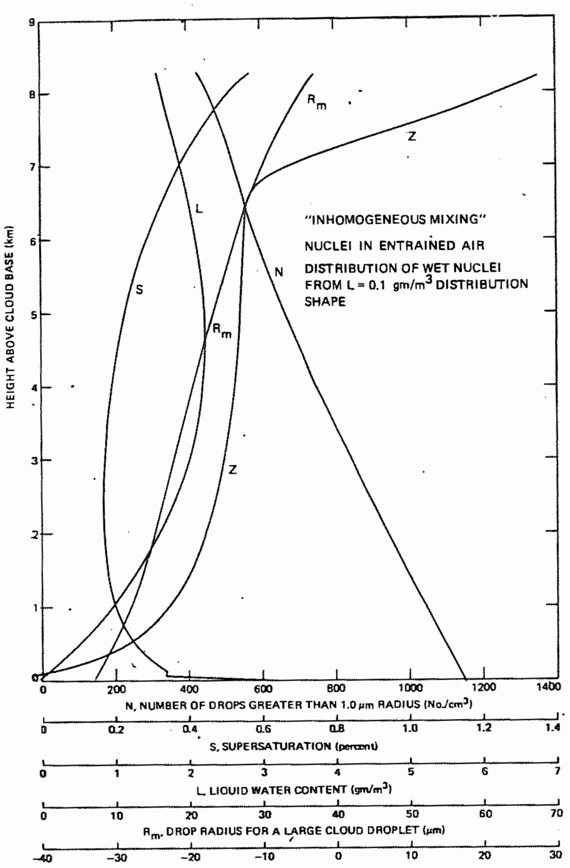

Fig. 6. Parameters computed in a parcel simulation with "inhomogeneous mixing".

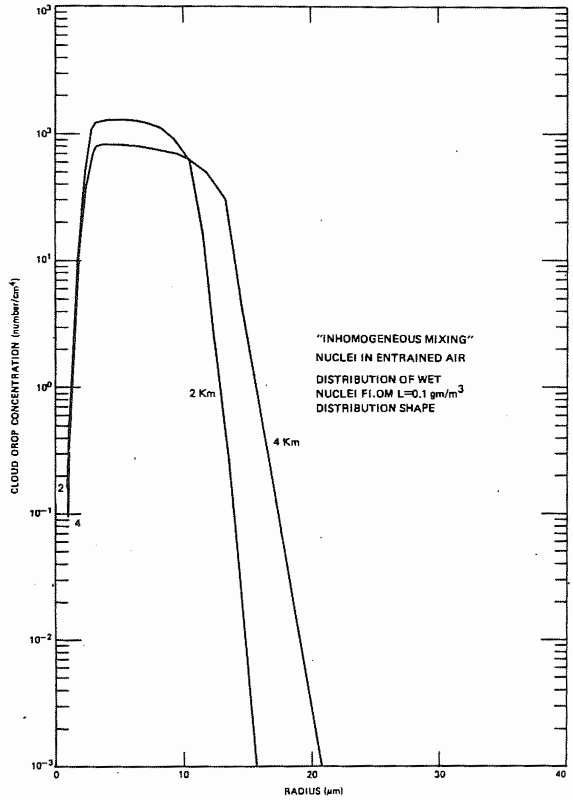

Fig. 7. Cloud droplet distributions predicted at 2 and 4 km above the L = 0.1 gm/kg level for a parcel simulation with "inhomogeneous mixing".

concentration may be more significant in these cases than the details of the mixing process. In addition the results of the simulations in which the tail of the nuclei distribution was included suggest the importance of large particles in precipitation initiation.

Acknowledgments. This research was supported by the Atmospheric Research Section of the National Science Foundation under grant NSFATM 8217615.

6. REFERENCES

1. Mason, B. J., and P. R. Jonas 1974, Quart. J. R. Met. Soc, 100, 23-38.

2. Lee, I. Y., and H. R. Pruppacher, 1977, Pageoph, 115, 523-545.

3. Baker, M. D., and J. Latham, 1979, J. Atmos. Sci., 36, 1612-1615.

4. Telford, J. W., and S. K. Chai, 1980, Pageoph., 118, 720-742.

5. Ochs, H. T., and C. S. Yao, 1978, J. Atmos. Sci., 35, 1947-1958.

6. Ochs, H. T., 1978, J. Atmos. Sci., 35, 1959-1973.

7. Ochs, H. T., and R. G. Semonin, 1979, J. Appl. Meteor, 18, 1118-1129.

8. Baker, M. D., R. G. Corbin and J. Latham, 1980, Quart. J. R. Met. Soc., 106, 581-598.

ANALYTICAL SOLUTIONS TO A KINETIC EQUATION FOR THE CLOUD DROP SIZE SPECTRUM FORMED BY CONDENSATION IN A TURBULENT MEDIUM

V. I. Smirnov and L. A. Nadeykina

Central Aerological Observatory, Moscow, USSR

In clouds condensation is affected by turbulence (Refs 1-6), nucleus matter solubility (Refs 7,8), the residence time (age) of droplets (Ref. 9), mixing between a cloud and the environment (Refs 10-12). In the present paper a kinetic equation is derived taking into account the factors mentioned above, and several analytical solutions of this equation are found.

We introduce a distribution function of cloud drops (spectrum) $f(t,x,r,c,\tau)$, where t denotes time, $f dx_1 dx_2 dx_3 dr dc d\tau$ is the mean (over a cloud ensemble) number of drops in a volume element $dx_1 dx_2 dx_3 = d\vec{x}$ with radii from r to r + dr, with nucleus condensational activity from c to c+dc, with age from τ to $\tau + d\tau$.

The equation for a drop growing by condensation can be written in the following well known form, e.g. Ref. 8:

$$\dot{r} = [A_0(T)/(r + r^*)\rho_s][\rho - \rho_s(1+\omega)], \quad (1)$$

where ρ is the vapour density in the environment, ρ_s is the saturated vapour density at temperature T, A_0 is a T function which depends on the vapour and medium parameters, too, r^* is a free-molecular parameter which includes the condensation coefficient, r^+ is the drop surface curvature parameter, $\omega = r^+/r - c/r^3$, the last term representing the nucleus solubility contribution.

Vapour supersaturation is defined through $\delta = (\rho - \rho_s)/\rho_s$.

The equation derived for f by a known method is

$$\frac{\partial f}{\partial t} + \nabla(\vec{v} f) + \frac{\partial}{\partial r}(\dot{r} f) + \frac{\partial f}{\partial \tau} = J(t,\vec{x},r,c,\tau), \quad (2)$$

where $\vec{v}$ is the drop velocity, J is a source and sink function describing nucleus activation and mixing between the cloud and its environment.

On the basis of the mass, momentum and energy conservation laws one can write, following Ref. 6, a set of equations

$$\dot{T} = -\gamma u_3 - a_3 J_*, \quad \nabla\vec{u} = u_3/\lambda - a_3 J_*/T$$
$$\dot{r} = \frac{D_e}{r F_1}\frac{\rho_s}{\rho_w}\left(a_1 u_3 + F_2 - \omega F_1 + a_2 J_*\right), \quad (3)$$

where $a_1 = (g c_p/R_a T)(L R_a/c_p T R_v - 1)a_3$, $a_2 = L a_3/R_v T^2$, $a_3^{-1} = c_p(1 + L^2\rho_s/c_p R_v T^2 \rho_a)$, $\gamma = g(1 + L\rho_s/R_a T\rho_a)a_3$, $\lambda^{-1} = (g/R_a - \gamma)/T$, $\rho_a(\rho_w)$ is the air (water) density, $\vec{u}$ is the air velocity, g is the gravity acceleration, x_3 is the vertical coordinate, c_p is the air specific heat at constant pressure, L is the latent heat of condensation, $R_a(R_v)$ is the gas constant for air (water vapour), J_* is the energy loss per a unit mass (e.g. due to radiation).

$$D_e = A_0(T)\rho_w/\rho_s(1 + r^*/r) \equiv D_0/(1 + r^*/r) \quad (4)$$

$$F_1 = 4\pi\iiint D_e r f \, dr\, dc\, d\tau$$
$$F_2 = 4\pi\iiint D_e r\omega f \, dr\, dc\, d\tau \quad (5)$$

the last expressions being generalized as compared to the F_1 and F_2 of Ref. 6. Starting from Eqs (2) and (3), upon averaging over an ensemble of turbulent clouds, we derive the following kinetic equation which generalizes and corrects the form derived in Ref. 6.

$$\frac{\partial f}{\partial t} + \frac{\partial}{\partial x_i}\left(u_i - v_s\delta_{i3}\right) f + \frac{\rho_s}{\rho_w F_1}\frac{\partial}{\partial r}\frac{D_e}{r} \times \Big\{ a_1 u_3 + F_2 - \omega F_1 + a_2 J_* + a_1 K_{3i} \times \Big[-\frac{d\ln\rho_s}{dT}\left(\frac{\partial T}{\partial x_i} + \gamma\delta_{i3}\right) + \frac{1}{F_1}\left(\frac{\partial F_1}{\partial x_i} + \frac{F_1}{\lambda}\delta_{i3}\right) + \frac{a_1}{F_1}\frac{\rho_s}{\rho_w}\tilde{A}_1\left(\frac{D_e}{r}\right)\delta_{i3}\Big]\Big\} f + \frac{\partial f}{\partial \tau} = \left(\frac{\partial}{\partial x_i} + \frac{a_1\rho_s}{F_1\rho_w}\delta_{i3}\frac{\partial}{\partial r}\frac{D_e}{r}\right) K_{ij}\left(\frac{\partial}{\partial x_j} + \frac{\delta_{3j}}{\lambda} + \frac{a_1\rho_s}{F_1\rho_w}\delta_{3j}\frac{\partial}{\partial r}\frac{D_e}{r}\right) f + J(t,\vec{x},r,c,\tau), \quad (6)$$

where K_{ij} is the turbulent diffusion tensor, v_s is the sedimentation velocity,

$$\tilde{A}_1(x) = 4\pi\iiint D_e r \frac{\partial}{\partial r}(x f)\, dr\, dc\, d\tau. \quad (7)$$

Eq.(6) does hold for a cloud which is dense enough for the supersaturation relaxation time to be short as compared to the time scale over which a spectrum is evolving.

The mean effective vapour supersaturation (which determines a mean growth rate of drop radii) is equal to

$$\delta = \frac{1}{F_1}\Big[a_1 u_3 + F_2 + a_1 K_{3l}\frac{\partial \ln F_1}{\partial x_l} + \left(\frac{a_1}{F_1}\right)^2\frac{\rho_s}{\rho_w}K_{33}\tilde{A}_1\left(\frac{D_e}{r}\right) - a_1\frac{d\ln\rho_s}{dT}K_{3i}\left(\frac{\partial T}{\partial x_i} + \gamma\delta_{3i}\right) + \frac{a_1}{\lambda}K_{33} + a_2 J_*\Big] \quad (8)$$

and differs from the mean supersaturation only by the term proportional to $d\ln\rho_s/dT$.

1. DROP SPECTRA IN A MODEL WHICH INCLUDES A STEADY-STATE LATERAL NUCLEUS INPUT INTO AND DROP LOSS FROM THE CLOUD

We consider a one-dimensional convective updraft exchanging air with its surroundings. Air outside the cloud is assumed to be nearly saturated, the temperature and its gradient outside the cloud being equal. Due to mixing the spectrum tends to be independent of height.
On adding the sink term $-Ef$ into the right side of Eq.(6), the source term being proportional to $\delta(r)$, one obtains a following equation for the drop age distribution $\chi(t)$

$$d\chi/d\tau = -E\chi \tag{9}$$

The solution to (9) is

$$\chi = E\exp(-E\tau) \tag{10}$$

1.1. Diffusion and mixing are taken into account, the nucleus activity being negligible and $r^+ = 0$

Upon integrating Eq.(6) over τ we come to[*]

$$\frac{\rho_s}{\rho_w F_1}\frac{\partial}{\partial r}\frac{\mathcal{D}_e}{r}\left[a_1 u_3^* + \left(\frac{a_1}{F_1}\right)^2\frac{\rho_s}{\rho_w}K_{33}\tilde{A}_1\left(\frac{\mathcal{D}_e}{r}\right)\right]f = \left(\frac{a_1\rho_s}{F_1\rho_w}\right)^2 K_{33}\frac{\partial}{\partial r}\left(\frac{\mathcal{D}_e}{r}\frac{\partial}{\partial r}\frac{\mathcal{D}_e}{r}f\right) - Ef \tag{11}$$

where $u_3^* = u_3 - (Lu_3/a_1R_vT^2 + K_{33}d\ln\rho_s/dT)(\partial T/\partial x_3 + \gamma)$.
Eq.(11) has an exact solution of the form

$$f(r) = n_0\alpha(r + r^*)\exp\left[-\alpha(r^2 + 2rr^*)/2\right], \tag{12}$$

where n_0 is the drop concentration, and α being determined by a rather complex nonlinear equation.
Assuming that $r^* \ll r$, which is commonly true for cloud drops, we find

$$f(r) = n_0\alpha r\exp(-\alpha r^2/2) \tag{13}$$

where $\alpha = 2\pi(n_0E\rho_w/a_1\rho_s u_3^*)^{2/3}$. The mean drop radius is $\bar{r}_1 = (\pi/2\alpha)^{1/2}$, the variability factor $\delta_0 = [\overline{r^2} - (\bar{r})^2]^{1/2}/\bar{r} = 0.523$.

[*] It is assumed that $K_{33}/\lambda \ll u_3$, $u_3/\lambda \ll E$ and $u_3(\partial T/\partial x_3 + \gamma)/T \ll E$ which leads to $a_2 J_* = -(Lu_3/R_vT^2)(\partial T/\partial x_3 + \gamma)$.

For the case, where $r^* \gg r$ (e.g. the condensation coefficient being small), we find

$$f(r) = n_0\alpha r^*\exp(-\alpha r^* r) \tag{14}$$

where $\alpha r^* = (8\pi En_0\rho_w/a_1\rho_s u_3^*)^{1/3}$. The mean drop radius is $\bar{r}_2 = 1/\alpha r^* = 0.69\bar{r}_1$, the variability factor equalling 1.
Note that the turbulence on vertical exerts no influence on both the spectrum shape and the variability factor but it affects strongly the mean drop size.
Alteration of the drop growth regime occurring due to decrease in the condensation coefficient results in a strong change in the spectrum shape implying a sharp increase in the large drop concentration.
The liquid water content (LWC) equals

$$w = Bu_3^*/E, \quad B = a_1\rho_s \tag{15}$$

being equal to the LWC gradient for an adiabatic process.
Condensation takes place when $u_3^* > 0$, which is possible when i) $u_3 > 0$, $\partial T/\partial x_3 + \gamma < \gamma^* = a_1R_VT^2/L$, ii) $u_3 > \tilde{u}_3 = K_{33}(d\ln\rho_s/dT)(\partial T/\partial x_3 + \gamma)/[1 - L(\partial T/\partial x_3 + \gamma)/a_1R_VT^2]$, $\partial T/\partial x_3 + \gamma < \gamma^*$, iii) $u_3 < 0$, $\partial T/\partial x_3 + \gamma > \gamma^*$.

1.2. The case, where $K_{33} = 0$, $E \neq 0$ (which holds when $K_{33} < u_3^2/E$)

The vapour supersaturation as determined by Eq.(8) being constant the radius of a drop is related to its age and nucleus activity by

$$\frac{\rho_w}{\rho_s}\int_{r_0(c)}^{r}\frac{x^4\,dx}{\mathcal{D}_e(x)(\delta x^3 - r^+x^2 + c)} = \tau \tag{16}$$

where $r_0(c)$ is the drop radius after the initial stage of condensation.
From Eqs (9) and (16), taking the nucleus activity distribution into account, we come to

$$f(r,c) = \frac{E\,g(c)\,r^4\rho_w}{\rho_s\mathcal{D}_e(r)(\delta r^3 - r^+r^2 + c)} \times \exp\left(-\int_{r_0}^{r}\frac{E\rho_w x^4\,dx}{\rho_s\mathcal{D}_e(x)(\delta x^3 - r^+x^2 + c)}\right), \tag{17}$$

$g(c)$ being the nucleus activity spectrum. According to Ref.13 and to the familiar formulae for an equilibrium particle size one has $g(c) = b_1c^{-(1+s)}$, where b_1, s are constant.
For $r \gg r_0$, $r \gg r^*$ we find that

$$f(r) = 5^{1+s}\,\Gamma(1+s)\,b_1\left(\mathcal{D}_0\rho_s/E\rho_w\right)^s r^{-(1+5s)} \tag{18}$$

An analogous relation can easily be derived for the case, where $r \ll r^*$, too: $f \sim r^{-(1+4s)}$.
The dependence of f upon r is the same as that found in Ref.7 for a non-turbulent cloud.

2. LARGE DROP SPECTRUM CONTROLLED BY DROP AGE AND THE NUCLEUS HYGROSCOPICITY

Neglecting r^+ and r^* in Eq.(1) one finds $r^5=5A_0c\tau$. Upon excluding a dependent variable r and letting $v_s=0$ we express the spectrum in a form of $g(t,\vec{x},c)\chi(t,\vec{x},\tau)$, the age distribution χ obeying a generalized equation of convective diffusion. The χ function being known, the drop size spectrum can be determined from the relation

$$f_1(t,\vec{x},r) = \int_0^\infty d\tau\, \chi(t,\vec{x},\tau)\, g(\vec{x},c)(dc/dr). \quad (19)$$

For $g \sim c^{-(1+s)}$ we find

$$f_1 \sim r^{-(1+5s)} \quad (20)$$

which is analogous to f in the case of a non-turbulent medium (Refs 7,8).
Thus the lateral mixing of updrafts with the environment appears to be the most powerful of the known mechanisms responsible for the broadening drop size spectra in convective clouds.
A proportional relation between LWC and air velocity for updrafts mixing with the environment is in striking contrast to the LWC dependence on height for adiabatic processes.
A conclusion that clouds can form in downdrafts under instability (the air vertical velocities being low enough) seems to be rather surprising.
An interesting fact revealed in this study is a spectrum breadening due to the condensation coefficient decrease which can occur when drop surfaces are contaminated.

3. REFERENCES

1. Belyayev, V.I., 1961, On the drop distribution in a cloud undergoing a condensation stage. Izv. Acad. Sci. USSR, Geophys. Series, No. 3, p.1209-1213.
2. Sedunov, Yu.S., 1965, A thin structure of clouds and its role in cloud drop spectrum formation. Izv. Acad. Sci. USSR, Atmospheric and Oceanic Physics, 1, No. 7, p. 722-731.
3. Levin, L.M. and Sedunov Yu.S., 1966, A kinetic equation describing microphysical processes in clouds. Dokl. Acad. Sci USSR, 170, No. 2, p. 323-326.
4. Smirnov V.I. and Kabanov A.S., 1970, An influence of the concentration inhomogeneity on horizontal of emerging drops on their size spectrum in cloud. Izv. Acad. Sci. USSR, Atmospheric and Oceanic Physics, 6, No. 12, p. 1262-1275.
5. Stepanov, A.S., 1975, Cloud drop growth by condensation in a turbulized atmosphere. Izv. Acad. Sci. USSR, Atmospheric and Oceanic Physics, 11, No. 1, p. 27-41.
6. Voloshchuk, V.M. and Sedunov,Yu.S., 1977, Kinetic equations of drop spectrum evolution on the condensation stage of cloud development. Meteorol. and Hydrol., No. 3, p. 3-14.
7. Smirnov,V.I. and Sergeyev,B.N., 1973, On the relation between the size distributions of condensation nuclei and large cloud drops. Dokl. Acad. Sci USSR, 208, No. 1, p. 87-90.
8. Smirnov, V.I. and Sergeyev, B.N., 1979, A system of atmospheric aerosol particle size spectra formed by vapour condensation on nuclei. Izv. Acad. Sci USSR, Atmospheric and Oceanic Physics, 15, No. 5, p. 540-549.
9. Mason, B.J., 1960, The evolution of droplet spectra in stratus cloud. J. of Meteorol., 17, No. 4, p.459-462.
10. Mason,B.J. and Chien, C.W., 1962, Cloud droplet growth by condensation in cumulus. Quart.J. Roy. Meteorol. Soc., 88, No. 376, p. 136-142.
11. Warner J., 1973, The microstructure of cumulus cloud: Part IV. The effect of the droplet spectrum of mixing between cloud and environment. J. Atmos. Sci, 30, No. 2, p. 256-261.
12. Sergeyev, B.N, 1980, Number modeling of growth by condensation of a drop ensemble in a convective cloud. Trudy Tsentr. Aerolog. Obs., No. 137, p. 27-28.
13. Twomey, S., 1959, The nuclei of natural cloud formation. Geofis. pura e appl., 43, No. 2, p. 243-249.

LOCAL PERTURBATION EFFECT ON MICROSTRUCTURE OF A TURBULIZED CLOUD

K.I. Vasilieva, V.M. Merkulovich, A.S. Stepanov

The Institute of Experimental Meteorology

Obninsk, USSR

The paper gives an analysis of microstructure evolution of a warm locally superheated or supercooled cloud layer.
Cloud medium state is described with an equation system including a kinetic equation for drop size distribution as well as an equation for heat and moisture balance. The kinetic equation for regular, stochastic condensation and gravitational coagulation is

$$\frac{\partial}{\partial t}\frac{f(r,\vec{x},t)}{\rho}=\hat{L}_1\frac{f(r,\vec{x},t)}{\rho}+\hat{L}_2\frac{f(r,\vec{x},t)}{\rho}. \quad (1)$$

Here the condensation operator $\hat{L}_1$ is given as in (Ref.1):

$$\hat{L}_1\frac{f}{\rho}=-\frac{\mathcal{D}\delta_0}{\rho_w}\frac{\partial}{\partial r}\frac{f(r,\vec{x},t)}{\rho}+kr\left[\frac{\partial}{\partial\vec{x}}+\frac{\partial S^*}{\partial\vec{x}}\frac{1}{r}\frac{\partial}{\partial r}\right]^2\frac{f(r,\vec{x},t)}{\rho}, \quad (2)$$

where

$$\frac{\partial S^*}{\partial\vec{x}}=\frac{\mathcal{D}\tau\rho}{\rho_w}\frac{c_p}{L}\cdot\left(\frac{\partial\theta}{\partial\vec{x}}-\frac{\partial\tilde{\theta}}{\partial\vec{x}}\right). \quad (3)$$

The coagulation operator $\hat{L}_2$ is a usual collision integral (Ref.2). For calculations of sedimentation rates and water drop capture coefficients approximate expressions were used (Refs. 3-5). Supersaturation, specific moisture and temperature are defined by equations as follows (Ref.1):

$$\delta_0=\frac{c_p}{L}\left(\frac{\partial\theta}{\partial\vec{x}}-\frac{\partial\tilde{\theta}}{\partial\vec{x}}\right)k\tau\left[\frac{2}{3}\frac{\partial}{\partial\vec{x}}\ln\frac{n}{\rho}+\frac{1}{3}\frac{\rho}{P}\frac{\partial}{\partial\vec{x}}\frac{P+\rho_{vs}}{\rho}-\frac{1}{3}\frac{\rho}{P}\frac{c_p}{L}(\gamma-1)\frac{\partial\tilde{\theta}}{\partial\vec{x}}\right]+k\tau\frac{c_p}{L}\frac{\partial\tilde{\theta}}{\partial\vec{x}}\frac{\partial\ln\gamma}{\partial\vec{x}}; \quad (4)$$

$$\gamma=1+\frac{\rho_{vs}}{\rho}\frac{L}{c_pT}\frac{L}{R_vT};$$

$$\left(\frac{\partial}{\partial t}-k\frac{\partial^2}{\partial\vec{x}^2}\right)\vec{B}=0,\qquad \vec{B}=\left(\theta-\frac{L}{c_p}\frac{P}{\rho},\frac{\rho_{vs}+P}{\rho}\right). \quad (5)$$

The system (1)-(5) has the following notations: t is the time; $\vec{x}(x, y, z)$ is the Cartesian coordinate system (the axis z is directed upwards; f is the drop size distribution; r, s are the radius and surface area of a drop; $\mathcal{D}$, k are molecular and turbulent diffusion coefficients; ρ, ρ_w are the air and water; ρ_{vs} is the density of saturated vapor above the flat surface of pure water; T is the temperature; θ, $\tilde{\theta}$ are the potential and pseudopotential temperatures; $\tau=[4\pi\mathcal{D}\int rf\,dr]^{-1}$ is the time constant for water vapor condensation; P is water constant; n is the drop concentration; c_p is the air heat capacity at constant pressure; L is the latent heat of condensation; R_v is the gas constant for water vapor.
When writing equations (1)-(5) the following assumptions were used: 1) a volume of interest is rather distant from cloud boundaries and sufficiently large to study cloud microstructure evolution in it under turbulence; 2) the effect of drop sedimentation and mean medium velocity on drop spectrum is not considered; 3) the drops are of such sizes that the influence of hygroscopicity and surface tension can be neglected. The first assumption makes it possible to use the operator $\hat{L}_1$ in the form of (2) (Ref.1). The second assumption is not a principal one and is used only to find a "pure" effect of drop spectrum evolution under stochastic condensation in a turbulized medium locally inhomogeneous in temperature on gravitational coagulation. The influence of sedimentation and convection arising under a local perturbation of medium on the drop spectrum is considered in (Refs.6,7).
Initial conditions of the equation system (1)-(5) are:

$$\left.\frac{P+\rho_{vs}}{\rho}\right|_{t=0}=C_w=const; \quad (6)$$

$$T|_{t=0}=\tilde{T}(z)+a_T\exp\left[-(z-z_0)^2/a_z^2\right]; \quad (7)$$

$$\left.\frac{f}{\rho}\right|_{t=0}=2r\cdot\Psi(\pi r^2-s^*), \quad (8)$$

where C_w is the medium specific moisture content; $\tilde{T}(z)$ is a solution of the equation $\frac{\partial\tilde{\theta}}{\partial z}=0$ at $T(z_0)=T_0$, z_0 is the height where the temperature perturbation maximum is located; a_T, a_z are the perturbation and the diameter of the turbulized zone; $\Psi(\pi r^2-s^*)$ is the solution of

$$\frac{\partial}{\partial t}\frac{f}{\rho}=\hat{L}\frac{f}{\rho}, \quad (9)$$

at $a_T=0$ for steady-state conditions.
Boundary conditions formulated under the assumption that the cloud medium surrounding the volume of interest is nonturbulized.
If $a_T\neq 0$ limitations appear for possible considered time ranges.
So a problem is considered of the cloud drop spectrum evolution under regular, stochastic condensation and gravitational coagulation in the cloud layer where a one-dimensional instant local temperature perturbation is preset. It is assumed that the microstructure immediately accomodates to the temperature variation. The spectrum shape is chosen so that in a nonperturbed cloud fraction the spectrum should not change due to condensation.
The kinetic equation (9) is known for fifteen years already. But during this time not a single attempt has been made to numerically solve this equation together with the equations for mass and water vapor transport. In the papers dealing with the kinetic equation of stochastic condensation its form has some way or other been changed. In (Ref. 8) the effect of turbulence on averaged over turbulence realizations water vapor saturation value is not considered and above all the drop distribution function is treated as a conservative substance. Due to the latter assumption the eddy liquid water flux proved to be proportional to liquid water gradient though in the case considered in (Ref. 10) it follows from equations of balance for heat and liquid water content that the turbulized liquid wa-

ter flux is proportional to the difference between dry- and moist-adiabatic gradients and does not approach zero at homogeneous liquid water distribution.
In (Ref. 9) the kinetic equation gives incorrect items describing the effect of turbulence on a drop spectrum. Therefore the equations for liquid water content obtained with the kinetic equation integration and by the balance equation for heat and moisture content do not coincide. Drop spectrum height variation in a steady-state turbulized cloud is studied analytically in (Ref. 10) where an erroneous conclusion is made that the solution of the stochastic condensation kinetic equation has a bimodal form:

$$f(s, z) = \frac{1}{2} f_o(s-\xi_1, z) + \frac{1}{2} f_o(s-\xi_2, z), \quad (10)$$

where $f_o(s)$ is the drop spectrum near the cloud base. When obtaining and analysing the solution of (10) the parameters ξ_1 and ξ_2 considered independent. It can be shown (Ref. 11) that the requirement to conserve the moisture leads to a dependence between the two parameters and ξ_1 becomes equal to ξ_2, i.e. both modes coincide.
The equation system (1)-(8) has been solved numerically with the following values of the parameters: $a_z = 0.5$; $r_o = 0.5\,\mu m$; $\Delta r = 0.25\,\mu m$; $\Delta z = 7.5$ m, where r_o is the minimum considered radius, Δr is the grid interval for radius for fine droplets. For large droplet spectrum part this interval is not constant and $\Delta r_{i+1}/\Delta r_i = 1.05$. The cloud layer height where the process of interest has taken place was 450 m. Other parameters were variable: $a_T = +1; -3.5; -10; -13; -20$ K; the initial relative dispersion $\sigma_r/\bar{r}$ was equal to 0.2; 0.4; the temperature perturbation maximum height z_o was 150; 225; 300 m; specific moisture content $C_w = 0.884 \cdot 10^{-2}$; drop concentration at z_o $n_o = 300$ cm^{-3}; eddy diffusivity coefficient k was 2.25; 9 m^2/s. Cloud drop spectra were obtained for different time points, then calculated were concentration, mean radius, dispersion, liquid water content, concentration n_r and liquid water content P_r for large drops.

$$n_r = \int_r^\infty f(r, z, t)\,dr; \qquad P_r = \frac{4}{3}\pi \rho_w \int_r^\infty r^3 f(r, z, t)\,dr.$$

As far as the initial drop size distribution implies the drop specific concentration homogeneous, local cooling causes drop concentration increase and heating leads to its decrease. Turbulent mixing (consider a certain case of local cooling gives a temperature increase with time near cooling maximum (the layer center at $z_o = 225$ m) and a temperature decrease with time at the layer periphery.
At small times the gravitational coagulation begins in the center of the perturbation zone where the drop concentration and mean drop radius are maximal. That is why at the beginning in the central part of the parturbation zone the concentration and liquid water content of large drops increase whereas the total drop concentration decreases. In the course of time the coagulation rate in the center becomes less intensive due to the drop concentration decrease because of turbulent mixing as well as due to decreasing of mean drop radius as a result of stochastic condensation. The appearance of large drops, drop concentration increase due to turbulence, mean radius and dispersion increase by stochastic condensation make the process of coagulation at the periphery more intensive. As far as liquid water content and mean drop radius increase with height the coagulation rate above the cloud layer center is more intensive.
As a whole in the course of time in the center of the cooling zone the drop concentration decreases monotonously by turbulence and coagulation. At the periphery the concentration at first increases due to turbulence. Then the coagulation retards the concentration increase and in some time causes its decrease. Table I gives percentage difference of initial drop concentration and that for a certain period of time. The first and the second columns show the variant for basic drop concentration (a_T=0) and the variant for the drop concentration without coagulation ($\hat{L}_2 \equiv 0$), respectively. At a_T=0 the coagulation leads to some variation of drop concentration with n_{100}~0.01 m^{-3} and n_{250} ~ 0.0002 m^{-3}. The turbulent mixing within the calculation uncertainties does not influence the drop concentration. Stochastic condencation and turbulent transport at a_T=-7 K result in a decrease of concentration in the center of the perturbed zone and its increase at the periphery.
The rate of coagulation growth of drops in the problem under consideration depends on the following characteristics of perturbation and cloud medium: amplitude, water and moisture content, drop concentration, eddy diffusivity coefficient.
Increasing of perturbation amplitude causes an increase of drop concentration, of mean drop radius and water content. Dispersion of the initial drop distribution decreases and the rate of dispersion increase becomes more intensive due to stochastic condensation. These factors provoke the coagulation (see tables I and 2). Turbulent "smearing" of perturbation smoothes the difference in coagulation rates with time. The data of table 2 indicate that by 30 minutes of the process $n_{100}(a_T$= 10 K$) < n_{100}(a_T$= -7 K$)$ in the center of the cooling zone. It can be explained by more intensive coagulation at a_T= -10 K and to some extent by enhancement of large drops exchange by turbulence caused by medium heterogeneity increasing.
Analytical studying of drop spectrum evolution under stochastic condensation (Refs. 17, 12) has shown that the spectrum dispersion in the center of local cooling zone as a function of the parameter kt/a_z^2 has a maximum. Therefore an increase of the eddy diffusivity coefficient may cause both the intensification and suppression of the coagulation process. The intensification of the perturbation "smearing" at increasing eddy diffusivity coefficient leads to suppression of coagulation by a fast decrease of drop concentration and mean radius in the cooling zone. The data obtained have shown that at least at $t \geq 5$ min the suppression of coagulation with increasing k prevails over the intensification (see tables 1 and 3). This is most important in appearance and growth of large particles and

their water content. At increasing k from 2.25 m^2/s to 9 m^2/s n_{250} and P_{250} give a decrease of an order of a value (table 3), but they are more than 10^4 higher the corresponding values in the basic case. At t= 40 min maximum values of n_{100} and P_{100} are attained at z =270 m and are: n_{100}= 1570 m-3 and P_{100}= 0.08570 m^{-3}.

Initial concentration decrease at given water content leads to mean radius increase that in its turn causes coagulation growth enhancement. This effect is more important for the processes at the periphery of the perturbation zone where temperature gradients are close to the environmental ones. Stochastic condensation in this case changes the drop spectrum insignificantly and the effect of initial conditions on coagulation kinetics is more pronounced.

Variations of maximum cooling level influences the drop growth rate as far as water content and drop concentration change with height. The behavior of concentration profiles(large drop water content, total concentration, etc.) is similar to that of corresponding parameters when maximum cooling takes place at the level of 225 m.

The results given above have been obtained for the specific moisture content of 0.834. 10^{-2} and T_o = 283 K. The water content at the level z_o is 1 g^{-3} at a_T= 0 and ~4.7 gm^{-3} at a_T=-7 K. A double decrease of specific moisture content results in a more abrupt decrease of coagulation rate of droplet growth, i.e. n_{100} at a_T=-7 K decreases for four orders of magnitude (see tables 1 and 4) To obtain data of such an order (as in case of C_w =0.834.10^{-2}) a_T should be decreased to -20 K. The data of table 4 illustrate the role of perturbation pulsations in the coagulation kinetics. When a_T decreases from -7 K to -20 K the concentration n_{100} and water content P_{100} increase for four orders in the center of the perturbation zone. The data of table 1 show that at decreasing water content in about 20 minutes the total drop concentration at the levels higher than 75 m above the center of the cooling zone is still growing, i.e.the turbulent mixing is more effective than the gravitational coagulation.

Local heating causes a decrease of drop concentration, mean drop radius, water content, drop spectrum dispersion at initial adjustment of cloud microstructure to perturbations. The system in this case tends to regain the unperturbed state; the time constant in this case is about 50 min. The coagulation rate is close to the initial one, large drops concentration and water captured by them do not practically differ from the initial values at z = 225 m, n_{100}~0.01m^{-3}; P_{100} ~ 0.1.10^{-6}gm^{-3}.

Of certain interest is studying of a drop spectrum in the medium undergoing recurrent local cooling. It was assumed that temperature perturbation occurred two or three times with the interval of 5 min. The following cases were considered: 1)T_o=283 K; C_w= 0.884.10^{-2} a_T=-3.5 K at t=0 and t=5 min; 2)T_o= 274 K; C_w= 0.442.10^{-2}; a_T=-7 at t = 0; 5 min and 10 min. The data obtained were compared with the results corresponding to the following parameter values: 3) T_o=283K, C_w = 0.884.10^{-2}, a_T=-7 K at t=0;4)T=274 K, C_w = 0.442.10^{-2}, a_T =-20 K at t=0. Fig.1 shows the behavior of n_{100} for these four cases. When analysing these data and the large drop water content one can see that in the center of the cooling zone at the nearest levels (the distance of 15-37.5 m) cooling results in a more intensive growth of large drops. The behavior of these parameters at the periphery is practically the same. The difference at the central levels can be explained by differences in turbulent mixing intensity. From the one hand, large temperature gradients(cases 3 and 4) cause more intensive mixing both of large and fine drops leading to a decrease of large drop number in the center of the perturbed zone as compared to cases 1 and 2, respectively. From the other hand, at the levels more distant from the center than mentioned above, an inverse picture can be seen, i.e. the number of large drops is greater at larger temperature gradients and correspondingly more intensive mixing. In case 2) a great number of drops with the radii more than 250 m form during 40 minutes, the variations in n_{250} being similar to that for n_{100}.

Thus the results obtained have shown that the drop spectrum evolution in a turbulized, locally cooled medium leads to intensification of gravitational coagulation. At the same time coagulation rate increases with cooling increasing with a decrease of eddy diffusivity coefficient and an increase of specific moisture content. In a medium with repeated local cooling the coagulation process enhances in the center of the perturbation zone. If in view of (Ref. 13) it is assumed that precipitations take place at $n_{100} \geq 1500$ m^{-3}, $P_{100} \geq 0.005$ g/m^3 (drizzle), then according to our data precipitation particles form if water content within the cooled zone reaches 3 - 4 g/m^3.

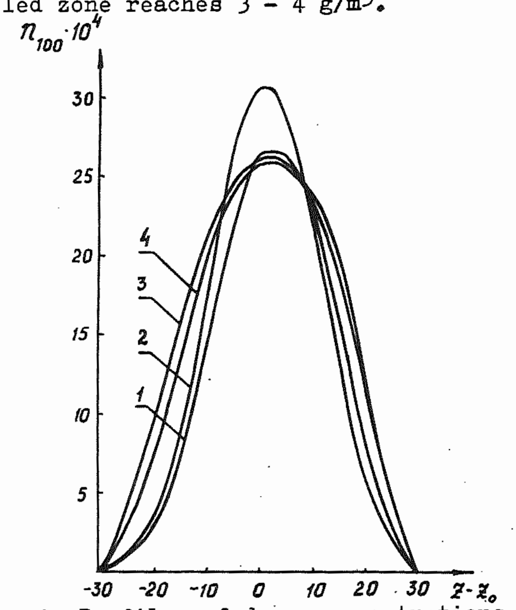

Fig. 1. Profiles of drop concentrations. Drop radii 100 μm, t=40 min. 1 - case 1; 2 - case 2; 3 - case 3; 4 - case 4.

Relative variation of total drop concentration. Left number corresponds to t = 20 min, right - to t = 30 min.

$z(m)$	T_o = 283 K; k = 2.25 $m^2 \cdot s^{-1}$: $a_T = 0$		$a_T = -7K$, $L_2 = 0$		$a_T = 1K$		$a_T = -7K$		$a_T = -10K$		$T_o = 283K$, $k = 9 m^2 s^{-1}$: $a_T = -7K$		$T_o = 274K$; $k = 2.25 m^2 s^{-1}$: $a_T = -10K$		$a_T = -20K$	
37.5	0.6	0.8	-0.6	-1.0	0.9	1.4	0	0.4	0.1	7.7	0	0.7	-1.1	-1.2	-1.3	-0.7
75	1.0	1.5	-1.6	-2.2	2.0	2.9	0	1.4	1.9	20.9	0.2	1.5	-3.2	-3.6	-3.7	-1.9
112.5	1.3	1.9	-2.8	-3.1	3.3	4.2	0.2	3.8	8.1	38.2	0.4	2.4	-5.7	-5.4	-5.9	-0.1
150	1.5	2.3	-3.9	-3.7	4.7	5.3	0.8	8.3	22.1	54.8	1.0	3.5	-7.6	-6.1	-6.8	6.3
187.5	1.7	2.6	3.8	4.5	3.2	3.4	6.9	18.2	43.7	69.9	9.6	12.3	9.8	12.1	15.6	32.0
225	1.9	2.8	5.1	5.9	-14.4	-14.2	6.7	21.8	51.4	75.5	11.4	14.4	14.7	17.3	16.6	36.0
262.5	2.1	3.1	3.2	3.9	2.6	2.9	6.8	20.6	46.7	73.6	9.4	12.6	9.0	11.4	14.0	32.6
300	2.2	3.3	-1.7	-1.4	3.9	4.7	3.3	14.1	29.5	62.0	3.8	6.8	-2.6	0.8	-1.5	13.9
337.5	2.3	3.3	-1.0	-1.0	3.2	4.2	2.6	9.2	14.7	36.7	3.1	5.9	-0.9	-0.04	-0.6	7.9
375	2.2	3.0	-0.4	-0.5	2.6	3.5	2.1	5.4	5.9	32.7	2.4	4.4	0.2	0.6	0.4	3.7
415.5	1.6	2.0	-0.1	-0.2	1.7	2.3	0.7	2.7	2.3	15.9	1.4	2.4	0.5	0.7	0.6	1.6

Table 2

Large drop concentration at different temperature local perturbations. T = 283 K, k= 2.25 m^2/s, C_w= .834.10^2, t=30 min, z_o=225 m

$z(m)$	$n_{100} (m^{-3})$ a_T (K)		$n_{250} (m^{-3})$ a_T (K)		$P_{100} (g \cdot m^{-3})$ a_T (K)		$P_{250} (g \cdot m^{-3})$ a_T (K)	
	-7	-10	-7	-10	-7	-10	-7	-10
75	446	1260	0.9	374	.02	.08	.02	.06
150	2190	2655	590	901	.13	.19	.10	.16
225	3620	3050	1040	1099	.22	.24	.17	.20
300	2990	2980	825	1010	.18	.22	.14	.18
375	1100	2020	265	613	.06	.13	.04	.10

Table 3

Large drop concentration and liquid water content at different eddy diffusivity coefficient. T 283 K, a_T=-7 K, C_w=.834.10^2, t=30' min, z_o=225 m.

$z(m)$	$n_{100} (m^{-3})$ $k (m^2 \cdot s^{-1})$		$n_{250} (m^{-3})$ $k (m^2 \cdot s^{-1})$		$P_{100} (g \cdot m^{-3})$ $k (m^2 \cdot s^{-1})$		$P_{250} (g \cdot m^{-3})$ $k (m^2 \cdot s^{-1})$	
	2.25	9	2.25	9	2.25	9	2.25	9
75	446	136	99	20	.02	.005	.02	.003
150	2190	357	590	56	.13	.013	.10	.008
225	3620	582	1040	97	.22	.022	.17	.015
300	2990	633	825	109	.18	.025	.14	.017
375	1100	410	265	70	.06	.016	.04	.011

Table 4

Values of n_{100} and P_{100} at C_w=.442.10^{-2}, T=274K, k=2.25 m^2/s, t=30 min, z_o= 225 m

$z(m)$	$n_{100} (m^{-3})$ a_T (K)		$P_{100} (g \cdot m^{-3})$ a_T (K)	
	-7	-20	-7	-20
75	0.006	220	$0.58.10^{-7}$	$0.91.10^{2}$
150	0.11	1509	$0.12.10^{-5}$	$0.76.10^{1}$
225	0.4	2865	$0.5.10^{-5}$	0.16
300	0.28	1925	$0.35.10^{-5}$	0.1
375	0.05	424	$0.6.10^{-6}$	$0.19.10^{1}$

REFERENCES

1. Vasilieva, K.I., Merkulovich, V.M., Stepanov, A.S., 1983. On behavior of cloud droplet spectrum formed by stochastic condensation, Meteorologiya i gidrologiya, No. 9, p. 50-57.
2. Voloshchuk, V.M., Sedunov, Yu.S. Coagulation processes in disperse systems, 1975, Leningrad, Gidrometeoizdat, 320 pp.
3. Berry, B.X., 1967, J. Atmos. Sci., 24, No6. p.688-701.
4. Long, A.B., Manton, M.J., 1974, On the collection kernel for the coalescence of water droplets, J. Atm. Sci., 31, No.4, p.1053-1057.
5. Scott, W.T., Chen, C.Y., 1970, Approximate formulas fitted to Davis-Sartor-Neiburger droplet collision efficiency calculations, J.Atmos., 27, No. 4, p.698-700.
6. Kabanov, A.S., Stepanov, A.S., 1978, Temperature inhomogeneities effect on cloud medium, Trudy IEM, 19(72), p. 10-23.
7. Stepanov, A.S., 1976, Turbulence effect on cloud drop spectrum under condensation, Izv.Acad.Sci.USSR, Atmospheric and Oceanic Physics. 12, No.3, p.281-291.
8. Clark, T.L., Hall, W.D., 1979, A numerical experiment on stochastic condensation theory, J.Atmos.Sci., 36, No.3, p.470-483.
9. Clark, T.L., 1976, Use of log-normal distribution for numerical calculations of condensation and collection. J.Atmos.Sci., 33, No. 5, p.810-821.
10. Manton, M.J., 1979, On the broadening of a droplet distribution near cloud base. Quart.J.Roy.Meteorol.Soc., 105, p.899-914.
11. Merkulovich, V.M., Stepanov, A.S., 1981, Comments on the paper "On the broadening of a droplet distribution by turbulence near cloud base" by Manton M.J. (Quart. J.Roy.Meteorol. Soc., 1979, 105), Quart. J.Roy.Meteorol. Soc., 107, No. 454, p.976-977.
12. Merkulovich, V.M., Stepanov, A.S., 1977, Hygroscopicity and surface tension forces effects at cloud droplet condensation growth by turbulence, Izv. Acad. Sci. USSR, Atmospheric and Oceanic Physics, 13, No. 2, p. 163-171.
13. Voit, F.Ya., Kornienko, E.E., Khusid, S.V., 1972, Some peculiarities of precipitation formation in cumulus clouds. Trudy UkrNIGMI, 118, p. 61-80.

AN ANALYTIC-NUMERICAL SOLUTION OF THE (KINETIC) SPECTRAL CONDENSATION EQUATION

Ulrike Wacker

Institut für Meteorologie und Geophysik der Universität Frankfurt/Main
D-6000 Frankfurt 1, Fed.Rep.Germany

1. INTRODUCTION

Microphysical processes in clouds depend basically on the present drop size distribution. Therefore, any detailed mathematical simulation of the development of clouds and precipitation requires the knowledge of the drop size spectrum changing in time by condensation, coagulation, nucleation etc., described in terms of the (kinetic) spectral budget equation for the distribution function.

In this paper we will deal with the condensation process, which plays a predominant role in the early stage of a cloud. Omitting all microphysical processes except condensation the corresponding prognostic equation for the drop mass distribution function $f = f(m,t)$ with m: drop mass, is the so called (kinetic) spectral condensation equation (hereafter referred to as SCE):

$$\frac{\partial f}{\partial t} + \frac{\partial f\dot{m}}{\partial m} = 0 \qquad (1)$$

This continuity equation is of the type of a non-linear advection equation, where the condensation growth rate $\dot{m}$ has the meaning of an 'advection velocity'.

The solution of Eq.(1) by means of purely numerical schemes as proposed by e.g. Richtmyer and Morton (1967; Ref.1) and Book (1981; Ref.2) for advection equations is basically connected with the difficulties resulting from the extremely steep gradients of f and $\dot{m}$ as well as a probable change of sign of the advection velocity $\dot{m}(m)$ along m. To circumvent the problem of integrating the SCE (1) most microphysical models (e.g. Takahashi and Lee, 1978; Ref.3; Fitzgerald, 1974; Ref.4) apply the imposed conservation condition for the number of drops in each class in connection with grid points moving along m according to $\dot{m}$. However, a severe limitation of this method is the distortion of the grid points in most important regions, namely where the growth rate $\dot{m}$ changes its sign.

To overcome these difficulties we will present in this paper an analytical method to solve the spectral condensation equation. The treatment of Eq.(1) in a Lagrangian space formalism leads to an exact solution $f(m,t)$ throughout the whole drop size range, even at those critical points of $\dot{m}$ mentioned above.

2. SOLUTION METHOD

The SCE (1) describes the evolution of the drop size spectrum $f(m,t)$ by condensation or evaporation as a function of drop mass m and time t. A necessary condition for solving Eq.(1) is the knowledge of the condensation growth rate $\dot{m}$. Here we use the formulation as given by Pruppacher and Klett (1978; Ref.5). The analytic integration of the SCE requires the assumption of constant relative humidity RH and temperature T.

To elaborate $f(m,t)$ we have to pay attention to the facts that the drop growth rate is a function of m, $\dot{m} = \dot{m}(m)$, that it may become zero and change its sign. Because of the type of the SCE (1) its solution requires a distinct treatment of masses with $\dot{m} = 0$ and $\dot{m} \neq 0$.

First we will consider the evolution of $f(m,t)$ for masses $m=m^*$ with vanishing growth rate, $\dot{m}(m=m^*) = 0$. Obviously, if $(\partial\dot{m}/\partial m)_{m^*}>0$ drops with $m>m^*$ grow steadily and drops with $m<m^*$ evaporate, so that all particles adjacent to m^* are moving away from that mass, and $f(m^*,t)$ will decrease in time. Hence, in this case we may interprete m^* as a 'divergence point' m_{div}.
On the contrary, if $(\partial\dot{m}/\partial m)_{m^*}<0$, i.e. drops with $m>m^*$ evaporate and those with $m<m^*$ condensate, all drops near m^* tend to approach that very point and contribute to an increase of drops at m^*. This feature causes a rising value of $f(m^*,t)$ and we call the point a 'convergence point' m_{con}.
The evolution of $f(m^*,t)$ is described quantitatively by the analytical solution of Eq.(1) for $m^* = m_{con}, m_{div}$:

$$f(m^*,t) = f(m^*,t_0)\ \exp\left[-\left(\frac{\partial\dot{m}}{\partial m}\right)_{m^*}(t-t_0)\right] \qquad (2)$$

The atmospheric conditions relative humidity, temperature and salt content of the drops decide, whether there exists only a convergence point, a convergence point as well as a divergence point or none of both, because of $\dot{m}>0$ for all drops.

Next we will reflect upon drops with nonvanishing growth rate. To integrate Eq.(1) analytically we adopt the Lagrangian point of view by following the trajectories of single particles resulting in an exact analytical solution for the evolution of the drop size spectrum:

$$f(m,t) = f(m_0,t_0)\ \frac{\dot{m}(m_0)}{\dot{m}(m)} \qquad (3)$$

The initial value $m_0 = m(t_0)$ is linked to the actual drop mass m by the drop growth rate $\dot{m}$.

From the interpretation of the zeros of $\dot{m}$ as convergence or divergence points it follows that the related growth rates $\dot{m}(m)$ and $\dot{m}(m)$ have equal signs. Therefore, Eq.(3) satisfies the necessary condition of a probability distribution function, namely $f(m,t)>0$.

The evaluation of the analytical solution of the SCE (1), i.e. Eq.(2) and (3), requires numerical procedures, which causes the appearance of difficulties. They are primarily connected with the convergence point, because a maximum of f(m,t) arises at m_{con} accompanied by very steep gradients comparable to the Dirac δ-function. This feature gives rise to large errors for the integration over the whole spectrum. To avoid the difficulty we consider only drops with $m>m_{con}$ and choose a minimum value of m, m_{min}, next to m_{con}. The discretization of the mass coordinate exhibits an extraordinary fine resolution for the smallest masses, and the grid points are kept fixed with respect to time. It should be noted that this scheme does not conserve the total number of drops, because evaporating drops migrate straight onto m_{con} and leave the prescribed mass range. However, the number of lost particles and the resulting error can be estimated from the conservation law. Moreover, in the presence of an additional divergence point the number of drops with an initial value $m_0>m_{div}$ must also be conserved; this condition serves as a test for the quality of the solution scheme of the SCE (1).

With regard to the divergence point the distribution function $f(m_{div}, t)$ is calculated directly from Eq.(2) without any further difficulties. In case of $\dot{m}>0$ for all drops sharp gradients do not arise because of the missing convergence point leading to a simpler treatment.

3. A CASE STUDY

Now we will discuss an example for the solution of Eq.(1) for RH = 100.1%, T = 283 K, p = 900 mb and a salt content $m_s = 1.1\times10^{-15}$ g NaCl for each drop. The corresponding growth rate for motionless drops is shown in Fig.1. For the given atmospheric conditions $\dot{m}$ is positive if $m < 2.9\times10^{-13}$ g and $m > 4.2\times10^{-12}$ g, and negative if $2.9\times10^{-13} < m < 4.2\times10^{-12}$ g, indicating a convergence point at $m_{con} = 2.9\times10^{-13}$ as well as a divergence point at $m_{div} = 4.2\times10^{-12}$ g.

The corresponding time development of f(m,t) is plotted in Fig.2 for t = 0,10,100 s. Because of constant RH and T the characteristic effects of the convergence and divergence point on the shape of f(m,t) are clearly illustrated.

As the distribution function is not calculated at the convergence point the curve of

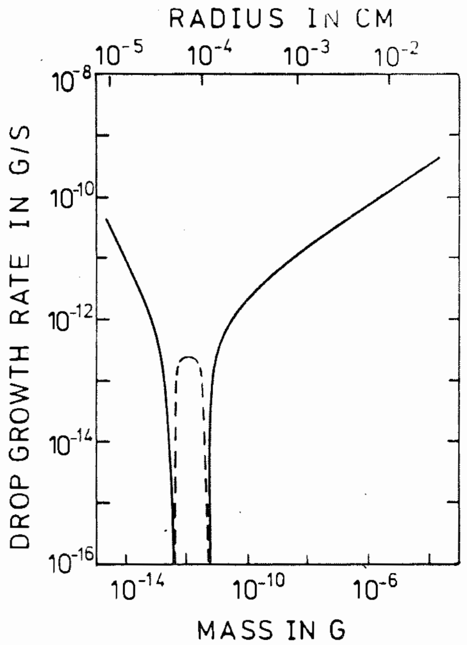

Fig.1:

Drop growth rate $\dot{m}$ as function of drop size for model conditions RH = 100.1%, T = 283 K, p = 900 mb, $m_s = 1.1\times10^{-15}$ g NaCl.
(——: positive values, ---: negative values)

f(m,t) is indicated in the range $m_{con} < m < m_{min}$ by a dashed line to point out the arising extremely steep gradient in that region.

Despite the low absolute values of $\dot{m}$ for smallest drops most droplets with $m_0<m_{div}$ reach their (stable) equilibrium value $m_{con} = 2.9\times10^{-13}$ g within less than 20 s; these are the unactivated particles under the given model conditions. The presence of the divergence point causes a minimum at $m_{div} = 4.2\times10^{-12}$ g becoming more and more pronounced. The growing drops with $m_0>m_{div}$ lead to a maximum at $m \approx 10^{-10}$ g at t = 100 s, which is augmented by more than a factor of 100 in comparison to the initial value of the distribution function. Within that peak most of the growing particles are concentrated. The conservation error for the total number of activated drops with $m_0 > m_{div}$ amounts to only 6% of the initial value.

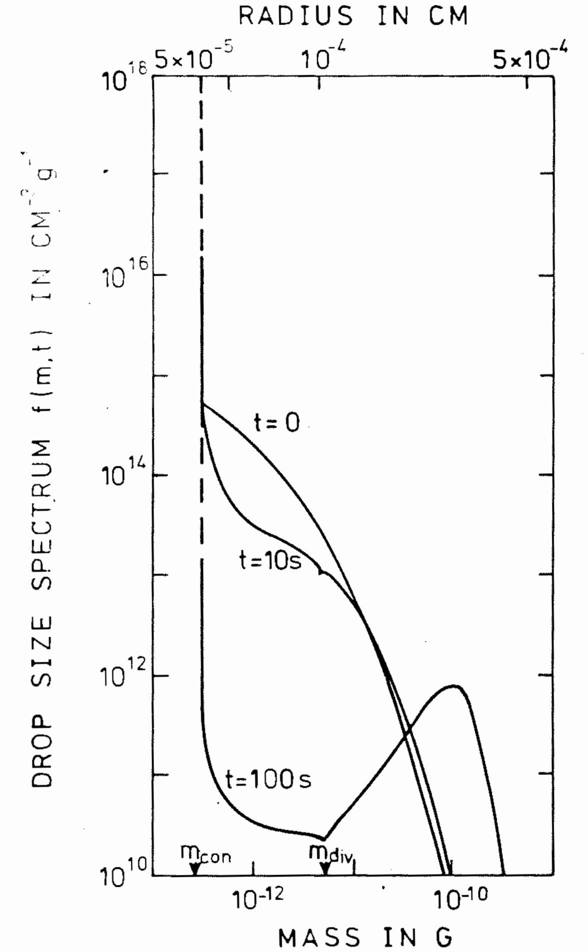

Fig.2:

Time development of the drop size distribution f(m) for t = 0, 10, 100 s, calculated with the semi-analytical integration scheme. Model conditions as in Fig.1. Dashed lines indicate f(m) for $m_{con}<m<m_{min}$.

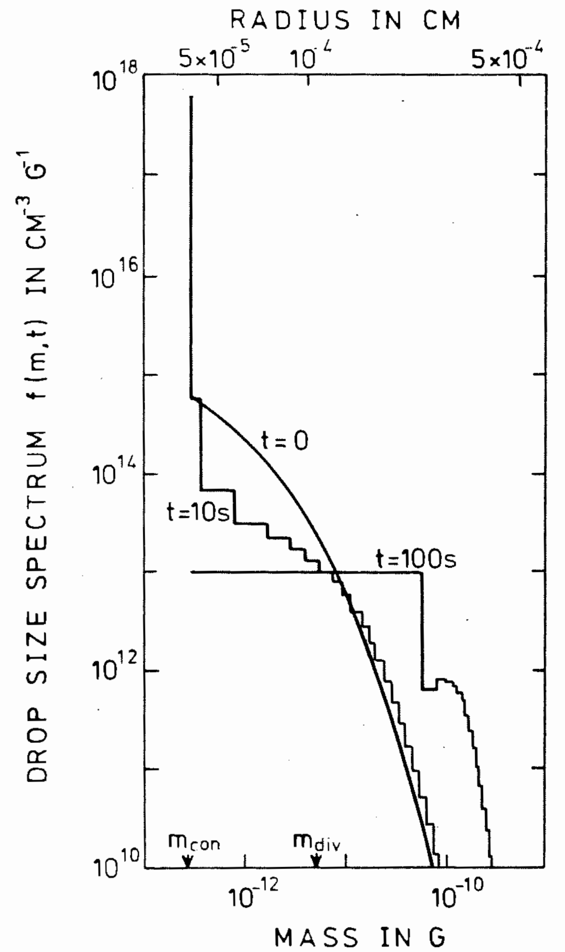

Fig.3:

As Fig.2, but calculated with a conventional model. For details see text.

4. CONCLUDING REMARKS

The ability of the presented semi-analytical solution of (1) is best illustrated by a comparison with the results obtained by a conventional model, i.e. using time dependent grid points and applying the drop number conservation for each class as carried out for instance by Fitzgerald, 1974 (Ref.4). Fig. 3 shows that the class containing initially m_{div} grows steadily throughout the whole integration time; at last it spreads over several orders of magnitude of m (including the convergence point), but characterized by just one value of f(m). Therefore, this interesting mass region cannot be resolved in sufficient detail. However, far away from the divergence point with $m > 10^{-10}$ g the models agree quite well for growing drops; the same feature holds true, if the model conditions cause $\dot{m} > 0$ for all drops.

To summarize the results it should be stated that the presented analytic-numerical solution of the (kinetic) spectral condensation equation and its verification are a real improvement over previous numerical schemes in mathematical and physical aspects. This applies especially to those cases, where the drop growth rate changes its sign, i.e. at subsaturation or low values of supersaturation as is often observed under atmospheric conditions.

5. REFERENCES

1. Richtmyer R D & Morton K W 1967, Difference Methods for Initial Value Problems, 2nd ed, New York, Interscience, pp 406.

2. Book D L (Ed) 1981, Finite-Difference Techniques for Vectorized Fluid Dynamics Calculations, New York, Springer, pp 226.

3. Takahashi T & Lee S 1978, The nuclei mass range most efficient for the initiation of warm cloud showers, J Atmos Sci 35,1934-1946.

4. Fitzgerald J W 1974, Effect of aerosol composition on cloud droplet size distribution: A numerical study, J Atmos Sci 31,1358-1367.

5. Pruppacher H R & Klett J D 1978, Microphysics of Clouds and Precipitation, Dordrecht, D Reidel Publ Co, pp 714.

AN ANALYSIS OF CLOUD DROPLETS SPECTRUM EVOLUTION BY COALESCENCE AND BREAKUP PROCESSES.

Isaac M. YEnukashvili

Depart. for Research, Israel Meteorological Service.
P.O.Box 25, Bet-Dagan, Israel.

Abstract.

A new algorithm of the numerical method of moments is developed for integrating the kinetic equation of coalescence and breakup of cloud droplets. Analytic expressions of autoconversion, accretion and breakup conversion of mass and number concentration describing the intraction between small cloud droplets portion of the spectrum and larger drops portion of the spectrum are derived. Numerical results are obtained for different initial droplet spectrum and for different coalescence/breakup kernels. Also droplets mass grid points and time steps are varied. The results of numerical experiments are compared with Berry's and Reinhardt's analysis for the autoconversion, accretion and larger drops selfcollection.

1. Introduction.

The microphysical processes of coalescence and breakup of cloud droplets are among the important processes governing the mass conversion from cloud droplets to larger drops in the problem of cloud droplets spectrum evolution. Coalescence of cloud droplets alone tends to formation of larger drops (autoconversion); coalescence alone between cloud droplets and larger drops (accretion) and coalescence between larger drops (selfcollection) tends to mass conversion from cloud droplets to larger drops (Ref.1). Cloud droplets and larger drops disintegration opposes this tendency and tends to mass conversion from larger drops to cloud droplets. If there is an equilibrium between these two tendencies a steady-state distributions of cloud droplets and larger drops may be developed as a result of simultaneous action of coalescence and breakup processes (Ref.5,6,7).

In this study a new algorithm of the numerical method of moments for integrating coalescence /breakup kinetic equation (Ref.2,3,4) is developed. Analytic expressions for time derivatives of number concentrations and liquid water contents of cloud droplets and larger drops each taken separately are derived. Numerical experiments are carried out to study the mass conversion process between cloud droplets and larger drops resulting from simultaneous action of coalescence and breakup processes.

2. The governing equations and computation method.

The coalescence/breakup kinetic equation for number density function n(x,t) can be written as:

$$\partial n(x,t)/\partial t=-n(x,t)\int_0^\infty \sigma(x,y)n(y,t)dy-n(x,t)P(x)+$$
$$+(1/2)\int_0^x \sigma(x-y,y)n(x-y,t)n(y,t)dy+\int_x^\infty P(y)Q(y,x)n(y,t)dy \qquad (1)$$

In this equation $\sigma(x,y)$ represents the coalescence kernel for two droplets of mass x and y; $P(x)$-the probability that a droplet of mass x will break up during a unit time and $Q(y,x)$-the number density function of fragment droplets of mass x formed due to breakup of a parent drop of mass y.

Multiplying (1) by dx and by xdx and integrating in both cases from 0 to S and from S to ∞ we have:

$$\partial N_1(t)/\partial t=-(1/2)\int_0^S n(x,t)dx\int_0^S \sigma(x,y)n(y,t)dy-(1/2)$$
$$\int_0^S n(x,t)dx\int_{S-x}^S \sigma(x,y)n(y,t)dy-\int_0^S n(x,t)dx\int_S^\infty \sigma(x,y)n(y,t)dy-$$
$$-\int_0^S P(x)n(x,t)dx+\int_0^S P(x)n(x,t)dx\int_0^x Q(y,x)dy+$$
$$+\int_S^\infty P(y)n(y,t)dy\int_0^S Q(y,x)dx \qquad (2)$$

$$\partial M_1(t)/\partial t=-\int_0^S xn(x,t)dx\int_S^\infty \sigma(x,y)n(y,t)dy-(1/2)\int_0^S n(y,t)dy$$
$$\int_{S-y}^S (x+y)\sigma(x,y)n(x,t)dx+\int_S^\infty P(y)n(y,t)dy\int_0^S xQ(y,x)dx \qquad (3)$$

$$\partial N_2(t)/\partial t=-(1/2)\int_S^\infty n(x,t)dx\int_S^\infty \sigma(x,y)n(y,t)dy+(1/2)$$
$$\int_0^S n(x,t)dx\int_{S-x}^S \sigma(x,y)n(y,t)dy-\int_S^\infty P(x)n(x,t)dx+$$
$$+\int_S^\infty n(y,t)P(y)dy\int_S^y Q(y,x)dx \qquad (4)$$

$$\partial M_2(t)/\partial t=\int_0^S xn(x,t)dx\int_S^\infty \sigma(x,y)n(y,t)dy+(1/2)\int_0^S n(y,t)dy$$
$$\int_{S-y}^S (x+y)\sigma(x,y)n(x,t)dx-\int_S^\infty P(y)n(y,t)dy\int_0^S xQ(y,x)dx \qquad (5)$$

In equations (2)-(5) $N_1(t)$,$N_2(t)$ represent number concentrations of cloud droplets and larger drops respectively; $M_1(t)$,$M_2(t)$-are liquid water contents of cloud droplets and larger drops respectively. **S** represents a droplet mass separating cloud droplets diapason from larger drops diapason of the spectrum. In equations (3) and (5) the first term on the right hand side represents the accretion term; The second term represents the autoconversion term; The third term describes breakup mass conversion from larger drops portion of the spectrum to the small cloud droplets portion of the spectrum.

In equations (2) and (4) the first term on the right hand side describes the decreasing of $N_1(t)$ and $N_2(t)$ respectively as a result of coalescence between cloud droplets in eq. (2) and between larger drops in eq. (4). The second term in equations (2) and (4) is the number concentration autoconversion term. The third term in eq.(2) represents the accretion term; The last three terms in eq. (1) and the last two terms in eq, (4) describe number concentration balance (variation) in (2) and (4) respectively as a result of cloud droplets and larger drops disintegration.

To compute the autoconversion,accretion and breakup conversion terms (double integrals),and also to solve the equations (2)-(5),the numerical method of moments (Ref.2,3,4) is used for integrating the kinetic eq.(1).Each separate droplet mass interval between droplets mass grid points (x_k,x_{k+1}) where $x_{k+1}=sx_k$ is considered as a droplet packet with its own number concentration,liquid water content and other moments and the unknown number density function $n_k(x,t)$ in each droplet packet is represented by an expansion in orthogonal polynomials with a given weighting function

$$n_k(z,t)=W_k(z,t)\sum_{i=0}^{\infty}a_{ik}(t)G_{ik}(z) \qquad (6)$$

where $z=x/x_k$ represents droplets nondimensional mass in the packet (x_k,x_{k+1}); $W_k(z,t)$-weighting function; $G_{ik}(z)$-are polynomials orthogonal in the range (1,s) with weighting function $W_k(z,t)$. $a_{ik}(t)$ are the expansion coefficients which are expressed as linear combinations of the moments of number density function $n_k(z,t)$.It should be noted that the first order approximation of the expansion (6) which includes the first two terms of the expansion (6) describes not only the case where the droplets in the packet(x_k,x_{k+1}) are spread over the whole mass interval (x_k,x_{k+1}) but also the case where droplets in the packet (x_k,x_{k+1}) are located only in the part of the whole mass interval (x_k,x_{k+1}) (Ref.3,4).In last case the bidimensional integration formula of Gaussian type is used to reduce the computer time required for numerical computation of the coalescence and breakup double integrals (Ref.3).

3.Numerical computations and concluding remarks.

The unknown number density function $n_k(z,t)$ in each separate droplet packet (x_k,x_{k+1}) is represented by an expansion in orthogonal polynomials with a given weighting function in the range (x_k, x_{k+1}).In this way the problem of solving the coalescence/breakup kinetic equation (1) is replaced by one of solving a set of coupled differential equations for the moments of the number density function $n_k(z,t)$. The convergence of the expansion (6) for the number density function $n_k(z,t)$ in terms of orthogonal polynomials with a given weighting functions in range (1,s) $(s\leq 2)$ is sufficiently rapid and for droplet mass grid points $x_{k+1}=sx_k$ $(s\leq 2)$ the approximation of $n_k(z,t)$ by means of the first two moments ,that is by means of the first two terms of the expansion (6) is sufficiently correct.

Analytic expressions for the values of autoconversion,accretion and breakup conversion for number concentrations and liquid water contents of cloud droplets and larger drops are derived.A numerical experiments and an analysis are carried out to study the variation of the autoconversion,accretion and breakup conversion terms in equations (2)--(5) in terms of time and number density function moments and to study the interaction between the small droplets portion of the spectrum and the larger drops portion of the spectrum as well.

For numerical integration of coupled differential equations for number concentrations and liquid water contents of the number density function $n_k(z,t)$ in each separate droplet packet (x_k,x_{k+1}) which are derived fro eq. (1) the method of fractional time steps is adopted.In this method it is assumed that the time step of integration is broken up into separate treatment of coalescence and breakup processes.Also numerical computations without using the method of fractional time steps are carried out. It is shown that for time steps $\Delta t\leq 5$sec. the difference between numerical results obtained by using and without using the method of fractional time steps is very small.

A development of an equilibrium steady-state distributions for cloud droplets and larger drops as a result of simultaneous action of coalescence and breakup processes is studied in terms of coalescence and breakup kernels and in terms of cloud droplets and larger drops initial spectra.A comparison is made between numerical results computed by using the whole kinetic eq.(1) and by using eq. (1) without breakup terms.It is shown that the peak values of the number density and mass density distribution functions are displaced towards the small droplets portion of the spectrum as a result of cloud droplets and larger drops disintegration.

Acknowledgments.The author wishes to thank the colleagues from Israel Meteorological Service Research Department for valuable discussions.

4.References.

1. Berry E.X. and R.Reinhardt,1974, An analysis of cloud drop growth by collection. J.Atmos. Sci.31, N7 and N8.
2. Bleck R. 1970, A fast approximative method for integrating the stochastic coalescence equation. J.Geophys. Res.,75, 5165-5171.
3. Enukashvily I.M. 1980, Anumerical method for integrating the kinetic equation of coal scence and breakup of cloud droplets. J.Atmos. Sci.37, 2521-2534.
4. Enukashvily I.M. 1981,A numerical method for integrating the kinetic equations of droplets spectrum evolution by condensation/evaporation and by coalescence/breakup processes.Proceedings of the second International Colloquium on Drops and Bubbles.Holliday Inn,Monterey,California,U.S.A. 19-21 November.
5. Gillespie J.R. and R.List,1978,Effects of collision-induced breakup on drop size distributions in steady rainshafts.Pure Appl. Geophys.117,599--626.
6. Lushnikov A.A. and N.Piskunov, 1977,Formation of steady-state distributions in koagulating systems with disintegrating particles. Colloid.J.,39, 760-764.
7. Srivastava R.C.,1982, A simple model of particle coalescence and breakup. J. Atmos. Sci. 39,1317--1322.

A NUMERICAL METHOD FOR INTEGRATING THE COALESCENCE KINETIC EQUATIONS FOR CLOUD DROPLETS AND ICE PARTICLES.

Isaac M. YEnukashvili

Depart. for Research, Israel Meteorological Service.P.O.Box 25, Bet-Dagan, Israel.

Abstract

An extension of numerical method of moments is developed for numerical integration of coupled coalescence kinetic equations for supercooled cloud droplets number density function $n_1(x,t)$ and for ice particles number density function $n_2(x,t)$.The time evolution of $n_1(x,t)$ is considered as a result of coalescence,breakup and collisions of supercooled droplets with ice particles.The $n_2(x,t)$ varies in time t as a result of coalescence and collisions of ice particles with supercooled droplets.The method is used for numerical modelling of hail growth by stochastic collection.

1. Introduction

Coalescence and breakup of supercooled cloud droplets,coalescence of ice particles and coalescence between ice particles and supercooled cloud droplets are among the important processes governing the formation and development of ice phase in mixed clouds.In (Ref.5) a set of coupled kinetic equations for supercooled droplets number density function $n_1(x,t)$ and ice particles number density function $n_2(x,t)$ is derived and the method of moments is used to compute the first moments of $n_1(x,t)$ and $n_2(x,t)$. In Beheng's (Ref.2) numerical simulation of graupel development the numerical method of Berry (Ref.1) is used.In (Ref.4) the method of Bleck (Ref.3) is used for numerical modelling of hail growth by stochastic collection.

The approximation of the number density functions $n_1(x,t)$ and $n_2(x,t)$ between supercooled droplets and ice particles mass grid points respectively is the main problem in the numerical integrating of the set of coupled coalescence kinetic equations for $n_1(x,t)$ and $n_2(x,t)$.In Berry's approximation of number density functions (Ref.1) neither the number concentrations nor the mass of supercooled droplets and ice particles are conserved.In Bleck's method (Ref.3) it is impossible to estimate the error of the approximate numerical solution and an assumption is made that in each separate supercooled droplets and ice particles packets all droplets and ice particles respectively are spread over the whole mass intervals (x_k,x_{k+1}).This Bleck's uniform distribution hypothesis gives as a result a significant increase of the mass conversion velocity from cloud droplets to larger drops and from cloud droplets to ice particles for real coalescence kernels.

In this study numerical method of moments (Ref.6,7) is used for integrating the set of coupled kinetic equations for $n_1(x,t)$ and $n_2(x,t)$ describing supercooled droplets and ice particles spectra evolution resulting from droplet-droplet,droplet-ice particle and ice particle-ice particle coalescences and from supercooled droplets breakup as well.

2. The governing equations and computation method.

The set of coupled kinetic equations for supercooled droplets number density function $n_1(x,t)$ and for ice particles number density function $n_2(x,t)$ can be written as (Ref.2,4,5):

$$\partial n_1(x,t)/\partial t=-n_1(x,t)\left(\int_0^\infty\sigma_{11}(x,y)n_1(y,t)dy+\int_0^\infty\sigma_{12}(x,y)n_2(y,t)dy\right)+(1/2)\int_0^x\sigma_{11}(x-y,y)n_1(x-y,t)n_1(y,t)dy-P(x)n_1(x,t)+\int_x^\infty P(y)Q(y,x)n_1(y,t)dy \quad (1)$$

$$\partial n_2(x,t)/\partial t=-n_2(x,t)\left(\int_0^\infty\sigma_{22}(x,y)n_2(y,t)dy+\int_0^\infty\sigma_{21}(x,y)n_1(y,t)dy\right)+(1/2)\int_0^x\sigma_{22}(x-y,y)n_2(x-y,t)n_2(y,t)dy+\int_0^x\sigma_{21}(x-y,y)n_2(x-y,t)n_1(y,t)dy \quad (2)$$

In these equations $\sigma_{11}(x,y)$ and $\sigma_{22}(x,y)$ represent the coalescence kernel for two supercooled droplets and for two ice particles interactions respectively; $\sigma_{12}(x,y)=\sigma_{21}(x,y)$ represents the coalescence kernel for supercooled droplet and ice particle interaction. $P(x)$ is the probability that a droplet of mass x will break up during a unit time,and $Q(y,x)$-the number density function of fragment droplets of mass x formed due to breakup of a parent drop of mass y.

Unknown number density functions $n_1(x,t)$ and $n_2(x,t)$ in each droplet packets and ice particle packets respectively are represented by an expansion in orthogonal polynomials with a given weighting functions (Ref.6,7)

$$n_{1k}(z,t)=W_{1k}(z,t)\sum_{i=0}^{\infty} a_{ik}(t)G_{ik}(z) \quad (3)$$

$$n_{2k}(z,t)=W_{2k}(z,t)\sum_{i=0}^{\infty} b_{ik}(t)P_{ik}(z) \quad (4)$$

where $z=x/x_k$ represents nondimensional mass of supercooled droplets or ice particles. $W_{1k}(z,t)$ and $W_{2k}(z,t)$ are weighting functions. $G_{ik}(z)$ and $P_{ik}(z)$ are polynomials orthogonal in the range $(1,s)$, $(s=x_{k+1}/x_k)$ with weighting functions $W_{1k}(z,t)$ and $W_{2k}(z,t)$ respectively. $a_{ik}(t)$ and $b_{ik}(t)$ are expansion coefficients which describe deviations of $n_{1k}(z,t)$, $n_{2k}(z,t)$ from $W_{1k}(z,t)$ and $W_{2k}(z,t)$ respectively. Expansion coefficients $a_{ik}(t)$ and $b_{ik}(t)$ are expressed as a linear combinations of the number density functions moments.In this way droplets and ice particles number concentrations ,masses and other moments in each corresponding packets are conserved and the problem of solving the coupled kinetic equations (1)-(2) is replaced by one of solving a following set of coupled differential equations for the number density functions-$n_{1k}(z,t)$ and $n_{2k}(z,t)$ moments (Ref.6).

$$\partial M^{m}_{1k}(t)/\partial t=-\sum_{i=1}^{J} A11^{m}_{ik} - \sum_{i=1}^{J} A12^{m}_{ik} + \sum_{i=1}^{k-1} A11^{m}_{i,k-1,k} +$$

$$+\sum_{i=1}^{k-1} A11^{m}_{i,k,k} - B^{m}_{k} + \sum_{i=k}^{J} B^{m}_{i,k} \tag{5}$$

$$\partial M^{m}_{2k}(t)/\partial t=-\sum_{i=1}^{J} A22^{m}_{ik} - \sum_{i=1}^{J} A21^{m}_{ik} + \sum_{i=1}^{k-1} A22^{m}_{i,k-1,k} +$$

$$+\sum_{i=1}^{k-1} A22^{m}_{i,k,k} + \sum_{i=1}^{k-1} A21^{m}_{i,k-1,k} + \sum_{i=1}^{k-1} A21^{m}_{i,k,k} \tag{6}$$

where $M^{m}_{1k}(t)$ and $M^{m}_{2k}(t)$ represent the mth order moments of the number density functions $n_{1k}(z,t)$ and $n_{2k}(z,t)$ respectively in the packets (x_k, x_{k+1}); J-the total number of supercooled droplets or ice particles packets.

$A11^{m}_{ik}$, $A12^{m}_{ik}$, $A11^{m}_{i,k-1,k}$, $A11^{m}_{i,k,k}$, $A22^{m}_{ik}$

$A21^{m}_{ik}$, $A22^{m}_{i,k-1,k}$, $A22^{m}_{i,k,k}$, $A21^{m}_{i,k-1,k}$, $A21^{m}_{i,k,k}$

are the coalescence double integrals;

B^{m}_{k} and B^{m}_{ik} are breakup integrals(Ref.6,7).

The computations of the coalescence and breakup double integrals require the values of number density functions $n_{1k}(z,t)$ and $n_{2k}(z,t)$ in each separate droplets and ice particles packets.Therefore approximating $n_{1k}(z,t)$ and $n_{2k}(z,t)$ by means of the first L terms of the expansions (3)-(4) respectively and substituting these approximations in the coalescence and breakup double integrals,and also replacing the expansion coefficients $a_{ik}(t)$ and $b_{ik}(t)$ by means of linear combinations of number density functions moments we obtain from (5)-(6) a finite set of coupled differential equations to compute the first L moments of $n_{1k}(z,t)$ and $n_{2k}(z,t)$.

The accuracy of the approximations of $n_{1k}(z,t)$ and $n_{2k}(z,t)$ by means of the first L terms of the expansions (3)-(4) respectively depend on the choice of weighting functions as well as on the choice of droplets,ice particles mass grid points $x_{k+1}=sx_k$.The number density functions $n_1(x,t)$ and $n_2(x,t)$ in experiments are determined only for the range (x,x+dx). If dx<<x the number density functions in each range (x,x+dx) represent a piece-wise constant functions and an arbitrary moments of $n_1(x,t)$ and $n_2(x,t)$ in the range (x,x+dx) are expressed by means of the zero order moments of corresponding number density functions.For numerical integrating the kinetic equations (1)-(2) it is impossible to choose mass grid points for which $(x_{k+1}-x_k)<<x_k$.Therefore for such grid points the zero-order approximation of the expansions (3)-(4) (L=1),which corresponds to Bleck's method (Ref.3,4) will be incorrect for an arbitrary weighting functions.It should be noted that the first order approximations of the expansions (3)-(4) (L=2) describe not only the case where supercooled droplets and ice particles in the packet (x_k, x_{k+1}) are spread over the whole mass interval (x_k, x_{k+1}) but also the case where supercooled droplets and ice particles in the packet $(x_k, x_{k+1})$are located only in the part of the whole mass interval (x_k, x_{k+1}).

3. Numerical computations and concluding remarks.

The unknown number density functions $n_{1k}(z,t)$ and $n_{2k}(z,t)$ in each separate supercooled droplets packets and ice particles packets are represented by an expansions in orthogonal polynomials with a given weighting functions in the range (x_k, x_{k+1}).In this way the problem of solving the kinetic equations (1), (2) is replaced by one of solving a set of coupled differential equations for the moments of the number density functions $n_{1k}(z,t)$ and $n_{2k}(z,t)$.The convergence of the expansions (3)-(4) in terms of orthogonal polynomials with a given weighting functions in the range (1,s) ($s\leq 2$) is sufficiently rapid.For droplets and ice particles mass grid points $x_{k+1}=sx_k$ ($s\leq 2$) the approximation of $n_{1k}(z,t)$ and $n_{2k}(z,t)$ by means of the first two terms of the expansions (3)-(4) respectively is sufficiently correct.

Analytic expressions for the time derivatives of ice phase number concentrations and ice phase water contents of small and larger portions of ice particles spectrum are derived.Also analytic expressions of mass and number concentration conversion double integrals describing formation and development of larger ice particles portion of ice phase are derived.Numerical results are obtained for different coalescence/breakup kernels and for different initial droplets and ice particles spectra.Also droplets and ice particles mass grid points intervals are varied. Weighting functions and integration time steps are varied as well.Numerical experiments are carried out simulating hailstones growth by stochastic collection and simulating mass conversion from liquid supercooled droplets to larger ice particles as well.The corresponding results of numerical computations are compared with Danielsen's and Bleck's numerical modelling of hail growth by stochastic collection(Ref.4).

Acknowledgments.The author wishes to thank the colleagues from Israel Meteorological Service Research Department for valuable discussions.

4.References

1.Berry E.X. and R.Reinhardt,1974, An analysis of cloud drop growth by collection.J. Atmos.Sci.,31, 1814-1831.
2.Beheng K. D. 1978, Numerical simulation of graupel development. J. Atmos. Sci.,35,683-689.
3.Bleck R. 1970, A fast approximative method for integrating the stochastic coalescence equation. J. Geophys. Res.,75,5165-5171.
4.Danielsen E.F.,R.Bleck and D.A.Morris, 1972, Hail growth by stochastic collection in a cumulus model. J. Atmos. Sci.,29,135-155.
5.Enukashvily I.M. 1967, On the coagulation in mixed atmospheric clouds. "Cloud physics"-collection of works of the Geophysical Institute of the Georgian Science Academy, vol.25,N1, 155-162.
6.Enukashvily I.M. 1980, A numerical method for integrating the kinetic equation of coalescence and breakup of cloud droplets. J.Atmos.Sci.,37,2521--2534.
7.Enukashvily I.M. 1981, A numerical method for integrating the kinetic equations of droplets spectrum evolution by condensation/evaporation and by coalescence/breakup processes.Proceedings of the Second International Colloquium on Drops and Bubbles. Holliday Inn,Monterey, California, U. S. A. 19-21 November.

A NUMERICAL METHOD FOR INTEGRATING THE KINETIC EQUATION OF DROPLET SPECTRUM EVOLUTION BY CONDENSATION AND EVAPORATION PROCESSES.

Isaac M. YEnukashvili

Depart. for Research, Israel Meteorological Service. P.O.Box 25, Bet-Dagan, Israel.

Abstract

An extension of the method of moments is developed for the numerical integration of the equations of droplet spectrum evolution by condensation and evaporation processes. Droplet packets between nonfixed droplet mass grid points $(x_k(t), x_{k+1}(t))$ depending on time t are considered and unknown number density function $n_k(x,t)$ in each such droplet packets is represented by an expansion in orthogonal polynomials with a given weighting function. In this way the problem of solving the condensation kinetic equation is replaced by one of solving a set of coupled differential equations for the moments of the number density function $n_k(x,t)$, and the first relationship between droplet total liquid water content M(t) and between vapor supersaturation S(t) is derived. The second relationship between M(t) and S(t) can be derived in the known manner using the equations of advection phenomena and thermodynamics.

1. Introduction

There exist three maijor difficulties in numerical computation Of droplet spectrum evolution by condensation/evaporation processes (Ref. 3-5). a)The problem of distribution of condensed or evaporated water between droplet packets requires a correct approximation of droplets number density function $n_k(x,t)$ in each droplet packets. b)For correct computation of vapor supersaturation the release of latent heat of condensation/evaporation should be taken into account. c)The small relaxation time of condensation/evaporation processes requires very small time steps for numerical integrating the corresponding equations.

To surmount these difficulties in this study a separate treatment of microphysics of condensation and evaporation processes (without advection phenomena) is adopted and these processes for sufficiently small time steps is considered as a space-homogenous process. Such consideration is based on the assumption that the time step of integration is broken up into separate treatment of the dynamic tendency and of the microphysical process, (Ref.3,5).

2. The Governing Equations and Computation Method.

Differential equations describing the microphysics of droplet spectrum evolution by condensation and evaporation processes can be written as::

$$\partial n(x,t)/\partial t+\partial((dx/dt)n(x,t))/\partial x=0 \qquad (1)$$

$$dx/dt=K(S(t)x^{2/3}-Bx^{1/3}+F(c)x^{2/3})/(x^{1/3}+\xi) \qquad (2)$$

$$S(t)=(Q(t)-Q_s(t))/Q_s(t) \qquad (3)$$

$$Q(t)+M(t)=Q(0)+M(0) \qquad (4)$$

$$\rho c_p(dT(t)/dt)=L(dM(t)/dt) \qquad (5)$$

$$dQ_s(T)/dT=(Q_s(T)/T)((L/R_vT)-1) \qquad (6)$$

Eq. (1) represents condensation kinetic equation Eq. (2)- the individual droplet diffusional growth equation which includes the terms due to surface tension $(Bx^{1/3})$ and solute effects $(F(c)x^{2/3})$; S(t)-supersaturation ratio; M(t)-droplets total liquid water content; Q(t)-vapor density; $Q_s(t)$-vapor saturation density at temperature T(t); Eq. (4) represents the mass conservation equation; Eq. (5)- the first law of thermodynamics; Eq. (6) represents the Clapeyron-Clausius equation.

For t=0 $(0\leq t\leq\tau)$, where τ is time step, we have initial conditions:

$$x_k(t=0)=x_k(0);\ x(y,0)=y;\quad n(x,0)=n_0(y);$$
$$Q(t=0)=Q(0);\quad M(t=0)=M(0);\quad T(t=0)=T(0); \qquad (7)$$

Multiplying (1) by $x^m dx$ and integrating from $x_k(t)$ to $x_{k+1}(t)$ and also taking into account that $n(x,t)dx=n_0(y)dy$, we have the set of number density function moments equations:

$$dM_k^m(t)/dt=m\int_{x_k(t)}^{x_{k+1}(t)} x^{m-1}(dx/dt)n(x,t)dx=$$
$$=m\int_{x_k(0)}^{x_{k+1}(0)}(x(y,t))^{m-1}(dx(y,t)/dt)n_0(y)dy \qquad (8)$$

where

$$M_k^m(t)=\int_{x_k(t)}^{x_{k+1}(t)} x^m n(x,t)dx=\int_{x_k(0)}^{x_{k+1}(0)}(x(y,t))^m n_0(y)dy \qquad (9)$$

represents the m-order moment of the number density function inthe droplet packet with nonfixed grid points $(x_{k+1}(t),x_k(t))$, that is in the droplet packet which for t=0 is contained within grid points $(x_k(0),x_{k+1}(0))$ and for time t transfers in the droplet packet $(x_k(t),x_{k+1}(t))$ as a result of the droplets diffusional growth.

From equation (8) we have for m=0 and m=1

$$dN_k(t)/dt=0;\quad dM_k(t)/dt=\int_{x_k(0)}^{x_{k+1}(0)}(dx(y,t)/dt)n_0(y)dy \qquad (10)$$

where $N_k(t)=M_k^0(t)$ and $M_k(t)=M_k^1(t)$ represent the number concentration and liquid water content respectively in the droplet packet $(x_k(t),x_{k+1}(t))$. Using

(10) we have for the droplets total liquid water content

$$dM(t)/dt = \sum_{k=1}^{J} \int_{x_k(0)}^{x_{k+1}(0)} (dx(y,t)/dt)\, n_0(y)\, dy \qquad (11)$$

where J-total number of droplet packets.

Picard's method of succesive approximations is used for the integration of differential equation (2) with initial condition for t=0 x=y. For sufficiently small time steps τ ($0 \leqslant t \leqslant \tau$) it is assumed that the droplet individual growth rate in the (j+1)th approximation is determined by the droplet mass in jth approximation. Substituting (2) in (11) and approximating $n_0(y)$ by means of the first two moments $N_k(0)$ and $M_k(0)$ (Ref.1,2) we obtain the first relationship between total liquid water content of droplets and between water vapor supersaturation:

$$dM^{(j)}(t)/dt = S^{(j)}(t)\Phi^{(j-1)}(t) + \Psi^{(j-1)}(t) \qquad (12)$$

where

$$\Phi^{(j-1)}(t) = K\sum_{k=1}^{J} \int_{x_k(0)}^{x_{k+1}(0)} ((x^{(j-1)}(y,t))^{2/3}\, n_0(y)\, dy)/ ((x^{(j-1)}(y,t))^{1/3} + \xi) \qquad (13)$$

$$\Psi^{(j-1)}(t) = K\sum_{k=1}^{J} \int_{x_k(0)}^{x_{k+1}(0)} n_0(y)\, dy((-B(x^{(j-1)}(y,t))^{1/3} + F(c)(x^{(j-1)}(y,t))^{2/3})/((x^{(j-1)}(y,t))^{1/3} + \xi)) \qquad (14)$$

are condensation/evaporation integrals (Ref.1,2).

The second relationship between $M^{(j)}(t)$ and $S^{(j)}(t)$ can be derived using equations (3)-(6) and expanding $Q_s(t)$ in Tailor's series; for smalltime steps, for which $(T(t)-T(0)) \ll T(0)$ we have:

$$S^{(j)}(t) = (Q(0)+M(0)-M^{(j)}(t))/(Q_s(T(0))+F(M^{(j)}(t)-M(0)))-1 \qquad (15)$$

where

$$F = ((LQ_s(T(0)))/\rho c_p T(0))((L/R_v T(0))-1)$$

and L-the latent heat of water vaporization.

Note that according to (10) number concentration $N_k(t)$ in the droplet packets with nonfixed grid points $(x_k(t), x_{k+1}(t))$ is constant and for initial monodisperse droplet spectrum $M(t)=N(0)x(t)$, where N(0) represents the total number concentration of droplets. Therefore for initial monodisperse droplet spectrum and for the case B=0 and F(c)=0 in eq.(2) there exist analytic solution of the set of eq.(2), (11), (15) which may be used for the test of the numerical method developed in this study.

3. Numerical Computations and Concluding Remarks.

The unknown number density function $n_k(x,t)$ in each separate droplet packet with nonfixed grid points is represented by an expansion in orthogonal polynomials with a given weighting function in the range $(x_k(t), x_{k+1}(t))$. In this way the problem of solving the condensation kinetic equation is replaced by one of solving a set of coupled differential equations for the moments of the number density function $n_k(x,t)$ and the first relationship between droplets total liquid water content M(t) and vapor supersaturation S(t) is obtained.

Numerical results are obtained for different individual droplet diffusional growth rate and for different initial droplets spectrum. Also droplet mass grid points intervals, weighting functions and integration time steps are varied.

The results of numerical computations of droplet spectrum evolution by condensation/evaporation processes indicate that the convergence of the Picard's method of the succesive approximations for equation (2) for small time steps is sufficiently rapid. It is shown that a simultaneous using of the Picard's method and of the method of moments gives reasonable results which for the initial monodisperse droplets spectrum and for the case B=0 and F(c)=0 in eq. (2) are very close to the existing analytic solution.

At the current stage the logical extension of numerical method developed in this study is to use this method for numerical integrating the equations describing droplets condensation/evaporation and ice particles sublimation/evaporation processes in mixed clouds.

Acknowledgments. The author wishes tu thank the colleagues from Israel Meteorological Service Research Department for valuable discussions.

4. References

1. Enukashvily I.M. 1980, A numerical method for integrating the kinetic equation of coalescence and breakup of cloud droplets, J.Atmos. Sci. 37, 2521-2534.
2. Enukashvily I.M. 1981, A numerical method for integrating the kinetic equations of droplet spectrum evolution by condensation/evaporation and by coalescence/breakup processes, Proceedings of the second International Colloquium on Drops and Bubbles, Holliday Inn, Monterey, California, U.S. 19-21 November.
3. Hall W.D. 1980, Adetailed microphysical model within a two-dimensional dynamic framework: model description and preliminary results, J. Atmos. Sci., 37, 2486-2507.
4. Pruppacher H.R. and I.D. Klett, 1978, Microphysics of clouds and precipitation, D. Reidel.
5. Soong S.T. 1974, Numerical simulation of warm rain development in an axisymmetric cloud model, J. Atmos.Sci., 31, 1962-1985.

SESSION II

MICROPHYSICAL PROCESSES IN CLOUDS AND PRECIPITATION

Subsession II-5

Hydrometeors
(raindrops, snow crystals, hailstones)

FROZEN DROP EMBRYOS IN ALBERTA HAILSORMS AND THEIR ORIGINS

Marianne English, Lawrence Cheng
Atmospheric Sciences Department
Alberta Research Council
Edmonton, Alberta, Canada

and

Nancy C. Knight
National Center for Atmospheric Research
Boulder, Colorado, U.S.A.

1. INTRODUCTION

Numerous hailstone samples have been collected from a number of severe hailstorms to obtain supporting evidence for hypotheses, derived from aircraft and radar data, concerning the origin of hail embryos in Alberta storms.

Some of the hail samples have been time-resolved having been collected with mobile vehicles especially equipped for hail sampling. In 1979, one vehicle was available for hail sampling. Two vehicles were made available in 1980 for hail sampling and, since 1981, three sampling vehicles have been in use. To augment the samples collected with the mobile vehicles, a network of volunteers was established who were instructed to collect time-integrated hail samples whenever it hailed on their property. In this manner, hail samples were collected at 5 to 35 different locations from a number of severe hailstorms. Some of these hailstones have been sectioned for embryo analysis. The hailstones collected in 1979 were photographed, measured and sectioned at NCAR (see Ref. 1 for details of the technique). Those collected since 1980 have been photographed and sectioned at the University of Alberta in Edmonton using very similar techniques.

The conceptual hailstorm model believed applicable to Alberta Storms is described in Section 2 of this paper. Section 3 presents the available data on hail embryo type in Alberta hailstorms and patterns in hail embryo type are discussed in Section 4. A discussion of the results obtained to date is presented in Section 5.

2. THE CONCEPTUAL HAILSTORM MODEL

Figure 1 represents a conceptual model of the precipitation processes leading to the formation of hail within a severe Alberta hailstorm. The dominant hail formation mechanism involves graupel particles which are grown within feeder clouds and then transported by the wind into the main storm where they grow to hailstones along the edges of the main updraft. (This concept is consistent with Ref. 2.) For storms where a relatively long time (~15 min as opposed to ~5 min) elapses between the initiation of graupel in the feeder clouds and the merger of the feeder clouds with the main storm, the graupel particles in the feeder clouds may have time to descend to the melting level. In such cases, frozen drop embryos may be found in hailstones collected at the ground, the frozen drop embryos being due to melted graupel (Ref. 3).

3. FROZEN DROP EMBRYOS IN ALBERTA STORMS

Knight (Ref. 1) analyzed numerous hailstones from a number of hail days in Alberta for embryo type and determined that, overall, 74% of the embryos were graupel. Furthermore, she determined that hailstorms in regions with warm cloud bases tend to produce more drop embryos than hailstorms in regions with cold cloud bases. In the present analysis, hailstones are analyzed on a storm by storm basis.

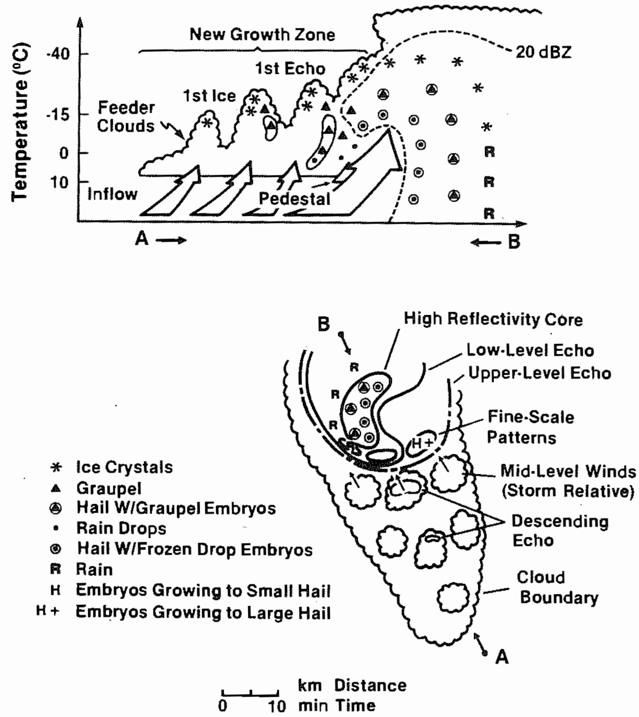

Figure 1. A conceptual model of the precipitation processes leading to the formation of hail within severe alberta hailstorms (from Ref. 3 and 5).

The average percentages of drop embryos found in the storms analyzed are shown in Table 1. Also shown in Table 1 are the number of samples, the total number of hailstones analyzed, and the cloud base temperature for each storm. (In the present analysis, time variations have been ignored and all samples collected at one location have been combined. The number of samples, therefore, is actually the number of locations at which samples were collected.) It is apparent that the percentage of drop embryos varies widely from storm to storm, the values shown in Table 1 varying from 0 to 58%. Furthermore, no obvious relationship with cloud base temperature is apparent.

4. PATTERNS IN EMBRYO TYPE

Knight and English (Ref. 4) analyzed hailstone embryos from the storms of 7 and 21 July 1979 and concluded that the percentage of drop embryos, as well as the hailstone sizes, were highest at the southern edges of the hailswaths. (In Alberta, most hailstorms travel from west to east with the southern edge of the storm being the upwind edge.) Furthermore, they hypothesized that if feeder clouds were the primary source of embryos for the storms, then embryos would be introduced mostly into the upwind edge of the updraft and the drop

Table 1
Proportion of Frozen Drop Embryos in Alberta Storms

Storm Date	Cloud Base[5] Temperature °C	Number of Samples	N_{TA}[1]	$\frac{N_{SA}}{N_{TA}}$[2]	$\frac{\bar{N}_S}{N_T}$[3]	Echoing[4] Feeder Clouds
7 July '79	10	7	363	28	42	y
21 July '79	11	28	467	58	58	y
16 July '80	8	14	218	0	0	y
23 July '80	10	35	461	2	3	n
26 July '80	6	25	364	2	1	y
27 July '80	8	26	907	1	1	n
2 August '80	12	17	358	15	16	n
30 June '82	6	9	242	20	19	y

1 N_{TA} is the total number of hailstones analyzed
2 N_{SA}/N_{TA} is the ratio of the total number of hailstones with drop embryos to the total number of hailstones analyzed
3 $(\bar{N}_S/N_T)$ is the average percentage of drop embryos in a sample
4 y indicates that the storm had echoing feeder clouds in the vicinity of the melting level
n indicates that the storm had no echoing feeder clouds in the vicinity of the melting level
5 cloud base temperatures were determined from aircraft observations or from surface temperature and dew point temperature observations; they are expected to be accurate to $\pm$ 1°C

embryos would be initially bigger/heavier and lower than the graupel embryos. Under such conditions the calculations of English (Ref. 2) suggest that drop embryos and large hail would predominate closest to the updraft, i.e. at the southern edge of the swaths and drop embryos should be found primarily in the largest hailstones.

Krauss (Ref. 3 and 5) examined radar data from the storms of 7 and 21 July 1979. He found that many of the feeder clouds produced echoes before merging with the main storm. Echoes often formed above the -10°C level, but due to the time and distance before merging with the main storm, most of the echoes were able to descend to below the melting level. Occassionally, such echoes were seen to rise when they approached the strong updrafts of the main storm, suggesting that melted graupel particles from the feeder clouds were being entrained into the main storms.

For these reasons, data from the storms listed in Table 1 were examined for evidence of spatial, size and radar echo patterns.

4.1 Spatial Patterns

It is apparent from Table 1 that only the storms of 7 July 1979, 21 July 1979, 2 August 1980 and 30 June 1982 produced significant numbers of frozen drop embryos. In all four storms, the same kind of embryo pattern is apparent, i.e. there is a tendency for more drop embryos to be found close to the southern edge of the hailswaths. As well, the biggest hailstones are found in the same location.

The change in embryo type is often quite marked even over small distances like a few kilometers, suggesting that the observed embryo type will be very strongly dependent upon the locatin of the sample. This may be a reason for the lack of a relationship between the average percentage of frozen drop embryos and cloud base temperature in the data of Table 1.

4.2 Embryo Type as a Function of Hailstone Size

Percentages of drop embryos and of graupel embryos have been plotted as a function of hailstone size for each of the four storms that exhibited significant numbers of frozen drop embryos. For hailstones collected from the storm of 2 August 1980, the percentages of frozen drop and graupel embryos seem to be more or less constant with size. In the other three storms (7 and 21 July 1979 and 30 June 1982) a marked tendency for greater numbers of frozen drop embryos with larger hailstone size is evident. Thus the hailstone size/embryo type pattern seen in the storms of 7 July 1979, 21 July 1979 and 30 June 1982 is consistent with the hypothesis that frozen drop embryos result from melted graupel in the feeder clouds. The pattern seen in the storm of 2 August 1980 does not seem to be cnsistent with the melted graupel from feeder clouds hypothesis.

4.3 Radar Echo Patterns

Because of the results of Krauss (Ref. 3 and 5), it seems reasonable to expect that feeder clouds, in which significant numbers of graupel particles descend to below the melting level, would produce a radar echo in the vicinity of the melting level. For this reason, radar data from the storms listed in Table 1 have been examined for evidence of echoing feeder clouds in the vicinity of the melting level. The results are indicated in Table 1. Of the four storms which produced significant numbers of frozen drop embryos only the storm of 2 August 1980 did not have echoing feeder clouds.

Five of the storms listed in Table 1 had echoing feeder clouds; only three of the five produced significant numbers of frozen drop embryos. The two storms that did not seem to produce significant numbers of drop embryos were those of 16 July 1980 and 26 July 1980. In both of these storms, hail sampling occurred only during two short, well separated periods and only a few of the sampling locations were at the southern edge of the hailswaths. Thus the embryo type data for these two storms may not be representative of the whole storms. Furthermore, a few of the storms which had echoing feeder clouds did not have such feeder clouds throughout their lifetime. Thus a closer coordination is required between the radar data and the hail samples before any conclusions can be drawn about these two storms.

5. CONCLUSIONS

From 7 to 35 samples, that is from 218 to 907 hailstones per storm have been analyzed for hail embryo type, samples having been collected from 8 Alberta storms. The results suggest that the percentage of frozen drop embryos varies considerably from storm to storm, values from 0 to 58% having been found in the storms analyzed here. In most storms, graupel embryos predominate. Within a storm, the percentage of drop embryos can vary markedly with sample location, so that it may be difficult to obtain a representative value for a storm.

Four of the 8 storms studied produced significant numbers of frozen drop embryos. For these 4 storms, patterns in embryo type, hailstone size and radar echo structure have been investigated. For three of the four storms, the patterns found are consistent with the hypothesis that the frozen drop embryos originated as melted graupel in feeder clouds. The hailstone size/embryo type pattern and the radar echo structure of the 4th storm, that of 2 August 1980, do not seem to be consistent with this hypothesis. In fact, these patterns seem to be consistent with the hypothesis that the frozen drops originated through coalescence in the main updraft (Ref. 6). The very warm cloud base temperature of this storm lends credance to the coalescence hypothesis as does also the evidence of a coalescence process operating in cumulus clouds in Yellowknife, N.W.T. (Ref. 7).

In conclusion then, the evidence suggests that many of the frozen drop embryos originate as melted graupel which has been entrained into the main storm from feeder clouds. However, it appears likely that in storms with particularly warm bases, significant numbers of embryos arise through a warm rain process.

6. ACKNOWLEDGMENTS

The authors are grateful to all the staff of the Alberta Research Council and the voluntes who participated in the sample collection. Profs. E. Lozowski and R. Charlton have been very helpful in sectioning the hailstones at the University of Alberta. Mr. B. Kochtubajda, Ms. B. Henderson, Ms. K. Finstad and Mr. Z. Miztal assisted with the data reduction. This research is funded by Alberta Agriculture and the Alberta Research Council. Mrs Knight's participation in the project was funded by the National Center for Atmospheric Research.

7. REFERENCES

1. Knight, N.C. 1981: The climatology of hailstone embryos. J. Appl. Meteor., 20, 750-755.

2. English, M., 1973: Alberta hailstorms, Part II: Growth of large hail in the storm. Meteor. Monogr., 14 (36), 37-98.

3. Krauss, T.W., 1981: The origin of drop hail embryos in an Alberta hailstorm. Preprints, 8th Conf. on Weather Modification, Amer. Meteor. Soc., Boston, Mass., 130-131.

4. Knight, N.C. and M. English, 1980: Patterns of hail embryo type in Alberta storms. J. Rech. Atmos., 14, 325-332.

5. Krauss, T.W., 1981: Precipitation processes in the new growth zone of Alberta hailstorms. Ph.D. thesis, University of Wyoming, Laramie, Wyo. 296 pp.

6. English, M., L. Cheng and N.C. Knight, 1982: Hail embryo type in Alberta storms. Preprints, 12th Conference on Severe Local Storms, Amer. Meteor. Soc., Boston, Mass. 9-12.

7. Isaac, G.A. and R.S. Schemenauer, 1979: Large particles in supercooled regions of Northern Canadian cumulus clouds. J. Appl. Meteor., 18, 1056-1065.

A MICROPHYSICAL ORIGIN OF GRAUPEL AND HAIL

N. Fukuta, N.-H. Gong* and A.-S. Wang**

Department of Meteorology, University of Utah
Salt Lake City, Utah 84112, U.S.A.

1. INTRODUCTION

In the atmosphers, ice crystals grow while falling. The falling constantly brings fresh environment to the crystal surface and causes a feed-back effect changing the rate and the mode of growth and subsequently the fall behavior. The ice crystal growth in natural environments is therefore difficult to estimate from that measured in static environments nor can it be evaluated by the growth data under unnatural or artificial draft. Our ice crystal growth study under free fall in supercooled fog started for this reason (Ref. 1) although the time for the growth was less than 1 min. The study allowed the crystal growth parameters to be combined with a single variable, i.e., time, under the given environmental condition. The growth time under free fall was extended to about 3 min by Ryan et al (Refs 2,3) Michaeli and Gallily (Ref. 4) and Fukuta et al (Ref. 5).

Recognizing the importance of ice crystal growth under free fall, we applied the wind tunnel technique to the problem using supercooled fog, first without specific stabilization mechanism for suspended crystals other than a simple honeycomb (Ref. 5). However, the study revealed formation of fast falling ice crystals at -10°C and its possible consequence of growing into graupel and hail embryos was speculated (Refs 6,7). To confirm the fate of ice crystals growing at -10°C and other temperatures, applying the previous experience and giving careful thought, we developed a vertical supercooled cloud tunnel (Refs 8,9). It has a number of new supporting mechanisms and extended the growth period drastically, as much as 30 min under some conditions. Details of the supercooled cloud tunnel and its operation have been reported (Refs 8,9). Fig. 1 shows the latest version of the tunnel which has further improvements on the fog by-pass mechanism and honeycomb design.

In this paper, we shall report results of measurements recently carried out using the supercooled cloud tunnel, and discuss the difference in growth mode switch over from the vapor diffusion to riming of graupel and hail type under different temperatures in comparison with the result of center crystal analysis obtained with natural graupel.

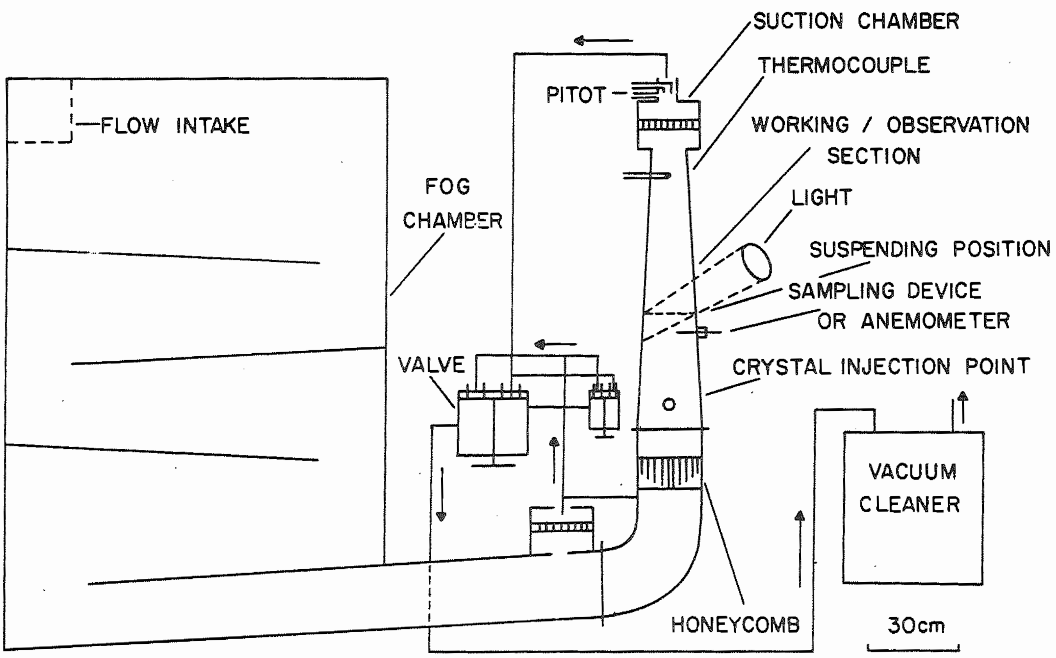

Figure 1. The new vertical, supercooled cloud tunnel.

* On leave from Lanzhou Institute of Plateau Atmospheric physics, Academia Sinica, Lanzhou, The People's Republic of China

** On leave from Institute of Atmospheric Physics, Academia Sinica, Beijing, The People's Republic of China

2. BEHAVIORS OF ICE CRYSTALS GROWING UNDER FREE FALL

The present supercooled cloud tunnel (see Fig. 1) has the following modifications since last report

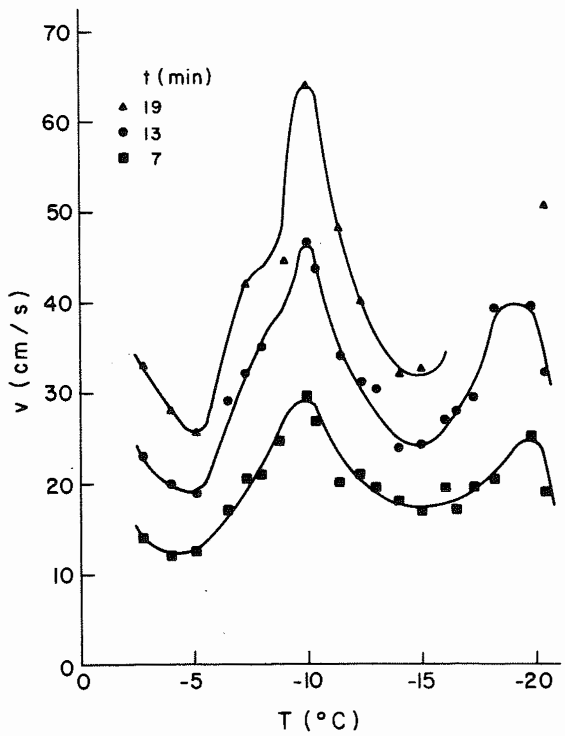

Figure 5. Ice crystal fall velocity v plotted as a function of temperature T at different growth time t.

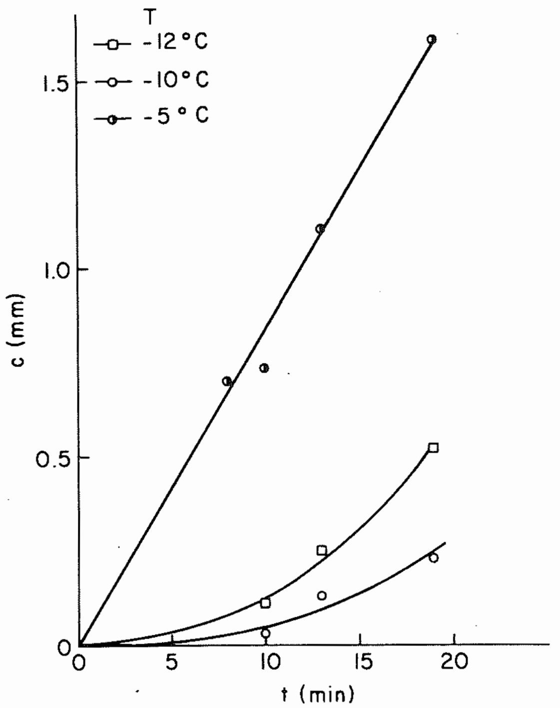

Figure 7. The ice crystal height c plotted as a function of growth time t at different temperature T.

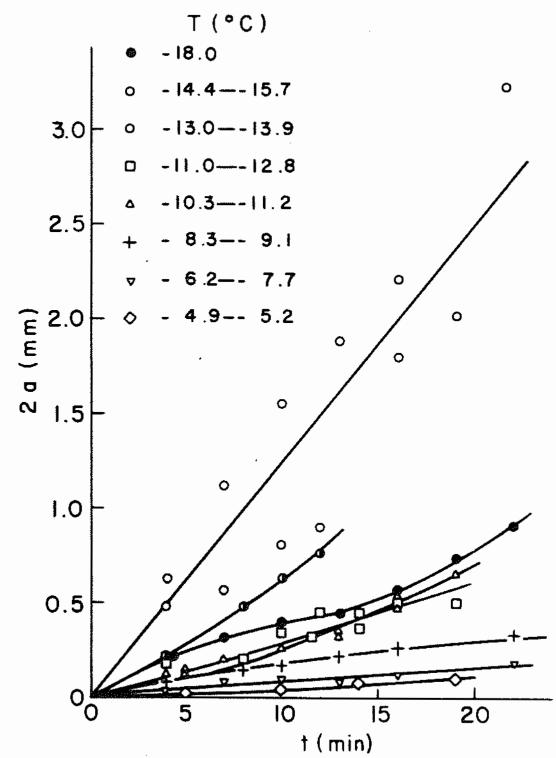

Figure 6. The ice crystal diameter 2a plotted as a function of growth time t at different temperature T.

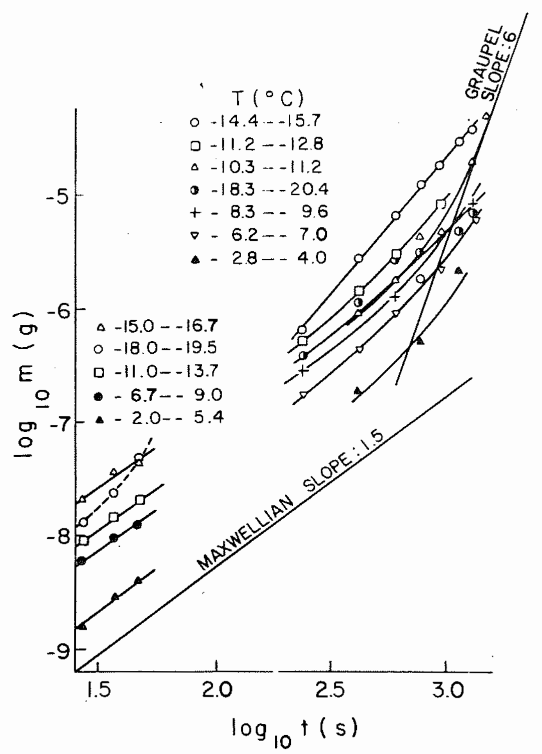

Figure 8. Ice crystal mass m plotted as a function of growth time t at different temperature T.

min of growth. However, after the period, the growth rate begins to deviate for all temperatures from the Maxwellian slope, showing additional effects such as ventilation and riming. The most remarkable is the behavior of -10°C crystals. As we have predicted (Ref. 6), the present data, though limited in number, seem to approach slope of 6 for graupel process.

(Ref. 9). The fog bypass mechanism was moved to a position close to the honeycomb so that fog free zone development under the honeycomb is avoided at the beginning of operation. The honeycomb made of plastic straws has now proportionally longer air path toward the middle to increase the resistance to the fog flow and secures the updraft profile gently concave upward. The liquid water content is now determined by the dew point hygrometer mechod. Fig. 2 shows an example of data recording during measurement. Fig. 3 shows photographs of ice crystals grown in the tunnel. The liquid water content varies from

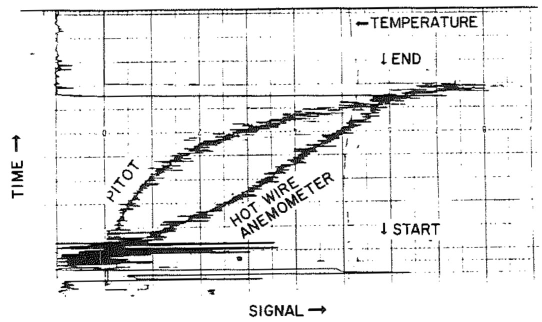

Figure 2. An example of temperature and air velocity recording in the supercooled cloud tunnel.

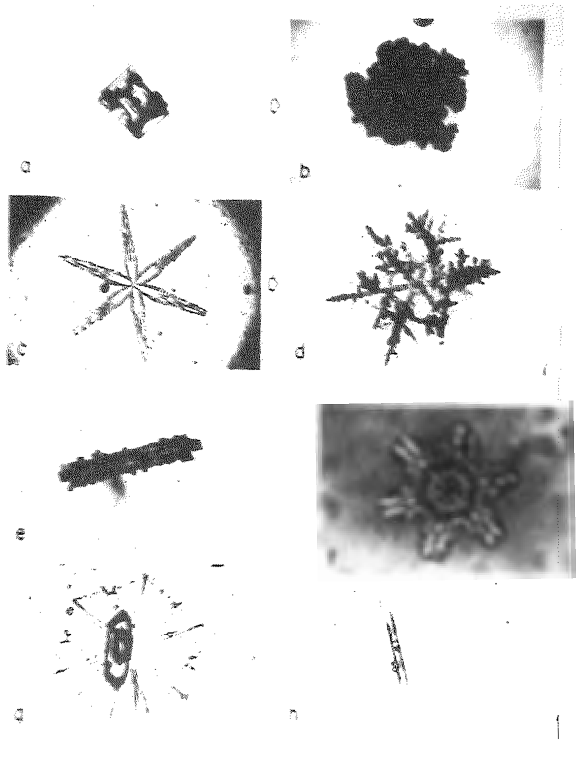

Figure 3. Ice crystals grown in the supercooled cloud tunnel. a: -9.5°C, 10 min growth, 0.14 mm long, b: -10.6°C, 25 min, 1.05 mm, c: -14°C, 7 min, 1.12 mm dia., e: -6.5°C, 16 min, 0.63 mm long, f: -13.0°C, 10 min, 0.63 mm, g: -12.1°C, 10 min, 0.66 mm, h: -11.2°C, 8 min, 0.47 mm.

0.4 gm^{-3} at 0°C to 1.5 gm^{-3} at -24°C.

The observed habit variation with temperature is in agreement with previous works (Refs 5,8,9); columns at temperatures between -4.5 and -7.0°C (Fig. 3e), isometric crystals at around -10°C (Fig. 3a), vaned and double plates between -10 and -12°C (Fig. 3, f, g, h), dendrites between -13 and -16°C (Fig. 3, c, d) and complex crystals below -18°C. The isometric crystals growing at -10°C have tendency to develop appendages and become graupel (Fig. 3, a,b). Whereas, ice crystals growing at around -15°C continue to develop dendritic structures (Fig. 3, c,d). The double plates which are often observed shortly after nucleation tend to become single plates because the upper plate is starved due to moisture extraction by the lower while falling. Fig. 3h indicates the effect.

2.1. The Fall Velocity

The fall velocity of ice crystals growing under free fall, as we pointed out earlier (Ref. 6), is of particular interest to understand the change of the growth mode. In the supercooled cloud tunnel, it is continuously monitored and measured through the updraft speed to suspend the crystal. Fig. 4 shows the

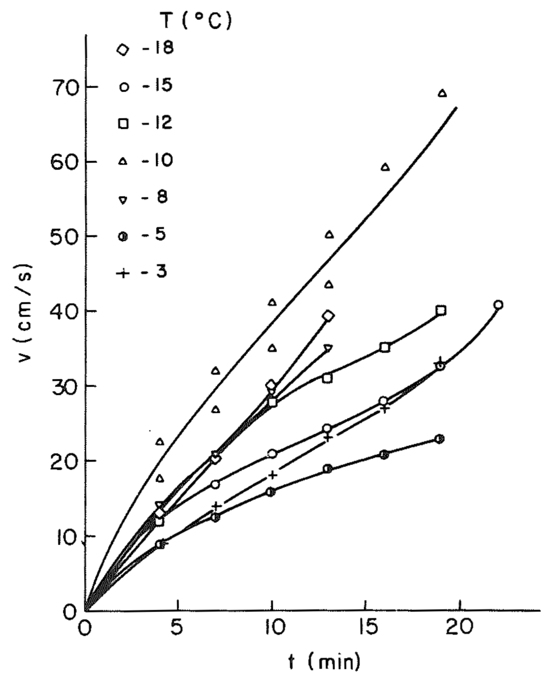

Figure 4. The ice crystal fall velocity v plotted as a function of growth time t at different temperature T.

fall velocity change with time at different temperature. As is evident in the figure, the fall velocity at -10°C, which was already the fastest after 3 min of growth (Ref. 5), continues to increase. Fig. 5 shows the fall velocity plotted as a function of temperature at different growth time. The general trend observed for shorter growth times, still continues with a maximum at -10°C and two minima at around -5 and -15°C.

2.2. The Mass and Crystal Dimensions

Figs. 6 and 7 show increase of the crystal dimensions with time, where 2a is the diameter and c the height. The maxima of each dimensions increase linearly with time. Fig. 8 shows the measured mass of crystal as a function of time in log-log plot at different temperature. From the figure, it is clear that the Maxwellian slope of 1.5 is sutained for initial 2-3

3. CENTER CRYSTALS OF NATURAL GRAUPEL

To check the natural occurrence of the fastest growth mode switchover, we collected graupel from 3 storms during the spring of 1983 in Salt Lake City; noon on March 23, midnight on April 2-3, and 5:50 pm on April 25. Graupel were preserved in silicone oil DC330 in a deep freezer. 250 graupel of average size 4 - 5 mm were carefully crushed and examined under the microscope in the silicone oil. Most of them did not contain ice crystals of recognizable size. However, 9 of them had ice crystals with size ranging from 0.5 - 2.0 mm. Classification of the crystals is as follows:

SHAPE OF CRYSTAL	NUMBER OF CASES
Plate	1
Column	3
Dendrite	1
Prism	1
Complex	3

Columns are obviously most common.

4. A MICROPHYSICAL ORIGIN OF GRAUPEL AND HAIL

As we have seen in Fig. 8 and discussed in our previous study (Ref. 6), the growth mode switchover from the diffusional growth where $m \propto t^{1/2}$ to the riming growth of spherical particles where $m \propto t^6$ happens in the shortest period of time with dense isometric crystals growing at -10°C. It is now believed to be due to the habit change between cloumn and plate (dendrite) occurring at that temperature which helps develop the fastest fall velocity due to aerodynamically small drag and large gravitational pull. Since $v \propto r^{1/2}$, where r is the radius, for graupel and hail, $m \propto v^6$. It is for this reason, the earliest graupel development is expexted with -10°C crystals.

For graupel development, a large effective fall distance is required which is found normally only in convective clouds. When a convective cloud develops strongly in isolation or without graupel feeding mechanism form preexisting clouds, -10°C is the zone where ice nucleation begins to provide a sufficient number of ice crystals for later graupel and hail development. The ice crystals nucleated at around -10°C have a longer growth time in the updraft compared with those nucleated at lower temperatures, and when they fall back to the undisturbed cloud updraft, they enjoy fast growth under high liquid water content, W_L. The high W_L again gives a strong advantage in the mass growth : $m \propto W_L^6$ (Ref. 6).

Although crystals nucleated at around -15°C are more numerous, they initially grow into plates and dendrites. Unless their dendritic growth of side stretching is overcome by riming growth to thicken, they are not likely to go into graupel growth. Whereas, crystals nucleated at temperatures warmer than -10°C can grow into graupel relatively easily but their number may not be significantly high due to low ice nucleation rate. There is a reason to believe that graupel and hail do not grow on weak crystals such as thin dendrites and snowflakes. The uneven aerodynamic drag which is common for large falling bodies may destroy such structures.

Cloud droplet coalescence followed by freezing does not provide a faster formation of graupel and hail compared with the -10°C ice crystal mechanism. Droplet growth rate is proportional to the supersaturation and in clouds the supersaturation is at the most 1%, normally much less. Whereas, ice supersaturation vailable for crystal growth at -10°C is about 10%, and since the crystal grown at that temperature is nearly spherical, the riming rate is considered to be as fast as the coalescence rate of a drop of equivalent size.

Thus, ice crystals grown at -10°C possess a microphysical advantage of further growing into graupel and hail. If, however, the ice nucleation at that level were insufficient, other graupel mechanisms may come into play. If the -10°C advantage were real for graupel and subsequent hail development, one may apply it for hail control jamming the route artificially although the dynamic motion of convective clouds, horizontal direction in particular, has to be properly utilized (Ref. 7). Although the above discussions are largely speculative, it is clear that the behavior of ice crystals at -10°C in supercooled convective clouds deserves special attention.

Acknowledgments. This work was supported by the Division of Atmospheric Sciences, National Science Foundation under Grant ATM-8106792 and by the Environmental Research Laboratories of the National Oceanic and Atmospheric Administration under Senior Academician Program (N.F.).

4. REFERENCES

1. Fukuta N 1969, Experimental studies on the growth of small ice crystals, *J Atmos Sci*, 26, 522 - 531.
2. Ryan B F et al 1974, The densities and growth rates of ice crystals between -5C and -9C, *J Atmos Sci*, 31, 2136 - 2141.
3. Ryan B F et al 1976, The growth rates and densities of ice crystals between -3°C and -21°C, *J Atmos Sci*, 33, 842 - 850.
4. Michaeli G & Gallily I 1976, Growth rates of freely falling ice crystals, *Nature*, 259, 110.
5. Fukuta N et al 1979, Laboratory studies of organic ice nuclei smoke under simulated seeding conditions: Ice crystal growth, *Final Rep to NSF* under Grant No. EMV77-15346, January 1979.
6. Fukuta N 1980, Development of fast falling ice crystals in clouds at -10°C and its consuquence in ice phase processes. *Preprints, 8th Internat Conf Cloud Phys*, Clermont-Ferrand 15 - 25 July 1980, 97 - 100.
7. Fukuta N 1981, "Side-Skim Seeding" for convective cloud modification, *J Weather Mod,* 13, 188 - 192.
8. Kowa M W 1981, Determination of ice crystal growth parameters in a supercooled cloud tunnel, *M.S. Thesis*, Univ of Utah, 1981.
9. Fukuta N et al 1982, Experimental and theoretical studies of ice crystal habit development, *Preprints, Conf on Cloud Phys,* Chicago 15 - 17 November 1982, 325 - 328.

Numerical Modelling of Hail to Rain Conversion

Paul Joe[1] and Roland List
Dept. of Physics, University of Toronto,
Toronto, Ont., Canada

1. INTRODUCTION

The shedding of millimeter sized drops during the wet growth of hailstones has been observed in laboratory experiments. Carras and Macklin (Ref. 4) studying the growth rate of hailstones recognized the loss of accreted water by the shedding of drops of about 1 mm in diameter. The major observation of icing experiments, closely simulating natural conditions, including hailstone aerodynamics and pressure effects, was that the net collection efficiency was less than unity because of shedding (Ref. 11, 12, 13, 21). The first quantitative experiments to measure the shed drop spectrum were performed on rotating cylinders at laboratory pressures (Ref. 9, 10).

Incomplete freezng of accreted water occurs because the heat transfer due to evaporation and convective cooling is less than the latent heat of fusion that is released during freezing. This results in the formation of spongy ice, in which the unfrozen water is incorporated into the ice matrix. However, the excess water may form a water skin which can disrupt and shed.

The object of this paper is to examine the significance of this process to the atmosphere via a numerical model. How does shedding affect hailgrowth? Does the shedding process produce enough millimeter sized droplets under atmospheric conditions? Can rain sized drops found in hailstorms be explained? The idea behind the model is not to simulate a case study but to investigate the possible roles that shedding may play in a hail cloud.

This is the first model to use measured collection efficiencies and measured shed drop size distributions. Orville and Kopp (Ref. 18) included shedding in their model by calculating the heat transfer from a hailstone and shedding the water component of the spongy ice and creating rain-sized drops.

2. THE SHED DROP SPECTRUM

Quantitative observations of the shed drop spectrum have been made from the icing of rotating cylinders (Ref. 9, 10) with an initial diameter of 2 cm. The experiments were conducted at the University of Toronto, in a closed circuit icing tunnel with a total length of 3.4m. The tunnel has a vertical measuring section 0.48m high and a 0.15m by 0.15m cross-section. The tunnel was contained in a 3.8m high cold room with horizontal dimensions of 7.4m by 2.7m. Deionized water was injected via an air atomizing nozzle positioned 1.8m below the measuring section. The mean volume diameter of the impinging drops was approximately 75 microns. The conditions of the experiments were:

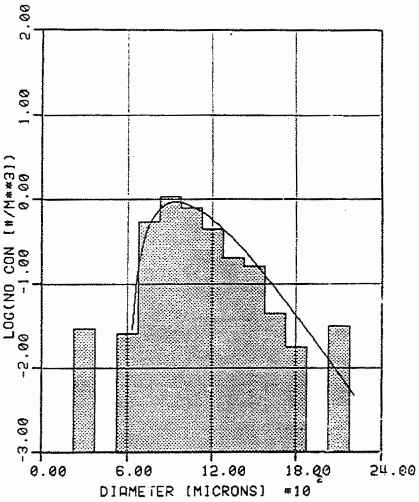

Figure 1: Number concentration of shed drops from a typical shedding experiment. The conditions were: initial size was 2 cm, temperature was -7C, liquid water content was 6.4 g/m**3 and the rotation rate was 1.4 Hz. The solid line is a curve fit by equation 1.

1. The temperature varied from 0 to -20 C.
2. The liquid water content (LWC) varied from 0.5 to 20.0 g/m**3. Shedding occurred at all liquid water contents depending on the temperature.
3. The relative air velocity was 22 m/s.
4. The rotation rates varied from 0 to 25 Hz.

The shed drop distributions were measured, 0.237 m downstream in the wake of the cylinder, using a two-dimensional grey-scale optical array spectrometer. Figure 1 shows a typical spectrum from an shedding experiment. Also drawn is a curve fit to the data. The main conclusions from these experiments were:

1. Shedding occurs at conditions that may be expected in a hail cloud.
2. Cloud droplets are instantaneously converted to rain-sized drops.
3. The shed drop sizes ranged from 0.5 mm to 2 mm with the mode size being 1140 microns in the mass distribution.
4. The shape of the spectrum may be described by a Gamma function of the form:

$$n(d)\,dd = n0 \exp(-(d-d0)/a)\,(d-d0)^{p-1}\,dd \quad (1)$$

where n(d) dd is the number concentration of drops in the range d to d + dd
d0 = 604 microns
a = 140.51 microns
p = 3.40
n0 is a constant determined by the shedding rate

[1] Present affiliation: Visiting fellow with the Cloud Physics group, Atmospheric Environment Service.

5. The net collection efficiency, Enet, defined as the "ratio of the net growth rate, as represented by the difference between the accretion of droplets and any loss by shedding and bouncing or similar mechanism, and the total droplet mass flux in the swept out air volume", (Ref. 12) and conversely the shedding rate (1-Enet) is given by:

$$Enet = \sum_{i=0}^{2}\sum_{j=0}^{2} Aij \times T^{**}i \times Wf^{**}j \qquad (2)$$

A00=0.4141
A01=-0.04556
A02=0.001184
A10=0.05617
A11=0.0008018
A12=0
A20=-0.0009143
A21=0
A22=0

where T is in degrees Celsius and Wf is in grams per cubic meter.

3. THE MODEL

While the experiments were carried out with rotating cylinders, the assumption was made that the basic results can be applied to growing hailstones. This has been a traditional approach (Ref. 16), the results exhibit similar trends (Ref. 21) and are totally adequate for this model. A one-dimensional steady-state microphysical model was formulated.

The dynamics are determined by the steady-state continuity equation with a height dependent air density. The updraft velocity is inversely proportional to the air density. That is:

$$\rho_a \, Vz = \text{constant} \qquad (3)$$

where ρ_a is the air density
and Vz is the updraft velocity

The environmental temperature is derived from 18 soundings in the Denver area (Ref. 1) and are not unlike those recorded during the National Hail Research Experiment (Ref. 22). The temperature is given by:

$$Tenv = 53 \ln (2.84 P) \qquad (4)$$

where the temperature (Tenv) is in degrees Kelvin and the pressure (P) in kilopascals.

The lifting condensation level (LCL) is taken as the cloud base and occurs at 3.5 km, with a pressure of 67.08 kPa, cloud base temperature of 5C and a mixing ratio of 0.00822. The cloud temperature is calculated assuming a moist adiabtic lapse rate. The model is steady-state so that the spectra evolve with height but not in time, a condition that would be expected in the mature phase of a hailstorm.

4. THE WATER SUBSTANCES

The model distinguishes seven different water substance components: vapour, cloud water, hailstones, rain water, water shed from hailstones, frozen rain water and frozen shed water. Rainwater differs from shed water in its origin; that is, a collision-coalescence mechanism versus the accretion-shedding mechanism, respectively. In order to investigate the origin of frozen hailstone embryos, the frozen rainwater is kept separate from the frozen shedwater.

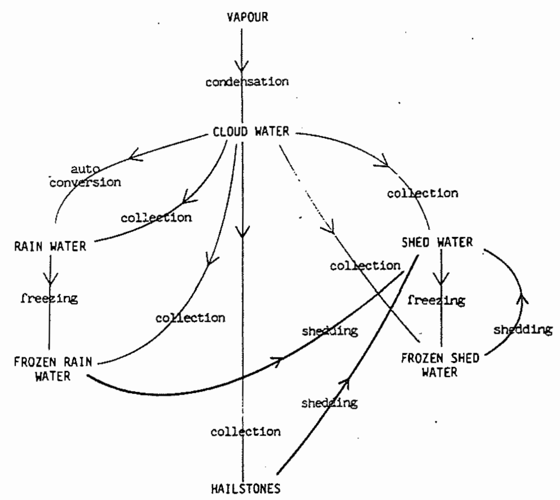

Figure 2: Interaction diagram. This figure shows the water substance components and their interactions with each other. The emphasis of the model is indicated on the diagram by heavy solid lines.

Figure 2 shows the interactions, which are considered to be continuous, among the various water components. Figure 2 shows the interactions among the various water components which are considered to be continuous. Each distribution is assumed to be stationary and thus self-interactions such as coalescence and breakup of raindrops are not explicitly modelled but assumed.

The spectra of the water substances are parameterized by Gamma functions of various orders except for the cloud water which is assumed to have negligible size and moves with the air. It is the only water component that interacts with the vapour phase through condensation and evaporation. The rain and hail is assumed to be parameterized by a zero order Gamma functions of the form:

$$n(d)\, dd = n0 \exp (\lambda \, d) \, dd \qquad (5)$$

valid for d < 3mm and d >= 3 mm for rain and hail, respectively; where, the parameters n0, λ, d have their usual definitions. The boundary at 3mm between rain and hail is based upon observations (Ref. 6, 20). The mean volume diameter of the rain is assumed to be 1mm and remains constant throughout the calculations. The initial hail embryo size is assumed to be 5mm in order to compare with calculations of previous models (Ref. 5); so that their more extensive computations may be employed to extend these results. The spectra of the shed water is defined by equation (1) which yields a mean volume diameter of 1.4 mm.

By assuming a Bigg's (Ref. 2) type freezing mechanism, the probability of freezing is proportional to drop volume; thus, the frozen drop spectra are proportional to their liquid counterparts multiplied by drop diameter to the third power (Ref. 7). The liquid components of the water substances have upper limits to their size distributions to reflect the size limiting mechanisms such as collision-breakup type (Ref. 14, 15). However, the solid phase components are not limited in this way and their upper limits extend to infinity.

Hailgrowth is initiated by 5mm embryos. These are assumed to be produced by feeder clouds and injected into the main updraft region (Ref. 3, 17, 19) at the 0C level of the cloud. The embryos ascend in the cloud and the calculations terminate when they reach their balance level where the hailstone terminal velocity is equal to the updraft velocity.

In order to examine the influence of the interactions on the size distributions that may be observed, the spectral parameters are calculated from the mixing ratios. This requires that for the frozen water substances, the mean size increases with mixing ratio. For the liquid components, an eqilibrium situation is assumed which implies that the mean size remains the same but the number concentration increases. As new substances are created, the initial characteristic sizes are allotted to the new particles and the spectrum parameters are recalculated assuming conservation of mass and number.

5. MODEL RESULTS AND DISCUSSION

This paper will restrict itself to examining the significance of just the shedding process. Future publications will address the role of shed drops as frozen drop embryos for further hail growth. Three cases will be described: no shedding, shedding only and shedding with rain and freezing.

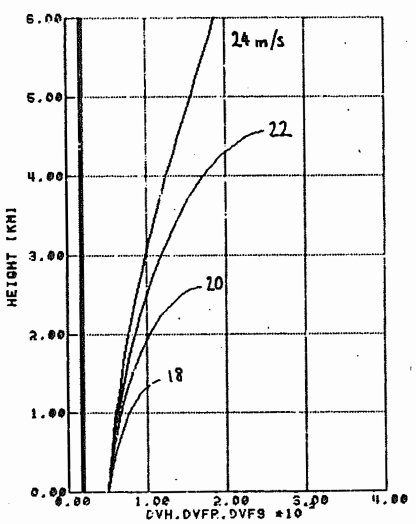

Figure 3: No shed case study with initial hail concentration of 1/m**3. Family of curves are for cloud base updraft velocities of 18, 20, 22 and 24 m/s. The mean volume diamter of the hailstones is plotted. Full width of the diagram is 4cm. The double line at about .2cm are the diameters of the frozen shed and rain drops which in this case do not exist. The curves trace the hail embryo trajectories from the 0C level to their balance level; the larger the updraft, the higher the balance level.

5.1 CASE 1: NO SHEDDING

Figure 3 presents the model results, with no shedding and no rain production for comparison purposes. A hail concentration of 1/m**3 is injected at the 0C level as in Charlton and List (Ref. 5). The figure presents the mean volume diameter of the hailstones for updraft velocities of 18, 20, 22 and 24 m/s. The results show that the larger the updraft, the larger the hail that is produced. This is as a result of longer residence times and hence growth times in the hail growing region. However, if the updraft velocity is too large, then the hail is carried out of the hail growing region without growing very much. Large hail (2 cm) may be produced in a reasonable amount of time, 10 minutes. The effect of larger hail concentration (not presented) is to deplete the cloud water more quickly which again results in slower growth and therefore larger hail.

5.2 CASE 2: SHEDDING WITHOUT FREEZING

Figure 4 presents the case with shedding, but no rain production and no freezing. Shedding slightly reduces the growth rate of the hailstones. The hailstones are carried up higher (by 1 km) in the cloud to colder regions where more effective growth may take place. This results in larger hailstones when compared to similar conditions without shedding. Thus, the updrafts required to produce large hail do not have to be as large as in the no-shed case.

Shedding occurs only in the lower and warmer (<3km) regions of the cloud which might have been expected but not obvious when both temperature and liquid water content are determining factors in the shedding process (see figure 5). The shed water may collect the cloud water, which slightly depletes it, (contributing to a lower hail growth rate) but is itself collected by the hailstones.

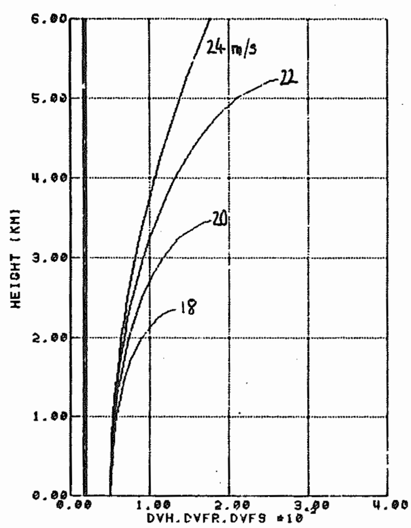

Figure 4: Same as figure 3 except for the shedding case. Shedding results in higher trajectories and slightly larger hailstones.

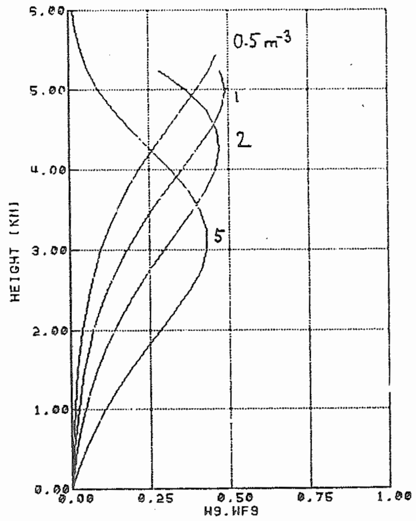

Figure 5: Liquid water content of the shed drops for the case of a 22m/s cloud base updraft. The hail concentration is varied from 0.5, 1, 2 and 5 per cubic meter. As the the hail concentration increases, the peak in the shed water content appears lower in the cloud. If the hail concentration becomes greater than 2/m**3, then the shed drops become totally depleted by the hailstones and is only an in-cloud feature.

These processes occur in roughly different regions of the cloud. Production occurs in the lowest few kilometers of the cloud, collection of cloud water in the next few kilometers and depletion by hail collection in the top few kilometers of the cloud. The shed water is not really lost to the hailstone; but rather, the water is temporarily stored in millimeter sized drops which may later be collected again. If the hail concentration is large enough (>2/m**3); then, the shed water may be totally depleted and the occurence of millimeter sized drops is only an in-cloud feature. The maximum water content of the shed drops is about 0.5 g/m**3. Clearly, there is a sensitive balance between the hail concentration and the observation of millimeter sized drops.

This model is dynamically limited; however, with realistic updrafts that may decrease with height after increasing to a maximum, (Ref. 8, 23) shed water may accumulate at its own balance level and form a zone of large drops.

Another important feature is in the spectral picture, presented in figure 6. There is sufficient water content in the shed drops to be noticable in the precipitation spectrum and produce a biexponential distribution not unlike those observed on the ground and in the air (Ref. 6, 20). A break appears in the spectrum, with the steeper negative slope being associated with the liquid particles. Figure 7 presents the spectral picture of hailgrowth with shedding, rain production and the freezing of both types of millimeter sized drops. With the addition of the warm rain process an unrealistic spectral picture occurs. The mass spectrum has a trimodal appearence. At the lower levels of the cloud, the number concentration has a biexponential look but the slopes of the distributions are in the wrong sense; the rain contribution to the spectrum is flatter than the hail part of the spectrum.

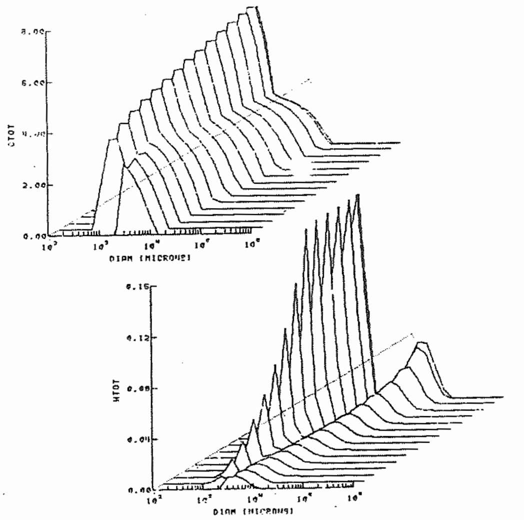

Figure 6: Three-dimensional spectral diagram of the precipitation particles. The horizontal axis is logarithmic drop size. The oblique axis is height above the 0C level. Full scale is 6km. The vertical axis is logarithmic number concentration (top) and linear water content (bottom). The distribution is drawn every 250m except for the top line which is the distribution at the balance level. This figure is for the case of shedding with an updraft velocity of 20 m/s and hail concentration of 1/m**3. Note the bimodal distribution not unlike those observed in nature.

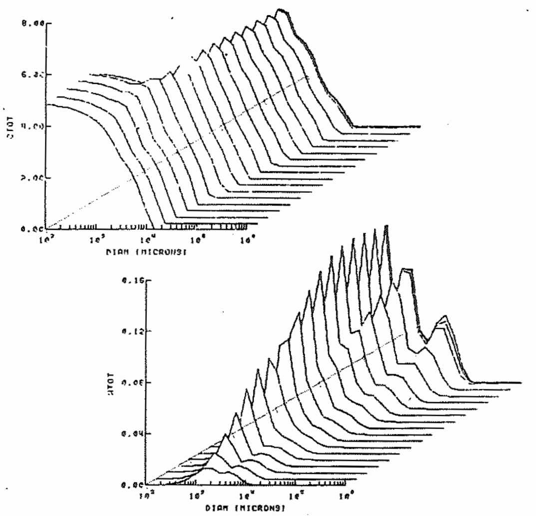

Figure 7: Same as in figure 6 except rain production and freezing of drops is included. Rain is produced by the autoconversion process only in the warm part of the cloud. There is a biexponential appearence at low levels but the slopes are in the wrong sense from those observed in nature and a trimodal appearence at higher levels.

6. CONCLUSIONS

The experiments have shown the existence of the shedding mechanism which instantaneously converts cloud droplets to rain-sized drops. The model shows that shedding is a significant process in the atmosphere. Shedding occurs in the lower levels of the hail growth region. Larger hail results because of slower growth rates and longer residence times. Therefore, lower updrafts are required to pr uce large hail.

The shed drops collect cloud water and are collected by the hail. The maximum water content of the shed drops is about 0.5 g/m**3. The collection by hail may dominate if the hail concentration is greater than about 2/m**3 such that all the shed drops may be depleted and are only an in-cloud feature.

The freezing of shed drops would possibly lead to frozen drop embryos. Inclusion of shedding produces distributions not unlike those observed in nature.

It is clear from this model that hail and rain are intimately linked and the consideration of one must include the other. Shedding provides a possible third mechanism for the formation of rain.

ACKNOWLEDGEMENTS: This research was supported by the Atmospheric Environment Service of Canada.

7. REFERENCES

1. Beckwith, W.B., 1957: Analysis of hailstorms in the Denver Network, 1949-1958, Physics of Precipitation, Geophysics Monograph No. 5, 348-353, American Geophysical Union, Washington, D.C.
2. Bigg, E.K., 1953: The supercooling of water, Proc. Phys. Soc., B66, 688-694.
3. Browning, K.A. and G.B.Foote, 1976: Air flow and hailgowth in supercell storms and some implications for hail suppression, QJRMS, 102, 499-533.
4. Carras, J.N. and W.C. Macklin, 1973: The shedding of accreted water during hail growth, QJRMS, 99, 639-648.
5. Charlton, R.B. and R. List, 1972: Hail size distributions and accumulation zones, JAS, 29, 1182-1193.
6. Federer, B. and A. Waldvogel, 1975: Hail and raindrop size distributions from a Swiss multicell strom, JAM, 14, 91-97.
7. Federer, B. and A. Waldvogel, 1978: Time-resolved halistone analyses and radar structure of Swiss storms, QJRMS, 104, 69-90.
8. Hitschfeld, W.F. and R.H. Douglas, 1963: A theory of hailgrowth based on studies of Alberta storms, ZAMP, 14, 554-562.
9. Joe, P.I., 1982: The shedding of millimeter sized drops in simulated hail formation, Ph.D. Thesis, U. of T., pp 360.
10. Joe, P.I., R. List and G.B. Lesins, 1981: Ice Accretions, Part II: Rain production by cloud water conversion, Journal de Recherches Atmospherique, 14, 357-364.
11. Joe, P.I., R. List, P.R. Kry, M.R. de Quervain, P.Y.K. Lui, P.W.Stagg, J.D. McTaggart-Cowan, E.P. Lozowski, M.C. Steiner, J. von Niederhausern, R.E. Stewart, E. Freire and G. Lesins, 1976: Loss of accreted water from a growing hailstone, International cloud physics conference, Boulder, Colorado,, July 26-August 6, 264-269.
12. List, R., 1977: Ice accretions on structures, J. Glaciology, 81, 451-465.
13. List, R., P.I. Joe, G. Lesins, P.R.Kry, M.R. de Quervain, J.D. McTaggart-Cowan, P.W. Stagg, E.P. Lozowski, E. Freire, R.E. Stewart, M.C. Steiner and J. von Niederhausern, 1976: On the variation of the collection efficiencies of icing cylinders, International cloud physics conference, Boulder, Colorado, July 26-August 6, 233-239.
14. Low, T.B., 1977: Products of interacting raindrops, experiments and parameterization, Ph.D. thesis, U. of T., pp 230.
15. McTaggart-Cowan, J.D. and R. List, 1975: Collision and breakup of water drops at terminal velocity, JAS, 32, 1401-1411.
16. Macklin, W.C., 1977: The characteristics of natural hailstones and their interpretation, Met. Mono., 16, no. 38, 65-88.
17. Musil, J.D., 1970: Computer modelling of hailstone growth in feeder clouds, JAS, 27, 474-482.
18. Orville, H.D. and F.J. Kopp, 1977: Numerical simulation of the life history of a hailstorm, JAS, 34, 1596-1595.
19. Schleusener, R.A., 1966: Project Hailswath: Final report, volume 2, reports from participating groups, Rapid City, South Dakota.
20. Smith, P.L., D.J. Musil, S.F. Weber, J.F. Spahn, G.N. Johnson and W.R. Sand, 1976: Raindrop and hailstone size distribution inside hailstorms, Preprints of the International conference on cloud physics, Boulder, July 26-August 6, AMS, 252-257.
21. Stewart, R.E., 1974: Analysis of the growth of spheroidal hailstones under simulated natural icing conditions, M.Sc., U. of T., pp72.
22. Summers, P.W., J.C. Fankhouser, G.M. Morgan Jr., G.B. Foote and A.C. Modhal, 1979: Results of a randomized hail suppresion experiments in northeast Colorado, VIII, the representative draw analysis, JAM, 18, 1618-1628.
23. Sulakvelidze, G.K., N. Sh. Bibilashvili and V.F. Lapcheva, 1967: Formation of precipitation and modification of hail processes. Gichrometeoizdat, Leningrad, 1965, Israel progrom for scientific translations, Jerusalem.

WET GROWTH OF HAILTONES: INTEGRATION OF MULTIPLE DOPPLER DATA AND HAILSTONE STRUCTURE ANALYSIS IN A KINEMATIC MODEL

Nancy C. Knight*, Stephan P. Nelson**, and Steven V. Vasiloff**

*National Center for Atmospheric Research
Boulder, Colorado

**National Severe Storms Laboratory
Norman, Oklahoma

1. INTRODUCTION

Analysis of properly collected and preserved hailstones may be used to verify trajectory modelling in Doppler flow fields. The method for such collection and preservation and the rationale for the technique has been reported by Knight and Knight (1968). The hailstones used in the investigation reported here were collected from a storm in central Oklahoma on 19 June 1980. The hailfall was of relatively short duration, lasting approximately five minutes, and over this period of time a total of 364 stones were collected on an area of one square meter. The stones ranged in size from 6 to 29 mm in longest dimension.

2. HAILSTONE STRUCTURE ANALYSIS

There are problems in using ground truth from hailstones, particularly in wet growth, and primarily because of the amount of recrystallization which occurs when the hailstone temperature is close to 0°C. The collection method used insures that the structure is preserved as it was when the hailstone arrived at the surface and that any evidence of recrystallization present in the stones is a result of processes occurring prior to their collection. Evidence of recrystallization is given in hailstone thin-sections by the presence of large, equi-dimensional crystals with straight, smooth boundaries and equi-dimensional air bubbles (Knight and Knight, 1968). The hailstones from the storm on 19 June exhibited all of these characteristics in varying degrees, as is illustrated by the thin-sections shown in Fig. 1, but because they were properly collected and preserved, one knows that the recrystallization features observed occurred before the stones reached the surface.

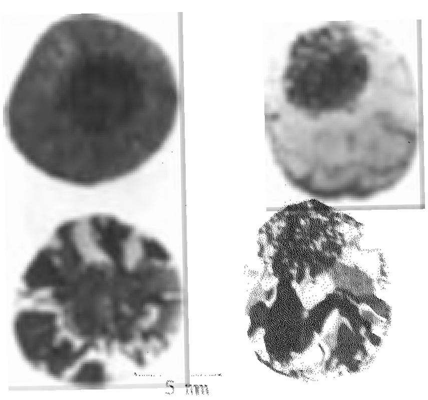

Fig. 1. Hailstone thin sections from 19 June 1980 in transmitted and polarized light. Note graupel embryos, large, equi-dimensional crystals and smooth crystal boundries. The transparent ice surrounding the embryo is evidence of wet growth.

The majority of the hailstones contained graupel embryos with all subsequent growth having been wet. Because of the recrystallization in these hailstones, it is more difficult to use crystal size as a determinant of growth conditions; however, one can conclude with considerable certainty that the outer sections of the stones grew wet and even slightly spongy because of the general transparency of the ice and the relationship between the air bubbles and the lobe structures (Knight and Knight, 1970). Quite similar hailstone structures have also been reported by Levi et al., (1970).

3. THE DOPPLER WIND FIELD AND THE KINEMATIC MODEL

The storm from which the hailstones were collected formed west of the National Severe Storms Laboratory (NSSL) in Norman, Oklahoma late in the evening and moved eastward as a complex of several cells among which one eventually intensified and turned toward the southeast. By 2320 hours this cell was located about 35 km southwest of NSSL and NSSL's two 10 cm wavelength Doppler radars began scanning it. (The characteristics of these radars are given in Sirmans et al., 1977.) The three dimensional wind field used here was obtained from the two measured radial velocities, the mass continuity equation, and an assumed terminal velocity/reflectivity relationship. Vertical velocities were obtained by downward integration of the continuity equation where the velocities were constrained to be zero at both the storm top and the earth's surface (Brown et al., 1981). The horizontal flow field at 8.5 agl that is correlated with the hailstone collections is shown in Fig. 2.

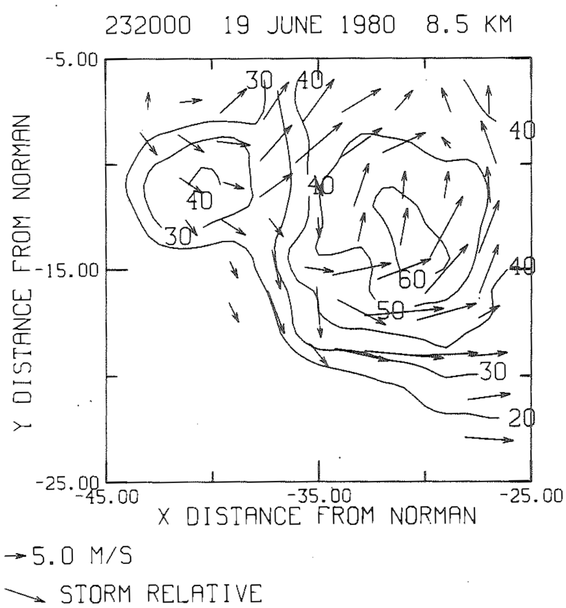

Fig. 2. Horizontal flow fields and equivalent radar reflectivity factors, Z_e, at 8.5 km AGL, 2320 hrs, 19 June 1980.

The details of the kinematic model used here are given in Nelson, 1983 and will be only briefly described. The hail growth model uses the three dimensional, multi-Doppler synthesized flow field as a framework. The winds are assumed to be steady over the hail growth times ($\sim$15 min). The model was initialized with 4 mm embryos. This dimension was determined from measurements of the average size of the embryos in the hailstone collections. The model embryos were distributed throughout the storm, released, and allowed to advect and grow. For each hailstone, the ambient conditions and surface temperature, and, therefore, the wet or dry growth mode, were calculated using the appropriate thermodynamic equations. The thermal and moisture conditions are assumed to be adiabatic in areas where the updrafts are greater than 10 m s^{-1} and equal to the environmental values outside of the updrafts.

4. RESULTS

The hailstones were collected at the ground between 2333 and 2338 hours. The pattern of reflectivity at 0.5 km agl and 2320 hours is given in Fig. 3 in which the vehicle position is also indicated. This position has been time-to-space adjusted to the radar reference time for the entire period of hail collection, using the storm motion vector. The model produced two predominant hail growth trajectories. The two trajectories gave fallout positions that were somewhat separate and that corresponded rather well with reflectivity maxima near the ground. One representative fallout position is given for each trajectory in Fig. 3. The trajectories for these particles and the vertical velocities at 8.5 km agl are shown in Fig. 4. In these figures particle #7 represents the trajectory and growth history corresponding to the hailstones in the ground collection. This modelled hydrometeor travelled very little in a horizontal direction, having been caught in a rotary flow centered at x $\simeq$ -35 and y $\simeq$ -14(Fig. 2). In agreement with the hailstones collected at the surface, all of the mass of the modelled hailstone, excepting the embryo, is accreted in the wet growth mode in which the hailstone surface temperature is constant at 0°C and the coldest ambient temperature is -17°C. The size of the modelled hailstone at the surface was 18 mm diameter.

As is evident from Figs. 3 and 4, the hailstones collected by the vehicle were not from the strongest area of the storm. The trajectory for modelled particle #9 is longer in horizontal extent and the stone encountered somewhat colder and drier conditions in the beginning of its growth history. However, it soon entered the wet growth regime and continued to grow wet, reaching a maximum diameter at the ground of 29 mm. Unfortunately, there were no surface collections from this area of the storm with which this stone might be compared.

5. CONCLUSIONS

Hailstones collected from an Oklahoma storm exhibited evidence of wet growth and recrystallization associated with hailstone surface temperatures close to 0°C. The kinematic, three dimensional model using multi-Doppler synthesized flow fields reproduced the wet growth conditions and produced hailstones grown on graupel embryos upon which all subsequent growth was wet and which were within the size range observed at the ground.

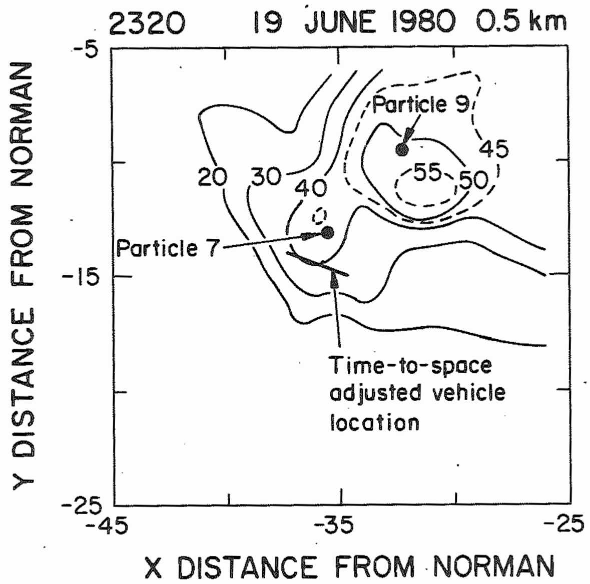

Fig. 3. Z_e at 0.5 km AGL, 2320 hrs, 19 June 1980. Representative fallout position for each modelled trajectory. Vehicle location is time-to-space adjusted. Particle 7 corresponds to the ground collections.

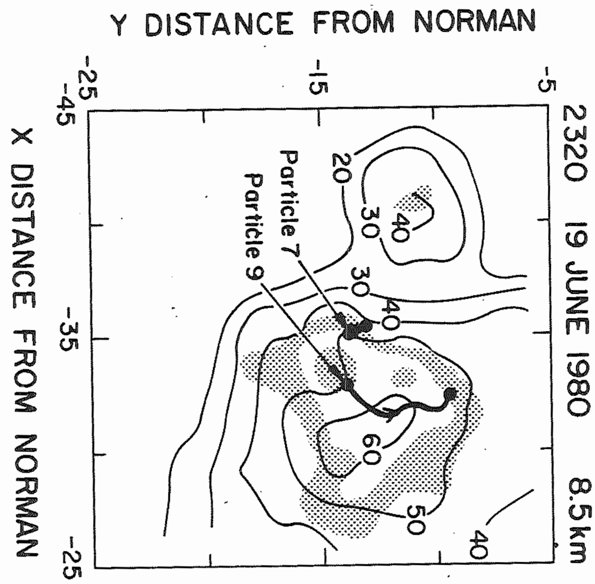

Fig. 4. Z_e at 8.5 km AGL, 2320 hrs. 19 June 1980. Vertical velocities are: outer shaded contour W $\geq$10 m s^{-1}; inner contour (unshaded) W >20 m s^{-1}; innermost shaded contours W >30 m s^{-1}. Modelled trajectories are given for particles 7 and 9.

Two basic hail growth trajectories were derived from the model which were related to the two observed reflectivity maxima. The horizontal flow patterns suggest that there may be two embryo source regions, one associated with a satellite (11 and the other with recycling in the main updraft. However, because of the long growth times required for the 4 mm embryos, time-varying solutions will be required to confirm this and they are not presently available.

6. REFERENCES

1. Brown, R. A., E. R. Safford, S. P. Nelson, D. W. Burgess, W. C. Bumgarner, M. L. Weible, L. C. Fornter, 1981; Multiple Doppler radar analysis of severe thunderstorms: Designing a general analysis system. NOAA Tech. Memo. ERL NSSL-92, 21 pp.

2. Knight, C. A. and N. C. Knight, 1968; The final freezing of spongy ice: Hailstone collection techniques and interpretations of structures. J. App Meteor., 5, 875-881.

3. Knight, C. A. and N. C. Knight, 1970: Lobe structures of hailstones. J. Atmos. Sci., 4, 667-671.

4. Levi, L., E. Achaval, and A. N. Aufdermaur, 1970: Crystal orientation in a wet growth hailstone. J. Atmos. Sci., 27, 512-513.

5. Nelson, S. P., 1983: The influence of storm flow structure on hail growth. J. Atmos. Sci., 40, 1965-1983.

6. Sirmans, D., J. T. Dooley and B. Bumgarner, 1977: Doppler radar quality control summary. NOAA Tech. Memo. ERL-NSSL-83, Section II., 79-130.

ANNEALING EFFECTS ON THE HAILSTONE STRUCTURE

Laura Levi* - Elena M. de Achaval - Enrique Ceppi**
Servicio Meteorológico Nacional - Buenos Aires - Argentina

* Comisión Nacional de Energía Atómica
** Instituto de Matemática Astronomía y Física
Universidad Nacional de Córdoba

1. INTRODUCTION

It has been generally observed that, when hailstones collected on the ground are analysed, the modifications due to annealing, that these have suffered both before collection and during storage, should be taken into account in order to correctly infer their growth conditions from their structure. Knight and Knight (Ref. 1) suggested that the original hailstone structure could be better preserved by quenching, that is, by directly receiving the precipitation particles in a cold bath. However, quenching may not avoid the annealing effects that might have occurred before precipitation, when the growth of external layers in wet or spongy regime keeps the stone at 0°C during a non negligible time. Finally, quenching itself could be a source of modifications of the hailstone structure, specially when spongy ice layers exist, for, in this case, the rapid freezing of the remaining water may generate new crystals not related with the growth conditions. For these reasons, the study of the annealing effects on the hailstone structure is still of interest.

The annealing effects on the structure of dry regime accretions have recently been studied by McCappin and Macklin (Ref. 2). According to these authors, the relations, observed in the studied samples between grain length and grain width, could be informative as to the annealing effects that the grains have suffered before analysis, so that the initial crystallographic structure of a stone layer could be derived from that observed in the annealed one. However, McCappin and Macklin did not try any direct application of their results, to interpret the sturcture actually found in natural hailstones. In fact, this structure differs, to some extent, from that of the dry growth accretions studied by these authors, possibly because of the frecuent formation of wet or spongy ice layers.

Considering that the annealing effect in natural hailstones has scarcely been studied, research on this phenomenon, using several large stones, has been presently carried out. The behaviour observed will be discussed by taking into account previous results on grain growth that were obtained for accreted ice (Refs. 2-4), for thin sheets of natural hailstones (Refs. 5,6) and for ice samples grown in the laboratory (Refs. 7,8).

2. CHARACTERISTICS OF THE SAMPLES AND EXPERIMENTAL METHODS

The studied hailstones, of 3-5 cm diameter, were from two different storms, that had occurred in Córdoba (17/11/81) and in Buenos Aires (20/7/82). The stones analysed from the first storm (X-stones) were about 150 samples collected on the ground during precipitation. They were stored in a container at dry ice temperature and, after five months, they were placed in a cold room at -15°C. Most samples were progressively prepared for structure analysis, whereas four of them were used for annealing experiments.

About 30 hailstones were collected on the ground during the second storm. They were stored in the cold room at -15°C and prepared for analysis about six months later. Five samples were used for the annealing experiments.
The datailed study of the hailstone structure was carried out by analysing plastic replicas of the thermally etched surfaces, in the microscope (Ref.9). Thin sheets were also observed in natural and polarized light. The samples were cut through their equatorial plane. They all presented evident prevalence of wet or spongy growth, as revealed both by the orientation of the crystals and by the presence of rather large air bubbles.

The X-stones usually consisted of a conical or a spherical embryo, frequently grown about a small but visible frozen droplet and of two succesive transparent and opaque ice layers, formed by large and small crystals respectively. There were evidences of a final transparent ice layer, partially melted during precipitation.

The C-stones consisted of an approximately spherical embryo, sometimes not definitely differentiated from the subsequent structure. The latter was formed by one or two layers of relatively large crystals and transparent ice. There was strong evidence of spongy growth as shown by the presence of pronounced lobes.

The samples used for the annealing experiments at $T \approx -10°C$ were cut through two orthogonal planes that contained the stone center, as shown in Fig. 1. Part 0 was not annealed, while parts 1, 2 and 3 were annealed in a thermostat during progressively larger times.

The temperature in the thermostat was measured by a thermocouple and electronically regulated to $\pm 0.2°C$.

After annealing, surfaces corresponding to the p-plane (Fig. 1) were prepared for analysis.

Figure 1. X-stone divided by two orthogonal planes through its center.

3. RESULTS

3.1. Effects of storage at -15°C.

The effects of annealing at -15°C have been derived from the comparison of the structure of X-stones sectioned and replicated for analysis at different times. Some results are given in Table 1, where $\bar{\sigma}$ is the mean grain area and $\bar{e}$ is the mean shape factor obtained as the ratio of the mean length to the mean width of the crystals. The table shows that samples selected for analysis from the dry ice container and inmediately sectioned and replicated, presented a structure very similar to that of samples prepared for analysis after about a year storage in the cold room. In all cases, the stones presented a layer of large crystals, (sometimes split into two slightly different zones) with mean area varying between 1 and 0.1 mm^2 and a layer of small crystals, with mean area varying between 0.03 and 0.07 mm^2. The initial mean shape factor varied between 1.2 and 2.1 ramaining in the same range after storage.

Table 1

Mean grain area $\bar{\sigma}$ and shape factor $\bar{e}$ for different storage times at -15°C.

Sample	Mean Grain Area mm^2	Shape factors $\bar{e}$	Storage time at -15°C months
X-38 A	0.45	1,7	0
X-38 B	0.057	1.3	0
X-39 A	0.15	1.8	0
X-39 B	1.1	2.1	0
X-39 C	0.042	1.2	0
X-33 A	0.16	1.7	12
X-37 A	0.36	1.6	14
X-37 B	0.15	1.6	14
X-37 C	0.037	1.5	14

It was concluded from these results that, if some modification of the grain size and shape occurred during a year annealing at -15°C, this was smaller than that corresponding to the lack of homogeneity of the samples. Thus, if annealing effects had modified the initial crystal structure of the samples, they should have operated previously to collection.

3.2. Annealing effects at $T \geqslant -10°C$

Most experiments were performed at annealing temperatures of 0°C and -2°C; in two cases this temperature was -6°C and -10°C. Representative examples of the results obtained for the mean grain radius $\bar{r}$ as a function of time are given in Fig. 2. Notice that, since the experimental points were calculated by writing $\bar{r} = \sqrt{\bar{\sigma}/\pi}$, the phenomenon was treated here as for spherical grains. The straight lines in Fig. 2 represent a least-square fit to experimental data corresponding to a given hailstone layer. For part 0 (Fig. 1) the annealing time was taken t = 30 min. Not all the series of points have been represented in Fig. 2 to avoid their superposition.

The linear correlation assumed in Fig. 2 between log $\bar{r}$ and log t corresponds to the application of the grain growth law

$$\bar{r} = k_n \, t^n \qquad (1)$$

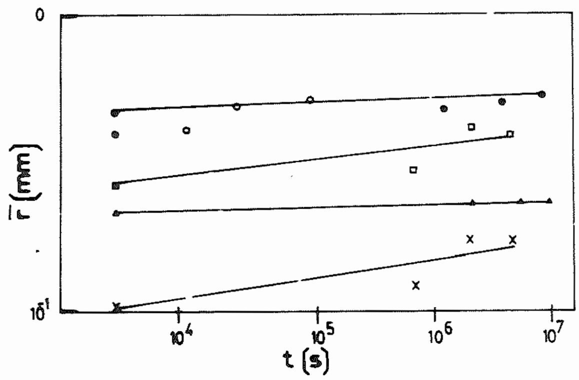

Figure 2. Radius $\bar{r}$ as a function of time, for different stones.

In Fig. 3 the n values obtained in the whole series of experiments are represented as a function of T. the results are quite scattered; however, the curve for long $\bar{n}$, where $\bar{n}$ is the mean value of n corresponding to each T, shows that, according to the present results, n would be temperature dependent, its value decreasing with T. At T = 0°C, the values of n are near those obtained for artificial accretions (Ref.2)

On the other hand, k_n represents the mean grain radius at t = 1 s. As it may be expected, it is slightly smaller but always of the same order of magnitud of $\bar{r}_o$.

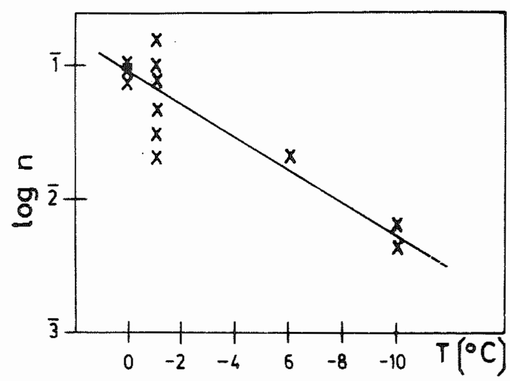

Figure 3. Log n as a function of temperature.

3.3. Shape factor

It has been shown that the shape factor $\bar{e}$ depends on the growth conditions of the accreted ice (air temperature, surface temperature and growth regime).

Now, it has been condidered of interest to determine its variations due to annealing at $T \geqq -10°C$. The results are exemplified in Table 2. It may be seen that, when the samples are heavily annealed at 0°C or -2°C, so that $\bar{r}$ increases markedly with time, $\bar{e}$ decreases slightly. However, the variation is weakly significant. Actually, even the smaller value of $\bar{e}$ found after annealing, $\bar{e}$ = 1.3, is comparable to the value $\bar{e}$ = 1.2 given in Table 1 for a non annealed ice layer, formed by crystals of about the same size.

Table 2

Grain radius and shape factor before and after annealing

Sample	T °C	t days	$\bar{r}_o$ mm	$\bar{r}_3$ mm	$\bar{e}_o$	$\bar{e}_3$
X-33	-6	100	0.71	0.89	1.7	1.7
C-40	-2	50	0.37	1.16	1.8	1.6
X-37 A	-2	50	0.34	0.58	1.6	1.4
X-37 B	-2	50	0.22	0.29	1.6	1.6
X-37 C	-2	50	0.11	0.21	1.5	1.3
C-30	0	0.26	0.60	0.86	2.4	2.0

3.4. Grain size frequency distributions

It has been observed that normal grain growth determines appromately gaussian distributions for the grain dimensions, that is for the mean radius r of singular crystals or, when the crystal shape is taken into account, for their length l and width w. These distributions are centered about a maximun, located near the mean value of the measured dimension $\bar{r}$, $\bar{l}$ or $\bar{w}$ respectively. When the phenomenon is quasi stationary and the frequency is given as a function of $r/\bar{r}$ or similar adimensional variables, the frecuency distributions obtained at succesive annealing times are similar to each other, despite the evolution of the absolute grain dimensions.

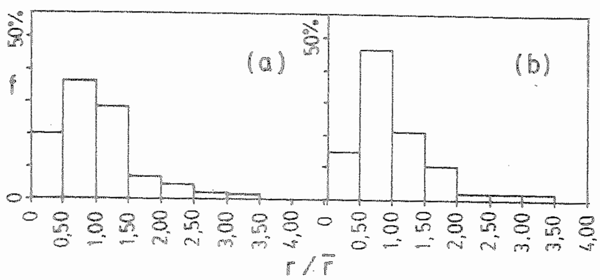

Figure 4. Frequency distributions of grain radius
a) before annealing
b) after 50 days annealing at -2°C

In the present work, frequency distributions of $r/\bar{r}$ have been obtained for the initial sample structure and for those corresponding to different annealing times. The results are exemplified by the hystograms in Fig. 4 corresponding to a hailstone layer initially formed by quite small crystals, with mean radius $\bar{r}_o = 0.3$ mm. After 50 days annealing at -2°C, it was $\bar{r}_3 = 1.1$ mm, that is $\bar{r}_3 = 3.5\ \bar{r}_o$. It may be observed that both distributions in Fig. 4, corresponding to the initial and final sample structure, have their maximum near $r/\bar{r} = 1$ so that they may be considered similar for their general shape. This result suggests that normal grain growth occurred along the whole process.

4. DISCUSSION

Following previous authors (Refs. 2,3,5,6), in section 3.2, the grain size has been represented as a function of time by applying Eq.1. It is known, however, that this law is only theoretically valid when the initial grain size is negligible with respect to that the annealed samples. In this case, it should be $n = 0.5$ and the factor k_n would have a theoretic expression depending on the grain boundary interface free energy and mobility. When the initial grain dimensions are not negligible, it should be written, instead of Eq. 1

$$\bar{r}^2 - \bar{r}_o^2 = K\ (t - t_o) \qquad (2)$$

where $K = k_n^2$ when $\bar{r}_o = 0$ for $t = 0$. The parameter K is usually given by

$$K = K_o \exp\ (-Q/kT) \qquad (3)$$

where Q is the activation energy for the grain boundary mobility. The values of K_o and Q characteristic of a given pure material would not depend on the temperature, as far as a given mechanism controls the boundary motion. It has been shown, however, that secondary features of the samples, such as impurities or inclusions, may hinder the grain growth process. This fact may be taken into account by introducing a retarding term in the equation wich relates the grain growth rate with the radius $\bar{r}$ or by modifying the value of K.

Now, it has been considered of interest to apply Eq.2 to the present results and to those obtained by previous authors for accreted ice (Refs. 2,3), in order to evaluate the rate factor K. The results are represented in Fig. 5, where ln K is given as a function of 1000 / T. The straight line in the figure was obtained by Levi and Ceppi (Ref. 8) after applying Eq.2 to their results and those obtained by Jellinek and Gouda (Ref. 7). It may be seen that several points are well distributed along this curve which corresponds to $Q \simeq 0.6$ eV. A similar value of Q was found by Azume and Higashi (Ref.10). The corresponding curve shows that, for $T \geq -3$°C, the Azume and Higashi's results are quite near those of previous authors (Refs. 7,8). However, for annealing temperatures closer to the melting point, K increases more rapidly, approaching the experimental point obtained by Levi and Ceppi at T = 0°C.
For T = 0°C, we have also indicated in Fig. 5 the interval inside which the values of K are scattered when Eq.2 is applied to the results of McCappin and Macklin.

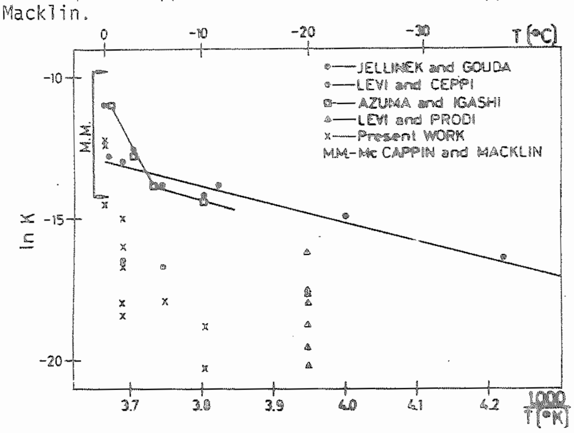

Figure 5. ln K as a function of 1000/T as derived from different experiments.

It may be interesting to observe that the scattering interval extends markedly above the straight line derived from Ref. 7, this behaviour being in agreement with the pronounced increase of K observed previously at this temperature (Refs. 8,10).

As for the experimental points corresponding to the natural hailstones studied in the present work, Fig. 5 shows that those corresponding to $T = 0°C$ are located in the same interval as the results of McCappin and Macklin. The results for $T < 0°C$ show that, at a given temperature, K may vary markedly with the sample, but that all the values obtained are distributed below the previously mentioned straight line. At $T = -10°C$, K is so small that the change in the grain size observed after 100 days storage may not be considered larger than the scattering of the results due to the non homogeneity of the samples. This last result could be considered in partial disagreement with those obtained by Prodi and Levi, who observed a small but nor really negligible annealing effect in artifical accretions, stored during 90 days at -19°C. This difference could be explained, however, by observing that the accreted ice studied by the above mentioned authors was stored at the annealing temperature inmediately after growth. On the contrary, all the hailstones had certainly undergone some annealing before the experiments took place. It is possible that during previous annealing, the migration of impurities or air bubbles to the boundaries had reduced the boundary mobility.

5. CONCLUSIONS

From the present comparative analysis of the grain growth behaviour observed in ice samples of different origin, it may be concluded that the curves in Fig. 5 give, with good approximation, the value of K which should be introduced in Eq. 2 so as to represent normal grain growth in pure ice samples. However, since ice is rarely pure, the grain boundary migration is usually hindered by impurities or air bubbles, this fact determining a strong decrease of K when $T < 0°C$.

It seems reasonable that, in these conditions, the values of K obtained at given temperature, for different samples, may differ markedly. In fact, these samples could differ in their impurity content as well as in their previous history. The considered retarding effects on the grain boundary motion would be weak or negligible at $T = 0°C$, where K would increase sharply, regardless of the sample structure.

As for the applications of the present results to the study of natural hailstones, it should be noted that protracted storage at $T < -10°C$ could determine modifications of the hailstone structure so slight, that they may be ignored, whenever this structure is interpreted in terms of the growth conditions.

On the contrary storage at higher temperatures would determine non negligible effects. In this case, the estimation of the initial grain size from that observed after storage could not be very precise, due to the dependence of the phenomenon on the initial sample structure itself.

The rapid annealing effects that occur at $T = 0°C$ have been already pointed out (Ref. 1). It is now interesting to observe that, at this temperature, a non negligible grain modification could take place during annealing times as short as 10-20 min. For instance, a structure containing grains of negligible initial size could attain mean grain dimensions of about 100 μm after about 10 min at 0°C.

This fact might account for the shape factor observed for natural hailstones which is smaller than for artificial accretions and which could be mainly due to annealing previous to collection.

6. ACKNOWLEDGEMENTS

The authors are indebted to Dr. F. Requena for helpful discussions and to A. M. Schnersch for contribution in experimental work.

The economic support of the Consejo Nacional de Investigaciones Científicas y Técnicas is also acknowledged.

7. REFERENCES

1. Knight C A and Knight N C 1968. Hailstone collection techniques and interpretation of structures, J.Appl. Meteor, 7, 875-888.
2. McCappin C J and Macklin W C, The crystalline structure of ice formed by droplet accretion, J.Atmos.Sci. in presse.
3. Prodi F and Levi L 1980, Aging of accreted ice, J. Atmos. Sci, 37, 1375-1384.
4. Knight C A et al 1978, Cylindrical ice accretions as simulation of hail growth, J. Atmos. Sci, 35, 443-452.
5. Carte A E 1961, Grain growth in ice, J. Graciol, 6, 411-420.
6. Jellinek H H G and Gouda V K 1969, Grain growth in polycrystalline ice, Phys Status Solidi, 31, 413-423.
7. Levi L and Ceppi E A 1982, Grain growth in ice, Il Nuovo Cimento, 5, 445-461.
8. Aufdermaur A N. et al 1968, Kristallachselagen in Hagelkörner, Z Angew Math Phys, 14, 574-589.
9. Azume N and Higashi A 1983, Effects of hydrostatic pressure on the rate of grain growth in antartic polycrystalline ice, J. Phys. Chem, 87, 4060-4063.

HAIL TO RAIN CONVERSION THROUGH MELTING

R. List, F. García-García, R.E. Stewart and D.B. McDonald

Department of Physics, University of Toronto
Toronto, Ontario, M5S 1A7, Canada

1. INTRODUCTION

Hailstones progress through different stages during their life cycle. A large number of laboratory studies have concentrated on the accretional growth of hailstones and have illustrated, in particular, that growth rates are typically limited by the shedding of millimeter-sized drops (Refs. 1,2,3 and 4). These represent instantaneously produced rain drops. Comparatively little attention has been directed towards the melting of hailstones, even though this phase is crucial for predicting hail characteristics on the ground and for determining the amount of and spectral distribution of the shed melt water.

The purpose of this paper is to report an investigation on the melting of hailstones under simulated natural conditions in a wind tunnel. Both spherical and spheroidal particles were investigated at terminal speeds and with rotational and gyrational modes of motion relative to the surrounding air-stream. Particular attention was given to the comparison of the observed melting and the theoretical predictions. The manner of the shedding itself was another focus of the investigation.

2. THE EXPERIMENT

The melting experiments were performed at the University of Toronto in a closed-circuit wind tunnel with controllable air speed, pressure and temperature. The air speed in the vertical measuring section is produced by a fan coupled to a motor assembly and can be varied from 7 to 40 ms^{-1}. A vacuum pump directly connected to the tunnel allows the tunnel air to reach a minimum pressure of 30 kPa. Cooling is provided by a compressor that can maintain a constant temperature as low as -30°C. A heating system located inside the tunnel is required to ensure steady state conditions for temperatures above -15°C. A unique feature of this tunnel is the double wall construction prior to and including the measuring section. The inner wall isolates the experimental region from the large temperature gradients near the outer wall. The measuring section (68.6 cm high, with a cross-section of 17.7 x 17.7 cm) consists of four aluminum outer plates and four plexiglass inner plates. Any plate may be modified for a specific function and mounted on any of the four faces, thus making the measuring section easy to adapt for any particular experiment.

For the melting experiments, four specially designed plates were used (Figure 1). A plate with an air tight door and a quick-release plexiglass plate provided access to the interior of the measuring section. The plate opposite to the door plate was designed to support the hailstone in the air stream and also to cause the particle to execute the fall mode of an oblate spheroid, called symmetric gyration (Ref. 5). A third plate was designed to provide proper illumination for photographic purposes and to hold a support system used to rotate spherical particles. The fourth plate provided photographic and video-recording camera mountings.

For the melting experiments, pressure (50 to 100 kPa), temperature (3 to 12°C) and air speed (19 to 28 ms^{-1}) were systematically varied. The experimental conditions were chosen to simulate melting conditions near, but below, the cloud base, using as a basis radiosonde observations taken on hail days in Colorado (Ref. 6). Vertical air speeds were set equal to the calculated terminal velocities of the hailstones. It should be noted that the relative humidity could not be varied over a wide range. Dry and wet bulb temperatures were measured with two iron-constantan thermocouples located at the measuring section. Relative humidity values ranged between 55 and 80%.

The hailstone models used for the experiments were made by freezing water in rubber molds. Ice oblate spheroids (2 cm major axis diameter and aspect ratio 0.67) were forced to gyrate symmetrically with a nutation/precession angle of 30° and at frequencies

Figure 1. Photograph of the measuring section of the wind tunnel.

between 5 and 30 Hz. Ice spheres (2 cm diameter) were rotated about a horizontal axis at frequencies between 0 and 20 Hz. The hailstones were allowed to melt for a known amount of time, then removed from the tunnel, weighed and measured. The change in particle diameter was always less than 10%.

3. DESCRIPTION OF THE SHEDDING

Observations of the shedding characteristics were made during the experiments and documented with the aid of photographs and video-tape recordings. As the hailstone began to melt, the melted water clung to the ice particle due to surface tension. As the water skin grew thicker, it started to accumulate on the surface of the hailstone. At this point, the accumulation of water is in balance under the forces due to the aerodynamic stress, the underlying friction, gravity, the surface tension and the angular motions of the hailstone (centrifugal forces).

In the case of non-rotating spheres, the water skin accumulated at both poles of the particle. For rotation cases, the water skin moved along the equator and formed a bulge on the side of the particle rotating against the airflow. The transition in the motion of the water skin from the poles to the equator took place at a rotation rate between 0.3 and 2.0 Hz. In the case of spheroids, the type of angular motion executed by the hailstone (symmetric gyration) affected the aerodynamic forces exerted on the water skin and the melted water was observed to collect slightly below the equator.

The major portion of the shedding originated from the water bulge. As the bulge became large enough, ripples started to form. The shedding, normally arising from these ripples, occurred mainly in the form of drops, but filaments that broke into drops were also observed (Figure 2). Bag breakups, as described in coalescence-breakup studies (Ref. 7), were also observed (Figure 3); however, this was a very rare event, accounting for less than 0.5% of the total number of shed drops observed.

The shedding of drops appears to be an instability phenomenon of the water skin, probably related to its size, shape, dynamics and temperature. However, the roughness of the hailstone surface affects the shedding characteristics. For hailstones with smooth surfaces, only shedding from the equatorial bulge was observed. For hailstones with rough surfaces, any lobe served as a collection point for the melted water and the excess of water was shed from these locations.

It is interesting to note that both the spherical and the spheroidal hailstone models preserved their shapes during melting.

4. SHED DROP SPECTRA OF SPHERICAL HAILSTONES

A series of experiments was recorded on video-tape, from which the shedding spectra of spherical hailstones were determined. Air temperature and rotation rate were varied between 5 and 10^{o}C, and 0 and 10 Hz, respectively. These experiments were carried out at laboratory pressure (100 kPa) and an air speed of 19 ms^{-1}. Illumination was provided by a strobolume unit set at a 60 Hz constant flashing rate, with a flash duration of 10 microseconds. A 35 mm lens was used and provided a magnification factor of 2.0 on the video monitor, from which the shed drops were counted in different size categories.

Shed drop spectra did not show major dependences on temperature or rotation rate. Shed drop distributions exhibited a unimodal pattern, with an average volume diameter of 0.95 mm. The minimum and maximum drop size observed were 0.3 and 2.0 mm, respectively.

A lognormal function was fitted to the relative number distribution of shed drops. This provided a reasonable fit to the data for all the experiments (Figure 4). The density function P(d), of the lognormal

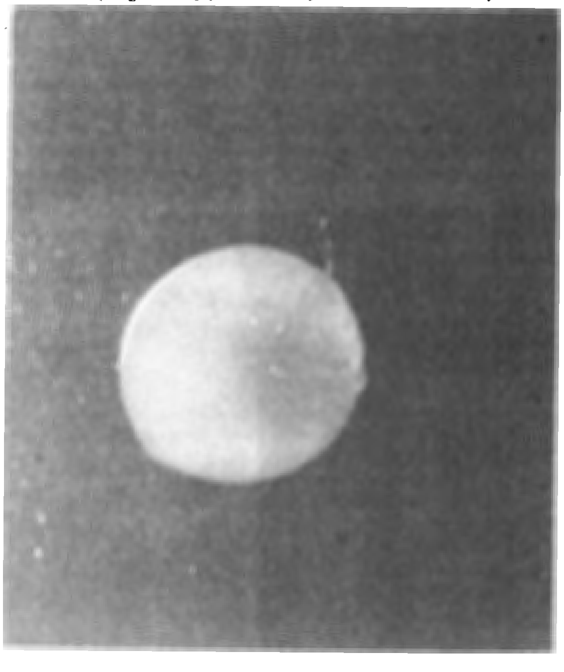

Figure 2. Photograph of a spherical ice particle showing shedding from a filament. Parameters: air temperature 5^{o}C, air pressure 67 kPa, air velocity 24 ms^{-1}, and rotation rate 5 Hz, clockwise.

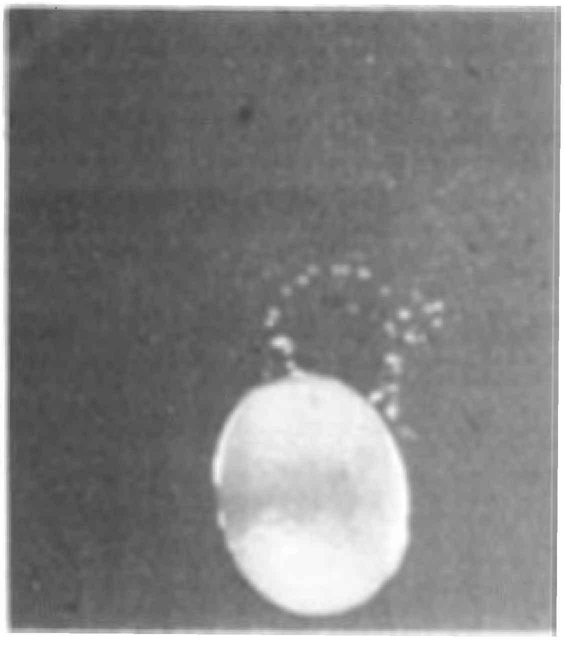

Figure 3. Photograph of an explosive shedding from a spheroid. The view is from the side of hailstone mount. Parameters: air temperature 5^{o}C, air pressure 100 kPa, air velocity 20 ms^{-1} and gyration frequency 10 Hz.

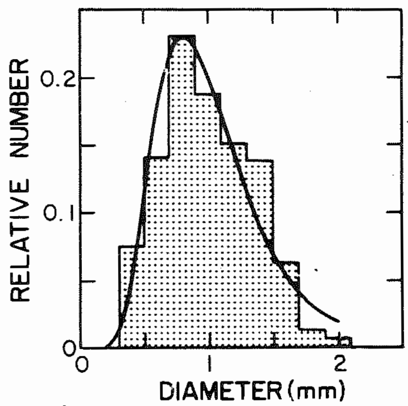

Figure 4. A typical shed drop spectrum for a spherical hailstone. Conditions for this experiment were: air temperature, 5°C; air pressure, 100 kPa; air velocity, 19 ms^{-1}; rotation rate, 5 Hz. The continuous line is a lognormal distribution given by Eq.1.

distribution is given by:

$$P(d) = \frac{H}{d} \exp\{-\frac{1}{2}(\frac{\ln d - \mu_o}{\sigma})^2\} \qquad (1)$$

where d is the diameter of the shed drop in mm, and the average values of the parameters of the distribution were found to be: H = 0.213, μ_o = -0.058 and σ = 0.389.

5. HEAT TRANSFER AND MELTING RATES OF HAILSTONES

The general heat balance equation for a growing hailstone under quasi steady state conditions is given by the experession:

$$Q^*_{CC} + Q^*_{ESC} + Q^*_{CP} + Q^*_{FM} = 0. \qquad (2)$$

The first three terms represent the direct and indirect heat flux between the particle and its environment by conduction and convection (Q^*_{CC}), by evaporation, sublimation or condensation (Q^*_{ESC}), and by accretion of water droplets (Q^*_{CP}). The term Q^*_{FM} represents the heat per unit time used to freeze the deposited water partly or entirely or to melt a part of the original hailstone. Expressions for each of these terms have been presented before for the cases of spheres (Refs. 8,9) and oblate spheroids (Ref.10).

The first two terms in Eq. 2 can be written as:

$$Q^*_{CC} = -\pi\gamma k\ D\ Nu\ (t_D - t_A) \qquad (3)$$

and

$$Q^*_{ESC} = -\frac{C\ \gamma\ D_{wA}\ D\ Sh}{T_A}(e_{sh} - U_w\ e_{sv}) \qquad (4)$$

where k is the thermal conductivity of air, D_{WA} is the diffusivity of water vapour in air, D is the diameter of the particle, γ is the surface area ratio of spheroid to sphere, Nu is the Nusselt number, Sh is the Sherwood number, U_w is the relative humidity of the air, t_D is the surface temperature of the hailstone; e_{sh} and e_{sv} are the saturation vapour pressures over the hailstone and over water, respectively; t_A and T_A are the ambient air temperature in degrees C and K, respectively; and C = 17025 K kg^2.

Environmental conditions below cloud-base represent the case of melting in which accretion of water droplets does not occur and melting drops are assumed to have a temperature equal to that of the surface skin, which is set equal to 0°C. In this case Q^*_{CP}=0. For the same reasons, Q^*_{FM} only accounts for the heat per unit time used to melt part of the original hailstone and can be expressed as:

$$Q^*_{FM} = L_f \frac{dm}{dt} \qquad (5)$$

where L_f is the latent heat of fusion and (dm/dt) is the melting rate of the hailstone.

Assuming that the physical processes involved in convecting heat away from the hailstone are similar to the ones convecting water vapour, it is possible to express Sh in terms of Nu using the empirical values given in Refs. 11 and 12, yielding the following relationship:

$$Sh = 0.95\ Nu\ . \qquad (6)$$

Substituting Eqs. 3 to 6 into Eq. 2, the following expression for the Nusselt number is obtained:

$$Nu = \frac{T_A\ L_f\ (dm/dt)}{D\gamma[\pi k\ T_A\ (t_D - t_A) + 0.95\ C\ D_{wA}(e_{sh} - U_w e_{sv})]} \cdot (7)$$

Using Eq. 7, Nu was calculated from the experimental data. The Nusselt number was found to be independent of the rotation and gyration frequencies. By introducing a consolidated heat transfer factor, χ, the experimental values of Nu can be summarized in terms of the Prandtl number, Pr, and the Reynolds number, Re, using Ranz and Marshall's empirical formula (Refs. 11 and 12) as follows:

$$Nu = \chi(0.6)\ Pr^{1/3}\ Re^{1/2}\ . \qquad (8)$$

The consolidated heat transfer factor has been introduced to take into account the effects on the heat flux due to the shape and the roughness of the hailstone, as well as any other effects such as those produced by the presence of the water skin on the surface of the particle. In the present investigation, χ was found to be equal to 1.12 ± 0.14 for rotating spheres, and 1.41 ± 0.15 for gyrating spheroids.

Melting rates can now be calculated for any set of environmental conditions by substituting Eq. 8 into Eq. 7. As an example, melting rates for 2 cm spherical hailstones are presented in Figure 5 for a selection of relative humidity values. The temperature-pressure profile model used is based on radiosonde observations taken on hail days in Colorado (Ref. 6) and can be expressed analytically (Ref. 9) in the form:

$$T_A = 53\ \ln\ (2.84\ p) \qquad (9)$$

where T_A is in degrees K and p is the environmental pressure in kPa. It should be noted that the results presented in Figure 5 represent instantaneous melting rates. This means that, once the diameter of the hailstone has changed, the particle will have a different surface area and its melting rate will change.

The calculated melting rates, combined with the parameterized shed drop distributions (Eq. 1), can now be used to obtain the number production rate of shed drops. For example, a 2 cm spherical hailstone melting at the cloud base (t_A = 5°C, p = 67 kPa and U_w = 100%) would produce 26 drops per second, with 4 of them having equivalent volume diameters between 1 and 2 mm. This result suggests that melting hailstones are an important source of rain drops through shedding.

6. SUMMARY AND CONCLUSIONS

Experiments on the melting of artificial hailstones were performed in a wind tunnel with controllable air

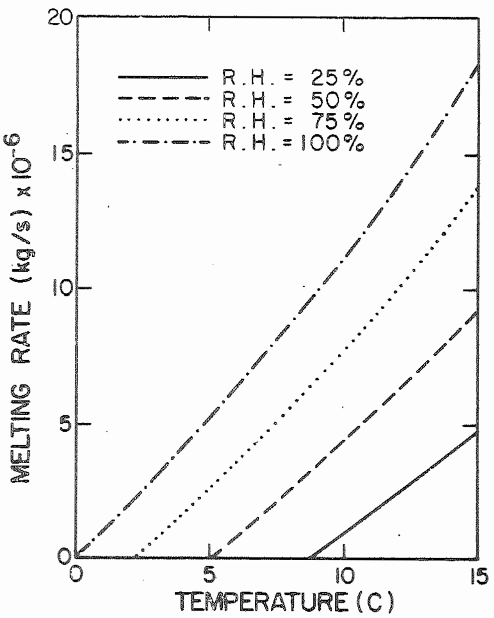

Figure 5. Instantaneous melting rates for a 2 cm diameter spherical hailstone as a function of temperature for different relative humidity values. Temperature and pressure are related according to Eq. 9.

speed, pressure and temperature. Two types of hailstone models were used: spheres (2 cm diameter) rotating about a horizontal axis at frequencies between 0 and 20 Hz, and oblate spheroids (2 cm major axis diameter, 0.67 aspect ratio) describing symmetric gyration at frequencies between 5 and 30 Hz. The varied environmental parameters were temperature (3 to 12°C), pressure (50 to 100 kPa) and air speed (19 to 28 ms^{-1}). The conclusions of the investigation are:

1. Melting hailstones are an important source of rain-sized drops through shedding.

2. Shed drops originate predominantly from a water accumulation zone on the surface of the hailstone and result from an instability of the water skin.

3. The observed shed drops from melting ice spheres had sizes between 0.3 and 2.0 mm, and an average volume diameter of 0.95 mm. Their spectra are basically independent of the temperature and the rotation rate, and can be parameterized using a log-normal distribution.

Shedding spectra of melting hailstones obtained in this study are similar to those obtained for the case of icing cylinders (Ref. 13), which show unimodal distributions with a mean volume diameter of about mm.

4. The Nusselt number was found to be independent of the rotation and gyration frequencies. Nu can be written in terms of Prandtl and Reynolds numbers by introducing the consolidated heat transfer factor, χ, which takes into account the effects on the heat flux due to the shape and the roughness of the hailstone, as well as any other effects such as those produced by the presence of the water skin. The values of χ obtained for rotating spherical and gyrating spheroidal hailstones while melting were 1.12 ± 0.14 and 1.41 ± 0.15, respectively.

The results obtained here can be used to more adequately model the life history of hailstones and the accompanying cold rain.

Acknowledgements: This work was sponsored by the National Science and Engineering Council of Canada. One of the authors (FGG) is indebted to Consejo Nacional de Ciencia y Tecnologia of Mexico for its financial support.

7. REFERENCES

1. List R, Joe P I, Lesins G, Kry P R, de Quervain M R, McTaggart-Cowan J D, Stagg P W, Lozowski E P, Freire E, Stewart R E, List C G, Steiner M C and Von Niederhausern J 1976, On the variation of the collection efficiencies of icing cylinders, International Cloud Physics Conference, Boulder 26-30 July 1976, 233-239.

2. Carras J N and Macklin W C 1973, The shedding of accreted water during hailstone growth, Quart J Roy Meteor Soc 99, 639-648.

3. Joe P I, List R, Kry P R, De Quervain M R, Lui P Y K, Stagg P W, McTaggart-Cowan J D, Lozowski E P, Steiner M C, Von Neiderhausern J, Stewart R E, Freire E and Lesins G 1976, Loss of accreted water from growing hailstones, International Cloud Physics Conference, Boulder 26-30 July 1976, 264-269.

4. Joe P I, List R and Lesins G 1980, Ice accretions Part II: Rain production by cloud water conversion, J Rech Atmos 14, 357-364.

5. Kry P R and List R 1974, Angular motions of freely falling spheroidal hailstone models, Phys Fluids 17, 1093-1102.

6. Beckwith W R 1960, Analysis of hailstorms in the Denver network 1949-1958, Physics of Precipitation, Geophys Monog No. 5, Amer Geophys Union, 348-353.

7. McTaggart-Cowan J D and List R 1975, Collision and breakup of water drops at terminal velocity, J Atmos Sci 32, 1401-1411.

8. List R 1963, General heat and mass exchange of spherical hailstones, J Atmos Sci 20, 189-197.

9. List R, Schuepp P H and Methot R G J 1965, Heat exchange ratios of hailstones in a model cloud and their simulation in a laboratory, J Atmos Sci 22, 710-718.

10. List R and Dussault J G 1967, Quasi steady state icing and melting conditions and heat and mass transfer of spherical and spheroidal hailstones, J Atmos Sci 24, 522-529.

11. Ranz W E and Marshall W R 1952, Evaporation from drops, Part I, Chem Eng Prog 48, 141-146.

12. Ranz W E and Marshall W R 1952, Evaporation from drops, Part II, Chem Eng Prog 48, 173-180.

13. Joe P 1982, The shedding of millimeter sized drops in simulated hail formation, Ph D Thesis, University of Toronto, 306 pp.

MELTING OF SNOWFLAKES IN THE ATMOSPHERE

Takayo Matsuo

Physical Meteorology Research Division, Meteorological Research Institute, 1-1, Nagamine, Yatabe-machi, Tukuba-gun, Ibaraki-ken, 305, Japan

ABSTRACT

The melting of snowflakes has been studied by analysis, laboratory experiment, theoretical calculation, and field observation (Refs. 1, 2, 3, 4, 5). The results indicated that the melting of snowflakes took place under the influence of air temperature, relative humidity, and precipitation intensity and that the melting brought about atmospheric cooling around a melting layer. The melting process of snowflakes is explained in terms of (1) heat transfer from the ambient air to snowflakes, (2) water vapor transfer on the snowflake surface accompanied with latent heat, and (3) melting of snowflakes related to the heat absorbed and released.

1. ANALYSIS OF SURFACE WEATHER OBSERVATION DATA

The analysis was made of the relationship between forms of precipitation and surface meteorological elements. Fig.1 shows an example of phase diagram for precipitation on the ground. A dashed line indicates a critical line for snow; precipitation is all snow below the line (solid phase). A solid curve shows a critical curve for rain; precipitation is all rain above the curve (liquid phase). Stippled area indicates the transition region from snow to rain: snow, sleet, and rain occur in the region (mixed phase). Precipitation varies depending on surface air temperature and relative humidity. Precipitation is likely to become rain with increasing air temperature and relative humidity.

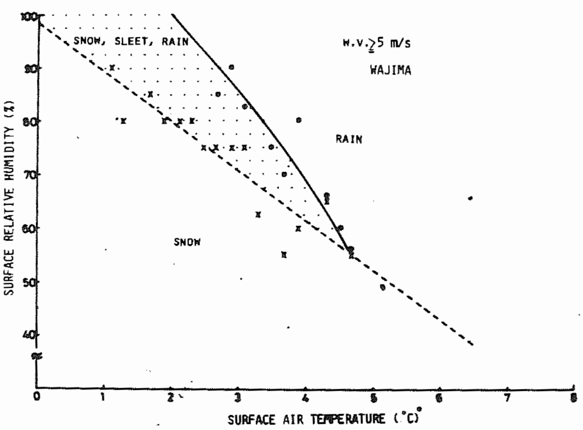

Fig.1 Phase diagram for precipitation on the ground at wind velocity above 5 m/sec at the Wajima Weather Station, Japan. The periods of analysis are the cold seasons (Jan.-Mar.) from 1973 to 1978. Symbols of crosses and open circles indicate the critical humidities for snow and rain at a temperature interval of 0.2 °C, respectively.

In the transition region sleet rather than rain took place frequently in association with high-intensity precipitation. An interpretation is that snowflakes are relatively large at that precipitation and it takes long time for them to melt completely (Ref. 1).

These results suggested that the melting of snowflakes in the atmosphere was influenced by not only air temperature but also relative humidity and precipitation intensity. Graupel is excluded in the Figure but a similar tendency is shown in Ref. 6.

2. LABORATORY EXPERIMENT OF MELTING

The melting experiment was carried out of freshly fallen snowflakes supported on a nylon net in a vertical wind tunnel at an airstream of 100 cm/sec in air velocity and of 5.5 °C in temperature. The morphological variations of snowflakes by melting were shown in a series of photographs taken every ten seconds. Fig.2 shows an example of a melting snowflake. The snowflake gradually melts to form a water drop at the end.

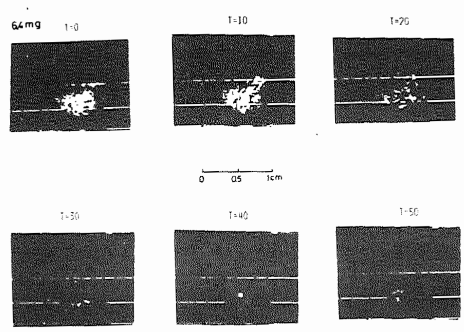

Fig.2 Photographs taken every ten seconds showing the shrinkage of a snowflake by melting. White horizontal and vertical lines are threads of a nylon net. Mass of the snowflake is indicated in the upper left-hand corner. Experimental set-up of airstream is 5.5 °C in temperature and 100 cm/sec in air velocity.

The examination revealed that the break-up of snowflake did not take place in melting and that the melt water did not accumulated on the snowflake surface but percolated into the inside. The percolation may be due to capillary action. From the above result, a micro-physical model was proposed of the snowflake in melting. Using the model, an empirical formula for the melting rate of snowflake, which is expressed as the rate of decrease in radius R by melting, was obtained to give the relation $dR/dt = -\varepsilon \tilde{a} (K\Delta T + L_v D\Delta\sigma)/L_f \rho_i R$. The coefficient ε is an adjustable parameter to bridge a gap between the experiment and theory, and evaluated as

1.75. $\tilde{a}$ is the ventilation coefficient of a sphere, K the thermal conductivity of air, L_v the latent heat of evaporation of water, D the coefficient of molecular diffusion of water vapor in air, ρ_i the density of snowflake, $\Delta\sigma$ the difference between water vapor density of airstream and equilibrium water vapor density on the snowflake surface, and ΔT the temperature difference between the snowflake and the ambient airstream.

3. SIMULATION OF MELTING OF SNOWFLAKES IN THE ATMOSPHERE

Using the formula as a basic equation, the simulation of melting of snowflakes in the atmosphere was made to estimate the effects of air temperature, relative humidity, and snowflake size and density on the process of melting. The result is illustrated in Fig.3, which shows variation in diameter of snowflakes with fall distance below 0 °C level, at a lapse rate of 6 °C/Km. Arrows indicate the fall distance for the onset of melting. Snowflakes gradually become small by sublimation of water vapor from the surface at the first stage of falling and after that they quickly shrink by melting to form raindrops at the end.

If the air below the 0 °C level is saturated, they begin to melt from just below the 0 °C level and those of ordinary size, with equivalent diameter 1-5 mm in raindrop, complete melting within several hundred meters below the 0 °C level. If the air is subsaturated, say 80 %, snowflakes do not melt as far as about 300 m distance below the 0 °C level. The distance for the onset increases with decreasing relative humidity. The distance for the completion increases with decreasing relative humidity and with increasing snowflake diameter.

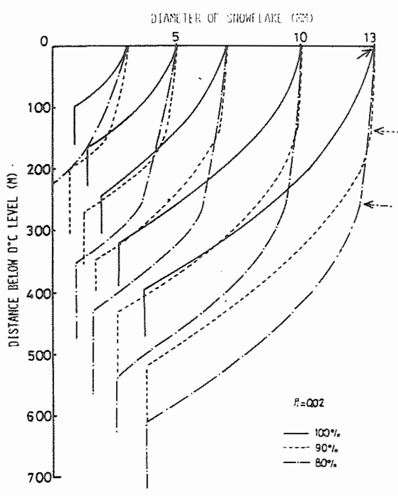

Fig.3 Variation in calculated snowflake diameter with distance below 0 °C level at given relative humidities of air. Initial density of snowflakes is 0.02 g/cm^3.

The result of calculation using various lapse rates is shown in Fig.4. The distance for the completion increases by 25-100 m per 1 °C/Km decrease in lapse rate. This exhibits the importance of air temperature on the melting.

The distance for the onset is explained in terms of wet-bulb temperature. The wet-bulb temperature decreases with decreasing relative humidity; snowflakes in the air having a wet-bulb temperature below 0 °C do not melt even if air temperature is above 0 °C. The distance for the completion is interpreted by heat transferred from the air to snowflakes, latent heat due to evaporation of water vapor from the snowflake surface, and heat capacity

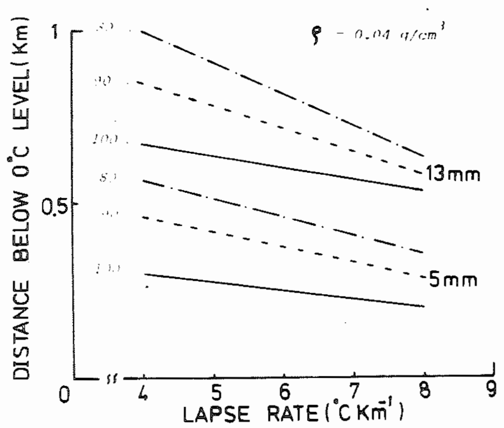

Fig.4 Calculated fall distance for the completion of melting as a function of lapse rate, at a given relative humidities of 80 %, 90 %, and 100 %. Initial snowflake diameters are 5 mm and 13 mm and the density is 0.04 g/cm^3.

of snowflakes. Snowflakes complete melting rapidly, 1) at high lapse rate, 2) at high relative humidity, and 3) with small mass.

4. FIELD OBSERVATION OF SNOW AND SLEET

The field observation was carried out of snowflake water content, fall velocity, mass, and cross-sectional area under various condition of surface air temperatures and relative humidities in January of 1978 and Feburuary of 1979 at Nagaoka City, Japan. The result showed that the fall velocity and the liquid water content of snowflakes were dependent on surface air temperature above 0 °C, relative humidity, and snowflake mass. The fall velocity increased with increasing air temperature and relative humidity. In snowfall at a high temperature above 0 °C, the fall velocity was almost constant with respect to snowlake mass or sometimes that of small mass was larger than that of large one. This finding shows a different tendency from the result mainly obtained from non-melting snowflakes so far (Refs. 7, 8). The water content increased with increasing surface air temperature and relative humidity. Percent water in snowflakes was highest at the highest air temperature of 1.8 °C during the snowfall period. Compared among the cases of the same air temperature, the percent water increased with increasing relative humidity. In the case of the same air temperature and relative humidity, it increased with decreasing mass. These observations agree with the result of simulation (Ref. 4).

5. ATMOSPHERIC COOLING BY MELTING SNOWFLAKES

Precipitations associated with a warm front of a low were observed by rawinsondes and a Doppler radar from 1981 t 1982 at the Tukuba District in Japan. The Doppler radar observation was made at the roof of the Meteorological Research Institute. The rawinsondes were released routinely at 9^h and 21^h at the yard of the Aerological Observatory 200 m north of the Doppler radar. Nine case observations of melting layers over the warm fronts were analysed using the Doppler and sonde data. Six cases displayed cooling of air around the bright band (B.B.) and three ones did not. The occurrence of cooling was related to precipitation intensity near the 0 °C level. No cooling was observed at a precipitation intensity below 0.3 mm/hr deduced from radar reflectivity, but above 0.3 mm/hr the cooling took place. The degree of cooling increased with increasing precipitation intensity. The typical feature of the atmospheric cooling by melting is shown in Fig. 5. The vertical profile of air temperature is shown by a solid line. The stippled area is bright band inferred from the rawinsonde and Doppler analysis. The shaded area, surrounded by a dashed and a solid lines, shows the cooling effect of melting snow and the temperature decrease of a few degrees takes place. A nearly isothermal layer about 800 m thick exists above and below the 0 °C level. The isothermal layer is lowered to the center of the bright band. The presence of isothermal layer above the 0 °C level suggests that some vertical mixing of air occurs through the 0 °C level.

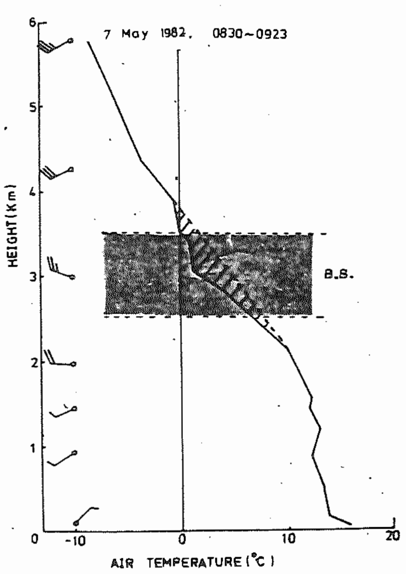

Fig.5 Sounding on 7 May 1982 on temperature-height diagram. B.B. is bright band.

6. MECHANISM OF SNOWFLAKE MELTING

It is concluded that the melting of snowflakes takes place under the control of 1) heat transferred from the ambient air to snowflakes, 2) latent heat accompanied with phase change of water vapor on the snowflake surface, and 3) heat capacity of snowflakes. The factors important in the process are air temperature, relative humidity, and snowflake size and density.

The heat transfer from the air to snowflakes causes the cooling of air.

ACKOWLEDGEMENT

The author relied heavily upon the advise and discussions of many staff members of the Meteorological Research Institute of the Japan Meteorological Agency and these contributions are gratefully ackowledged. Special recognition must be made of Dr. Y. Sasyo who provided useful comments and assistance in field observation of snow. Mr. Y. Sato provided valuable assistance with the analysis of surface weather data. Dr. J. Aoyagi, Mr. H. Sakakibara, and Mr. K. Matsumura contributed most helpfully with his analysis of Doppler Data. His appreciation is extended to Mr. J. Kubo and Dr. T. Okabayashi for their encouragements.

REFERENCES

1. Matsuo, T. , Y. Sasyo, and Y. Sato, 1981, Relationship between types of precipitation on the ground and surface meteorological elements, J. Met. Soc. Japan 59, 462-476.
2. Matsuo, T. and Y. Sasyo, 1981, Non-melting phenomena of snowflakes observed in subsaturated air below feezing level, J. Met. Soc. Japan 59, 26-32.
3. ———— and ————, 1981, Empirical formula for the melting rate of snowflakes, J. Met. Soc. Japan 59, 1-9.
4. ———— and ————, 1981, Melting of snowflakes below freezing level in the atmosphere. J. Met. Soc. Japan 59, 10-25.
5. Matsuo, T. , H. Sakakibara, J. Aoyagi, and K. Matsumura, 1983, Vertical temperature profile in precipitation associated with a warm front of a low, Proc. Autumn Meeting in 1983, Japan Met. Soc. 232 (in Japanese).
6. Matsuo, T. and Y. Sasyo, 1982, Melting of snow pellets in the atmosphere, Pap. Met. Geophys. 33, 55-64.
7. Magono, C. , 1953, On the growth of snowflake and graupel, Sci. Rep. Yokohama Nat. univ., Sec. 1 No. 2, 18-40.
8. Langleben, M. P. , 1954, The terminal velocity of snowflakes, Quart. J. R. Met. Soc. 80, 174-181.

PROPERTIES OF ICE ACCRETED IN A TWO STAGE GROWTH

Franco Prodi, Anna Franzini and G.Santachiara
Istituto FISBAT-CNR, Rep.Nubi e Precipitazioni, 40126 Bologna, Italy

1.INTRODUCTION

The laboratory investigation of accreted ice in controlled conditions remains the major way of broadening our knowledge of the phenomenon (Ref.-1), and at the same time more specific and attainable goals are assigned to it. Though the extreme difficulty of effectively simulating natural conditions in the laboratory is now clear, a number of important albeit partial results may be reached by investigating simplified or extreme situations which cannot be treated theoretically: very low density accreted ice, water shedding, and, the subject of the present paper, ice accreted in a two stage growth, mostly by the superposition of a wet or spongy growth over a previously formed porous structure.

The first experimental evidence that hailstone growth might take place in two stages has been provided by Prodi (Ref.2) from local density measurements performed by a contact microradiographic technique on slices of natural hailstones and artificially accreted cylinders.

Previous suggestions regarding the possible role of low density ice in hailstone growth (Refs.3-4) were not followed due to the paper of Browning et al, (Ref.5) predicting ice density close to 0.9 g cm^{-3} for hailstones larger than 0.5 cm. The suggestion that two-stage growth may be more frequent than previously suspected has been taken up by Pflaum (Ref.6), who has produced numerous computations of the effect of porous ice densification on the terminal velocity of a solid sphere. These computations were prompted by win- tunnel experiments on riming groupels (Ref.7).

The present investigation involves the laboratory study of ice accreted in a two stage growth and examines the possibility of using the results in the interpretation of natural hailstones features.

2.EXPERIMENTAL

The experiment has been conducted in a vertical wind tunnel alongside a cold room, with supercooled droplets impinging on a rotating cylinder, described in previous works (Refs.8 to 10) to which the reader should refer for anything here left unspecified.

The technique for local ice density measurements is the same as described in Refs 1 and 11.

Three slices of each deposit were cut by a band saw and machined plane by a microtome. The thickness of one slice was accurately calibrated and it was used for contact microradiography. The polycrystalline bulk ice grown on the plastic embryo and visible in the reflected light pictures of the cross sections as a clear inner ring of ice, served as a reference for bulk ice density on the x-ray micrographs, when the optical density of the film was converted into the density of the accreted ice. The optical densitometer has been used with a small circular beam (35 μm size) for more localized observations, and with the rectangular beam (35 X 636 μm, perpendicular to the inspected path) in order to obtain the average value on a wider strip. The second slice was photographed in reflected light and, once thinned to about 300 μm, in cross polarized light. The third was used to obtain formvar replicas following the technique described in Ref.12, and analyzed with an optical microscope, for both crystal size parameters (average grain size, mean maximum length and width) and crystal orientations.

To study the first stage of the deposit, the cylinder was taken off the inner, 6 mm diameter, plastic rod, and the three perpendicular sections of the deposit were cut out of its central region in order to perform the first series of analyses. The two remaining pieces of the deposit were rejoined by the reinsertion of the plastic rod for

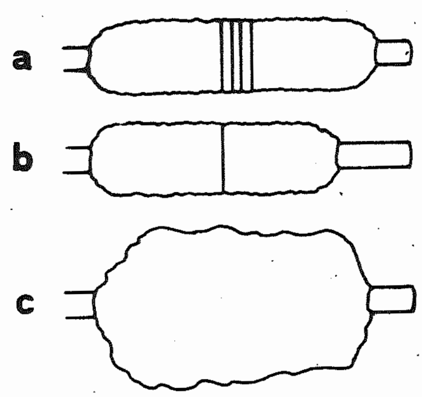

Fig.1 Scheme of operations. After growth of the first stage, three slices were cut out (a), the remaining pieces were placed on the rotating rod (b), and the second stage was grown on it (c).

the next stage of growth (Fig.1). To obtain different densities of the accreted ice the vertical velocity was made to vary from 5 to 29 m sec^{-1}, which was expected to produce,according to the Macklin's relationship (Ref.13), a wide range of ice densities.

3.RESULTS AND DISCUSSION.

The results are presented as a comparison between the findings relating to the first stage of growth and those of the same layer once the second stage has been grown over, indicating the modifications that have thereby been introduced into the first structure. Data are also added regarding the layer entirely grown during the second stage of growth, to be compared with the former results. The two growth conditions chosen for the first stage were such as to give in one case ice of rather high density (TS2, from 0.88 to 0.84 g cm^{-3}, decreasing with increasing radius) and in the other case rather low density ice (TS3, from about 0.55 to 0.38 g cm^{-3}).

3.1Growth TS2

Growth conditions	1st st.	2nd st.	Ext layer
T_a, °C	-26.7	-17.5	-17.5
T_d, °C	-15.8	0°	0
Impact vel.,$msec^{-1}$	29	29	29
Mean vol. rad., a, µm	8.5	8.5	8.5
Rot. rate, Hz,	1.75	1.75	1.75
Results			
Local density, g cm^{-3}	0.88 to0.84	0.88 to .90	
Crystall. param.:			
Av. grain size,σ mm^2	$2.1\ 10^{-3}$	$5\ 10^{-3}$	$6.4\ 10^{-2}$
Mean max.length, l,mm	0.062	0. 89	0.28
Mean max.width, w,mm	0.040	0.058	0.13

There was a slight penetration of liquid water into the previous structure, but it was limited in quantity since the ice density was quickly raised near the wet-spongy growth values. The second growth stage was very spongy and had a typical fan-like appearance (Ref.14), fronts of bubbles and well-defined wet growth lobes (Fig.2). It did not alter drastically the appearance of the first layer, exept by making the first opaque deposit more transparent. Interestingly enough the crystallographic parameters revealed an observable annealing process which might be accounted for by the minutes spent at or near 0°C during the second stage. Average crystal sizes more than doubled. Both mean maximum length and mean maximum width increased. The outer layer presents values typical of spongy growth at that temperature (Ref.15) following a thin intermediate layer of smaller size crystals. In summary, as regards this growth we may say that the main effect introduced by the second stage is in the annealing of the fist stage crystals and in a slight increase of the local density values. This is of importance in the analysis of natural hailstones, implying that it will be almost impossible to find very small crystals due, apart from any other reason, to the effect of annealing during the hailstone fall. For the same reason, during melting, the density of layers originally grown at low density will increase due to penetration of melted water.

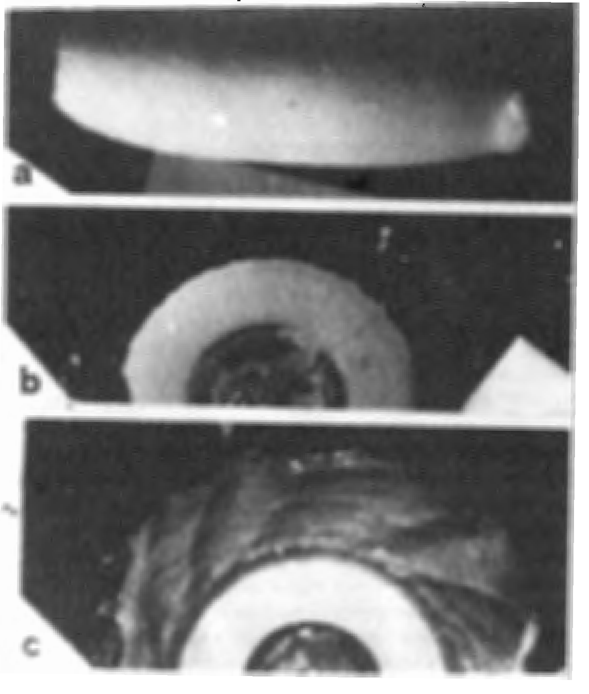

Fig.2. Growth experiment TS2. External appearance of the first stage deposit (a), part of its cross section (b), and part of the cross section of the completed deposit (c). Scale in this and in Fig.3 is given by the external 1 cm. diameter of the inner transparent bulk ice ring.

3.2 Growth TS3

	1st st.	2nd st.	Ext layer
Growth conditions: T_a	-22 to-20	-24	-24
T_d , °C	-15	0	0
Impact vel.,m sec^{-1}	5	29	29
Mean vol. rad.,a,µm	8.5	8.5	8.5
Rot.rate,Hz,	3	3	3
Results:			
Local density,g cm^{-3},	see text		
Crystall. param.:			
Av.grain size,σ,mm^2	$5.5\ 10^{-4}$	$4.6\ 10^{-2}$	$8.9\ 10^{-2}$
Mean max. length,l,mm	0.027	0.23	0.30
Mean max. width,w,mm	0.022	0.18	0.2

This growth was a case of a rather porous first stage. The low density was obtained by reducing the updraft velocity to 5 m sec^{-1}. The deposit presents a fragile feathery structure. The reflected light picture and the x-ray micrograph cross-section demonstrate the appearance of lobes and tiny channels right from the very beginning of

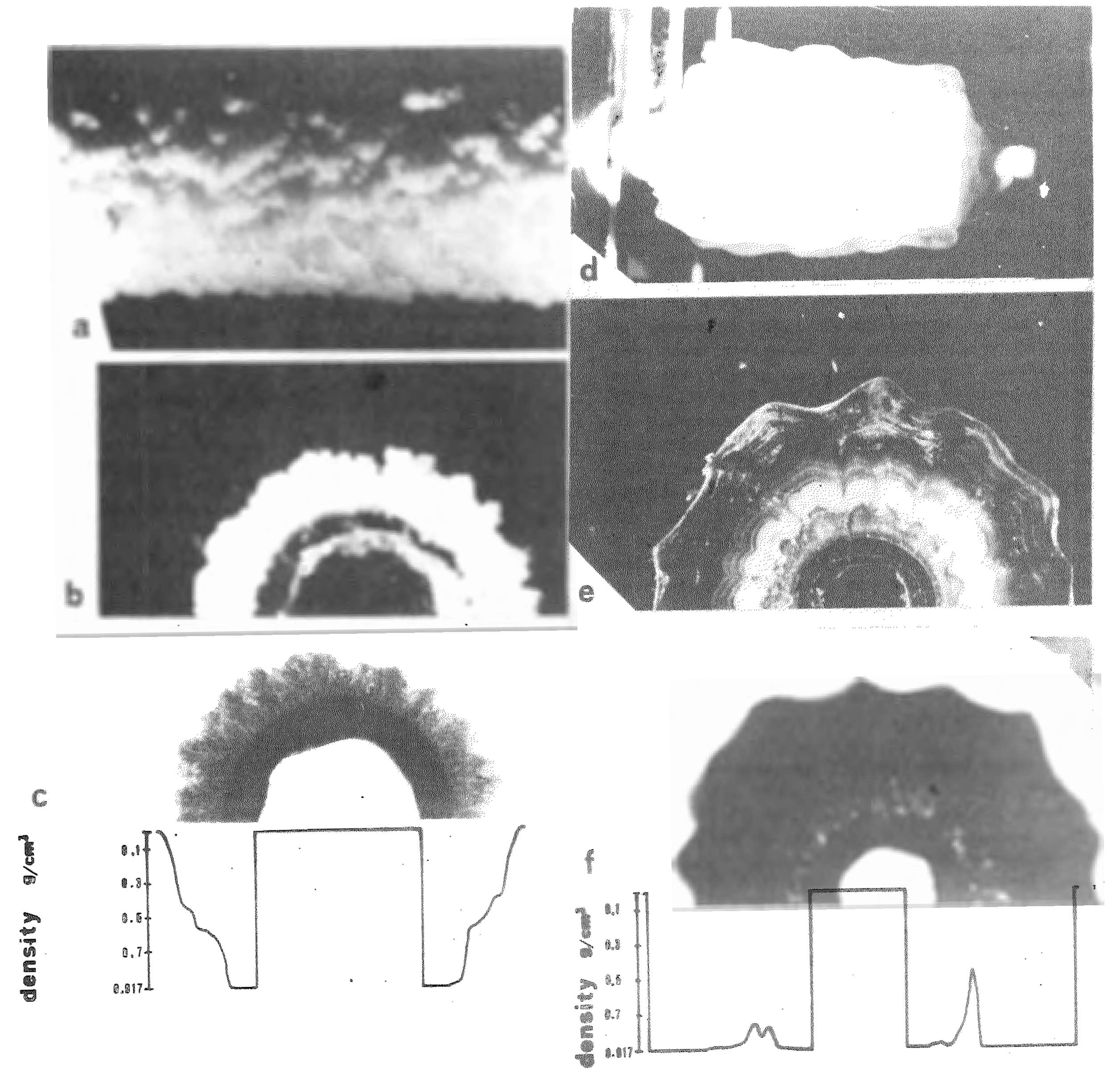

Fig. 3. Growth experiment TS3. External appearance of the full deposit of the first stage of growth (a), reflected light picture (b) and x-ray micrograph (c) of a part of a cross section of the same stage. External appearance of the full deposit after the second stage has been grown on it (d). Reflected light picture (e) and x-ray micrograph (f) of part of a cross section of the two stage deposit. In (g) a magnified detail of (e) is shown indicating the morphological changes of the first deposit due to the superposition of the second stage; note the resemblance to feature frequently observed in natural hailstones. In (c) and (f) the graph of the local density of ice derived by the optical density of the x-ray film along a diameter of the slice is shown. As in Fig.2 scale is given by the external 1 cm. diameter of the inner transparent bulk ice ring.

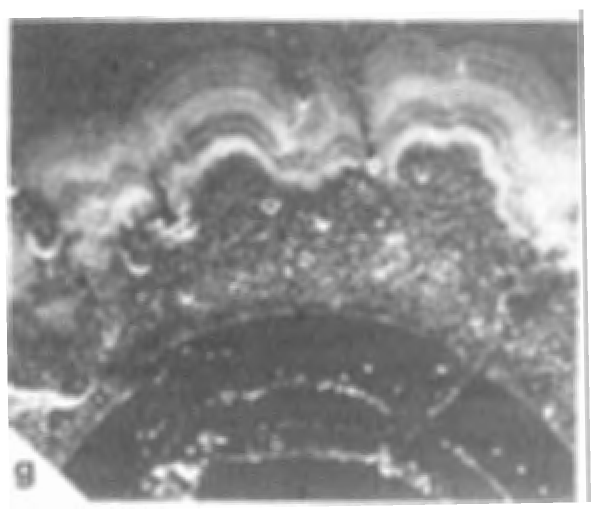

the accretion. In the case of this growth the change in cross-section morphology due to the superposition of the second stage of growth is striking and is demonstrated by all the analyses. The reflected light picture reveals that the first three millimeters of accreted deposit are transformed from entirely milky to quasi-transparent with a lot of medium size air bubbles. Continuing outwards there is a layer of curved opaque lobes which at least in the inner part still correspond to the area occupied by previous first stage growth. Over this there is a dry layer with clearly defined bubble rings formed by the new growth stage before the wet growth takes over, and finally there is wet-spongy growth. The local density path is combined in the Figs 3c and 3f. Fig.3c clearly indicates that the density of the ice fabric decreases with increasing raddius as the feathery-channel structure develops, from a value of 0.5 g cm^{-3} near the embryo to 0.4-0.38 g cm^{-3} at the branches; here one has to take into account the possible effect on the measurements of the rupture of the branch tips and the resulting reduction in the thickness of the slice. However, these local density values rise drastically due to the second stage of growth, approaching wet growth values, except at the large radial bubbles which provide the main record of the previous porous structure. In the large bubble layer an average density (0.75 g cm^{-3}) far greater than the original first stage density is obtained, and values in areas near the large bubbles are 0.86 g cm^{-3}, -much closer to the wet growth values. Remarkably enough, the morphology of the full deposit resembles that of a typical natural hailstone, with the irregular array of lobes and the radial lines of elongated air bubbles between the lobes. The crystallographic parameters reflect the dramatic change equally well. The crystal size is increased by approximately two orders of magnitude, much more than would be expected by a simple annealing effect during the few minutes at 0°C.

4.CONCLUDING REMARKS

The main result of the experiment consists in showing the evolution of morphological features, local density and crystallographic parameters in the two-stage growth of accreted ice deposits. It has been shown that especially when the first stage is of low density, the change in all parameters is striking, and more important features typical of natural hailstones are easily reproduced. The two stage growth seems to leave typical and unequivocal marks which more than in the case of single stage growth, can greatly help in the interpretation of natural hailstone features. In particular, large radially elongated air bubbles are the clear indication of such a process. The x-ray micrography technique is a useful tool in resolving variations of accreted ice local density variations. Further combinations of experimental conditions are under investigation, among which the melting of a porous structure.

5. REFERENCES

1. List R. 1977.Response to "The characteristics of natural hailstones and their interpretation": Laboratory hail research - A critical assessment. Met. Monographs, Vol.16, N.38, Am.Met.Soc. Publ., 89-91.
2. Prodi F., 1970. Measurements of local density in artificial and natural hailstones. J.Appl.Met. 9, 903-910.
3. List R. 1958. Kennzeichen atmosphärischer Eispartikeln. 2.Teil: Hagelkörner. Z.Angev.-Math. Phys.,9A, 217-234
4. Kidder R.E. and A.E.Carte 1964. Structures of artificial hailstones.J.Rech.Atmos.,1, 169-181.
5. Browning K.A., Ludlam F.H. and Macklin W.C. 1963 The density and structure of hailstones.-Quart.J.Roy.Met. Soc.,89, 75-84.
6. Pflaum J.C. Hail formation via Microphysical Recycling.J.Atmos.Sc.37, 160-173.
7. PflaumJ.C. and Pruppacher H.R. 1978. A wind tunnel study of the growth of groupels initiated from frozen drops. J.Atmos.Sc.36, 680-689.
8. Prodi F. 1975 Chlorides in natural and artificial hailstones.J.Appl.Met. 14,120-124.
9. Levi L. and Prodi F. 1978. Crystal size in ice grown by droplet accretion. J.Atmos.Sc.35, 2181-2189.
10. Levi L. and Prodi F., 1983. Effects of growth temperatures and surface roughnesson crystal orientation of ice accreted in a dry regime.-J.Atmos.Sc.40, 1281-1299.
11. Prodi F. and Wirth E., 1973 Mesoscale and microphysical investigation of an isolated hailstorm. Riv.It.Geofisica,XXII,n.3/4, 165-185
12. Aufdermaur A.N., List R. and De Quervain M.R. 1963. Kristallachsenlagen in Hagelkörnern. Z.Angev.Math.Phys.,14, 574-589.
13. Macklin W.C. 1962. The density and structure of ice formed by accretion. Quart.J.Roy.Met.-Soc.88, 30-50.
14. Prodi F. and Levi L. 1980. Hyperfine bubble structures in ice grown by droplet accretion. J.Rech.Atmos., 14, 373-384.
15. Prodi F., Levi L. Franzini A. and Scarani C. 1982. Crystal size and orientation in ice grown by droplet accretion in wet and spongy regimes. J.Atmos.Sc. 39, 2301-2312.
16. McCappin C.J. and Macklin W.C. 1984 The crystalline structure of ice formed by droplet accretion: I Fresh sasmples. J.Atmos. Sc.,forthcoming.
17. Ashworth E, Ashworth T. and Knight C.A. 1980. Cylindrical ice accretions as simulations of hail growth: III Analysis techniques and application to trajectory determination. J.-Atmos.Sc. 37,846-854 .

MICROPHYSICAL CONDITIONS OF HAIL FORMATION IN CLOUDS

M.I. Tlisov and V.G. Khorguani

High Mountain Geophysical Institute, Naltchik, 360030, USSR

1. HAILSTONE EMBRYO TYPES

Study of the physical nature and conditions for hailstone embryo formation is of great importance for understanding hail formation processes and hail modification. There are two major concepts of the hail embryo origin. According to the first one, hail grows from graupel which forms on ice crystals of various shapes and dimensions. A primary crystal might be formed due to the crystallization of a droplet several microns in diameter. According to the second concept hail embryos are large frozen drops several millimeters in diameter. In other words the aim is to determine which of the known mechanisms of precipitation formation is responsible for embryo formation (through the ice phase or coalescence of cloud droplets).

Rather extensive, but not always representative and contradictory data on the investigation of hail embryo nature are available at present in literature. A simultaneous attempt was made to arrange these data into a system (Refs. 1, 2), but it would be reasonable to come back to this subject once again. Table 1 gives a summary of total percentage of hail embryo types obtained by various researchers in various regions of the globe. Statistical representativeness of the given data is unequal. However, in qualitative terms Table 1 shows a common regularity, i.e. hail embryos may be graupel particles as well as frozen drops. Unfortunately, there is no information about the number of studied hailstones and hailstorms in works (Refs. 4, 8), which makes the interpretation difficult. Analysis (Ref. 10) of $1.2 \cdot 10^3$ hailstones from five hailfalls showed that in four of them embryos were mostly graupel particles. However, the total statistical sample shows the predominance of droplet embryos. Statistical weight of samples is not equivalent and that makes the obtained conclusions doubtful. Data from other authors show the predominance of graupel embryos.

In order to get a regional and seasonal trend of the embryo type ratio one should have representative samples of individual hailfalls. The average statistical sample should have maximum conformity with the general one. Relying on our experiments we found (Ref. 12) that the shape of the curve of the hailstone size spectrum for an individual hailfall becomes stable when the total number of particles amounts to 2×10^3. This value has been chosen as a criterion of statistical confidence of our studies. As seen from the Table, the study of 28 hailstorms in 1972-76 in the North Caucasus (Ref. 11) shows that hail forms mostly on graupel embryos.

General ratio of embryo types - "graupel/frozen drop" (68:32) - remained practically unchanged after the following study of another 8 hailstorms. At the same time, predominance of droplet embryos was observed in 9 individual hailstorms out of 36. Embryo type ratio within the ranges of the hailstone size spectrum for individual hailstorms seems to be of greater importance, as compared to the embryo size, the boundary of which is difficult to establish.

Table 1
Type ratio for hail embryos from the data by different authors

Ref.	Embryo ratio Type % Frozen drop	Graupel	Total No. of hailstones	Total No. of hailstorms
/3/	20	80	$6,7 \times 10^3$	3
/4/	90	10	-	2
/5/	25	75	$6,4 \times 10^2$	-
/6/	25	65	4×10^2	40
/2/	9	87	$3,6 \times 10^3$	58
/2/	62	17	$1,1 \times 10^3$	27
/7/	32	68	2×10^4	10
/8/	99	1	-	-
/9/	35	65	$2,9 \times 10^4$	15
/10/	63	37	$1,2 \times 10^3$	5
/11/	32	68	$6,1 \times 10^4$	28

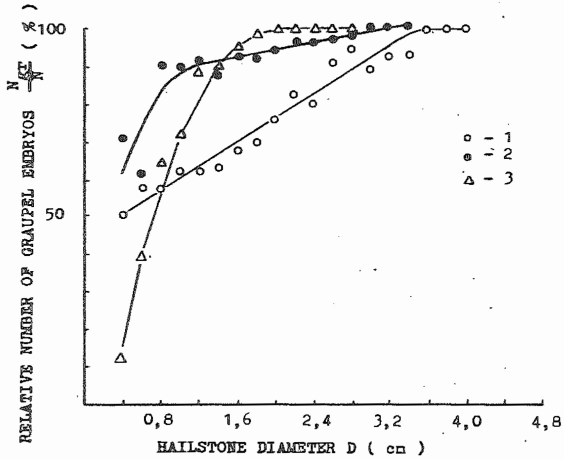

Fig. 1. Relative number of graupel embryos as a function of hail size. 1 - averaged curve for samples of 15 hailfalls; 2 - June 29, 1972; 3 - June 9, 1976.

Fig. 1 shows that the fraction of graupel embryos increases with D, both in samples averaged over 15 hailstorms (curve 1) and in samples corresponding to individual hailfalls (curves 2-3). Such ratio of embryo types within different size ranges was determined for 15 hailstorms classified as multicells. Graupel embryos dominated in all samples. Assuming that the size of hailstones is determined by their residence time within the cloud, with other parameters being equal, it appears that graupel embryos form earlier than large drop embryos. Drop embryos seem to form later during the transition of cloud cells into the hail stage.

No definite regularity in the change of the embryo type ratio within hailstone size spectra for other single cells, supercells, multicells and unclassified storms was observed. In a single cell of June 19, 1974, total embryo ratio - "drop/graupel" (67:33) - remained constant for all ranges of size spectrum with maximum hailstone diameter D_{max} = 2.1 cm. It is interesting to note, that all embryonic graupels were conical in shape. In five single cell storms (Ref. 11) hail entirely formed on graupel particles and reached 1.5 - 1.8 cm in diameter. Height on the warm part of the clouds in these cells was insignificant ($\Delta H \sim$ 1.5 km). With the exception of the above five cells hail always used to form on embryos of both types. Hailstone samples from supercells are characterized by close percentage of drop and graupel embryos. Based on the calculation of informativeness of aerosynoptical and radar parameters of hailclouds (Ref. 11), probability of hail formation on large frozen drops is shown to increase with the decrease of temperature at the maximum velocity level.

2. BUBBLE STRUCTURE OF HAILSTONE EMBRYOS

Laboratory experiments on water drop crystallization (D = 0.1 - 0.6 cm) in a vertical wind tunnel (Ref. 13) showed that the relation between the environmental temperature T_{∞} (°C) and mean arithmetic diameter of the bubbles d_a might be expressed empirically: $d_a = -493/\ (T_{\infty}\ -2)$. Instrumental errors in estimates of T do not exceed ±2 °C and d_a ±10 %. Size distribution of air bubbles in frozen drops is fairly well approximated by the lognormal law with the dispersion of the logarithm of the bubble diameter σ_ℓ = 0.92 ÷ 0.63. Results of the laboratory investigations were used to study the structure of the drop embryos. Theoretical estimation (Ref. 14) shows that the freezing temperature of the drop (D = = 0.2 cm) growing inside the cloud environment with water content 4 $g \cdot m^{-3}$, is approximately 1-2 °C higher as compared to the conditions of isolated crystallization. Based on these considerations, hailstones were analyzed only when the large embryonic drop was clearly seen and the following layer was distinctly "dry" in its crystal structure. Each sample from 7 analyzed hailfalls included on the average 50 hailstones and practically the whole size spectrum for each hailfall was covered. Fig. 2 (curves 1-3) shows integral curves of the number of embryonic drops in natural hailstones, calculated by the bubble structure, as a function of their freezing temperature. Embryonic drops in these three hailfalls froze in the temperature range from -2 to -16 °C, with 90 % of embryos nucleated at temperatures higher than -10 °C. Most probable temperature range (about 75 %) was -6 ÷ -10 °C. Data on the embryo bubble structure can be qualitatively compared to the results of the experimental study of crystallization for large drops obtained from melted central regions of hailstones (Ref. 15). Opposite to raindrops the above drops underwent complete crystallization at relatively high temperatures -17 °C, and about 40 % - at temperatures -7 ÷ -8 °C.

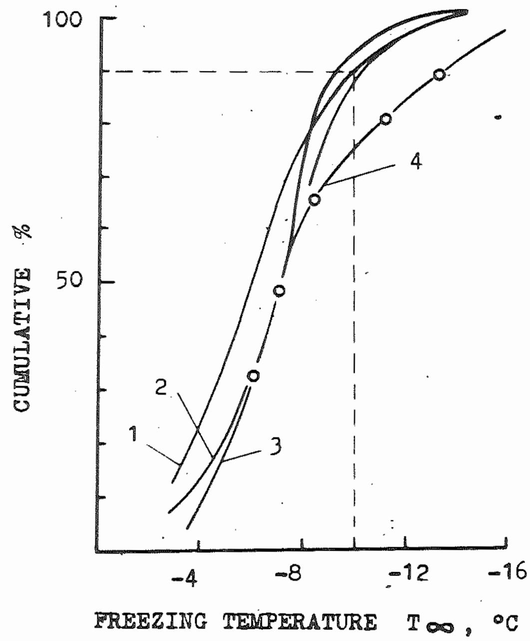

Fig. 2. Integral curves of the number of embryonic drops as a function of their freezing temperatures reproduced by the bubble structure. 1 - June 23, 1974; 2 - May 19, 1975; 3 - May 15, 1975; 4 - direct crystallization of drops from data (Ref. 15).

Thus the above results suggest that formation of hail embryos from large drops mostly takes place at temperatures above -10 °C as a result of heterogeneous ice nucleation. It should be noted that preliminary results of hail embryo analyses for deuterium are also in agreement with the above conclusion.

3. AEROSOL STRUCTURE OF HAILSTONES

Air bubble structure of graupel embryos is extremely complex and difficult both for reproduction under laboratory conditions and for analysis. Therefore it is assumed that rather useful information may be obtained from estimating the temperature of primary crystal initiation on aerosol particles contained in hail embryos. All the more, microstructural characteristics and ice-forming properties of aerosol particles contained in hail and other kinds of atmospheric precipitation differ essentially (Ref. 16). The investigation procedure for sampled hailstones (Table 2) was the following. The embryo was cut out of the hailstone and placed on a special substrate. The sample was then inserted into a thermal diffusion chamber and evaporated avoiding liquid phase. The aerosol deposit was then activated at water saturation, and ice-forming properties of aerosol particles were studied. Initiation of crystals was observed through a long-focus-length microscope. More complete description of the investigation procedure and equipment is available (Refs.17, 18).

Table 2 shows that primary crystals formed on aerosol particles within hail embryos at temperatures -6 °C ÷ -13 °C and more often large nuclei with diameters over 10 μm were centres of ice formation.

Table 2
Primary crystal initiation temperature

No.	Date of hailfall	No. of hailstones	Temperature range for crystal initiation
1.	13.06.73.	6	-13 ÷ -17
2.	19.06.74.	12	-13 ÷ -17
3.	15.06.74.	12	-8 ÷ -13
4.	21.05.75.	14	-8 ÷ -13
5.	31.07.75.	15	-8 ÷ -13
6.	14.04.76.	7	-8 ÷ -17
7.	17.07.78.	36	-6 ÷ -14
8.	Storm rain	10	-17 ÷ -20

In other words, giant and supergiant particles are, as a rule, high temperature iceforming nuclei. Nuclei concentration in the drop embryos is usually several times higher than in the graupel embryos (Ref. 17). In the storm rain samples first crystals developed at lower temperatures and nuclei concentration was one order of magnitude less. Comparison of Table 2 and Fig. 2 shows, that the range of temperatures for the initiation of first crystals on aerosol particles within hail embryos and freezing temperatures of embryonic drops practically coincide, but for more accurate comparison the knowledge of the nucleation mechanism is needed.

Table 3
Relation of ice-forming nuclei concentration N_{IN} to total concentration of aerosol particles (N_T) from hail embryos of two hailfalls 1 - July 17, 1978; 2 - July 22, 1978, and the atmospheric surface layer (N_{IN}/N_T x 106).

Type of aerosol sample	-6 °C	-10 °C	-14 °C	-18 °C
Drop embryo 1	6	51	186	349
Graupel embryo 1	5	16	32	55
Drop embryo 2	90	245	469	735
Graupel embryo 2	18	50	69	104
Atmospheric aerosol	0,03	0,14	0,8	4,5

Table 3 shows that fraction of ice-forming nuclei in aerosol deposits of hail embryos is 1-3 orders higher than that of ice-forming nuclei in atmospheric aerosols. It should be noted that the difference between ice crystal concentration inside the cloud and ice-forming nuclei concentration in the vicinity of the cloud may depend not only on ice multiplication processes but on the growth activity after their transition through the cloud. Estimation indicates (Ref. 16) that hailstone concentration in the cloud is comparable to ice-forming nuclei concentration only at temperatures above -10 °C - -12 °C and to the concentration of giant aerosol particles, if their diameter is above 60-70 μm. Concentration of ice-forming nuclei and giant aerosol particles in the atmosphere is on the whole 2-3 orders higher than the hailstone concentration within clouds. Thus there is a surplus of ice-forming nuclei in the atmosphere, which are potential hail embryos and formation of hail on them is apparently of a selective nature. A number of studies were dedicated to the investigation of the microstructural characteristics of aerosol deposits from hailstones, aimed at reproducing hailstone history of origin and growth (Refs 1, 16, 19-20 etc.). Analysis (Ref. 19) of hailstones from two hailfalls of different intensity (July 17, 22, 1978, D_{max} = 2 cm and 3, 4 cm respectively) showed conformity of embryo crystal structure and hailstone layers with aerosol particle dispersion. The average statistical curves of size distribution of embryo aerosol particles and hailstone layers are shown in Fig. 3 in coordinates of the inverse-power distribution.

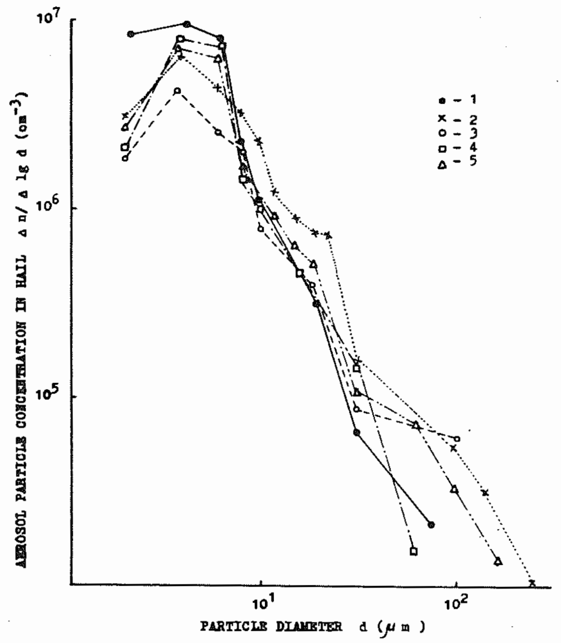

Fig. 3. Size distribution of aerosol particles contained in hailstones. 1 - dry growth layers; 2 - wet growth layers; 3 - mixed growth layers; 4 - graupel embryos; 5 - frozen drop embryos.

The largest root-mean-square diameter of particles $\bar{d}_2 \approx$ 11 μm corresponds to those hailstone layers, which formed in wet growth and the smallest $d_2 \approx$ 5 μm - to the dry growth layers and graupel embryos. The presence of supergiant aerosol particles (d > 30 μm) in aerosol deposits is of special interest, since they can function as active centers of coagulation in the cloud and possess high ice-forming and condensation characteristics (Refs. 1, 16, 17). These particles are found in hailstones in relatively small numbers. Particles exceeding 60 μm in diameter are practically not present in graupel and layers of dry growth, while their size reaches 250 μm in drop embryos and layers of wet growth. Fig. 3 gives a satisfactory approximation of curves by the inverse-power distribution $\Delta N/ \Delta \lg d = a\, d^{-\alpha}$ in the size range

$4 < d < 30\,\mu m$, α takes values from 2.2 to 3.7 which in fact agrees with the values of Young and others for aerosols in free atmosphere (Ref. 22). Different aerosol structure of drop and graupel embryos probably indicates different aerosol medium in which they form. Thus graupel embryos may form in a small drop medium in relatively weak updrafts which might occur in a new developing cell (multicell process) or at the edge of a major updraft (supercell process). It is assumed (Refs. 20, 21) that air is entrained into the flows, where graupel particles form, from higher by-cloud levels containing high-dispersion aerosols. This is confirmed by a shorter size spectrum of particles from the dry growth layers and graupel embryos, and by their relatively low ice-forming efficiency. The assumption that graupel formation is related to the initial stage of multicell processes and that graupel embryos are "older" than drop embryos (see Section 1) also agrees with the above said. One can assume that at later stages of hailstorm evolution with the development of strong updrafts, entrainment levels descend to the ground surface and supergiant aerosol particles are lifted from the surface layer and form large hailstone drop embryos. Results obtained in this study suggest that only negligible fraction of embryos grow into hail. These embryos form at relatively high cloud temperatures, mainly above -10 °C. Study of the hail embryo nature indicates a dominating role of the ice phase and the absence of a single mechanism in hail embryo formation. Hail embryos of different types apparently form at different development stages or in different parts of a hail cloud. With few exceptions both known mechanisms of precipitation formation succeed in operation in one and the same hailstorm.

REFERENCES

1. Tlisov, M.I., Khorguani, V.G., 1982. On conditions of hail embryo development in clouds (in Russian). Izv. Acad. Sci. USSR, Atmospheric and Oceanic Physics. 18, No. 3, 251-255.
2. Knight, C.A. and Squires, P., 1982. The national hail research experiment. Boulder, Colorado, 282 pp.
3. List, R., 1958. Kennzeichen atmosphärischer Eispartikeln, I Teil. Graupeln als Wachstumzentren von Hagelkorne. Angew. Math. Phys., 9a, No. 3, 180-182.
4. Macklin, W.C., Strauch, E., Ludlam, F.H., 1960. The density of hailstones collected from a summer storm. Nubila, 3, 12-17.
5. Carte, A.E., Kidder, R.E., 1966. Transvaal hailstones. Quart. J. Roy. Met. Soc., 92, No. 93, 382-391.
6. Knight, C.A., Knight, N.C., 1970. Hailstone embryos. J. At. Sci., 27, No. 3, 659-666.
7. Tlisov, M.I., 1974. Study of natural hailstone embryos (in Russian). Express Information, 6 (27), 10-12.
8. Bartishvili, G.S., 1975. Hail embryos and hail nuclei (in Russian). Trudy VGI, 32, 3-15.
9. Khorguani, V.G., Tlisov, M.I., 1976. On embryo nature and hailstone concentration in clouds (in Russian). Rept. Acad. Sci. USSR, 227, No. 5, 1108-1111.
10. Federer, B., Waldvogel, A., 1978. Time-resolved hailstone analysis and radar structure of Swiss storm. Quart. J. Roy. Met. Soc., 104, No. 439, 69-90.
11. Tlisov, M.I., 1979. Some aspects of hail embryo formation (in Russian). Trudy VGI, 44, 100-107.
12. Khorguani, V.G., Tlisov, M.I., 1974. On function of size distribution of hailstones (in Russian). Izv. Acad. Sci. USSR, Atmospheric and Oceanic Physics, 10, No. 4.
13. Tlisov, M.I., 1977. Results of studies of air bubbles in hail embryos (in Russian). Col. papers II All-Union Conf. Young Scientists, Hydrometservice USSR, M. Gidrometeoizdat, 194-200.
14. Zhekamukhov, M.K., 1979. On the influence of coagulative growth upon the process of supercooled drop freezing (in Russian). Trudy VGI, 44, 14-22.
15. Kazankova, Z.P., Medaliev, Kh.Kh., 1972. Some features of raindrop crystallization (in Russian). Trudy VGI, 21, 70-76.
16. Khorguani, V.G., 1979. On the role of giant aerosol particles and ice-forming nuclei in hail embryo formation (in Russian). Izv. Acad. Sci. USSR, Atmospheric and Oceanic Physics, 15, No. 9, 920-927.
17. Tlisov, M.I., Berezinski, N.A., 1983. Ice-forming properties of aerosol particles contained in hailstones (in Russian). Trudy VGI, 48, 65-73.
18. Berezinski, N.A. et. al., 1980. Equipment procedure and results of studies of atmospheric ice-forming nuclei (in Russian). Meteorologia i gidrologia, No. 8, 106-110.
19. Berezinski, N.A., Tlisov, M.I., 1982. Size distribution and ice-forming properties of aerosol particles contained in hailstones (in Russian). Prepr. IV All-Union Conf. Aerosols, Erevan, USSR, 81-82.
20. Rosinski, J., Browning, K.A., Langer, C., Nagamoto C.T., 1976. On the distribution of water insoluble particles in hailstones and its possible value as an indication of the hail growth history. J. Atm. Sci., 33, No. 3, 530-536.
21. Rosinski, J., Knight, Ch.A., Nagamoto, C.T., Morgan, G.M., Knight, N.C., Prodi, F. Further studies of large water-insoluble particles within hailstones. J. Atm. Sci., 36, No. 5, 862-867.
22. Rassul, S.M., 1976. Chemistry of low atmosphere (in Russian), Izd. "Mir", 406 pp.

AUTHOR INDEX
of Volume I

Академия наук Эстонской ССР
Институт астрофизики и физики атмосферы

Труды 9-й международной конференции по физике облаков. Таллин, СССР, 21-28 августа, 1984. Том 1.

На английском языке. Художник-оформитель Р. Мягар. Таллин, "Валгус".
Toimetajad V. Russak ja H. Heinoja.

ИБ № 4835.

Trükkida antud 04.06.84. MB-08004. Formaat 60x84/8. Trükipaber nr. 1. Masinakiri. Ofsettrükk. Tingtrükipoognaid 33,95. Tingvärvitõmmiseid 34,64. Arvestuspoognaid 32,74. Tellimise nr.933-1172. Trükiarv 600. Hind rbl. 5.-. Tellitud. Kirjastus "Valgus", 200 090 Tallinn, Pärnu mnt. 10. Eksperimentaalkombinaadi "Bit" rotaprint, 200 001 Tallinn, Pikk t. 68.

Cover:

The example of radar reflectivity pattern and vertical air velocity in Cb. These data were obtained by means of airborne doppler radar for vertical sounding, installed on board the IL-18 instrumented aircraft. Measurements were performed in the area of Alma-Ata (Kazakhstan), 30 September 1981, when flying above the top of Cb. The special processing methods permitted to eliminate errors in air velocity measurements caused by aircraft linear and angular movements. The technique and device were developed in the Central Aerological Observatory (for further explanation see: Vostrenkov, V.M. and Melnichuk, Yu. V. Measurements of vertical air velocities in clouds and precipitation by means of airborne doppler radar for vertical sounding. Preprints of the 6th All-Union Meeting on Radar Meteorology, Tallinn, 1982).

На обложке:

Пример распределения радиолокационной отражаемости и вертикальных воздушных скоростей в Св. Данные получены с помощью бортового допплеровского радиолокатора вертикального зондирования, установленного на самолете-метеолаборатории ИЛ-18. Измерения выполнены в районе г. Алма-Ата (Казахстан) 30 сентября 1981 г. при полете самолета над верхней границей Св. Использована специально разработанная методика исключения ошибок измерений скоростей воздушных потоков, обусловленных собственными линейными и угловыми перемещениями самолета. Методика и аппаратура разработаны в Центральной аэрологической обсерватории (подробнее см.: Vostrenkov, V.M. and Melnichuk, Yu. V. Measurements of vertical air velocities in clouds and precipitation by means of airborne doppler radar for vertical sounding. Preprints of the 6th All-Union Meeting on Radar Meteorology, Tallinn, 1982).

5.-.

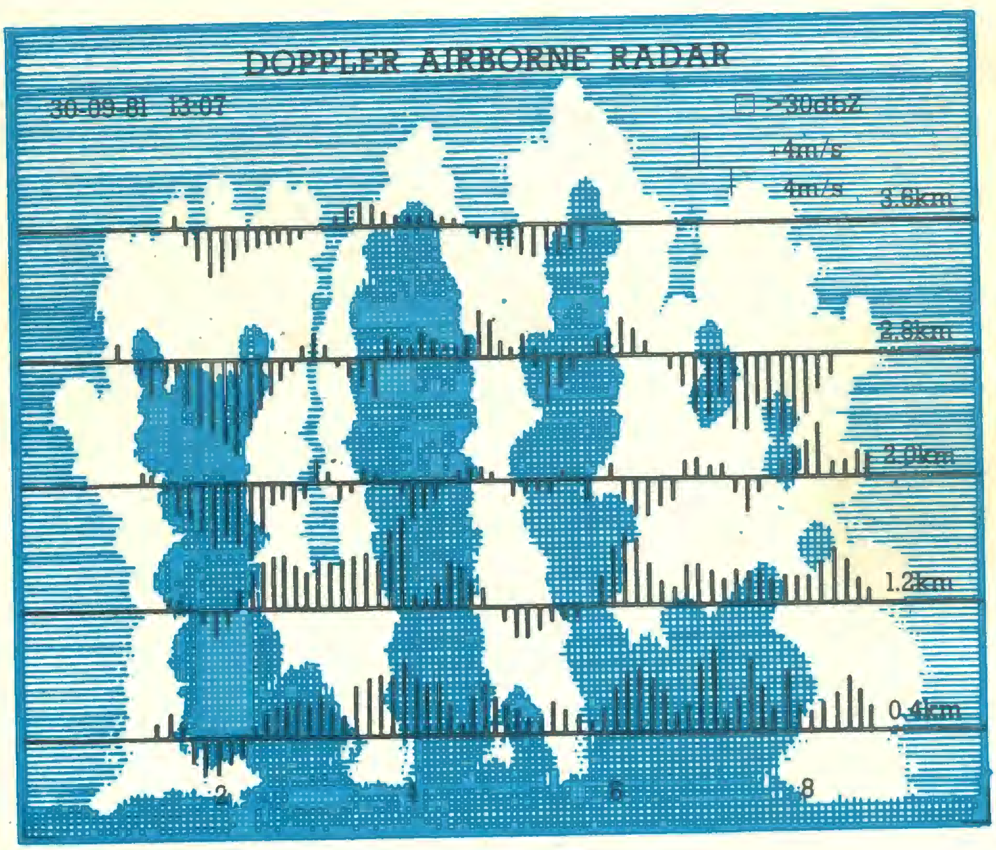
DOPPLER AIRBORNE RADAR
30-09-81 13:07
>30dbZ
+4m/s
4m/s
3.6km
2.8km
2.0km
1.2km
0.4km
2
4
6
8